PHYSIK-DEPARTMENT

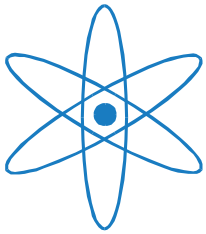

From few- to many-body physics with ultracold atoms

Dissertation

von

Richard Schmidt

TECHNISCHE UNIVERSITÄT
MÜNCHEN

TECHNISCHE UNIVERSITÄT MÜNCHEN

Physik Department

Lehrstuhl T34, Univ.-Prof. Dr. Wilhelm Zwerger

From few- to many-body physics with ultracold atoms

Richard Schmidt

Vollständiger Abdruck der von der Fakultät für Physik
der Technische Universität München zur Erlangung des akademischen Grades eines

Doktors der Naturwissenschaften (Dr. rer. nat.)

genehmigten Dissertation.

Vorsitzender:		Univ.-Prof. Christian Pfleiderer, Ph.D.
Prüfer der Dissertation:	1.	Univ.-Prof. Dr. Wilhelm Zwerger
	2.	Univ.-Prof. Dr. Walter Metzner Universität Stuttgart

Die Dissertation wurde am 21.05.2013 bei der Technische Universität München eingereicht und durch die Fakulät für Physik am 14.06.2013 angenommen.

Abstract

In this thesis field theoretical methods are applied to few- and many-body systems of strongly interacting ultracold quantum gases, mainly using the functional renormalization group (fRG). First, the quantum mechanical three-body problem of resonantly interacting bosons is solved exactly within a two-channel model. It is shown how the recently observed universality of the three-body parameter in Efimov physics can be explained from two-body physics only. In a derivative expansion the four-body problem is analyzed. The four-body sector is governed by a limit cycle flow and one finds that no additional four-body parameter is introduced in the renormalization procedure. The second part of this thesis studies a single impurity immersed in a majority Fermi sea. The impurity undergoes a transition from a polaron state to a molecule for increasing attraction. In this context we develop a new, numerical fRG technique which allows the computation of Green's functions with full frequency and momentum dependence including full self-energy feedback. We compute the decay rates of excited states, predict the existence of a highly excited repulsive polaron state and propose a radio-frequency experiment to measure the impurity spectral function. Using a non-self-consistent T-matrix approximation the impurity problem in two spatial dimensions as well as for mass imbalance is studied. Our results are in excellent agreement with recent experiments and exemplify the intricate interplay between few- and many-body physics in ultracold atomic systems.

Kurzfassung

In dieser Dissertation werden feldtheoretische Methoden auf Wenig- und Vielteilchenssysteme stark wechselwirkender, ultrakalter Quantengase angewandt, hauptsächlichlich unter Verwendung der funktionalen Renormierungsgruppe (fRG). Zuerst leiten wir die exakte Lösung des Dreikörperproblems resonant wechselwirkender Bosonen in einem Zwei-Kanal-Model her. Es wird gezeigt, wie die kürzlich beobachtete Universalität des Dreikörperparameters allein auf Basis von Zweiteilchen-Physik erklärt werden kann. In einer Ableitungsentwicklung wird das Vierteilchen-Problem analysiert. Der Vierteilchensektor wird bestimmt durch einen Limit-Cycle-Fluss und man findet, dass kein weiterer Vierkörperparameter in der Renormierungsprozedur eingeführt wird. Der zweite Teil dieser Dissertation betrachtet ein Fremdatom im Fermisee einer Majoritätsspezies. Für wachsende Attraktion vollzieht das Fremdatom einen Übergang von einem polaronischen Zustand zu einem Molekül. In diesem Zusammenhang entwickeln wir eine neue, numerische fRG Methode, welche, unter Einbindung der vollen Selbstenergie-Rückwirkung, die Berechnung von Greensfunktionen mit voller Impuls- und Frequenzabhängigkeit erlaubt. Wir berechnen die Zerfallsraten der angeregten Zustände, sagen die Existenz eines hoch angeregten, repulsiven Polaronzustandes voraus, und schlagen ein Radiofrequenz-Experiment vor um die Spektralfunktion des Fremdatoms zu messen. Anhand einer nicht-selbstkonsistenten T-Matrixnäherung analysieren wir das Fremdatom-Problem in zwei räumlichen Dimensionen. Unsere Ergebnisse sind in exzellenter Übereinstimmung mit Experimenten und veranschaulichen das komplizierte Zusammenspiel von Wenig- und Vielteilchenphysik in ultrakalten, atomaren Systemen.

Contents

Chapter One

Introduction

In a system of many particles without any interactions, the single particle is ignorant of the others and some might regard the systems as rather simple and uninteresting. As soon as interactions are switched on the situation becomes, however, much more complex and intriguing. The particles start to influence each other and instead of non-interacting 'bare' particles one deals with 'dressed' quasiparticles – effective degrees of freedom – whose properties, such as their dispersion relation or their mutual interactions differ from the non-interacting case.

Due to instabilities in the effective interactions and the resulting symmetry breaking, even truly new degrees of freedom may emerge such as composite Cooper pairs, molecules or magnons. The description of this transformation from the simple to the complex is one aim of theoretical physics. Since, furthermore, it is the microscopic few-body interactions that lay the basis for the complicated, macroscopic many-body physics, a deep understanding of the link between both the few- and many-body physics becomes indispensable.

When interactions are weak many well-controlled, theoretical approaches exist to describe many-body systems [1, 2, 3, 4, 5]. The story becomes, however, increasingly complicated when strong interactions are at work and no small parameter is available. In order to improve the theoretical tools to tackle such problems, it is desirable to find experimentally realizable systems which allow a reliable comparison of theory and experiment. Ultracold atoms provide such a system [6] and in this theoretical thesis we apply functional renormalization group techniques to ultracold atomic systems in the intricate strong coupling regime. The functional renormalization group provides a way to study problems ranging from few- to many-body physics in a unified framework. For this reason the link between few- and many-body physics becomes particularly transparent in this approach which helps to systematically improve the approximations used in the solution of many-body problems. Along this line we obtain results in excellent agreement with experimental findings and predict effects which have subsequently been observed in cold atom experiments.

The role of ultracold atoms

Dilute vapors of atoms can be confined in magnetic and optical traps using the intrinsic polarizability and magnetic moment of the atoms. Using various experimental techniques [7] these vapors can then be cooled to extremely low temperatures of $\mathcal{O}$(nK) which makes them to what is today known as *ultracold atoms*. In terms of absolute temperatures ultracold atoms are

among the coolest matter known in nature.[1] With the exception of liquid Helium, at such low temperatures the absolute ground state of the system is a solid and the ultracold gas is therefore in a metastable state. The decay of the ultracold vapor towards the solid state takes mainly place due to three-body recombination collisions of atoms [11]. To increase the lifetime of the ultracold atomic samples these processes have to be suppressed which is why the atomic gas has to be made very dilute. Although in consequence the typical interparticle distance d becomes rather large, it is because of the ultracold temperatures that the thermal de Broglie wavelength of the atoms can by far exceed the interparticle spacing d and quantum (statistical) effects become relevant. Exploiting this fact and the progress in experimental techniques led to the first realization of an almost ideal Bose-Einstein condensate (BEC) in 1995 [12, 13], awarded with the Nobel prize in 2001. Similarly, a degenerate, two-component Fermi gas was achieved in 1999 [14], leading to the observation of superfluid pairing and the realization of the BEC-BCS crossover [15], see also [16].

Ultracold atoms can be described exceptionally well by theoretical physics for various reasons. Most importantly, the interactions between the atoms can be modeled in very simple terms although at first sight the interaction potential $V(r)$ of two colliding atoms is rather complicated. In terms of this interaction potential, the corresponding interaction Hamiltonian is given by

$$\hat{H}_{\text{int}} = \int d^3 r \int d^3 r' \hat{\psi}^\dagger(\boldsymbol{r}')\hat{\psi}(\boldsymbol{r}')V(|\boldsymbol{r}-\boldsymbol{r}'|)\hat{\psi}^\dagger(\boldsymbol{r})\hat{\psi}(\boldsymbol{r}). \tag{1.1}$$

with creation and annihilation operators $\hat{\psi}^\dagger$, $\hat{\psi}$ of bare atoms of mass m and where at large distances r the atoms interact via a van-der Waals type potential with a tail $\sim 1/r^6$ [17] which is a short-range potential [18]. The ultralow temperatures imply a very small collision energy $E = \hbar^2 k^2/m$ of the atoms. The scattering amplitude – which carries the full information about the non-relativistic two-body scattering – is then given by the (s-wave) low-energy expansion (in three spatial dimensions)[2]

$$f(k) = \frac{1}{-1/a - ik + \mathcal{O}(k^2)}. \tag{1.2}$$

The key to simplicity and an efficient description of ultracold atoms is that this scattering amplitude remains the exactly same no matter which concrete short-range interaction potential is chosen. This applies in particular to the simple contact interaction $V(r) \sim \delta(r)$ so that ultracold atoms can theoretically be described by the much simpler Hamiltonian

$$\hat{H}_{\text{int}} = g_\Lambda \int d^3 r \hat{\psi}^\dagger(\boldsymbol{r})\hat{\psi}(\boldsymbol{r})\hat{\psi}^\dagger(\boldsymbol{r})\hat{\psi}(\boldsymbol{r}). \tag{1.3}$$

[1] In relative scales the temperatures are not as cold as they might seem: for instance, in experimentally realizable two-component Fermi gases the Fermi temperature T_F itself is very low so that the lowest achievable relative temperature T/T_F is today only on the percent level. This is comparable but not less than what is found in typical metals at room temperature [8] or neutron stars [9, 10].

[2] Unless stated otherwise, we will work in 'natural' units $\hbar = 2m = k_B = 1$.

Here, the coupling constant g_Λ is chosen such that it yields the desired scattering length a in Eq. (1.2). As long as all scales such as temperature or a possible Fermi energy are small the low-energy limit is justified and the Hamiltonian (1.3) is a valid representation of the true interaction Hamiltonian (1.1). In fact here we encounter a first example of the consequences of the concept of *universality* to be discussed in more detail in Chapter 2 and which is a guiding principle in the description of systems ranging from few- to many-body physics: the observable macrophysics, e.g. $f(k)$, is independent of the exact realization of the microphysics, e.g. $V(r)$, and it is described in terms of a few relevant parameters only; here the scattering length a.

As a theorist one then arrives at a very pleasant situation: in contrast to other (strong coupling) systems such as high-T_c superconductors or the quark-gluon plasma, we deal not only with a Hamiltonian in whose validity we have large confidence – in contrast, e.g. to the question of how well the Fermi-Hubbard model describes the physics of high-temperature superconducting materials – but which is also rather simple – in contrast, e.g., to the standard model governing the phase diagram of QCD.

There are also other advantages to cold atoms which make them interesting, among them in particular Feshbach resonances and optical lattices. Using so-called Feshbach resonances it is possible to adjust the interaction parameter g_Λ and accordingly the scattering length a almost at will. This tunability of the interaction strength opens up a whole new realm of possibilities and allows to enter the strong coupling regime in an experimentally controlled and rather simple way. Furthermore, using optical lattices, the kinetic part of the Hamiltonian can be manipulated and lattice Hamiltonians, such as the Fermi- or Bose-Hubbard model, can be implemented. This led for instance to the observation of the Mott-Insulator to superfluid transition [19] and the detailed experimental study of the phase diagram of the Fermi-Hubbard model is under way [20]. Using similar techniques, lower spatial dimensions with $d < 3$ can be studied. Today imaging techniques are available which even allow for the single-site resolved detection of atoms in optical lattices [21, 22] and which admit the study of the real-time evolution of correlation functions in lattice systems far from equilibrium [23].[3]

It is important to keep in mind that there are also severe limitations to ultracold atoms. For instance, cold atomic systems are finite systems and they are subject to the external trapping potential which complicates the direct comparison of experimental data to theoretical calculations which are often performed for bulk systems and in the thermodynamic limit. Also the experimental analyzing techniques are rather limited in comparison to the plethora of methods available for solid state systems. Most information about the cold atom clouds is obtained from absorption imaging. During the imaging process the sample is unfortunately destroyed so that experiments have to repeated very often to collect the necessary statistics. Furthermore, the more sophisticated the data, the more relevant corrections to 'ideal' physics become: range corrections, the intricate calibration of the temperature and atom number measurement, and the relevance of transversal modes in reduced dimensions are among the com-

[3] There are many more possibilities to be listed: dipolar gases [24], reduced and mixed dimensions [25, 26], (multiflavor) fermions [27], mass- [28] and spin-imbalance [29], artificial gauge fields [30], deterministic single-lattice site preparation of many-body states [31], and many more (for a comprehensive overview and review see e.g. [6, 32]).

plications. Finally, it should be emphasized that ultracold atoms are after all artificial systems which indeed help to understand complex physics' questions. But in the end, it is worthwhile to take the step back to, e.g., hard condensed matter physics, and apply the knowledge gained.

Despite these limitations, we have seen that ultracold atoms provide a large toolbox to set up systems virtually at will, which is why ultracold atomic gases are often highlighted for their role as universal *quantum simulators* [20] reviving Feynman's original idea [33]. The idea is that Hamiltonians, whose physics is too complicated to be solved analytically or by numerical means on a classical computer, can be designed in the laboratory and it is nature, namely the experiment itself, which then performs the calculation. In a sense, the experiment can be viewed as an instance of a very specialized quantum computer, and much research is focused on proposals of how to experimentally realize Hamiltonians of interest. Recent experiments studying the unitary Fermi gas [34, 35] or the realization of the Bose-Hubbard Hamiltonian [19, 36] can be interpreted as such quantum simulations, where ultracold atoms provide an ideal basis for testing theoretical many-body techniques versus experimental data. In this regard, in particular the excellent agreement between experiment and theory for the unitary Fermi gas, a long standing, strong coupling many-body problem [16], is truly remarkable [35, 37]. The possibility to improve our theoretical methods as well as our understanding of many-body physics on the basis of detailed experiments which can directly test the theoretical predictions makes ultracold atoms so appealing for many branches of theoretical physics, ranging from hard condensed matter physics [38], to quantum information processing [39, 40], to nuclear matter [41], to high-energy and black-hole physics [42, 43].

Outline

Few-body Efimov physics. In the first part of this thesis, cf. Chapters 2 and 3, we focus on the few-body aspect of cold atoms. This is an important aspect on its own since the few-body physics ultimately determines the stability of the cold atomic samples. On the other hand a thorough investigation of the few-body physics leads to effects not present in standard condensed matter systems. A prominent example is the Efimov effect [44] which is introduced in detail in the beginning of Chapter 2: three particles interacting via resonant short-range potentials form an infinite number of three-body bound states which obey universal scaling relations. These states exist even in a regime where the two-body interaction does not support a bound state. Although predicted in 1970 in the context of nuclear physics, Efimov states have been first observed in ultracold atoms [45].

We study the Efimov effect from a functional renormalization group (fRG) perspective.[4] One finds that the well-known unitary, non-Gaussian renormalization group fixed point in the two-body sector is supplemented by a universal RG limit cycle running of the six-point correlation function. The Efimov effect has profound consequences regarding universality as a new three-body parameter has to be introduced in addition to the scattering length a which fixes the overall phase of this limit cycle. A priori this three-body parameter is not expected to be a universal number. Nonetheless, recent observations [47] suggest such a universality of the

[4] For a review on the application of the fRG to the Efimov effect in the case of zero-range interactions, see [46].

three-body parameter and its origin had been unclear. On the basis of an exact solution of the three-body problem, we show in Chapter 2 how the observed universality can quantitatively be explained in terms of the standard two-channel model of ultracold atoms close to a Feshbach resonance. This model is of great relevance for the many cold atom experiments that employ Feshbach resonances. By studying also the non-universal corrections due to the finite range of the microscopic interaction potentials, our results give further insight into the limitations of universality in cold atomic systems in general and how the microscopical details governing the collisions of atoms and molecules have impact on the observable physics.

Furthermore, it had been an open question whether further parameters are necessary when going to the four-body problem. From the numerical solution of the four-body problem for the *lowest* four-body bound states, Greene and coworkers [48] conjectured that no such parameters are needed. They however could not access the particularly interesting, scale-invariant unitarity point for infinite scattering length at the scattering threshold where physics truly becomes universal. In Chapter 3 we study the four-body problem using RG equations. Within a derivative expansion we are able to support the conjecture that indeed no four-body parameter is needed for the consistent renormalization of four-body physics by studying the problem directly for the highly excited states in the scaling limit.

Many-body polaron physics. The second part of this thesis is related to the quantum simulation aspect of cold atoms and the question: can the Stoner transition to itinerant ferromagnetism be realized in a Fermi gas of ultracold atoms? This question has recently been debated [49, 50, 51, 52, 53, 54, 55, 56] and first measurements seemed in favor of such a transition [49]. The situation exemplifies how subtle differences between the paradigm condensed matter and cold atom systems can complicate an attempted quantum simulation. These subtle differences arise from the microscopic physics and can be understood from a simple argument: consider a three-dimensional electron gas with screened interactions (the condensed matter system) versus a two-component, ultracold Fermi gas (the quantum simulator). Both systems are described by an effective Hamiltonian $\hat{H}$ with a contact interaction $\sim g_\Lambda(\hat{\psi}^\dagger\hat{\psi})^2$ as given by Eq. (1.3). In the electron gas the interaction represents the screened Coulomb interaction which is *repulsive*, i.e. $g_\Lambda > 0$. Contrarily, the contact interaction in the cold atomic system is determined by the short-range interatomic van der Waals potential which is *attractive* and thus $g_\Lambda < 0$. In consequence, although both the cold atom as well as the condensed matter system may feature the same positive scattering length a, the former system remains microscopically attractive – and features an associated molecular bound state – and thus can simulate the screened electron gas only in a very limited regime [49, 50, 51].

In Chapter 4 we study this highly controversial problem [49, 50, 51, 52, 53, 54, 55, 56] in the limit of extreme spin imbalance where a single $\downarrow$-impurity is immersed in a Fermi sea of $\uparrow$-atoms. In the context of this so-called Fermi polaron problem, we developed a new, numerical fRG technique which allows to study the RG flow of full spectral functions. In terms of diagrams, our method is similar to a selfconsistent Ward-Luttinger approach [37, 57, 58]. The results from the fRG are in excellent agreement with recent diagrammatic Monte Carlo calculations [59, 60] for various ground state properties and depending on the interaction

strength one finds a transition in the ground state from a molecular to a dressed impurity state which interacts attractively with the majority atoms. Additionally, the algorithm allows the calculation of the decay rates of the molecule and attractive polaron across the transition.

But most importantly, the resulting spectral function reveals that the impurity can also propagate as a highly excited, metastable repulsive polaron. In the limit of a going to zero from above, quasiparticle weight is shifted towards the repulsive polaron excitation which, in this regime, becomes stable. This can be viewed as an a posteriori justification for using a weakly-coupled effective (Fermi liquid) field theory for stable, repulsively interacting polarons in the limit of small positive scattering length a. Only in this limit a quantum simulation of the repulsive Fermi gas of 'standard' condensed matter physics is possible. Contrarily, when approaching the regime of strong repulsion the repulsive polaron decays into the low-lying molecular states via three- and higher-body processes and the attempted quantum simulation becomes impossible. For this reason the Stoner transition to ferromagnetism in a spin-imbalanced, repulsive Fermi gas cannot be straightforwardly studied using ultracold atoms.

Using a non-selfconsistent T-matrix approach, we study the polaron problem in two spatial dimensions in Appendix A and find that it has very similar features compared to the three-dimensional case. Calculating the radio-frequency response, we show that a recent experiment by the group of Köhl in Cambridge [61] can be reinterpreted in terms of polarons rather than confinement induced molecules. Following our predictions [62, 63] (cf. also Appendix B), repulsive polarons have recently been observed experimentally in two and three dimensions using radio-frequency spectroscopy [64, 65].

Chapter Two

Efimov physics beyond universality

In this chapter we present an exact solution of the quantum three-body problem using functional renormalization. Three particles interacting via resonant, short-range interaction potentials build a series of three-body bound states. Their existence is connected to a universal discrete scaling symmetry and the appearance of a new *three-body parameter* which had been presumed to be a non-universal quantity. Recent experiments with cold atomic gases close to Feshbach resonances suggest, however, that this parameter exhibits universal behavior. In the following, we present an extended yet simple model for Bose gases close to Feshbach resonances and derive the exact solution of the corresponding three-body problem. Our results explain the observed behavior of the three-body parameter and we provide new predictions for the deviation from universal scaling of the lowest Efimov states which can be tested in future experiments.

In Section 2.1 we give a brief review on Efimov physics which is largely based on the excellent review by Braaten and Hammer, see [66]. Section 2.2 explains the main methods how Efimov trimers have experimentally been measured and we elucidate the observed apparent universality of the three-body parameter. In Section 2.3 we then introduce a simple two-channel model describing the physics of ultracold atoms close to a Feshbach resonance and determine the model parameters by solving the corresponding two-body problem. The following Section 2.4 introduces the functional renormalization group method used to solve the three-body problem, the truncation of the effective action is given and the renormalization group equations are derived, which are solved in Section 2.5. In Section 2.6 we develop a numerical procedure to determine the bound state spectrum and we present the results in Section 2.7. In Sections 2.8 and 2.9 we study the extent of universality for the low-lying Efimov states. We compare our result to experiments and conclude in Section 2.10.

2.1 Universality in cold atoms

In cold quantum gases, one deals with atoms interacting via pairwise short-range potentials. The scattering properties of these systems can be described solely in terms of the s-wave scattering length a, when their average interparticle distance $d = 1/n^{1/3}$, as well as their de-Broglie wave length $\lambda = h/p$ is much larger than the characteristic length scale of their potential range r_0, that is $d \gg r_0$ and $p \ll 1/r_0$. As we have seen in the introduction in Chapter 1, these conditions are fulfilled for dilute atomic gases at ultralow temperatures and they ensure that the kinetic energy of the atoms is so small that they are neither able to resolve the short-range

details of the interaction potential nor can they probe these short distances by merely being located 'on top of each other'.

Being characterized by a single parameter, cold atoms are an example of a system which exhibits universality. Quite generally, a phenomenon is called universal, if the observables are independent of the microscopic details such that the system is characterized by a few variables only. Universality appears, for instance, in the physics close to critical points. A critical point is the end point of a line of a first order phase transition. One of the most prominent examples is the liquid-gas transition. As illustrated in the pressure-temperature phase diagram shown in Fig. 2.1, a line $T = T(P)$ marks the phase transition from a liquid to a gaseous phase with an associated discontinuity of the density. This line terminates in the critical point beyond which the phase transition becomes a crossover. The gas and the liquid phase have the same density ρ_c at the critical point, which is approached according to a power law, $\rho - \rho_c = C(T - T_c)^\beta$ [66]. While the coefficient C is non-universal, the exponent β is the same for a whole class of systems. It does not matter which specific gas of particles is chosen and, even more impressively, the same *critical exponent* β appears in systems which are at first sight completely unrelated to the liquid-gas transition as for example in solids featuring a ferro- to paramagnetic phase transition. All these systems are then said to belong to the same *universality class* and they are described by a common universal effective field theory which has only a few parameters as input.

In the context of cold atoms, there is a more narrow notion of universality and physics is termed *universal* if observables depend only on the scattering length a and on no other parameter [11, 67, 68]. For instance, the physics of a weakly interacting Bose-Einstein condensate can universally be described by the expansion parameter na^3. One speaks of non-universal corrections when there are residual dependencies on microscopic details such as the scale r_0, which characterizes the range of the interatomic potentials.

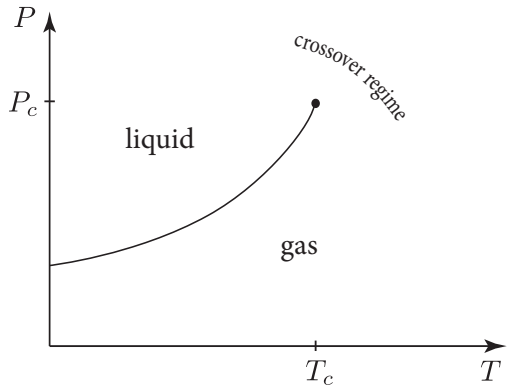

FIGURE 2.1: *Phase diagram of the liquid gas transition [66]. The critical line (solid) terminates in the so-called critical point (dot) beyond which the phase transition becomes a crossover. Physics close to such a critical point is related to the existence of a renormalization group fixed point and exhibits universality as well as scale invariance.*

The appearance of universality is intimately related to the existence of renormalization group fixed points [69, 70]. Various theories, although being different on the microscopic level, may flow to the same fixed point and thus, at large distances, lead to the same observable physics. The non-relativistic system of cold atoms is governed by the existence of two fixed points [71, 72, 73]. One is a weak coupling or so-called Gaussian fixed point, the other a strong coupling fixed point which corresponds to unitary interactions. In the context of Bose-Einstein condensation, universality is usually connected to the Gaussian fixed point and is thus a weak coupling phenomenon.

In the following we will be interested in the universality associated to the non-perturbative fixed point. Here, the system is characterized by a large scattering length, $|a| \gg r_0$, and universality applies as well. The most simple example of a universal observable is the existence of a weakly bound molecule (the so-called *dimer*) with binding energy

$$\epsilon_D = \frac{\hbar^2}{ma^2}, \tag{2.1}$$

where $\hbar$ is Planck's constant and m the mass of the atoms. Other examples are found in the case of a two-component Fermi gas. In the unitarity limit where the scattering length diverges, $a \to \infty$, the chemical potential of the Fermi gas is measured to be [34][1]

$$\mu = \xi \epsilon_F, \quad \xi = 0.376(4), \tag{2.2}$$

which is in excellent agreement with theoretical results [37, 75, 76, 77]. Here ξ is the so-called Bertsch parameter [78] which is a universal number. Similar, excellent agreement between theory and experiment is found for the critical temperature T_c/T_F [34, 37, 79, 80]. It is one of the remarkable consequences of universality that theoretical insight and methods developed with having cold atoms in mind can then be applied to other systems ranging from neutron stars [41] to hard condensed matter physics [6, 38].

The Efimov effect

When three identical bosons interact with resonant short-range potentials ($a \gg r_0$) a new universal quantum phenomenon is revealed. This was first realized by Vitaly Efimov in 1970. He showed the existence of an infinite series of three-body bound states in the resonance limit, $a \to \infty$ [44, 81].[2] The binding energies of the so-called Efimov trimers form a geometric spectrum so that the binding energies of consequent levels exhibit a constant ratio[3]

$$\frac{E_n^{\mathrm{T}}}{E_{n+1}^{\mathrm{T}}} = e^{\frac{2s_0}{\pi}} = 515.03\ldots, \quad s_0 = 1.00624\ldots \tag{2.3}$$

[1] An improved experimental analysis of the Feshbach resonance position in the ^{6}Li Fermi gas by Zürn *et al.* yields a corrected value of the Bertsch parameter $\xi = 0.370(5)(8)$ [74].

[2] The Efimov effect occurs quite generally if two out of three pairs of the participating particles are interacting with a large scattering length [66].

[3] Here the universal number s_0 is given for the case of identical bosons.

when the *unitarity point* $1/a = E = 0$ is approached. At this point two bosons are just at the verge of being bound into the weakly bound dimer.

We show a typical Efimov bound state spectrum in Fig. 2.2 where the axis are rescaled in order to make several of the three-body bound states visible. Each of the infinitely many

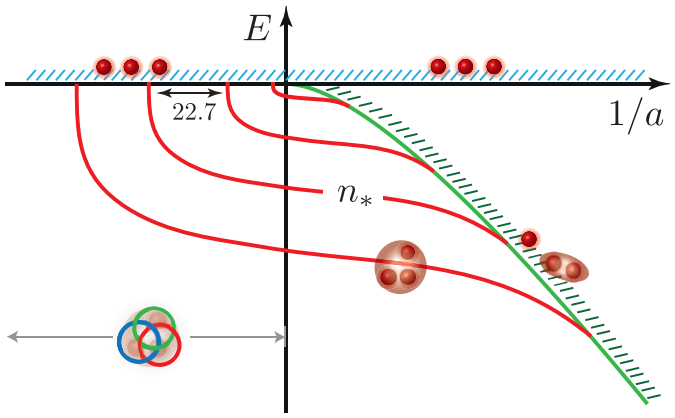

FIGURE 2.2: *Illustration of the Efimov energy spectrum. The Efimov trimers (red solid) extend from the atom threshold (blue hatching) at vanishing energy $E = 0$ and $a < 0$ to the side of positive scattering length $a > 0$ where they merge into the atom-dimer threshold (green solid). For negative a, the trimers are of Borromean nature as they exist in a regime where no two-body bound state exist – a purely quantum phenomenon not present in classical mechanics.*

Efimov states evolves from the three-atom threshold (dashed blue hatching) for $a < 0$ across the resonance and merges into the atom-dimer scattering threshold for $a > 0$ (green line). Quite counterintuitively, the trimer states exist even in a regime where no two-body bound state is present. In this regime the Efimov states are sometimes called Borromean in reference to the legendary Italian family: take one of the three away and the whole system falls apart.

Eq. (2.3) is a universal law as it does not depend on any short-range details. The only important ingredients are: short-range interactions, a large scattering length $|a| \gg r_0$, and energies $|E| \ll \hbar^2/(m r_0^2)$. The Efimov effect is a strong coupling phenomenon taking place in the vicinity of the two-body strong-coupling RG fixed point. It was predicted by Efimov in the context of nuclear physics and it took more than thirty years to find experimental evidence for its existence. Its observation is an example of the broad implications of universality: instead of being found in a nuclear system, the Efimov effect was observed using ultracold atoms close to a Feshbach resonance [45]. Unfortunately, the search for Efimov states in the nuclear matter context has been quite unsuccessful so far, despite much effort such as the decades of research devoted to the search for the elusive ^{3}He trimer [82, 83].

The Efimov effect, which existence was rigorously proven by Amado and Noble [84, 85], demands the introduction of a new notion of universality. Although the existence of the Efimov states, the relation (2.3), as well as the shape of the spectrum shown in Fig. 2.2 is

universal, the absolute value of the binding energies is not universally fixed. In fact, the whole Efimov spectrum in Fig. 2.2 can be shifted arbitrarily while leaving universal ratios such as Eq. (2.3) unaffected. This arbitrariness necessitates the introduction of an additional *three-body parameter* (3BP). This is made explicit by rewriting the Efimov binding energies as [66]

$$E_T^{(n)} = \left(\frac{1}{515.03}\right)^{n-n^*} \frac{\hbar^2 \varkappa_*^2}{m}, \tag{2.4}$$

where n^* denotes the number of some reference Efimov state as indicated in Fig. 2.2. The wave number $\varkappa_*$ is a free parameter which is chosen to set the overall position of the spectrum. $\varkappa^*$ can be regarded as the three-body parameter but this is not a unique choice. From Fig. 2.2 it is evident that one may choose any observable which fixes the overall position of the spectrum. This could, for instance, also be the value of the scattering length $a_-^{(n^*)} < 0$, where the reference trimer n^* meets the three-atom threshold. As shown by Efimov, the trimers meet the atom threshold at values [86] (see also [66])

$$a_-^{(n)} = 22.6942^{n-n^*} a_-^{(n^*)}, \tag{2.5}$$

for large $|a|/r_0 \gg 1$.

Due to the Efimov effect, two-body universality is violated: not only the scattering length a is needed in order to characterize the physics but an additional parameter. While in the two-body problem non-universal corrections scale as positive powers of $r_0/|a|$ and hence are suppressed for large $|a|$, the three-body parameter $\varkappa^*$ never disappears. It reflects the ignorance of the short-range details of the interatomic potentials and thus it had – until recently – been regarded as a non-universal number.

From Efimov's results (2.3) and (2.4) it follows that there are infinitely many *weakly* bound trimers. But how does the spectrum behave for the *deeply* bound states? In order to answer this question let us define two important limits. We argued that non-universal corrections to the two-body scattering scale as powers of $r_0/|a|$, for a detailed discussion see [66]. There are two limits in which these corrections go to zero. One is the so-called:

Unitary or ***resonance limit*** **[66]**

$$|a| \to \infty, \quad r_0 \text{ finite.} \tag{2.6}$$

In this limit infinitely many, *weakly* bound trimer states exist. One may go away from the resonance limit by lowering the absolute value of the scattering length $|a|$. When the inverse wavenumber of the nth bound state $1/\varkappa^{(n)}$ or the corresponding scattering length $a_-^{(n)}$, where it meets the atom threshold, becomes of order r_0, the Efimov states cease to exist due to the finite range of the interaction potentials. Hence there will be a *lowest* Efimov state. The

Efimov states in this situation are illustrated as solid red lines in Fig. 2.3. As also indicated, the low-lying states can not be expected to obey the universal geometric scaling, since here non-universal corrections of order $r_0/|a|$ become relevant. For this reason one expects that the specific position of the lowest state is highly dependent on microscopic details. This explains why the three-body parameter is expected to be a non-universal number.

The resonance limit is a very physical limit and it can be realized using a shape resonance as depicted in Fig. 2.4(a) and (b) for the case of a square well potential. Keeping the potential range constant, the depth of the potential is fine-tuned to a critical value V_{cr} at which a two-body bound state just vanishes into the continuum. Another possibility to reach the resonance limit is the use of so-called Feshbach resonances [87, 88, 89, 90, 91, 92]. This mechanism is employed in cold atoms and we will investigate it in more detail in Section 2.3.

The second limit in which the corrections $r_0/|a|$ go to zero is the

---

Zero-range or ***scaling limit*** [66]

$$|a| \text{ fixed}, \quad r_0 \to 0. \tag{2.7}$$

This limit is illustrated in Fig. 2.4(c). It was explicitly studied in the context of Efimov physics first by Frederico *et al.* [93]. In this limit, which is often referred to as scaling limit, the purely theoretical, idealized situation of contact interactions is realized and the two-particle interaction potential reads $V(\mathbf{r}'-\mathbf{r}) = g\,\delta(\mathbf{r}'-\mathbf{r})$. The scattering phase shift becomes exactly $k\cot\delta_0(k) = -1/a$ for the partial s-wave and vanishes identically for all higher partial waves, $\delta_L \equiv 0$ for $L > 0$. At first sight the zero-range limit seems quite unphysical, as interaction

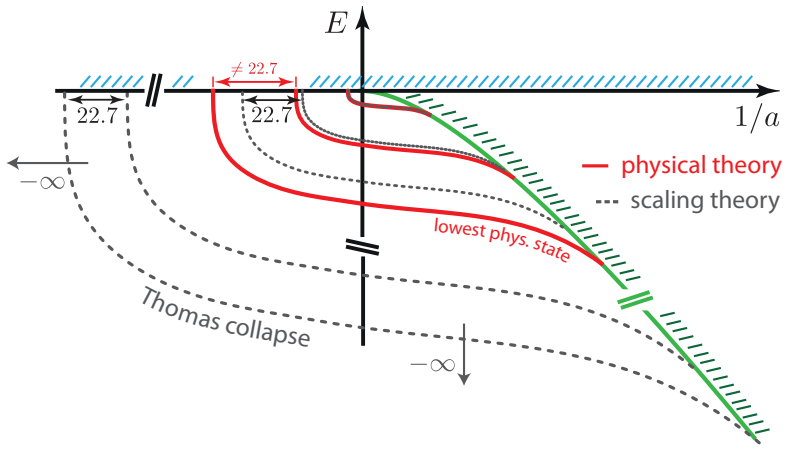

FIGURE 2.3: *Illustration of the Efimov spectrum obtained from scaling theory (dashed black) compared to a (physical) finite range model (solid red).*

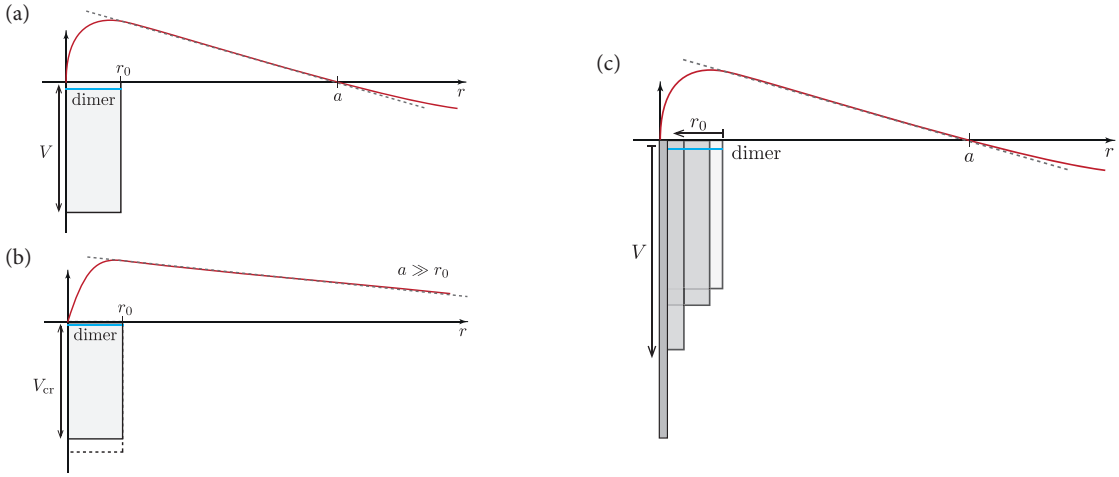

FIGURE 2.4: *(a) and (b): Shape resonance. The depth of a square well potential is fine-tuned to a critical value where the scattering length diverges and the weakly bound molecule disappears into the scattering continuum. (c) Zero-range limit. While keeping the scattering length a fixed the range of the potential is sent to zero. In (a-c) also the wave function, which defines the scattering length a, is indicated.*

potentials in non-relativistic physics are never contact interactions. The non-universal corrections due to the true physical range vanish, however, as powers of $r_0/|a|$ so that in the limit of large scattering length the scaling limit yields accurate results (cf. the discussion in Chapter 1). The zero-range limit has the advantage that it makes calculations feasible and in Section 2.2 we will encounter various examples where the scaling limit is used to derive analytical results.

However, as soon as $|a|$ or the relevant, inverse wave numbers $1/\varkappa$ become of order of r_0, the scaling limit leads to unphysical or even pathological results: there are not only infinitely many weakly bound trimer states but also infinitely many *infinitely deeply* bound states. The reason for this pathological behavior is the absence of any scale r_0 which prevents the system from collapsing to infinite binding energies - and thus the collapse of the trimers to infinitely small size. Obviously this collapse is prevented in nature by the presence of a finite potential range and, theoretically, it is prevented by the presence of a regulating effective range term $\sim r_e k^2/2$ in the inverse scattering amplitude $f(k)$, see Eq. (2.26) below. Such an effective range r_e is for instance introduced when the range r_0 is kept fixed as previously discussed following Eq. (2.6). Furthermore, due to the absence of any short-range scale, *all* Efimov states exactly obey the universal scaling relations such as Eqn. (2.4) and (2.5). The corresponding Efimov states are illustrated as dotted lines in Fig. 2.3. However, the dependence on the three-body parameter $\varkappa^*$, cf. Eq. (2.4), is still present, and $\varkappa^*$ has to be fixed to determine the overall position of the spectrum. It is of importance – and unfortunately often not properly taken into account in the literature – to realize that the scaling limit only leads to valid predictions

when $|a|$ is *much* larger than the range r_0.[4] For the deep Efimov states accessible in experiments with cold atoms this is typically not realized, and, strictly speaking, scaling theory *cannot* be applied.

As mentioned above, it is, however, very tempting to apply results from scaling theory because it allows to derive analytical expressions for many physical observables. For example, already Efimov showed [81, 86] that the atom-dimer scattering length a_{AD} at the atom-dimer scattering threshold (green solid line in Fig. 2.3) obeys [66]

$$a_{AD} = (b_1 - b_0 \tan[s_0 \ln(a\varkappa_*) + \beta]a \tag{2.8}$$

where the b_i are universal coefficients, first calculated in [94]. Universal results like this can easily be used to fit experimental data, but once again, they are applicable only if $|a| \gg r_0$.

The collapse of the trimer states to infinite binding energies is connected to what was found by Thomas prior to the calculation by Efimov [95]. He considered atoms interacting via a square well potential where he performed the scaling limit $r_0 \to 0$ while keeping a constant, cf. Fig. 2.4 (c). He showed that there exists a three-body bound state with binding energy $E_{\text{tri}} \sim -\hbar^2/(m r_0^2) \to -\infty$. In 1979, Efimov succeeded to connect Thomas' and his own work and showed that there are the above mentioned infinitely many, deep trimer states where the deepest of those scales as $E_{\text{tri}} \sim -\hbar^2/(m r_0^2) \to -\infty$ [86].

Efimov effect and the renormalization group. The Efimov effect also leaves its traces in a renormalization group analysis of the three-body problem [66] and it presents one of the extremely rare cases where a renormalization group limit cycle [97, 98] is realized in nature.

[4] As we will see below, $|a|$ has often to be up to two orders of magnitude larger than of r_0 or $|r_e|$ to be safely in the scaling regime.

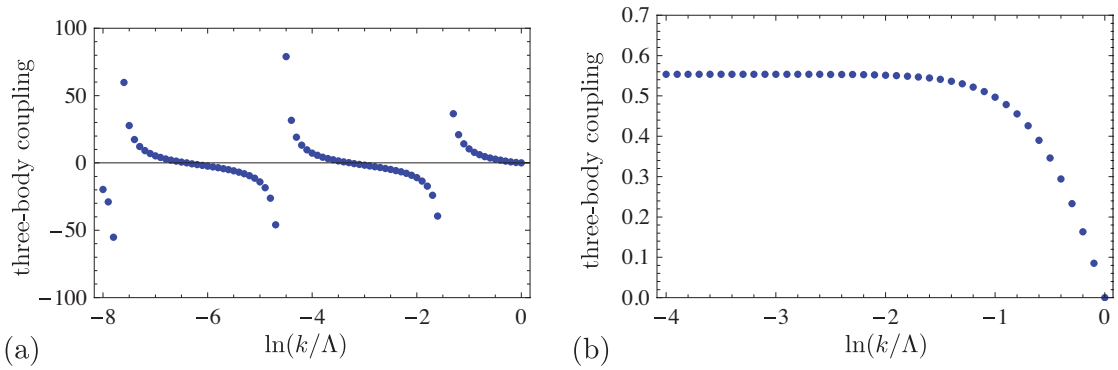

FIGURE 2.5: *Renormalization group flow of the three-body coupling constant with logarithmic RG scale k in units of the UV cutoff scale Λ as computed in [96] for (a) bosons, (b) SU(2) fermions.*

The connection between limit cycles and Efimov physics was first discussed in [99] and studied in detail using effective field theory by Bedaque, Hammer, and van Kolck [100, 101]. Later the connection was also analyzed in [96, 102, 103, 104, 105, 106].

As mentioned before, the two-body sector is governed by a strong coupling fixed point [70, 72, 73, 107]. The existence of the fixed point directly implies that the system exhibits scale invariance so that the system is invariant under the *continuous* scale transformations [66, 108, 109, 110]

$$a \to \lambda a \qquad \boldsymbol{r} \to \lambda \boldsymbol{r} \qquad t \to \lambda^2 t. \tag{2.9}$$

The Efimov effect changes the situation. One finds that the running of the three-body coupling exhibits a flow which is log-periodic in the RG momentum scale k as shown in Fig. 2.5(a). This result was obtained from the functional renormalization group [96] and it is similar to the calculation performed by Bedaque *et al.* [100, 101]. The period of the flow is given by the Efimov number s_0, which Efimov showed to obey [44]

$$s_0 \cosh \frac{\pi s_0}{2} = \frac{8}{\sqrt{3}} \sinh \frac{\pi s_0}{6}. \tag{2.10}$$

The log-periodic structure of the limit cycle flow reflects the geometric spectrum (2.4): when the RG scale is changed by a multiple factor of $\exp \pi/s_0$ new divergencies appear in the flow of the three-body coupling and these divergencies correspond to the appearance of new bound states. The three-body parameter $\varkappa_*$ also appears in the renormalization group framework and it sets the overall phase of the renormalization group flow. In a sense [66], $\varkappa_*$ labels a continuous set of universality classes. The periodic structure of the flow with its fixed frequency π/s_0 reveals that the continuous scale invariance present in the two-body problem is broken and only a *discrete scale invariance* remains. This symmetry breaking is purely quantum, and one may speak of a quantum anomaly as discussed in [111, 112, 113]. The system is now invariant only under the discrete scale transformations [66]:

$$\varkappa_* \to \varkappa_* \qquad a \to \lambda_0^n a \qquad \boldsymbol{r} \to \lambda_0^n \boldsymbol{r} \qquad t \to \lambda_0^{2n} t$$

with

$$\lambda_0 = e^{\pi/s_0}. \tag{2.11}$$

The quantum anomaly is connected to the physics of two particles interacting via an inverse square potential. The reason is that the quantum mechanical solution of the three-body problem can be reduced to the solution of a Schrödinger equation with an $1/R^2$ potential [66]. We studied this problem and its connection to the renormalization group limit cycle in [111].

It is worth mentioning that scale invariance is a very important feature when considering many-body systems such as the unitary Fermi gas [16]. It allows to derive many exact relations such as the vanishing of the bulk viscosity [109] or the exact time evolution of the system [114, 115, 116, 117, 118]. Contrarily, if one considers unitary bosons, scale invariance is broken rendering calculations much more difficult. For two-component fermions with a mass-imbalance smaller than a factor of 13.6 [119, 120] no Efimov effect, however, takes place. Instead of showing a periodic limit cycle the atom-dimer coupling exhibits an RG fixed point

tied to the renormalization group running of the two-body sector, cf. Fig. 2.5(b). Thus no quantum anomaly appears, scale invariance is preserved, and calculations can safely exploit this important symmetry.

2.2 Observation of Efimov physics with ultracold atoms

Basically there are two experimental routes which have been taken to reveal Efimov physics with cold atoms. One is the direct photo association of Efimov trimers using radio-frequency spectroscopy. The other is an indirect detection by measuring three-body loss enhancements caused by Efimov physics. For the latter one exploits the instability of cold atomic gases caused by the recombination of atoms into molecular bound states. The binding energy gained in the formation of a molecule is transferred into kinetic energy of the atoms participating in the process. When this energy exceeds the trap depth, the atoms have sufficient momentum to escape from the trapping potential. Having escaped from the trap, these atoms are obviously not present in a subsequent absorption image, by which the number of trapped atoms is determined experimentally. By measuring the remaining fraction of atoms as function of time the loss rate can then be inferred.

In order for momentum to be a conserved quantity, such collisional loss processes have to involve at least three atoms.[5] The third atom ensures momentum conservation by carrying away a portion of the binding energy released in the recombination process. Since three atoms are involved, the loss rate is proportional to the third power of density [11],

$$\dot{n} = -K_3 n^3, \tag{2.12}$$

where K_3 is the three-body loss coefficient and n the density of atoms. As discussed in Chapter 1, the existence of loss processes in ultracold atomic gases is quite natural: after all, the true ground state of the system is not the gas of atoms but a solid – with the exception of the helium where the atoms would form a liquid. In consequence, ultracold gases are in a metastable state and the loss process discussed above is one of the many ways by which the system can reach its true ground state.

Let us now briefly discuss three observables which are related to three-body decay and which can be used to detect Efimov physics.

Three-atom recombination maxima for $a < 0$. The first possibility to find evidence for Efimov states is the measurement of the loss coefficient K_3 in dependence of negative scattering length a. In the scaling limit, cf. Eq. (2.7), K_3 can be expressed as [66]

$$K_3 = 3C(a)\frac{\hbar^2 a^4}{m}. \tag{2.13}$$

When no Efimov state is present, one finds a pure a^4 scaling with a constant coefficient $C(a)$ [121, 122]. This scaling is due to the process schematically shown in Fig. 2.6(a), where two

[5] Two-body decay processes are also possible. These can, however, be often made sufficiently small in order to be neglected [11].

atoms form a virtual scattering state (dashed line). This state subsequently interacts with a

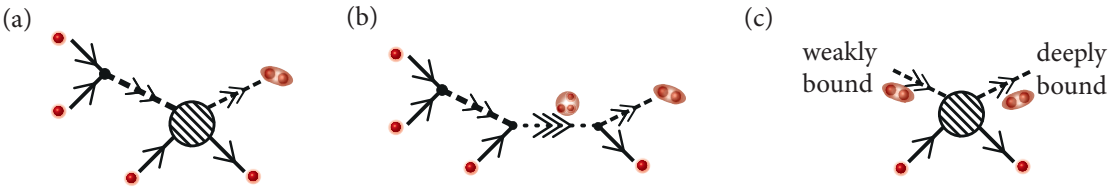

FIGURE 2.6: *Collisional processes leading to three-body decay of ultracold atomic gases. Solid lines represent atoms, dashed lines molecules and dotted lines with three arrows Efimov trimers. (a) Three-atom recombination. (b) In the presence of a trimer a new decay channel opens up. (c) Atom-dimer recombination at the atom-dimer scattering threshold.*

third atom (dashed vertex). The outgoing, deeply bound molecule as well as the outgoing atom can be on-shell, physical scattering states. The evaluation of the corresponding matrix element yields Eq. (2.13).

The situation changes, when an Efimov state is nearby or even crosses the atom scattering threshold at the scattering length a where the measurement is performed. In this case a new, fast decay channel opens up. The new process contributing to Fig. 2.6(a) is schematically depicted in Fig. 2.6(b). When the third atom enters, a new state, the trimer, can be formed. This trimer has typically a very short lifetime and it decays quickly into deeply bound states. Furthermore, when the trimer is energetically close to the atom threshold at zero energy, it is almost gapless and thus the corresponding matrix element becomes very large. This leads to a large enhancement of the loss which is visible as a resonance in $K_3 = K_3(a)$.

This additional modification due to Efimov physics is described by the scattering length dependent prefactor $C(a)$ in Eq. (2.13), which, in the resonance limit, has to obey $C(22.7a) = C(a)$ due to the discrete scale invariance of Efimov physics. The loss process for $a < 0$ was first discussed by Esry, Greene and Burke [123] and shortly after in [124, 125, 126, 127]. Using effective field theory, Braaten and Hammer succeeded to derive an analytical expression for $C(a)$ *in the scaling limit* [126]

$$C(a) = 4590 \, \frac{\sinh(2\eta_-)}{\sin^2[s_0 \ln(a/a_-)] + \sinh^2 \eta_-}. \tag{2.14}$$

Here a_- is a representative of the three-body parameter as described in the previous section and η_- reflects the finite lifetime of the trimer state involved. By fine-tuning the parameters a_- and η_-, Eq. (2.14) can be used to fit the experimental results. Three-body loss enhancements due to Efimov physics have been found in many cases [45, 47, 128, 129, 130, 131, 132, 133, 134, 135, 136] and in Fig. 2.7 we show two examples. While in Fig. 2.7(a) the first measurement of an Efimov loss resonance for identical bosons [45] is shown, Fig. 2.7(b) displays the loss coefficient in a three-component ^{6}Li Fermi gas [128] compared to a functional renormalization group calculation [137].

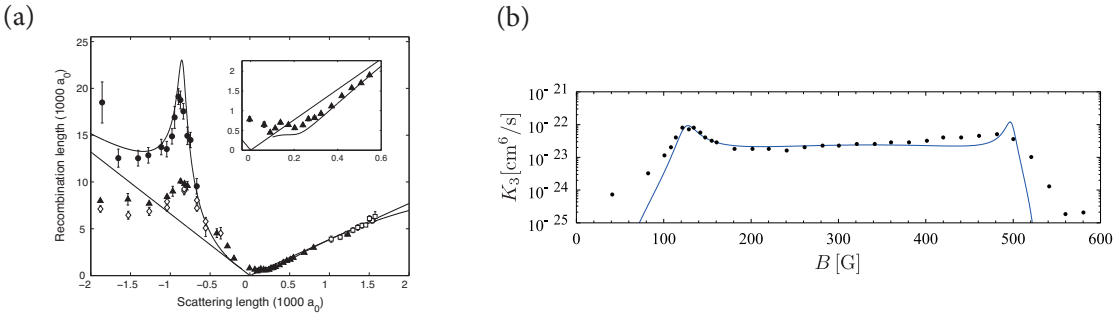

FIGURE 2.7: *(a) First indirect observation of an Efimov trimer in a ultracold gas of* ^{133}*Cs atoms. The measured recombination length (symbols) is shown versus the scattering length a and compares well with results from scaling theory (solid curve) [Figure taken from [45] by courtesy of R. Grimm]. (b) Three-body loss coefficient* K_3 *as function of magnetic field in a three-component* ^{6}*Li Fermi gas. The resonances are due to Efimov states. Experimental data from [128] (symbols) versus a functional renormalization group calculation [137].*

Three-atom recombination minima for $a > 0$**.** For $a > 0$, three atoms at the atom threshold at $E = 0$, cf. Fig. 2.2, can recombine into the weakly bound dimer state (green solid line in Fig. 2.2). In this case the two processes shown in Fig. 2.6(a) and (b) do not lead to enhancement but rather a reduction of losses, since both processes conspire in such a way that the corresponding matrix elements interfere destructively with each other. In the scaling limit, the corresponding coefficient $C(a)$ obeys the equation [66, 125]

$$C(a) = 67.1\, e^{-2\eta_+}(\cos^2[s_0 \ln(a/a_+)] + \sinh^2 \eta_+) + 16.8\,(1 - e^{-4\eta_+}). \tag{2.15}$$

Similarly to Eq. (2.14), a_+ is a possible representative of the three-body parameter and η_+ determines the lifetime of the trimer responsible for the minimum. Recombination minima were for instance observed in [45], cf. Fig. 2.7(a, inset). The existence of these minima may become of great importance for many-body physics as they might help to stabilize strongly interacting repulsive Bose or SU(N) Fermi gases for $a/r_0 \gg 1$.

Loss resonances in atom-dimer scattering. It is also possible to prepare a mixture of weakly bound dimers and free atoms in which both constituents interact with each other. During this process, depicted in Fig. 2.6(c), the weakly bound dimer can fall into a deeply bound molecular state and the participating atoms leave the trap. Similar to the discussion below Eq. (2.13), a close-by trimer state leads to an enhanced loss and the corresponding loss rate is parametrized by [138][6]

$$\dot{n}_D = \dot{n}_A = -\beta(a) n_D n_A. \tag{2.16}$$

[6]Here we neglect dimer-dimer scattering as well as the three-atom recombination also present in these mixtures.

In the scaling limit, the coefficient β has been calculated using effective field theory [139] and has the form

$$\beta(a) = C_{AD}(a)\frac{\hbar a}{m}, \tag{2.17}$$

with

$$C_{AD}(a) = 20.3\frac{\sinh(2\eta_*)}{\sin^2[s_0\ln(a/a_*)] + \sinh^2\eta_*}, \tag{2.18}$$

and where again, a_* and η_* are representatives of the three-body parameter and the lifetime of the trimer, respectively. The enhanced atom-dimer loss has been studied for instance in [138, 140]. Note that in the case of $a > 0$, non-universal corrections become generally particularly important, as the atom-dimer threshold itself (green solid line in Fig. 2.2) exhibits a strong dependence on microscopic details when a becomes of the order of r_0.

Photo association of trimers. The last possible route taken to detect Efimov physics is the direct formation of Efimov trimers. Recently the group of Jochim succeeded to use radio-frequency (rf) modulations to associate trimers from a mixture of atoms and dimers in an two-component mixture of ^{6}Li atoms [141]. By applying an rf pulse, one hyperfine spin is flipped and a trimer is associated in the final state. By measuring the rf response it was then possible to directly determine the binding energy of the Efimov bound state, which, however, is very short-lived. Similar results have been reported in [129, 142].

The apparent universality of the three-body parameter

In Section 2.1 we have seen that for potentials with a finite range r_0 there always exists a lowest Efimov state in the spectrum. From now on, we will identify this state with the number $n = 0$. As discussed above, one key experimental signature of Efimov physics is the resonant enhancement of the three-body recombination rate when the nth Efimov state meets the atom threshold at a scattering length $a_-^{(n)}$. In practice, it is, however, often only the lowest Efimov state at $a_- \equiv a_-^{(0)}$ that can be observed because of large atom losses as the scattering length increases, cf. Eq. (2.13). As more experimental data have been accumulated in recent years [47, 128, 129, 130, 131, 132, 133, 134, 135], a puzzling observation came to light: in most experiments, the measured values for a_- clustered around $a_- \approx -9.45\, l_{\rm vdw}$, no matter which alkali atoms were used. In consequence, this observation suggests a three-body parameter which is indeed independent of the microscopic details. But where does this apparent 'universality of the three-body parameter' come from? A possible answer to this question is based on the observation that, typically, Efimov trimers which are accessible with ultracold atoms appear in a situation where the scattering length is tuned via a Feshbach resonance. Here the scattering length is greatly modified and enhanced due to the presence of a molecule in a closed scattering channel. Thus the underlying microscopical mechanism is similar in all experiments. If the three-body parameter is additionally not too sensitive to the remaining differences, the observed 'universality' may appear not too surprising after all.

Feshbach resonances are characterized by an additional parameter, the width r^*, which introduces a new scale into the system. In the following we present a theory for the three-body physics of ultracold atoms close to a Feshbach resonance of arbitrary width. For so-called open-channel dominated resonances, where $r^*/l_{\rm vdw}$ is very small, we find as a main result that the lowest Efimov state appears at $a_- \approx -8.3\, l_{\rm vdW}$ consistent with experiments. These open-channel dominated Feshbach resonances can, under certain conditions, be described by a single-channel picture. Such a single-channel picture has been employed in recent, independent work by Wang and coworkers [143] and Chin [144] where results similar to ours have been found. Irrespective of the short distance behavior, single-channel potentials with a van der Waals tail are known to have $l_{\rm vdw}$ as the only relevant length scale at energies much smaller than the depth of the potential well [145]. In the absence of genuine three-body forces, it is plausible that this result extends to the three-particle Efimov problem and thus, that $l_{\rm vdw}$ provides the characteristic scale for the three-body parameter.

While being consistent with the observed correlation between a_- and the van der Waals length $l_{\rm vdw}$ for a number of different alkalis, such a single-channel description does not apply in general and suggests a universality of the ratio $a_-/l_{\rm vdw}$ which is far too general even within the constraint that only two-body interactions play a role. In particular, a single-channel description cannot apply for closed-channel dominated Feshbach resonances. In this case, it is known that the three-body parameter is set by the intrinsic length $r^\star$ which determines the strength of the Feshbach coupling [146, 147].

In the following, we present an exact solution for the Efimov spectrum within a standard two-channel model [92] which incorporates the finite range of the Feshbach coupling and properly recovers both limits of open-channel *and* closed-channel dominated resonances. It provides a complete description of the trimer spectrum in terms of only two, experimentally accessible, parameters: the van der Waals length $l_{\rm vdw}$ and the intrinsic length $r^\star$. Depending on the dimensionless resonance strength $s_{\rm res} = 0.956\, l_{\rm vdw}/r^\star$ [92], there is a continuous change in the relation between the trimer energy and the scattering length, with the lowest Efimov state appearing at $a_- \approx -8.3\, l_{\rm vdw}$ as $s_{\rm res} \gg 1$ while $a_- \approx -10.3\, r^\star$ in the opposite limit $s_{\rm res} \ll 1$. This model provides a minimum description of the Efimov spectrum which is based on two-body physics only and has no adjustable parameter. It explains why the ratio $a_-/l_{\rm vdw}$ is in the observed range for open-channel dominated resonances and predicts strong deviations from this in the intermediate regime $s_{\rm res} = \mathcal{O}(1)$.

2.3 Two-channel model

In cold atoms the scattering length a can be tuned by means of Feshbach resonances [87, 88]. Here one takes advantage of the fact that during a collision the pair of atoms can virtually change their spin configuration. In the different spin configuration they interact then via a different scattering potential, which is, due to the Zeeman effect, shifted with respect to the potential of the incoming atoms when an external magnetic field is applied. For an illustration, see Fig. 2.8. If the Zeeman energy shift $\sim \mu B$ is larger than the typical kinetic energy of the colliding particles (in the so-called open channel), the scattering states of the spin-flipped chan-

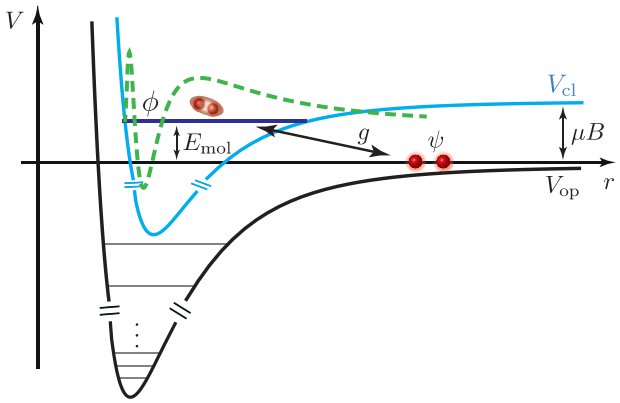

FIGURE 2.8: *Feshbach resonance model. During their collision the atoms ψ in the open channel can virtually flip their hyperfine spin state. The presence of a magnetically tunable molecule ϕ in the closed channel leads to an enhanced scattering cross section. A detailed discussion is given in the main text.*

nel are energetically inaccessible. Thus the latter is called the closed channel. Both the open and the closed channel typically support many vibrational bound states. When tuning the magnetic field, vibrational bound states of the closed channel cross the scattering threshold of the open channel which causes an enhancement of the scattering cross section. In the following we explain this mechanism, which leads to so-called Feshbach resonances, by introducing a simple two-channel model.

Let us concentrate on one of the closed-channel molecular states which we denote by the field ϕ, cf. Fig. 2.8. Its *bare* energy is detuned by an amount E_{mol} from the open-channel threshold. Due to the coupling of the open and closed channel, the closed-channel molecule is renormalized and becomes a quantum mechanical superposition of open- and closed-channel states. When this *renormalized* state is crossing the threshold it causes a resonance in the scattering length which can be parametrized by the phenomenological formula [92]

$$a(B) = a_{\mathrm{bg}} - \frac{2}{r^* \mu (B - B_0)}. \tag{2.19}$$

Here, μ is the difference in the magnetic moment between the molecule and the open-channel atoms, and B_0 is the magnetic field where the divergence in a appears. a_{bg} denotes the background scattering length caused by the scattering solely in the open channel when no coupling to the closed channel is present. The parameter r^* characterizes the width of the resonance as function of the magnetic field. It is determined by the dimensionless 'strength' s_{res} of the Feshbach resonance which is given by [92]

$$s_{\mathrm{res}} = \frac{\bar{a}}{r^*}, \tag{2.20}$$

and where we introduced the so-called mean scattering length [148]

$$\bar{a} = \frac{4\pi}{\Gamma(1/4)^2} l_{\mathrm{vdw}} = 0.95598\ldots l_{\mathrm{vdw}}. \tag{2.21}$$

We will find that r^* plays an important role in our study of non-universal corrections in Efimov physics. Feshbach resonances characterized by $s_{\mathrm{res}} \ll 1$ ($s_{\mathrm{res}} \gg 1$) are termed *closed-(open-)channel dominated resonances*.

Our goal is to explain the observed universality of the three-body parameter mentioned in Section 2.2 within a simple model. The experimental observations indicate that the first Efimov bound state appears for rather large scattering lengths a of order $a_- \sim -10\, l_{\mathrm{vdw}}$. Typical background scattering lengths are of the order of the van der Waals length[7] [92], such that the scattering length needed to enter the regime of Efimov trimers is mainly due to the second term in Eq. (2.19), which originates from the coupling of the open to the closed channel. Based on the dominant role of this term, we are justified to neglect the first term in Eq. (2.19). The scattering length is then given by

$$a(B) = -\frac{2}{r^* \tilde{\nu}(B)}, \qquad \tilde{\nu}(B) = \mu(B - B_0), \tag{2.22}$$

where $\tilde{\nu}(B)$ defines the renormalized dimer binding energy. Neglecting the background interaction potential altogether, the system is described by the following classical action for non-relativistic bosons [91, 149, 150, 151, 152],

$$\begin{aligned} S &= \int_{\mathbf{r},t} \left\{ \psi^*(\mathbf{r},t)[i\partial_t - \nabla^2]\psi(\mathbf{r},t) + \phi^*(\mathbf{r},t) \overbrace{\left[i\partial_t - \nabla^2/2 + E_{\mathrm{mol}}(B) \right]}^{P_\phi^{\mathrm{cl}}} \phi(\mathbf{r},t) \right\} \\ &+ \frac{g}{2} \int_{\mathbf{r}_1,\mathbf{r}_2,t} \chi(\mathbf{r}_2 - \mathbf{r}_1) \left[\phi\left(\frac{\mathbf{r}_1 + \mathbf{r}_2}{2}, t \right) \psi^*(\mathbf{r}_1,t)\psi^*(\mathbf{r}_2,t) + c.c. \right], \end{aligned} \tag{2.23}$$

where we use natural, non-relativistic units $\hbar = 2m = 1$. Here, ψ denotes the atoms in the open channel and ϕ the molecule in the closed channel. We introduced the *bare* detuning of the closed-channel molecule $E_{\mathrm{mol}}(B) = \mu(B - B_{\mathrm{res}})$, cf. Fig. 2.8, where B_{res} describes the threshold crossing of the molecule when no closed- to open-channel coupling were present. The molecule ϕ has the same classical, Schrödinger propagator as the atoms besides a factor of two reflecting that the molecule consists of two atoms and thus has twice the mass.

The term $\sim g$ describes the conversion of two atoms into the closed-channel molecule with coupling strength g: two atoms ψ at separation $|\boldsymbol{r}_2 - \boldsymbol{r}_1|$ are annihilated and a molecule ϕ is created at the corresponding center of mass coordinate. Note, that for a description of

[7] ^{6}Li and ^{133}Cs are examples of alkalis which feature a large background scattering length, $|a_{\mathrm{bg}}|/l_{\mathrm{vdw}} \gg 1$. While ^{6}Li is fermionic and thus less relevant for our study, ^{133}Cs has a background scattering length which is large and *positive*. As the Efimov phenomenon we are after appears for *negative* scattering length, however, the second term in Eq. (2.19) is even more dominant in this case.

universal features of Efimov physics, like the asymptotic ratio $a_-^{(n+1)}/a_-^{(n)} \to e^{\pi/s_0}$, this atom-molecule conversion amplitude $\sim g$ may be taken as pointlike in coordinate space [66, 100, 101] which simplifies calculations considerably. In reality, however, it is apparent that the conversion coupling has a finite range σ which is determined by the scale of the wave function overlap between the open- and closed-channel states. As has been pointed out by a number of authors [149, 150, 153, 154, 155, 156], this can be accounted for by a form factor $\chi(r)$ in Eq. (2.23). Although the precise form of $\chi(r)$ depends on the (short-range) details of the interatomic potentials, and thus is unknown, we choose an exponential form factor $\chi(r) \sim e^{-r/\sigma}/r$. This form mimics the asymptotics of the bound state wave function in the closed channel (green dashed line in Fig. 2.8) which is a weakly bound state for the usually small magnetic fields employed in experiments. In momentum space this leads to $\chi(p) = 1/(1+\sigma^2 p^2)$.

As we will show below, the characteristic range σ is given by the van der Waals or the mean scattering length $\bar{a} \approx 0.96\, l_{\rm vdw}$. In physical terms, this reflects the fact that the classical turning point in the closed-channel states is of the order of $l_{\rm vdw}$ because, as just mentioned, for typical magnetic field-tuned Feshbach resonances, it is only the weakly bound states in the closed channel which are close to the continuum threshold that are experimentally accessible. In contrast to the more standard Gaussian cutoff [149, 150, 153], our choice for $\chi(r)$ is optimal in the sense that the resulting effective range $r_e = 3\bar{a}$ of two-body scattering near an open-channel dominated Feshbach resonance (see Eq. (2.34) below) agrees very well with the standard result $r_e \approx 2.92\,\bar{a}$ [145] for a single-channel potential with an $1/r^6$ tail.

The action (2.23) has three open parameters: g, $B_{\rm res}$, and σ. Our goal is to fix these by experimentally observable two-body physics. All three-body observables will then be a prediction with no adjustable parameters at all. In order to achieve this let us derive the two-body scattering properties of the model (2.23).

Determination of model parameters

The two-body problem can be solved exactly by computing the renormalization of the dimer propagator $P_\phi^{\rm cl}$, cf. Eq. (2.23). Evaluating the standard ladder diagram one obtains the full inverse, retarded dimer propagator $\mathcal{G}_\phi^{-1}$ which reads

$$\mathcal{G}_\phi^{-1}(E,\mathbf{q}) = -E + \frac{\mathbf{q}^2}{2} + E_{\rm mol}(B) - i\epsilon - \frac{g^2/(32\pi)}{\sigma\left[1+\sigma\sqrt{-\frac{E}{2}+\frac{\mathbf{q}^2}{4}-i\epsilon}\right]^2}, \tag{2.24}$$

and where the last term can be interpreted as the self-energy of the dimer. Note that due to the finite range of the 'Yukawa'-type coupling $\sim g$ the regularization of the ladder is automatically taken care of such that the corresponding integral can be straightforwardly evaluated.

The scattering of two atoms in the open channel is mediated by the exchange of the molecule ϕ. Evaluating the tree-level diagram shown in Fig. 2.9 (where the dashed (solid) line denotes the propagation of a *full* dimer (atom) and the dot represents the Yukawa coupling

$\sim g$) one obtains the scattering amplitude

$$f(k) = \frac{g^2 \chi(k)^2}{16\pi} \mathcal{G}_\phi(2k^2, \mathbf{0}). \tag{2.25}$$

Here, the scattering is evaluated in the center of mass frame with incoming atoms of momenta $\pm\boldsymbol{k}$ and total energy $E = 2k^2$ with $k = |\boldsymbol{k}|$. The low-energy expansion of the scattering amplitude defines the scattering length and effective range:

$$f(k) = \frac{1}{-1/a + r_e k^2/2 + \mathcal{O}(k^4) - ik}. \tag{2.26}$$

By expanding the exact solution (2.25) in small k and comparing the result with Eq. (2.26) the experimentally accessible scattering length can be extracted from our model. One finds

$$\frac{1}{a} = \frac{1}{2\sigma} - \frac{16\pi}{g^2} E_{\mathrm{mol}}(B). \tag{2.27}$$

The bound state energy spectrum can in turn be obtained from the poles of dimer Green's function $\mathcal{G}_\phi(E, \mathbf{0})$ in Eq. (2.24). It is shown in Fig. 2.10(a) in dependence of the magnetic field for finite coupling $g > 0$ (solid line) and also for the case when no open- to closed-channel coupling is present, $g = 0$ (dashed line). It is possible to derive an analytical expression for the dimer energy $E_D = E_D(B)$ but as it is a very lengthy expression we refrain from showing it here explicitly. In Fig. 2.10(b) we display the scattering length obtained from Eq. (2.27) in dependence of B for the same parameters as in Fig. 2.10(a).

Without any coupling between the open and closed channel, i.e. $g = 0$, the bound state spectrum is very simple. There is the two-atom threshold at $E = 0$ and the closed-channel molecule at $E = \mu(B - B_{\mathrm{res}})$. Contrarily, for nonzero g the position where the dimer reaches the threshold and then vanishes in the scattering continuum, is shifted by[8] $\Delta B = B_{\mathrm{res}} - B_0$ and accordingly the resonance in $a(B)$ appears at B_0, cf. Fig. 2.10(b). The resonance shift ΔB is readily obtained from Eq. (2.27) evaluated at $B = B_0$, and one finds

$$\mu \Delta B = \mu(B_0 - B_{\mathrm{res}}) = \frac{g^2}{32\pi\sigma}. \tag{2.28}$$

[8]Note, ΔB must not be confused with the *magnetic* width of the Feshbach resonance.

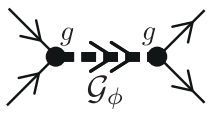

FIGURE 2.9: *Tree level diagram yielding the effective atom-atom scattering amplitude Eq.* (2.25).

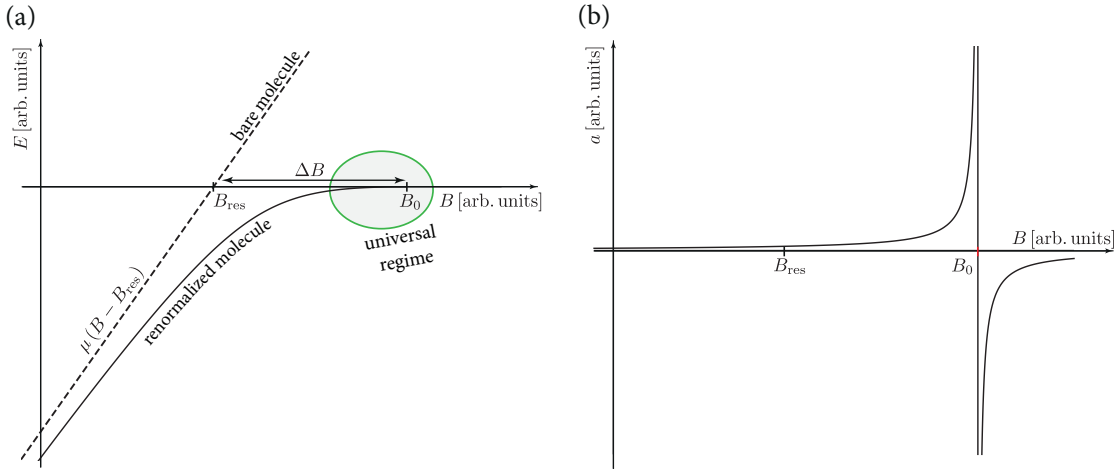

FIGURE 2.10: *(a) Energy spectrum of the two-channel model* (2.23)*. The energy of the molecular state ϕ is shifted with respect to the non-interacting, bare state (dashed line) due to the a nonzero coupling of closed- and open-channel states for $g \neq 0$ (solid line) (b) Scattering length a as function of magnetic field B for the same parameters as in (a).*

The magnetic field dependence in Eq. (2.27) can be compared to Eq. (2.22):

$$a = \frac{1}{\frac{1}{2\sigma} - \frac{16\pi}{g^2}\mu(B - B_{\text{res}})} = -\frac{2}{r^*\mu(B - B_0)}. \tag{2.29}$$

The insertion of μB_{res} from Eq. (2.28) into this expression gives the identification of the coupling g,

$$g^2 = \frac{32\pi}{r^*}. \tag{2.30}$$

The Feshbach range r^* is accessible from the experimentally measured Feshbach resonance profiles $a(B)$ or from a fit of the dimer binding energy close to resonance. Since the resonance position B_0 is experimentally measurable as well, Eq. (2.28) fixes the parameter B_{res} in our model. The only parameter now left is the range σ. Here we exploit that the resonance shift ΔB, cf. Eq. (2.28), which is always positive in our model, has previously been calculated by Julienne and coworkers using quantum defect theory for a multi-channel model with microscopic interaction potentials that have a van der Waals tail [157]. They obtain (see Eq. (15) in [150])

$$\mu\Delta B = \frac{2}{r^*\bar{a}} \frac{1 - a_{\text{bg}}/\bar{a}}{1 + \left(1 - a_{\text{bg}}/\bar{a}\right)^2} \overset{a_{\text{bg}}\to 0}{=} \frac{1}{r^*\bar{a}}. \tag{2.31}$$

Comparing this with Eq. (2.28) finally yields[9]

$$\sigma = \bar{a}. \tag{2.32}$$

All parameters of our model are now fixed by two-body physics only. Let us summarize the identifications made:

from scattering length profile $a(B)$:	g	$\Longleftrightarrow$	r^*
from resonance shift Eq. (2.28) compared to measurement of B_0:	$\mu B_{\rm res}$	$\Longleftrightarrow$	μB_0
from resonance shift Eq. (2.28) compared to quantum defect theory, Eq. (2.31):	σ	$\Longleftrightarrow$	$l_{\rm vdw}$

Finally we comment on the effective range approximation which has been employed in recent work on Efimov physics [158, 159]. Within the effective range approximation one uses in the three-body calculation the scattering amplitude $f(k)$ expanded up to order k^2

$$f(k) = \frac{1}{-1/a + r_e k^2/2 - ik}, \tag{2.33}$$

where in our model the effective range r_e is obtained from expanding the exact $f(k)$ in Eq. (2.25),

$$r_e = -2r^* + 3\sigma\left(1 - \frac{4\sigma}{3a}\right). \tag{2.34}$$

It has to be emphasized that the use of Eq. (2.33) together with Eq. (2.34) is an approximation. It will *not* be employed in our following three-body calculation. We comment on this approximation at this point, as on the one hand the analysis of the effective range Eq. (2.34) is instructive and on the other hand we want to comment on the range of applicability of the effective range approximation.

In the limit where the physical range σ goes to zero the effective range is given by

$$r_e = -2r^* < 0 \quad (\sigma = 0), \tag{2.35}$$

which is negative as required by the causality bound derived by Wigner [160], see also [161]. The resulting model respecting Eq. (2.35) is known as the effective range or resonance model.

[9] Note, alternatively σ can also be determined from a fit of the measured dimer energy spectrum.

It will be studied in detail in Section 2.8. Taking the additional limit $r^* \to 0$ corresponds to the scaling limit.

We emphasize that for finite $\sigma > 0$ the limit $r^* \to 0$ is well-defined and yields the physics of open-channel dominated Feshbach resonances with an effective range given by $r_e = 3\sigma$ on resonance. In this case, upon integrating out the field ϕ in the action (2.23), one obtains an effective action for the atoms ψ where the dynamical part of the inverse propagator P_ϕ^{cl} can be completely neglected as can be seen from evaluating the corresponding tree-level diagram shown in Fig. 2.9. The action then describes a single-channel model with an effective range of the atom-atom coupling which is in good agreement with the value obtained from a single-channel model with true van der Waals potentials [145]. Thus we may expect that our model also describes situations well where the scattering physics is solely dominated by a background scattering potential with a van der Waals tail. This also explains the good agreement of our results, to be derived in the following, with the one obtained in the single-channel calculations by Wang *et al.* [143]. Note however, that as long as $\sigma > 0$, the single-channel model obtained from integrating out the field ϕ in the limit of open-channel dominated Feshbach resonances is still *not equivalent* to a single-channel model featuring a van der Waals type interaction. The difference is that in such a 'standard' single-channel model the van der Waals interaction takes place in the *density channel* while the two-channel model, after integrating out ϕ, becomes equivalent to a single-channel model with an interaction of finite range in the *pairing channel*.

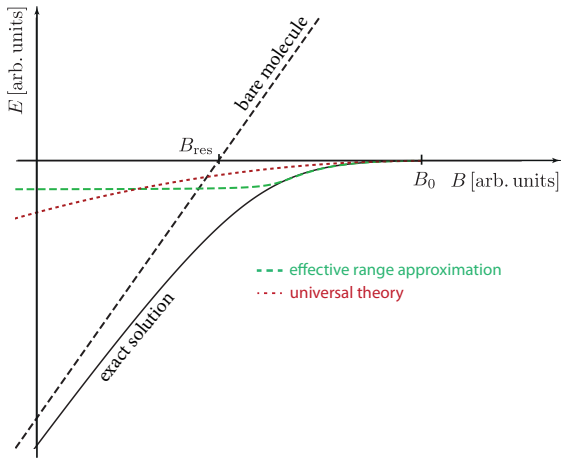

FIGURE 2.11: *Molecule energy obtained from the exact expression* (2.25) *(solid black) compared to the effective range approximation Eq.* (2.36) *and* (2.34) *(dashed green). The result for the universal dimer energy* $E_D = -2/a^2$ *is shown as dotted, red line.*

Coming back to the effective range approximation, we compare the exact bound state spectrum as shown in Fig. 2.10(a) to the spectrum obtained from Eqn. (2.33) and (2.34) in order to estimate the range of validity of this approximation. The result is shown in Fig. 2.11 (dashed line) for a relatively open-channel dominated resonance with $s_{\mathrm{res}} = 10$. We also show

the universal formula $E_D = -2/a^2$ (dotted line). Within the effective range approximation the scattering amplitude has a pole corresponding to a bound state energy

$$E_D = -\frac{2}{r_e^2}\left(1 - \sqrt{1 - \frac{2r_e}{a}}\right)^2 . \tag{2.36}$$

The apparent breakdown for $a < 2r_e$ and $r_e > 0$ is prevented by the scattering length dependence of r_e itself, cf. Eq. (2.34). Note that keeping an effective range independent of the scattering length is not sufficient. The effective range expansion has a wider range of applicability when the closed-channel character of the resonance increases, $s_{\rm res} \to 0$, since then r^* dominates Eq. (2.34).

2.4 *Functional renormalization group approach*

In the following we will exactly solve the three-body problem for the action given by Eq. (2.23) using the functional renormalization group. Although there is no three-body coupling present in the action (2.23), quantum fluctuations will generate an effective interaction between atoms and dimers described by a term

$$\sim \int_{Q_1,Q_2,Q_3} \lambda_3(Q_1,Q_2,Q_3)\phi^*(Q_1)\psi^*(Q_2)\phi(Q_3)\psi(Q_1+Q_2-Q_3), \tag{2.37}$$

where the four-momenta $Q_i = (E_i, \boldsymbol{q}_i)$ include energy and momentum. A process leading to the generation of the vertex λ_3, even in absence of a microscopic three-body coupling, is given by the diagram

$\lambda_3 \sim$  (2.38)

where dashed lines denote (full) dimer propagators, solid lines atom propagators, and the vertex dots represent the atom-dimer conversion (Yukawa) coupling $\sim g$. The vertex λ_3 develops a complicated energy and momentum dependence and poles in this vertex signal the presence of Efimov bound states.

Within a standard effective field theory approach the solution of the three-body problem amounts to a self-consistent solution of the set of integral equations shown in Fig. 2.12 [100, 101, 163]. When few-body physics is concerned only, the set of equations corresponding to these diagrams yields the exact solution of the three-body problem. It is rather remarkable how small the set of equations is considering that one is dealing with a strong-coupling problem. And indeed, in a *many*-body problem, the situation is much more complex. In this case, one has to deal with the fact that in general there is an infinite hierarchy of coupled equations

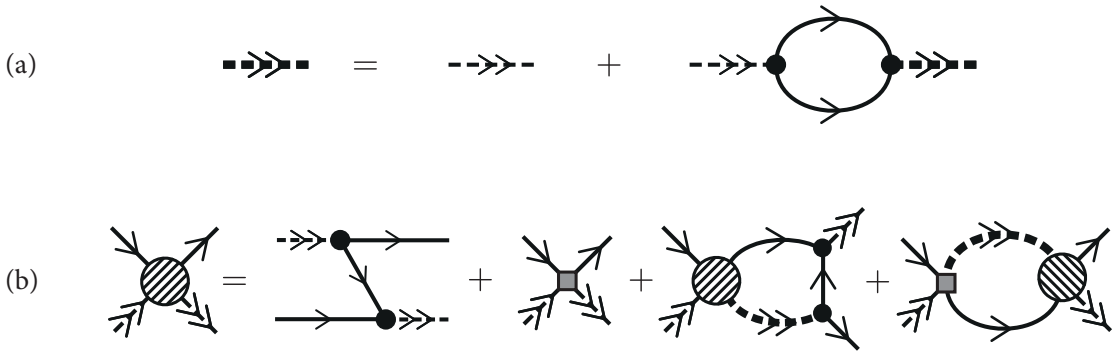

FIGURE 2.12: *Integral equations for the (a) two-body problem (Lippmann-Schwinger equation) and the (b) three-body problem (Skornyakov-Ter-Martirosyan (STM) equation [162]). Thick, dashed lines denote the full dimer propagator, thin lines atoms. Further symbols are: Yukawa coupling (small circle), bare atom-dimer coupling (gray square), and full atom-dimer vertex (dashed, big circle).*

describing infinitely high n-body couplings.[10] For instance, consider the vertex $\lambda_4(\phi^*\phi)^2$ which belongs to the four-body sector. It describes dimer-dimer scattering and is generated by quantum fluctuations of the type

(2.39)

In the generic many-body setting, it couples back to the two-body sector by a tadpole diagram as shown in Fig. 2.13(a). The same 'backfeeding' takes place for the atom-dimer coupling λ_3. In the many-body problem it influences the one- and two-body sector via the diagrams shown in Fig. 2.13 (b-c). These diagrams in turn would yield additional contributions to the integral equation in Fig. 2.12, rendering the exact solution of the problem inaccessible.

In the few-body problem, however, the density of particles is zero and thus no holes can be present. This is a direct consequence of the fact that in non-relativistic few-body physics one studies the excitations out of the vacuum state and not out of a many-body ground state, which for example may be a filled Fermi sea or a Bose-Einstein condensate. Diagrams generating a coupling belonging to an n'-body sector which involve a higher-n-body vertex with $n > n'$, always involve the propagation of at least one hole and thus they vanish.

This can also be understood from the statistical physics point of view. While in the many-body problem the partition function is taken with respect to the set of many-body states

[10] In the following we will often use the notion of n-body couplings or sectors. This shall define the set of (interaction) terms which describe n in- and outgoing particles. Here the fundamental field ψ counts as one particle, while the composite field ϕ corresponds to two particles as given by their respective charge under the global U(1) symmetry.

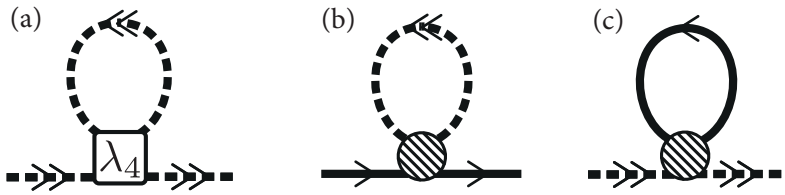

FIGURE 2.13: *Diagrams where higher n-body couplings feed back into lower $n' < n$-body sectors. They vanish in the few-body problem.*

compatible with the desired particle number (or, if grand-canonical, the chemical potential), in the few-body problem the partition function is taken with respect to the vacuum only. In non-relativistic physics, it is impossible to annihilate a particle out of this vacuum. This is different from relativistic, 'few-body' high-energy physics where in a sense the vacuum reminds much more of non-relativistic many-body physics. Here, antiparticles can be excited out of the vacuum, and thus arguments applying to non-relativistic few-body physics do not hold anymore. In summary, with the arguments outlined above one can show the so-called vacuum hierarchy [46, 66] which states that in the few-body problem the n-body sector cannot influence the n'-body sectors for $n' < n$. Note that in the context of fRG flow equations the argument becomes more subtle [164, 165]. As recently shown by Tanizaki [164], depending on the choice of regulators there are additional equations to be considered to close the set of few-body flow equations. In the following we, however, employ a regulator scheme which respects the vacuum hierarchy as also pointed out in [164].

Since we only want to solve the three-body problem, we can ignore the quantum generation of the four-body and higher order couplings by virtue of the vacuum hierarchy. Therefore the only equations to be solved are the ones displayed in Fig. 2.12. These equations have to be solved self-consistently which means that the *full*, exact dimer propagator, cf. Fig. 2.12(a), has to be inserted into the equation for the three-body coupling λ_3, displayed in Fig. 2.12(b). The solution of the three-body problem thus consists of several steps: the two-body problem has to be solved, the three-body integral equation has to be derived, and finally, it has to be solved as well. In order to achieve this we choose to use the functional renormalization group for two reasons. First, the derivation of the three-body equation becomes particularly simple in this approach, and secondly, it offers the solution of the few-body problem within a framework which allows not only to tackle the few-body problem but also the much more complex many-body problem within the same, unified approach.

The functional renormalization group (fRG) is introduced in Appendix C and some computational details will be covered in Chapter 4. For detailed reviews, we refer to [166, 167, 168, 169, 170, 171, 172, 173, 174, 175]. In brief, the fRG uses an RG scale k dependent generating functional Γ_k – the so-called *effective average action* – which interpolates between the classical action $S = \Gamma_{k=\Lambda}$, when k equals the UV cutoff scale Λ of the theory, and the full (quantum) effective action $\Gamma = \Gamma_{k=0}$, when k reaches the infrared, by successively including quantum fluctuations on momentum scales $p \gtrsim k$.

The effective action $\Gamma = \Gamma[\psi, \phi]$ is the generating functional of all 1PI vertex functions and

thus the knowledge of Γ is equivalent to having solved the many-body Schrödinger equation. The evolution of Γ_k with the RG scale k is governed by the non-perturbative renormalization group equation [176]

$$\partial_k \Gamma_k = \frac{1}{2}\mathrm{Tr}\frac{1}{\Gamma_k^{(2)} + R_k}\partial_k R_k. \tag{2.40}$$

Using this RG equation we derive the *exact* effective action Γ of the three-body problem in the s-wave channel described by the underlying action (2.23). This problem presents one of the rare examples where the RG evolution of a non-trivial problem can actually be solved exactly. As such, it is of interest from an RG perspective alone, since it offers the possibility to study the consequences of regulator choices in (2.40) on the basis of an exact solution. This has to some extent been done in a similar context studying SU(2) fermions in [177] and open questions concerning an observed regulator dependence have been resolved in [164].

The functional $\Gamma[\psi, \phi]$ contains all possible terms of ψ and ϕ allowed by the symmetries. The first step in solving Eq (2.40) is to single out a truncation of Γ_k which contains the *complete* information about the three-body problem. In general, infinitely many couplings of arbitrarily high order are generated during the RG flow, e.g. terms $\sim (\psi^*\psi)^n$, $\sim \phi^*\phi^*\psi^4$ etc. By the virtue of the vacuum hierarchy, however, the $n \geq 4$-body sector does not feed back to the lower $n \leq 3$ body sectors. It is for this reason that we can write down an exact and complete vertex truncation of Γ_k for the three-body problem. It reads

$$\begin{aligned}\Gamma_k &= \int_{\mathbf{r},t}\Big\{\psi^*(\mathbf{r},t)[i\partial_t - \nabla^2]\psi(\mathbf{r},t) + \phi^*(\mathbf{r},t)P_{\phi,k}(i\partial_t, \nabla^2/2)\phi(\mathbf{r},t)\Big\} \\ &+ \frac{g}{2}\int_{\mathbf{r}_1,\mathbf{r}_2,t}\chi(\mathbf{r}_2-\mathbf{r}_1)\Big[\phi(\frac{\mathbf{r}_1+\mathbf{r}_2}{2},t)\psi^*(\mathbf{r}_1,t)\psi^*(\mathbf{r}_2,t) + c.c.\Big] + \Gamma_k^{\mathrm{3B}},\end{aligned} \tag{2.41}$$

where Γ_k^{3B} is the three-body term generated by quantum fluctuations which reads [cf. Eq. (2.37)]

$$\Gamma_k^{\mathrm{3B}} = -\int_{Q_1,Q_2,Q_3}\lambda_3^{(k)}(Q_1,Q_2,Q_3)\phi^*(Q_1)\psi^*(Q_2)\phi(Q_3)\psi(Q_1+Q_2-Q_3). \tag{2.42}$$

Note, that there are more terms in Eq. (2.41) allowed by the symmetries of the problem such as e.g. $\lambda_2(\psi^*\psi)^2$, or $\xi_3(\psi^*\psi)^3$, which would be generated by diagrams of the form shown in Fig. 2.14. These diagrams however vanish because holes appear in the loops. Note, the coupling $\lambda_2(\psi^*\psi)^2$ generated by the diagram in Fig. 2.14(a) would induce a flow of the Yukawa coupling g. Since λ_2 remains, however, zero during the flow, the Yukawa coupling is not renormalized, $\partial_k g \equiv 0$. For this reason the only running couplings to be introduced in the truncation of Γ_k are the inverse dimer propagator $P_{\phi,k}$ and the atom-dimer coupling $\lambda_3^{(k)}$. Both couplings are complicated functions of momenta and frequencies so that one technically has to deal with an infinite set of coupled flow equations.

The flow equations for $P_{\phi,k}$ and $\lambda_3^{(k)}$ are derived upon insertion of Eq. (2.41) into Eq. (2.40) and by taking the suitable functional derivatives with respect to the fields at fixed external momenta. The flow equations are displayed in terms of diagrams in Fig. 2.15.

FIGURE 2.14: *(a) Diagram generating an atom-atom scattering term* $\sim \lambda_2(\psi^*\psi)^2$ *which belongs to the two-body sector. Since it contains holes in the loop, it vanishes in the non-relativistic vacuum. (b) Diagrams generating a three-atom scattering term* $\sim \gamma(\psi^*\psi)^3$ *which belongs to the three-body sector. Since the diagrams contain holes in the loop, they vanish as well.*

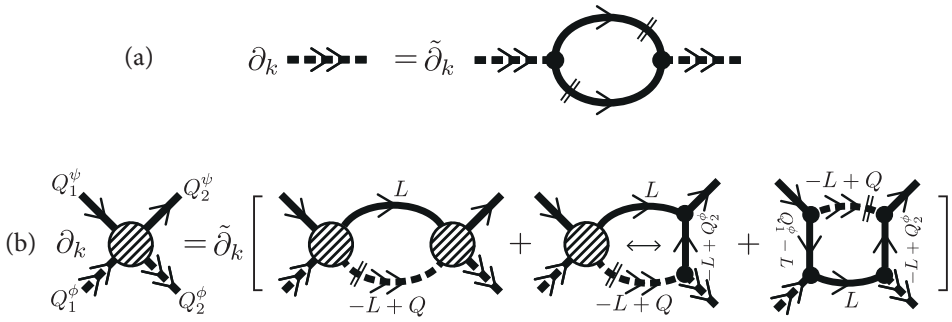

FIGURE 2.15: *RG flow equations in terms of Feynman diagrams. Lines with one (two) arrows denote atoms (dimers). The two thin lines cutting internal lines denote regulated, inverse propagators* $P^c_{\psi/\phi} = P_{\psi/\phi} + R_{\psi/\phi}$. *(a) Flow equation of the inverse dimer propagator* $P_{\phi,k}$. *(b) Flow equation of the atom-dimer coupling* $\lambda_3^{(k)}$.

We have now to devise an RG scheme which yields infrared vertices $P_\phi = P_{\phi,k=0}$ and $\lambda_3 = \lambda_3^{(k=0)}$ which in turn solve the self-consistent equations displayed in Fig. 2.12. In order to achieve this we have to first integrate the flow of the dimer propagator and then insert its infrared solution into the flow of $\lambda_3^{(k)}$. Remarkably, this RG flow prescription can be implemented by a specific choice of regulators R_ψ and R_ϕ which we put forward in [96]. It is based on the observation that in every diagram belonging to the three-body sector one dimer appears in the loop while in the two-body sector only atoms are present. Thus we can choose a dimer regulator which stays extremely large while we are lowering the atom regulator R_ψ to zero in a first RG step. The result is then the *full*, exact solution of the two-body problem. In a second RG step we then lower the dimer regulator R_ϕ. By inspection of Fig. 2.15(b) we see that the internal atom lines are then not regularized anymore and only a regulator on the dimer lines remains. As a result of this second RG step we obtain the full, exact solution of the three-body problem. A similar scheme has been used by Diehl *et al.* for the solution of the atom-dimer scattering problem of fermions [177]. Moroz *et al.* then introduced the notion of

the two-step RG prescription [111] for the solution of the three-body Efimov problem in the scaling limit. Here we adapt this method to solve the three-body problem for the finite-range action (2.23) for arbitrary energies and scattering lengths, cf. [178].

In the end, this prescription amounts to solving first the two-body problem exactly, and then using the resulting dimer propagator $\mathcal{G}_\phi = 1/P_{\phi,k=0}$ as input for the flow equation of $\lambda_3^{(k)}$ depicted in Fig. 2.15. We already derived the solution of the two-body problem in Section 2.3, cf. Eq. (2.24). It is however instructive to re-derive this result using the fRG method. For similar treatments, see [46, 96, 177].

Exact solution of the two-body problem

The flow equation of $P_{\phi,k}$ is given by

$$\partial_k P_{\phi,k}(Q) = -\frac{1}{2}\int_P \tilde{\partial}_k \frac{g^2 \chi(|\mathbf{p}+\mathbf{q}/2|)^2}{[P_\psi(-P)+R_\psi(-P)][P_\psi(Q+P)+R_\psi(Q+P)]}. \tag{2.43}$$

Here, the symbol $\tilde{\partial}_t$ implies that the scale derivative only acts on the explicit k dependence of the regulators R_ψ. Equation (2.43) can be solved analytically for various regulators R_ψ. The particle-particle loop shown in Fig. 2.15(a) would diverge in the case of zero-range interactions if no regulator were present and each choice of R_ψ represents a different regularization scheme for this loop. Here we use the particularly simple form

$$R_{\psi,k}(Q) = k^2 \tag{2.44}$$

which simply adds a static gap to the atoms. Note that the Yukawa coupling g can be placed in front of the integral, because $\tilde{\partial}_k$ acts only on the regulator and furthermore g is not dependent on k anyway. After having performed the frequency integration, the flow equation reads

$$\partial_k P_{\phi,k}(\boldsymbol{q},E) = -\frac{g^2}{2}\tilde{\partial}_k \int \frac{d^3p}{(2\pi)^3}\frac{\chi(|\boldsymbol{p}|)^2}{-E+2\boldsymbol{p}^2+\boldsymbol{q}^2/2+2k^2}, \tag{2.45}$$

where used a shift in the integration variable $\boldsymbol{p} \to \boldsymbol{p}-\boldsymbol{q}/2$ which makes the angular integration trivial. Since no coupling appearing in Eq. (2.45) is k-dependent we are allowed to replace $\tilde{\partial}_k$ by ∂_k upon which we can directly perform the RG flow by integrating the flow equation from $k = 0$ up to the UV cutoff scale $k = \Lambda$. We obtain the infrared, (retarded) inverse dimer propagator

$$\begin{aligned}\mathcal{G}_\phi^{-1}(E,\mathbf{q}) &= P_\phi(\boldsymbol{q},E) = P_{\phi,\Lambda}(\boldsymbol{q},E) + \frac{g^2}{8\pi^2}\int_0^\infty d\,p\,p^2\chi(p)^2 \\ &\quad\times\left[\frac{1}{-E+2p^2+\boldsymbol{q}^2/2+2\Lambda^2-i\epsilon} - \frac{1}{-E+2p^2+\boldsymbol{q}^2/2-i\epsilon}\right].\end{aligned} \tag{2.46}$$

Here, $P_{\phi,\Lambda}(E,p)$ equals P_ϕ^{cl} defined in Eq. (2.23).

For a finite value $\sigma > 0$ the momentum integral is regularized by the finite range of $\chi(r)$ which gives an additional $1/\boldsymbol{p}^2$ decay for large momenta. We may therefore directly take the UV limit $\Lambda \to \infty$. Note, that this is different from the case of zero-range potentials which has been discussed previously in the context of the fRG [46, 96, 177] and which is subject of most literature on Efimov physics [66]. In this case, $\chi(p) = 1$ and the limit $\Lambda \to \infty$ cannot be taken right away since then the second term in Eq. (2.46) diverges upon integration. Instead, Λ has to be kept finite so that the first term in the bracket in Eq. (2.46) is responsible for the regularization. The now convergent integral is evaluated, the Λ-dependence absorbed in the definition of the UV dimer propagator (renormalization) and *in the end* the limit $\Lambda \to \infty$ can be taken. We note that the limits $\Lambda \to \infty$ and $\sigma \to 0$ *are not* interchangeable.

In our present case, where we have the physical cutoff $1/\sigma$ given by the range of the conversion coupling g, no artificial UV regularization is needed. After having taken the UV limit $\Lambda \to \infty$ we obtain the result previously obtained, cf. Eq. (2.24), which we display again

$$\mathcal{G}_\phi^{-1}(E,\mathbf{q}) = -E + \frac{\boldsymbol{q}^2}{2} + E_{\mathrm{mol}}(B) - i\epsilon - \frac{g^2/(32\pi)}{\sigma\left[1+\sigma\sqrt{-\frac{E}{2}+\frac{\mathbf{q}^2}{4}-i\epsilon}\right]^2}. \tag{2.47}$$

Having solved the two-body problem and having fixed all parameters of our model as discussed in the previous Section we can now turn to the solution of the three-body problem.

2.5 Exact solution of the three-body problem

In our two-step RG scheme, we are now left with the final step to derive and solve the flow equation for the vertex $\lambda_3^{(k)}$ using the full, infrared propagator (2.47) as input.

Derivation of the flow equation

The derivation of the flow equation for $\lambda_3^{(k)}$ follows the previous works [96, 177] which we extend to account for finite range potentials as well as finite scattering energies and scattering length a. In our scheme the atoms ψ are not regulated while the molecules ϕ are supplemented with a sharp momentum regulator, such that

$$\frac{1}{P_\phi(E,\boldsymbol{q}) + R_{\phi,k}(E,\boldsymbol{q})} = \frac{1}{P_\phi(E,\boldsymbol{q})}\theta(|\boldsymbol{q}|-k). \tag{2.48}$$

The starting point of the second RG step is the truncation (2.41) with $P_{\phi,k}$ replaced by its infrared counterpart in Eq. (2.47). The only running coupling is then $\lambda_3^{(k)}$ which depends on three four-momenta Q_1, Q_2, and Q_3. Following [177] this complexity can be simplified by performing the calculation in the center-of-mass frame (CMF). The definitions for the kinematic variables is equivalent to our choice in Ref. [96] and it is summarized in Fig. 2.16.

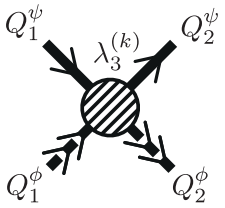

$$Q_1^\psi = (E_{\psi 1}, \mathbf{q}_1) \qquad Q_2^\psi = (E_{\psi 2}, \mathbf{q}_2)$$

$$Q_1^\phi = (E - E_{\psi 1}, -\mathbf{q}_1) \qquad Q_2^\phi = (E - E_{\psi 2}, -\mathbf{q}_2)$$

FIGURE 2.16: *Kinematics of the vertex* $\lambda_3^{(k)}(E_{\psi 1}, \boldsymbol{q}_1; E_{\psi 2}, \boldsymbol{q}_2; E)$.

In the CMF, the vertex depends only on 9 variables and we write it as[11]

$$\lambda_3^{(k)} = \lambda_3^{(k)}(\overbrace{E_{\psi 1}, \boldsymbol{q}_1}^{Q_1^\psi}; \overbrace{E_{\psi 2}, \boldsymbol{q}_2}^{Q_2^\psi}; E) \tag{2.49}$$

where E denotes the total incoming energy of the atom and dimer. The flow equation, diagrammatically shown in Fig. 2.15, then reads

$$\begin{aligned}
\partial_k \lambda_3^{(k)}(Q_1^\psi, Q_2^\psi; E) \;=\; & \tilde{\partial}_k \int_L \frac{\theta(|\mathbf{l}| - k)}{P_\psi(\omega, \boldsymbol{l}) P_\phi(-\omega + E, -\boldsymbol{l})} \times \\
& \Bigg[\lambda_3^{(k)}(Q_1^\psi, L; E) \lambda_3^{(k)}(L, Q_2^\psi; E) \\
& + g^2 \lambda_3^{(k)}(L, Q_2^\psi; E) \frac{\chi(|\boldsymbol{q}_1 + \frac{\boldsymbol{l}}{2}|)\chi(|\boldsymbol{l} + \frac{\boldsymbol{q}_1}{2}|)}{P_\psi(-\omega + E - \boldsymbol{q}_1^2, -\boldsymbol{l} - \boldsymbol{q}_1)} \\
& + g^2 \lambda_3^{(k)}(Q_1^\psi, L; E) \frac{\chi(|\boldsymbol{q}_2 + \frac{\boldsymbol{l}}{2}|)\chi(|\boldsymbol{l} + \frac{\boldsymbol{q}_2}{2}|)}{P_\psi(-\omega + E - \boldsymbol{q}_2^2, -\boldsymbol{l} - \boldsymbol{q}_2)} \\
& + \frac{g^2 \chi(|\boldsymbol{q}_2 + \frac{\boldsymbol{l}}{2}|)\chi(|\boldsymbol{l} + \frac{\boldsymbol{q}_2}{2}|)}{P_\psi(-\omega + E - \boldsymbol{q}_2^2, -\boldsymbol{l} - \boldsymbol{q}_2)} \frac{g^2 \chi(|\boldsymbol{q}_1 + \frac{\boldsymbol{l}}{2}|)\chi(|\boldsymbol{l} + \frac{\boldsymbol{q}_1}{2}|)}{P_\psi(-\omega + E - \boldsymbol{q}_1^2, -\boldsymbol{l} - \boldsymbol{q}_1)} \Bigg],
\end{aligned} \tag{2.50}$$

where $L = (\omega, \boldsymbol{l})$ is the loop and $Q = (E, \mathbf{0})$ the 'external' momentum. We may now apply the residue theorem to evaluate the ω integration. Here it is important to note that we assume that singularities (bound states) arise in $\lambda_3^{(k)}$ solely from singularities in the last argument E belonging to three-body bound states and not from the first two arguments. This is similar to the reasoning leading to decompositions of vertex functions into bilinears as done by Giering, Husemann, Metzner, and Salmhofer [179, 180, 181, 182]. In our case this assumptions holds exactly as verified by our final result. Since the loop frequency only appears in the first two

[11] In the following, various definitions of $\lambda_3^{(k)}$ are used, which only differ in their momentum dependence. Which of the definitions we use shall be implied by the corresponding kinematic arguments.

arguments of $\lambda_3^{(k)}$ we may safely integrate Eq. (2.50). Furthermore we consider only energies $E \leq 0$ below the atom ($a < 0$) and atom-dimer threshold ($a > 0$), respectively, so that we do not pick up additional bound state poles from the dimer propagator when closing the frequency integration contour. Note that this would become a subtle issue when solving the three-body problem for more complicated atomic potentials featuring deeply bound states.

The frequency integration puts the atom appearing in the first line in Eq. (2.50) on-shell, $\omega \to \boldsymbol{l}^2$, cf. [46, 66, 96, 177], such that it is only required to track the flow of a 'half-on, half-off shell vertex' $\lambda_3^{(k)}$, defined by

$$\lambda_3^{(k)}(\boldsymbol{q_1}, \boldsymbol{q_2}; E) = \lambda_3^{(k)}(E_{\psi 1} = \boldsymbol{q}_1^2, \boldsymbol{q}_1; E_{\psi 2} = \boldsymbol{q}_2^2, \boldsymbol{q}_2; E) \tag{2.51}$$

Differently to the solution of the two-body problem, we are not allowed to make the replacement $\tilde{\partial}_k \to \partial_k$ in Eq. (2.50) as the integrand includes k-dependent couplings. Instead we perform the $\tilde{\partial}_k$ derivative which acts only on the step function. The flow equation then reads

$$\begin{aligned}
\partial_k \lambda_3^{(k)}(\boldsymbol{q}_1, \boldsymbol{q}_2; E) \;=\; & -\int \frac{d^3 l}{(2\pi)^3} \frac{\delta(|\mathbf{l}| - k)}{P_\phi(E - \boldsymbol{l}^2, -\boldsymbol{l})} \Bigg[\lambda_3^{(k)}(\boldsymbol{q}_1, \boldsymbol{l}; E) \lambda_3^{(k)}(\boldsymbol{l}, \boldsymbol{q}_2; E) \\
& + g^2 \lambda_3^{(k)}(\boldsymbol{q}_1, \boldsymbol{l}; E) \frac{\chi(|\boldsymbol{q}_2 + \frac{\boldsymbol{l}}{2}|)\chi(|\boldsymbol{l} + \frac{\boldsymbol{q}_2}{2}|)}{-E + \boldsymbol{q}_2^2 + \boldsymbol{l}^2 + (\boldsymbol{q}_2 + \boldsymbol{l})^2 - i\epsilon} \\
& + g^2 \frac{\chi(|\boldsymbol{q}_1 + \frac{\boldsymbol{l}}{2}|)\chi(|\boldsymbol{l} + \frac{\boldsymbol{q}_1}{2}|)}{-E + \boldsymbol{q}_1^2 + \boldsymbol{l}^2 + (\boldsymbol{q}_1 + \boldsymbol{l})^2 - i\epsilon} \lambda_3^{(k)}(\boldsymbol{l}, \boldsymbol{q}_2; E) \\
& + g^4 \frac{\chi(|\boldsymbol{q}_1 + \frac{\boldsymbol{l}}{2}|)\chi(|\boldsymbol{l} + \frac{\boldsymbol{q}_1}{2}|)}{-E + \boldsymbol{q}_1^2 + \boldsymbol{l}^2 + (\boldsymbol{q}_1 + \boldsymbol{l})^2 - i\epsilon} \frac{\chi(|\boldsymbol{q}_2 + \frac{\boldsymbol{l}}{2}|)\chi(|\boldsymbol{l} + \frac{\boldsymbol{q}_2}{2}|)}{-E + \boldsymbol{q}_2^2 + \boldsymbol{l}^2 + (\boldsymbol{q}_2 + \boldsymbol{l})^2 - i\epsilon} \Bigg].
\end{aligned} \tag{2.52}$$

The collisions of atoms take place in the low-energy limit. Thus we may perform an s-wave projection of the atom-dimer scattering and define [96, 177]

$$\lambda_3^{(k)}(q_1, q_2; E) = \frac{1}{2g^2} \int_{-1}^{1} d\cos\theta \, \lambda_3^{(k)}(\boldsymbol{q}_1, \boldsymbol{q}_2; E), \qquad \theta = \angle(\boldsymbol{q}_1, \boldsymbol{q}_2), \tag{2.53}$$

where the prefactor is defined for later convenience.[12] Taking the angular average of Eq. (2.52) and evaluating the delta function leads to the rather simple expression[13]

$$\begin{aligned}
\partial_k \lambda_3^{(k)}(q_1, q_2; E) \;=\; & -\frac{g^2}{2\pi^2} \frac{k^2}{P_\phi(E - \boldsymbol{k}^2, k)} \times \\
& \Big[G_E(q_1, k) \lambda_3^{(k)}(k, q_2; E) + \lambda_3^{(k)}(q_1, k; E) G_E(k, q_2) \\
& + G_E(q_1, k) G_E(k, q_2) + \lambda_3^{(k)}(q_1, k; E) \lambda_3^{(k)}(k, q_2; E) \Big]
\end{aligned} \tag{2.54}$$

[12] With this choice the coupling $\lambda_3^{(k)}$ is rescaled by the quasiparticle weight $Z_\phi \sim 1/g^2$ of the molecule at resonance in the zero-range and broad resonance limit.

[13] For computational details on the angular average we refer to Appendix E.

where we defined

$$G_E(p,q) \equiv \frac{1}{2}\int_{-1}^{1} d\cos\theta \frac{\chi(\left|\mathbf{p}+\frac{\mathbf{q}}{2}\right|)\chi(\left|\mathbf{q}+\frac{\mathbf{p}}{2}\right|)}{-E+\mathbf{p}^2+\mathbf{q}^2+(\mathbf{p}+\mathbf{q})^2-i\epsilon}. \tag{2.55}$$

The function $G_E(p,q)$ can be calculated analytically for a Gaussian as well as the exponential shape function $\chi(r)$. The resulting expression is however quite lengthly. In the limit of vanishing range $\sigma \to 0$ it reduces to the well-known expression [66, 163, 177]

$$G_E(q,p) = \frac{1}{4qp}\log\frac{q^2+p^2+qp-\frac{E}{2}-i\epsilon}{q^2+p^2-qp-\frac{E}{2}-i\epsilon}. \tag{2.56}$$

Remarkably, the flow equation (2.54) can be integrated exactly [177]. The final result will be a modified version of the famous Skornyakov-Ter-Martirosyan (STM) equation [162]. For the derivation we follow closely the derivation in [177] extended to our problem.

First note that Eq. (2.54) is in a binomial (matrix) form. This is the key to be able to integrate this equation exactly. In order to do so it is convenient to define the quantities

$$g_E(q_1,q_2) = 16q_1q_2G_E(q_1,q_2), \tag{2.57}$$

$$\tilde{\lambda}_E^{(k)}(q_1,q_2) = 16q_1q_2\lambda_3^{(k)}(q_1,q_2;E), \tag{2.58}$$

$$f_E^{(k)}(q_1,q_2) = g_E(q_1,q_2)+\tilde{\lambda}_E^{(k)}(q_1,q_2), \tag{2.59}$$

and finally

$$\zeta_E(l) = -g^2\mathcal{G}_\phi(E-l^2,l)/(32\pi^2). \tag{2.60}$$

Using Eqs. (2.57)-(2.60) the differential flow equation (2.54) can be written in the compact form

$$\partial_k f_E^{(k)}(q_1,q_2) = \zeta_E(k)f_E^{(k)}(q_1,k)f_E^{(k)}(k,q_2). \tag{2.61}$$

which can be expressed as [96, 177]

$$\partial_k f_E^{(k)}(q_1,q_2) = \int_0^\infty dl\int_0^\infty dl' f_E^{(k)}(q_1,l)A_E^{(k)}(l,l')f_E^{(k)}(l',q_2) \tag{2.62}$$

with

$$A_E^{(k)}(l,l') = \zeta_E(k)\delta(k-l)\delta(k-l'). \tag{2.63}$$

Interpreting Eq. (2.62) as a matrix equations with matrices of a continuous index we may formally write Eq. (2.62) as

$$\partial_k \boldsymbol{f}_E^{(k)} = \boldsymbol{f}_E^{(k)}\cdot\boldsymbol{A}_E^{(k)}\cdot\boldsymbol{f}_E^{(k)} \tag{2.64}$$

$$\Longrightarrow \quad \partial_k(\boldsymbol{f}_E^{(k)})^{-1} = -\boldsymbol{A}_E^{(k)}. \tag{2.65}$$

It is remarkable how the complicated three-body problem is reduced to such a simple flow equation. Before integrating this equation, we have to specify the initial condition at the UV scale $k = \Lambda$ for $f_E^{(k)}$. For now we assume that there are no sizable microscopic three-body forces, so that $\tilde{\lambda}_3^{(\Lambda)} = 0$ in Eq. (2.59). This implies

$$f_E^{\mathrm{UV}}(q_1, q_2) = g_E(q_1, q_2). \tag{2.66}$$

In reality, there are, however, genuine three-body forces and we will qualitatively study their influence in Section 2.9. Respecting the initial condition (2.66), Eq. (2.65) is integrated from k to Λ which yields

$$[f_E^{(k)}]^{-1}(q_1, q_2) = g_E^{-1}(q_1, q_2) + \int_k^\Lambda dk' A_E^{(k')}(q_1, q_2). \tag{2.67}$$

The inversion of this result gives the following expression in matrix representation – note, in this step the resummation of infinitely many diagrams takes place –

$$\boldsymbol{f}_E^{(k)} = \left[\boldsymbol{I} + \boldsymbol{g} \cdot \int_k^\Lambda dk' \boldsymbol{A}_E^{(k')} \right]^{-1} \cdot \boldsymbol{g} \tag{2.68}$$

From this equation, when integrating down to the infrared scale $k = 0$, we then finally obtain[14]

$$\boxed{f_E(q_1, q_2) = g_E(q_1, q_2) - \int_0^\Lambda dl \; g_E(q_1, l) \zeta_E(l) f_E(l, q_2)} \tag{2.69}$$

When inserting the definition of f_E, Eq. (2.59), into Eq. (2.69) one finds that this is a modified version of the famous STM equation [162] (see also [66]) – here in a version for the irreducible vertex function λ_3 and for finite range potentials. In 'standard' treatments of Efimov physics using zero-range potentials, the integral in (2.69) is UV divergent and the regularization with the cutoff Λ has to be kept. Adjusting Λ one can then control the actual position of the Efimov states in the $(1/a, E)$ plane of the bound state spectrum. Therefore, in the zero-range case, the UV cutoff Λ can be regarded as a representation of the three-body parameter.

In our case the situation is fundamentally different. Having a physical range σ present, the integral is not divergent anymore by virtue of the form factor $\chi(r)$ appearing in the terms g_E as well as ζ_E. Thus we can safely take the limit $\Lambda \to \infty$. In a sense, nature takes care of the regularization by itself and the artificial three-body parameter Λ disappears from the theory.

Numerical renormalization group flow of $\lambda_3^{(k)}$

Equations (2.68) or (2.69), respectively, have to be solved numerically. For this purpose, it is advantageous to put the vertex f_E and all other functions such as g_E on a logarithmic grid in

[14] When Eq. (2.69) is solved for energies E above the atom-dimer threshold for $a > 0$, a pole in ζ is picked up in the l-integration in Eq. (2.69) leading to an imaginary part of f_E. This is responsible for a finite recombination rate at the atom-threshold.

momentum space. In this way, one can then easily follow the RG evolution of, for instance, $\lambda_3^{(k)}(q_1, q_2)$. The numerical procedure is stable and robust due to the fact that Eq. (2.68) is not an implicit integral equation unlike the standard STM equation (2.69). Specifically, we use dimensionless quantities and measure the momenta and RG scale k with respect to the inverse range of the potential $\Lambda_\sigma \equiv 1/\sigma$ and define

$$t = \ln \frac{k}{\Lambda_\sigma}, \quad t_i = \ln \frac{q_i}{\Lambda_\sigma}, \quad t_{\max} = \ln \frac{\Lambda}{\Lambda_\sigma} \tag{2.70}$$

where $t_{\max}$ is larger than zero. If one considers the zero-range limit, $\sigma \equiv 0$, then Λ_σ is traded for the UV cutoff scale Λ itself such that $t_{\max} = 0$. In the case of $\sigma > 0$ any choice $\Lambda \gg \Lambda_\sigma$ can be used and Λ only appears because of the numerical implementation. On a discrete logarithmic grid with spacing Δt and extension $(t_{\min} \dots t_{\max})$, Eq. (2.68) reads in discretized form

$$[f_E]_{t_1,t_2} = \left[\delta_{t_1,t'} + \Delta t \sum_{t_l=t_1}^{t_{\max}} [g_E]_{t_1,t_l} \zeta_E(t_l) \delta_{t_l t'} \right]^{-1}_{t_1,t'} [g_E]_{t',t_2}, \tag{2.71}$$

where t_1, t_2, t', t_l, and t denote discrete indices labeling the points on the logarithmic RG scale and momentum grid, respectively. In the numerical solution $t_{\max}$ and thus Λ is chosen to be much larger than $1/\sigma$ so that the integral in (2.68) has converged within the numerical accuracy. In Fig. 2.17 we show an exemplary RG flow of $\lambda_3^{(k)}$ for external energy $E = 0$ and a finite, negative $1/a < 0$. In the beginning of the flow the vertex $\lambda_3(t_1, t_2, E = 0)$, which is symmetric in momentum space, remains zero, cf. Fig. 2.17(a), until it reaches the scale $k \approx 1/\sigma$ [Fig. 2.17(b)]. From this scale on, high momentum modes become renormalized and a log-periodic pattern, characteristic for an RG limit cycle, develops, cf. Fig. 2.17(c-d). When the RG scale reaches the scale given by the scattering length $1/|a|$ the RG flow is effectively stopped, cf. Fig. 2.17(e), and a finite number of periodic patterns remains [Fig. 2.17(f)]. The development of each of these periodic patterns is related to the appearance of a resonant enhancements of $\lambda_3^{(k)}$ during the flow. This in turn gives rise to the presence of a bound state and therefore the number of periodic patterns along the diagonal $t_1 = t_2$ axes gives the number of Efimov states. From this observation it is already evident that when $|a|$ becomes of the order of σ no Efimov states can be present as essentially no flow is generated at all.

Fig. 2.17 was derived for a large value of $s_{\text{res}} \approx 100$. If s_{res} is chosen to be small, then it is the scale $1/r^*$ which suppresses the flow of the atom-dimer vertex in the UV so that the flow is started only on a much smaller RG scale k. For this reason much larger values of $|a|$ are needed in order for λ_3 to support bound states. It is important to note that a finite energy $|E|$ takes also the role of an IR cutoff scale such that the flow at $1/a = 0$ but at finite $E < 0$ looks very similar to the one shown in Fig. 2.17.

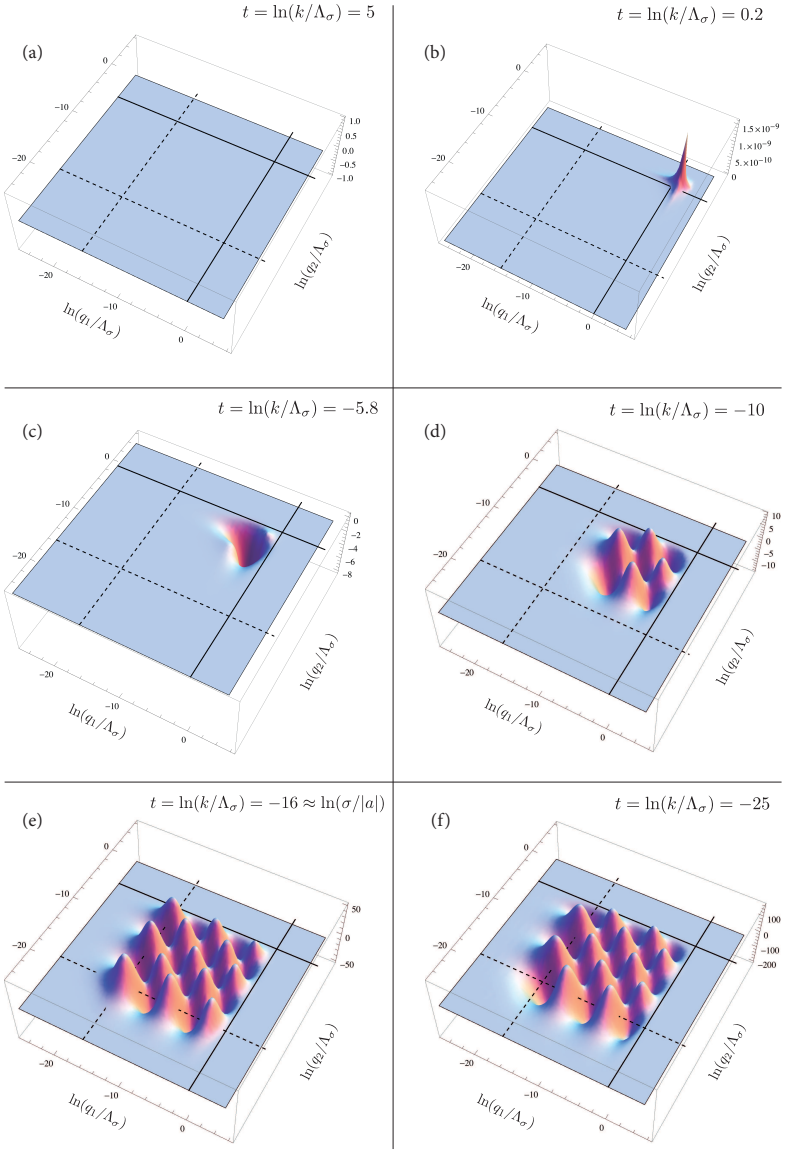

FIGURE 2.17: *Renormalization group flow of the atom-dimer vertex* $\lambda_3^{(k)}(q_1, q_2, E = 0)$. *The solid lines represent the scale* $q_i = 1/\sigma$ *and the dashed lines the inverse scattering length* $q_i = 1/|a|$. *For a detailed discussion, see main text.*

2.6 Determination of the bound state spectrum

The knowledge of the full vertex λ_3 at the infrared scale gives all information about the scattering of three bosons, such as bound states, recombination rates, and lifetimes, by evaluating the corresponding tree-level diagrams [66]. In the following we compute the trimer bound state

spectrum by identifying the poles of $\lambda_3(q_1,q_2;E)$ as a function of the energy E. As shown recently [48], such poles also exist in higher order vertices λ_N for $N \geq 4$ which are not considered in this chapter. In Chapter 3, we will study the four-body problem using renormalization group equations and show that the Efimov effect extends to the four-body sector. Indeed, it is likely that there are N-body bound states for arbitrary large N, a conjecture consistent with a recent theorem by Seiringer [183] which states that any pairwise interaction potential with negative scattering length a has an N-body bound state for some value of N, no matter how small $|a|$ may be. So far, the existence of N-body Efimov states has been shown numerically up to $N = 13$, see [184].

Three-body bound states are determined by the poles in the vertex function λ_3 as function of total incoming scattering energy of the atom and the dimer, cf. Fig. 2.16. Basically, the procedure is similar to the case of simple two-atom scattering which is determined by the scattering amplitude $f(E)$ in Eq. (2.25). The difference is that the vertex λ_3 is a more complicated quantity depending also on the momenta of the in- and outgoing atoms. Close to its poles λ_3 can be parametrized by [66]

$$\lambda_3^{(n)}(q_1,q_2;E) \approx \frac{\mathscr{B}(q_1,q_2)}{E + E_T^{(n)} + i\,\Gamma_T^{(n)}}, \tag{2.72}$$

where $\Gamma_T^{(n)}$ accounts for the possibility of unstable trimer states and $\mathscr{B}$ represents the momentum dependent residue of the bound state pole. In our case we have neglected the background scattering potential and use a closed-channel potential which supports only a single bound state such that no deeply bound molecular states are present. In consequence, there are no decay channels for the trimers and $\Gamma_T^{(n)} \equiv 0$. The pole structure of $\lambda_3(q_1,q_2;E)$ in Eq. (2.72) carries over to the vertex $\tilde{\lambda}_3$ defined by Eq. (2.58). Since g_E, as defined by Eq. (2.57) is a regular function of energy at $E = -(E_T^{(n)} + i\Gamma_T^{(n)})$, it can be neglected in Eq. (2.59) such that indeed

$$f_E^{(n)}(q_1,q_2) \approx \frac{\tilde{\mathscr{B}}(q_1,q_2)}{E + E_T^{(n)} + i\,\Gamma_T^{(n)}}. \tag{2.73}$$

In order to determine the bound state energies, Eq. (2.73) is inserted into the modified STM equation (2.69). This equation is evaluated for energies close to a possible bound state pole so that the regular function g_E can be neglected. This finally yields the matrix equation

$$\tilde{\mathscr{B}}(q_1,q_2) = \frac{g^2}{32\pi^2}\int_0^\Lambda dl\,\frac{g_E(q_1,l)}{P_\phi(E-l^2,l)}\,\tilde{\mathscr{B}}(l,q_2). \tag{2.74}$$

As before, as long as $\sigma > 0$, the UV cutoff Λ can be sent to infinity. Eq. (2.74) can conveniently be written in matrix representation as

$$\tilde{\mathscr{B}} = \mathscr{C}\cdot\tilde{\mathscr{B}} \tag{2.75}$$

with

$$\mathscr{C}(q_1,q_2;E)=\frac{g^2\xi}{8(3+\xi)\pi^2}\frac{g_E(q_1,q_2)}{P_\phi(E-q_2^2,q_2)}. \tag{2.76}$$

Eq. (2.75) is a homogeneous matrix equation which has non-trivial solutions for $\tilde{\mathscr{B}}$ only if

$$\mathscr{D}\equiv\det[\mathscr{C}-\boldsymbol{I}]=0. \tag{2.77}$$

It is straightforward to repeat the proceeding derivation for the case of three interacting (mass-balanced) SU(2) fermions and for completeness we included a factor ξ in Eq. (2.75) which is $\xi=1$ for bosons and $\xi=-1$ for fermions. Since the second fraction in Eq. (2.76) is positive, it is directly evident that there cannot be an Efimov effect for SU(2) fermions.

Numerical procedure

In order to find the bound state spectrum of the two-channel model (2.23) we have to calculate the zeros of the determinant $\mathscr{D}$ in Eq. (2.77) where $\mathscr{D}$ is a function of the scattering length, energy, resonance strength, and potential range, $\mathscr{D}=\mathscr{D}(1/a,E,g,\sigma)$. To evaluate $\mathscr{D}$ numerically, the function $\mathscr{C}-\mathbf{1}$ from Eq. (2.77) is put on a logarithmic momentum grid as defined by Eqn. (2.70). This grid extends from high momentum modes of order $q_{\max}\approx 5/\sigma$ down to low momenta of order $q_{\min}\approx 0.01 q_{\mathrm{IR}}$ where q_{IR} is determined by the lowest out of $1/|a|$ or $|E|^{1/2}$. The choice of the interval $q_{\min/\max}$ ensures convergence within numerical precision. The unitarity point $E=1/a=0$ can be treated analytically, which we have done in Ref. [96].

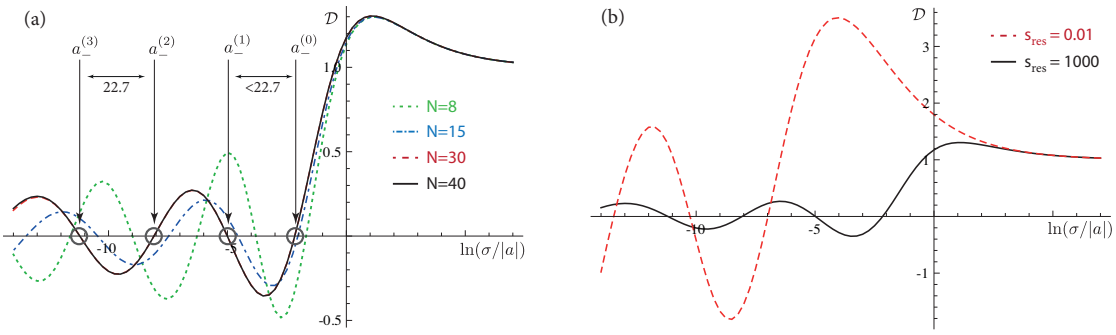

FIGURE 2.18: *Determinant $\mathscr{D}$ evaluated for zero energy, as function of scattering length $a<0$ and conveniently rescaled by a positive factor of $(1+e^{-\ln|\sigma/a|/2})$. (a) Comparison of the flow for various grid sizes used for the numerical representation of $\mathscr{C}$. Note, the results for $N=30,40$ lie almost on top of each other. (b) Determinant $\mathscr{D}$ as function of negative scattering length for two values of resonance strength. The smaller s_{res} the larger $|\sigma/a|$ has to be to allow the formation of an Efimov trimer.*

In Fig. 2.18(a) we show the determinant $\mathscr{D}$ for an open-channel dominated resonance characterized by $g^2=100/\sigma$ at $E=0$ as function of $\ln|\sigma/a|$ for a varying number of grid points $N\times N$. For the displayed range of $\sigma/|a|$, one finds convergence of the results for $N\approx 40$.

The number of necessary grid points depends on the range $q_{\min} \dots q_{\max}$. This follows also directly from our discussion of the RG flow shown in Fig. 2.17: the smaller $|a|$ or $|E|$, the wider the range where $\lambda_3(q_1, q_2; E)$ has a non-trivial structure in momentum space. In this way Fig. 2.18(a) nicely illustrates the necessity to keep a constant (high) resolution of logarithmic momenta as higher excited Efimov states are studied and thus $q_{\min}$ is lowered. This constraint is implemented in our numerical procedure and we find that a resolution of logarithmic momenta with a grid spacing of $\Delta t = 0.2$ leads to convergent results. As a consequence of the logarithmic scaling of the Efimov states this implies that, for instance, about 10^6 grid points are needed for the study of the fourth excited Efimov state, in particular when closed-channel dominated Feshbach resonances are considered.

In Fig. 2.18(a) each zero-crossing of $\mathcal{D}$ (indicated by the circles) corresponds to the existence of an Efimov state reaching the atom threshold and the first four Efimov states are visible in this figure. From this picture we may thus directly read off the ratio of the various scattering length $a_-^{(n)}$. While the first Efimov states with low numbers n show deviations from the universal scaling (2.5), this scaling is quickly recovered as unitarity, $1/a = 0$, is approached. In Fig. 2.18(b) the determinant $\mathcal{D}$ is shown, again as function of $\ln|\sigma/a|$ at $E = 0$, and we compare an open-channel dominated resonance with $s_{\text{res}} = 1000$ to a closed-channel dominated resonance, where $s_{\text{res}} = 0.01$. Similarly, we show $\mathcal{D}$ for the same values of s_{res} as function of

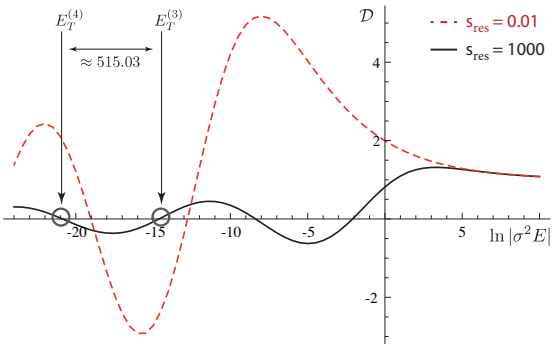

FIGURE 2.19: *Determinant $\mathcal{D}$ as function of energy $|E|$ in the resonance limit $1/a = 0$ for two values of resonance strength. The smaller s_{res} the smaller $|E\sigma^2|$ has to be to allow the formation of an Efimov trimer.*

$\ln|\sigma^2 E|$ in Fig. 2.19 in the *resonance limit*, $a = \infty$. Again, one can nicely read off the approach of universality as $|E|$ is lowered. From Figs. 2.18 and 2.19 one of our main results becomes already apparent: as the parameter s_{res} is decreased one finds that the overall Efimov spectrum is pushed towards the unitarity point $E = 1/a = 0$. This crossover of the spectrum will be explored in detail in the following section.

2.7 Universal Efimov spectrum

The numerical procedure to find the bound state poles in $\lambda_3(q_1, q_2; E)$ as described in the previous section can be used for arbitrary values in the $(E, 1/a)$ plane. In Fig. 2.20 we show the resulting Efimov spectrum including the atom-dimer threshold for an open-channel dominated Feshbach resonance of $s_{\mathrm{res}} = 100$ [Fig. 2.20(a)], and for a resonance of intermediate strength, $s_{\mathrm{res}} = 1$ [Fig. 2.20(b)]. The position of the trimer states in the $(1/a, E)$ plane is completely

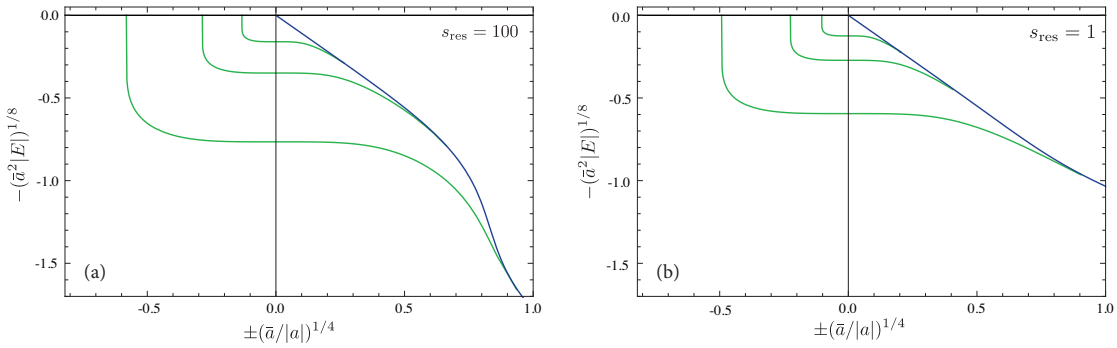

FIGURE 2.20: *Rescaled Efimov spectra. (a) The Efimov spectrum in dimensionless units for an open-channel dominated Feshbach resonance of strength $s_{res} = 100$. (b) The spectrum for a resonance of intermediate strength $s_{res} = 1$. The dimer binding energy is shown in blue.*

fixed by our calculation. We choose a convenient rescaling of the axis to make several Efimov states visible. A rescaling as applied in Fig. 2.20 is made in most plots of Efimov spectra found in literature. One should, however, keep in mind that this rescaling somewhat hides the true shape of the levels. For this reason we find it instructive to show the spectra in Fig. 2.21 also without rescaling of the axis. On the one hand this reveals the actual ratio of energy levels, which is so large that the excited states are not even visible in the plots. On the other hand the non-universal shape of the atom-dimer threshold becomes much more apparent – note in particular the large deviations in the energy scale when comparing resonances of different strength. The overall appearance of the spectrum remains similar as the strength of the resonance s_{res} is varied. As discussed in the previous section, it gets pushed towards the unitarity point $E = 1/a = 0$ in the limit $s_{\mathrm{res}} \ll 1$, while for open-channel dominated resonances it reaches a maximal extent in the $(1/a, E)$ plane.

The detailed position of the lowest energy levels depends on both the value of the van der Waals length l_{vdw} – which equals σ in our model[15] – and the resonance strength s_{res}. Only in the experimentally hardly accessible limit of highly excited Efimov states, $n \gg 1$, the ratios of $a_-^{(n)}$, $a_*^{(n)}$ (the scattering length for which the trimer meets the atom-dimer threshold), and $E^{(n)}$ of consecutive levels approach their universal values. It is instructive to quantify to which extent the lowest states deviate from this scaling within our model. In Table 2.1 we show our results for various dimensionless ratios for Feshbach resonances of widely different strengths.

[15] Up to a factor of ≈ 0.96, cf. Eq. (2.21).

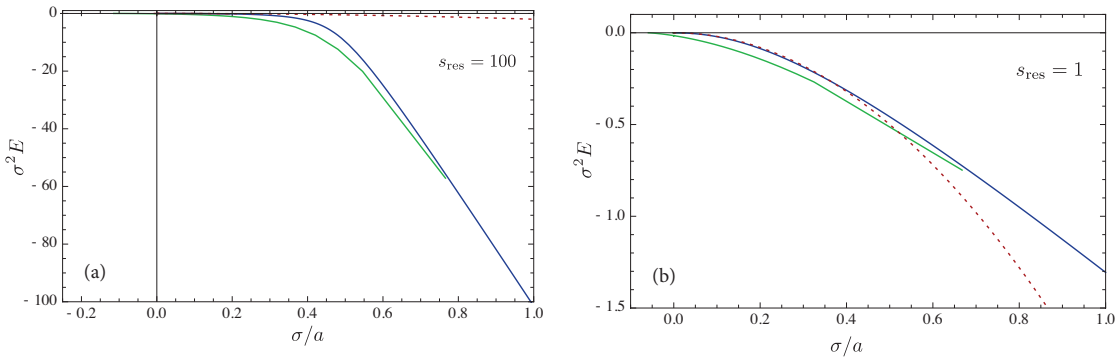

FIGURE 2.21: *Efimov spectra without rescaling of the axis. (a) The Efimov spectrum in dimensionless units for a open-channel dominated Feshbach resonance of strength $s_{res} = 100$. (b) The spectrum for a resonance of intermediate strength $s_{res} = 1$. The dimer binding energy is shown in blue. The universal dimer binding energy is shown as dotted red line.*

A plot of these ratios as a continuous function of the resonance strength is shown in Fig. 2.22. Already for the third state the results are close to the asymptotic behavior determined by the universal Efimov number $s_0 \approx 1.00624$, regardless of the value of $s_{\rm res}$.

$s_{\rm res}$	n	0	1	2	$n \gg 1$
100	$E^{(n)}/E^{(n+1)}$	530.871	515.206	515.035	515.028
	$a_-^{(n+1)}/a_-^{(n)}$	17.083	21.827	22.654	22.694
	$a_*^{(n+1)}/a_*^{(n)}$	3.980	40.033	23.345	22.694
	$\kappa_*^{(n)} a_-^{(n)}$	2.121	1.573	1.512	1.5076
1	$E^{(n)}/E^{(n+1)}$	515.830	515.039	515.035	515.028
	$a_-^{(n+1)}/a_-^{(n)}$	22.869	22.650	22.690	22.694
	$a_*^{(n+1)}/a_*^{(n)}$	17.183	22.303	22.716	22.694
	$\kappa_*^{(n)} a_-^{(n)}$	1.500	1.511	1.508	1.5076
0.1	$E^{(n)}/E^{(n+1)}$	521.273	515.059	515.010	515.028
	$a_-^{(n+1)}/a_-^{(n)}$	26.230	22.964	22.71	22.694
	$a_*^{(n+1)}/a_*^{(n)}$	26.965	21.286	22.48	22.694
	$\kappa_*^{(n)} a_-^{(n)}$	1.296	1.489	1.506	1.5076

TABLE 2.1: *The ratio between consecutive trimer energies $E^{(n)} = \hbar^2(\kappa_*^{(n)})^2/m$ and threshold scattering lengths $a_{-,*}^{(n)}$ as well as the product $a_-^{(n)}\kappa_*^{(n)}$ for an open-channel ($s_{res} = 100$), intermediate ($s_{res} = 1$) and closed-channel dominated ($s_{res} = 0.1$) Feshbach resonance for the three lowest-lying Efimov states $n = 0, 1, 2$. The rightmost column shows the ratios in the universal scaling limit ($E = 1/a = 0$).*

By contrast, the experimentally most relevant lowest states ($n = 0, 1$) exhibit large deviations. Remarkably, our prediction $a_-^{(1)}/a_- = 17.08$ for open-channel dominated resonances is in reasonable agreement with recent measurements of the position of the second Efimov trimer in ^{6}Li, which find a ratio near 19.7 [140, 185], definitely smaller than the asymptotic value 22.69. Surprisingly, for intermediate Feshbach resonances ($s_{\rm res} \approx 1$), the interplay between the scales r^* and σ leads to ratios close to their asymptotic ones even for the lowest states (see Fig. 2.22). Note that the values of $a_*^{(n)}$ for small n are highly sensitive to the precise form of the two-body bound state spectrum which, on its own, is strongly non-universal, cf. Fig. 2.21 and the discussion in Section 2.3. The ratios between the lowest $a_*^{(n)}$ are therefore in general not suitable for a measurement of universal ratios. As also apparent from Fig. 2.21, for open-channel dominated resonances $a_*^{(0)}$ approaches in our model values of $a_*^{(0)} \approx 1.3\, l_{\rm vdw}$. This is of the order of the van der Waals length and thus comparable with typical background scattering lengths. Since we completely neglected any background interaction potentials, our model is not valid in this regime. Nonetheless, even in more elaborate models including the background scattering, the atom-dimer threshold will remain non-universal in the regime where the lowest Efimov state merges into it. In order to observe universal Efimov physics in the regime of positive scattering length a one has to access the states with $n \gg 1$ near threshold, where the dimer binding energy has the universal form $\epsilon_b = \hbar^2/ma^2$. In fact, the latter can be regarded as a good measure to test if one reached the universal regime, both in theory and experiment, cf. also Fig. 2.11.

To investigate generic features of the trimer spectrum which are independent of the precise form of the dimer energy, we study the dependence of $a_-^{(n)}$ and $\varkappa_*^{(n)}$ on the strength of the Feshbach resonance. In Fig. 2.23 the behavior for the lowest, experimentally accessible, state is shown. For open-channel dominated resonances $a_-/\bar{a}$ and $\bar{a}\varkappa_*$ become independent of $s_{\rm res}$ and we find

$$a_- \approx -8.27\, l_{\rm vdw} \tag{2.78}$$

and

$$\varkappa_* l_{\rm vdw} = 0.26. \tag{2.79}$$

This is in agreement with the results by Wang *et al.* [143] who find $\varkappa_* l_{\rm vdw} = 0.226(2)$ and $a_- \approx -9.73(3)\, l_{\rm vdw}$ using a purely single-channel model with interaction potentials which feature a van der Waals tail.

In the limit of closed-channel dominated resonances, the van der Waals length becomes irrelevant, and the scale for the Efimov spectrum is set by r^*. This is also reflected by the dominant role of r^* in the effective range r_e, cf. Eq. (2.34). Specifically, we find

$$\begin{aligned} a_-^{(n)} &= \xi^{(n)} r^* \\ \varkappa_*^{(n)} r^* &= \eta^{(n)}, \end{aligned} \tag{2.80}$$

with numbers $\xi^{(n)}$ and $\eta^{(n)}$ which approach universal values as $n \to \infty$. In fact, we accurately reproduce the results for the scaling limit ($n \gg 1$) of closed-channel dominated Feshbach reso-

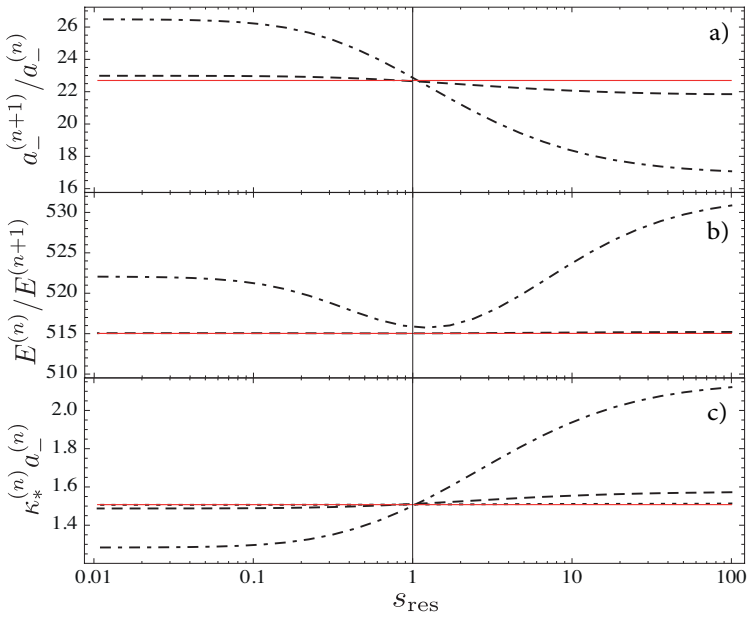

FIGURE 2.22: *Various dimensionless ratios as function of the Feshbach resonance strength s_{res}. Shown are the results for the lowest level (dot-dashed), first excited state (dashed), and second excited state (dotted). The universal scaling result is shown in red. a) Ratio of scattering lengths $a_-^{(n+1)}/a_-^{(n)}$ where the consecutive trimer states meet the atom threshold at $E = 0$. b) Ratio $E^{(n)}/E^{(n+1)}$ of the consecutive trimer energies at unitarity $1/a = 0$. c) Ratio $\kappa_*^{(n)} a_-^{(n)}$ as a measure of the distortion of the trimer levels from their universal shape in the (a, E) plane.*

nances,

$$\begin{aligned} a_-^{(n\gg 1)} &= -12.90\, r^* \\ \kappa_*^{(n\gg 1)} &= 0.117/r^* \qquad (s_{\rm res} \to 0, \text{ scaling limit}) \end{aligned} \tag{2.81}$$

which were previously derived within an effective range model with $\sigma \equiv 0$ yet $r^* > 0$ [146, 147]. For the low-lying Efimov states scaling theory, however, does not apply as discussed in Section 2.1. For this reason these low-lying states deviate from the limiting scaling behavior in Eq. (2.81) and our model predicts for example for the lowest Efimov state the ratios[16]

$$\begin{aligned} a_-^{(n=0)} &= -10.9\, r^* \\ \kappa_*^{(n=0)} &= 0.118/r^* \qquad (s_{\rm res} \to 0, \text{ lowest Efimov state}) \end{aligned} \tag{2.82}$$

At first sight, one expects that the precise numbers which quantify the deviations (2.82) from the universal scaling predictions (2.81) are specific for our model (2.23) with an exponential

[16] Note, to obtain these values r^* has to be chosen as large as $\mathcal{O}(10^6)\sigma$.

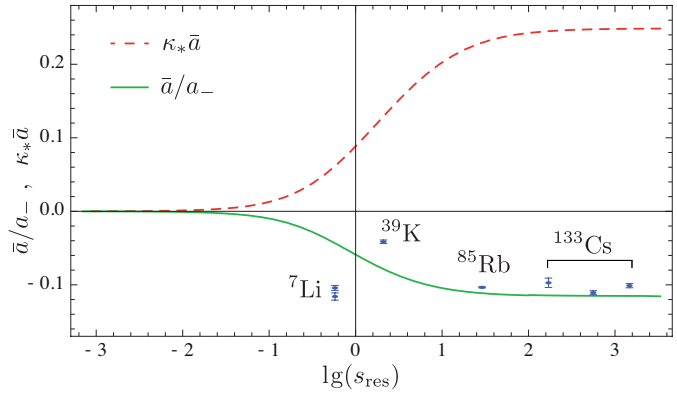

FIGURE 2.23: *Inverse threshold scattering length a_- (solid line) and wavenumber $\varkappa_* = \varkappa_*^{(0)}$ (dashed line) in units of $\bar{a}$ as functions of the resonance strength s_{res}. The dots with error bars show the experimental results for ^{7}Li [131, 134], ^{39}K [132], ^{85}Rb [135] and ^{133}Cs [47].*

form factor $\chi(r)$. As it turns out however, there is a larger degree of universality involved here. As we will see in Sections 2.8 and 2.9, the deviations from the universal scaling relations in the limit of $r^*/\bar{a} \gg 1$ are themselves universal again so that the numbers $\xi^{(n)}$ and $\eta^{(n)}$ are, remarkably, not dependent on microscopic details. Note that it is possible to study the deviations from universal scaling using a systematic expansion in the small parameter $l_{vdw}/|a|$ within effective field theory as done by Ji and coworkers [186]. Such an approach, however, requires not only an adjustable three-body parameter, but in addition further counterterms which are necessary to renormalize the theory with an interaction of finite range at finite scattering lengths a.

2.8 Effective range model

In this section we derive the Efimov physics of the so-called effective range or resonance model which corresponds to the zero-range limit $\sigma \to 0$ of the model (2.23). In this limit the scattering amplitude $f(k)$ is exactly given by the expansion of $f(k)$ up to order k^2 [cf. Eq. (2.33)]

$$f(k) = \frac{1}{-1/a + r_e k^2/2 - ik}. \tag{2.83}$$

This can be seen from the solution of the two-body problem which is obtained by the evaluation of the ladder diagram, cf. Fig. 2.12(a). Since in the resonance model $\chi(r) \equiv 1$, a ultraviolet regularization is necessary. The resulting UV scale dependence is absorbed in the definition of $E_{\rm mol}$ in Eq. (2.23), which takes the role of a scattering length dependent UV counterterm (renormalization). The final expression for the dimer propagator then reads

$$\mathcal{G}_\phi^{-1}(E,\mathbf{q}) = -E + \frac{\mathbf{q}^2}{2} - i\epsilon + \frac{g^2}{16\pi}\left[-1/a + \sqrt{-\frac{E}{2} + \frac{\mathbf{q}^2}{4} - i\epsilon}\right], \tag{2.84}$$

which yields, upon evaluation of Eq. (2.25), the expression (2.83) for $f(k)$ with

$$r_e = -\frac{64\pi}{g^2} = -2r^* < 0. \tag{2.85}$$

The three-body problem is straightforwardly solved along the same lines as in Section 2.5 with Eq. (2.84) as input in the STM equation (2.69). However, note that the UV regularization has to be kept due to the absence of a regulating form factor $\chi(p)$. The bound state spectrum is determined as described in Section 2.6 from the solution of Eqn. (2.76) and (2.77) where g_E and P_ϕ are given by Eq. (2.56) and Eq. (2.84), respectively. The numerical procedure is analogous to the discussion in Section 2.6 below Eq. (2.77), with the choice $q_{\max} = \Lambda$.

In the following we measure all quantities in units of the ultraviolet scale $\Lambda = \alpha a_0^{-1}$ with a_0 conveniently chosen to be the Bohr radius and where α is an open parameter. This parameter can be tuned to fit the results of experiments and represents as such a reincarnation of the three-body parameter. The resulting Efimov spectra are very similar to the results shown for instance in Fig. 2.20 and one finds that the extent of the bound states in the $(1/a, E)$ plane is dependent on the dimensionless width $\tilde{r}^* = r^*\Lambda$.

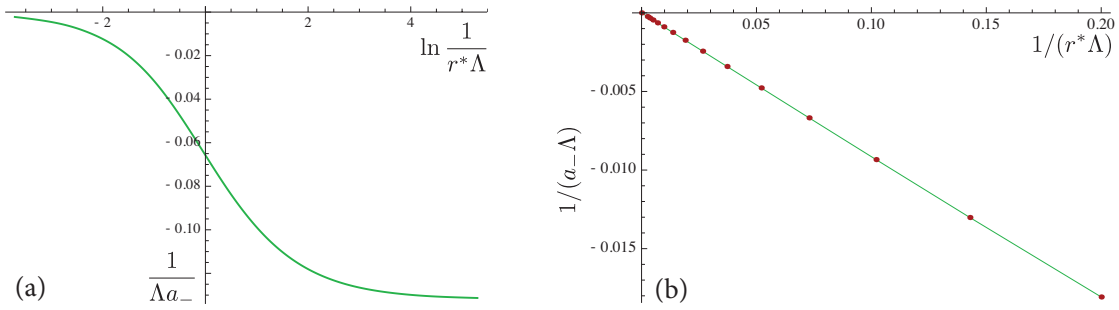

FIGURE 2.24: *(a) Scattering length $a_- = a_-^{(0)}$ where the lowest Efimov trimer meets the atom threshold as function of the dimensionless width $r^*\Lambda$. (b) For large dimensionless values $r^*\Lambda$ the scaling of a_- becomes independent of the cutoff scale Λ and scales linearly with r^*.*

In this section we concentrate on the scattering lengths $a_-^{(n)}$ where the trimers meet the atom threshold and the wave numbers $\varkappa_*^{(n)}$ corresponding to the energy of the trimer at unitarity. In Fig. 2.24 we show $a_- = a_-^{(0)}$ in units of Λ as function of $\tilde{r}^*$. As shown in Fig. 2.24(a) we find that for $r^*\Lambda \ll 1$ the scattering length a_- approaches a maximal value $a_- = \beta/\Lambda$ with β a numerical constant dependent on the regularization scheme chosen; here a sharp momentum cutoff. Although the relation $a_- \sim 1/\Lambda$ is similar to the result $a_- \sim l_{\rm vdw}$ derived in Section 2.7, it is important to note that here Λ is an artificial cutoff scale which serves as a free parameter. Note, from the relation $a_- \sim 1/\Lambda$ we recover the Thomas collapse in the limit $\Lambda \to \infty$.

For $r^*\Lambda \gg 1$, that is for a large effective range $|r_e|$, the situation is different, cf. Fig. 2.24(b). Due to its linear behavior we find that a_- becomes independent of the cutoff scale Λ and

$a_-^{(n)} = \xi^{(n)} r^*$ as in Eq. (2.80). In Table 2.2 we show $\xi^{(n)}$ and $\eta^{(n)}$ for various n and similar to Section 2.7 we find deviations from the universal scaling, Eq. (2.81), for low n. We find that the values $\xi^{(n)}$ and $\eta^{(n)}$ turn out to be new *universal numbers for all n* which do not depend on the specific model or regularization scheme chosen as long as the model features a large value of r^*, see also Section 2.9.

n	0	1	2	3	4
$\xi^{(n)} e^{-\frac{n\pi}{s_0}}$	-10.90	-12.72	-12.89	-12.897	-12.899
$\eta^{(n)} e^{\frac{n\pi}{s_0}}$	0.118	0.117	0.117	0.117	0.117
$a_-^{(n+1)}/a_-^{(n)}$	26.48	22.98	22.713	22.698	-

TABLE 2.2: *Approach of universal scaling of the lowest Efimov states in the limit* $r^*\Lambda \gg 1$.

In Table 2.2 we also quantify how the ratios $a_-^{(n+1)}/a_-^{(n)}$ quickly approach their universal value 22.694 as $n \to \infty$. We find that the decrease of the deviations from universal scaling is relatively well described by a the phenomenological formula

$$\frac{a_-^{(n+1)}}{a_-^{(n)}} \approx 22.694 + \gamma_1 e^{-\gamma_2 n}, \tag{2.86}$$

where $\gamma_1 = 63(20)$ and $\gamma_2 = 2.7(3)$. The large error in the numerical constants is due to the very large momentum grid needed in the regime $r^* \to \infty$.

Since we find that the deviations from the universal scaling, Eq. (2.81), itself is again universal, we conjecture that there exists a universal relation of a form similar to Eq. (2.86) governing the approach of $a_-^{(n+1)}/a_-^{(n)}$ towards the universal value 22.694 with universal numbers γ_i.

2.9 Test of universality

Let us now address the question to which extent the properties of the lowest Efimov state, such as the scaling of a_- with $l_{\rm vdw}$ and r^*, cf. Eq. (2.78) and (2.82), depend on the microscopical details of our model (2.23). We will test two possible sources of such non-universal corrections: first, a modification of the form factor determining the atom-molecule conversion and, secondly, non-universal corrections due to a non-zero three-body force.

Form of the atom-molecule conversion coupling $\chi(r)$. Our original idea was, cf. Section 2.2, that the apparent universality of the three-body parameter is due to the fact that in all experiments having measured a_-, ultracold atoms close to a Feshbach resonance have been used. This led us to the assumption that it is the Feshbach mechanism itself which causes the observed, apparent universality. In order to support this picture we introduced the simple two-channel model (2.23) with the specific, physically motivated form factor $\chi(r) \sim e^{r/\sigma}/r$. This choice is, however, by far not the only, unique choice and we may use the freedom of

choosing different form factors χ to test the degree of universality involved in the solution of the corresponding three-body problem.

Specifically, we study here the results for a Gaussian form factor often employ in literature [149, 150, 153],

$$\chi(q) = e^{-q^2\sigma^2/2}, \tag{2.87}$$

which in coordinate space yields $\chi(r) \sim e^{r^2/(2\sigma^2)}$. Using this form factor the solution of the two-body problem is slightly modified. In particular we find

$$\begin{aligned} \mathscr{G}_{\phi}^{-1}(E,\mathbf{q}) &= -E + \frac{\mathbf{q}^2}{2} + E_{\rm mol}(B) - i\epsilon + \frac{g^2}{16\pi^{3/2}\sigma} + \frac{g^2}{16\pi^2}\sqrt{-\frac{E}{2} + \frac{\mathbf{q}^2}{4} - i\epsilon} \\ &\times \exp\left[\sigma^2\left(-\frac{E}{2} + \frac{\mathbf{q}^2}{4} - i\epsilon\right)\right] \operatorname{erfc}\left[\sigma\sqrt{-\frac{E}{2} + \frac{\mathbf{q}^2}{4} - i\epsilon}\right], \end{aligned} \tag{2.88}$$

which gives, upon expansion of the scattering amplitude $f(k)$, the identifications

$$\frac{1}{a} = -\frac{16\pi}{g^2}E_{\rm mol}(B) + \frac{1}{\sqrt{\pi}\sigma}, \tag{2.89}$$

$$r_e = -2r^* + \frac{4\sigma}{\sqrt{\pi}}\left(1 - \frac{\sqrt{\pi}\sigma}{2a}\right), \tag{2.90}$$

$$r^* = \frac{32\pi}{g^2}, \tag{2.91}$$

and by comparing the resonance shift with the quantum defect calculation by Julienne and coworkers [157], as described in Section 2.3, we find

$$\sigma = \frac{2}{\sqrt{\pi}}\bar{a}. \tag{2.92}$$

The three-body problem is solved analogous to Section 2.5-2.7 with the Gaussian form factor (2.87) used in the corresponding expressions. Subsequently the three-body bound state spectrum can be determined. As a measure for the extent of universality we concentrate on the dependence of $a_-^{(n)}$ on r^* and $l_{\rm vdw}$. In Fig. 2.25 we show the crossover of $\bar{a}/a_-$ from the closed- to the open-channel dominated limit (solid line) and compare the results to the one obtained in Section 2.7 (dashed line).

In the limit of open-channel dominated resonances, $s_{\rm res} \gg 1$, we find

$$a_- = -7.40\, l_{\rm vdw}. \tag{2.93}$$

This shows that, while the functional form of the scaling of a_- with $l_{\rm vdw}$ for open-channel dominated resonances is universal, the specific prefactor is a non-universal quantity which, however, is of the order of $\mathcal{O}(10) l_{\rm vdw}$. Comparing the result Eq. (2.93) with the result derived

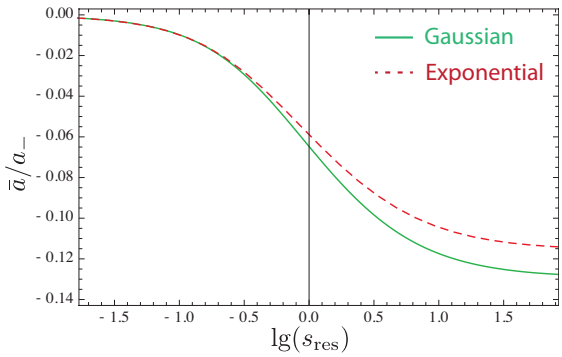

FIGURE 2.25: *Inverse threshold scattering length a_- in units of $\bar{a}$ as functions of the resonance strength s_{res}. We compare the result using the exponential form factor (dashed), cf. Section 2.3, to the Gaussian form factor in Eq.* (2.87) *(solid).*

in Section 2.7 we conjecture that in the limit of open-channel dominated resonances the typical deviations from the experimentally observed scaling around the mean value $a_- \approx -9.45 l_{\rm vdw}$ can be expected to be at the 10% level. This is also consistent with the findings of Wang *et al.* [143] who find similar non-universal deviations using a variation of the depths of the two-body potentials employed in their single-channel model calculation.

Similarly to Section 2.7, we find for closed-channel dominated resonances, $s_{\rm res} \ll 1$, that a_- scales with the resonance width r^* according to

$$a_- = -0.118\, r^*. \tag{2.94}$$

Contrary to the relation (2.93) this scaling turns out to be independent of the microscopic model chosen. It is the same for the exponential, the Gaussian, as well as a delta-function like form factor employed in the effective range model in Section 2.8. For *all* Efimov states we recover exactly the results shown in Table 2.2. The underlying reason for this *new, extended universality* can be found by inspection of the expression for the effective range in the various models, cf. Eqn. (2.34), (2.85), and (2.89). When r^* is large, the effective range r_e is dominated by this scale, the effective atom-atom scattering is determined by the term $r_e = -2r^*$, and the observable physics becomes independent of the microscopical details.

Influence of a three-body force. When studying the dipole-dipole interactions between neutral atoms in third-order perturbation theory, one finds that they induce a microscopic three-body interaction (or *force*)

$$W_{\rm AT} = \gamma \frac{1 + 3\cos\theta_{12}\cos\theta_{23}\cos\theta_{31}}{r_{12}^3 r_{23}^3 r_{31}^3}, \tag{2.95}$$

where θ_{ij}, r_{ij} are the angles and sides of the triangle spanned by the three atoms. The interaction (2.95) is known as the Axilrod-Teller potential [187] and it is valid at large atomic

separations r_{ij} [17, 188]. The coefficient γ depends on the specific atoms chosen and it has been calculated to high precision for various mixtures of atom species by Babb and coworkers [188]. The short distance behavior of the three-body force is largely unknown and presumed to be highly dependent on microscopic details. Also exchange interactions play a major role at short and intermediate interparticle distances.

Here we want to study the consequences of a microscopic three-body force for the scaling of the lowest Efimov trimers in a simple approximation. Eq. (2.95) is a very complicated function of momenta which renders the exact solution of the three-body problem intractable. In order to, nonetheless, get some insight into the question how strong the influence of the three-body force is on the observable three-body physics, we introduce a phenomenological atom-dimer contact interaction $\tilde{\lambda}_3^{(\Lambda)}$ [cf. Eq. (2.58)] in our model (2.23). Integrating out the dimer field ϕ in the classical action yields an effective momentum dependent, microscopic three-atom interaction $\sim(\psi^*\psi)^3$ which is determined by the evaluation of the tree-level diagram shown in Fig. 2.26(a).

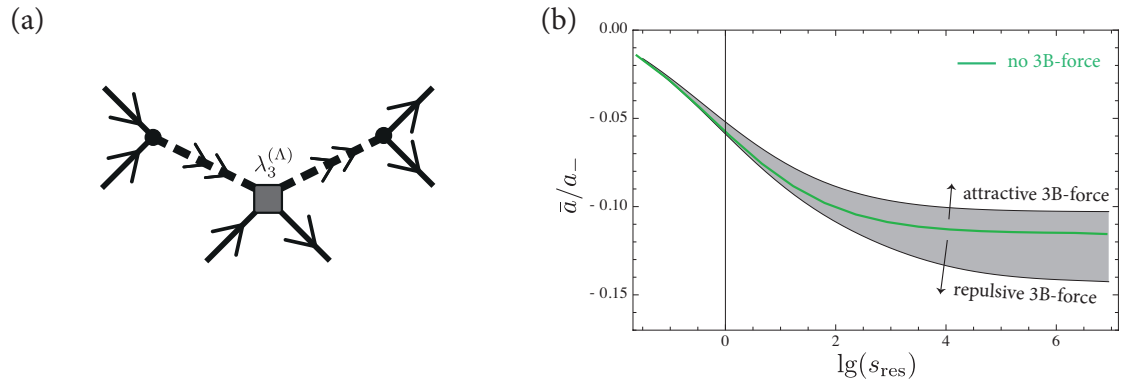

FIGURE 2.26: *(a) Tree-level diagram which gives the effective, microscopic three-body force* $\sim(\psi^*\psi)^3$ *upon integrating out the composite molecular field* ϕ*. (b)* $\bar{a}/a_-$ *as function of* s_{res}*. The shaded region corresponds to the result obtained including a microscopic three-body force with values* $\tilde{\lambda}_3^{(\Lambda)}=-0.1$ *(attraction) up to* $\tilde{\lambda}_3^{(\Lambda)}=0.01$ *(repulsion) in units of* $\bar{a}$*. Here we use the exponential form factor* χ *employed in Section 2.7.*

As a result of the introduction of the microscopic atom-dimer force $\tilde{\lambda}_3^{(\Lambda)}$ one finds a new, modified STM equation,

$$f_E(q_1,q_2)=g_E(q_1,q_2)+\tilde{\lambda}_3^{(\Lambda)}(q_1,q_2)-\int_0^\Lambda dl\,[g_E(q_1,l)+\tilde{\lambda}_3^{(\Lambda)}(q_1,l)]\,\zeta_E(l)f_E(l,q_2). \quad (2.96)$$

The bound state spectrum is derived in a similar way as in Section 2.6. In Fig. 2.26(b) we show $\bar{a}/a_-$ as function of $s_{\rm res}$. While the solid line displays our result from Section 2.7 ($\tilde{\lambda}_3^{(\Lambda)}=0$), the shaded region corresponds to choices of $\tilde{\lambda}_3^{(\Lambda)}\in(-0.1\ldots0.01)$ in units of σ.

Note that our choice of the three-body force is purely with the aim to find some insight into the question to which extent three-body forces induce non-universal corrections. In fact our choice of a constant $\tilde{\lambda}_3^{(\Lambda)}$ in momentum space leads to a momentum dependence of $\lambda_6(\psi^*\psi)^*$ which does not bear much resemblance with the momentum structure of Eq. (2.95). In particular our model leads to irrelevant three-body forces in the limit of closed-channel dominated Feshbach resonances. Furthermore, evaluating the tree-level diagram in Fig. 2.26(a) we find that our phenomenological three-body force carries a dependence on the external magnetic field due to the appearance of dimer propagators in the tree-level diagram. Nonetheless, although we employ here only this simple toy model, we expect that the strong influence of a three-body force on our results, cf. Fig. 2.26(b), will carry over to the inclusion of the correct, yet unfortunately unknown, microscopic three-body interaction.

Specifically, we find that the effect of the three-body force is much more pronounced for a repulsive three-body interaction. Contrarily, for attractive interactions, we find that the value of a_-/σ is shifted towards larger values. Remarkably, our results for a_-/σ converge to a finite value even for an arbitrarily large three-body force $\tilde{\lambda}_3^{(\Lambda)} \to \infty$ with a shift of $a_-/\bar{a}$ of not more than 15%. Since we expect the real three-body force to be indeed attractive due to the induced dipole-dipole interactions this observation might explain why the influence of three-body force appears to be rather weak for open-channel dominated resonances. This interpretation is also in agreement with the experimental results which show only a weak scattering of the data for a_- around the isotope averaged mean value $a_- \approx -9.45 l_{\mathrm{vdw}}$. In summary, from our results this remaining scattering of a_- can be attributed to a combined effect of microscopical details of the Feshbach model, such as the form factor χ, as well as a non-zero, attractive three-body force. We estimate that both effects yield corrections on the $10-15\%$ level.

2.10 Comparison to experiment and conclusion

We have presented a simple, exactly solvable model for the three-body physics of ultracold bosonic atoms, containing only r^* and l_{vdw} as experimentally accessible parameters, in which the full Efimov spectrum is fixed without an adjustable three-body parameter. Our results provide an explanation for the observed proportionality between the scattering length a_- where the first Efimov trimer appears and the van der Waals length l_{vdw}, which is often interpreted as a 'universality' of the three-body parameter. This relation applies for open-channel dominated resonances. With regard to three-body forces we showed, using a simple model, that the presence of these forces, if attractive and short ranged, only yields a weak correction to the results. For increasing values of $r^\star$, a continuous crossover is found into the regime of closed-channel dominated resonances, where the scale for the three-body parameter is set by r^* alone, recovering previous exact solutions [146, 147].

Comparing to the experimental data, see Fig. 2.23, the open-channel dominated resonances in ^{85}Rb [135] and in ^{133}Cs [47] fit well into our prediction. The 12 % deviation between the value $a_- \approx -9.45\, l_{\mathrm{vdw}}$ inferred from averaging the results from different experiments and our ratio -8.27 shows the absence of a true universality of the three-body parameter in a strict

sense: short range physics which enters, for instance, into the details of the form factor $\chi(r)$ leads to slightly different numbers. From both the experimental data [see Fig. 2.23] and a study of how much our numbers change for various choices of the form factor $\chi(r)$ [cf. Section 2.9] we conclude that they are generically at the ten percent level.

As mentioned above, the van der Waas length does not set the scale for the Efimov spectrum in general. In particular, in the regime of Feshbach resonances of intermediate strength $s_{\rm res} \approx 1$ both scales r^* and σ become relevant. Our approach equally applies to this regime, which is realized, e.g., in the case of ^{39}K, where $s_{\rm res} \simeq 2.1$ [132]. As shown in Fig. 2.23, the observation [132] of a considerable deviation from the result $a_- \approx -9.45\, l_{\rm vdw}$ in this case is in qualitative agreement with our model.[17] By contrast, the case of ^{7}Li, which seems to follow nicely the result $a_- \approx -9.45\, l_{\rm vdw}$ [131, 134] for open-channel dominated resonances despite the even smaller value $s_{\rm res} \simeq 0.58$ [134] of the resonance strength is not consistent with our prediction.

A possible origin of this discrepancy may be three-body forces of or beyond the Axilrod-Teller type [187]. Whether it is indeed three-body forces or other effects not captured by our model that will account for the discrepancy between the observed a_- in ^{7}Li, ^{39}K and our prediction is unknown at present. Note, however, that an explanation of the observed result for a_- in ^{7}Li within a single-channel description [143] is likely to be inadequate due to the rather small value of $s_{\rm res} \simeq 0.58$.

Studying in detail models with various form factors χ, we revealed a new extended universality for bosonic three-body systems which feature a large width r^*. For these systems, even deviations from the $n \gg 1$ scaling are universal themselves. Finally, we have shown that for the lowest Efimov states within a given trimer spectrum, there are appreciable deviations from the asymptotic scaling relations, consistent with experiments. Clearly, a more systematic experimental investigation of these non-universal ratios and of resonances with intermediate strength $s_{\rm res} = \mathcal{O}(1)$ is necessary to clarify to which extent the generic features of the Efimov effect in ultracold atoms are captured by our simple model, in which the complete trimer spectrum is obtained without any adjustable parameter from two-body physics only.

[17] New experimental data suggests that the value of $l_{\rm vdw}/a_-$ reported in [132] has to be corrected and is shifted to a larger value [136].

Chapter Three

Renormalization group study of the four-body problem

As discussed in the previous Chapter, few-body physics saw a renewed interest in recent years following the observation of three-body Efimov states in experiments using cold atoms. The findings of Kraemer *et al.* [45] stimulated extensive activity in the field of three-body physics, both experimentally and theoretically and as a result the Efimov effect in three-body systems is a well-understood phenomenon today. The next natural step is then to raise the question:

"What is the physics of four particles interacting with strong, short-range interactions?"

Early attempts towards an understanding of this system were made in the context of nuclear physics using a variety of approaches [189, 190, 191, 192]. Also the four-body physics of ^{4}He atoms has been investigated in much detail, for an overview see e. g. [193, 194, 195]. The simpler four-body physics of fermions with two spin states, relevant for the dimer-dimer repulsion, has been studied in [196], while the four-body problem of fermions with isospin symmetry was investigated in the context of α-particle condensation in [197, 198, 199].

In their pioneering work, Platter and Hammer *et al.* [200, 201] investigated the four-body problem using effective interaction potentials and made the conjecture that the four-boson system exhibits universal behavior. Calculating the energy spectrum of the lowest bound states in dependence on the scattering length a the existence of two tetramer (four-body bound) states associated with each trimer was conjectured. In 2009, von Stecher, D'Incao, and Greene [48, 202] investigated the four-body problem in a remarkable quantum mechanical calculation. They found that the Efimov trimer and tetramer states always appear as sets of states with two tetramers associated with each of the trimer levels and calculated the bound state energy spectrum of the lowest few sets of states. The calculation suggests that the energy levels within one set of states are related to each other by universal ratios, which were obtained from the behavior of these lowest sets of states.

The experimental detection of tetramer states follows similar steps as described in Section 2.2. It is, however, even more challenging and requires extremely precise measurements. Remarkably, Ferlaino *et al.* were able to observe signatures of the lowest two of the tetramer states in a recent experiment [203] which was supported by several other observations [131, 132, 204, 205], verifying the predictions by Stecher *et al.* [48, 202], Platter and Hammer *et al.* [200, 201], and the work which will be presented in the following [106]. Also the further

step towards the experimental observation of five-body bound states has been taken [205]. Recently, Stecher was even able to show theoretically the existence of N-body bound states for up to $N = 13$ [184].

In Chapter 2 we have seen that when one uses zero-range, two-body interactions to study the three-body problem, a three-body parameter in addition to the scattering length a has to be introduced in order to characterize the problem completely. Similarly, one may ask if there is a new *four-body parameter* entering the physics in order to renormalize the four-body problem. This would, in accordance with the discussion in Section 2.1, reduce the universality of the few-body problem further because more parameters are introduced in the theory. The question of the existence or absence of a four-body parameter has been much debated in recent years with contradictory results. While Yamashita *et al.* [206] conclude that a four-body parameter enters the problem at leading order, the calculations [48, 200, 201, 202, 207] suggest otherwise.

While the calculations by Platter et al. [200, 201] and von Stecher *et al.* [48, 202] rely on quantum mechanical approaches, in this work we want to shed light onto the four-body problem from a different perspective. A lot of insight into the three-body problem had been gained from effective field theory and renormalization group methods [66, 96, 100, 101, 208] and it is desirable to apply these also to the four-body problem. In this Chapter we will make a first step towards such a description that is complementary to previous quantum mechanical approaches. Of special interest is the further investigation of universality and the role of a possible four-body parameter. In this context the so-called unitarity point, defined by $E = 1/a = 0$, is of particular importance. In this limit not only the scattering length a is infinite but also all binding energies in the problem accumulate at the atom threshold at zero energy. Only at this point the non-universal corrections which scale with powers of $r_0/|a|$ or $r_0^2|E|$, respectively, vanish and physics becomes completely universal so that, for example, the ratio between the binding energies of consecutive trimer levels assumes exactly its universal value, $E_{n+1}/E_n = \exp(-2\pi/s_0)$. For this reason the unitarity point is of particular interest. Unfortunately, in the previous calculations [48, 200, 201, 202] the unitarity point was inaccessible and only the few lowest lying states were determined. As we have seen in the previous Chapter, the Efimov spectrum for these lowest states is, however, not yet perfectly in the universal regime. The major advantage of the present RG approach is that it allows to investigate analytically the complete spectrum and, in particular, to address directly the unitarity point in order to extract the universal relations between the three- and four-body bound states.

While we solved the three-body problem in Chapter 2 exactly using the vertex expansion of the effective average action Γ_k in Eq. (2.41), the four-body problem is so complicated that we have to rely on an approximate, yet simple and physically intuitive model. This model is based on a derivative expansion of the average action Γ_k and neglects the momentum dependence of the three- and four-body vertices. As discussed in Chapter 2, the Efimov effect reveals itself as a limit cycle RG flow of the three-body coupling. The three-body parameter sets the overall 'phase' of this flow which has a period given by s_0/π when studied at the unitarity point. Similarly, the presence of a four-body body parameter would naturally appear as an additional feature in the RG flow of the four-body couplings with a new parameter needed to characterize the structure of the four-body flow. In the following we will show, however, that the three-body limit cycle enforces a more complicated limit cycle flow of the four-body sector which is

strictly attached to the limit cycle of the three-body sector. In turn, this strict connection of the three- and four-body sector leaves no room for any four-body parameter.

Furthermore the RG method allows for computations away from the unitarity point. From a two-channel model we calculate the bound state energy spectrum and investigate how the relations between tetramer and trimer states approach the universal limit as one comes closer to the unitarity point. The Chapter is structured as follows. In Section 3.1 we set up and explain the microscopic model. Sections 3.2 and 3.3 are devoted to the FRG analysis of the two- and three-body sector. In Section 3.4 we discuss the four-body sector and present our numerical results while in Section 3.5 we comment on a rebosonization technique used for the numerical solution. Our findings are summarized in Section 3.6.

3.1 Definition of the model

In the following we will solve the four-body problem approximately by the use of the functional renormalization group and follow the RG evolution of the average action Γ_k governed by the exact RG equation (2.40). Instead of an exact solution using a vertex expansion of Γ_k as in the previous Chapter, we employ here a derivative expansion of Γ_k where the vertex functions $\Gamma_k^{(n)}$ are expanded in terms of energy and momentum. While this makes the analytical derivation and solution of the flow equations possible, it leaves us only with approximate results. The model shall again describe atoms close to a Feshbach resonance, but contrarily to Chapter 2 we consider a zero-range approximation of Eq. (2.23) with $\sigma \to 0$. The truncation for the Euclidean flowing action is given by

$$\begin{aligned}\Gamma_k &= \int_x \{\psi^*(\partial_\tau - \Delta - E_\psi)\psi + \phi^* \overbrace{\left[A_{\phi,k}(\partial_\tau - \frac{\Delta}{2}) + m^2_{\phi,k}\right]}^{P_{\phi,k}} \phi \\ &+ \frac{g}{2}(\phi^*\psi\psi + \phi\psi^*\psi^*) + \lambda_{3,k}\phi^*\psi^*\phi\psi \\ &+ \lambda_{\phi,k}(\phi^*\phi)^2 + \beta_k(\phi^*\phi^*\phi\psi\psi + \phi\phi\phi^*\psi^*\psi^*) + \gamma_k\phi^*\psi^*\psi^*\phi\psi\psi\}, \end{aligned} \tag{3.1}$$

where Δ denotes the Laplace operator and we again use the natural, non-relativistic convention $2m = \hbar = 1$ with the atom mass m. ψ denotes the field of the elementary bosonic atom, while the dimer, which equals the closed-channel molecule at $k = \Lambda$, is represented by the field $\phi \sim \psi\psi$. The atom is supplemented with a non-relativistic propagator with gap E_ψ. The explicit dependence on E_ψ will allow us to capture some of the energy dependence of the higher order vertices as we will argue below. The dimer propagator is given by a derivative expansion where Galilean symmetry enforces the expansion coefficient $A_{\phi,k}$ to be the same in front of the frequency and momentum. Furthermore, the gap term $m^2_{\phi,k}$ equals the detuning E_{mol} in Eq. (2.23) for $k = \Lambda$. Although this approximation of $P_{\phi,k}$ is obviously not exact, cf. Eq. (2.24), the dynamics of $P_{\phi,k}$ allows us to capture essential details of the momentum dependence of the two-body interaction. For instance, the wave function renormalization

factor A_ϕ allows us to correctly account for an anomalous dimension η of the dimer field ϕ. This anomalous dimension is unity at unitarity as can be seen from Eq. (2.24) by evaluating the square root structure of the dimer propagator and $\eta = 1$ is recovered correctly in our simple model (3.1).

The only nonzero interaction, present at the microscopic UV scale $k = \Lambda$, is taken to be the Yukawa-type term with the coupling g. As discussed in detail in Chapter 2, the two-atom interaction is given by the tree-level exchange diagram shown in Fig. 2.9. From the evaluation of this diagram we will show below that the Yukawa interaction g and the wave function renormalization A_ϕ can be connected to the effective range r_e in an effective range expansion. We furthermore assume that no three- or four-body forces are present, so that the atom-dimer interaction λ_3 as well as the various four-body interactions λ_ϕ, β, and γ vanish at the UV scale and are built up only via quantum fluctuations during the RG flow. All couplings present in Eq. (3.1) are allowed to flow during the RG evolution and are taken to be momentum-independent in Fourier space.

In the general case of nonzero density and temperature one works in the Matsubara formalism and the integral in Eq. (3.1) sums over homogenous three-dimensional space and over imaginary time $\int_x = \int d^3x \int_0^{1/T} d\tau$. Although our method allows us to tackle the full, many-body problem at finite temperature in this way, we are here interested solely in the few-body physics, for which the density n and temperature T vanish. For $T = 0$, $\int_x$ reduces to an integral over infinite space and time as it was also the case in Chapter 2. Our truncation (3.1) is again based on the simple structure of the non-relativistic vacuum and, as discussed in Section 2.4 numerous simplifications occur when solving the exact RG equation (2.40) compared with the general, many-body case.

The flowing action (3.1) has a global $U(1)$ symmetry which corresponds to particle number conservation. In the vacuum limit it is also invariant under spacetime Galilei transformations which restricts the form of the non-relativistic propagators to be functions of $\partial_\tau - \Delta$ for the atoms and $\partial_\tau - \Delta/2$ for the dimers. Similar to the arguments given in the previous Chapter, one can shown that the truncation (3.1) includes every possible interaction term which can be built up due to quantum fluctuations. All other U(1) symmetric couplings belonging to the $N \leq 4$-body sectors like, for instance, $\sim (\psi^*\psi)^2$, $\sim (\psi^*\psi)^4$, or $\sim \phi^*\phi^*\psi^4$ vanish identically as no diagram can generate them. Thus the truncation (3.1) is complete within the leading order derivative expansion. Due to the vacuum hierarchy, the different N-body sectors can be solved in subsequent steps [177]. In this spirit we first solve the two-body sector, then investigate the three-body sector in order to finally study the four-body problem.

The model (3.1) is equivalent to a zero-range, single channel model in the limit of open-channel dominated Feshbach resonances, where $g \to \infty$. In this limit the momentum dependence of $P_{\phi,\Lambda}$ can be neglected. Then, upon integrating out the molecular field, one obtains an effective atom-atom coupling $\lambda_\psi(\psi^*\psi)^2$ with $\lambda_\psi = g^2/m_\phi^2$ which is a zero-range interaction.

In Eq. (3.1) the higher-order couplings carry no explicit momentum or energy dependence. This makes the derivation of flow equations much simpler as we may project onto couplings at zero external momentum and frequency. The use of the energy gap E_ψ, however, allows to 'recapture' the energy dependence in an implicit way in the center-of-mass frame. The reason

for this is an additional semi-local gauge symmetry of the action (3.1). This symmetry has been discussed in detail in [105, 209, 210] and it leaves the real-time microscopic action $S = \Gamma_{k=\Lambda}$, cf. Eq. (3.1), invariant under the time-dependent U(1) transformations [105]

$$\psi \to e^{-iEt}\,\psi \qquad \phi \to e^{-i2Et}\,\phi, \tag{3.2}$$

when additionally the gap E_ψ is shifted by

$$E_\psi \to E_\psi + E. \tag{3.3}$$

This symmetry corresponds to an overall energy shift in the (real frequency) atom propagator. As a consequence, we may, instead of evaluating P_ψ explicitly at a finite external frequency E and $E_\psi = 0$, that is $P_\psi(\omega = E, \boldsymbol{q}; E_\psi = 0)$, equally well evaluate it at zero external frequency but at a finite gap $E_\psi = E$, $P_\psi(\omega = 0, \boldsymbol{q}; E_\psi = E)$. As we will see below this argument carries over to the dimer propagator and allows also to correctly capture the energy dependence of $\lambda_3(\boldsymbol{q}_1, \boldsymbol{q}_2; E)$, cf. (2.51), so that only the dependence on the momenta $\boldsymbol{q}_1$ and $\boldsymbol{q}_2$ is neglected. What we gain is a very simple and efficient way to derive flow equations as only zero external frequencies have to be considered while still keeping the energy-dependence of the vertices. Note, for few-body physics the energy gap E_ψ is always negative, $E_\psi < 0$. In the case of finite density, E_ψ is replaced by the chemical potential μ which is adjusted to yield the correct density $n = -1/V\,\partial\Gamma/\partial\mu$.

Beside the ansatz of Γ_k we must choose a suitable regulator function R_k in order to solve Eq. (2.40). Based on our treatment of the closely related three-fermion problem [105, 137], we choose the regulators,

$$\begin{aligned} R_\psi &= (k^2 - q^2)\theta(k^2 - q^2), \\ R_\phi &= \frac{A_\phi}{2}(k^2 - q^2)\theta(k^2 - q^2), \end{aligned} \tag{3.4}$$

with $q = |\boldsymbol{q}|$. These regulators are optimized in the sense of [172, 211] and allow the derivation of analytical results.

3.2 Two-body sector

The solution of the two-body problem can be found analytically in our approximation[1] (for the analogous problem considering fermions, see [105, 212]). The only running couplings in the two-body sector are the dimer gap m_ϕ^2 and the wave function renormalization A_ϕ. As there are no possible nonzero flow diagrams for the Yukawa coupling g, it does not flow in the vacuum limit. The flow equations of the two-body sector are shown in terms of Feynman diagrams in Fig. 3.1(a). The resulting expressions are given by

[1] The inverse atom propagator (one-body sector) is not renormalized in the non-relativistic vacuum.

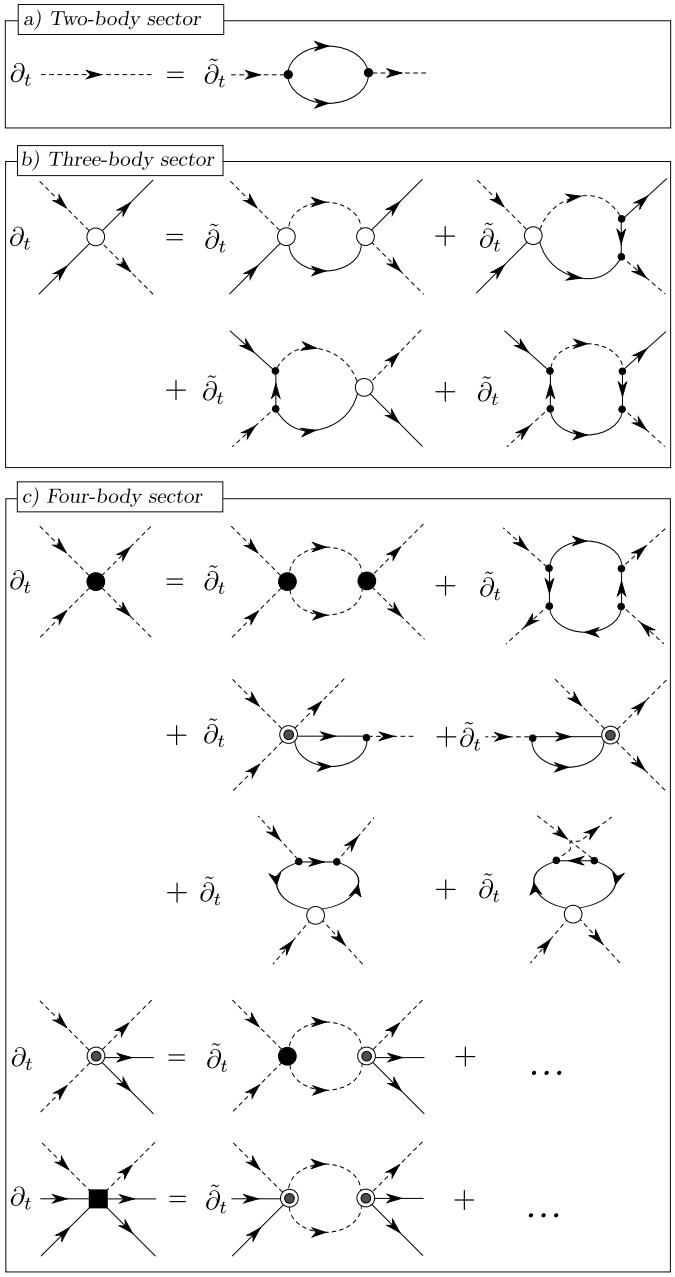

FIGURE 3.1: *The flow equations in terms of Feynman diagrams for the (a) two-body, (b) three-body, and (c) four-body sector. All internal lines denote full, regularized propagators. The scale derivative $\tilde{\partial}_t$ on the right hand side of the flow equations acts only on the regulators. Solid lines represent elementary bosons ψ, while dashed lines denote composite dimers ϕ. The vertices are: Yukawa coupling g (small black dot), atom-dimer vertex λ_{AD} (open circle), dimer-dimer coupling λ_ϕ (black circle), coupling β (two circles), and the atom-atom-dimer vertex γ (black square). Due to the large number of diagrams for the latter two vertex functions, we only show two exemplary diagrams.*

$$\begin{aligned}\partial_t m_\phi^2 &= \frac{g^2}{12\pi^2}\frac{k^5}{(k^2-E_\psi-i\epsilon)^2},\\ \partial_t A_\phi &= -\frac{g^2}{12\pi^2}\frac{k^5}{(k^2-E_\psi-i\epsilon)^3},\end{aligned} \tag{3.5}$$

where $t=\ln\frac{k}{\Lambda}$. In contrast to the derivation of similar equations in [71, 105, 106, 137, 212, 213, 214, 215, 216] we keep here explicit the infinitesimal $i\epsilon$ terms, which will be useful when identifying our model parameters with the two-body scattering physics.

The flow equations (3.5) can be solved analytically by direct integration from $k=0\ldots\Lambda$. The UV cutoff Λ of the theory effectively corresponds to a finite inverse range of our model which is of the order of $\Lambda\sim 1/l_{\rm vdw}$. In the true zero-range limit we have to take $\Lambda\to\infty$ which yields the scaling limit and correspondingly leads to the artificial Thomas collapse in the three-body problem, cf. Section 2.1. Here we take Λ large but finite and Λ will serve as the three-body parameter fixing the overall position of the Efimov spectrum. Also we will measure length and energy scales in terms of Λ. We assume that the cutoff scale is much larger than any other scale in the system, so that in particular $|E_\psi|/\Lambda^2\ll 1$. Under this condition the solution of Eqn. (3.5) reads:

$$m_\phi^2(k=0) = m_{\phi,\Lambda}-\frac{g^2}{12\pi^2}\Lambda+\frac{g^2}{16\pi}\sqrt{-E_\psi-i\epsilon}, \tag{3.6}$$

$$A_\phi(k=0) = A_{\phi,\Lambda}-\frac{g^2}{64\pi}\frac{1}{\sqrt{-E_\psi-i\epsilon}}. \tag{3.7}$$

When working at the unitarity point where $E_\psi=0$, it is useful to have the full RG scale k-dependent solution of the flow equations. As easily seen from Eqn. (3.5) the resulting expressions are

$$m_\phi^2(k,E_\psi=0) = m_{\phi,\Lambda}-\frac{g^2}{12\pi^2}(\Lambda-k), \tag{3.8}$$

$$A_\phi(k,E_\psi=0) = A_{\phi,\Lambda}-\frac{g^2}{12\pi}\left(\frac{1}{k}-\frac{1}{\Lambda}\right). \tag{3.9}$$

The next step is to fix the values of the parameters $A_{\phi,\Lambda}$, $m^2_{\phi,\Lambda}$, and g. Since the average action at the UV scale has to equal the classical action, $\Gamma_\Lambda=S$, and because we deal with a physical molecular state in the Hamiltonian, see also Eq. (2.23), we have $A_{\phi,\Lambda}=1$. Furthermore, $m^2_{\phi,\Lambda}$ is given by

$$m^2_{\phi,\Lambda}=\frac{g^2}{12\pi^2}\Lambda-2E_\psi+\delta m_\phi^2, \tag{3.10}$$

where the first term represents a counterterm taking care of the UV regularization of the two-body sector. The second term $-2E_\psi$ is enforced by the semi-local gauge symmetry (3.2)

and physically accounts for the fact that a dimer consists of two atoms. The additional term δm_ϕ^2 and the Yukawa coupling g are fixed by experimentally observable two-body scattering physics and the procedure is similar to the steps described in Section 2.3.

The two-body scattering amplitude $f(q)$ is obtained from the evaluation of the tree-level process shown in Fig. 2.9 at the infrared scale $k = 0$. Using the shift symmetry (3.2) the corresponding expression reads

$$f(q) = \frac{1}{16\pi} \frac{g^2}{P_{\phi,k=0}(\omega = 0, \mathbf{0}; E_\psi = q^2)}. \tag{3.11}$$

Here, P_ϕ is not evaluated at finite frequency $\omega = 2q^2$ and $E_\psi \equiv 0$ as done in the exact case, cf. Eq. (2.25). Instead it is evaluated at $\omega = 0$ and at $E_\psi \equiv q^2 > 0$, which is positive since we deal with the scattering of two atoms of momenta $\pm\boldsymbol{q}$ *above* the atom threshold at $E = 0$ and *each* of these atoms carries a kinetic energy $E_\psi = q^2$. We then obtain

$$\begin{aligned} f(q) &= \frac{1}{16\pi} \frac{g^2}{\delta m_\phi^2 - 2q^2 + \frac{g^2}{16\pi}\sqrt{-q^2 - i\epsilon}} \\ &= \frac{1}{\frac{16\pi\delta m_\phi^2}{g^2} - \frac{32\pi}{g^2}q^2 - iq} \\ &= \frac{1}{-1/a + \frac{1}{2}r_e q^2 - iq}. \end{aligned} \tag{3.12}$$

where in the last line we compare our result to the effective range expansion of $f(q)$. This then yields the identification $\delta m_\phi^2 = -g^2/(16\pi a)$ and g is given by the effective range,

$$r_e = -\frac{64\pi}{g^2} = -2r^*. \tag{3.13}$$

Here r^* denotes the characteristic 'range' of the underlying Feshbach resonance as defined in Eq. (2.22). We then obtain for the dimer gap:

$$m_\phi^2(k = 0, E_\psi) = -2E_\psi + \frac{g^2}{16\pi}\left(-\frac{1}{a} + \sqrt{-E_\psi - i\epsilon}\right). \tag{3.14}$$

In the following we derive the bound state energy spectrum of the four-body problem in the $(1/a, E)$ plane by using E_ψ to determine the energy of the various bound states. Thus we are only interested in negative energies which is why $E_\psi < 0$ and the $i\epsilon$ terms in Eqn. (3.6), (3.7), and (3.14) can safely be sent to zero.

The model (3.1) features a dimer bound state and in order to determine its binding energy ϵ_D we calculate the pole of the dimer propagator, corresponding to the condition $m_\phi^2(k =$

$0; E_\psi)|_{E_\psi=\epsilon_D/2} = 0$, which yields in the limit $E_\psi/\Lambda^2 \ll 1$

$$\begin{aligned} \epsilon_D = 2E_\psi &= -2\left(\frac{g^2}{64\pi} - \sqrt{\frac{g^4}{(64\pi)^2} + \frac{g^2 a^{-1}}{32\pi}}\right)^2 \\ &= -\frac{2}{r_e^2}\left(1 - \sqrt{1 - \frac{2r_e}{a}}\right)^2, \end{aligned} \tag{3.15}$$

where we used in the first equation that the dimer consists of two atoms of energy E_ψ each. In the limit $g \to \infty$, corresponding to $r^* \to 0$ one recovers the well-known result $\epsilon_D = -2/a^2$. The dimer bound state energy is shown as a function of the inverse scattering length in Fig. 3.3 (black solid line). The deviation from the universal $\sim 1/a^2$ scaling for large inverse scattering lengths is due to the finite size of g which is taken to be $g^2/\Lambda = 10$. In the regime of small scattering length a one finds a crossover of the dimer binding energy to the limiting behavior $\epsilon_D = -4/(ar^*)$.

3.3 Three-body sector

In the previous Chapter, we found that the bound state spectrum of the three-body sector is much richer than its two-body counterpart. Let us summarize some of our findings: in his seminal papers [44, 81, 86, 120] Efimov showed the existence of an infinite series of three-body bound states for strong two-body interactions. These energy levels exhibit a universal geometric scaling law as one approaches the unitarity point $E = a^{-1} = 0$. Remarkably, these three-body bound trimer states exist even for negative scattering lengths a where no two-body bound state is present; they become degenerate with the three-atom threshold for negative scattering length and merge into the atom-dimer threshold for positive a. Within a zero-range model one has to introduce an additional three-body parameter in order to determine the actual positions of the degeneracies [100, 101]. The fitting of such a three-body parameter becomes obsolete if one however starts from a truly physical model as done in Chapter 2. In the present Section we want to shortly review how Efimov physics can be treated within a derivative expansion. For a more detailed account on this matter and an application to the three-component ^{6}Li Fermi gas we refer to [96, 105, 137]. For a recent review on fRG applications to Efimov physics, see [46].

In our truncation, the three-body sector contains a single, pointlike[2] $\phi^*\psi^*\phi\psi$ term with a coupling λ_3, which is assumed to vanish in the UV. It is build up by quantum fluctuations during the RG flow and the corresponding Feynman diagrams of the flow equation for λ_3 is shown in Fig. 3.1(b). The derivation of the flow equation of λ_3 follows essentially the same

[2]We denote a vertex as pointlike if it carries no *explicit* energy and momentum dependence.

steps as outlined in Section 2.5. The starting point is the flow equation

$$\partial_k \lambda_3^{(k)}(E) = -\tilde{\partial}_k \int_L \frac{1}{P_\psi^R(\omega,\boldsymbol{l}) P_{\phi,k}^R(-\omega+E,-\boldsymbol{l})} \left[\lambda_3^{(k)}(E) + \frac{g^2}{P_\psi^R(-\omega+E,-\boldsymbol{l})} \right]^2, \qquad (3.16)$$

which can be derived from Eq. (2.50) and (2.52), respectively, with the difference that the propagators are regulated additively, $P^R_{\psi,\phi} = P_{\psi,\phi} + R_{\psi,\phi;k}$ and a projection onto zero external momenta has been performed $\lambda_3(E) \equiv \lambda_3(\mathbf{0},\mathbf{0};E)$. Furthermore, note the relative minus sign compared to Eq. (2.50) which is due to a different sign convention for λ_3. The form factors χ are absent as we are considering only the limit $\sigma \to 0$ in this chapter. Since we are working in the pointlike approximation we furthermore perform the projection onto zero external *energy* E, $\lambda_{3,k} = \lambda_3^{(k)}(E)|_{E=0}$.

At this point, note that the propagators in Eq. (3.16) are defined for vanishing atom gap E_ψ as also done in the Chapter 2. The shift symmetry (3.2) can now be used to retain the energy dependence of $\lambda_3^{(k)}$ despite the projection onto zero energy. To see this, note that the energy E is the total energy which the *three* atoms have which enter the atom-dimer collision, cf. Fig. 2.16, and thus each atom carries an energy $E_\psi = E/3$. Furthermore the dependence on E in Eq. (3.16) and Eq. (2.54) appears in the last argument of $\lambda_3^{(k)}(q_1,q_2;E)$. It is thus a pure 'external' parameter which is not influenced by the loop momenta[3]. We may now perform a shift $\omega \to \omega + E_\psi$ of the real loop frequency and use the identification $E = 3E_\psi$ to find that the evaluation of $\partial_k \lambda_3^{(k)}(E)$ at $E_\psi = 0$ is identical[4] to the evaluation of the RHS of Eq. (3.16) at vanishing E but for a finite $E_\psi = E/3$. Due to this equivalence we can use the dependence on E_ψ of the *pointlike* coupling λ_3 to recover the energy dependence of the atom-dimer vertex. This dependence will be used below to determine the Efimov spectrum at finite energy. Note, that the *momentum* dependence of $\lambda_3^{(k)}(q_1,q_2;E)$ is *not* resolved in our approximation. This, together with the approximation of the dimer propagator P_ϕ, leads to deviations in the Efimov scaling and the corresponding number s_0.

Three-body limit cycle

In this Chapter, we are mostly interested in the unitarity point where the scattering length diverges and where the energy E is at the atom-threshold and thus vanishes, $E = 0$. Remarkably, it is possible to obtain an *analytical* solution for the flow equation of λ_3 in this limit, while away from unitarity we have to rely on a numerical solution. In our approximation the dimer field ϕ develops a large anomalous dimension $\eta = -\frac{\partial_t A_\phi}{A_\phi} = 1$ at unitarity which is consistent with the exact solution of the two-body sector [96, 177]. As the atom and dimer propagators

[3] This is different in the four-body sector. Here the coupling λ_3 appears in a different momentum configuration in the loop such that the loop momentum appears in the last argument of $\lambda_3^{(k)}$. This can be seen from the last two flow equations depicted for the flow of λ_4 in Fig. 3.1(c).

[4] Due to the shift symmetry the exact dimer propagator obeys $P_\phi(\omega + 2E', \boldsymbol{p}, E_\psi = 0) = P_\phi(\omega, \boldsymbol{p}, E_\psi = E')$.

have vanishing gaps in the IR the two-body sector respects a continuous scaling symmetry. This reflects that at the unitarity point all intrinsic length scales drop out of the problem and the system becomes classically scale invariant. Furthermore, the Yukawa coupling g is dimensionless due to the anomalous dimension $\eta = 1$ and the only length scale present is the inverse ultraviolet cutoff Λ^{-1}, which defines the validity limit of our effective theory. When furthermore the limit $\Lambda \to \infty$ is taken all scales are gone and the system is perfectly scale invariant. Contrary to the analogous fermionic system, for bosons this continuous scaling symmetry is broken by the Efimov effect.

In order to find the solution of the three-body sector we switch to the rescaled, dimensionless coupling $\tilde{\lambda}_3 \equiv \frac{k^2}{g^2}\lambda_3$. With this choice the flow equation of $\tilde{\lambda}_3$ becomes independent of the RG scale k and Yukawa coupling g,

$$\partial_t \tilde{\lambda}_3 = \underbrace{\frac{24}{25}\left(1-\frac{\eta}{15}\right)}_{a}\tilde{\lambda}_3^2 \underbrace{-\frac{14}{25}\left(1-\frac{4\eta}{35}\right)}_{b}\tilde{\lambda}_3 + \underbrace{\frac{26}{25}\left(1-\frac{\eta}{65}\right)}_{c}. \tag{3.17}$$

The terms proportional to η are due to the $\tilde{\partial}_k$ derivative acting on the wave function renormalization A_ϕ in $R_{\phi,k}$, cf. Eq. (3.4). In order to make the fixed point structure of the three-body RG flow apparent it is useful to rewrite Eq. (3.17) as

$$\partial_t \tilde{\lambda}_3 = \frac{112}{125}(\tilde{\lambda}_3 - c_1)(\tilde{\lambda}_3 - c_2) \tag{3.18}$$

with $c_{1/2} = (31 \pm i5\sqrt{535})/112$. We see that the limit cycle character of the RG flow is signaled by the fact that the fixed points are not real but complex numbers! Since the coupling $\tilde{\lambda}_3$ is a real number its winding around the (in the complex plane symmetrically located) fixed points $c_{1/2}$ leads to periodic divergencies of the RG flow of $\lambda_3 \in \mathbb{R}$. To visualize the flow of $\tilde{\lambda}_3$ it is helpful to use the idea of complex extension, developed in [111]. Here, the flow of $\tilde{\lambda}_3 \equiv \tilde{\lambda}_1 + i\tilde{\lambda}_2$ is studied in the complex plane and it is depicted in Fig. 3.2(a). The terminology of a limit *cycle* becomes even more apparent when the flow is stereographically projected onto the Riemann sphere as shown in Fig. 3.2(b).

As was demonstrated in [96, 111, 217], the behavior of the solution of this type of flow equation is determined by the sign of the discriminant D of the right hand side of Eq. (3.17) which is negative, $D = b^2 - 4ac < 0$. Eq. (3.17) can be solved analytically and one finds[5]

$$\tilde{\lambda}_3(t) = \frac{-b + \sqrt{-D}\tan\left(\frac{\sqrt{-D}}{2}(t+\delta)\right)}{2a}, \tag{3.19}$$

where δ is connected to the three-body parameter and determines the initial condition. Remarkably, the three-body sector exhibits a quantum anomaly: the RG flow of the renormalized coupling $\tilde{\lambda}_3$ exhibits a limit cycle, which, due to its periodicity, breaks the classically

[5]Here, a denotes the first coefficient in Eq. (3.17) and not the scattering length.

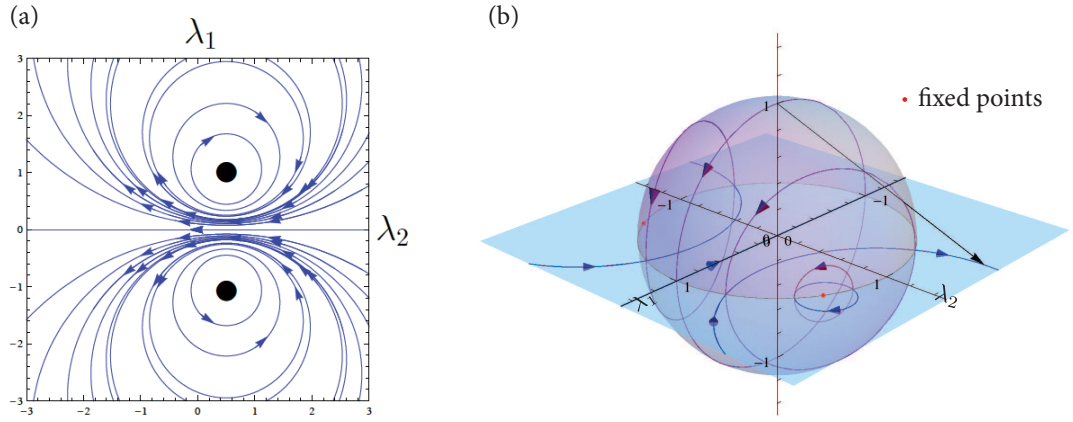

FIGURE 3.2: *Three-body RG limit cycle in the complex plane. (a) The phase portrait of the flow equations Eq.* (3.18). *(b) RG flows in the complex plane and the corresponding map onto the Riemann sphere. The pink dots represent the two complex fixed points. The solid lines with arrows, pointing towards the UV, correspond to different RG trajectories. Additionally, the black straight solid line from the north pole illustrates the stereographic projection of the Riemann sphere S^2 onto the complex plane $\mathbb{C}$.*

continuous scaling symmetry to the discrete subgroup Z. The Efimov parameter can be determined from the period of the limit cycle [96] and is given in our approximation by

$$s_0 = \frac{\sqrt{-D}}{2} = \sqrt{\frac{107}{125}} \approx 0.925203. \tag{3.20}$$

As we have seen and derived in Chapter 2, the exact result is given by $s_0 \approx 1.00624$ [66]. Considering the simplicity of our pointlike approximation, which, as discussed above, does not resolve any momentum structure of the interaction vertex of the three-body sector, the agreement is quite good and suggests that our model should provide a solid basis for an approximate solution of the four-body problem.

Efimov spectrum

The presence of N-body bound states leads to divergencies in the corresponding N-body vertices. The periodic divergencies in the analytical solution of $\tilde{\lambda}_3$ in Eq. (3.19) correspond therefore to the presence of the infinitely many Efimov trimer states at the unitarity point. We can use the divergencies in λ_3 to calculate the bound state spectrum also away from the unitarity point. In Chapter 2 we showed that the trimer energies can be extracted from the poles of λ_3 as function of E. From the discussion before we know that the explicit energy dependence of $\lambda_3(E)$ can be extracted from the dependence of λ_3 on E_ψ. The trimer energy can then be calculated by determining the atom energies E_ψ for which $\tilde{\lambda}_3$ exhibits divergencies in the IR

as function of a^{-1}. The trimer binding energies are then given by $E_T = 3E_\psi$. The resulting three-body spectrum is shown in Fig. 3.3 (green lines). For calculational purposes we switch to the static trimer approximation which is equivalent to our two-channel model in Eq. (3.1). We describe this procedure in Section 3.5.

Similar to the exact result in Chapter 2 we find that as the unitarity point is approached the trimer binding energies form a geometric spectrum and the ratio between adjacent levels is given by

$$\frac{E_T^{(n+1)}}{E_T^{(n)}} = e^{-\frac{2\pi}{s_0}}. \tag{3.21}$$

This can also be understood from the limit cycle flow of λ_3. At each scale $k = \Lambda e^t$, where λ_3 diverges, one hits a trimer state. The RG scale k can in turn be connected to the atom energy E_ψ [96, 105, 137] and as the divergencies appear periodically in t one easily obtains Eq. (3.21).

There is an additional universal relation obeyed by the trimer energy levels which we may take as a measure of the quality of our approximation. It is given by the relation of the trimer binding energies $E_T^{(n)}$ at unitarity and the value of a for which the trimers become degenerate with the atom-dimer ($a_*^{(n)}$) and three-atom threshold ($a_-^{(n)}$), respectively. For comparison with the literature, it is useful to define a wave number $\varkappa^*$ given by $E_T = -\hbar^2\varkappa^{*2}/M$ (in our convention, $E_T = -2\varkappa^{*2}$). We then find

$$a_-^{(n)}\varkappa_*^{(n)} \approx -1.68, \quad a_*^{(n)}\varkappa_*^{(n)} \approx 0.08 \qquad (n \to \infty) \tag{3.22}$$

which may be compared with the exact result $a_-^{(n)}\varkappa_*^{(n)} = -1.5076$, $a_*^{(n)}\varkappa_*^{(n)} = 0.07076$ from the fully momentum-dependent calculation in [66, 100, 101] and as also recovered in our calculation in Chapter 2. Again, the good agreement with our approximate solution suggests that our model should provide a solid basis for the step to the four-body problem.

3.4 Four-body sector

Recently, the solution of the four-body problem in the low-energy limit has gained a lot of interest. In quantum mechanical calculations the existence of two tetramer (four-body bound) states was conjectured for each of the infinitely many Efimov trimers [200, 201]. By calculating the lowest few sets of bound state levels von Stecher *et al.* [48, 202] concluded that the ratios of the binding energies of the two tetramers with respect to the energy of the trimer state approach universal constants. However, with the quantum mechanical approach the calculation directly at the unitarity point ($a^{-1} = E = 0$), marked by a star in Fig. 3.3, has so far been impossible, although this point is of great interest when one wants to gather evidence for universality of the four-body system. In fact, in the three-body sector the universal, infinite RG limit cycle appears only exactly at the unitarity point and only here all non-universal corrections vanish identically. It is one of the advantages of the fRG approach that, in contrast to the quantum mechanical calculation, the unitarity regime can be directly accessed.

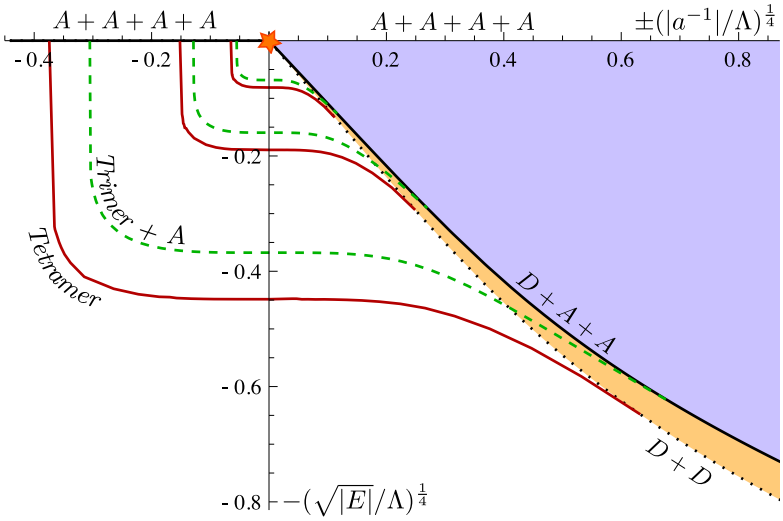

FIGURE 3.3: *The generalized Efimov plot for four identical bosons. We plot the energy levels of the various bound states as a function of the inverse s-wave scattering length a as numerically calculated in our approximative, effective theory. In order to improve the visibility of the energy levels we rescale both the dimensionless energy E/Λ^2 and the dimensionless inverse scattering length a^{-1}/Λ where Λ denotes the UV cutoff of our model. Also, we only show the first three sets of Efimov levels. The solid black line denotes the atom-atom-dimer threshold, while the dotted black line gives the dimer-dimer threshold. In the three-body sector one finds the well known spectrum of infinitely many Efimov trimer states (green, dashed) which accumulate at the unitarity point $E = a^{-1} = 0$, indicated by the orange star. In our pointlike approximation the four-body sector features a single tetramer (solid, red) associated with each trimer state.*

In order to investigate the four-body sector we include all possible, U(1) symmetric, momentum independent interaction vertices in the effective flowing action Γ_k. As discussed in Section 3.1 one can show by the use of the vacuum hierarchy [96, 165, 177, 210] and under the assumption that all three- and four-body couplings vanish in the microscopic action, $S = \Gamma_\Lambda$, that from all these possible vertices only the three couplings λ_ϕ, β, and γ are built up by quantum fluctuations. These are thus included in our truncation, Eq. (3.1). Very recently Tanizaki showed that the vacuum hierarchy may be violated in the RG evolution when the atoms and composite dimers are integrated out simultaneously [164]. While our RG scheme in Chapter 2 respects fully the vacuum hierarchy, the regulator choice in this Chapter may mildly violate the decoupling of n-body sectors. From [164] we, however, expect that the deviations due to this violation are small compared to the corrections introduced by using the approximate derivative expansion.

Four-body limit cycle and universality

Let us first analyze the unitarity point. Here it is helpful to switch to rescaled, dimensionless couplings

$$\tilde{\lambda}_\phi = \frac{k^3}{\pi^2 g^4}\lambda_\phi, \quad \tilde{\beta} = \frac{k^4}{g^3}\beta, \quad \tilde{\gamma} = \frac{\pi^2 k^5}{g^2}\gamma. \tag{3.23}$$

The corresponding flow equations are obtained by inserting the effective flowing action Γ_k, Eq. (3.1), into the Wetterich equation (2.40). By the use of the rescaled couplings we find three coupled ordinary differential equations, which are again coupled to the two- and three-body sectors, but become independent of an explicit g and k. The diagrammatic representation of the flow equations is shown in Fig. 3.1(c). Considering the $\mathcal{O}(10^2)$ Feynman diagrams which have to be evaluated it is quite remarkable that the flow equations at the unitarity point take the fairly simple, analytical form[6]

$$\partial_t \tilde{\lambda}_3 = \frac{128}{125} - \frac{62}{125}\tilde{\lambda}_3 + \frac{112}{125}\tilde{\lambda}_3^2, \tag{3.24}$$

$$\partial_t \tilde{\lambda}_\phi = \frac{1}{16} + \frac{1}{3}\tilde{\beta} - \frac{1}{6}\tilde{\lambda}_3 + 3\tilde{\lambda}_\phi + \frac{128}{15}\tilde{\lambda}_\phi^2, \tag{3.25}$$

$$\begin{aligned}\partial_t \tilde{\beta} &= \frac{188}{125}\tilde{\beta} + \frac{1}{6}\tilde{\gamma} + \frac{128}{125}\tilde{\lambda}_3 \\ &+ \frac{224}{125}\tilde{\lambda}_3\tilde{\beta} - \frac{156}{125}\tilde{\lambda}_3^2 + \frac{4384}{375}\tilde{\lambda}_\phi \\ &+ \frac{128}{15}\tilde{\beta}\tilde{\lambda}_\phi - \frac{3968}{375}\tilde{\lambda}_3\tilde{\lambda}_\phi,\end{aligned} \tag{3.26}$$

$$\begin{aligned}\partial_t \tilde{\gamma} &= \frac{4592}{375} + \frac{8768}{375}\tilde{\beta} + \frac{128}{15}\tilde{\beta}^2 \\ &+ \frac{1}{125}\tilde{\gamma} - \frac{79072}{1875}\tilde{\lambda}_3 - \frac{7936}{375}\tilde{\beta}\tilde{\lambda}_3 \\ &+ \frac{448}{125}\tilde{\gamma}\tilde{\lambda}_3 + \frac{74368}{1875}\tilde{\lambda}_3^2 - \frac{5376}{625}\tilde{\lambda}_3^3.\end{aligned} \tag{3.27}$$

We pointed out in the last section that the appearance of bound states is connected with divergent vertex functions $\Gamma_k^{(n)}$ and we exploit this behavior to determine the bound state spectrum of the four-boson system. These infinities are complicated to handle in a numerical solution of the theory. In particular, the numerical treatment of unbounded limit cycles is problematic due to the periodic infinities during the RG flow. In order to circumvent this difficulty we use the method of inverse couplings.

The basic idea is quite simple. In the beginning of the RG flow one follows the rescaled couplings $\tilde{\lambda}_\phi$, $\tilde{\beta}$, and $\tilde{\gamma}$ according to Eqn. (3.24)-(3.27). When the couplings reach a critical

[6]For illustrative purpose we show the analytical form of the flow equations at the unitarity point only. Away from this limit their explicit expressions become much more complex.

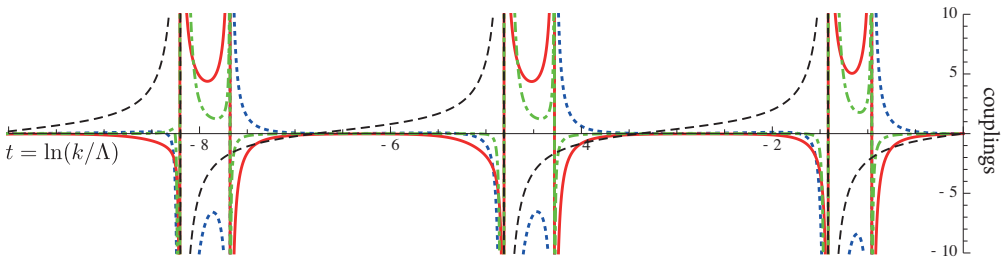

FIGURE 3.4: *Renormalization group limit cycle behavior of the three- and four-body sector at the unitarity point* $E = a^{-1} = 0$. *The rescaled, dimensionless couplings* $\tilde{\lambda}_3$, $4\tilde{\lambda}_\phi$, $\tilde{\beta}/6$, *and* $\tilde{\gamma}/1000$ *are plotted as functions of* $t = \ln(k/\Lambda)$. *Not only the three-body coupling* $\tilde{\lambda}_3$ *(dashed, black) exhibits a limit cycle behavior, but also the four-body sector couplings* $\tilde{\lambda}_\phi$ *(red, solid),* $\tilde{\beta}$ *(blue, dotted), and* $\tilde{\gamma}_1$ *(green, dotdashed) obey a limit cycle attached to the three-body sector with the same period.*

numerical value in the close vicinity of a tetramer resonance at the (logarithmic) RG scale $t = t_T^{(n)}$, one switches to the flow of the inverse couplings $\bar{\lambda}_3 = 1/\tilde{\lambda}_3$, $\bar{\lambda}_\phi = 1/\tilde{\lambda}_\phi$, $\bar{\beta} = 1/\tilde{\beta}$, and $\bar{\gamma} = 1/\tilde{\gamma}$. In the corresponding flow equations at first sight potentially dangerous terms such as the expression $\bar{\lambda}_\phi^2/\bar{\beta}$ appearing in the flow $\partial_t \bar{\lambda}_\phi$ approach in fact well-defined, finite values as both $\bar{\lambda}_\phi$ and $\bar{\beta}$ tend to zero at $t = t_T^{(n)}$. In order to handle the additional zero-crossings of $\bar{\lambda}_3$ when the flow approaches a trimer resonance at $t = t_{\mathrm{Tri}}^{(n)}$, a different approach has to be taken. It turns out that in this case numerically stable results can be achieved by studying the evolution of the rescaled couplings $\hat{\lambda}_\phi = \tilde{\lambda}_\phi/\tilde{\lambda}_3$, $\hat{\beta} = \tilde{\beta}/\tilde{\lambda}_3^2$, $\hat{\gamma} = \tilde{\gamma}/\tilde{\lambda}_3^3$.

The result of the numerical calculation of the four-body sector at unitarity is shown in Fig. 3.4. Here, we display the RG flows of all nonzero three- and four-body sector couplings as a function of the logarithmic RG scale $t = \ln(k/\Lambda)$. The three-body coupling $\tilde{\lambda}_3$ (black dashed line) exhibits the well-known limit cycle behavior, described in Section 2.5, with the period being connected to the Efimov parameter s_0. Remarkably, there is an additional limit cycle in the flow of the four-body sector couplings with a periodic structure of exactly the same frequency as the three-body sector. This four-body sector limit cycle exhibits resonances which are shifted with respect to the ones belonging to the three-body system. The magnitude of this shift is given by a new universal number, which is inherent to the four-body sector.

Our observation is that the four-body sector is intimately connected with the three-body sector at the unitarity point. Its flow is permanently attached to the running of the three-body sector from the first three-body resonance on. For $k \ll \Lambda$ the flow reaches its 'final' periodic structure. Due to the tight bond between the three- and four-body sector, no room is left for an additional four-body parameter.

We have explicitly checked the universal aspects of the flow by using, for instance, finite initial values of the four-body couplings in the UV. The result is shown in Fig. 3.5. Note in

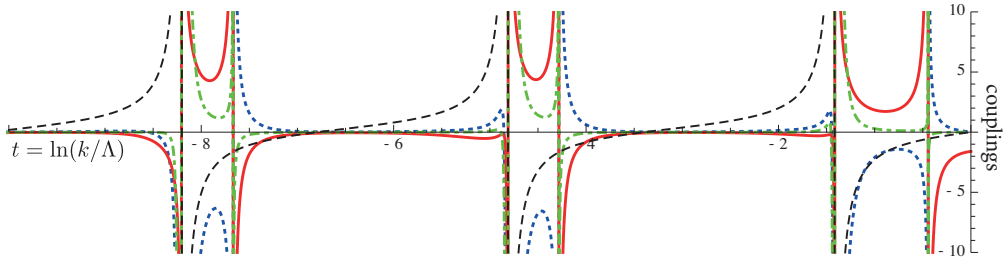

FIGURE 3.5: *Check of universality. Renormalization group limit cycle behavior of the three- and four-body sector at the unitarity point* $E = a^{-1} = 0$. *The rescaled, dimensionless couplings* $\tilde{\lambda}_3$ *(dashed, black),* $4\tilde{\lambda}_\phi$ *(red, solid),* $\tilde{\beta}/6$ *(blue, dotted), and* $\tilde{\gamma}/1000$ *(green, dotdashed) are plotted as functions of* $t = \ln(k/\Lambda)$. *In contrast to Fig. 3.4 nonzero UV values for the four-body couplings have been used. Although different in the UV the flow approaches its universal infrared limit cycle very quickly.*

particular the shift of the first tetramer resonance. While the position of the first tetramer and even its existence is highly non-universal, the higher tetramer states approach the universal, infrared result very quickly and we find that arbitrary choices of initial values lead to the same infrared behavior. Furthermore, the Yukawa coupling g, which is connected to the strength of the Feshbach resonance by Eq. (3.13), completely disappeared in the flow equations at unitarity: again an indicator of universality. Having done this calculation directly at the unitarity point our conclusion is, that, within our simple approximation, the four-body sector behaves truly universal and independent of any four-body parameter confirming the conjecture made by Platter *et al.* [200, 201] and von Stecher *et al.* [48, 202]. We expect that universality will also hold for an improved truncation and maybe even for N-body bound states with $N > 4$.

Origin of the degenerate tetramer resonance

Naively one expects that each resonance in the flow of the vertex functions is connected to the presence of a bound state. As one observes there are also additional resonances in the four-body sector being degenerate with the three-body sector resonances. At first sight one may arrive at the conclusion that these resonances are pure artifacts of our approximation and that they will disappear as one includes further momentum dependencies in the field theoretical model. On the other hand one can also take a different perspective on these resonances by taking into account that the RG scale k-dependence of vertices is related to their respective energy dependence.[7] For this reason the divergencies at $t_{\text{Tri}}^{(n)}$ may carry some deeper physical insight. In fact, these divergencies may be due to non-analyticities of the energy dependence

[7]By a simple argument, one can see that there is such a relation between the RG scale k-dependence of a coupling and its 'true' energy dependence: Let us consider the energy dependence of the full, inverse dimer propagator P_ϕ which is a solution of the fully energy dependent flow equation (2.45) in Chapter 2 which we have to continue to real energies E. In a standard ladder summation in Eq. (2.45) no k^2 regulator term were present. The energy

of the four-body vertices which are *not* connected to bound state *poles*. Indeed, as the energy of a tetramer becomes larger than the energy of the lowest trimer state, the tetramer can decay into a trimer and a free atom, which is in this case the energetically favorable configuration. The trimer energy in this respect marks the atom-trimer scattering threshold. It is well-known that such continuum thresholds are connected to branch cuts in the respective vertex function, with a branch point exactly where the continuum emerges. Although in our pointlike approximation such non-analyticities cannot be resolved by the vertex λ_3 itself, they can show up as spurious divergencies in the RG scale k-dependent $\lambda_3 = \lambda_3(k)$. At first sight one may guess that these divergencies cannot be distinguished from divergencies belonging to true bound state poles within a derivative expansion. This is, however, not quite true.

In order to show this, we use the method of complex extension developed in [96]. The idea is to extend the domain of the running couplings to the complex plane

$$\begin{aligned} \lambda_3 &\to \lambda_{3,1} + i\lambda_{3,2} & \lambda_\phi &\to \lambda_{\phi,1} + i\lambda_{\phi,2} \\ \beta &\to \beta_1 + i\beta_2 & \gamma &\to \gamma_1 + i\gamma_2. \end{aligned} \tag{3.28}$$

This effectively doubles the number of real flow equations and additional initial conditions must to provided. We choose a small value $\lambda_{3,2}/\Lambda^2 = \epsilon = 10^{-5}$ in our numerical calculation and take all other imaginary parts to be zero in the UV. In physical terms, by the complex extension we convert the stable bound states into metastable resonances. One may compare this with the procedure of Braaten and Hammer [126, 139, 218] who introduce a parameter η^* in order to model the decay of the trimers to deeply bound states which have not been explicitly included in the effective model.[8] In this line we view our complex extension as a way to, on the one hand, include these deeply bound states in the fRG calculation. On the other hand, this allows us to study the evolution of the imaginary part of the four-body vertices as the trimer resonance, which represents energetically the atom-trimer threshold, is crossed. Specifically, we find that for $\epsilon \ll 1$ the decay width of the n$^{\text{th}}$ Efimov trimer $\Gamma^{(n)}_{\text{Tri}}$ is given by $\Gamma^{(n)}_{\text{Tri}} = 4\epsilon E^{(n)}_{\text{Tri}}$ at unitarity. This is in agreement with the result in [66]

$$\Gamma^{(n)}_{\text{Tri}} \approx \frac{4\eta^*}{s_0} E^{(n)}_{\text{Tri}} \tag{3.29}$$

which holds for small η^*. Thus, for $\epsilon \ll 1$, the relation to the parameter η^* introduced by Braaten and Hammer is given by

$$\epsilon = \frac{\eta^*}{s_0}. \tag{3.30}$$

E itself however serves as an effective infrared cutoff. In a pointlike RG approximation we project this equation onto zero external energy. Instead we, however, have the regulator k^2 in the denominator of Eq. (2.45). One can now directly see that we may trade the energy E in the full energy dependent ladder expression with the term $2k^2$ in Eq. (2.45). In the resulting k-dependent solution $P_{\phi,k}$ the k-dependence is equivalent to the dependence on the energy E in the limit of $g \to \infty$.

[8] The parameter η^* has for instance been measured in a system of ^{7}Li atoms where one finds $\eta^* \approx 0.2$ [134].

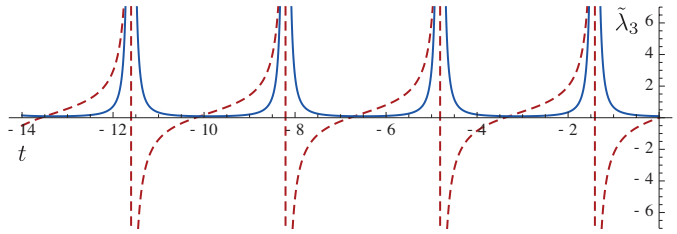

FIGURE 3.6: *Renormalization group limit cycle behavior of the dimensionless, complex coupling $\tilde{\lambda}_3$: real part (red, dashed), imaginary part (blue, solid).*

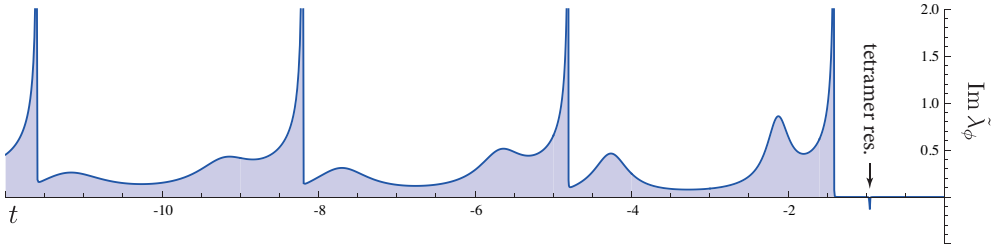

FIGURE 3.7: *Renormalization group flow of the imaginary part of dimensionless coupling $\tilde{\lambda}_\phi$.*

In Fig. 3.6 we show the flow of the real and imaginary part of the three-body coupling $\tilde{\lambda}_3$ as function of the logarithmic RG scale t. This plot corresponds directly to what was shown in Fig. 3.2 before. In the three-body sector the trimers are only unstable due to the decay to the deeply bound states not explicitly included in our model. We observe that there is a resonant enhancement of $\tilde{\lambda}_{3,2}$, with a shape of a typical bound state resonance everytime a trimer resonance is passed. These resonances have a constant width obeying Eq. (3.29).

The situation is different for the four-body couplings. In Fig. 3.7 we show the flow of the imaginary part of the coupling $\tilde{\lambda}_\phi$. As the coupling encounters the first tetramer state, the flow shows a peak in the imaginary part much like in the case of λ_3 and its width can be interpreted as due to the decay to the deeply bound states; other decay channels are not present for this state. Having crossed this resonance the imaginary part goes back to its small value. As the k^2 dependence of the flow of couplings resembles to some extent the energy dependence of the full vertices, the behavior of λ_ϕ corresponds just to what one would expect from a bound state pole.[9] The flow changes its characteristics, however, dramatically when it crosses the first trimer state at $t = t^{(0)}_{\mathrm{Tri}}$. Here the imaginary part experiences a large enhancement which

[9]The bound state peak in $\mathrm{Im}\tilde{\lambda}_\phi$ has the wrong sign when using the adhoc replacement (3.28). Strictly speaking, one should take the $i\epsilon$ prescription for the propagators involved in the theory and carry them through the calculation for a finite ϵ. We then expect this resonance to have the correct signature. Since we are only interested in an heuristic argument we carry on with the more simple prescription (3.28).

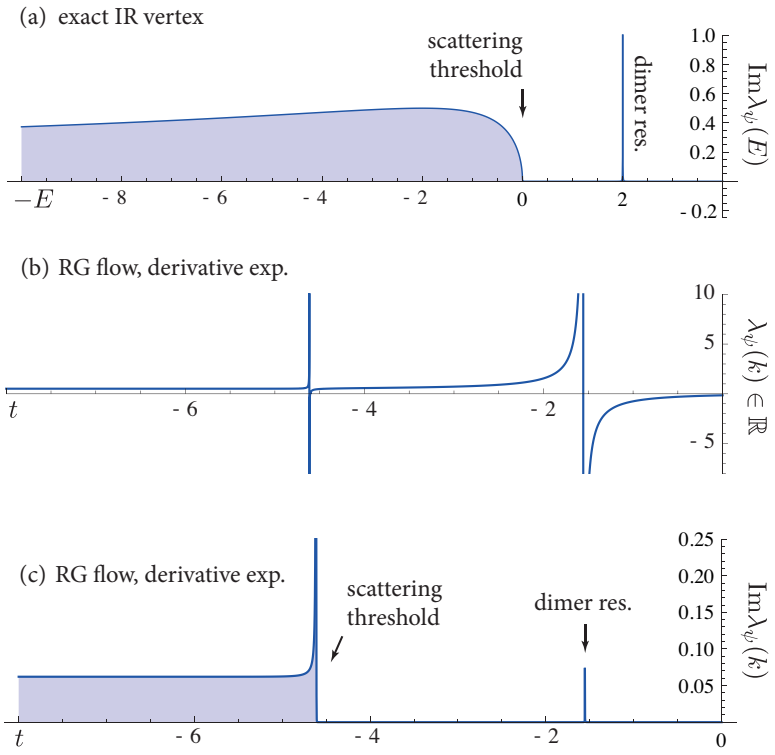

FIGURE 3.8: *(a) Imaginary part of the full two-atom scattering vertex λ_ψ (T-matrix) as function of energy for $a = 1$. (b) RG flow of the purely real coupling $\lambda_\psi(k)$ given by Eq.* (3.32) *evaluated for a positive energy E_ψ above the atom threshold. (c) RG flow of the imaginary part of $\lambda_\psi = \lambda_{\psi,1} + i\,\lambda_{\psi,2}$ as function of the logarithmic RG scale $t = \ln(k/\Lambda)$ for $E_\psi > 0$.*

does not go back to small values after the resonance. The k-dependence of this enhancement reminds of the typical energy dependence of the threshold behavior of a scattering vertex.

A similar threshold behavior can, for instance, be seen when evaluating the energy dependence of the full two-atom scattering vertex $\lambda_\psi(E)$ which, taking the single-channel limit of Eq. (2.47), has the form

$$\lambda_\psi(E)^{-1} \propto -\frac{1}{a} + \sqrt{-E/2 - i\epsilon}. \tag{3.31}$$

The resulting imaginary part is shown in Fig. 3.8(a) for a scattering length $a = 1$.

We can use the two-body problem as an analogy in order to support our expectation that the divergencies in the four-body couplings at the position of the trimer states are indeed due to a atom-trimer scattering threshold behavior. To do so we calculate the RG flow of the two-atom vertex λ_ψ in a leading order derivative expansion, i.e. in the pointlike limit. The flow

can be derived from Eq. (3.5) using $\lambda_\psi = -g^2/m_\phi^2$ with the resulting expression

$$\partial_t \lambda_\psi = -\frac{\lambda_\psi^2}{12\pi^2} \frac{k^5}{(k^2 - E_\psi)^2}. \tag{3.32}$$

This flow equation can be solved numerically for such an initial value $\lambda_\psi(k = \Lambda)$ such that a weakly bound state exists, i.e. $a > 0$, and for energies E_ψ above the atom threshold. One then encounters divergencies during the flow which can be handled similarly as for the case of the four-body coupling using the inverse coupling $1/\lambda_\psi$. The result is shown in Fig. 3.8(b). Two divergencies appear, and the first belongs to a bound state resonance. At first sight the second resonance, which reminds of the degenerate resonances we encounter in the four-body couplings, could be mistaken as a bound state resonance. When the flow equation is, however, evaluated in the complex coupling plane ($\lambda_\psi = \lambda_{\psi,1} + i\,\lambda_{\psi,2}$), and using the strict $i\epsilon$ prescription for the propagators, the true nature of the resonance becomes clear, see Fig. 3.8(c) where we show the RG flow imaginary part $\lambda_{\psi,2}$. The first resonance features a large enhancement of $\lambda_{\psi,2}$ which has the characteristics of a bound state resonance. In the vicinity of the second enhancement of λ_ψ from Fig. 3.8(b), $\lambda_{\psi,2}$ behaves differently and very similar to what we found in the case of the four-body coupling: the coupling $\lambda_{\psi,2}$ shows an enhancement which does not vanish after crossing the resonance. In this case we, however, know that this resonance is indeed connected to the non-analyticity of the full solution $\lambda_\psi(E)$ which corresponds to the atom-atom scattering threshold. Having this analogy in mind, it is reasonable to assume that the additional resonances of the four-body couplings λ_ϕ, β, and γ at the trimer resonances are indeed due to non-analyticities in the full energy dependent couplings, which are *not* connected to bound states, but merely to the onset of the atom-trimer scattering continuum.

Missing tetramer state

We can already infer from the calculation at unitarity that within our approximation we are only able to resolve a single tetramer state attached to each trimer. In contrast, the 'exact' quantum mechanical calculations in [48, 200, 201, 202] predict the existence of two tetramer states which have been observed in 2009 by Ferlaino *et al.* [203]. As one includes further momentum dependencies, it is well possible that new, genuine resonances associated with the 'missing' tetramer state will appear. Such an effect occurs for example in the three-body problem. There, it is essential to include the momentum dependent two-atom vertex. Only under this condition one arrives at the quadratic equation (3.17) which gives rise to the Efimov effect. This can easily be seen by inspection of the flow equation of λ_3 depicted as Feynman diagrams in Fig. 3.1(b). The assumption of a momentum independent two-atom interaction corresponds to a momentum (and frequency) independent dimer propagator. In this approximation the first term on the RHS of Fig. 3.1(b) vanishes because all poles of the loop frequency integration lie in the same complex frequency half-plane. This directly leads to the loss of the Efimov effect in this crude level of approximation.

There is, however, also a much simpler explanation for why there is only a single tetramer state in our approximation. In order to understand the reasoning let us consider solely the flow $\tilde{\lambda}_\phi$, Eq. (3.25). The coefficients in this equation are sensitive to the approximation chosen as well as to the regulators employed. In order to keep the argument simple, we neglect the inter-four-body sector coupling given by the term $\sim \tilde{\beta}$. When solving the resulting flow equation one does find a single tetramer state in the spectrum. However, as argued above, the coefficients in Eq. (3.25) will change as the approximation is altered. It turns out that by changing the coefficient in front of $\tilde{\lambda}_3$ it is possible to produce an arbitrary number of tetramer states attached to each trimer. For instance, in Fig. 3.9 we show the solution of the equation

$$\partial_t \tilde{\lambda}_\phi = \frac{1}{16} - c\,\tilde{\lambda}_3 + 3\tilde{\lambda}_\phi + \frac{128}{15}\tilde{\lambda}_\phi^2 \tag{3.33}$$

up to the first trimer resonance with $c = 10$ [Fig. 3.9(a)], and $c = 2$ [Fig. 3.9(b)]. In the latter

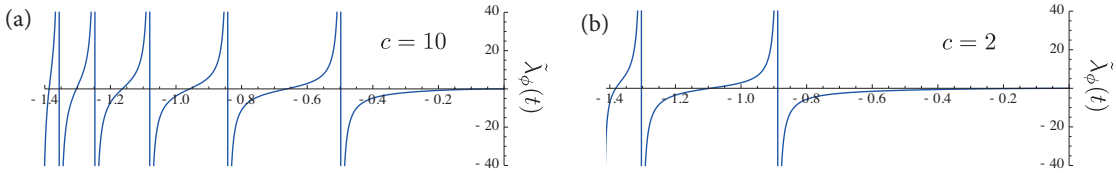

FIGURE 3.9: *(a) RG flow of the coupling λ_ϕ given by Eq.* (3.33) *up to the first trimer resonance. The number of tetramer resonances is sensitive to the value of the coefficient c, here $c = 10$. (b) Same as in (a) but with $c = 2$.*

case we find exactly two tetramer states attached to the trimer. From this simple result we are led to the conclusion that it is likely that for a more elaborate truncation the coefficients in the flow equations change in such a way that exactly two tetramers appear in the spectrum. We thus also expect that more generally, for instance, for changing mass ratios it is well possible that a different number of tetramers might appear in the spectrum.

Spectrum away from the unitarity point

Similar to our solution of the three-body problem, cf. Section 3.3, we can also use our model to investigate the bound state energy spectrum of the four-body problem away from the unitarity point by solving the flow equations for arbitrary values of the scattering length a. The energy levels of the various bound states are determined by varying the energy of the fundamental atoms E_ϕ such that one finds a resonant four-body coupling in the IR. The result of this calculation is shown in Fig. 3.3, where we plot the energy levels of the various bound states versus the inverse scattering length. We find one tetramer state attached to each of the Efimov trimer states. These tetramer states become degenerate with the four-atom threshold for negative scattering length and merge into the dimer-dimer threshold for positive a. In the experiment this leads to the measured resonance peaks in the four-body loss coefficient [203].

In order not to overload the plot we show only the first three sets of levels, although the fRG method allows to calculate an arbitrary number of them. One also observes that the shape of the tetramer levels follows the shape of the trimer levels. In analogy to the three-body sector one can calculate a universal formula relating the tetramer binding energies $E_{\mathrm{Tet}}^{(n)*} = -2(\kappa_{\mathrm{Tet}}^{(n)*})^2$ at $a \to \infty$ with the corresponding scattering length at which the tetramers becomes degenerate with the four-atom threshold $a_{\mathrm{Tet,-}}^{(n)}$ and the dimer-dimer threshold $a_{\mathrm{Tet,+}}^{(n)}$, respectively. We find

$$a_{\mathrm{Tet,-}}^{(n)} \kappa_{\mathrm{Tet}}^{(n)*} \approx -1.75, \quad a_{\mathrm{Tet,+}}^{(n)} \kappa_{\mathrm{Tet}}^{(n)*} \approx 0.20 \qquad (n \gg 1). \tag{3.34}$$

In their quantum mechanical calculation von Stecher *et al.* were able to calculate the lowest few sets of bound state energy levels [48]. From their behavior it was inferred that the ratio between the tetramer and trimer binding energies approaches a universal number within these first few sets of levels. It is therefore expected that the universal regime in the energy plot in Fig. 3.3 is reached very fast as one goes to smaller a^{-1} and E_ψ.

In order to investigate this observation made by von Stecher *et al.*, we calculate the behavior of two ratios as a function of the number n denoting the set of level for which they are determined. The first ratio relates the negative scattering lengths $a_{\mathrm{Tet,-}}^{(n)}$ and $a_{\mathrm{Tri,-}}^{(n)}$ for which the n^{th} tetramer and trimer become degenerate with the four-atom threshold. The second is the ratio between the binding energies of the n^{th} tetramer $E_{\mathrm{Tet}}^{(n)*}$ and the n^{th} trimer $E_{\mathrm{Tri}}^{(n)*}$ at resonance, $a \to \infty$. The resulting plots are shown in Fig. 3.10. We calculate the ratios for different values of the microscopic couplings in order to test the degree of universality of the various sets of energy levels. To test the dependence on the resonance strength $s_{\mathrm{res}} \propto g^2$ we show the results for various values of the Yukawa coupling g. As one sees, only the first of the ratios depend on the microscopic details. Already from the second set of levels on the microscopic details are washed out and the ratios become independent of the choice of initial conditions: The regime of universality is reached extremely fast and as a^{-1} and E_ψ are lowered one will ultimately find the four-body limit cycle described above.

For the asymptotic ratios we find ($n \gg 1$)

$$a_{\mathrm{Tet,-}}^{(n)} \approx 0.518\, a_{\mathrm{Tri,-}}^{(n)}, \tag{3.35}$$

$$E_{\mathrm{Tet}}^{(n)*} \approx 4.017\, E_{\mathrm{Tri}}^{(n)*}. \tag{3.36}$$

Von Stecher *et al.* obtain $a_{\mathrm{Tet,-}}^{(n)}/a_{\mathrm{Tri,-}}^{(n)} \approx 0.43$ for the deeper bound tetramer and $E_{\mathrm{Tet}}^{(n)*}/E_{\mathrm{Tri}}^{(n)*} \approx 4.58$, respectively. Considering the simplicity of our model the agreement is quite good. With an ultracold bosonic gas of Cesium atoms Ferlaino *et al.* measured $a_{\mathrm{Tet,-}}^{(n)}/a_{\mathrm{Tri,-}}^{(n)} \approx 0.47$. In this experiment only the lowest set of tetramer states in the energy spectrum had been accessible due to the particular scattering length profile. Considering our observation that the deepest set of levels is still strongly dependent on the microscopical details, in accordance with our findings in Chapter 2, one cannot expect to find the universal numbers in this particular setting. Therefore more experiments for bosons interacting via larger scattering lengths would be desirable.

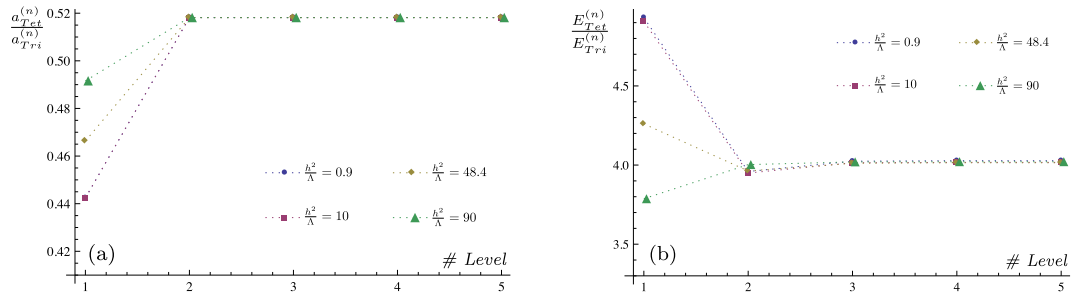

FIGURE 3.10: *Calculation of universal ratios for the lowest five set of levels. The calculation is done for different values of the Yukawa coupling g^2/Λ which determines the effective range in our model (in the figure: $h \equiv g$). The dotted lines are only guide for the eye. (a) Ratios between the values of scattering lengths $a^{(n)}_{Tet,\cdot}$ and $a^{(n)}_{Tri,\cdot}$ for which the tetramer and corresponding trimer become degenerate with the four-atom threshold. (b) Ratios between the values of binding energies $E^{(n)*}_{Tet}$ and $E^{(n)*}_{Tri}$ at resonance $a \to \infty$.*

3.5 The trimer approximation and rebosonization

In this section we will apply the rebosonization method developed in [219] to our model (3.1). By a Hubbard-Stratonovich transformation in the atom-dimer scattering channel, we introduce an additional trimer field $\chi \sim \phi\psi$, representing the bound state of three bosons, which mediates the atom-dimer interaction, see Eq. (3.37) below. A similar procedure had already been used a long time ago by Fonseca and Shanley [192] in the context of nuclear physics and was recently employed by us in [105, 137] for the treatment of the three-component Fermi gas. There are several reasons for employing this procedure. First, it is useful to reduce the number of resonances one has to integrate through in the RG flow. Instead of calculating the divergent coupling λ_3 one only has to calculate zero-crossings of the trimer energy gap which is numerically much easier to handle. Secondly, by the introduction of a dynamical trimer field one is able to mimic some of the complicated momentum structure of the atom-dimer interaction in a simple way which could be sufficient to find the missing tetramer state in our calculation. A third reason is that the four-body problem allows to study the method of rebosonization in a context where the resulting field dependencies are more involved as compared to typical applications put forward so far [105, 214, 220].

But most importantly, the rebosonization scheme allows to describe the many-body problem based on the action (3.1) in a physically intuitive way and in particular in the symmetry broken phases of the system. In order to explain this point in more detail, note that the analysis of the three- and four-body problem considered in the previous sections works equally well when considering a three-component SU(3) Fermi gas, with the exception that there exist no tetramer states due to the Pauli principle.[10] Employing continuity arguments, the phase

[10] One may also consider the bosonic case. Here the gas becomes unfortunately unstable for negative scattering length at homogeneous finite density. This is the reason why we analyze the fermionic case here.

diagram of this system has been discussed in [105]. In the few-body system (cf. Fig. 2.2), for small, negative scattering length $|a| \ll l_{\rm vdw}$, the ground state is given by unbound fermions. Increasing the density to finite values one expects that the ground state is given by attractively interacting fermions which build an extended 'color' superfluid phase. At a critical coupling $a \approx a_-$ the ground state changes character and becomes a gas of fermionic trimers, which can be expected to be an almost ideal Fermi gas deep in the unitary regime where the trimers feature a large energy gap.[11] Similarly, for $a = a_*$, in the few-body problem, the trimers merge into the atom-dimer channel and the dimer is now the ground state. This will be reflected also by the many-body problem and one expects that for $a \approx a_*$ a new color superfluid phase of repulsive molecules appears. Since the symmetry of the trimer phase is different from the color superfluid phases, there have to be quantum phase transitions, with possible associated quantum critical regions in between.

The proper description of these quantum critical regimes is a complicated task and up to now no attempts for solving this problem have been made in the case of a continuum system. For the similar problem of SU(3) fermions on the lattice we refer to [221, 222, 223]. The main difficulty is the competition of various degrees of freedom which are in this case composite particles with varying particle content. In order then to describe the phase transitions properly, quantum fluctuations of all relevant degrees of freedom have to be included. For instance, at the quantum phase transition at $a \approx a_-$ fluctuations of the superfluid order parameter field $\sim \phi$, unbound atoms $\sim \psi$ *and* trimers $\sim \chi$ will be important. We already see from this argument that an intuitive way to describe this situation is the use of the relevant *effective* degrees of freedom. From this perspective the introduction of a trimer field is quite natural. Note, that in principle the system can be described in terms of the atoms ψ only. This would, however, necessitate the evaluation of the fully frequency and momentum dependent vertices of the three- and four-body sector which seems to be an impossible task.

Even having introduced the trimer field, the calculation remains difficult close to the phase transitions. For instance, close to $a \approx a_-$ collisions between trimers and atoms $\sim \chi^* \psi^* \chi \psi$ or collisions converting a trimer and an atom into two Cooper pairs $\sim \chi^* \psi^* \phi \phi$ will be important. As these couplings belong to the four-body sector our previous discussion of four-body physics becomes of relevance even for the many-body problem. In order to describe the system properly all couplings belonging to the four-body sector will be important in the effective average action Γ_k. One may then hope[12] that the introduction of the trimer field together with the inclusion of all these interaction vertices in the effective average action Γ_k allows a rather accurate description of the system.

Technically, the trimer field is introduced by a Hubbard-Stratonovich transformation at the UV scale, $\lambda_3 \sim h^2/m_\chi^2$, which replaces the atom-dimer scattering *in the UV* by a trimer exchange. The main problem of a standard application of a Hubbard-Stratonovich transformation is that the regeneration of the replaced coupling by quantum fluctuations on lower

[11] Unless they feature a small effective attraction, for instance in the p-wave channel [105].

[12] Since one deals with a strong coupling problem, also *all* higher order couplings might potentially become relevant.

momentum scales is typically not taken into account. For instance the critical temperature of conventional superconductors given by BCS theory can be derived from a model in which the atom-atom attraction is replaced by a pair exchange (for a detailed discussion see [214] and Appendix D). In BCS theory the regeneration of the vertex $(\psi^*\psi)^2$ is neglected. Taking into account this vertex yields a correction to T_c as large as a factor of almost two, which is the famous Gorkov correction to BCS theory. The method of rebosonization allows to account for these contributions in a systematic way. In the Efimov problem it is even solely for these contributions that the Efimov effect appears [105]. Having a future application of the results of the previous sections to many-body physics in mind, it is thus the first step to study the rebosonization for the trimer field. In contrast to our previous work [105], we will here also include the four-body couplings which, as discussed above, will be important in a proper description of the atom-trimer-molecule quantum phase transitions.

In the three-body sector the atom-dimer coupling λ_3 exhibits divergencies when the energy gap of the fundamental atoms E_ψ is tuned such that one hits a trimer bound state in the IR. In the *static* trimer approximation,[13] the coupling λ_3 is mediated by the exchange of a trimer field χ with the non-dynamical, inverse propagator $P_\chi = m_\chi^2$, which can be depicted as

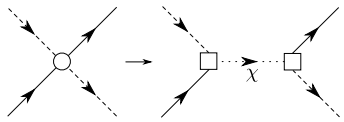

The trimer field $\chi \sim \phi\psi$ is introduced on the microscopic scale by a Hubbard-Stratonovich transformation and our ansatz for the effective average action, motivated by the resulting classical action, reads

$$\begin{aligned}
\Gamma_k \;=\; & \int_x \{\psi^*(\partial_\tau - \Delta + E_\psi)\psi \\
& + \phi^*\left(A_\phi(\partial_\tau - \frac{\Delta}{2}) + m_\phi^2\right)\phi + \chi^* m_\chi^2 \chi \\
& + \frac{g}{2}(\phi^*\psi\psi + \phi\psi^*\psi^*) + \lambda_3 \phi^*\psi^*\phi\psi \\
& + h(\chi^*\phi\psi + \chi\phi^*\psi^*) \\
& + \lambda_\phi(\phi^*\phi)^2 + \beta(\phi^*\phi^*\phi\psi\psi + \phi\phi\phi^*\psi^*\psi^*) \\
& + \gamma\phi^*\psi^*\psi^*\phi\psi\psi + \delta_1\chi^*\psi^*\chi\psi \\
& + \delta_2(\chi^*\psi^*\phi\phi + \chi\psi\phi^*\phi^*) \\
& + \delta_3(\chi^*\psi^*\phi\psi\psi + \chi\psi\phi^*\psi^*\psi^*)\}. \qquad (3.37)
\end{aligned}$$

The Yukawa interaction h couples the trimer field to the dimer and atom field. The δ_i are the additional U(1) symmetric four-body couplings which are generated by quantum fluctuations.

[13] In the case of many-body physics this can be extended to account for a dynamical trimer field, e.g., with a derivative expansion for the inverse trimer propagator.

By virtue of the vacuum hierarchy, all other possible couplings can be shown to stay zero during the RG evolution provided they vanish at the UV scale. The coupling λ_3 is regenerated through a box diagram in the RG flow. However, it is possible to absorb *all* emerging couplings δ_i and λ_3 by the use of the rebosonization procedure. For this matter we promote the trimer field χ to be explicitly scale dependent, $\chi \to \chi_k$, $\chi^* \to \chi_k^*$ and the Wetterich equation generalizes to[14]

$$\begin{aligned}\partial_k \Gamma_k[\Phi_k] &= \frac{1}{2}\mathrm{Tr}\left(\Gamma_k^{(2)}[\Phi_k] + R_k\right)^{-1}\partial_k R_k \\ &\quad + \left(\frac{\delta}{\delta\Phi_k}\Gamma_k[\Phi_k]\right)\partial_k\Phi_k,\end{aligned} \tag{3.38}$$

where Φ_k now includes all fields including the trimer fields (χ_k, χ_k^*). The additional term in the generalized flow equation (3.38) allows for the absorption of the reemerging couplings since one has the freedom to conveniently choose the scale dependence of the trimer fields as a function of fields. In order to continuously eliminate the couplings λ_3 and δ_i during the flow, we choose

$$\begin{aligned}\partial_k \chi_k &= \phi\psi\zeta_{a,k} + \psi^*\chi_k\psi\zeta_{b,k} \\ &\quad + \psi^*\phi\phi\zeta_{c,k} + \psi^*\phi\psi\psi\zeta_{d,k}, \\ \partial_k \chi_k^* &= \phi^*\psi^*\zeta_{a,k} + \psi\chi_k^*\psi^*\zeta_{b,k} \\ &\quad + \psi\phi^*\phi^*\zeta_{c,k} + \psi\phi^*\psi^*\psi^*\zeta_{d,k}.\end{aligned} \tag{3.39}$$

Upon inserting Eq. (3.39) into the generalized Wetterich equation (3.38) the condition that the flows of λ_3 and δ_i vanish leads to

$$\begin{aligned}\zeta_a &= -\frac{\partial_k\lambda_3}{2h}, \quad \zeta_b = -\frac{\partial_k\delta_1}{2m_\chi^2} \\ \zeta_c &= -\frac{\partial_k\delta_2}{m_\chi^2}, \quad \zeta_d = -\frac{\partial_k\delta_3 + h\zeta_b}{m_\chi^2}.\end{aligned} \tag{3.40}$$

When one calculates now the flow equations of the remaining flowing couplings by projecting Eq. (3.38) onto them, one obtains new contributions due to the presence of additional terms arising from Eq. (3.39). Note that in particular the term ζ_a takes care of the reemerging atom-dimer vertex.

In our static trimer approximation the trimer field has no dynamical propagator and the model given by Eq. (3.37) is equivalent to the two-channel model in Eq. (3.1). Furthermore, no regulator has to be specified for the trimer field since in our approximation the original atom-dimer coupling λ_3 is solely replaced by h^2/m_χ^2. At this point it becomes clear why the

[14] There is a correction to this result when the trimer is a dynamical degree of freedom and the flow equation is then modified [172, 220].

modified flow equations will be easier to handle numerically: instead of calculating a divergent λ_3 in the three-body sector one has only to deal with zero crossings of m_χ^2 at the values of k where originally λ_3 had divergencies. The modified flow equations are given by

$$\begin{aligned} \partial_t h &= \partial_t h|_{\Phi_k} + m_\chi^2 \zeta_a, \\ \partial_t \beta &= \partial_t \beta|_{\Phi_k} + h\zeta_c, \\ \partial_t \gamma &= \partial_t \gamma|_{\Phi_k} + 2h\zeta_d, \end{aligned} \tag{3.41}$$

where the first terms in the flows are the original flow equations with the trimer field taken to be scale independent. In fact, by expressing all flow equations in terms of the coupling $H \equiv h^2$ one can also get rid off the problematic h in the denominator of ζ_a in Eq. (3.40), cf. [46, 105]. We point out that the static trimer approximation allows to calculate easily the three-body sector and, remarkably, it allows for an analytical solution of the flow of λ_3 in the complex coupling plane [111]. In the four-body sector the original divergencies of λ_3 still appear since trimers χ appear in the corresponding flow diagrams and therefore one has to deal with terms $\sim 1/m_\chi^2$. These difficulties can, however, be resolved in a similar fashion as described in Section 3.4. Finally, the bound state spectrum of the trimers can be computed by calculating the poles of the trimer propagator, $m_\chi^2(k = 0, E_\psi) = 0$, in a straightforward manner.

3.6 Conclusion

In this chapter, we investigated the four-body problem with the help of the functional renormalization group. Employing a simple two-channel model with pointlike three- and four-body interactions we were able to study universal properties at the unitarity point $a \to \infty$, $E = 0$ as well as to perform computations away from it.

In the RG language the Efimov physics of the three-body problem manifests itself as an infinite RG limit cycle behavior of the three-body coupling constant at unitarity. We found that also the four-body sector is governed by such a limit cycle which is solely induced by the RG running of the three-body sector, signaling the absence of a four-body parameter.

We computed the energy spectrum away from unitarity and were able to obtain the universal relations between four- and three-body observables in our approximation. Our calculation provides an explanation for the findings of von Stecher *et al.* [48], who found that these ratios approach universal constants very quickly for higher excited states. We also found a dependence of the ratios for the lowest level on microscopic details such as the strength of the underlying Feshbach resonance. This is of relevance for the experimental observations by Ferlaino and coworkers [203]. In this experiment only the lowest tetramer states have been observed and hence one cannot expect to find the exact universal relations between them.

Considering the simplicity of our model, we find good agreement with the previous studies in [48, 200, 201]. There had been disagreement in literature about universality and the absence or existence of a four-body parameter, see e.g. [206, 224, 225]. Our renormalization group

results support the conclusion that the four-body system is universal and independent of any four-body parameter.

An important shortcoming of the pointlike approximation is the absence of the shallower of the two tetramer states. We presented ways how this shortcoming might be overcome, either by the use of a truncation with an improved momentum and energy dependence of the vertices or by a different choice of regulators. From the energy spectrum in Fig. 3.3 it becomes also evident that the excited tetramer states can decay into an energetically lower lying trimer plus an atom. The higher excited states in the four-body system are therefore expected to have an intrinsic finite decay width [201]. Whether this width has a universal character, however, still remains an open question. Using the method of complex extension of RG flows [111] we presented a method for how to infer this width from a functional renormalization group analysis even in a simple, lowest order derivative expansion.

The inclusion of the full momentum dependencies in the three- and four-body sector seems to be a rather complicated task. In the effective field theory study of the three-boson system the introduction of a dynamical dimer field, often called the di-atom trick [66], has been a decisive step towards the exact solution of the three-body problem. From this perspective we suggest that the inclusion of a dynamical trimer field in the effective action might help to simplify the momentum dependent calculation. Furthermore, we indicated how this approximation gives a good starting point for a many-body calculation addressing possible quantum phase transitions in the system and we showed how the method of rebosonization may be used to simplify the calculations.

Chapter Four

Full spectral functions and excitation spectra near the polaron-to-molecule transition from the fRG

As we have seen in the previous Chapters, in three spatial dimensions the ground state of two interacting fermions of different species changes its character at the critical unitary interaction strength $1/a = 0$. While for $1/a < 0$ it is given by two unbound, free atoms, it becomes a weakly bound molecular state with universal binding energy $\epsilon_b = -\hbar^2/(ma^2)$ for $1/a > 0$. How this situation changes when one of these species, say the $\uparrow$-atoms, has a finite density $n_\uparrow = k_F^3/(6\pi^2)$ characterized by the Fermi wave vector k_F, is one of the main questions we will address in this Chapter.

In this case, one deals with a polaron problem where an impurity, the $\downarrow$-atom, is immersed in an environment, the $\uparrow$-Fermi sea. In general, a polaron is an impurity immersed into some environment which changes the single particle properties of the impurity due to the interactions with the bath [226]. Impurity problems are ubiquitous in physics with many prominent examples ranging from lattice polarons [227] to Kondo physics [228, 229, 230]. In the present polaron problem, the single $\downarrow$-spin atom constitutes a mobile impurity in the environment of $\uparrow$-fermions and below a critical dimensionless interaction strength $\vartheta = 1/(k_F a) < \vartheta_c$ the ground state is given by the so-called Fermi polaron, a single particle excitation with well-defined quasiparticle properties [3]. For increasing microscopic attraction, $\vartheta > \vartheta_c$, the ground state changes its character, and the impurity forms a molecular state with an atom of the $\uparrow$-Fermi sea. This qualitative change of the ground state marks the so-called *polaron-to-molecule transition* and has been predicted by Prokof'ev and Svistunov [59, 60]. It has not only been studied extensively theoretically [59, 60, 72, 231, 232, 233, 234, 235, 236, 237, 238, 239], but also has been verified experimentally [240].

As it turns out, not only the ground state features interesting physics but also the excitation spectrum across the transition exhibits a rich structure. On the one hand, as shown from a microscopic calculation in this chapter (see also [62]) and in a phenomenological two-loop calculation by Bruun *et al.* [241], the polaron (molecule) remains a well-defined excited quasiparticle of finite lifetime for $\vartheta > \vartheta_c$ ($\vartheta < \vartheta_c$) with a power-law decay of its lifetime confirming the first-order nature of the polaron-to-molecule transition [59, 60]. On the other hand, a new quasiparticle appears for large microscopic attraction ($1/a > 0$) at positive energies: the *repulsive polaron*.

In order to access these excited states it is necessary to calculate the full energy and momentum dependent self-energies of the impurity and the molecular state. So far, there had been a lack of theoretical work which studies all the features in the polaron-to-molecule transition in

a unified approach. In this Chapter we present a new, numerical functional renormalization group method [62] which allows such a unified description.

The polaron-to-molecule transition is of great relevance for many-body physics as it constitutes a two-component Fermi gas in the limit of extreme spin imbalance. While the repulsive polaron sheds light on the question if the *attractive* Fermi gas prepared on the so-called *repulsive* branch [49] is stable enough to reach the phase transition to (Stoner) ferromagnetism [49, 50, 52, 53, 54, 55, 56, 242, 243, 244] the ground state of the polaron-to-molecule transition provides information about the phase diagram of the imbalanced BEC/BCS crossover [16, 245].

Motivated by this many-body perspective, we will first briefly review the phase diagram of the imbalanced Fermi gas in Section 4.1, after which we introduce the Fermi polaron physics in more detail (Section 4.2). In Section 4.3 we derive the RG flow equations and analyze the ground state properties using a simple derivative expansion. The discussion of the advantages and disadvantages of such an approximation then leads to the question of how to calculate the RG flow of full spectral functions in Section 4.4. After we analyze the spectral properties in Section 4.5, we use the full Green's functions to predict the radio-frequency response in a mixture of ^{6}Li atoms using linear response theory in Section 4.6. We summarize our results in Section 4.7.

4.1 Aspects of the phase diagram of an imbalanced Fermi gas

A spin-balanced, two-component Fermi gas with attractive interactions becomes superfluid – and superconducting if the fermions carry charge – at low temperatures, as first observed by Onnes in 1911 [246] and sucessfully explained many years later, in 1957, by Bardeen, Cooper, and Schrieffer [247]. As shown by Cooper [248], the combination of arbitrary weak attractive interactions and the presence of a Fermi surface leads to the formation of so-called Cooper pairs, which, as bosonic degrees of freedom, condense and build the superfluid BCS-state. In fact, the attraction can even be so weak that in the corresponding two-body problem no bound state exists.

The transition temperature for BCS-suprafluidity is exponentially suppressed,

$$T_c/T_F = \frac{8e^\gamma}{\pi e^2} e^{-\frac{\pi}{2}\frac{1}{k_F|a|}}, \tag{4.1}$$

with γ the Euler constant, T_F the Fermi temperature, k_F the Fermi wave vector, and a the scattering length. This result, as derived by Bardeen *et al.* [247], is, however, not exact but receives a correction by a factor of $1/(4e)^{1/3}$ due to particle-hole fluctuations known as the Gorkov-Melik-Barkhudarov correction to BCS theory [249]. For a derivation of both results from the functional renormalization group we refer to Appendix D. Low temperatures as in Eq. (4.1) in the weak coupling regime $k_F|a| \ll 1$, where BCS theory becomes valid, can presently not be achieved with ultracold atoms. However, the use of Feshbach resonances allows to enhance the attraction so much that the strong coupling regime $k_F|a| \gg 1$ is accessible

where $T_c \sim \mathcal{O}(T_F)$ which is well in reach of cold atom experiments. This finally allowed the observation of fermionic superfluidity in ultracold gases by the MIT group [15, 29].[1] In fact, at unitarity, the critical temperature has been measured to be $T_c/T_F = 0.167(13)$ [34] which is in excellent agreement with various theoretical predictions ranging from a self-consistent Ward-Luttinger approach that gives $T_c/T_F = 0.16$ [37] to Monte Carlo calculations which give $T_c/T_F = 0.152(7)$ [79] and 0.171(5) [80].

The tunability of the interactions allows to realize the so-called BCS-BEC crossover (for a collection of related articles we refer to [16]): while for negative and small $k_F a$ the formation of highly non-local Cooper pairs takes place, for positive scattering lengths a the fermions form molecules which become tightly bound in the BEC-limit $k_F a \to 0^+$. In this limit the tightly bound molecules with the universal binding energy $\epsilon_B = \hbar/(ma^2)$ form a weakly interacting, repulsive and thus stable BEC of bosonic molecules with the standard BEC transition temperature [1][2]

$$T_{c,\mathrm{BEC}}/T_F \approx 0.218. \tag{4.2}$$

Within standard BCS theory for a spin-balanced Fermi gas, the superfluid state is protected by an energy gap Δ which vanishes at the transition temperature in a second order phase transition. But what happens when a spin imbalance is introduced? Such an imbalance can be enforced in cold atoms by choosing an actual imbalance in the densities $n_\uparrow \neq n_\downarrow$ of $\uparrow$- and $\downarrow$-atoms which, in a grand canonical description, implies a finite difference in the chemical potentials $h = (\mu_\uparrow - \mu_\downarrow)/2 \neq 0$. This is similar to an electron gas in an external magnetic field B which likewise leads to an imbalance in the chemical potentials $h = (\mu_\uparrow - \mu_\downarrow)/2 = \gamma B/2$ with γ the gyromagnetic ratio.

Contrarily, a finite value of h does, however, not necessarily imply a imbalance in the fermion densities. In fact, due to the protecting energy gap Δ, a finite effective magnetic field h can be applied before the superfluid state breaks down at a critical value h_c due to the large mismatch of the Fermi surfaces. While the superfluid phase for $h < h_c$ has a vanishing polarization $P = (n_\uparrow - n_\downarrow)/(n_\uparrow + n_\downarrow)$, the phase for $h > h_c$ is characterized by $P \neq 0$. The finite jump in the polarization (and density) implies a first order phase transition at h_c. Note, that the existence of such a jump has been indicated by the experiment at MIT [29] but it is yet not theoretically proven.

In Fig. 4.1 a tentative phase diagram at zero temperature is shown where the axis are given by the dimensionless effective magnetic field h/ϵ_F and coupling constant $1/(k_F a)$.[3] Two lines are of particular importance: the Clogston field h_c and the so-called saturation field h_S. As discussed above, h_c marks the phase transition from a balanced superfluid (SF_0) to a normal, partially polarized Fermi gas (N_{pp}). In weak coupling, it equals the so-called Clogston-Chandrasekhar limit of the breakdown of superfluidity [250, 251] which, in mean-field theory,

[1] A historical side remark: Remarkably, one of the two first, Nobel prize rewarded, BECs in 1995 [12] as well as the superfluid fermionic system [15, 29] were created at the MIT with the same machine.

[2] That the interaction between the molecules becomes indeed weak in the deep BEC limit was shown in a four-body calculation by Petrov *et al.* [196].

[3] In this Section we use the definitions $n = n_\downarrow + n_\uparrow = k_F^3/(3\pi^2)$ and $\epsilon_F = k_F^2$ in natural units $\hbar = 2m = 1$, whereas in the following Sections as well as in Fig. 4.1 we use the different convention $n = n_\uparrow = k_F^3/(6\pi^2)$.

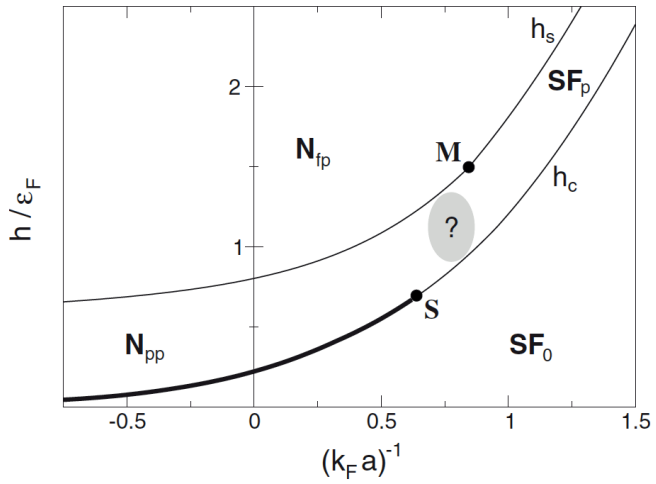

FIGURE 4.1: *Schematic plot of the zero temperature phase diagram of the spin-imbalanced Fermi gas. The axis are given by the dimensionless interaction strength* $1/(k_F a)$ *and the difference in chemical potentials* $h = (\mu_\uparrow - \mu_\downarrow)/2$ *in units of* ϵ_F*. In this figure the convention* $n_\uparrow = k_F^3/(6\pi^2)$ *is used. The figure is taken from Punk* et al. *[236] with courtesy of W. Zwerger.*

is given by

$$h_c = \frac{\Delta}{\sqrt{2}} \quad \text{(Clogston-Chandrasekhar limit).} \tag{4.3}$$

If the magnetic field h is above the saturation field h_s the system undergoes a second order phase transition to a fully polarized, single component Fermi gas of majority $\uparrow$-atoms. At low temperatures, interactions are frozen out due to the Pauli principle and the phase $h > h_s$ corresponds to an ideal $\uparrow$-Fermi gas.

Due to the first order phase transition for $k_f a \to 0^-$ from a superfluid state SF_0 with zero polarization P_1 to the normal, spin-polarized state N_{pp} with high polarization P_2 for $h > h_c$, there is a jump in the densities of $\uparrow$- and $\downarrow$-atoms at h_c as predicted by Bedaque *et al.* [252] and experimentally verified by Shin *et al.* [253]. This implies that there is a regime of polarizations P^* with $P_1 < P^* < P_2$ which are not allowed in the system. This regime is sometimes termed the forbidden region or the phase separated state. The latter terminology is easily understood considering a cold atomic system, where particular particle densities $n_\uparrow$ and $n_\downarrow$ can be prepared which correspond to a 'forbidden' P^*. Given such a P^*, it is energetically favorable for the system to form two types of domains of finite size in space: one type consists of a balanced superfluid while the other consists of a normal Fermi gas of finite polarization. Adding now more minority $\downarrow$-atoms, the superfluid domains will grow, while the other domains shrink. This is similar to bubble nucleation in the liquid gas transition [170]. This first order phase transition is shown as thick line in Fig. 4.1. It terminates at the so-called splitting point S where the transition along h_c turns second order. As discussed by Son [254] using

effective field theory, the point S marks a sharp transition at $T = 0$ but becomes a crossover at finite temperature and it is related to a characteristic change in the dispersion relation of the fermions in a balanced superfluid [76, 255]. While the fermionic excitation spectrum $E(k)$ in the balanced situation has a minimum at momentum $k = 0$ for $\vartheta > \vartheta_S$, it has its minimum at a finite momentum for $\vartheta < \vartheta_S$.

In the weak coupling regime, where the fermions are barely renormalized, the saturation field h_s is obtained in lowest order by setting $\mu_\downarrow = 0$ which yields $h_s = \mu_\uparrow/2 = \epsilon_F/2$. The first order correction due to interactions is in mean field theory given by $\mu_\downarrow = gn$ which results in $h_s = \epsilon_F(1/2 + 2/(3\pi|\vartheta|) + \ldots)$ [256]. As shown in Fig. 4.1, h_s increases towards the BEC side. The point M marks the endpoint of this second order phase transition from a non-interacting $\uparrow$-Fermi gas with $P = 1$ to a normal, partially polarized Fermi gas with $P \neq 1$. For couplings ϑ beyond the point M, h_s determines the transition from an ideal $\uparrow$-Fermi gas to a polarized superfluid (SF_p), where superfluid molecules are immersed in excess majority $\uparrow$-atoms. In [257] Pilati and Giorgini argue, based on a fixed-node Monte Carlo (FN-QMC) calculation, that for couplings $\vartheta > \vartheta_M$ the line h_s marks a first-order phase transitions to the phase SF_p due to the large atom-dimer repulsion in the regime close to the point M. Further in the BEC regime, for $\vartheta > \vartheta_T > \vartheta_M$, it this first order transition turns second order, with ϑ_T marking a tricritical point. Due to the phase separation between atoms and dimers for $\vartheta \gtrsim \vartheta_M$ the point M might be difficult to observe in experiments. For decreasing values of h within the SF_p phase, a second phase transition takes place to a balanced superfluid which is a continuous Lifschitz transition with a vanishing Fermi surface of $\uparrow$-atoms [256]. Similarly, for $\vartheta < \vartheta_M$ and at $T = 0$, there is also a Lifschitz transition along the line h_s, since here the Fermi surface of $\downarrow$-atoms vanishes; for finite $T > 0$ this transition becomes a crossover, while the SF_0-SF_p transition remains second order at $T > 0$ [256].

Along the line of the saturation field h_s the system is just on the verge of having a finite occupation of $\downarrow$-atoms and thus it gives the energy of a single down impurity in a $\uparrow$-Fermi gas. The point M then represents the position of the polaron-to-molecule transition. Since the point M plays such a prominent role in the phase diagram of a spin-imbalanced Fermi gas, its quantitative determination is of great importance. As we will show in the following sections, we determine the point M to be localized at the interaction strength $\vartheta_M = 0.904(5)$ which is in excellent agreement with the result from diagrammatic Monte Carlo, $\vartheta_M = 0.90(2)$. From this perspective our fRG approach builds a good starting point to explore the more involved dynamical aspects of the polaron-to-molecule transition.

4.2 The Fermi polaron problem

The remainder of this Chapter is devoted to the Fermi polaron problem, that is, as described in the introduction, a single $\downarrow$-atom[4] immersed in an $\uparrow$-Fermi sea. This situation is realized along the saturation field h_s in Fig. 4.1. Some of the questions to be addressed in this Chapter

[4] As long as there is only a single impurity, the statistics of the impurity plays no role and consequently the $\downarrow$-atom can also be a boson. We will, however, refer to the $\downarrow$-atom as a fermion of the same mass as the $\uparrow$-atoms since we are interested in the relevance for the phase diagram of an imbalanced Fermi gas.

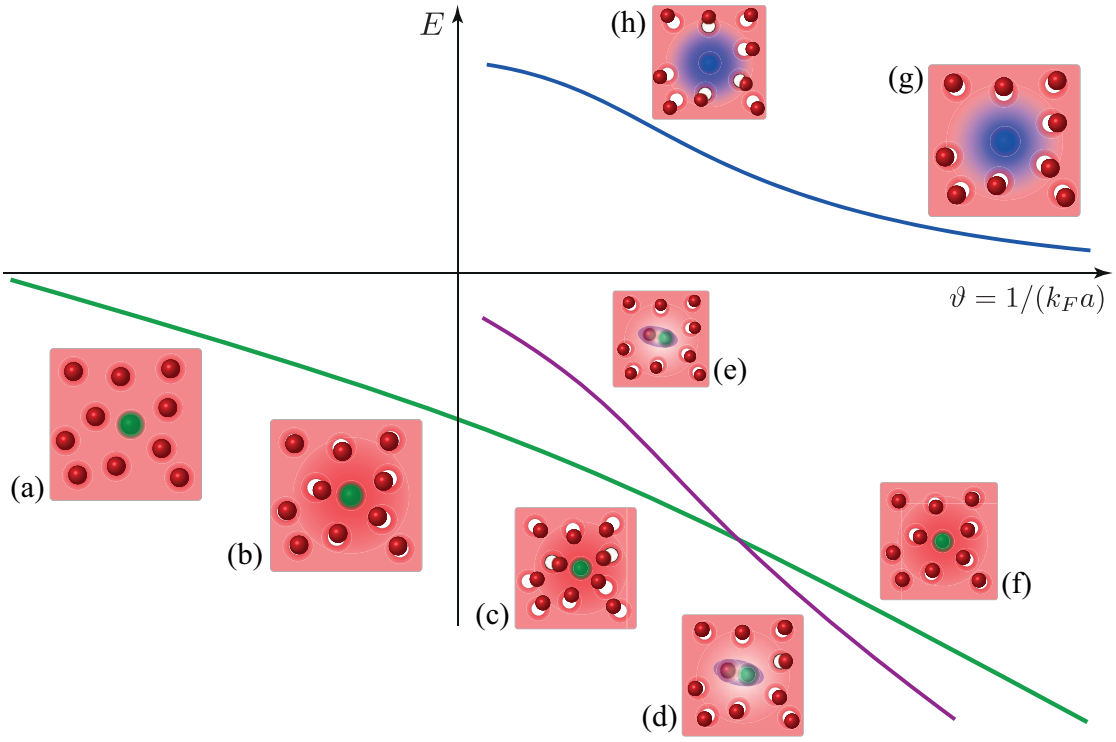

FIGURE 4.2: *Sketch of the basic features of the excitation spectrum of the Fermi polaron problem. (a) For very weak attraction the impurity is barely renormalized. (b-c) As the microscopic attraction increases the impurity becomes dressed with ↑-fermions and is a renormalized quasiparticle, the attractive polaron. (d) Beyond a critical interaction strength $\vartheta_c = (k_F a_c)^{-1}$ the molecule becomes the ground state of the system. (e-f) The attractive polaron and the molecule exist as excited states above their respective ground state also across the polaron-to-molecule transition. (g-h) A new quasiparticle excitation, not present in the microscopic action – the repulsive polaron – appears at positive energies. Also shown are the energies of the attractive polaron (green), molecule (purple), and repulsive polaron (blue).*

are: what is the ground state of the system? At which energy and interaction strength does the polaron-to-molecule transition occur? What is the nature of this phase transition? What is the quasiparticle excitation spectrum and what are the corresponding quasiparticle properties?

In Fig. 4.2 we schematically show some of the main features of the excitation spectrum of the Fermi polaron problem as function of the dimensionless interaction strength $\vartheta = 1/(k_F a)$. On the left side of the figure, Fig. 4.2(a), the impurity is interacting only very weakly with the ↑-Fermi sea; the ↓-atom can propagate almost freely through the medium and is barely renormalized. As the microscopic attraction is increased, $\vartheta \to 0$, the ↓-atom becomes a strongly renormalized quasiparticle, c.f. Fig. 4.2(b-c), with corresponding Landau quasiparticle parameters such as an effective mass m_* and wave function renormalization Z. Furthermore the interaction between the ↑- and ↓-atoms is effectively screened by the medium. In the following

we will call this quasiparticle the *attractive polaron*. Due to the attraction, interaction energy is gained when the impurity is added to the ↑-Fermi sea as indicated by the green line in Fig. 4.2.

At a critical interaction strength $\vartheta_c > 0$ the ground state changes character and it becomes energetically favorable to form a molecular bound state composed of the ↓- and an ↑-fermions, cf. Fig. 4.2(d). This bosonic molecule is an impurity itself in the surrounding ↑-Fermi sea. It is a renormalized quasiparticle as well, but, contrarily to the attractive polaron, it interacts via effective repulsive interactions with the Fermi sea. The energy gained by forming the molecule is indicated by the purple line in Fig. 4.2. The crossing of the energy levels of the molecule and the attractive polaron marks the polaron-to-molecule transition. It corresponds to the point M discussed in the previous Section. Note that the attractive polaron and the molecule exist as well-defined quasiparticle excitations even across the transition, cf. Fig. 4.2(e-f). As excited states they can decay into their respective ground state, but as we will see, this decay is a very slow process. The corresponding decay rates are calculated in Section 4.5 and indicate a true level crossing of the polaronic and molecular state, which confirms the first order nature of the polaron-to-molecule transition [59, 60].

As we will see in the following Sections, there is, however, a further excitation in the system at positive energies: the *repulsive polaron* [cf. Fig. 4.2(g-h)]. The repulsive polaron is a quasiparticle excitation which is highly unstable for $1/(k_F a) \to 0$, but which becomes a stable excitation in the limit $k_F a \to 0$. In this limit it is in fact *the* quasiparticle in the system with unity weight $Z \to 1$. This finding justifies perturbative methods for ultracold atoms in the 'weak coupling limit' $k_F a \to 0^+$.[5] The repulsive polaron has been studied by Cui and Zhai [243] as well as by Massignan and Bruun [258] using a non-selfconsistent T-matrix approximation. We will discuss the properties of the repulsive polaron and its relevance in detail in Section 4.5 using fRG methods which go far beyond previous studies. In a sense the polaron-to-molecule transition can be regarded as a modification of the two-body problem due to medium effects [62], see Fig. 4.3. In this picture, one may regard the emergence of the attractive and repulsive poloron branch as an effective level repulsion and splitting of the original free atom threshold due to many-body effects.

The ground state of the polaron-to-molecule transition, cf. Fig. 4.2(a)-(d), has been extensively studied theoretically [59, 60, 72, 231, 232, 233, 234, 235, 236, 237, 238, 239]. A quantity of interest is for instance the energy $E_\downarrow$ of the polaron. In particular at unitarity, where the scattering length a diverges and perturbation theory breaks down, the polaron problem provides an ideal benchmark for many-body methods. The polaron energy at unitarity has been calculated in a state-of-the-art diagMC calculation and it is found to be $E_\downarrow = -0.615\epsilon_F$ [59, 60] whereas a standard MC approach yields $E_\downarrow = -0.59\epsilon_F$ [232]. Furthermore the polaron energy can be calculated from a simple variational wave function with a single particle-hole excitation [231, 233]. The result $E_\downarrow = -0.607\epsilon_F$ is in remarkable, and at first sight rather surprising, agreement with the diagMC result. It can be shown, that this approach is equivalent to a next-to-leading order $1/N$ expansion [107], non-selfconsistent T-matrix [233], and Nozierés-

[5] From an RG perspective the microscopic problem is *strongly* coupled in this limit as the microscopic attraction is largest here. The *effective, infrared degrees of freedom*, namely the molecule in the ground state and the repulsive polaron in the excited state are, however, *weakly* coupled with the environment.

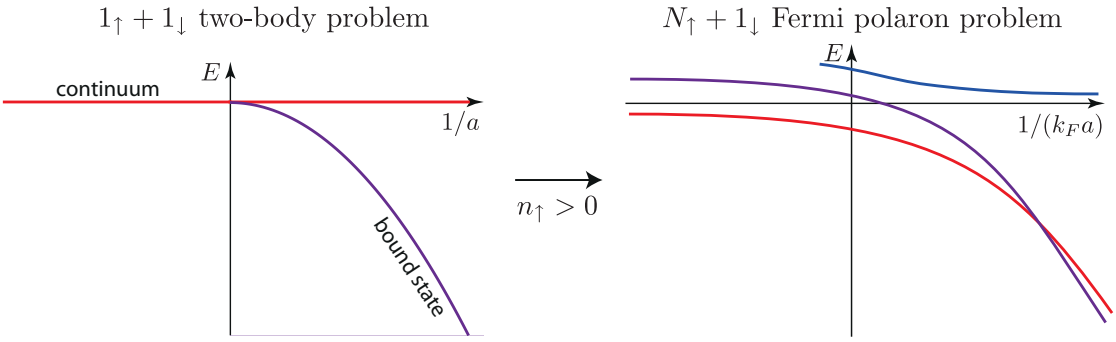

FIGURE 4.3: *The polaron problem may be regarded as the emergence of an effective two-level system. Due to many-body physics the degenerate atom threshold at zero energy undergoes an energy splitting and the interacting levels repel each other, as typical for a two-state system. In this picture the molecule can be regarded as rather an additional spectator mediating the interactions.*

Schmitt-Rink [259] calculation. Combescot *et al.* systematically studied the influence of multiple particle-hole fluctuations and the result converges to the value $E_\downarrow = -0.616\epsilon_F$ [234]. Experimentally, the group of Zwierlein at MIT measured the polaron energy at unitarity using radio-frequency spectroscopy and find $E_\downarrow = -0.59\epsilon_F$ [240]. Similar, excellent agreement has been found for various other ground state properties so that by now the ground state of the polaron problem can be considered to be well understood.

4.3 RG flow equation and analysis in a simple derivative expansion

Model and most general truncation

In the following Sections we closely follow our results as presented in [62]. We study a two-component Fermi gas at $T = 0$ in the limit of extreme population imbalance. The system is described by the microscopic, euclidean action

$$S = \int_{\boldsymbol{x},\tau} \Big\{ \sum_{\sigma=\uparrow,\downarrow} \psi_\sigma^* [\partial_\tau - \Delta - \mu_\sigma] \psi_\sigma + g \psi_\uparrow^* \psi_\downarrow^* \psi_\downarrow \psi_\uparrow \Big\}, \tag{4.4}$$

with imaginary time τ. The Grassmann-valued, fermionic fields $\psi_\uparrow$ and $\psi_\downarrow$ denote the $\uparrow$- and $\downarrow$-spin fermions, which have equal mass m. The associated chemical potentials μ_σ are adjusted such that the $\uparrow$-fermions have a finite density $n_\uparrow = k_F^3/(6\pi^2)$ while there is only a single impurity $\downarrow$-atom. The atoms interact via a contact interaction with coupling constant g which is related to the s-wave scattering length a. The scattering T-matrix acquires a complicated frequency and momentum dependence in the strong-coupling limit and the pairing is due to

a pole in the particle-particle scattering channel. It is then convenient to perform a Hubbard-Stratonovich transformation of the action (4.4) introducing a bosonic molecule (pairing) field $\phi \sim \psi_\downarrow \psi_\uparrow$ which mediates the two-particle interaction $\sim g\psi^*_\uparrow \psi^*_\downarrow \psi_\downarrow \psi_\uparrow$. The resulting action is given by

$$S = \int_{\boldsymbol{x},\tau} \Big\{ \sum_{\sigma=\uparrow,\downarrow} \psi^*_\sigma [\partial_\tau - \Delta - \mu_\sigma]\psi_\sigma + \phi^* G^{-1}_{\phi,\Lambda}\phi + h(\psi^*_\uparrow \psi^*_\downarrow \phi + h.c.)\Big\} \tag{4.5}$$

with a real Yukawa coupling h for the conversion of two fermions into a molecule. In Eqn. (4.4) and (4.5) we suppress the dependence of the fields on the coordinate $\boldsymbol{x}$ and imaginary time τ. Integrating out the bosonic field ϕ in the standard path integral shows that Eq. (4.5) is equivalent to the single-channel model (4.4) provided that $-h^2 G_{\phi,\Lambda} = g$. Within the two-channel model, $G_{\phi,\Lambda}$ may include a momentum dependent, closed-channel contribution as discussed in Chapters 2 and 3. In this case the model becomes equivalent to a single-channel model only in the limit $h \to \infty$ [72, 260]. As we have seen in Chapter 2, the characteristic range r^* of the Feshbach resonance is inversely proportional to the Yukawa coupling $h^2 \sim 1/r^*$ such that this limit corresponds to open-channel dominated Feshbach resonances [6, 62, 178].

Physical properties such as quasiparticle weights or energies can be accessed via Green's functions which are derivable from generating functionals. The one-particle irreducible vertex functions $\Gamma^{(n)}$ are obtained from the effective quantum action Γ, which can, for instance, be computed approximately in a loop expansion within perturbation theory. As we are interested in the intrinsically non-perturbative regime of fermions close to a Feshbach resonance where the scattering length a diverges we again employ the functional renormalization group where the evolution of the effective average action Γ_k is given by the exact renormalization group equation

$$\partial_k \Gamma_k = \frac{1}{2}\mathrm{STr}\left(\frac{1}{\Gamma^{(2)}_k + R_k}\partial_k R_k\right) = \frac{1}{2}\tilde{\partial}_k \mathrm{STr}\ln[\Gamma^{(2)}_k + R_k], \tag{4.6}$$

as introduced in Appendix C. Since we are working now with fermions the standard trace is replaced by the supertrace STr which includes an additional minus sign when the sum is performed over fermionic degrees of freedom. $\Gamma^{(2)}_k$ is the full, field dependent inverse two-point Green's function at scale k, and R_k is a regulator taking care of the successive inclusion of momentum scales. Γ_k is in general a functional of the fields and contains all possible operators of the fields allowed by the symmetries. For this reason its exact calculation is usually impossible and one has to rely on approximations for Γ_k. Here let us first perform a vertex expansion of

Γ_k of the form

$$\begin{aligned}
\Gamma_k &= \int_{\mathbf{p},\omega} \left\{ \psi_\uparrow^*[-i\omega + \mathbf{p}^2 - \mu_\uparrow]\psi_\uparrow + \psi_\downarrow^* G_{\downarrow,k}^{-1}(\omega,\mathbf{p})\psi_\downarrow + \phi^* G_{\phi,k}^{-1}(\omega,\mathbf{p})\phi \right\} \\
&+ \int_{P_1,P_2} h_k(P_1,P_2)[\psi_\uparrow(P_1)^*\psi_\downarrow(P_2)^*\phi(P_1+P_2) + h.c.] \\
&+ \int_{P_1,P_2,P_3} \lambda_{\psi,k}(P_1,P_2,P_3)[\psi_\uparrow(P_1)^*\psi_\downarrow(P_2)^*\psi_\downarrow(P_3)\psi_\uparrow(P_1+P_2-P_3)] \\
&+ \sum_{\sigma=\uparrow,\downarrow} \int_{P_1,P_2,P_3} \lambda_{\phi\sigma,k}(P_1,P_2,P_3)[\psi_\sigma(P_1)^*\phi(P_2)^*\psi_\sigma(P_3)\phi(P_1+P_2-P_3)] \\
&+ \int_{P_1,\ldots,P_6} \lambda_{6,k}(P_1,\ldots P_5)\delta(P_1+P_2+P_3-P_4-P_5-P_6) \\
&\quad \times[\psi_\uparrow(P_1)^*\psi_\uparrow(P_2)^*\psi_\downarrow(P_3)^*\psi_\downarrow(P_4)\psi_\uparrow(P_5)\psi_\uparrow(P_6)]
\end{aligned} \tag{4.7}$$

with Matsubara frequency ω, and where we made explicit the dependence of the interaction vertices on the various four-momenta $P_i = (\omega_i, \boldsymbol{p}_i)$ of the in- and outgoing particles. In the low-energy limit this truncation is complete, that is, all terms contributing to the exact solution of the polaron problem have been included.[6] This can be seen from the following arguments: as there is only a single $\downarrow$-atom in the system there cannot be the formation of a macroscopic BEC of molecules. Due to the absence of the corresponding finite occupation of a macroscopic mode with finite expectation value $\rho = \sqrt{\phi^*\phi}$, there is no functional dependence of the vertices $\Gamma^{(n)}$ on ρ. For the same reason, there are no anomaleous terms for the fermionic propagators $\sim \psi_\downarrow\psi_\uparrow$. Furthermore, the majority $\uparrow$-atoms are renormalized only by the single impurity $\downarrow$-atom to order $1/N_\uparrow$. Hence one can neglect the renormalization of the $\uparrow$-atoms in the thermodynamic limit, and the chemical potential $\mu_\uparrow = \epsilon_F = k_F^2/(2m)$ is that of a free Fermi gas [59, 60].[7] Because there is only a single $\downarrow$-atom, all terms contributing to the polaron problem can only have at most a single $\downarrow$-atom involved, either directly or as a component inside the composite field ϕ. For example, although terms $\sim (\phi^*\phi)^n$ are generated during the flow, they do not couple back to the operators containing only a single $\downarrow$-atom. Accordingly the only interaction terms which have to be kept are given by the third-sixth line in Eq. (4.7). The four-fermion coupling λ_ψ, the atom-dimer scattering term $\sim \lambda_{\phi\sigma}$ describing the scattering of a fermion of spin σ with a molecule, and the six-fermion scattering vertex $\sim \lambda_6$ vanish in the UV and are generated solely by quantum fluctuation. Note that in particular the term $\sim \lambda_{\phi\downarrow}$ can be ignored as it includes two $\downarrow$-fermions and thus does not belong to the polaron problem.

In a sense, these arguments reflect, that the polaron problem may be viewed as in between a few- and many-body problem, since similar arguments like in the Chapters on few-body

[6] We exclude the scale dependent pressure p_k in this argument as it does not couple back to the other flow equations.

[7] We work in units where the Fermi momentum $k_F = 1$ so that $\epsilon_F = 1$.

physics can be applied. Furthermore, the most general momentum dependencies respecting translational symmetry have been kept in Eq. (4.7) and assuming low-energy scattering, only spin-antisymmetric terms in the four-fermion scattering have been included. Note that already the problem of two polarons is much more involved as then a possible p-wave pairing between the two minority atoms is possible [261, 262]. This effect would be reflected by a term $\sim (\psi_\uparrow^* \psi_\uparrow)^2$, and many others, not present in Eq. (4.7).

Derivation of the flow equations

Since the vertices in Eq. (4.7) are momentum dependent, the couplings $G_\downarrow$, G_ϕ, h, λ_ψ, and $\lambda_{\phi\downarrow}$ represent formally an infinite number of couplings. In order to derive their flow equations $\Gamma^{(2)}$ has to be calculated,

$$\Gamma^{(2)}[\chi](P,Q) = \frac{\delta^2 \Gamma[\chi]}{\delta\chi(Q)\delta\chi(P)}, \tag{4.8}$$

where χ denotes the 'superfield' $\chi = (\psi_\uparrow, \psi_\downarrow, \psi_\uparrow^*, \psi_\downarrow^*, \phi, \phi^*)$. The expression $\Gamma^{(2)}[\chi] + R_k$ may then be separated into a field dependent part $\mathscr{F}$ and a field independent part $\mathscr{P}$ according to

$$\Gamma^{(2)}[\chi] + R_k = \mathscr{P} + \mathscr{F}[\chi] = \mathscr{P}(1 + \mathscr{P}^{-1}\mathscr{F}[\chi]). \tag{4.9}$$

The logarithm or denominator in Eq. (4.6), respectively, can be expanded in terms of $\mathscr{P}^{-1}\mathscr{F}[\chi]$. Then the desired flow equations for $\Gamma_k^{(n)}$ are derived by taking the suitable field derivatives. For complicated expressions including their intricate momentum dependence this derivation is done using a computer algorithm developed in [106].

In terms of diagrams, each field derivative corresponds to pulling out one external leg of the full field-dependent propagator loop in Eq. (4.6). The resulting flow equations can be diagramatically expressed as displayed in Fig. 4.4. Here, only a few representative diagrams are shown and only those which contribute in the polaron problem. For example, a tadpole diagram contributing to the molecule self-energy due to scattering off a virtual molecule is zero as it is proportional to the boson occupation number n_B which is zero in the polaron problem. This holds as long as $T = 0$. For finite temperatures one obtains finite molecule and $\downarrow$-atoms occupations n_B and $n_\downarrow$ due to the finite temperature.

The solution of the complete set of flow equation, depicted in Fig. 4.4, with fully momentum and frequency dependent vertices gives the exact solution of the polaron problem. Finding the solution is, however, computationally impossible and we have to use a suitable truncation of the effective average action Γ_k in Eq. (4.7).

Besides keeping the most relevant terms, which, since we are working in the strong coupling regime, will be partially based on at least some physical intuition, one should obviously also include the vertices corresponding to the observables one is interested in. In our case this is the excitation spectrum of the polaron-to-molecule transition. It is determined by the analytical structure of the Green's function of the impurity $G_\downarrow$ and molecule G_ϕ. Additionally, the dominant contribution to the interaction between the $\uparrow$- and $\downarrow$-fermions comes from the exchange of the molecule field ϕ. Based on this argument, we devise a truncation which takes

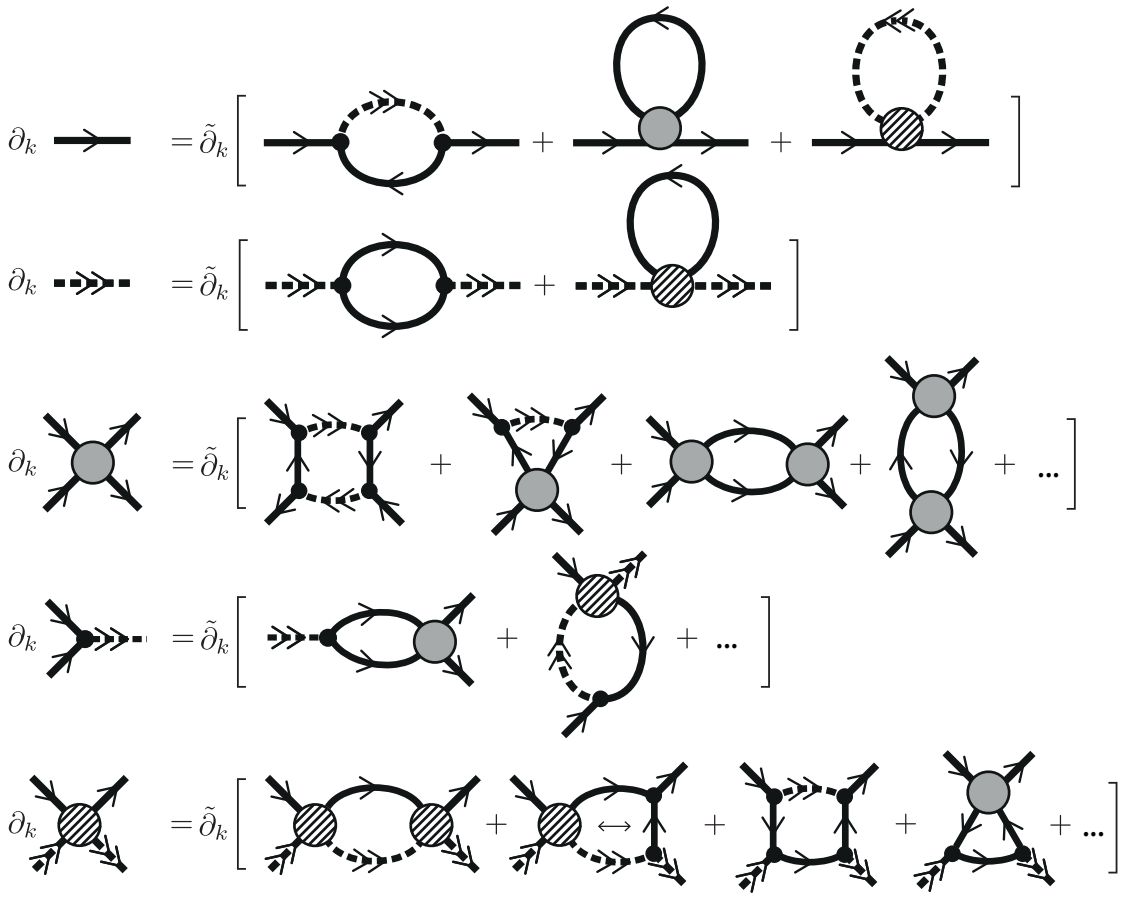

FIGURE 4.4: *Full set of Feynman diagrams contributing to the RG flow of the polaron problem. Their calculation yields the exact solution of the polaron problem. The flow equation generating the coupling λ_6 is not shown.*

into account the renormalization of $G_\downarrow$ and molecule G_ϕ while neglecting the couplings λ_ψ, $\lambda_{\phi\uparrow}$ and λ_6. The effective average action then reads

$$\begin{aligned}\Gamma_k &= \int_{\mathbf{p},\omega} \Big\{ \psi^*_\uparrow [-i\omega + \mathbf{p}^2 - \mu_\uparrow]\psi_\uparrow + \psi^*_\downarrow G^{-1}_{\downarrow,k}(\omega,\mathbf{p})\psi_\downarrow + \phi^* G^{-1}_{\phi,k}(\omega,\mathbf{p})\phi \Big\} \\ &+ \int_{\boldsymbol{x},\tau} h(\psi^*_\uparrow \psi^*_\downarrow \phi + h.c.), \end{aligned} \tag{4.10}$$

where we keep the full frequency and momentum dependence of the Green's functions $G_\downarrow$ and G_ϕ. Within the truncation (4.10) the Yukawa coupling h is not renormalized which can be seen as follows: in Eq. (4.10) we neglect the term $\psi^*_\uparrow \psi^*_\downarrow \psi_\downarrow \psi_\uparrow$. This term, although replaced at the UV scale with the boson exchange would be regenerated during the flow by

particle-hole fluctuations, cf. Fig. 4.4 [214, 263].[8] This does not imply, however, that our truncation only includes particle-hole fluctuations in lowest order as in a Chevy- or in the T-matrix approximation, see below. Contrarily, in our approach an infinite number of particle-hole fluctuations is taken into account. Similarly to the term $\sim \lambda_\psi$, the term $\sim \psi_\uparrow^* \phi^* \psi_\uparrow \phi$ for the atom-dimer interaction has been omitted. Both terms, $\sim \lambda_\psi$ and $\sim \lambda_{\phi\sigma}$ would lead to a renormalization of h as can be seen by inspection of the flow equations shown in Fig. 4.4. Due to their omission, however, there is no diagram generating a flow of h which is why

$$\partial_k h \equiv 0 \tag{4.11}$$

and h remains independent of frequency and momentum.

In consequence, the only running couplings are the Green's functions $G_\downarrow$ and G_ϕ which are themselves functions of both frequency ω and momentum $\boldsymbol{p}$. Their flow equations are derived by standard means, taking the appropriate functional derivatives of Eq. (4.6) with respect to the fields upon insertion of Eq. (4.10) into (4.6). One obtains

$$\begin{aligned} \partial_k P_{\downarrow,k}(P) &= h^2 \tilde{\partial}_k \int_Q G^c_{\phi,k}(Q) G^c_{\uparrow,k}(P+Q) \\ \partial_k P_{\phi,k}(P) &= -h^2 \tilde{\partial}_k \int_Q G^c_{\downarrow,k}(Q) G^c_{\uparrow,k}(P-Q) \end{aligned} \tag{4.12}$$

with multi-indices $P = (\omega, \mathbf{p})$ and $Q = (\nu, \boldsymbol{q})$. The functions $P_k \equiv G_k^{-1}$ on the left-hand side are the flowing inverse propagators *without* the regulator from Eq. (4.10), while the propagators G_k^c on the right-hand side are regulated:

$$G_k \equiv 1/P_k \qquad\qquad G_k^c \equiv 1/(P_k + R_k). \tag{4.13}$$

As usual, the tilde on $\tilde{\partial}_k$ indicates that the derivative with respect to the RG scale k acts only on the regulator term R_k in the cutoff propagators G_k^c: specifically, the single-scale propagators read $\tilde{\partial}_k G_k^c = -(G_k^c)^2 \partial_k R_k$. This set of flow equations is depicted in Fig. 4.5 and it will be investigated in the remainder of the chapter.

Previous diagrammatic approaches to the polaron problem used mainly a non-self-consistent T-matrix approximation [233, 258] which is equivalent to the solution via a variational wave function proposed by Chevy [231, 232, 236, 237, 239]. In such an approach the molecule propagator (second diagram in Fig. 4.5) is renormalized only by the *bare* fermion propagators. The resulting full T-matrix given by G_ϕ is then used to calculate the $\downarrow$-atom self-energy. Our approach is fundamentally different and goes beyond the non-selfconsistent T-matrix approximation: the flow equations (4.12) have a one-loop structure but contain the *full* propagators at scale k. By integrating the flow, diagrams of arbitrarily high loop-order are generated and constantly fed back into each other. For this reason in the fRG approach also the full propagator of

[8] This type of particle-hole fluctuations are the ones responsible for the Gorkov-Melik-Barkhudarov correction to BCS theory as described below Eq. (4.1).

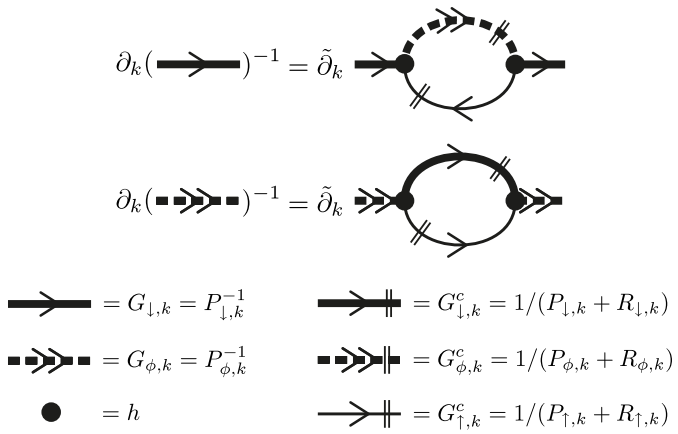

FIGURE 4.5: *Diagrammatic representation of the fRG flow equations* (4.12) *for the impurity and molecule propagators.*

the ↓-atom (at scale k) appears in the renormalization of the molecule Green's function unlike in the non-selfconsistent T-matrix approximation [231, 232, 233, 237, 239, 258]. In this way our approach is diagrammatically similar to a Ward-Luttinger approach [37, 58, 264, 255, 265] where the diagrammatic series in Fig. 4.5 is solved self-consistently. While in this approach all momentum and energy modes are integrated out in a single step, in the RG approach the integration is performed stepwise

Derivative expansion

In order to get some insight in the ground state properties of the polaron-to-molecule transition – answering for instance the question whether and for which interaction strength this transition takes place – we first devise a very simple, further truncation of Eq. (4.10), which allows the derivation of the flow equations (4.12) in analytical form. In particular, we are interested in the calculation of the ground state energy and quasiparticle weights. In order to address these, it is sufficient to keep only a limited momentum and frequency dependence of the Green's functions $G_\downarrow$ and G_ϕ, namely those at low energies close to the ground state pole. We may thus perform a derivative – also called gradient – expansion of Γ_k and expand the propagators $G^{-1}_\downarrow(\omega, \boldsymbol{p})$ and $G^{-1}_\phi(\omega, \boldsymbol{p})$ in powers of momentum and frequency,

$$\begin{aligned} G^{-1}_\downarrow(\omega, \boldsymbol{p}) &= S_\downarrow[-i\omega + \boldsymbol{p}^2] + m^2_\downarrow, \\ G^{-1}_\phi(\omega, \boldsymbol{p}) &= S_\phi[-i\omega + \boldsymbol{p}^2/2] + m^2_\phi, \end{aligned} \tag{4.14}$$

where the gap terms $m^2_\downarrow$ and m^2_ϕ are related to the flowing static self-energies $\Sigma_{\downarrow,\phi}(0,0)$, e.g. $m^2_\downarrow = -\mu_\downarrow - \Sigma_\downarrow(0,\mathbf{0})$.

Note that we allow only for a common prefactor $S_{\downarrow,\phi}$ in front of frequency and momentum. In the few-body problem this is valid as a consequence of Galilean symmetry [209]. This

constraint does not hold, however, for finite density, e.g. an effective mass corresponds to a different prefactor in front of $\boldsymbol{p}^2$. Note, that this does not imply a breaking of Galilean invariance which still holds at finite density and it is guaranteed by a relation of the effective mass to the four-fermion vertex (see, for instance, Eq. (19.2) in [2]). Being interested only in the ground state energy and quasiparticle weight, and for the sake of simplicity we use the simpler approximation (4.14). In Section 4.4 this constraint will be completely relaxed.

The quasiparticle weights $Z_{\downarrow,\phi}$ are given by

$$Z_{\downarrow,\phi} = 1/[\partial_\omega \, P_{\downarrow,\phi}(\omega, \boldsymbol{p}=0)]\Big|_{\omega=\omega^*} = 1/S_{\downarrow,\phi} \tag{4.15}$$

where the frequency derivative is evaluated at the respective ground state pole ω^*. Note again, that the majority fermions are not renormalized, $S_\uparrow = 1$ and $\mu_\uparrow = \varepsilon_F$.

So far we did not specify the regulator terms $R_\downarrow$ and R_ϕ in Eq. (4.13). We choose sharp cutoff functions R_k which allow to write the regulated Green's functions G_k^c in the particularly simple, multiplicative form (for unoccupied $\downarrow$-atoms)

$$\begin{aligned} G^c_{\downarrow,k}(\omega,\mathbf{p}) &= \frac{\theta(|\mathbf{p}|-k)}{P_{\downarrow,k}(\omega,\mathbf{p})}, \\ G^c_{\phi,k}(\omega,\mathbf{p}) &= \frac{\theta(|\mathbf{p}|-k)}{P_{\phi,k}(\omega,\mathbf{p})}, \\ G^c_{\uparrow,k}(\omega,\mathbf{p}) &= \frac{\theta(|\mathbf{p}^2-\mu_\uparrow|-k^2)}{P_{\uparrow,k}(\omega,\mathbf{p})}. \end{aligned} \tag{4.16}$$

This corresponds to a (additive) regulator of the form

$$R_{\downarrow,k}(\mathbf{p}) = P_{\downarrow,k}(\omega,\mathbf{p}) \left[1 - \frac{1}{\theta(|\mathbf{p}|-k)}\right] \tag{4.17}$$

$$R_{\phi,k}(\mathbf{p}) = P_{\phi,k}(\omega,\mathbf{p}) \left[1 - \frac{1}{\theta(|\mathbf{p}|-k)}\right] \tag{4.18}$$

$$R_{\uparrow,k}(\mathbf{p}) = P_{\uparrow,k}(\omega,\mathbf{p}) \left[1 - \frac{1}{\theta(|\mathbf{p}^2-\mu_\uparrow|-k^2)}\right]. \tag{4.19}$$

A few comments are in order: the regulators (4.17)-(4.19) are solely momentum and not frequency dependent. This implies directly that they break Galilean invariance as boosts in momentum are intimately connected to shifts in energy. At first sight this seems to be a severe violation because symmetries should not be destroyed by the choice of regulator.[9] In the present case, however, the few-body problem, where Galilean invariance holds exactly, can be

[9]This problem of breaking of Galilean symmetry appear also, although subtly hidden, in other theoretical approaches to the cold atoms [266, 267].

solved exactly as demonstrated in Chapter 2. Being the exact solution, the IR result of the RG flow becomes necessarily regulator independent and thus Galilean symmetry, although artificially broken during the flow, finally gets restored at the end of the renormalization group flow. Since Galilean invariance of the propagators would be broken anyway by the finite density on the quantum level ($k = 0$), we assume that the contribution to the symmetry breaking induced by the regulator, keeping in mind the exactness of the few-body flow, is subleading.

Furthermore, were we to take a Galilean invariant regulator with a momentum and frequency dependence[10] we would face a new problem. The resulting frequency dependence could give new, artificial poles in the complex frequency plane of the regulated Green's functions G^c. This in turn would entail a severe breaking of the vacuum hierarchy. As the vacuum hierarchy lies at the heart of the solution of the few-body problem, such a violation is not acceptable. There is, however, a quite simple choice of regulator which keeps Galilei invariance: the mass-like k^2-regulator. We solved the polaron problem also for this regulator and we find that the artificial breaking of Galilean symmetry does indeed not have an important impact on the results.

For the $\downarrow$- atoms and molecules the sharp regulators (4.17)-(4.19) strictly exclude low momentum modes with $|\boldsymbol{p}| < k$ which implements the Wilsonian RG idea of shell-wise integration of momentum modes. The majority fermions have a finite density and thus their pole is not at zero momentum but at momenta $\boldsymbol{p}$ on the Fermi surface. These low energy modes have to be integrated out at the end of the flow which is why the $\uparrow$-atom regulator has the modified form (4.19). Note, that the correct pole structure is automatically kept due to the propagator $P_\uparrow$ appearing in the prefactor of $R_\uparrow$. For example, if one uses a masslike, additive k^2 regulator one has to carefully implement the correct pole structure by using the sign function inside the regulator of the $\uparrow$-fermions, $R_{\uparrow,k} = \mathrm{sign}(\boldsymbol{p}^2 - \mu_\uparrow)k^2$.

Having specified the regulators the flow equation for the running couplings $S_{\downarrow,\phi}$, $m^2_{\downarrow,\phi}$ can be obtained in a straightforward manner. The frequency as well as momentum integration can be performed analytically and one obtains

$$\partial_k S_\downarrow = -\frac{2h^2 k}{\pi^2 S_\phi}\theta(\mu_\uparrow - 2k^2)\Big[\frac{\sqrt{\mu_\uparrow - k^2}}{(k^2 + \mu_\uparrow + 2m^2_\phi/S_\phi)^2} + \frac{k}{(-k^2 + 2\mu_\uparrow + 2m^2_\phi/S_\phi)^2}\Big], \quad (4.20)$$

$$\partial_k m^2_\downarrow = \frac{h^2 k}{\pi^2 S_\phi}\theta(\mu_\uparrow - 2k^2)\Big[\frac{\sqrt{\mu_\uparrow - k^2}}{k^2 + \mu_\uparrow + 2m^2_\phi/S_\phi} + \frac{k}{-k^2 + 2\mu_\uparrow + 2m^2_\phi/S_\phi}\Big], \quad (4.21)$$

[10] It is desirable to have a momentum dependent regulator in order to keep the flow maximally local in theory (momentum) space [172].

$$\partial_k S_\phi = -\frac{h^2 k}{2\pi^2 S_\downarrow} \frac{\sqrt{\mu_\uparrow + k^2}}{(2k^2 + \mu_\uparrow + m_\downarrow^2/S_\downarrow)^2}, \tag{4.22}$$

$$\partial_k m_\phi^2 = \frac{h^2 k}{2\pi^2 S_\downarrow} \frac{\sqrt{\mu_\uparrow + k^2}}{(2k^2 + \mu_\uparrow + m_\downarrow^2/S_\downarrow)}. \tag{4.23}$$

In the derivation the step functions appear due to the pole structure in the zero-temperature frequency integration.

The RG flow equation (4.6) is a (functional) differential equation and the resulting system of coupled differential equations (4.20)-(4.23) has to be supplemented with appropriate initial conditions at the ultraviolet scale $k = \Lambda$. In the UV, physics does not resolve large distances. To be more precise, if we choose Λ to be on the order of a few thousand Fermi wave vectors $\Lambda \sim \mathcal{O}(10^3 k_F)$ then the system is completely insensitive to the scale set by the density. For this reason the initial condition is dictated by few-body physics.[11]

As already discussed in Chapter 2, the s-wave vacuum scattering amplitude for the interaction of an $\uparrow$- and $\downarrow$-fermion with momenta $\boldsymbol{q}$, $-\boldsymbol{q}$ in the center-of-mass frame is given by ($q = |\boldsymbol{q}|$)

$$f(q) = \frac{1}{-1/a - iq}. \tag{4.24}$$

$f(q)$ is related to the full, retarded molecule propagator $G^{\text{vac}}_{\phi,\text{R}}$ evaluated at the infrared RG scale $k = 0$,

$$f(q) = \frac{h^2}{8\pi} G^{\text{vac}}_{\phi,\text{R}}(\omega = 2q^2, \mathbf{p} = 0), \tag{4.25}$$

where $\omega = 2q^2$ is the total kinetic energy of the interacting atoms. The subscript R indicates that the analytical continuation to the retarded function of real frequencies ($i\omega \to \omega + i0$) has been performed. As calculated from the fRG in Chapter 2 the exact vacuum molecule propagator $G^{\text{vac}}_{\phi,\text{R}}$ in the limit of microscopic contact interactions has the form

$$[G^{\text{vac}}_{\phi,\text{R}}(\omega, \mathbf{p})]^{-1} = \frac{h^2}{8\pi} \left(-a^{-1} + \sqrt{-\frac{\omega}{2} + \frac{\mathbf{p}^2}{4} - i0} \right). \tag{4.26}$$

This expression for $G^{\text{vac}}_{\phi,\text{R}}$ reproduces the correct scattering amplitude (4.24) when inserted into Eq. (4.25), and dictates the form of the UV propagator $G^{-1}_{\phi,\Lambda}$ for a given choice of regulator. In particular, the square root appearing in Eq. (4.26) is responsible for the term iq in the scattering amplitude (4.24). As we do not account for the square root structure of the molecule propagator using the simple derivative expansion (4.14), this term cannot be recovered in this approximation. We therefore focus on the correct calculation of the scattering length a at zero

[11] In fact, as we will see below, the RG flow will only deviate from its few-body trajectory in theory space when k becomes of the order of k_F. Only at this scale the particles 'become aware' of the many-body environment.

momentum. In order to do so, we have to solve the flow equation $\partial_k m_\phi^2$ in the vacuum limit, where neither the $\uparrow$- nor the $\downarrow$-atoms are renormalized and $\mu_\downarrow = \mu_\uparrow = 0$. Then the flow of the molecule gap can be integrated analytically and we obtain

$$(m^{\text{vac}}_{\phi,k=0})^2 = m^2_{\phi,\Lambda} - \frac{h^2\Lambda}{4\pi^2}. \tag{4.27}$$

In order to reproduce the correct (infrared) scattering length a the molecule gap has to fulfill the infrared condition $(m^{\text{vac}}_{\phi,k=0})^2 = -h^2/(8\pi a)$. This leads to the UV condition for the molecule gap,

$$m^2_{\phi,\Lambda} = \frac{h^2}{8\pi}(2\Lambda/\pi - a^{-1}), \tag{4.28}$$

which incorporates the correct regularization of the UV divergence $\sim \Lambda$ in Eq. (4.27). At the UV scale the momentum and frequency dependence of $P_{\phi,\Lambda}$ can be neglected due to the large bosonic gap $m^2_{\phi,\Lambda}$, and we set $S_{\phi,\Lambda} = 1$.

For finite density the initial condition for the fermions is given by their form in the microscopic action (4.5), $G^{-1}_{\sigma,k=\Lambda}(\omega,\mathbf{p}) = -i\omega + \mathbf{p}^2 - \mu_\sigma$. This corresponds to initial values $m^2_{\sigma,\Lambda} = -\mu_\sigma$ and $S_{\sigma,\Lambda} = 1$. After having specified the initial conditions we can solve the system of differential equations (4.20) numerically.

But how to extract the ground state energy and how to determine where the polaron-to-molecule transition takes place? In order to answer this, we note that the chemical potential $\mu_\downarrow$ is the energy required to add one $\downarrow$-atom to the system [3],

$$\mu_\downarrow = E(N_\downarrow) - E(N_\downarrow - 1). \tag{4.29}$$

The chemical potential $\mu_\downarrow$, as a Legendre parameter, is independent of the cutoff scale k and the interaction effects on the $\downarrow$-fermion, which are successively included during the flow, are captured by the k-dependent wave function renormalization $S_\downarrow$ and static selfenergy $\Sigma_\downarrow(0,0)$. In the polaron problem we are interested in a two-component Fermi gas in the limit of extreme population imbalance where one considers only a single $\downarrow$-atom, $N_\downarrow = 1$, and the relation (4.29) can be used to determine the ground-state energy of the system. On the other hand $\mu_\downarrow$ adjusts the density of $\downarrow$-atoms and thus its value marks the phase transition from a degenerate, fully polarized $\uparrow$-Fermi gas to a phase of finite $\downarrow$-fermion density [236], which is just the critical line given by h_s discussed in Section 4.1. Accordingly, for all choices of $\mu'_\downarrow \leq \mu_\downarrow$ there has to be a vanishing occupation of both $\downarrow$-fermions and molecules at every RG scale k, which leads to the condition

$$P_{\downarrow,k}(0,\mathbf{0},\mu'_\downarrow) \geq 0, \quad P_{\phi,k}(0,\mathbf{0},\mu'_\downarrow) \geq 0 \quad \forall\, \mu'_\downarrow \leq \mu_\downarrow. \tag{4.30}$$

In order to have only a single $\downarrow$-atom or molecule, $\mu_\downarrow$ has to be determined self-consistently such that either the $\downarrow$-atom or the molecule ϕ is gapless in the infrared, $P_{\downarrow/\phi,k=0}(0,\mathbf{0}) = 0$ (ground state), see also Table 4.1.

coupling	$(k_F a)^{-1} < (k_F a_c)^{-1}$	$(k_F a)^{-1} > (k_F a_c)^{-1}$
ground state	polaron	molecule
$\downarrow$ gap	$P_\downarrow(0,\mathbf{0}) = m_\downarrow^2 = 0$	$P_\downarrow(0,\mathbf{0}) = m_\downarrow^2 > 0$
ϕ gap	$P_\phi(0,\mathbf{0}) = m_\phi^2 > 0$	$P_\phi(0,\mathbf{0}) = m_\phi^2 = 0$

TABLE 4.1: *Conditions for the polaron and molecule ground states. The polaron-to-molecule transition occurs at the critical interaction strength* $(k_F a_c)^{-1}$ *at which* $m_\phi^2 = m_\downarrow^2 = 0$.

We indeed find that depending on the value of the dimensionless coupling $(k_F a)^{-1}$, either the polaron or the molecule becomes the ground state. The polaron-to-molecule transition occurs at the critical interaction strength $(k_F a_c)^{-1}$ at which $m_\phi^2 = m_\downarrow^2 = 0$.

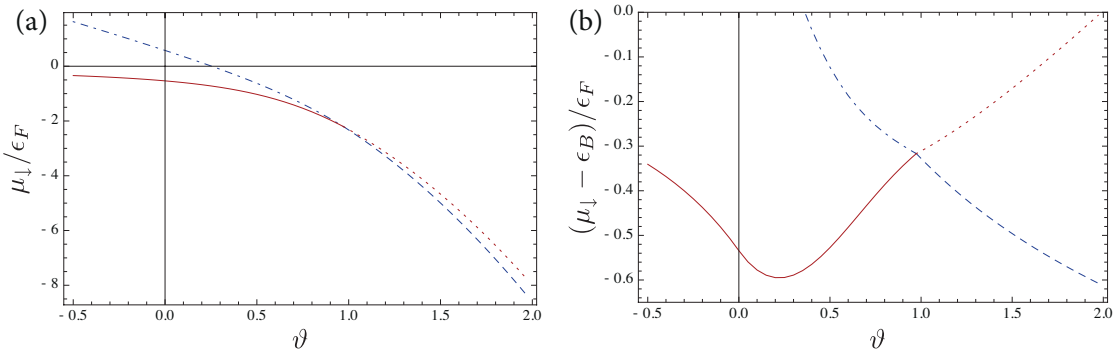

FIGURE 4.6: *(a) Ground state energy spectrum of the Fermi polaron problem from a derivative expansion. The attractive polaron (solid) is the ground state for* $\vartheta < \vartheta_c$. *In this regime the molecule (dot-dashed) is an excited state. For* $\vartheta > \vartheta_c$ *the molecule (dashed) becomes the ground state while the polaron exists as an excited state (dotted). (b) Same as (a) with the universal dimer binding energy substracted.*

In Fig. 4.6(a) we show the ground state energy spectrum for a broad Feshbach resonance of width $r^* k_F = 0.005$ as function of ϑ within the derivative expansion (4.14), using the sharp regulators (4.17)-(4.19). Indeed, the ground state switches from being an attractive polaron to a molecule at a critical interaction strength $\vartheta_c = 0.972$. In order to make this transition more visible it is convenient to substract the two-body binding energy $\epsilon_B = -2/a^2$, cf. Fig. 4.6(b). Only a single ϵ_B has to be subtracted since at most only a single molecule can be formed in the system. The value $\vartheta_c = 0.972$ compares quantitatively well with the diagMC result $\vartheta_c = 0.90(2)$ [59, 60]. Comparing energies of different variational wave functions for the molecule and the polaron one obtains $\vartheta_c = 0.84$ [236, 237]. Considering the simplicity of our approximation the agreement is quite remarkable.

A further benchmark is the energy of the polaron at unitarity, $a \to \infty$. Here, we find $\mu_\downarrow/\epsilon_F = -0.534$ which has to be compared with $\mu_\downarrow/\epsilon_F = -0.615$ (diagMC [59, 60]), -0.59 (MC [232]), -0.607 (Chevy's variational ansatz [231], T-matrix [233, 268]), -0.6158 (multiple particle/hole excitations [234]), and -0.59 from experiment [240].

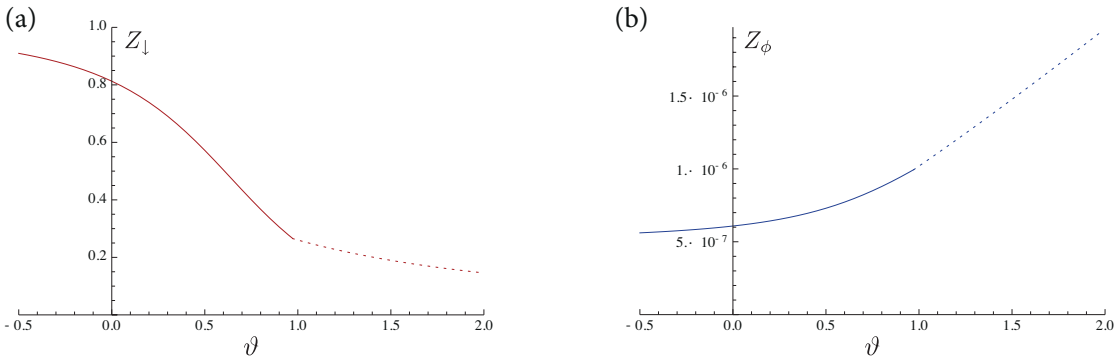

FIGURE 4.7: *(a) Spectral weight of the polaron as function of the dimensionless interaction strength ϑ. The non-analyticity at the transition is an artifact of the truncation. (b) Spectral weight of the molecule across the polaron-to-molecule transition. The molecule's small weight is due to its high degree of compositeness as discussed in Section 4.5.*

We also calculated the quasiparticle weights of the attractive polaron and the molecule as shown in Fig. 4.7. The attractive polaron has a weight $Z_\downarrow$ close to unity for small attraction and looses weight as the interaction is increased towards the transition. Already at this point we may rise the question: where is the spectral weight lost to? This question is often simply ignored in studies in the context of critical phenomena where one is solely interested in the low-energy degrees of freedom. However, it is an important physical question, as we know that the spectral function of a particle $\mathcal{A}$, given by

$$\mathcal{A}_{\downarrow/\phi}(\omega, \mathbf{p}) = 2\mathrm{Im}G_{\downarrow/\phi,\mathrm{R}}(\omega, \mathbf{p}) \tag{4.31}$$

has to obey the sum rule

$$\int \frac{d\omega}{2\pi} \mathcal{A}(\omega, \mathbf{p}) = 1, \tag{4.32}$$

no matter the interactions involved. Obviously, this sum rule is broken in the derivative approximation where the spectral function for the impurity reads

$$\mathcal{A}_\downarrow(\omega, \boldsymbol{p}) = 2\pi Z_\downarrow \delta(\omega - \boldsymbol{p}^2 + \frac{\mu_\downarrow + \Sigma_\downarrow}{S_\downarrow}). \tag{4.33}$$

The question of loss of spectral weight is also closely related to a further drawback of the simple derivative expansion which concerns the excited states in the system. We will see in the following that indeed a new well-defined quasiparticle appears in the spectrum which corresponds to a polaron excitation interacting repulsively with the majority atoms. This state will

be the one absorbing most of the spectral weight lost in Eq. (4.33). Furthermore we will also see that the attractive polaron as well as the molecule exist as excited states above their respective ground state across the transition at ϑ_c. This is indicated by the dotted (dashed-dotted) lines for the polaron (molecule) in Fig. 4.6. These lines have, however, to be considered with care, because it is not straightforward to extract these energies within a derivative expansion.

To understand this difficulty, we recall that a quasiparticle excitation is given by the poles of the retarded Green's function $G_R(\omega, \mathbf{p})$. Near each quasiparticle pole the retarded propagator can be approximated by a pole expansion of the form

$$G_{\mathrm{R}}(\omega, \mathbf{p}) \approx \frac{Z}{\omega_{\mathrm{qp}} - \omega - i0} = \frac{Z}{E_{\mathrm{qp}}(\mathbf{p}) - \omega - i\Gamma_{\mathrm{qp}}} \tag{4.34}$$

where Z is the quasiparticle weight, Γ_{qp} its decay width, and $E_{\mathrm{qp}}(\mathbf{p})$ its dispersion so that ω_{qp} is a complex number. Let us concentrate on the excited polaron state.[12] The Green's function of the polaron is given by Eq. (4.14) which is easily continued to real frequencies and yields the spectral function in Eq. (4.33). In this expression, we have no freedom to adjust the chemical potential $\mu_\downarrow$. As described above, it has to be chosen such that there is no finite occupation of polarons. For $\vartheta < \vartheta_c$, where the polaron is the ground state the condition $m_\downarrow^2 = 0$ gives the spectral function $\mathcal{A}_\downarrow(\omega, \boldsymbol{p}) = 2\pi Z_\downarrow \delta(\omega - \boldsymbol{p}^2)$ while for $\vartheta > \vartheta_c$, the gap $m_\downarrow^2$ is finite and the spectral function reads

$$\mathcal{A}_\downarrow(\omega, \boldsymbol{p}) = 2\pi Z_\downarrow \delta(\omega - \boldsymbol{p}^2 - m_\downarrow^2/S_\downarrow), \tag{4.35}$$

since the quasiparticle pole is located at the *real* finite frequency $\omega_{\mathrm{qp}} = m_\downarrow^2$. Here we see another drawback of the derivative expansion: it does not account for the finite lifetime expected for an excited state. In order to extract the energies shown in Fig. 4.6 we used the identification $\omega_{\mathrm{qp}} = m_\downarrow^2/S_\downarrow$. But this is obviously not the correct value. Within the derivative expansion we assume, up to the wave function renormalization Z, a frequency independent self-energy $\Sigma_\downarrow$. It is extracted from the flow by the projection onto the gap $m_\downarrow^2$,

$$\partial_t m_\downarrow^2 = \partial_t P_\downarrow(\omega, \mathbf{p})\Big|_{\omega=0, \mathbf{p}=0}, \tag{4.36}$$

evaluated at *zero* frequency. In general the self-energy Σ is, however, frequency dependent and to extract the correct quasiparticle energy ω_{qp} we need the self-energy to be evaluated not at zero frequency but at the quasiparticle pole, *after* continuation to real frequencies. This leads to a complicated implicit equation which is impossible to solve in a straightforward manner. In other words, for excited states we expand around the wrong expansion point of the Taylor expansion in frequency and only for the ground state we perform the correct projection to extract the quasiparticle energy because here the correct expansion point is indeed $\omega = 0$. For this reason the data in Fig. 4.6 has to be at most understood as a qualitative estimate of the exact quasiparticle energies. The same reasoning applies to the quasiparticle weights of the excited

[12] The reasoning is analogous for the molecule.

states shown in Fig. 4.7. The quasiparticle weight is evaluated from Eq. (4.35) which is again obtained from a projection at $\omega = 0$ and not at the true quasiparticle pole. This is the reason for the non-analyticity in $Z_\downarrow$ visible at ϑ_c which is an artifact of the derivative expansion.

In conclusion, we see that a derivative expansion is a very simple approximation which yields reasonable results when ground state properties are concerned. For non-universal quantities and dynamical properties it is, however, not sufficient. In the following we derive a new numerical fRG method which copes correctly with the various drawbacks indicated above and which allows us to extract the full quasiparticle spectrum of the polaron problem.

4.4 RG for full spectral functions

The main goal of this Chapter is to solve the system of flow equations (4.12) without imposing any constraints on the frequency and momentum dependence of the polaron and molecule propagators $G_{\downarrow/\phi,k}(\omega,\mathbf{p})$. This formally corresponds to the evaluation of the flow of infinitely many coupling constants which is impossible analytically and one has to resort to a numerical solution. In order to do so, the inverse, flowing Green's functions $P_{\downarrow/\phi,k}(\omega,\mathbf{p})$ are evaluated on a discrete grid in frequency and momentum space,

$$\begin{aligned} P_{\downarrow,k}(\omega,\mathbf{p}) &\to P_{\downarrow,k}(\omega_i,p_j) = P^{ij}_{\downarrow,k} \\ P_{\phi,k}(\omega,\mathbf{p}) &\to P_{\phi,k}(\omega_i,p_j) = P^{ij}_{\phi,k}. \end{aligned} \tag{4.37}$$

The propagator of the majority atoms is not renormalized and it is kept in its analytical form. For $P_{\downarrow/\phi,k}(\omega,\mathbf{p})$ we choose a logarithmically spaced, finite grid with $\omega_i \in (0,\ldots,\omega_{\max})$ and $p_j \in (0,\ldots,p_{\max})$. As a result of rotational invariance the propagators depend only on the magnitude of spatial momentum $p = |\mathbf{p}|$, and due to the condition $P^*(\omega) = P(-\omega)$ for Euclidean (Matsubara) propagators it is sufficient to consider positive frequencies only [2]. Later we will perform the analytical continuation to real frequencies. Therefore it is necessary to resolve the structure of the propagators well for small frequencies and momenta where most of the interesting physics takes place. For this reason we choose to sample the propagators in two regions separately with different grid resolutions. In Fig. 4.8(a) we show a typical grid on a logarithmic scale as well as on a linear scale in Fig. 4.8(b). In both, the small (ω,p) (green area) and the high (ω,p) regions (blue area) we choose to sample the same number of nodes. In the polaron case, we find that this sampling is the best compromise between efficiency and accuracy.

During the RG flow we keep then only track of the finite number of couplings $P^{ij}_{\downarrow/\phi,k}$ which are complex numbers. From these the full (ω,p) dependence of the inverse propagators is reconstructed by cubic spline interpolation,

$$\begin{aligned} P_{\downarrow/\phi,k}(\omega,p) &= \mathrm{Spline}(\{P^{ij}_{\downarrow/\phi,k}\}) \\ &= \sum_{\xi,\vartheta=0}^{3} c^{ij,\xi\vartheta}_{\downarrow/\phi,k}(\omega-\omega_i)^\xi (p-p_j)^\vartheta, \end{aligned} \tag{4.38}$$

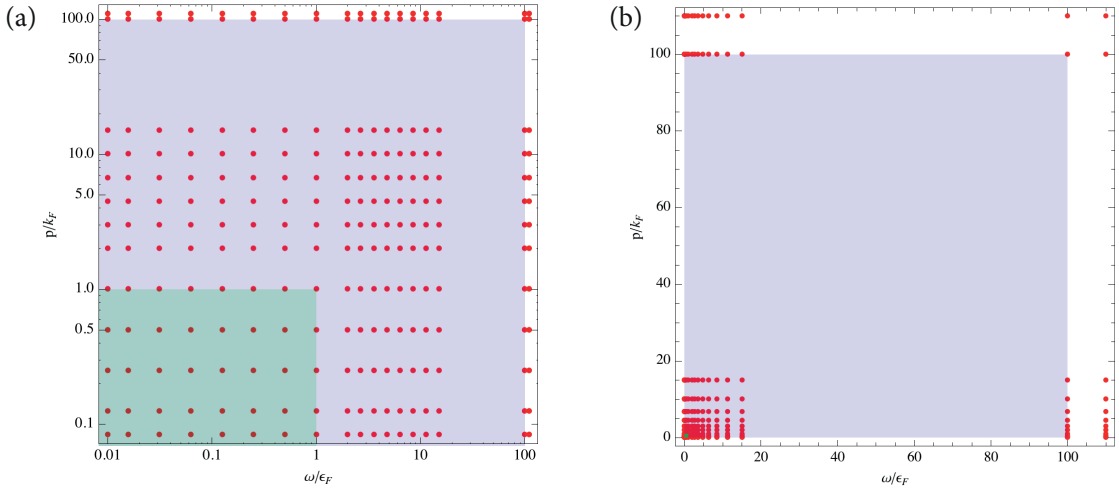

FIGURE 4.8: *Illustration of the frequency and momentum grid (red dots) chosen for the numerical representation of the inverse propagators $P_{\downarrow,\phi}$ on a logarithmic scale (a) and linear scale (b). Two different regions are employed with a higher resolution in the low frequency and momentum regime (green area). The additional outer points are used for the fit of the asymptotic behavior of the Green's functions.*

with $\omega \in (\omega_i, \omega_{i+1})$, $p \in (p_j, p_{j+1})$ and $c^{ij,\xi\vartheta}_{\downarrow/\phi,k}$ the corresponding spline coefficients. The grid only extends up to frequencies $\omega_{\max}$ and momenta $p_{\max}$. For the asymptotics of the propagators for high frequency and momentum modes we rely on the property that these modes are practically not renormalized. Their form can then be approximated by simple fit models for $\omega > \omega_{\max}$ and/or $p > p_{\max}$, and we choose

$$P^{>}_{\downarrow,k}(\omega,\mathbf{p}) = -i\omega + \mathbf{p}^2 - \mu_{\downarrow} \tag{4.39}$$

$$P^{>}_{\phi,k}(\omega,\mathbf{p}) = \frac{h^2}{8\pi}\left(-a^{-1} + \sqrt{-\frac{i\omega}{2} + \frac{\mathbf{p}^2}{4} + f_{\phi,k}}\right),$$

with $f_{\phi,k}$ determined by a continuity condition from the numerical value of $P_{\phi,k}$ for the largest momenta $|\mathbf{p}| = p_{\max}$. We find that this procedure yields the desired numerical accuracy which is higher than the accuracy of the numerical differential equation solver employed later on.

In the grids shown in Fig. 4.8, we chose $\omega_{\max} = 100\epsilon_F$ and $p_{\max} = 100k_F$. Note that there are additional grid points visible at even higher frequency and momenta which are situated in rather close vicinity of $\omega_{\max}$ and $p_{\max}$. We also track these additional points which are necessary for two reasons. First, they are used to determine the coefficients in our fit models for high frequency and momenta. More important is, however, that they guarantee a higher numerical stability of the spline interpolation. This can be seen by considering the inverse, infrared dimer propagator in vacuum, shown in Fig. 4.9. At high frequencies the propagator has

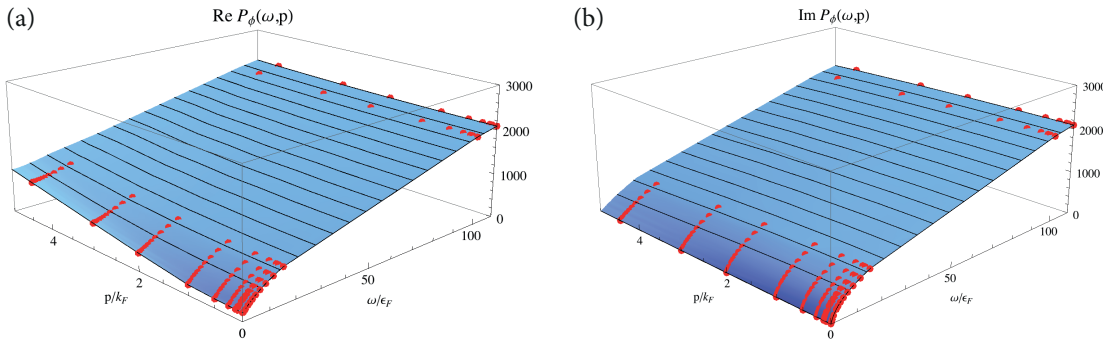

FIGURE 4.9: *Infrared solution of the flow of the inverse dimer propagator $P_\phi(\omega,\boldsymbol{p})$ in vacuum. (a) Real part of $P_\phi(\omega,\boldsymbol{p})$. (b) Imaginary part of $P_\phi(\omega,\boldsymbol{p})$.*

a fairly simple structure and the two narrowly spaced, high frequency grid points prevent the cubic spline algorithm to overshoot between the quite distant sampling points at intermediate scales. At each RG step the flow equations have to be evaluated with the interpolated Green's functions (4.38) as input.

In order to keep the numerical cost of computing the flow equations (4.12) low it is advantageous to employ the sharp momentum regulator functions $R_{\downarrow,k}$, $R_{\uparrow,k}$, and $R_{\phi,k}$ defined by Eq. (4.16). This reduces the number of loop integrations by one. The flow equations evaluated by our algorithm are then given by

$$\begin{aligned}
\partial_k P_{\downarrow,k}(\omega,\mathbf{p}) &= -\frac{h^2}{(2\pi)^3}\int_{-1}^{1} dx \int_{-\infty}^{\infty} d\nu \int_0^{\infty} q^2\, dq \\
&\quad \times \frac{\chi_k^+(p,q,x)}{P_{\phi,k}(\nu,\boldsymbol{q})P_{\uparrow,k}(\omega+\nu,\mathbf{p}+\boldsymbol{q})} \\
\partial_k P_{\phi,k}(\omega,\mathbf{p}) &= \frac{h^2}{(2\pi)^3}\int_{-1}^{1} dx \int_{-\infty}^{\infty} d\nu \int_0^{\infty} q^2\, dq \\
&\quad \times \frac{\chi_k^-(p,q,x)}{P_{\downarrow,k}(\nu,\boldsymbol{q})P_{\uparrow,k}(\omega-\nu,\mathbf{p}-\boldsymbol{q})}
\end{aligned} \tag{4.40}$$

where we have defined the characteristic functions

$$\begin{aligned}
\chi_k^{\pm}(p,q,x) &= \delta(q-k)\theta(|(\mathbf{p}\pm\boldsymbol{q})^2-\mu_\uparrow|-k^2) \\
&+ 2k\,\theta(q-k)\delta(|(\mathbf{p}\pm\boldsymbol{q})^2-\mu_\uparrow|-k^2)
\end{aligned} \tag{4.41}$$

and $x=\cos\theta$ expresses the angle θ between the momentum vectors $\mathbf{p}$ and $\boldsymbol{q}$ such that $|\mathbf{p}\pm\boldsymbol{q}|^2 = p^2+q^2\pm 2pqx$.

The q integration can be performed analytically and results in the evaluation of the δ-distributions and thus a replacement of q in Eq. (4.40). Note, that the stepfunctions θ depend

on the angular variable x and evaluate to zero depending on the value of x. It is advantageous to evaluate their argument in analytical form to keep the numerical cost of the following x-integration as low as possible. Finally one ends up with expressions for the flow equations of the schematic form

$$\begin{aligned} \partial_k P_{\downarrow/\phi,k}(\omega_i, p_j) &= \sum_\alpha \int_{-1}^{1} dx \int_{-\infty}^{\infty} d\nu \\ &\times \frac{f_\alpha(\omega_i, p_j, x, \nu, k, h, \mu_\uparrow)}{P_{\downarrow/\phi,k}(\nu, q^{(\alpha)}_{\downarrow/\phi}(p_j, x)) P_{\uparrow,k}(\omega \pm \nu, q^{(\alpha)}_{\uparrow}(p_j, x))} \end{aligned} \tag{4.42}$$

where the sum over the index α comprises the various contributions from the evaluation of the δ-distributions in Eq. (4.40). The function $f_\alpha(\omega_i, p_j, x, \nu, k, h, \mu_\uparrow)$ contains the checks of the step functions as mentioned above and the $q_{\downarrow/\phi/\uparrow}$ denote the magnitude of momenta for which the propagators appearing in the loop have to be evaluated.

In the numerical algorithm a number of about $\mathcal{O}(10^3 - 10^4)$ couplings is necessary to reach the desired numerical accuracy. We find that the numerical cost of a direct computation of the frequency integration is much too large so that we need a different approach to cope with this. As a way out, we find that the computational speed can be greatly enhanced by mapping the numerical integration onto an *analytical* integration using the spline polynomials in the interval $(-\omega_{\max}, \omega_{\max})$. In order to do this we are forced to perform the frequency integration *before* the angular x-integration. As mentioned above, $\omega_{\max}$ is chosen such that the error in the ω integration of the outer regime $\omega > \omega_{\max}$ introduced due to the approximation (4.39) is smaller than the accuracy of the numerical solution of the system of differential equations (4.12). Since the analytical form of $P_\uparrow$ is known the frequency ν-integration can be greatly simplified. It requires then only the evaluation of a sum of terms of the form

$$\sim \int_{\omega_i}^{\omega_{i+1}} d\omega \frac{1}{a + b\omega + c\omega^2 + d\omega^3} \frac{1}{e + f\omega} \tag{4.43}$$

which can be done analytically. The computation involves the finding of roots ω_n of cubic polynomials which is not only numerically stable but also fast. For the final angular integration in $x = \cos\theta$ on the right-hand side of the flow equation (4.42) we use a numerical integration with adaptive nodes in order to cope with discontinuities of the integrand.

At this stage, let us summarize the algorithm which is executed at each RG step at scale k:

- Input: $P^{ij}_{\phi,\downarrow}$ at scale k.
  For each external ω_i, p_j, do
  1. Evaluate the q-integration in Eq. (4.40) by appropriate replacements of q
  2. Perform numerical angular x integration with adaptive stepsize by evaluating
     a) Compute the complex coefficients $a - f$ in Eq. (4.43) for each ω_i-interval
     b) Perform the (inner) ω-frequency integration from $-\omega_{\max}$ to $\omega_{\max}$

c) Perform the (outer) frequency integrations $(-\infty, -\omega_{\max})$ and $(\omega_{\max}, \infty)$

3. Check precision of x-integration.

- Output: $\partial_k P^{ij}_{\phi,\downarrow}$ at scale k.

The system of ordinary differential equations for $P^{ij}_{\phi,\downarrow}$ is straightforwardly solved using a Runge-Kutta algorithm, which we have implemented in a version with adaptive stepsize in RG time $t = \ln(k/\Lambda)$. An adaptive stepsize is essential in order to detect the kinks in the RG flow of the $\downarrow$-propagator due to the sharp Fermi surface of the $\uparrow$-fermions at zero temperature. The values k where these kinks appear are dependent on the external momenta p_j. They appear due to the sharp regulator as well as the pole structure of the integrand of $\partial_k P_\downarrow$ in the complex frequency plane. For example for zero external momentum, the flow of $\partial_k P_\downarrow$ remains identically zero down to the scale $k/k_F = 1/\sqrt{2}$. If fact, until the scale $k = k_F$ is reached only the molecule flows and thus $P_{\phi,k}$ at this scale is equivalent to the result of a leading order $1/N$ expansion in presence of a sharp infrared regulator for modes $p > k$. Finally, we observe that about 10^4 adaptive RG steps are necessary to obtain an error smaller than $\epsilon \sim 10^{-5}$.

The algorithm is started at the UV scale $k = \Lambda$, where the initial condition is specified. It is determined by the few-body calculation (4.26). As we employ no approximation for the momentum and frequency dependence of the molecule propagator we are able to incorporate the *exact* two-body scattering amplitude (4.24). This is in contrast to the calculation in the previous Section using the derivative expansion where this is not possible. The vacuum problem can be solved exactly using the sharp regulators (4.16), which leads to the UV molecule propagator

$$P_{\phi,\Lambda}(\omega, \mathbf{p}) = -\frac{h^2}{8\pi a} + \frac{h^2\Lambda}{4\pi^2} - \frac{h^2}{2}\int_{\boldsymbol{q}} \left[\frac{\theta(|\boldsymbol{q} - \frac{\mathbf{p}}{2}| - \Lambda)\,\theta(|\boldsymbol{q} + \frac{\mathbf{p}}{2}| - \Lambda)}{q^2 + (-\frac{i\omega}{2} + \frac{\mathbf{p}^2}{4} - \mu_{\text{vac}})} - \frac{\theta(q - \Lambda)}{q^2} \right], \quad (4.44)$$

which is evaluated numerically at the beginning of the RG flow.

In Figs. 4.10 and 4.11 we show an exemplary flow of the molecular, inverse propagator from the UV scale to the IR scale at $k = 0$. One observes that the inverse euclidean propagators are perfectly smooth in frequency and momentum which is essential for the applicability of our spline algorithm. The drawback of working in the imaginary frequency domain is, however, that we have to perform the *numerical* continuation to real frequencies at the end of the flow.

The flow of the dimer in Fig. 4.10 nicely illustrates some basic properties of the RG flow. At the UV scale one starts with the classical action (the bare Hamiltonian) where we deal with a short-range interaction. As we see from Fig. 4.10(a), the dimer propagator is flat in momentum space which reflects that one deals with a contact interaction. Indeed, were we to integrate out the dimer field ϕ in Eq. (4.5) we would find that the resulting term $(\Psi^\dagger\Psi)^2$ is proportional to $h^2/P_{\phi,\Lambda}$ which becomes momentum independent as $\Lambda \to \infty$ (and thus the effective range goes to zero). Note, within a derivative expansion one only follows the flow of

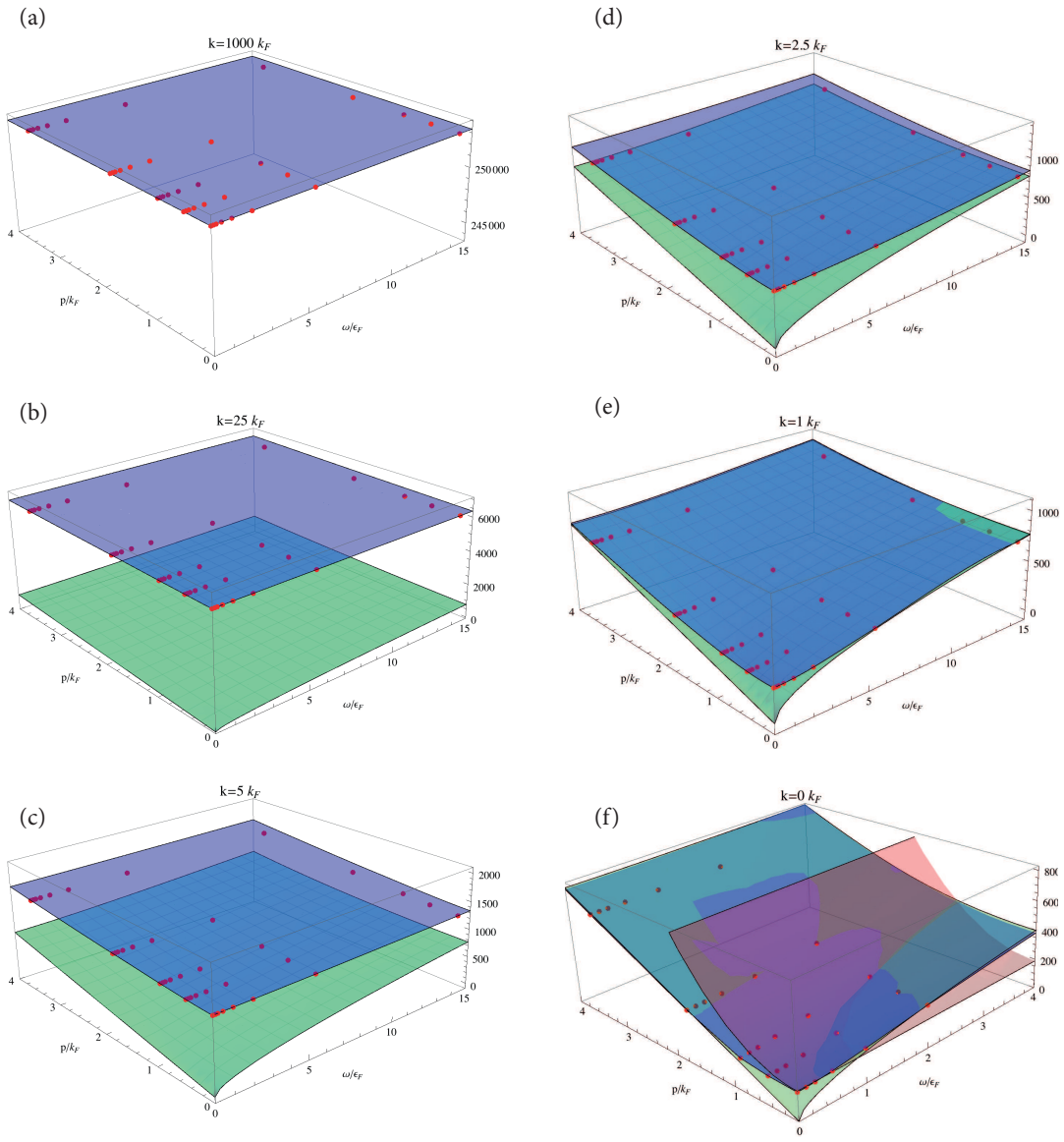

FIGURE 4.10: *Renormalization group flow of the real part of the euclidean, inverse molecule propagator $P_\phi(\omega, \mathbf{p})$ with RG scale k (blue surface) for unitary interactions. The red dots are the actual data computed with our new renormalization group algorithm. In green the exact infrared vacuum solution is shown. Note the different scale in the z-axis for the various figures. In red the result of the derivative expansion in the infrared is shown.*

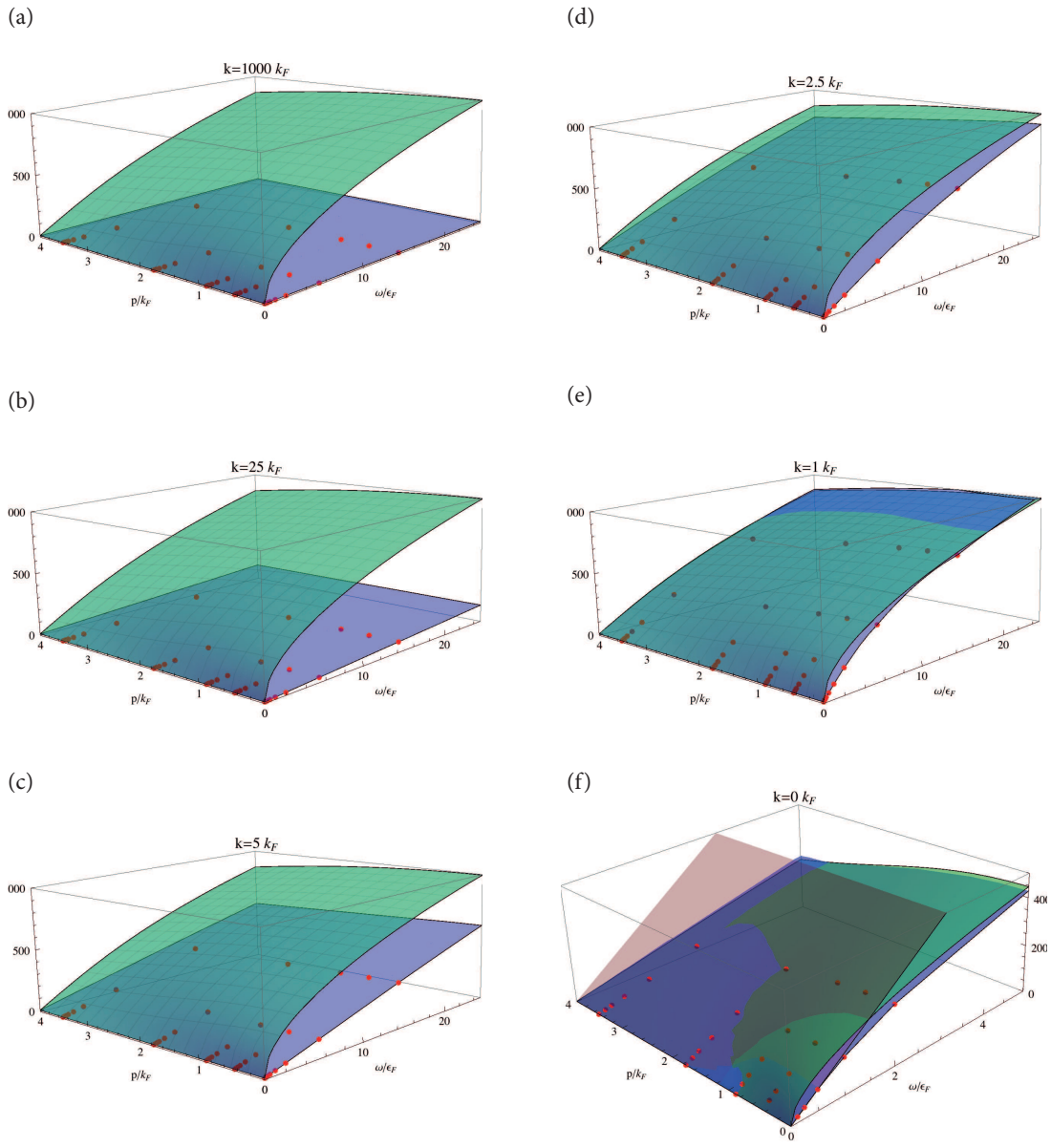

FIGURE 4.11: *Renormalization group flow of the imaginary part of the euclidean, inverse molecule propagator $P_\phi(\omega, \mathbf{p})$ with RG scale k (blue surface) for unitary interactions. The red dots are the actual data computed with our new renormalization group algorithm. In green the exact infrared vacuum solution is shown. In red the result of the derivative expansion in the infrared is shown.*

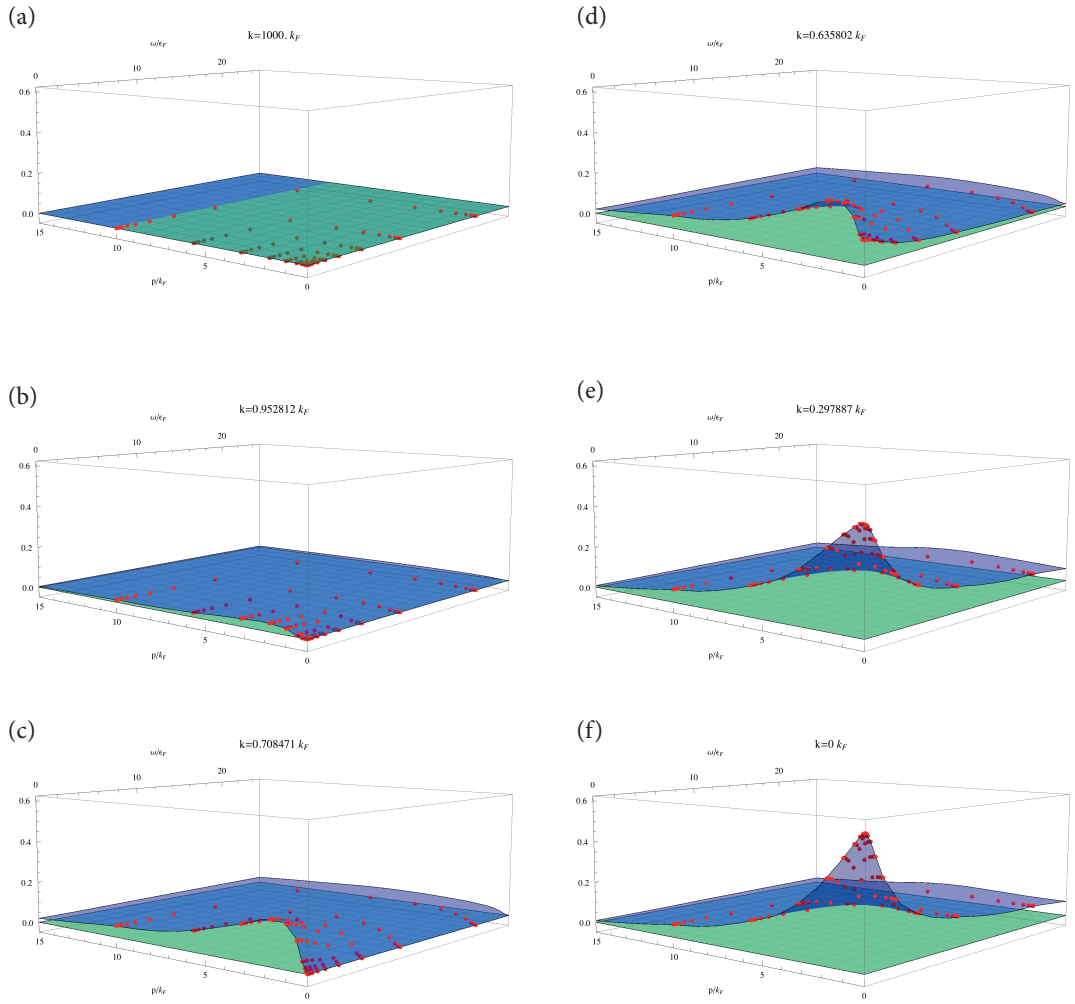

FIGURE 4.12: *Renormalization group flow of the real part of the self-energy* $\Sigma_{\downarrow}(\omega, \mathbf{p})$ *of the euclidean, inverse impurity propagator* $P_{\downarrow}(\omega, \mathbf{p})$ *with RG scale k (blue surface) for unitary interactions. The red dots are the actual data computed with our new renormalization group algorithm.*

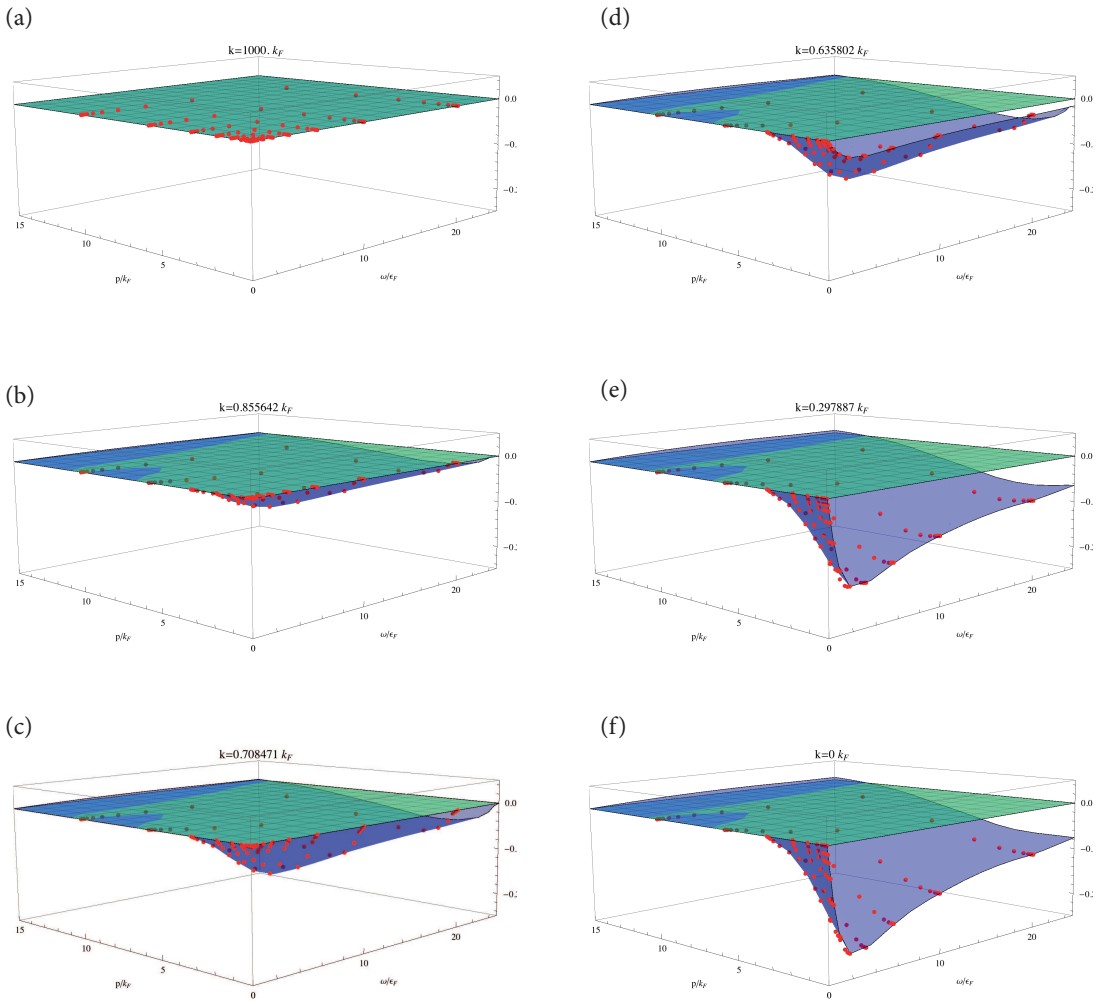

FIGURE 4.13: *Renormalization group flow of the imaginary part of the self-energy* $\Sigma_\downarrow(\omega, \mathbf{p})$ *of the euclidean, inverse impurity propagator* $P_\downarrow(\omega, \mathbf{p})$ *with RG scale k (blue surface) for unitary interactions. The red dots are the actual data computed with our new renormalization group algorithm.*

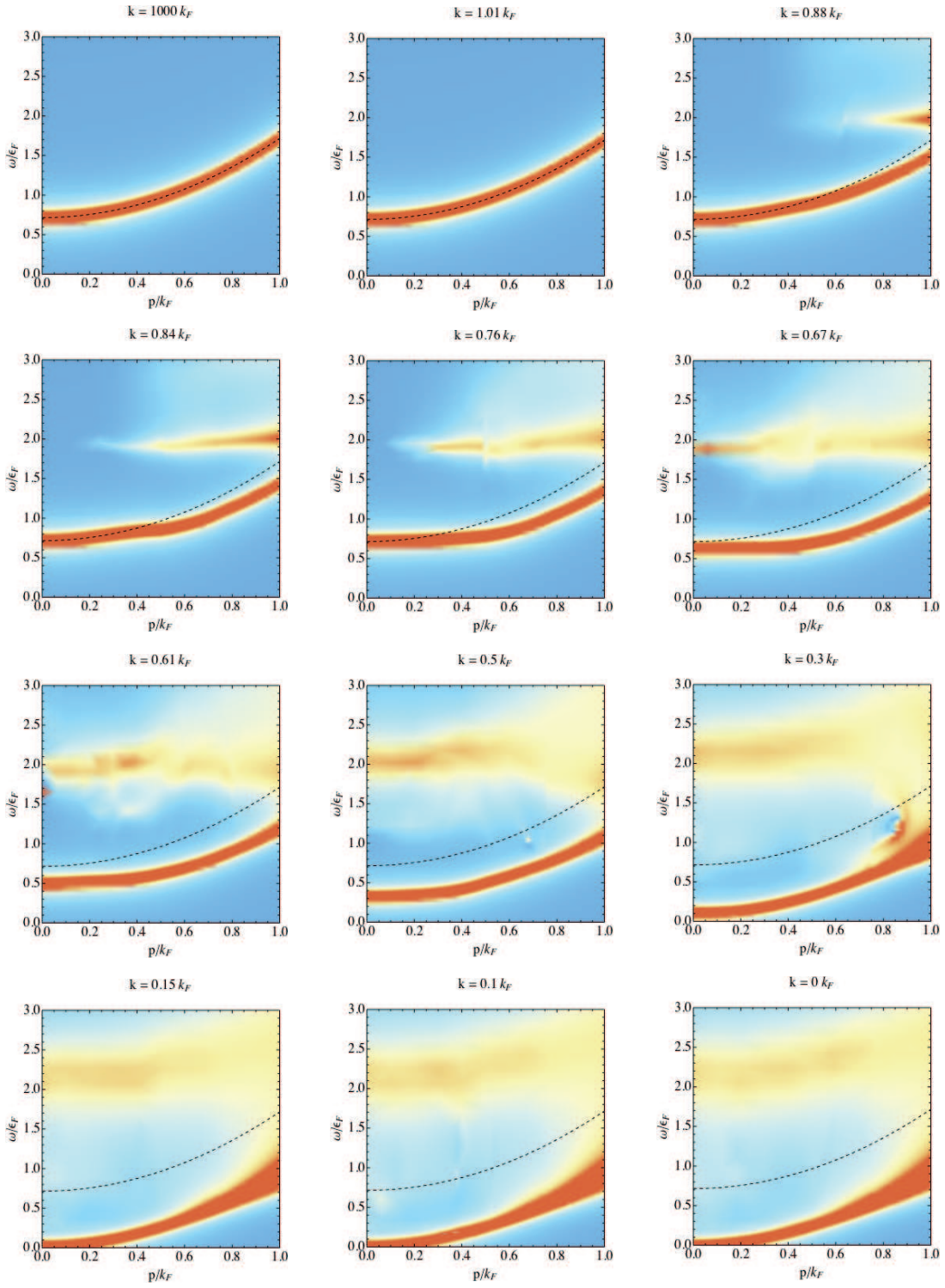

FIGURE 4.14: *Renormalization group flow of the spectral function of the impurity $A_\downarrow(\omega, \mathbf{p})$ with RG scale k from the UV (upper left) to the IR (down left) for unitary interactions. When the flow 'hits' the scale k_F spectral weight is transferred from the lower, attractive polaron branch to the upper, repulsive polaron branch. High momentum modes are renormalized first. In order to make the δ-function peak for the ground state visible we introduced an artificial width of the quasiparticles of* $0.03\,\epsilon_F$.

two couplings instead of the $\mathcal{O}(10^3)$ couplings employed here. Going to this complexity allows us to resolve the square root structure in Eq. (4.26), which is impossible within a derivative expansion. In Fig. 4.10(f) we also show the molecule propagator resulting from the derivative expansion where we subtracted an overall constant to allow for direct comparison. While it fits well in the low-energy region – as it should – it becomes completely wrong for high frequencies. In fact, at high frequencies one finds again the consequence of the anomaleous dimension of unity found in Chapter 2: the square root will always prevail at scales $|\omega|, \boldsymbol{p}^2 \gg k_F$.

In Figs. 4.12 and 4.13 we show the flow of the impurity self-energy. Note that it does not flow until the RG scale $k/k_F = 1$ is reached. Finally, when the flow reaches the infrared, $k = 0$, we end up with the full Matsubara Green's functions $G_{\downarrow,k=0}(\omega, p)$ and $G_{\phi,k=0}(\omega, p)$. The initial value of $\mu_\downarrow$ for a given $k_F a$ is adjusted such that a vanishing macroscopic occupation of $\downarrow$-atoms and molecules is obtained at the end of the flow, as discussed in Section 4.3. In order to access the spectral functions we perform the analytical continuation to real frequencies using a Padé approximation.

4.5 Full spectral functions

We now present the numerical results for the spectral functions of the polaron and molecule across the whole transition region. To clarify our notation we also recall the conventions of the definition of spectral properties which we will use in the following.

At the end of the RG flow, the Matsubara Green's functions $G_{\downarrow/\phi,k=0}(\omega, \mathbf{p})$, are continued analytically to retarded Green's functions $G_{\downarrow/\phi,\mathrm{R}}(\omega, \mathbf{p})$ of real frequency, using the Padé approximation. The spectral functions are defined as

$$A_{\downarrow/\phi}(\omega, \mathbf{p}) = 2\,\mathrm{Im} G_{\downarrow/\phi,\mathrm{R}}(\omega, \mathbf{p}). \tag{4.45}$$

As an example the spectral function $A_\downarrow(\omega, \mathbf{p})$ of the impurity at unitary is shown in Fig. 4.15.

The coherent single-particle excitations at zero momentum are determined by the solutions ω_{qp} of the equation

$$G^{-1}_{\downarrow/\phi,\mathrm{R}}(\omega, \mathbf{p} = 0)\Big|_{\omega=\omega_{\mathrm{qp}}} = 0 \tag{4.46}$$

for ω in the complex lower half-plane and we show the zero-momentum spectral functions $A_{\downarrow/\phi}(\omega, \mathbf{p} = 0)$ as functions of frequency and coupling $(k_F a)^{-1}$ in Fig. 4.16. Near each quasiparticle pole the retarded propagator can be approximated by the form

$$G_{\downarrow/\phi,\mathrm{R}}(\omega, \mathbf{p} = 0) \approx \frac{Z_{\downarrow/\phi}}{\omega_{\mathrm{qp}} - \omega - i0} \tag{4.47}$$

where the real part of ω_{qp} determines the quasiparticle energy

$$E_{\mathrm{qp}} = \mu_\downarrow + \mathrm{Re}[\omega_{\mathrm{qp}}]. \tag{4.48}$$

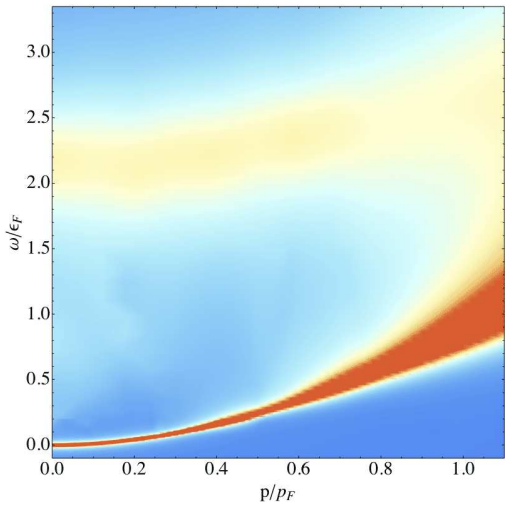

FIGURE 4.15: *Full momentum and frequency dependence of the polaron spectral function* $A_\downarrow(\omega, \mathbf{p})$ *at unitarity* $(k_F a)^{-1} = 0$. *In order to make the* δ*-function peak for the ground state visible we introduced an artificial width of the quasiparticles of* $0.007\,\epsilon_F$.

We have shifted the ground-state energy, which is zero in our calculation (vanishing gap), to the conventional value $\mu_\downarrow$ from Eq. (4.29). The imaginary part of the pole $\omega_{\rm qp}$ determines the decay width

$$\Gamma_{\rm qp} = -{\rm Im}[\omega_{\rm qp}]. \tag{4.49}$$

A Fourier transform in time relates the decay width to the quasiparticle lifetime

$$\tau_{\rm qp} = \hbar/\Gamma_{\rm qp}. \tag{4.50}$$

The quasiparticle weight $Z_{\downarrow/\phi}$ is obtained from the frequency slope at the complex pole position,

$$Z^{-1}_{\downarrow/\phi} = -\frac{\partial}{\partial\omega} G^{-1}_{\downarrow/\phi,{\rm R}}(\omega, \mathbf{p}=0)\Big|_{\omega=\omega_{\rm qp}}. \tag{4.51}$$

Note that an alternative definition of the decay width, often used in literature, see e.g. [258], has to be treated with care. It is defined in terms of the self-energy evaluated not at the complex pole position but on the real frequency axis,

$$\Gamma_{\rm alt} = {\rm Im}\Sigma_{\downarrow/\phi,{\rm R}}(\omega, \mathbf{p}=0)\Big|_{\omega={\rm Re}[\omega_{\rm qp}]}, \tag{4.52}$$

and agrees with our definition for $\Gamma_{\rm qp}$ only for a single quasiparticle pole (4.47) with $Z = 1$. This is however not the generic case as demonstrated in the polaron problem where further excited states are present and $Z < 1$. Hence, only $\Gamma_{\rm qp}$ from Eq. (4.49) can be interpreted as the half-width of the peaks in the spectral function and as the inverse lifetime.

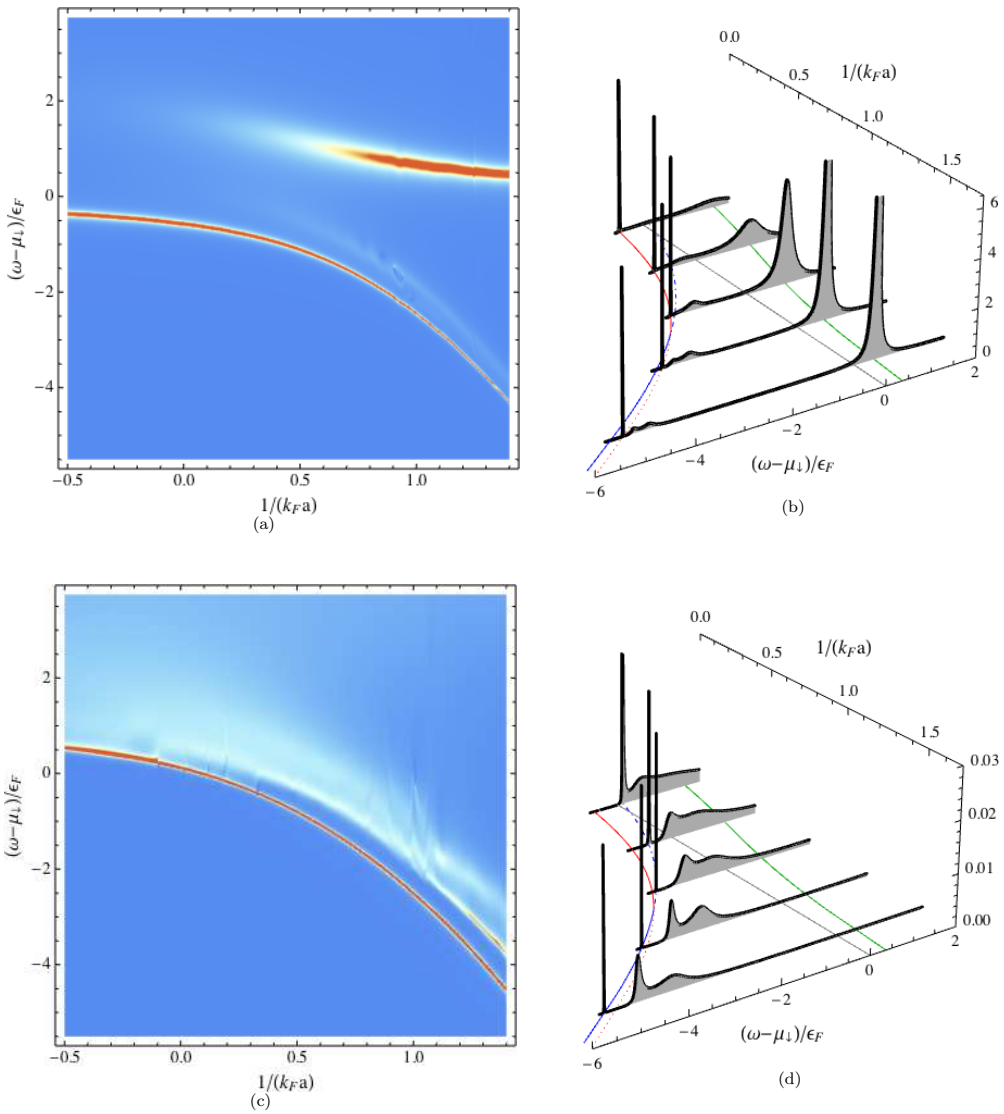

FIGURE 4.16: *Spectral functions at zero momentum in dependence on* $1/(k_F a)$. *(a), (b): Polaron spectral function* $A_\downarrow(\omega, \mathbf{p} = 0)$. *(c), (d): Molecule spectral functions* $A_\phi(\omega, \mathbf{p} = 0)$. *In order to make the* δ*-function peak for the ground state visible we introduced an artificial width of the quasiparticles of* $0.007\,\epsilon_F$.

We will now in turn discuss the features seen in the spectral functions: the peak position (E_{qp}), width (Γ_{qp}) and weight (Z), first for the polaron (upper row of Fig. 4.16) and then for the molecule (lower row of Fig. 4.16).

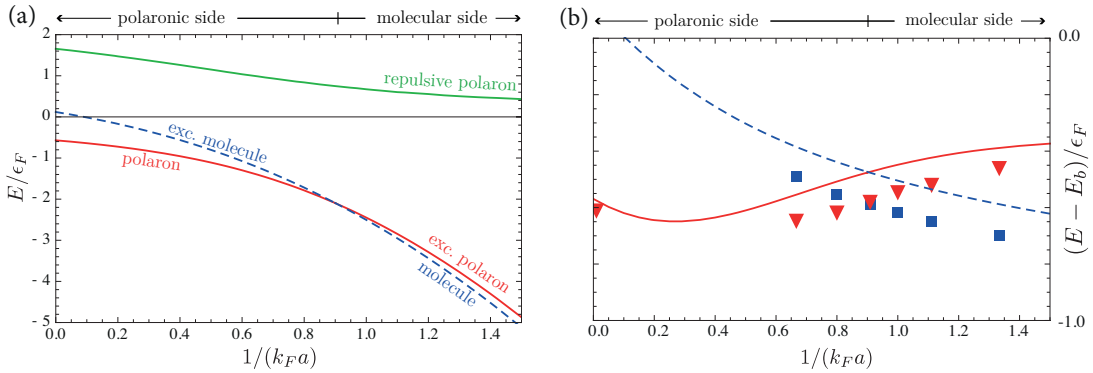

FIGURE 4.17: *(a) Energy spectrum of the single-particle excitations of the polaron-to-molecule transition. (b) fRG result for the ground-state energy (with the universal dimer binding energy $E_b = -\hbar^2/(ma^2)$ subtracted) in comparison to the results obtained with diagMC by Prokof'ev and Svistunov [59, 60] (symbols).*

Attractive and repulsive polaron

Energy spectrum. First, we analyze the energy spectrum of the quasiparticle excitations depicted in Fig. 4.17 in dependence on the coupling strength $(k_F a)^{-1}$. From our data we find two coherent quasiparticle states for the $\downarrow$-atom, the attractive and the repulsive polaron, and one bound state for the molecule. The attractive polaron (red solid line) is the ground state for $(k_F a)^{-1} < (k_F a_c)^{-1}$ (polaronic side) but becomes an excited state for $(k_F a)^{-1} > (k_F a_c)^{-1}$ (molecular side). Conversely, the molecule is the ground state on the molecular side (blue dashed line) and an excited state on the polaronic side, in accordance with the results using the derivative expansion in Section 4.3. For the critical coupling strength we obtain $(k_F a_c)^{-1} = 0.904(5)$, which agrees very well with the value $(k_F a_c)^{-1} = 0.90(2)$ obtained using diagrammatic Monte Carlo (diagMC) by Prokof'ev and Svistunov [59, 60]. At this point we already see, how the inclusion of the full frequency and momentum dependence significantly improves our results. This does not come as a surprise when considering the large discrepancy between the approximated propagators and the full result visible in Fig. 4.10(f) and 4.11(f). Also note that we expect the critical value $k_F a_c$ not to be a universal number. The value of $1/k_F a_c = 0.904$ is the result for a contact interaction and we expect it to be dependent on microscopic detail such as the width of the Feshbach resonance. Moreover, $k_F a_c$ changes with the mass ratio, cf. Appendix B.

As shown in Fig. 4.17(b), also the values for the energies agree well with diagMC (symbols). At unitarity, $(k_F a)^{-1} = 0$, we obtain the ground-state energy $\mu_\downarrow = -0.57\,\epsilon_F$ while diagMC gives the value $\mu_\downarrow = -0.615\,\epsilon_F$. Note that any non-analyticity in the energy spectrum across the transition has disappeared in contrast to the results from the derivative expansion, cf. Fig. 4.6. Having treated the full frequency and momentum dependence of the propagators in the truncation (4.10), we can attribute the major part of the residual deviation in the ground state energy to the omission of the terms $\psi^*_\uparrow \psi^*_\downarrow \psi_\downarrow \psi_\uparrow$ and $\phi^* \psi^*_\sigma \phi \psi_\sigma$. The latter term

describes the atom-dimer interaction and is expected to further reduce the ground-state energy in the transition regime in accordance with the results from the variational wave function approach [236, 237]. The term $\psi^*_\uparrow\psi^*_\downarrow\psi_\downarrow\psi_\uparrow$, generated by particle-hole fluctuations, is expected to give the main correction in the unitarity regime [234]. Both terms can be included in the fRG flow as additional flowing couplings, or implicitly by using the Katanin scheme [269] or rebosonization [219].

Until recently [49] most experiments with ultracold Fermi gases have focused on the lower, attractive branch on the BEC side $(k_F a)^{-1} > 0$. There exists, however, also the repulsive polaron branch (solid green line) which corresponds to a higher excited state of the $\downarrow$-atom interacting *repulsively* with the $\uparrow$-Fermi sea. Our results for the energy of the repulsive branch agree with the weak-coupling results [270] for $(k_F a)^{-1} \gtrsim 1$. In the strong-coupling regime our energies lie between the result from the non-selfconsistent T-matrix approach [258] and results for square well potentials numerically computed by Monte Carlo methods [242]. In the polaron spectral function, cf. Fig. 4.16(b), one can clearly discern the attractive polaron branch as a very sharp peak at low frequencies, and the much broader repulsive polaron branch at higher frequencies. In a recent experiment by the Innsbruck group using a mass-imbalanced mixture of ^{6}Li and ^{40}K fermions, the repulsive polaron in three dimensions has been measured for the first time [64]. The radio-frequency (rf) spectroscopy used in this experiments has been essential identical to the one proposed in our earlier theoretical work [62] which we discuss in Section 4.6. In Appendix B we will briefly comment on our results which predict the rf spectrum for the case of a mass-imbalanced mixture using a simple, leading order $1/N$ expansion.

Decay widths. The repulsive polaron has a large decay width Γ_{rep}, as calculated from Eq. (4.49) and depicted in Fig. 4.18(a), and correspondingly a short lifetime. The leading-order decay channel for the repulsive polaron is the process shown as tree-level diagram in Fig. 4.18(b, left) where the repulsive polaron, which is an excited state, decays to the attractive, and energetically lower lying, polaron due to the interaction with an $\uparrow$-atom. This diagram can be translated via the optical theorem into a contribution to the imaginary part of the $\downarrow$-atom self-energy, as depicted in Fig. 4.18(b, right). This self-energy diagram is already included in the non-selfconsistent T-matrix propagator $P^{\text{nsc}}_\downarrow$, and has been studied recently using this approximation [258]. Of course, this diagram is also included in our fRG approach. Note, that in the fRG approach also higher-order decay processes are included due to the constant feedback of the impurity self-energy into the flow of the molecular propagator.

In the weak-coupling limit $(k_F a)^{-1} \to \infty$ the excitation becomes sharp, $\Gamma_{\text{rep}} \to 0$, and the repulsive polaron is a well-defined quasiparticle. Towards unitarity, Γ_{rep} grows but remains a well-defined, finite quantity even at unitarity. We find that indeed Γ_{rep}, and not the approximation $\Gamma^{\text{alt}}_{\text{rep}}$ from Eq. (4.52), is the correct half-width at half-height of the respective peak in the polaron spectral function in Fig. 4.16(b). For $(k_F a)^{-1} < 0.6$ the energy E_{rep} of the repulsive branch exceeds the bath Fermi energy, $E_{\text{rep}} > \epsilon_F$. At this point it is energetically favorable to spin-flip or 'phase separate' the impurity atom, which can be interpreted as the

condition for the onset of saturated ferromagnetism [55, 243]. At the same time the decay width $\Gamma_{\text{rep}} > 0.2\,\epsilon_F$ is large, which destabilizes the transition to a ferromagnetic phase [50]. Note, that here we discuss a Nagaoka type problem [271] as discussed by Barth and Zwerger [55], while [50] deals with the balanced gas within a random phase approximation extended beyond the putative Stoner instability.

On the polaronic side $(k_F a)^{-1} < (k_F a_c)^{-1}$ the attractive polaron is the stable ground state with decay width $\Gamma_{\text{att}} = 0$, while on the molecular side it is an excited state with finite lifetime and decay width $\Gamma_{\text{att}} > 0$, cf. Fig. 4.19(a). This decay is much weaker and also qualitatively different from the repulsive channel. The attractive polaron can decay by a three-body recombination process as shown in Fig. 4.19(b, left). Via the optical theorem this process can be translated into a contribution to the $\downarrow$-atom self-energy as depicted in Fig. 4.19(b, right), plus an additional contribution with crossed lines. This decay channel has recently been studied using a phenomenological three-loop calculation [241]. The resulting finite lifetime cannot be seen in the non-selfconsistent T-matrix approximation, where the self-energy corrections of the $\downarrow$-atom – indicated by the inner white box $P_\downarrow$ – are *not* fed back into the T-matrix $\sim P_\phi^{-1}$ [233, 258]. In contrast to the non-selfconsistent T-matrix calculation, our fRG includes the full feedback of both the $\downarrow$ and ϕ self-energies, denoted by bold internal lines in the flow equations in Fig. 4.5. Therefore, the contributions from the decay diagram in Fig. 4.19(b), and many more, are automatically included in our approach.

Quasiparticle weights. Fig. 4.20 depicts the quasiparticle weights of the attractive and repulsive polaron computed using Eq. (4.51). On the polaronic side the attractive polaron state contains most of the weight, but as one moves towards the molecular side the spectral weight gradually shifts to the repulsive branch, and the corresponding peak in the polaron spectral function in Fig. 4.16(b) becomes larger. This can also nicely be seen from the flow of the impurity spectral function depicted in Fig. 4.14, where quasiparticle weight is transfered to the repulsive branch when the RG scale hits the scale given by the density, $k = k_F$. We find

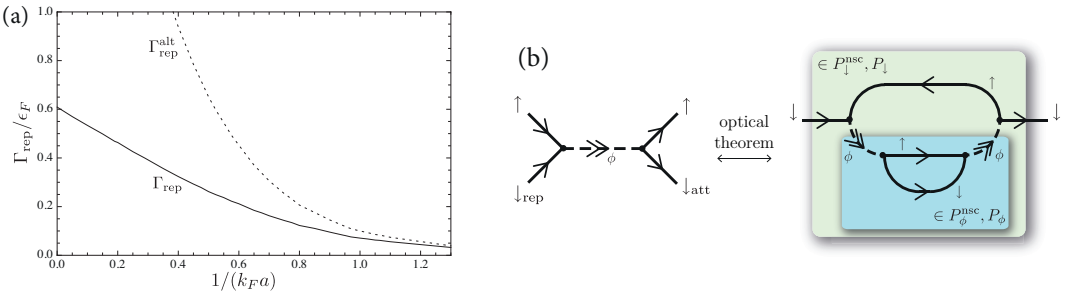

FIGURE 4.18: *(a) Decay width Γ_{rep} of the repulsive polaron as a function of the coupling $(k_F a)^{-1}$. We also show the width according to the approximate formula Eq.* (4.52) *(dotted line). (b) Decay channel for the repulsive polaron.* ***(left)*** *Two-body process which leads to the decay of the repulsive polaron.* ***(right)*** *Corresponding contribution to the $\downarrow$-atom self-energy via the optical theorem.*

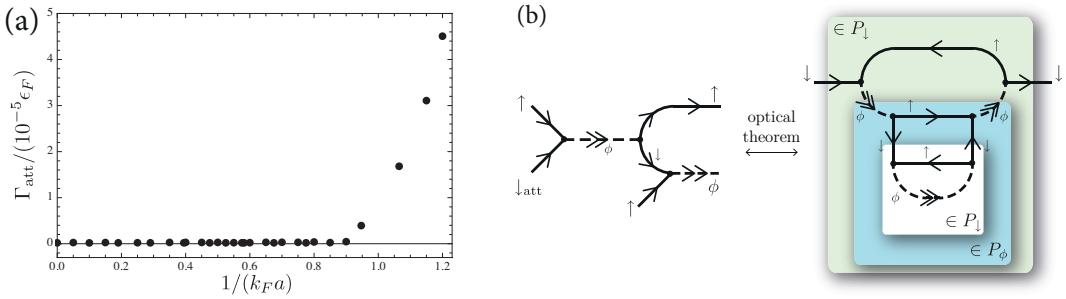

FIGURE 4.19: *(a) Decay width Γ_{att} of the attractive polaron as a function of the coupling $(k_F a)^{-1}$. (b) Decay channel for the attractive polaron.* ***(left)*** *Three-body recombination process which leads to the decay of the attractive polaron.* ***(right)*** *Corresponding contribution to the $\downarrow$-atom self-energy via the optical theorem (there is also a contribution with crossed lines).*

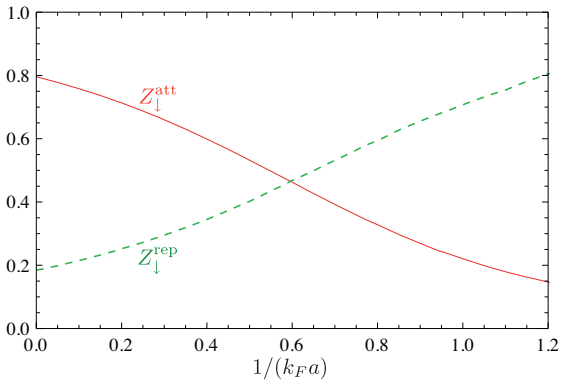

FIGURE 4.20: *Quasiparticle weight $Z_\downarrow$ of the attractive (solid line) and repulsive (dashed line) polaron. The weights of the two quasiparticle peaks in the $\downarrow$-spectral function make up almost completely the total spectral weight, and the contribution from the incoherent background is very small.*

that the attractive and repulsive branches almost completely make up the total spectral weight, hence the contribution from the incoherent background is very small. This is also apparent in the polaron spectral function in Fig. 4.16(b). Note that the contribution of the incoherent background is enhanced when considering a closed-channel dominated resonance (see also Appendix B).

Our results for the quasiparticle weights agree well with those from the non-selfconsistent T-matrix and variational wave-function approaches. At unitarity we obtain for the attractive polaron $Z_{\downarrow,\rm att} = 0.796$ compared to the variational value $Z_{\downarrow,\rm att} = 0.78$ [231, 256]. For the repulsive polaron at $(k_F a)^{-1} = 1$ we find $Z_{\downarrow,\rm rep} = 0.71$, in agreement with the recent non-selfconsistent T-matrix calculation [258].

Note that there is an alternative definition of the quasiparticle weight [256]

$$Z_{\downarrow}^{\mathrm{alt}} = \lim_{t\to\infty} \left| G_{\downarrow}(t, \mathbf{p}=0) \right|. \tag{4.53}$$

This definition has to be treated with care: on the molecular side of the transition the polaron acquires a finite decay width $\Gamma_{\downarrow} > 0$ but nonetheless continues to be a well-defined quasiparticle with finite spectral weight, as can be seen from Fig. 4.16. However, definition (4.53) yields zero as soon as $\Gamma_{\downarrow} > 0$ and in this case cannot be interpreted as a measure of spectral weight anymore. In contrast, the definition (4.51) remains correct for a finite decay width and accordingly our data for $Z_{\downarrow}$ shows no discontinuity at the transition. In the experiment the finite lifetime of the attractive polaron on the molecular side complicates the direct measurement of $Z_{\downarrow}$ by radio-frequency spectroscopy because the molecular state and not the attractive polaron becomes occupied as the initial state (cf. Section 4.6). Finally, note that all problems of extracting the quasiparticle properties have disappeared in our new approach compared to the derivative expansion.

Molecule

Energy spectrum. The molecule spectral function in Fig. 4.16(d) displays a sharp quasiparticle peak of the bound state at low frequencies, followed by an incoherent background at higher frequencies which actually carries most of the spectral weight. This background is neither taken into account in the simple derivative expansion discussed in the previous section nor in the Wilsonian RG approach [235] as for example popularized by Shankar [272]. On the molecular side $(k_F a)^{-1} > (k_F a_c)^{-1}$ the molecule is the ground state and is clearly separated from the incoherent continuum. On the polaronic side of the transition the molecule becomes an unstable, excited state and develops a clearly visible finite decay width in the spectral function.

Decay widths. The leading decay channel of the excited molecule state is via the three-body recombination process shown in Fig. 4.21(a, left). Via the optical theorem this process can be translated into a contribution to the molecule self-energy as depicted in Fig. 4.21(a, right). Similarly to the attractive polaron, in the non-selfconsistent T-matrix approximation the $\downarrow$-atom self-energy corrections in $P_{\downarrow}$ are *not* fed back into the T-matrix $\sim P_{\phi}^{-1}$, and the molecule does not decay in the vicinity of the polaron-to-molecule transition. In contrast, the diagram Fig. 4.19(b, right) is included in the fRG, which leads to the visible broadening in the spectral function.

Ref. [241] shows, by an analytical calculation of the phase space for three-loop diagrams of the type in Fig. 4.21(a), that the decay width of the molecule scales as

$$\Gamma_{\phi} \propto \Delta\omega^{9/2} \qquad\qquad \Delta\omega = E_{\phi} - E_{\downarrow,\mathrm{att}} \tag{4.54}$$

where $\Delta\omega$ is the difference between the energy levels of the excited molecule and the attractive polaron ground state. In Fig. 4.21(b) we show Γ_{ϕ} as a function of $\Delta\omega$ in a double logarithmic

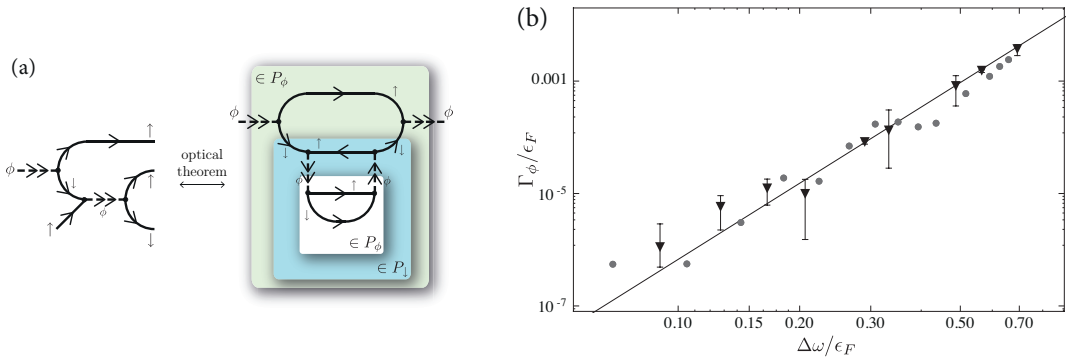

FIGURE 4.21: *(a) Leading decay channel for the excited molecular state.* ***(left)*** *Three-body recombination process which leads to the decay of the molecular state.* ***(right)*** *Corresponding contribution to the molecule self-energy via the optical theorem (there is also a contribution with crossed lines). (b) The decay width Γ_ϕ of the excited molecular state as a function of the energy difference $\Delta\omega = E_\phi - E_{\downarrow,att}$ between the excited molecule and attractive polaron ground state. The solid line indicates the power-law scaling $\Gamma_\phi \propto \Delta\omega^{9/2}$.*

plot. The large fluctuations of our numerical data are due to the accuracy of the Runge-Kutta integration as well as due to the restriction to a finite number of Matsubara frequencies. We have estimated the corresponding error by comparing the results for different grids with varying number and position of (Matsubara) frequencies. The solid line in Fig. 4.21(b) indicates the power law $\Delta\omega^{9/2}$. The triangles in Fig. 4.21(b) correspond to a calculation with a higher number of frequency grid points and we find convergence to the solid curve for decay widths larger than our numerical integration accuracy $\epsilon = 10^{-5}$. This indicates that the error for larger Γ_ϕ can be attributed to the Padé approximation, while for $\Gamma_\phi < \epsilon$ the accuracy of our results becomes limited by the absolute error of our numerical integration. Specifically, we find

$$\frac{\Gamma_\phi}{\epsilon_F} \approx 0.021 \left(\frac{\Delta\omega}{\epsilon_F}\right)^{9/2}. \tag{4.55}$$

With our fRG calculation we are thus able to verify the prediction by Bruun and Massignan [241] now from a microscopic calculation. The correctness of the power law attests to the strength of our method to describe many features of the polaron-to-molecule transition in one unified approach.

Quasiparticle weight and compositeness. The quasiparticle weight Z_ϕ of the molecular bound state in the spectral function in Fig. 4.16(d) is very small, $Z_\phi \approx 0.002$ at unitarity, and increases slowly towards the molecular limit, see Fig. 4.22(inset). For open-channel dominated resonances, $h^2 \sim \Delta B \to \infty$, the two-channel model (4.5) is equivalent to the single-channel, zero-range model (4.4) and $Z_\phi \equiv 0$ [260]. Specifically, we obtain for the weight of the bound

state in vacuum

$$Z_\phi = \frac{32\pi}{h^2 a} \qquad \text{(vacuum, } \Lambda \to \infty\text{)}. \tag{4.56}$$

This is consistent with the interpretation of Z_ϕ as the closed-channel admixture (cf. Eq. (29) in [6]). In our calculation we set the physical UV cutoff scale to $\Lambda = 10^3 k_F$, which is of the order of the inverse Bohr radius, and choose $h^2 < \infty$. We observe $Z_\phi \propto 1/k_F a$ on the BEC side and a deviation from the vacuum scaling close to unitarity, which may be due to a combination of finite density corrections and the admixture of closed-channel molecules in the microscopic action by choosing finite values of h and Λ. Starting from the two-channel model (2.23) in Chapter 2 we find that $Z_\phi \to 1$ for $a \to 0^+$.

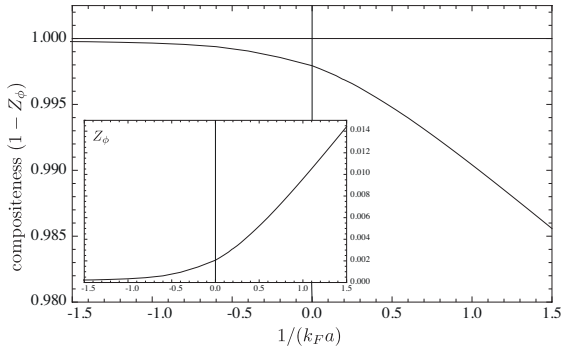

FIGURE 4.22: *Compositeness* $(1 - Z_\phi)$ *of the molecular bound state. A value of* 100% *would indicate that the molecule has no overlap with elementary closed-channel bosons. Inset: Molecular residue* Z_ϕ.

The quasiparticle weight Z can be interpreted as the overlap between the 'true' particles and the 'elementary', or bare, particles in the microscopic action (4.5). The attractive Fermi polaron becomes elementary, $Z_{\downarrow,\text{att}} \to 1$, in the BCS limit ($k_F a \to 0^-$), while in the opposite limit of $k_F a \to 0^+$ the repulsive Fermi polaron becomes elementary, $Z_{\downarrow,\text{rep}} \to 1$. Near unitarity, both excitations have a sizable weight. In contrast, the molecular bound state is almost exclusively a composite particle in the whole transition region. Indeed, the deviation of the quasiparticle weight from unity, $1 - Z_\phi$, is a well-established measure of compositeness in nuclear physics [273], and in Fig. 4.22 we show that for our choice of the Yukawa coupling h the compositeness of the molecule is very large ($> 98\%$). This is consistent with the measurement of a small molecular weight Z_ϕ for a balanced ^{6}Li Fermi gas close to a open-channel dominated Feshbach resonance by Partridge *et al.* [274]. In experiments with a closed-channel dominated Feshbach resonance the compositeness will decrease in particular away from resonance and a single-channel description becomes invalid. This has recently been verified by the Innsbruck experiment using a mass-imbalanced Fermi gas [64].

In the vacuum there exists no molecular state for negative scattering length a as can easily be seen from Eq. (4.26), which then has no bound-state pole. In the presence of a medium of

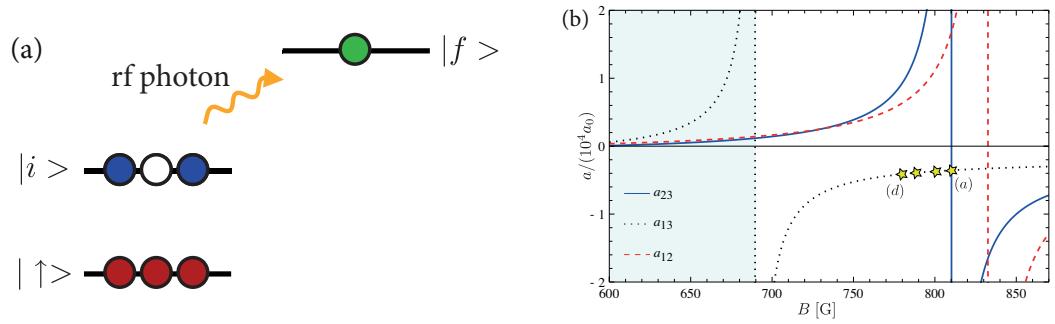

FIGURE 4.23: *(a) Radio frequency spectroscopy. Using rf photons atoms in a hyperfine state $|i>$ are driven to a final state $|f>$, while the second species in the initial mixture, $|\uparrow>$, is unaffected. (b) Scattering length profile of ^{6}Li atoms in the three lowest hyperfine states as calculated by P. S. Julienne based on the model described in [275]. The stars indicate the magnetic field values for which we determine the rf-response of the imbalanced Fermi gas in Fig. 4.24.*

$\uparrow$-fermions, however, the molecule propagator develops an excited bound-state pole also for negative scattering length a. This bound state will become the superfluid ground state when the impurity density exceeds a critical threshold [256].

4.6 *Rf-response of the ^{6}Li Fermi gas*

As a final application we connect our results for the polaronic spectral function to experimentally observable radio-frequency (rf) spectra. The attractive branch of the polaron-to-molecule transition has been studied experimentally by Schirotzek *et al.* [240] using a population imbalanced, two-component mixture of ^{6}Li atoms. In the experiment the rf-response of the system has been used to infer information about the low-frequency behavior of the fermionic spectral functions. For instance, the ground-state energy and the residue $Z_\downarrow$ of the $\downarrow$-fermions were measured and confirmed the theoretical predictions.

In order to measure the rf-response, an rf-pulse is applied to the system which drives the transition of the atoms to a third, initially empty state, cf. Fig. 4.23(a). In Fig. 4.23(b) we show the scattering length profile of ^{6}Li versus the magnetic field. In the experiment [240] a mixture of fermions initially in the hyperfine states $|1\rangle$ and $|3\rangle$ had been prepared in a range of the external magnetic field $B = 630\ldots690\,\mathrm{G}$ (shaded area). In this regime the scattering length a_{13} in the initial state is large and positive, while the final state scattering lengths a_{12}, a_{23} are rather small.

Information about the spectral function can be accessed from rf-spectroscopy, for example by populating the particle under investigation up to the energies one is interested in. Then one drives the transition to a weakly interacting final state for which the spectral function is well-known. This route had been taken for the study of the attractive polaron. For the repulsive polaron branch, on the other hand the protocol has to be different. The main complication is that the repulsive polaron has a very short lifetime in the strong-coupling regime of interest

[cf. Fig. 4.18(a)]. Hence, its macroscopic population is inhibited on longer time scales, and even after a fast ramp to the desired magnetic field most minority atoms may have decayed into the respective ground state. A similar situation arises in the detection of Efimov trimers in a three-component mixture of ^{6}Li atoms [141, 142]. The decay of the repulsive branch is also of relevance for the balanced system and the competition between ferromagnetic order and molecule formation [49, 50].

In this section we propose an experimental procedure to circumvent these difficulties and directly analyze the spectral function of the repulsive polaron. This protocol has by now been implemented successfully by the Innsbruck group for a mixture of ^{6}Li and ^{40}K atoms [64]. It led to the first observation of the repulsive polaron in three dimensions. Here, we focus on a prescription for the detection of the repulsive polaron in a strongly imbalanced two-component ^{6}Li Fermi gas, which we have put forward [62] prior to the observation [64]. The ^{6}Li Fermi gas is prepared in hyperfine states $|1\rangle$ and $|3\rangle$ for magnetic fields $B > 690\,\mathrm{G}$ across the (1,3) Feshbach resonance. In this regime the initial scattering length is negative, $a_{13} < 0$. One then drives an rf-transition to the final state $|2\rangle$ which is characterized by large, positive scattering lengths a_{12} and a_{23} and thus strong interactions. Because the attractive polaron spectral function of the initial state, with its negative scattering length a_{13}, is well understood both experimentally and theoretically, the final-state spectral function can then be analyzed in a controlled fashion.

Within linear response theory the induced transition rate from the initial state $|i\rangle$ to the final state $|f\rangle$ is given by [256, 255, 268]

$$I(\omega_L) = 2\Omega^2 \mathrm{Im}\chi_{\mathrm{R}}(\mu_f - \mu_i - \omega_L) \tag{4.57}$$

where the Rabi frequency Ω is given by the coupling strength of the rf-photon to the atomic transition, μ_i (μ_f) the initial (final) state chemical potential, and ω_L denotes the rf-frequency offset with respect to the free rf-transition frequency. Neglecting the momentum of the rf-photon, the retarded rf-susceptibility χ_{R} is given by the analytical continuation to real frequencies of the correlation function in imaginary time τ (Matsubara frequency ω)

$$\chi(\omega) = -\int_{\mathbf{r}}\int_{\mathbf{r}'}\int_{\tau} e^{i\omega\tau}\langle T_\tau \psi_f^\dagger(\boldsymbol{r},\tau)\psi_i(\boldsymbol{r},\tau)\psi_i^\dagger(\boldsymbol{r}',0)\psi_f(\boldsymbol{r}',0)\rangle, \tag{4.58}$$

where T_τ is the imaginary time-ordering operator. Eq. (4.58) leads to various diagrammatic contributions which are in general difficult to handle if the final-state interactions are not negligible [263]. Here we will evaluate Eq. (4.58) in a simple approximation with full Green's functions but without vertex corrections. In this approximation Eq. (4.58) yields the susceptibility in Matsubara frequency

$$\chi(\omega) = \int_{\boldsymbol{k},\nu} G_i(\boldsymbol{k},\nu)\, G_f(\boldsymbol{k},\nu+\omega). \tag{4.59}$$

The rf-response in real frequency is then given by

$$I(\omega_L) = \Omega^2 \int_{\boldsymbol{k}}\int_0^{\mu_i-\mu_f+\omega_L} \frac{d\nu}{2\pi} A_f(\boldsymbol{k},\nu)\, A_i(\boldsymbol{k},\nu+\mu_f-\mu_i-\omega_L) \tag{4.60}$$

	B field [G]	$(k_F a_{13})^{-1}$	$(k_F a_{23})^{-1}$	$(k_F a_{12})^{-1}$
(a)	810.3	-1.88	0.0	0.39
(b)	800.8	-1.80	0.2	0.58
(c)	788.2	-1.70	0.5	0.86
(d)	780.6	-1.62	0.7	1.04

TABLE 4.2: *Interaction parameters at the four transitions indicated in Fig. 4.23(b), using* $k_{F\uparrow} = 0.00015\, a_0^{-1}$.

where $\mu_i - \mu_f + \omega_L > 0$.

In Eq. (4.60) the initial-state spectral function A_i is probed for negative frequencies only. Hence, there is no rf-response for the pure polaron problem at vanishing density and chemical potential $\mu_\downarrow^{(0)}$. In the experiment one has, however, a small but finite concentration $x = n_\downarrow/n_\uparrow$ of $\downarrow$-fermions which leads to an observable rf-response. In order to describe the experimental situation we therefore need a calculation for a finite minority ($\downarrow$) density characterized by a chemical potential $\mu_i = \mu_\downarrow > \mu_\downarrow^{(0)}$. Within the fRG framework such a calculation requires the regulator $R_\downarrow$ in Eq. (4.16) to be adjusted in order to cope with the finite Fermi surface of $\downarrow$-fermions which complicates the computation. Fortunately, our calculation for the polaron problem shows that for negative scattering length, where the polaron is the ground state and decay processes do not matter, the fRG results are in excellent agreement with the results from a non-selfconsistent T-matrix approach. We may therefore use the T-matrix approach instead of a full-feedback fRG for the calculation of the imbalanced Fermi gas of finite densities $n_\uparrow$ and $n_\downarrow$ in order to determine the initial-state spectral function. The non-selfconsistent calculation was also done by Punk and Zwerger [268] and is obtained in our fRG formulation by simply switching off the feedback of the $\downarrow$-atom self-energy into the molecule flow.

Because the occupation of $\downarrow$-atoms is small, only the low-momentum modes are relevant. The $\downarrow$-atoms form a degenerate Fermi gas of polaronic quasiparticles and the spectral function can be approximated by [232]

$$A_i(\omega, \mathbf{p}) = 2\pi Z_i\, \delta\Big(\omega - \frac{\mathbf{p}^2}{2m_\downarrow^*} + \Delta\Big), \tag{4.61}$$

where Z_i is the residue, $m_\downarrow^*$ the effective mass of the impurity atoms, and Δ determines the impurity concentration x.

We have calculated the parameters $m_\downarrow^*$, Z_i, and Δ as functions of $(k_F a)^{-1}$ via the non-feedback (non-selfconsistent T-matrix) calculation. μ_i is determined self-consistently to ensure the correct impurity density. Inserting the spectral function Eq. (4.61) into the susceptibility (4.60) we obtain for the rf-response

$$I(\omega_L) = \frac{\Omega^2 Z_i}{2\pi^2} \int_0^{\sqrt{2m_\downarrow^*\Delta}} d\boldsymbol{k}\boldsymbol{k}^2\, A_f\Big(\boldsymbol{k}, \mu_i - \mu_f + \omega_L - \Delta + \frac{\boldsymbol{k}^2}{2m_\downarrow^*}\Big). \tag{4.62}$$

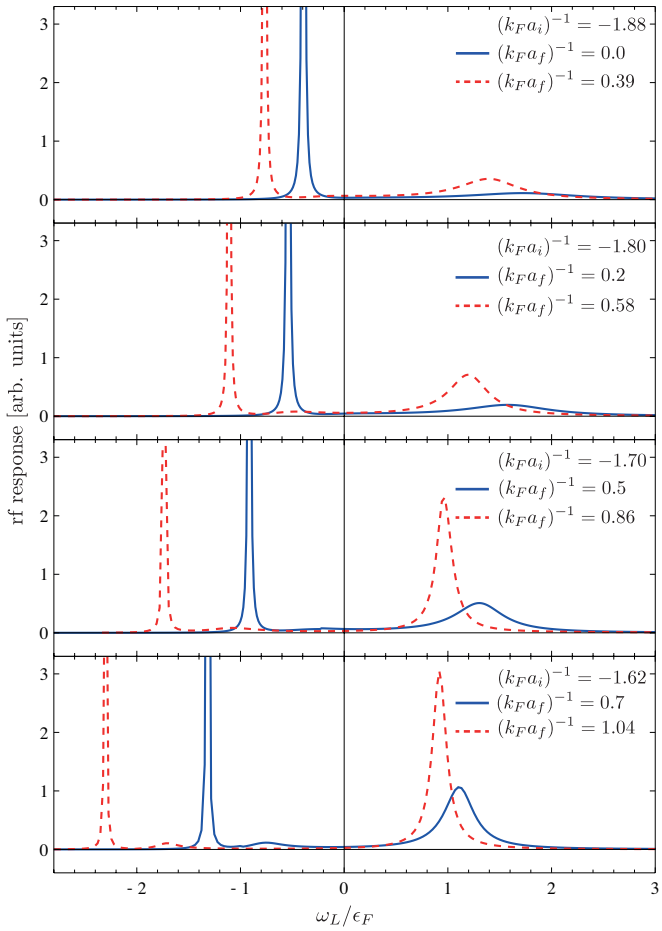

FIGURE 4.24: *Rf-spectra $I(\omega_L)$ for minority species $|1\rangle$ (solid blue lines) and minority species $|3\rangle$ (dashed red lines). The interaction parameters correspond to the four magnetic field values marked in Fig. 4.23(b), and listed in Table 4.2: (a) top—(d) bottom.*

For the final state $|f\rangle$ we use the spectral function obtained in Section 4.5 from the full fRG calculation. In Fig. 4.15 we show an example of the full final-state spectral function in dependence of frequency and momentum which enters the momentum sum in Eq. (4.62). One can clearly discern the broadening of the attractive polaron branch at larger momenta, as well as the broad repulsive branch at higher frequencies. A similar feature appears in the spectral function for the balanced Fermi gas above T_c as calculated by Haussmann *et al.* [255]. In this work the fermionic spectral function and rf-spectra were determined using a state-of-the-art *self-consistent* T-matrix (2PI) calculation and forms the basis for a full linear response calculation of transport coefficients like the spin diffusion [276] and shear viscosity including vertex corrections [110].

Initially, the gas is prepared in a $|1\rangle$ and $|3\rangle$ mixture, and both states can serve as minority

or majority species, for example, $|\uparrow\rangle = |3\rangle$ and $|\downarrow\rangle = |1\rangle$ such that $|i\rangle = |1\rangle$ and $|f\rangle = |2\rangle$. The initial occupation of the minority $|\downarrow\rangle$ states is small and for our numerical calculation we use $x = n_\downarrow/n_\uparrow = 0.01$. The energy scale is set by the Fermi momentum of the majority species $k_{F\uparrow} = 0.00015\, a_0^{-1}$ as appropriate for the MIT experiment [240]. We calculate the rf-spectra at four values of the magnetic field indicated as stars in Fig. 4.23(b), and listed in Table 4.2. The resulting spectra are shown in Fig. 4.24: the solid blue lines indicate the response for minority species $|1\rangle$, while the dashed red lines correspond to minority species $|3\rangle$. In the latter case the sign of the frequency offset ω_L is changed because the state $|3\rangle$ is energetically above the final state.

The position of the sharp attractive polaron peak at negative frequency offset ω_L shifts with the interaction parameter $(k_F a_f)^{-1}$ in accordance with the energy spectrum in Fig. 4.17. One observes that the attractive polaron looses quasiparticle weight on the molecular side, cf. Fig. 4.20. In contrast, the repulsive polaron branch gains quasiparticle weight towards the molecular side, and the respective peak in the rf-spectra becomes both larger and narrower, and one can read off the increasing lifetime.

The spectra in Fig. 4.24 are convolved with a sinc function $\mathrm{sinc}^2(\omega T/2)$ which gives the response to an rf-pulse with a rectangular profile of length $T = 20\,\mathrm{ms}$ [255]. While our curves are computed for zero temperature, a finite temperature $\sim 0.01\, T_F$ would lead only to a slight broadening of the experimental rf-peaks. The broadening of the attractive polaron due to the finite lifetime on the molecular side $(k_F a_f)^{-1} > (k_F a_c)^{-1}$, however, is too small to be resolved. Note that we have included both final-state and initial-state interaction in our calculation: the knowledge of the spectral function for the initial state allows for a detailed study of the final-state spectral function.

4.7 Conclusion

We have presented a new computational method to solve the non-perturbative, exact renormalization group equation (4.6) and have demonstrated its efficiency for the Fermi polaron problem as a specific example. The inclusion of the full frequency and momentum dependence of the propagators opens up new perspectives to apply the functional renormalization group to problems where the detailed dynamics of the relevant degrees of freedom becomes important [277]. In particular, the method draws its strength from the possibility to successively bosonize further channels of the interaction via additional auxiliary fields (Hubbard-Stratonovich transformation) [179, 180, 181, 182]. In this way one can partially capture the complicated analytical structure of higher-order vertex functions $\Gamma^{(n)}$, including possible quasiparticle poles and branch cuts, as we have explicitely shown for the s-wave scattering channel in the polaron problem. In combination with the recently developed flowing rebosonization technique [219] our numerical method can be extended to also incorporate re-emerging vertices. Our approach complements a related proposal for bosons [278] and it is a first example where a 'full' solution of the fRG equations has been demonstrated for a problem involving fermions with the inclusion of their self-energy.

For the Fermi polaron problem we achieve a unified description of many dynamical ef-

fects beyond thermodynamics. We verify the non-trivial power-law scaling of decay rates [241] and determine the properties of the repulsive polaron with a method beyond the non-selfconsistent T-matrix approximation [243, 258]. This is of value in the ongoing debate about the possible occurrence of ferromagnetism in ultracold Fermi gases with short-range interactions [49, 50, 52, 55, 242, 243, 258]. The polaron problem sheds light on this question in the limit of strong population imbalance. For the repulsive polaron we find the critical interactions strength $k_F a = 1.57$ from our numerical data (Fig. 4.17). This is just the value when the energy of the repulsive polaron is above the Fermi energy ϵ_F, but due to the fast decay with $\Gamma_{\text{rep}}/\epsilon_F \approx \mathcal{O}(1)$ there is no real critical behavior here [55]. Going to a finite density of $\downarrow$-fermions is straightforward within the fRG and involves only a slight modification of the regulator of the $\downarrow$-fermions (4.16) as long as no spontaneous symmetry breaking occurs. By continuity we can infer that the repulsive branch will remain to exist for small but finite $\downarrow$-population and will exceed the critical energy ϵ_F for the presumed onset of saturated ferromagnetism. It is an open question whether for larger impurity concentrations the repulsive branch is so strongly renormalized that saturated ferromagnetism can be ruled out [55], or whether competition with molecule formation may preclude the observation of ferromagnetic domains [50]. Answering these questions will require a full non-equilibrium calculation.

There has been much theoretical progress on the repulsive Fermi gas with short-range interactions, but relatively few experiments have been completed. While the repulsive ^{3}He Fermi gas has been studied extensively in experiment, it is not dilute and has a large repulsive hard-core potential [279]. In contrast, ultracold Fermi gases offer the realization of a proper contact interaction of tunable strength. We predict rf-transition rates for the repulsive branch and propose a possible route to measure these excited states in a ^{6}Li Fermi gas. This is a challenging problem because the final repulsive polaron state is highly unstable. Following our work these obstacles have recently been overcome by Kohstall *et al.* using a mixture of ^{6}Li and ^{40}K atoms [64]. In this experiment the repulsive polaron energy as well as its quasiparticle weight have been measured and fit remarkably well the theoretical predictions (see Appendix B).

The repulsive polaron in two spatial dimensions had not been studied so far. We analyze this problem in Appendix A using a simple non-selfconsistent T-matrix approach and find that the physics is rather similar the three-dimensional case. Using a calculation of the rf spectrum including the specific trap specifications of a recent experiment [61], we show that this experiment can be interpreted in terms of polaron physics. Following our work [63], the repulsive polaron in two dimensions has very recently been directly observed experimentally by Koschorreck *et al.* [65].

Chapter Five

Conclusions and outlook

In this thesis we theoretically studied the physics of ultracold quantum gases ranging from few- to many-body problems. Of particular interest was the application of the functional renormalization group (fRG) which allows the description of the few- and many-body physics in a unified field theoretical framework. In Chapter 2 we solved the quantum mechanical three-body problem of bosons interacting with short-range interactions for an extended two-channel model which accounts for the finite physical range σ of the pairwise interaction potential. Using renormalization group equations we derived a modified STM equation and calculated the bound state spectrum of the system. While universality, governed by the strong coupling unitary fixed point for infinite scattering length $a \to \infty$ and scattering energy at the threshold $E = 0$, is approached quickly for the highly excited Efimov states, the experimentally accessible low lying trimer states show deviations from universal scaling. We predicted, from two-body physics alone, the scattering lengths $a_-^{(n)}$ where the n-th Efimov states reach the atom threshold as function of r^*/σ where r^* characterizes the width of the Feshbach resonance. In the limit of open-channel dominated resonances $r^*/\sigma \to 0$ our results explain the experimentally observed 'universality' of the so-called three-body parameter $a_- = a_-^{(0)} \approx -9.45 l_{\mathrm{vdw}}$ [47] in terms of the 'standard model' of cold atoms and we predict a crossover to a scaling $a_- \sim r^*$ for closed-channel dominated resonances. Since the zero-range version of our model is a typical starting point for many-body theory of cold atoms our results attest to the validity of this model but also show its limitations. We analyzed in detail the universality of our results by using various forms of the atom-to-molecule conversion coupling and studied the influence of a microscopic three-body force. We found that they – in the open-channel dominated limit – generically lead to deviations from the 'universal' result $a_- = a_-^{(0)} \approx -9.45 l_{\mathrm{vdw}}$ on the ten percent level. Finally, we showed that in the closed-channel dominated limit a new class of universality arises where even the deviations from the scaling limit for the lowest Efimov states become universal themselves.

In Chapter 3 we extended the study of few-body physics to the four-body problem using a derivative expansion of the effective flowing action Γ_k. We solved the flow equations at the unitarity point and found that a four-body RG limit cycle is attached to the three-body limit cycle. This shows that no additional four-body parameter is needed for the renormalization of the four-body problem. In order to solve the RG equations we relied on an extension of the flow to the complex plane developed in [111]. The quantum mechanical calculation by Stecher *et al.* [48, 184] for the lowest four-body bound states away from the unitarity point predicts the existence of two tetramer states attached to each trimer. In our approximation

we are only able to resolve a single of these states but we showed ways of how our calculation can be extended to account also for the second tetramer. Furthermore we studied how the intrinsic lifetime and threshold behavior of the excited tetramer states can be inferred from the flow of pointlike couplings in the complex plane. In order to connect our results to many-body physics we studied how the method of rebosonization [137, 172, 219] can be used for the introduction of a trimer field which accounts for these trimers as new effective and physically propagating degrees of freedom. Finally we discussed the relevance of this approach when studying e.g. the quantum phase transitions in an SU(3) Fermi gas or the strongly coupled Bose gas.

The second part of this thesis dealt with aspects of the many-body physics of cold atoms. In particular we focussed on the Fermi polaron problem where a single, mobile impurity is immersed in a Fermi sea of majority atoms. Compared to many other methods the RG has the advantage that it can describe intrinsically non-perturbative situations and in this respect the Fermi polaron is a case in point. Typically, however, in standard RG approaches for fermions [272] one follows only a few relevant coupling constants so that one retains only a very poor spectral resolution of Green's functions. In Chapter 4 we developed a new numerical functional RG technique, which removes this disadvantage and which allows the study of the flow of fully momentum and frequency dependent vertex functions. This gave us access to the RG flow of the full spectral function of the impurity which we in turn used to predict the excitation spectrum of the system across the polaron-to-molecule transition. Besides finding accurate results for the ground state properties which compete with recent state-of-the-art diagMC results [59, 60] we were also able to access the excited states in the spectrum. We found that the attractive polaron and the molecule remain to exist as well-defined quasiparticles across the polaron-to-molecule transition with a lifetime τ which increases quickly as the transition is approached according to $\tau \sim \Delta E^{-9/2}$, where ΔE is the energy difference between the excited and the ground state. The finding of this power law, which is not possible to obtain for instance in a leading order $1/N$ expansion, attests to the strength of the fRG. The scaling $\sim \Delta E^{-9/2}$ had been conjectured on a basis of a phenomenological two-loop calculation in [241], and in Chapter 4 we derived it directly from microscopic physics. Furthermore we found that spectral weight is transferred from the attractive polaron to a new, emerging quasiparticle in the spectrum at positive energies: the repulsive polaron. We calculated the energy, lifetime, and quasiparticle weight of the repulsive polaron and found that it becomes a stable excitation of unit weight in the BEC limit. It interacts repulsively with the surrounding Fermi sea and its energy exceeds the Fermi energy for a critical interaction strength. At this point it becomes energetically favorable to add an additional majority atom to the system instead of a minority impurity which can be interpreted as an instability of the system towards ferromagnetism. However, at this presumed transition the repulsive polaron is a very short-lived quasiparticle which shows that molecule formation may be the true, leading instability. This prohibits cold atoms as a quantum simulator of a strongly repulsive Fermi gas. Finally we proposed a radio-frequency spectroscopy experiment to measure the impurity spectral function which has been implemented by the Innsbruck group [64]. In Appendix B we presented our calculation of the rf spectrum expected for this specific experimental setup which studies a mass-imbalanced Fermi gas of ^{6}Li and ^{40}K atoms. Our results are in remarkable agreement

with the experimental data.

In two spatial dimensions the excitation spectrum of the polaron problem had not been studied so far and in Appendix A we presented the calculation of the spectrum using a Nozieres-Schmitt-Rink approach. We found that the spectral properties are rather similar to the three-dimensional case. We compared our results to the experimental situation by approximately taking into account the quasi two-dimensional character of the optical lattice employed in experiments and performed a trap averaged calculation of the rf signal of the system within linear response theory. We showed that a experiment by Fröhlich *et al.* [61] can find a reinterpretation in terms of polaron physics. Recently, our results have been experimentally tested by Koschorreck *et al.* [65] and the data agrees well with our prediction.

In the context of the physics studied in this thesis, many open questions remain. Concerning few-body physics, one such question is the fate of N-body bound states. In his recent work [184] von Stecher found evidence for the existence of series of N-body bound states attached to each trimer. The ratio of scattering lengths $a^{(n)}_{N,-}/a^{(n)}_{\mathrm{Tri,-}}$ and energies $E^{*(n)}_{\mathrm{Tri}}/E^{*(n)}_{N}$ seem to be universal numbers for large n, with the ratios increasing as the particle number N grows. Experimentally, the lowest states are the ones which are most easily accessible. Combining our knowledge gained in the Chapters 2 and 3 together with the finding that the ratios $a^{(n)}_{N,-}/a^{(n)}_{\mathrm{Tri,-}}$ grow with N indicates that there might be a maximum number N_{max} as soon as a true finite range of the interaction potential is considered. Whether the number N_{max} is universal in cold atomic systems, similarly to what we found for a_-, or if the influence of N-body forces becomes particularly important for these lowest N-body bound states poses questions far from being answered.

An important shortcoming of the pointlike approximation used in our study of the quantum four-body problem is the absence of the shallower of the two tetramer states. In fact, it would be interesting to use the principle of minimal sensitivity used in the context of RG flow optimization [172, 211] within the present simple, pointlike truncation. One could use, for instance, the existing universal ratios such as $a^{(n)}_{\mathrm{Tet,-}}/a^{(n)}_{\mathrm{Tri,-}}$ as an optimization criterion. Then, parameters of regulators could be tuned to yield extremal results (principle of minimal sensitivity). As a result, it is well possible that the relevant coefficients in the flow equations of the four-body couplings are modified in such a way as to yield the expected two tetramer states. Similarly the extension of our truncation to account for a dynamical trimer field may be sufficient to find the missing tetramer state.

The Efimov effect is an example of a quantum anomaly in non-relativistic physics which breaks the scale invariance of the system and can be understood in terms of an effective three-body, inverse square potential [66]. This mechanism becomes of particular interest as symmetry arguments suggest that the conformal field theory emergent in recent studies [280] of non-Fermi liquids using the AdS/CFT correspondence [281] might be conformal quantum mechanics with an inverse square potential. We studied this problem in the context of this thesis and developed a method to extend RG flows to the complex plane [111]. By comparing our results to the low-energy behavior of the real and imaginary parts of the retarded Green's functions computed numerically by McGreevy and coworkers within the AdS/CFT

framework [282], we found further evidence for this correspondence. This suggests that the complex extension of RG flows might become useful for a better understanding of non-Fermi liquids from the AdS/CFT correspondence. The extend of this analogy is, however, still far from being understood.

Concerning the polaron problem it is still an open question what the fate of two impurities strongly coupled to a bath of majority fermions is in two or three spatial dimensions. This question is of great relevance for the phase diagram of the imbalanced Fermi gas as well as the stability of ferromagnetism in the case of repulsive interactions and it combines the many- and few-body aspect of cold atoms: for example in the case of two bosonic impurities the Efimov effect in presence of a Fermi sea will become important while for fermionic impurities the mediating force of the bath might lead to the formation of a p-wave molecule [261].

Finally our numerical fRG technique can be extended to study the question of how competing orders change physics in a possibly associated quantum critical regime [283]. Conventional ordering is signaled by singularities in higher point correlation functions $\Gamma^{(n)}$. Using an expansion of $\Gamma^{(n)}$ in the singular momentum and spin structure, the RG algorithm provides a means to study the competition of potentially critical channels including their interrelated backreaction which is very difficult using other diagrammatic methods such as diagrammatic Monte Carlo [284]. Similar to the scheme used by Giering, Husemann, Metzner, and Salmhofer for the study of the Fermi-Hubbard model at van Hove fillling [179, 180, 181, 182] in our approach the full self-energies are taken into account and can be used to compute nontrivial linear response properties, such as radio-frequency signals or transport coefficients. Using these observables, our numerical fRG method could then be benchmarked against experiments with ultracold atoms. This in turn could provide insight into the question how competing orders influence critical transport properties as well as which signatures they have in the resulting quasiparticle spectrum. An example for a system of interest in this regard is the microscopically repulsive Fermi gas in two and three dimensions. Similar to the Hubbard model, where d-wave superconductivity competes with antiferromagnetism, in the itinerant, repulsive Fermi gas, ferromagnetism may compete with the onset of p-wave superfluidity [285]. Whether such a scenario, partially reminiscent of the physics of ^{3}He [279], prevents the system from turning ferromagnetic is yet unresolved, and an fRG study including the competing channels as well as full self-energies might shed new light on this. Furthermore, taking the full momentum dependence of vertices into account, the fRG allows to start with arbitrary microscopic interactions which can be used to study the phase transition to ferromagnetism also in the case of dipolar gases trapped in lower-dimensional geometries.

Appendix A

The two-dimensional polaron and its observation

In this Appendix we theoretically analyze radiofrequency (rf) spectroscopy experiments in two-component Fermi gases and follow closely our work [63]. Similar to Chapter 4, we consider a small number of impurity atoms interacting strongly with a bath of majority atoms. While in Chapter 4 we studied impurities in three spatial dimensions, we consider here two-dimensional geometries and find that the main features of the rf spectrum correspond again to an attractive polaron and a metastable repulsive polaron. Our results suggest that the attractive polaron has been observed in a recent experiment [61] and new experimental results now directly support our predictions [65, 286].

The behavior of a mobile impurity (polaron) interacting strongly with a bath of particles is one of the basic many-body problems studied in condensed matter physics [287, 288, 289, 290]. With the advent of ultracold atomic gases [6], the Fermi polaron problem in which a single spin-$\downarrow$ atom interacts strongly with a Fermi sea of spin-$\uparrow$ atoms, has become a subject of intensive research [245]. In three dimensions we found that the polaron state splits into two branches, a low-energy state interacting attractively with the bath of fermions, and the repulsive polaron, which is an excited, metastable state, cf. [62, 243, 258]. In this way the polaron exemplifies a more general paradigm of a many-body system driven into a nonequilibrium state where a small number of high energy excitations interact strongly with the surrounding degrees of freedom [291, 292]. The polaron is the limiting case of a Fermi gas with strong spin imbalance, and the repulsive polaron provides insight into the question whether a quenched, repulsive Fermi gas may undergo a transition to a ferromagnetic state even though it is highly excited [49, 50, 62, 243, 258]. Similarly, the ground state of the polaron problem has important implications for the phase diagram of a strongly interacting Fermi gas [240, 256, 293].

It is a key question how many-body properties are affected by reduced dimensionality, and the polaron is a case in point. The combination of optical lattices and Feshbach resonances [6] provides a unique setting to experimentally study strongly interacting low dimensional systems using ultracold atoms [61, 294]. Recent advances in radiofrequency (rf) spectroscopy afford to measure energy spectra [240] and give access to excited states as well as full spectral functions using momentum resolved rf [295, 296]. So far, only the ground state of the two-dimensional polaron problem has been investigated theoretically [297, 298, 299] with the focus on a possible polaron-to-molecule transition. This is similar to the three-dimensional situation, considered in Chapter 4, where for strong interactions it becomes energetically favorable for the impurity to form a molecular bound state [59, 60]. The structure of high energy excitations and the experimental polaron signatures in rf spectroscopy have remained open questions which we address in this Appendix.

We introduce the microscopic Hamiltonian and discuss the few-body scattering in quasi two-dimensional geometries in Section A.1. The few-body T-matrix is modified by the medium and we use the Nozieres–Schmitt-Rink approach, which is equivalent to the leading order in a $1/N$ expansion [110], to calculate the corresponding corrections in Section A.2. Furthermore the properties of the dressed molecular state are discussed. In Section A.3 we derive the impurity spectral function and find that the impurity state splits into the attractive and the repulsive branch. We compute rf spectra for homogeneous 2D systems as well as for the experimentally relevant quasi-2D geometries in Section A.4. Finally, we argue that our calculation provides an alternative explanation of the recent experiment by Fröhlich et al. [61] in terms of the polaron picture.

A.1 Model and physics of quasi two-dimensional scattering

We consider a two-component 2D Fermi gas in the limit of extreme spin imbalance, described by the grand canonical Hamiltonian

$$H = \sum_{\boldsymbol{k}\sigma} (\varepsilon_{\boldsymbol{k}\sigma} - \mu_\sigma) c^\dagger_{\boldsymbol{k}\sigma} c_{\boldsymbol{k}\sigma} + \frac{g}{A} \sum_{\boldsymbol{k}\boldsymbol{k}'\boldsymbol{q}} c^\dagger_{\boldsymbol{k}\uparrow} c^\dagger_{\boldsymbol{k}'\downarrow} c_{\boldsymbol{k}'-\boldsymbol{q}\downarrow} c_{\boldsymbol{k}+\boldsymbol{q}\uparrow},$$

with single-particle energies $\varepsilon_{\boldsymbol{k}\sigma} = \boldsymbol{k}^2/2m_\sigma$ for species σ ($\hbar = 1$), chemical potentials μ_σ and system area A. Having in mind the experiment of Ref. [61], we focus on the case of equal masses $m_\uparrow = m_\downarrow = m$. Generalizations to mass imbalanced situations are straightforward [297, 298]. In the low-energy limit the attractive s-wave contact interaction g can act only between different species due to the Pauli principle. The majority atoms are not renormalized by the presence of a single impurity with finite mass such that $\mu_\uparrow = \varepsilon_F = k_F^2/2m$ at zero temperature. The chemical potential $\mu_\downarrow$ of the impurity atom is determined such that the impurity state $|\downarrow\rangle$ has vanishing density. Furthermore, $\mu_\downarrow$ is negative due to the attractive interaction between $\uparrow$- and $\downarrow$-atoms.

Quasi two-dimensional scattering

The two-body scattering of a spin-$\uparrow$ atom and a spin-$\downarrow$ atom in two spatial dimensions is described by the exact two-body T-matrix [300]

$$T_0(E) = \frac{4\pi/m}{\ln(\varepsilon_B/E) + i\pi}\,. \tag{A.1}$$

The pole of the T-matrix at $E = -\varepsilon_B$ corresponds to a molecular bound state, and the associated vacuum scattering amplitude for two particles with relative momenta $\boldsymbol{k}$ and $-\boldsymbol{k}$ in the center-of-mass frame is $f(k = |\boldsymbol{k}|) = mT_0(2\varepsilon_{\boldsymbol{k}}) = 4\pi/[\ln(1/k^2a_{2\mathrm{D}}^2) + i\pi]$ [6]. In the latter expression, the scattering amplitude is parametrized in terms of the so-called 2D scattering length a_{2D}.

Experimentally it is not possible to realize a perfect two-dimensional geometry. Instead a quasi-2D geometry can be designed using an optical lattice in one direction with associated trapping frequency ω_z. The atoms are then trapped in separate sheets of laser light, where the sheets have a finite transversal extent. In the case of such a confinement, a confinement induced two-body bound state exists for an arbitrarily weak microscopic attractive interaction [18, 300, 301] with binding energy $\varepsilon_B > 0$. The spatial extent of the bound state is related to the 2D scattering length given by $a_{2D} = \hbar/\sqrt{m\varepsilon_B} > 0$.

The bound state energy allows to relate our results to harmonically confined Fermi gases. In order to do so, we have to connect the strict 2D calculation to the quasi-2D geometry relevant to experiments [6, 301]. Well below the confinement energy $\hbar\omega_z$ where only the lowest transverse mode is occupied, this can be done by replacing ε_B with the exact quasi-2D two-body binding energy. In harmonic confinement ε_B is given by ([301], cf. Eq. (82) in [6])

$$\frac{\ell_z}{a_{3D}} = \int_0^\infty \frac{du}{\sqrt{4\pi u^3}} \left(1 - \frac{e^{-\Omega u}}{\sqrt{(1-\exp(-2u))/(2u)}}\right), \tag{A.2}$$

where $\Omega = \varepsilon_B/(\hbar\omega_z)$. In consequence, ε_B becomes a function of both the 3D scattering length a_{3D} and the confinement length $\ell_z = \sqrt{\hbar/m\omega_z}$. Using the *parametrization* $\varepsilon_B = \hbar/(ma_{2D}^2)$, the 2D scattering length a_{2D} can then be expressed in terms of its three-dimensional counterpart a_{3D} and ℓ_z. One finds that in the weak coupling BCS regime of small 3D scattering length $a_{3D} < 0$ the dimers are large and weakly bound ($\varepsilon_B \ll \hbar\omega_z$) [6], while in the BEC limit of small $a_{3D} > 0$ the weakly interacting molecules are too tightly bound to feel the confinement ($\varepsilon_B \sim \hbar^2/(ma_{3D}^2) \gg \hbar\omega_z$). Around the Feshbach resonance ($a_{3D}^{-1} = 0$) there is a strong coupling regime where the binding energy attains the universal value $\varepsilon_B = 0.244\,\hbar\omega_z$ [6, 301].

A.2 Nozieres-Schmitt-Rink approach and the many-body T-matrix

At finite density the majority atoms form a Fermi gas with Fermi energy ε_F and the two-body scattering is replaced by many-body scattering which gives rise to important qualitative differences, most notably the emergence of two polaron branches. In the presence of a Fermi sea of spin-↑ atoms, the molecular state itself is dressed by fluctuations and it is described by the many-body T-matrix. This can be calculated in the Nozieres–Schmitt-Rink approach [259], as done in the 2D case by Engelbrecht and Randeria [302, 303]. We generalize these results to the case of spin imbalance and compute the many-body T-matrix in the ladder approximation which is represented diagrammatically in Fig. A.1d. This yields

$$T^{-1}(\boldsymbol{q},\omega) = T_0^{-1}(\omega + i0 + \mu_\uparrow + \mu_\downarrow - \varepsilon_{\boldsymbol{q}}/2) + \int \frac{d^2k}{(2\pi)^2} \frac{n_F(\varepsilon_{\boldsymbol{k}} - \mu_\uparrow) + n_F(\varepsilon_{\boldsymbol{k}+\boldsymbol{q}} - \mu_\downarrow)}{\omega + i0 + \mu_\uparrow + \mu_\downarrow - \varepsilon_{\boldsymbol{k}} - \varepsilon_{\boldsymbol{k}+\boldsymbol{q}}}, \tag{A.3}$$

with the Fermi function $n_F(\varepsilon)$. At zero temperature where $\mu_\uparrow = \varepsilon_F$ and $\mu_\downarrow < 0$, we obtain a very compact analytical expression for the many-body T-matrix

$$T(\boldsymbol{q},\omega) = T_0\left(\tfrac{1}{2}z \pm \tfrac{1}{2}\sqrt{(z-\varepsilon_{\boldsymbol{q}})^2 - 4\varepsilon_F\varepsilon_{\boldsymbol{q}}}\right) \tag{A.4}$$

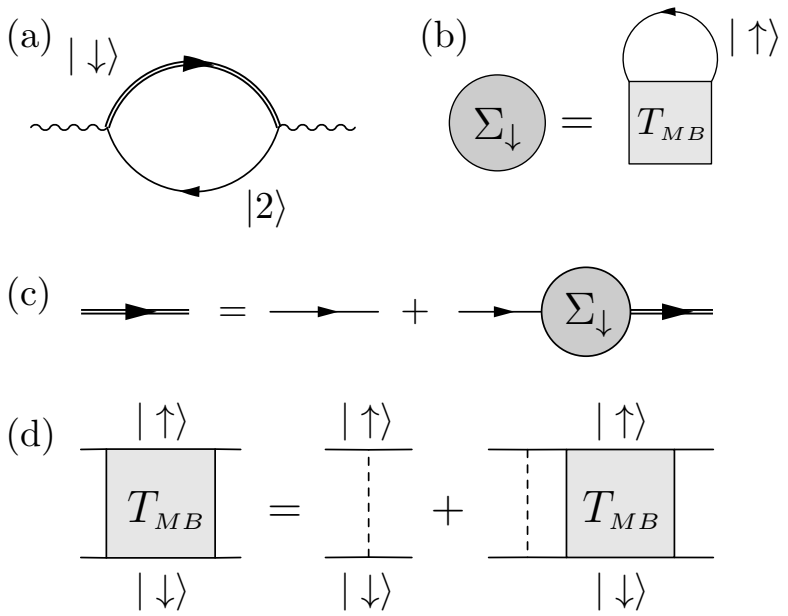

FIGURE A.1: *Diagrammatic representation of (a) the rf photon self-energy, (b) the self-energy of spin-↓ atoms, (c) the Dyson equation for the dressed Green's function $G_\downarrow$, and (d) the many-body T-matrix between states $|\uparrow\rangle$ and $|\downarrow\rangle$.*

with $z = \omega + i0 - \varepsilon_F + \mu_\downarrow$ and $\pm = \mathrm{sgn}\,\mathrm{Re}(z - \varepsilon_{\boldsymbol{q}})$. Remarkably, within the simple Nozieres–Schmitt-Rink approach the many-body T-matrix can be expressed as the two-body T-matrix, cf. Eq. (A.1), with shifted argument. The spectral function $\mathscr{A}_{\mathrm{mol}}(\boldsymbol{q},\omega) = -2\mathrm{Im}T(\boldsymbol{q},\omega)$ of the molecule is shown in Fig. A.2 for several values of the interaction strength parametrized by the two-body binding energy ε_B. One observes a bound state peak at low energies and the particle-particle continuum at higher energies.

The continuum of dissociated molecules arises mathematically from the branch cut of the square root (A.4) in the region $\omega_-(q) < \omega < \omega_+(q)$, $\omega_\pm = \varepsilon_F(1 \pm q/k_F)^2 - \mu_\downarrow$ (dash-dotted/solid lines), as well as from the branch cut of the logarithm (A.1) for $\omega > \omega_+(q)$ and for $\omega_0 = \varepsilon_{\boldsymbol{q}}/2 - \varepsilon_F - \mu_\downarrow < \omega < \omega_-(q)$ if $q > 2k_F$ (dashed lines).

The bound state arising from the pole of the many-body T-matrix has the dispersion relation [297]

$$\omega_b(\boldsymbol{q}) = \frac{\varepsilon_{\boldsymbol{q}}/2(\varepsilon_{\boldsymbol{q}}/2 - \varepsilon_F) + \varepsilon_B(\varepsilon_F - \varepsilon_B)}{\varepsilon_{\boldsymbol{q}}/2 + \varepsilon_B} - \mu_\downarrow \tag{A.5}$$

which changes qualitatively with the two-body binding energy ε_B. For large binding $\varepsilon_B > 2\varepsilon_F$ (Fig. A.2d), the bound state has minimum energy $\omega_b = \varepsilon_F - \varepsilon_B - \mu_\downarrow$ at $q = 0$ and we find an effective mass $m^*/m|_{q=0} = 2/(1 - 2\varepsilon_F/\varepsilon_B) > 2$.[1] For smaller binding $\varepsilon_B < 2\varepsilon_F$

[1]Note that the T-matrix does not yield the correct binding energy in the BEC limit [298]. However, in this

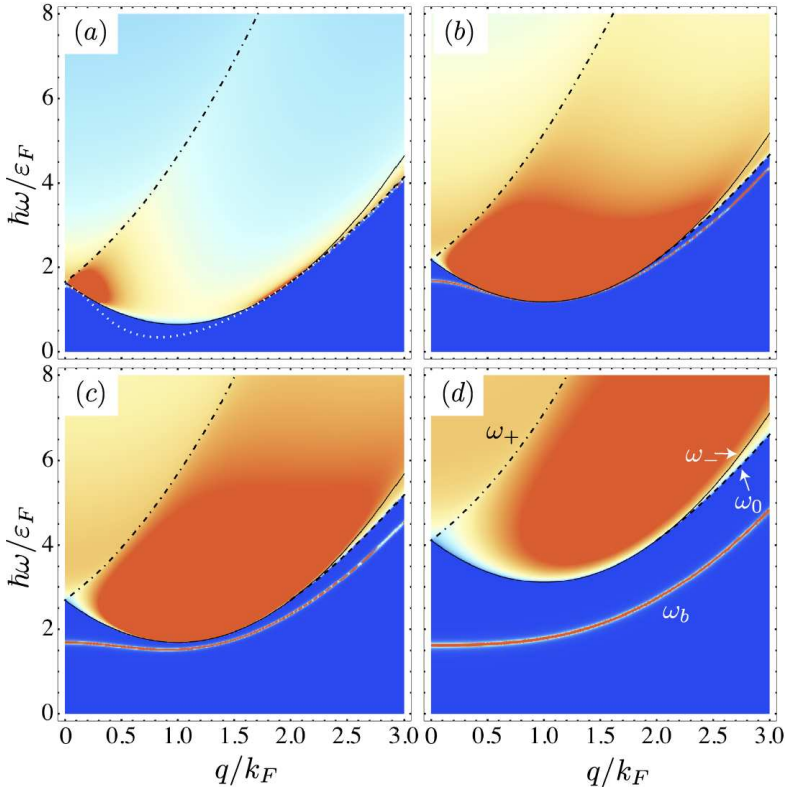

FIGURE A.2: *Molecular spectral function $\mathcal{A}_{mol}(\mathbf{q},\omega)$ for different values of the two-body binding energy $\varepsilon_B/\varepsilon_F$: (a) 0.1, (b) 0.5, (c) 1.0, (d) 2.5. The dashed lines mark the log continuum ω_0, dash-dotted and solid the root continuum $\omega_\pm$.*

(Fig. A.2b-c), the effective mass at $q=0$ becomes negative and a new minimum appears at finite wave vector $q_c = 2\sqrt{k_F a_{2D} - 1}/a_{2D}$ [297] and with positive effective mass $m^*/m|_{q=q_c} = [2 - 2/(k_F a_{2D})]^{-1} > 0$. For decreasing binding energy ε_B the bound state eventually touches the continuum at momenta $q_\pm/k_F = 1 \pm \sqrt{1 - 2\varepsilon_B/\varepsilon_F}$ (dotted line in Fig. A.2a). For $q_- < q < q_+$ the bound state has negative residue ($m^* < m$) and it ceases to exist.

A.3 Polaron and quasiparticle properties

The impurity atom is dressed with virtual molecule-hole excitations and becomes a renormalized quasiparticle. Its self-energy is given by scattering an ↑-hole off a molecule as depicted in

limit the repulsive polaron is the relevant excitation and its energy is correctly reproduced in our approximation.

Fig. A.1b. Explicitly, the self-energy reads

$$\Sigma^R_\downarrow(\boldsymbol{q},\omega) = \int \frac{d^2k}{(2\pi)^2}\frac{dz}{\pi} \quad \Big[\quad n_B(z) G^A_\uparrow(\boldsymbol{k}-\boldsymbol{q}, z-\omega)\mathrm{Im}T(\boldsymbol{k},z) \\ - \quad n_F(z)\mathrm{Im}G^R_\uparrow(\boldsymbol{k},z)\,T(\boldsymbol{k}+\boldsymbol{q}, z+\omega)\Big] \tag{A.6}$$

where $G^{A,R}_\uparrow$ refers to advanced/retarded $\uparrow$-Green's functions. The first contribution comes from the pole and branch cuts of the T-matrix. In the polaron problem neither the $\downarrow$-state nor the molecular state are macroscopically occupied at zero temperature, hence the molecular spectral function $\propto \mathrm{Im}T$ has weight only at positive frequencies $z > 0$ where $n_B(z)$ vanishes, cf. Fig. A.2. The second contribution of (A.6) with the bare $\uparrow$-spectral function $\mathrm{Im}G^R_\uparrow(\boldsymbol{k},z) = -i\pi\delta(z-\varepsilon_{\boldsymbol{k}}+\mu_\uparrow)$ directly yields [268, 303]

$$\Sigma_\downarrow(\boldsymbol{q},\omega) = \int_{k<k_F} \frac{d^2k}{(2\pi)^2}\, T(\boldsymbol{k}+\boldsymbol{q}, \varepsilon_{\boldsymbol{k}}-\mu_\uparrow+\omega), \tag{A.7}$$

which, in three spatial dimensions, leads to the same ground state energy as a variational ansatz [233]. The $\downarrow$-self-energy yields the $\downarrow$-Green's function via the Dyson equation (A.8) depicted in terms of Feynman diagrams in Fig. A.1c. We perform the integral in (A.7) numerically and obtain the spectral function of impurity atoms

$$\mathscr{A}_\downarrow(\boldsymbol{q},\omega) = -2\mathrm{Im}[\omega + i0 + \mu_\downarrow - \varepsilon_{\boldsymbol{q}} - \Sigma_\downarrow(\boldsymbol{q},\omega)]^{-1}. \tag{A.8}$$

The frequency and momentum dependence of the spectral function is shown in Fig. A.3 (left panel) for three values of the interaction strength. In Fig. A.4 we display the spectral function $\mathscr{A}_\downarrow(q=0, E-\mu_\downarrow)$ at zero momentum versus the interaction parameter $\eta = \ln(k_F a_{2D}) = -\ln(\varepsilon_B/2\varepsilon_F)/2$. In both figures we set the reference energy to the free atom threshold by subtracting the chemical potential $\mu_\downarrow$.

At weak binding $\varepsilon_B \ll \varepsilon_F$ (Fig. A.3a) the attractive polaron is a well-defined quasiparticle at small momenta but for $q \gtrsim k_F$ it scatters off virtual molecules and acquires a large decay width. Similarly to the three-dimensional case, for intermediate binding (Fig. A.3b) a new repulsive polaron state appears at positive energies. It is a metastable state with broad decay width, and it is shifted to higher energy due to the repulsive interaction with the Fermi sea of spin-$\uparrow$ atoms. The dispersion of the repulsive polaron has a minimum at finite momentum $q \sim k_F$ reflecting a similar feature in the molecular spectral function (Fig. A.2c); for larger momenta it approaches the free particle dispersion. Finally, for strong binding (Fig. A.3c) both polaron branches are well separated and the repulsive polaron becomes an increasingly long-lived and stable quasiparticle. Between the attractive and the repulsive polaron branches appears the molecule-hole continuum (see also Fig. A.4). Its spectral weight is small in the case of a broad Feshbach resonance studied here, but it is enhanced for narrow resonances by an admixture of closed-channel molecules [62].

It is instructive to see how the quasiparticle properties of the polaron change as the interaction parameter η is varied. The right inset of Fig. A.4 shows a continuous crossover where the

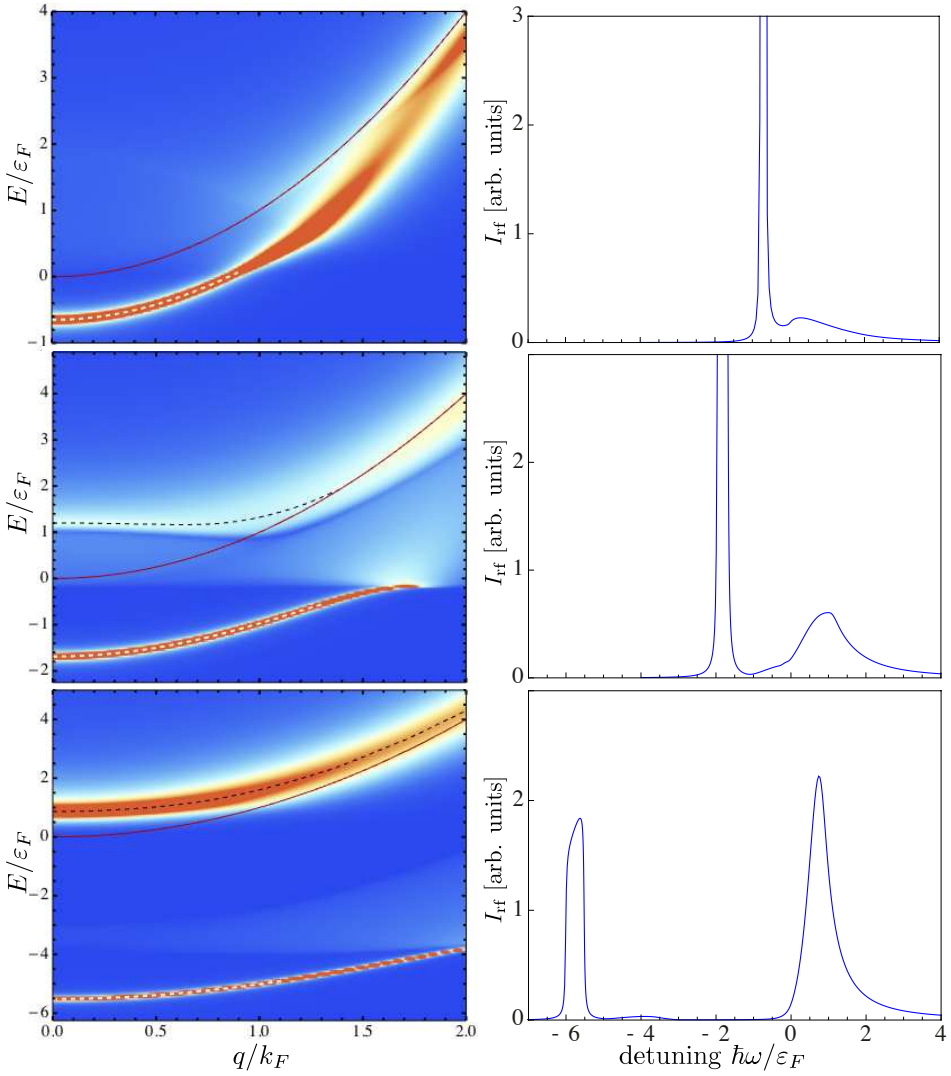

FIGURE A.3: ***Left panels:*** *spectral function $\mathcal{A}_\downarrow(q, E-\mu_\downarrow)$ for impurity atoms interacting with a 2D Fermi sea. Red lines indicate the free particle dispersion and white (black) dashed lines mark the dispersion of the attractive (repulsive) polaron.* ***Right panels:*** *corresponding rf spectra illustrating how weight is shifted from the attractive polaron state (peak at negative frequencies) to the new repulsive polaron state at positive frequencies. The two-body bound state energy is (a) $\varepsilon_B/\varepsilon_F = 0.1$, (b) $\varepsilon_B/\varepsilon_F = 1$, (c) $\varepsilon_B/\varepsilon_F = 5$.*

quasiparticle weight shifts from the attractive and to the repulsive polaron branch: for small binding ($\eta > 0$), the attractive polaron is the dominant excitation and the weight is gradually transferred toward the repulsive branch for increasing binding ($\eta < 0$). This crossover is also reflected in the effective mass m^*/m (Fig. A.4 left inset). Our strong coupling calculation re-

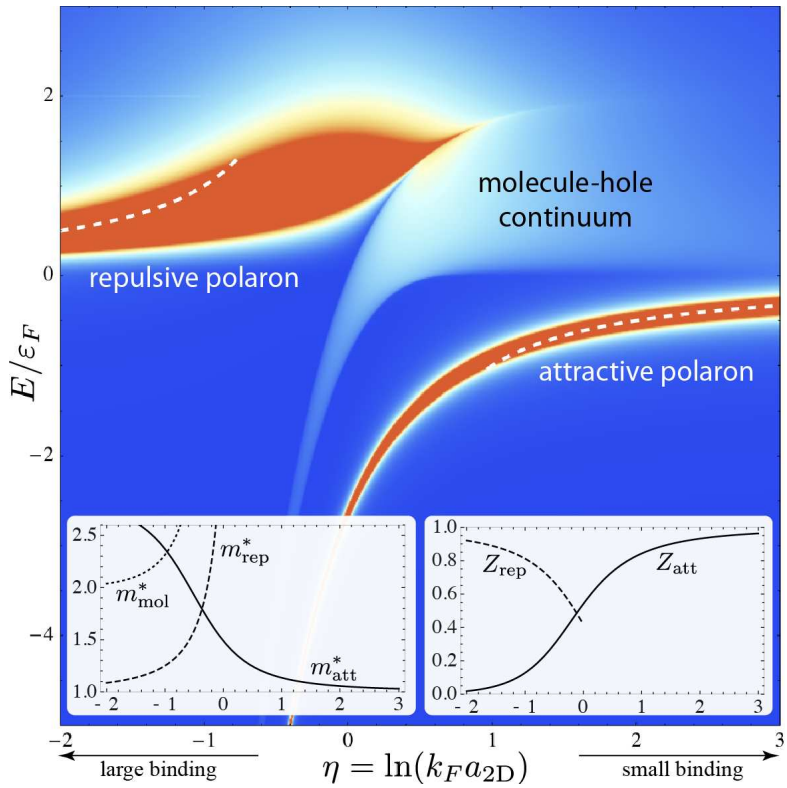

FIGURE A.4: *Polaron spectral function $\mathcal{A}_\downarrow(q=0, E-\mu_\downarrow)$ versus the interaction parameter η. The dashed lines indicate the perturbation theory of Ref. [304]. **Left inset:** effective mass m^*/m of the attractive and repulsive polaron as well as the molecule. **Right inset:** crossover of the quasiparticle weight Z from the repulsive to the attractive polaron.*

produces the perturbative results [304] for the attractive and repulsive polaron energies in the weak and strong binding limits (dashed lines in Fig. A.4). Therefore, we expect our results to be reliable also in the intermediate regime of strong coupling ($\eta \to 0^{\pm}$) where perturbation theory in $1/\eta$ breaks down and the confinement induced resonance appears [6, 305].

A.4 Radiofrequency spectroscopy and comparison to experiment

The spectral properties of the imbalanced Fermi gas can be accessed experimentally using rf spectroscopy. We assume that an rf pulse is used to drive atoms from an initial state $|i\rangle$ to an initially empty final state $|f\rangle$. We choose the final state to be strongly interacting with a bath of a third species $|\uparrow\rangle$ such that $|f\rangle$ is the impurity state, $|f\rangle = |\downarrow\rangle$. This inverse rf procedure interchanges the roles of $|i\rangle$ and $|f\rangle$ with respect to Ref. [240]; it has been proposed in Refs. [62, 258] and it is described in detail in Chapter 4. It has been realized in the experiment using two-dimensional Fermi gases by Fröhlich et al. [61].

Within linear response theory, the rf transition rate is given by [255]

$$I_{\rm rf}(\omega_{\rm rf}) = 2\Omega_{\rm rf}^2 {\rm Im}\chi^R(-\omega_{\rm rf} - \mu_i + \mu_f) \tag{A.9}$$

where $\Omega_{\rm rf}$ is the Rabi frequency, $\omega_{\rm rf}$ the detuning of the rf photon from the bare transition frequency and $\mu_{i(f)}$ the initial (final) state chemical potential. The retarded correlation function χ^R can be computed from the corresponding time-ordered correlation function $-i\theta(t-t')\langle[\psi_f^\dagger({\rm r},t)\psi_i({\rm r},t), \psi_i^\dagger({\rm r}',t')\psi_f({\rm r}',t')]\rangle$ [153, 268]. In general vertex corrections are crucial [110, 263], but we find that they vanish in the case of negligible initial state interactions as appropriate for the experiment [61]. At $T = 0$, we obtain

$$I_{\rm rf}(\omega_{\rm rf}) = \Omega_{\rm rf}^2 \int_{\varepsilon_{\boldsymbol{q}} < \mu_i} \frac{d^2q}{(2\pi)^2} \mathscr{A}_\downarrow(\boldsymbol{q}, \omega_{\rm rf} + \varepsilon_{\boldsymbol{q}} - \mu_\downarrow). \tag{A.10}$$

Eq. (A.10) is calculated numerically and the resulting rf spectra are shown in Fig. A.3 (right panel). The rf probes the final $|\downarrow\rangle$ state spectral function along the free-particle dispersion up to the initial state chemical potential μ_i. As in the experiment [61], we assume a balanced initial state mixture with $\mu_i = \mu_\uparrow$. We find a peak in the rf spectrum once the detuning $\omega_{\rm rf}$ reaches the final state chemical potential $\mu_\downarrow$ ($\mu_\downarrow$ is negative in the polaron problem). Similar to the situation in three spatial dimensions, cf. Fig. 4.24, the transfer of spectral weight from the attractive to the repulsive polaron can be directly observed in Fig. A.3.

Comparison to experiments

Recently a quasi-2D geometry has been realized experimentally with a Fermi gas of ^{40}K atoms [61]. Following the inverse rf procedure described above, an initially non-interacting balanced mixture is driven into a strongly interacting final state. As long as its occupation remains small the final state is a Fermi polaron, and our calculation predicts the experimental rf response.

In Fig. A.5 we show our trap averaged rf spectra versus magnetic field. We use the experimental parameters of Ref. [61] with $\omega_z = 2\pi \times 80$ kHz, $\omega_\perp = 2\pi \times 125$ Hz, and express $a_{\rm 3D}$ in terms of the magnetic field as described in Section A.1, cf. [6, 306]. We incorporate the radial trapping in the 2D plane using the local density approximation. In the experiment [61] not only a single (central) 2D layer is populated but also additional pancakes along the axial direction. For each of these layers we calculate the rf response

$$I_{\rm trap}^{(\nu)}(\omega) = \int d^2r\, \rho_{\rm LDA}^{(\nu)}({\rm r}) I_{\rm rf}^{(\nu)}(\omega, {\rm r}). \tag{A.11}$$

The various pancakes are indicated by the index ν and $\rho_{\rm LDA}^{(\nu)}({\rm r}) = m\varepsilon_F^{(\nu)}(r)/2\pi\hbar^2$ is the Thomas-Fermi distribution of the density of non-interacting fermions within a single layer. $I_{\rm rf}^{(\nu)}(\omega, {\rm r})$ is the rf response Eq. (A.10) computed for a homogeneous system with local Fermi energy $\varepsilon_F^{(\nu)}(r)$ and interaction parameter $\eta(r) = -\ln(\varepsilon_B/2\varepsilon_F^{(\nu)}(r))/2$. In the experiment [61] 30 layers have been populated. To obtain the complete rf response of the trapped system we thus finally

sum over 30 contributions $I^{(\nu)}_{\mathrm{trap}}$ where we assume that the peak density of each layer, $\epsilon^{(\nu)}_F(0)$, varies according to a Thomas-Fermi profile in axial direction with confinement frequency $\omega_\perp$. The local Fermi energy is $\varepsilon_F(r) = \varepsilon_F - m\omega_\perp^2 r^2/2$ with peak Fermi energy $\varepsilon_F = 9$ kHz.

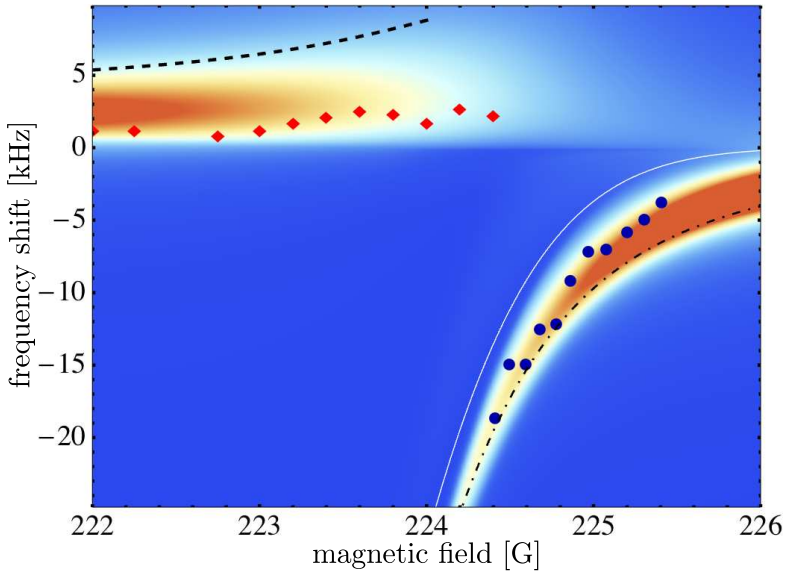

FIGURE A.5: *Trap averaged rf spectra of a quasi-2D Fermi gas: rf detuning versus magnetic field B. The experimental data points (blue and red diamonds) are taken from Ref. [61]. Also shown are the energy of the repulsive (dashed) and attractive (dash-dotted) polaron as well as the two-body binding energy (solid, white) in a homogeneous system.*

We observe that the lower branch of the experimental spectra (circles) agrees well with the attractive polaron picture (Fig. A.5) and our calculation provides an alternative interpretation to the two-body bound state (solid line) put forward in Ref. [61]. We note that also the measured frequency shift in 3D as shown in [61] fits the polaron picture [62]. Our results show a second rf peak at positive detunings corresponding to the repulsive polaron. The dashed line in Fig. A.5 indicates its quasiparticle energy in the bulk (cf. Fig. A.4). As similar for the attractive polaron energy (dash-dotted line) the trap average leads to a significant shift of the rf peaks to lower energies. The experimental data (diamonds) in this magnetic field range agrees qualitatively with our calculation. One possible reason for the remaining discrepancy is the large final state occupation in the experiment.

Influence of shape and length of the rf pulse. The line shape of the rf spectra has a strong dependence on the rf pulse shape. The rf pulse used in Ref. [61] is approximately rectangular with duration $T = 100\,\mu$s. We compute the experimental rf signal as the convolution of

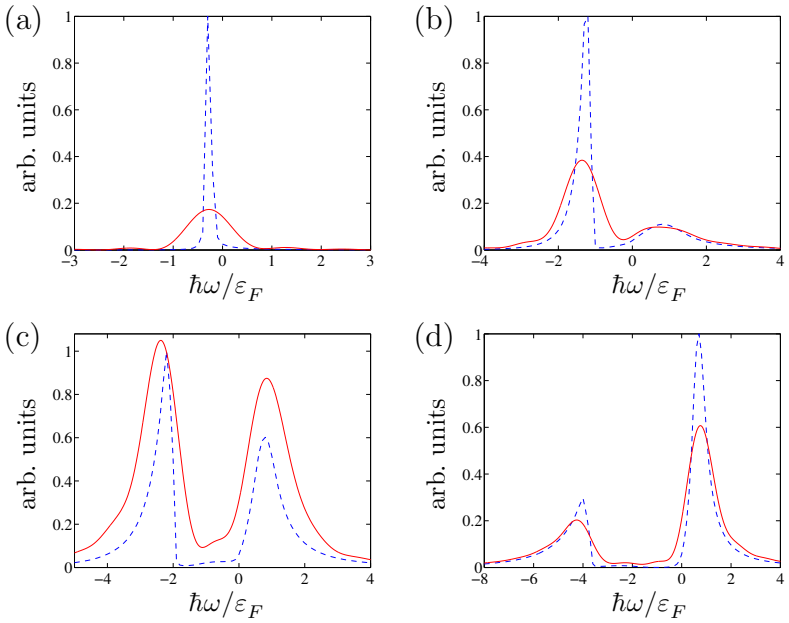

FIGURE A.6: *RF spectrum of a trapped quasi-2D Fermi gas for (a) $B = 227$ G, (b) $B = 225$ G, (c) $B = 224.5$ G, and (d) $B = 224$ G. The attractive polaron gives rise to the peak at negative frequencies and the repulsive polaron corresponds to the peak at positive frequencies. The dashed line depicts the trap averaged signal I_{trap} while the solid line shows the expected experimental signal I_{exp} which takes into account a rectangular rf pulse of duration $T = 100$ μs (not to scale) [61].*

$I_{\rm trap}(\omega)$ with the Fourier spectrum of the rf field [255]

$$I_{\rm exp}(\omega) = \frac{T}{2\pi}\int d\omega' \, I_{\rm trap}(\omega-\omega')\,\mathrm{sinc}^2(\omega' T/2). \tag{A.12}$$

In Fig. A.6 we show the resulting rf spectra for different values of the external magnetic field. Note that the broadening may shift the apparent peak position, see e.g. Fig. A.7b.

A.5 Conclusion

In conclusion, we studied Fermi polarons in two dimensions which exhibit an attractive and repulsive branch and computed their rf spectra. Additional work is needed to understand discrepancies between theory and experiment for repulsive polarons. As an example, pump and probe experiments in the form of a sequence of two short pulses may shed further light on this issue. Recently the attractive and repulsive polaron has been measured in experiments [65, 286]. The observation agrees well with the results from the simple NSR approach presented in this Appendix. We expect, however, that corrections to this result will become of relevance

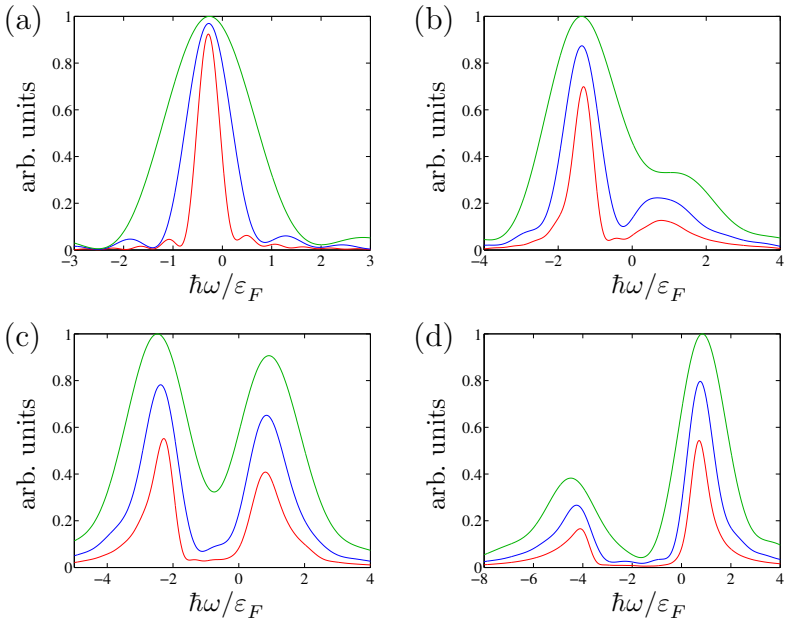

FIGURE A.7: *Same as Fig. A.6 but for different rf pulse duration (from top to bottom)* $T = 50\,\mu s$, $T = 100\,\mu s$, *and* $T = 200\,\mu s$ *(not to scale).*

in future experiments with quasi-two dimensional Fermi gases, in particular at finite density of both species, so that a more involved analysis using, for instance, methods such as those presented in Chapter 4 will be necessary.

Appendix B

Polaron in a mass-imbalanced Fermi gas

In this Appendix we present and summarize theoretical results which we obtained in collaboration with the group of Grimm in Innsbruck and which was related to the interpretation of an at the time ongoing experiment aiming at the measurement of the excitation spectrum of the polaron problem across the polaron-to-molecule transition.[1] In this experiment a spin-imbalanced, two-component mixture of ^{6}Li and ^{40}K atoms was prepared with the lighter ^{6}Li atoms being the majority species. In the initial state the two species were in a non-interacting state. Then an rf pulse was applied, driving a transition between hyperfine states of the minority ^{40}K atoms to a strongly interacting final state. In this way the proposal for an inverse rf procedure to measure the excitation spectrum of an impurity across the polaron-to-molecule transition, put forward by us in [62] and by Massignan and Bruun in [258] and as discussed in detail in Chapter 4, was experimentally realized.

The two major differences to the protocol discussed in Chapter 4 are the mass imbalanced situation and the fact that one deals with a Feshbach resonance of a relatively 'narrow' character. Here, the term 'narrow' has to be understand in the sense that the dimensionless quantity $k_F r^*$ is of order one or larger. The experiment focussed in particular on the measurement of the impurity's energy spectrum and its quasiparticle weight. As we have seen in Chapter 4, these properties can be described relatively well in a simple, non-self-consistent T-matrix approach [259].[2] We employed such a non-self-consistent T-Matrix approach already in Appendix A for the description of the polaron in two spatial dimensions and we apply this formalism here to the impurity problem in a mass-imbalanced situation (For similar, recent treatments we refer to [64, 307, 308]).

The microscopic action describing the system of fermions of masses $m_\uparrow$ and $m_\downarrow$ with a mass ratio $m_\uparrow/m_\downarrow = c$ close to a Feshbach resonance of finite width r^* is given by[3]

$$\begin{aligned} S &= \int_{\boldsymbol{x},\tau} \Big\{ \psi_\uparrow^*[\partial_\tau - \Delta - \mu_\uparrow]\psi_\uparrow + \psi_\downarrow^*[\partial_\tau - c\Delta - \mu_\downarrow]\psi_\downarrow \\ &\quad + \phi^* \left[\partial_\tau - \frac{c}{1+c}\Delta + E_{\mathrm{mol}}(B) \right] \phi + g(\psi_\uparrow^*\psi_\downarrow^*\phi + h.c.) \Big\}, \end{aligned} \tag{B.1}$$

[1] The experimental results have by now been published [64].

[2] Note, if one is, however, interested in a detailed quantitative description of these observables or, for instance, the lifetime of the excited molecule and attractive polaron branch, more involved methods such as the fRG approach presented in Chapter 4 are indispensable.

[3] We neglect a possible background scattering potential which for the ^{6}Li -^{40}K mixture, where background scattering length takes the small value $a_{\mathrm{bg}} = 63a_0$, is a good approximation.

where we introduced the units $2m_\uparrow = \hbar = 1$. In this convention, $m_\downarrow = 1/(2c)$ and the reduced mass becomes $m_r = \frac{1}{2}\frac{1}{1+c}$. The bare detuning of the molecule ϕ in the closed channel is given by $E_{\mathrm{mol}} = \mu(B - B_{\mathrm{res}})$ with μ the molecule's magnetic moment.

B.1 Two-body problem

First we solve the two-body problem as it lays the basis of the renormalization of the model and allows to connect the model parameters B_{res} and g to physical two-body observables. Evaluating the standard particle-particle ladder yields the inverse, retarded dimer propagator

$$\begin{aligned} P^R_{vac,\phi}(\omega, \boldsymbol{q}) &= -\omega + \frac{c}{1+c}\boldsymbol{q}^2 + E_{\mathrm{mol}}(B) - i0^+ \\ &\quad - \frac{g^2}{4\pi}\left[\frac{2\Lambda}{(1+c)} - \frac{1}{1+c}\sqrt{\frac{-\omega}{1+c} + \frac{c}{(1+c)^2}\boldsymbol{q}^2 - i0^+}\right]. \end{aligned} \tag{B.2}$$

The theory is renormalized by a redefinition of the bare detuning E_{mol} which cures the UV divergency. It can be inferred from the scattering amplitude which in the mass-imbalanced case is given by

$$f(k) = \frac{\hbar^2 m_r}{2\pi}\frac{g^2}{P^R_{vac,\phi}(\omega = (1+c)k^2, \mathbf{0})} = \frac{1}{4\pi(1+c)}\frac{g^2}{P^R_{vac,\phi}(\omega = (1+c)k^2, \mathbf{0})} = \frac{1}{-1/a - ik}. \tag{B.3}$$

Furthermore, the scattering length in dependence of the magnetic field close to the Feshbach resonance is given by

$$a(B) = -\frac{\hbar^2}{2m_r \mu r^*(B - B_0)} = -\frac{1+c}{\mu r^*(B - B_0)}. \tag{B.4}$$

From (see Eq. (B.3))

$$P^R_{vac,\phi}(0, \mathbf{0}) = -\frac{g^2}{4\pi(1+c)a} \tag{B.5}$$

then instantly follows the identification

$$g^2 = \frac{4\pi(1+c)}{r^*} \tag{B.6}$$

for the Yukawa coupling g, and for the resonance shift $\Delta B = \mu(B_0 - B_{\mathrm{res}})$ we find

$$\mu(B_0 - B_{\mathrm{res}}) = \frac{2(1+c)}{r^*}\Lambda. \tag{B.7}$$

For contact interactions, Λ goes to infinity and the resonance shift becomes infinite. Using Eqn. (B.6) and (B.7) we obtain the inverse, molecule propagator in vacuum

$$\begin{aligned} P^R_{vac,\phi}(\omega,\boldsymbol{q}) &= -\omega + \frac{c}{1+c}\boldsymbol{q}^2 - i0^+ + \overbrace{\mu(B-B_0)}^{-\frac{1+c}{r^* a}} \\ &\quad + \underbrace{\frac{g^2}{4\pi(1+c)}}_{(1+c)/r^*} \sqrt{\frac{-\omega}{1+c} + \frac{c}{(1+c)^2}\boldsymbol{q}^2 - i0^+}. \end{aligned} \tag{B.8}$$

It is instructive to analyze the spectrum of this propagator in some detail and compare it to the spectrum obtained from the molecule propagator of the two-channel model which features a finite, physical range σ and which we studied in Chapter 2, cf. Eq. (2.24). In view of our discussion of compositeness in Section 4.5, we focus in particular on the quasiparticle weight Z_ϕ of the molecule across the Feshbach resonance.

Spectrum of the resonance model ($\sigma = 0$). In Fig. B.1(a) we show the spectral function A_ϕ as defined in Eq. (4.45) with $G^R_\phi = 1/P^R_{vac,\phi}$ from Eq. (B.8) at zero momentum as function of the inverse, dimensionless scattering length r^*/a. One clearly discerns the bound state peak at negative frequencies and positive scattering length a with energy given by the generalization of Eq. (2.36) to mass-imbalance,

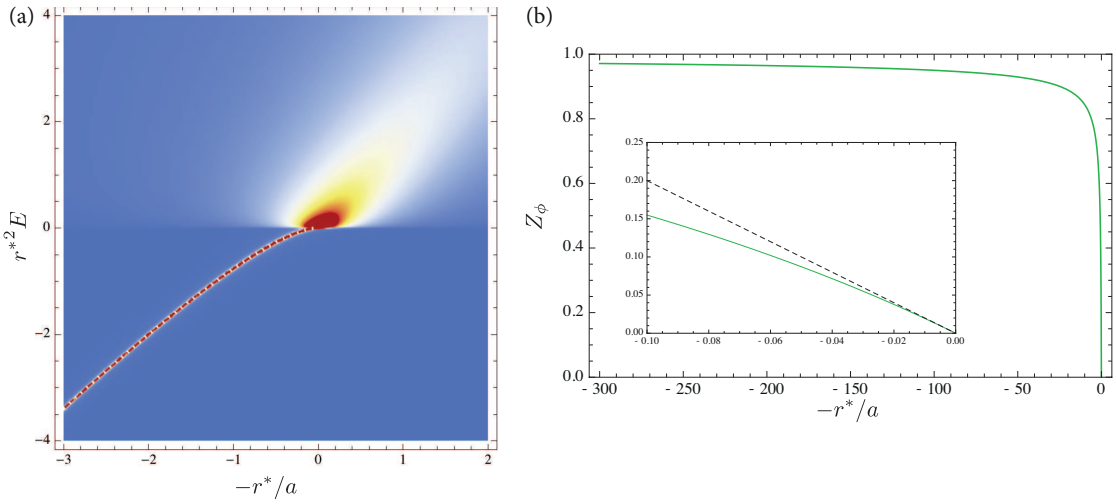

FIGURE B.1: *(a) Spectral function $A_\phi(\omega,\mathbf{0})$ of the molecule in vacuum at zero momentum in units of r^*. (b) Quasiparticle weight Z_ϕ of the molecule. Inset: Spectral weight Z_ϕ close to resonance. For both figures we choose the mass-balanced situation, $c = 1$.*

$$E_D = -\frac{1+c}{4r^{*2}}\left(1-\sqrt{1-\frac{4r^*}{a}}\right)^2 . \tag{B.9}$$

For positive a far away from resonance the molecule is an elementary particle – it has complete overlap with its bare counterpart – and its quasiparticle weight approaches unity, see Fig. B.1(b). For the resonance model (B.1) is possible to derive an analytical expression for Z_ϕ which is given by

$$Z_\phi = 1/\left(1+\frac{1}{1-\sqrt{1+4r^*/a}}\right), \tag{B.10}$$

and which is independent of the mass ratio c. As the Feshbach resonance is approached the molecular bound state looses its quasiparticle weight, which is transferred into the continuum of states of unbound atoms at positive frequencies. This continuum of states then carries most of the spectral weight. Note that $A_\phi(\omega, \boldsymbol{q})$ fulfills the sum rule Eq. (4.32) for arbitrary values of a. At the resonance $a \to \infty$, Z_ϕ goes to zero and the molecule dissolves completely, see Fig. B.1(b,inset). For negative scattering length $a < 0$ the quasiparticle pole ceases to exist and the molecule is a purely composite particle with $C = 1 - Z_\phi = 1$. Remarkably, the molecule remains purely composite for arbitrary values of $a < 0$. This is due to the infinite resonance shift given by Eq. (B.7) which prohibits the interacting molecule to approach the bare molecular state even far from resonance although the interactions are weak in this regime. This is fundamentally different in the more realistic two-channel model of finite range σ as discussed below and in Chapter 2.

Spectrum of a realistic finite range model ($\sigma > 0$). Let us now analyze the spectrum of the molecule propagator for the more realistic two-channel model (2.23) in Chapter 2. In this model $P_{vac,\phi}$ is given by Eq. (2.24). First note that the spectral function again fulfills the sum rule (4.32) for an arbitrary value of a.

In Fig. B.2(a) we show the spectral function $A_\phi(\omega, \mathbf{0})$ as function of σ/a for a closed-channel dominated resonance of width $r^*/\sigma = 3$, whereas in Fig. B.2(b) the spectrum for an open-channel dominated resonance characterized by $r^*/\sigma = 0.05$ is shown. Note that in the, compared to the resonance model (where $\sigma = 0$), more realistic finite range model (2.23) σ sets the scale of the two-body problem. Only this allows the definition of open- and closed-channel dominated resonances by comparing the actual short-distance scale σ to r^*. Contrarily, in the resonance model such a comparison is not possible as $\sigma \to 0$, and only a notion of narrow or broad resonances in the sense of $k_F r^*$ being large or small, respectively, is possible. From this perspective the finite range model with $\sigma > 0$ allows for a much more detailed study of physics at a Feshbach resonance. Nonetheless, for the many-body problem considered below we will focus on the simpler resonance model because it allows already a quite accurate description of the physics at low energies and close to resonance.

In Fig. B.3(a) we show the quasiparticle weight of the molecule for the open-channel dominated resonance of width $r^*/\sigma = 0.05$, cf. Fig. B.2(b). As the resonance is approached the bound-state molecule (green line) becomes a composite particle. In fact, the universal dimer

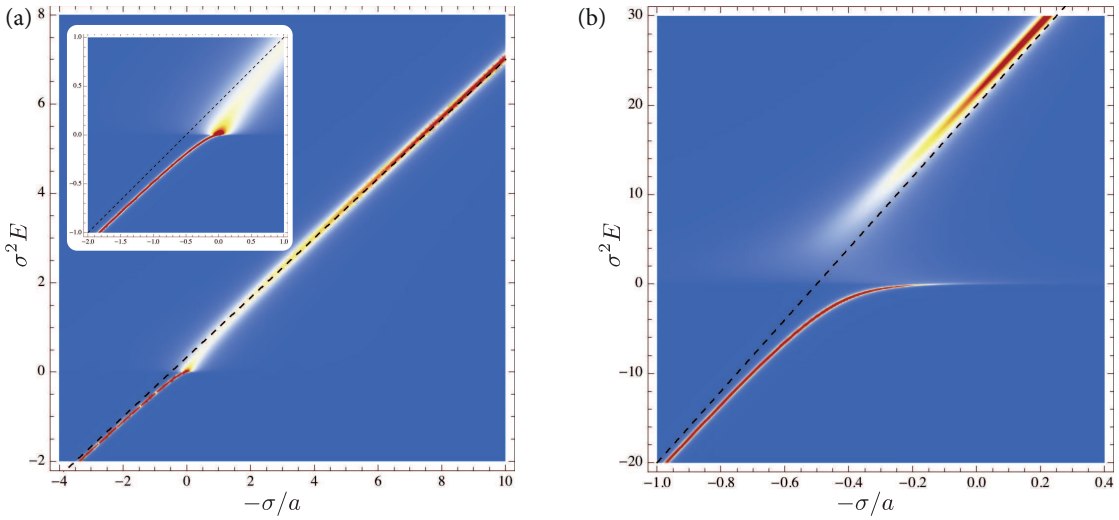

FIGURE B.2: *Spectral function $A_\phi(\omega, \mathbf{0})$ of the molecule in vacuum at zero momentum in dependence of the dimensionless inverse scattering length σ/a for the finite range two-channel model* (2.23). *(a) Closed-channel dominated resonance of width $\sigma/r^* = 1/3$; inset: same spectrum close to the resonance. (b) Open-channel dominated resonance of width $\sigma/r^* = 20$.*

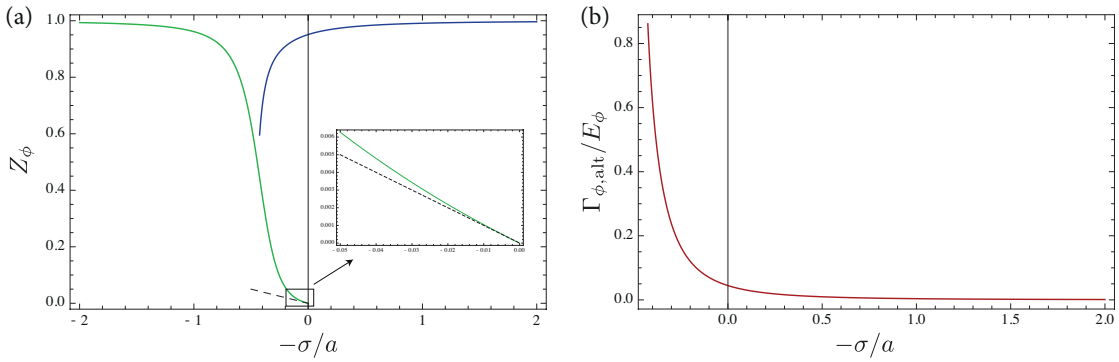

FIGURE B.3: *(a) Quasiparticle weight Z_ϕ of the molecule in vacuum as function of the dimensionless inverse scattering length σ/a for an open-channel dominated resonance. The bound state at negative energy (green line) looses weight which is mostly transferred to the renormalized closed-channel bound state at positive energies (blue line). Only a fraction of the weight is found in the scattering continuum; inset: weight of the bound state close to resonance. (b) Decay width Γ_ϕ according to the approximate formula* (4.52) *of the renormalized closed-channel molecule at positive energy compared to its energy E_ϕ. Although carrying a substantial fraction of spectral weight the closed-channel molecule is highly unstable close to the resonance due to the decay into unbound atoms in the scattering continuum. It becomes, however, a well-defined quasiparticle away from resonance reflected by $Z_\phi \to 1$ and $\Gamma_\phi/E_\phi \to 0$.*

has again a quasiparticle weight which vanishes linearly in $1/a$ close to the resonance (black dashed line). Contrarily to the resonance model, however, most of the lost spectral weight is transferred to the closed-channel molecular state at positive energy, visible as a rather broad peak in Fig. B.2(b), and which carries most of the weight (blue line Fig. B.3(a)). This is different from the resonance model where the weight lost in the bound state at negative energy is transferred solely into the scattering continuum at positive energies. From our analysis here, the reason for this difference becomes apparent: in the resonance model, the resonance shift is infinite so that there is just no bare state at finite, positive energies into which the weight could be transferred.

The molecular state in the finite range model at positive energies can decay into unbound atoms in the scattering continuum due to the coupling between the open and closed channel. For this reason the molecular state is relatively short-lived close to the resonance. We show the width Γ_ϕ/E_ϕ (using the approximate formula (4.52)) of the molecular state at its quasiparticle energy $E_\phi > 0$ in Fig. B.3(b). We find that the molecule is indeed not a well defined particle close to resonance. For $a \to 0^-$ it becomes, however, again a stable quasiparticle excitation with almost no composite character, $C_\phi = 1 - Z_\phi \to 0$.

B.2 In-medium molecule propagator

After having analyzed the two-body problem in some detail, let us come back to the many-body polaron problem. Within the non-self-consistent T-matrix approximation we have to first derive the many-body T-matrix which is, within our bosonic-fermionic model Eq. (B.1) equivalent to the molecule propagator $\mathcal{G}_\phi$ in the medium of the $\uparrow$-Fermi sea. It is given by the resummed ladder diagram and separates into two parts:

$$\begin{aligned}\mathcal{G}_\phi^{-1}(\nu,\boldsymbol{q}) &= \overbrace{P_\phi^\Lambda - \frac{g^2}{(2\pi)^2}\int_0^\Lambda d\,p\,p^2 \int_{-1}^{1} dx \frac{1}{-i\nu + c(\boldsymbol{p}+\boldsymbol{q})^2 + \boldsymbol{p}^2 - \mu_\downarrow - \mu_\uparrow}}^{\text{A}} \\ &+ \underbrace{\frac{g^2}{(2\pi)^2}\theta(\mu_\uparrow)\int_0^{\sqrt{\mu_\uparrow}} d\,p\,p^2 \int_{-1}^{1} dx \frac{1}{-i\nu + c(\boldsymbol{p}+\boldsymbol{q})^2 + \boldsymbol{p}^2 - \mu_\downarrow - \mu_\uparrow}}_{\text{B}}. \quad \text{(B.11)}\end{aligned}$$

While the terms denoted by A are given by the solution of the two-body problem when including the additional chemical potentials into Eq. (B.8), the term B represents the effect of the medium. It can be calculated in an analytical form which facilitates a fast numerical calculation of the polaron selfenergy in Eq. (B.13) below.

In the calculation the minority chemical potential $\mu_\downarrow$ is fixed to yield the desired density of $\downarrow$-atoms. In Fig. B.4 we show the in-medium spectral function of the field ϕ at unitarity for two different mass ratios and for a finite density of *both* the $\uparrow$- and $\downarrow$-atoms in the case of an open-channel dominated Feshbach resonance: in Fig. B.4(a) for the mass-balanced case $c = 1$ and in Fig. B.4(b) for $c = 6/40$ as appropriate for a mixture of ^{6}Li and ^{40}K atoms.

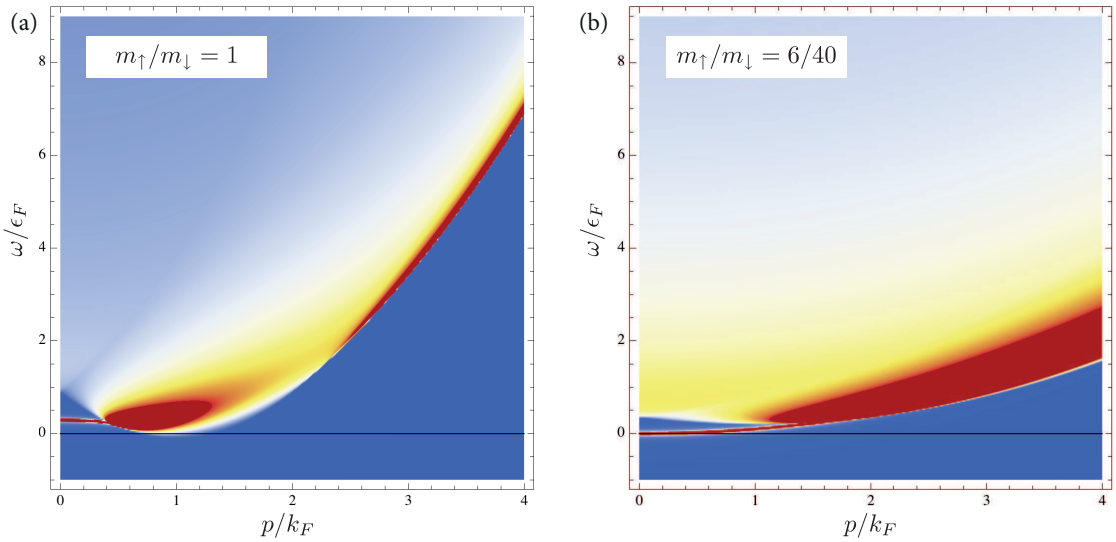

FIGURE B.4: *In-medium spectral function A_ϕ at unitarity for the two mass ratios $c = 1$ [(a)] $c = 6/40$ [(b)]. The minority chemical potential is chosen to take the value of the critical 'magnetic field' $h_\phi = (\mu_\uparrow - \mu_\downarrow)/2$ at which the molecule starts to have spectral weight at negative frequencies implying a finite occupation of dimers.*

In both cases the chemical $\mu_\downarrow$ is chosen to be at the critical value $h_\phi = (\mu_\uparrow - \mu_\downarrow)/2$ where the spectral function $A_\phi(\omega, \boldsymbol{p})$ begins to have weight at negative frequencies, so that a finite occupation of dimers emerges. Since the calculation was performed at zero temperature, these dimers condense and the system becomes superfluid. Remarkably, in the mass-balanced case the minimum of the dimer spectral function is at a *finite* momentum which may be interpreted as the onset of the transition to a superfluid of the FFLO type [309, 310]. Note, whether at finite density FFLO is really the ground state is an open problem. For mass imbalance $c > 1$ this effect is even more pronounced. It is, however, likely that this effect will disappear when the feedback of the fermion selfenergy into the T-matrix loop is properly included. For a mass imbalance $c = 6/40$ [Fig. B.4(b)] the minimum of A_ϕ remains at zero momentum (corresponding to a positive effective mass of the dimer) and the non-selfconsistent T-matrix approach thus predicts a transition to a 'standard' superfluid of the BCS type. Also note that the spectral function of the dimer A_ϕ bears much resemblance with the two-dimensional case, see f.e. Fig. A.2 in Appendix A.

B.3 Polaron spectral function

Let us now analyze the polaron problem of the mass-imbalanced Fermi gas with mass ratio $c = 6/40$. The calculation is analogous to the case of two spatial dimensions and the polaron

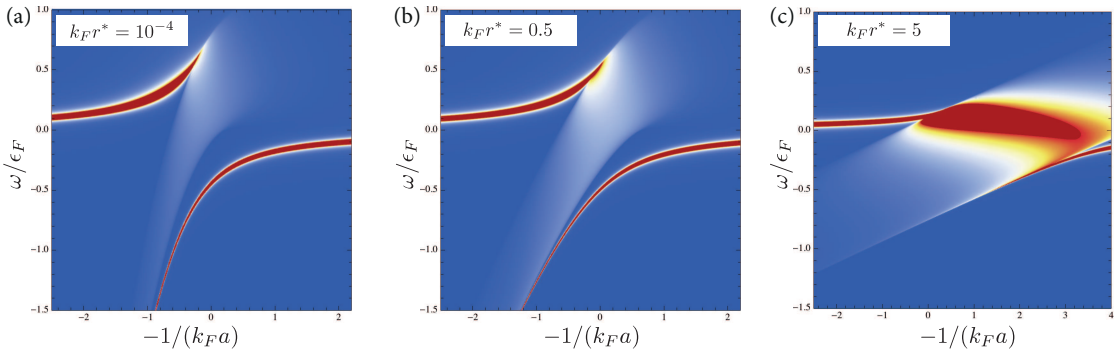

FIGURE B.5: *Polaron spectral function* $A_\downarrow(\omega, \boldsymbol{q} = 0)$ *versus dimensionless, inverse scattering length for various widths of the Feshbach resonance and mass ratio* $c = 6/40$. *(a)* $k_F r^* = 10^{-4}$ *(b)* $k_F r^* = 0.5$ *(c)* $k_F r^* = 5$.

spectral function

$$A_\downarrow(\omega, \boldsymbol{q}) = 2\mathrm{Im}[-\omega - i0 - \mu_\downarrow + \varepsilon_{\boldsymbol{q}} + \Sigma_\downarrow(\boldsymbol{q}, \omega)]^{-1} \tag{B.12}$$

is derived from the calculation of the polaron selfenergy which is given by

$$\Sigma_\downarrow(\boldsymbol{q}, \omega) = g^2 \int_{k<k_F} \frac{d^3k}{(2\pi)^3} \mathcal{G}_\phi(\boldsymbol{k} + \boldsymbol{q}, \varepsilon_{\boldsymbol{k}} - \mu_\uparrow + \omega), \tag{B.13}$$

with the dimer propagator from Eq. (B.11). As discussed in detail in Chapter 4, in the polaron problem the chemical potential $\mu_\downarrow$ is fixed such that neither the dimer nor the impurity has a finite occupation.

In Fig. B.5 we show the polaron spectral function $A_\downarrow(\omega, \boldsymbol{q} = 0)$ at zero momentum as function of the dimensionless interaction strength $1/(k_F a)$ for a mass-imbalanced Fermi gas with mass ratio $c = 6/40$. In Fig. B.5(a) and (b) the results for a broad and a resonance of intermediate width $k_F r^* = 10^{-4}$ and $k_F r^* = 0.5$, respectively, are shown and they are similar to the result for the mass-balanced case. The spectrum, however, changes dramatically when a narrow resonance is considered as shown e.g. in Fig. B.5(c) for $k_F r^* = 5$. On the one hand, the attractive polaron branch appears only for very weak attraction $k_F a \to 0^-$ and spectral weight is transferred to a more pronounced molecule-hole continuum close to resonance and in between the two polaron branches (note, the plot-range of $A_\downarrow$ is the same for all plots in Fig. B.5). On the other hand, the repulsive polaron shows an enhanced lifetime. This indicates that narrow resonances help to stabilize the repulsive Fermi gas of cold atoms. Note, however, that the energy of the repulsive polaron is shifted to lower energies. In fact, the energy of the repulsive polaron remains *below* the Fermi energy of the majority for arbitrary interaction strength. Therefore it is always preferable to inject an impurity into the ↑-Fermi sea instead of increasing the density of majority atoms. This shows that the increase of the lifetime of the repulsive branch comes at a prize as it becomes at the same time impossible

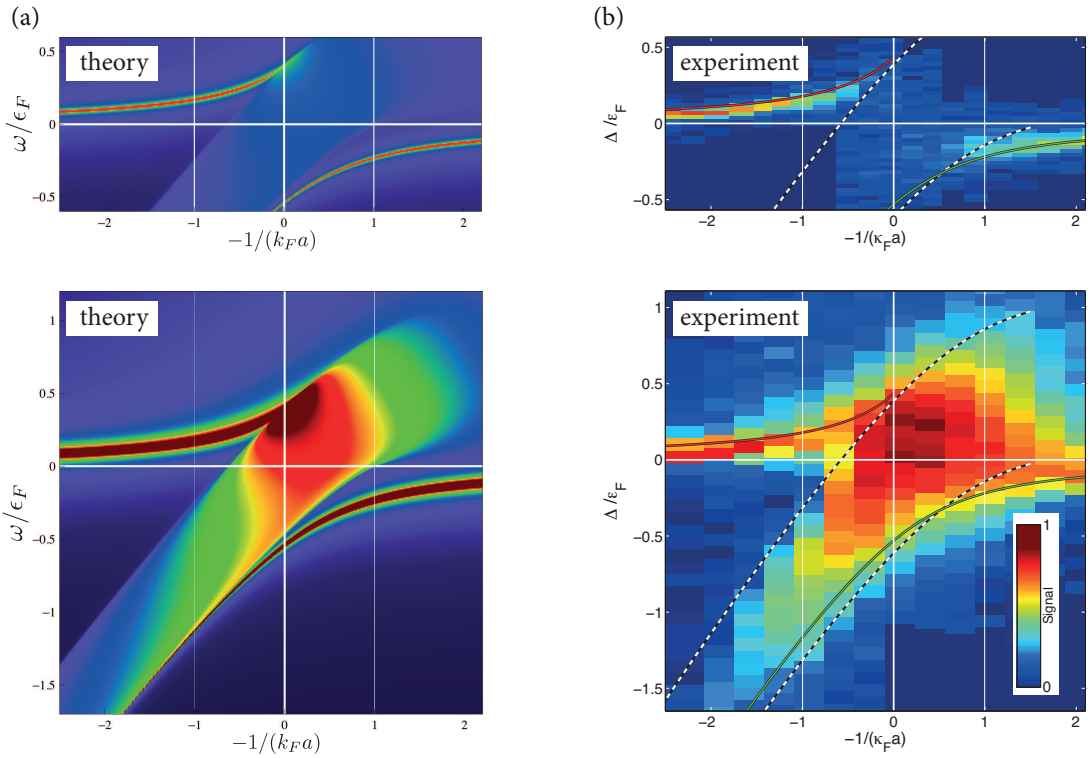

FIGURE B.6: *As discussed in Chapter 4, for small occupation of the minority species in the initial state, the rf response is accurately described by* $A_\downarrow(\omega, \boldsymbol{q} = 0)$ *and can be compared to the experimental rf response. (a) Polaron spectral function* $A_\downarrow(\omega, \boldsymbol{q} = 0)$ *versus dimensionless, inverse scattering length for a Feshbach resonance of width* $k_F r^* = 0.95$*. Both panels show the same spectral function. In the lower panel the plot range is chosen so that the molecule-hole continuum is saturated at unitary in order to mimic the high power rf pulse used in the experiment [64]. (b) Experimental rf response of an resonance of the same width* $k_F r^* = 0.95$*.* ***(upper panel)*** *Low power rf spectrum.* ***(lower panel)*** *High power rf spectrum which allows to access the final state spectral function in regions of small weight. The experimental figures in (b) are taken from [64] with the courtesy of Grimm* et al..

to cross the threshold to the onset of saturated ferromagnetism: again, the Stoner transition defies a quantum simulation with cold atoms.

Finally, we compare our results to experimental data. The polaron problem has been studied experimentally in [64]. In the following we calculate the polaron spectral function for parameters as appropriate for this experiment [64], where a mixture of ^{6}Li and ^{40}K atoms had been prepared with a Fermi energy of the majority ^{6}Li atoms of $\epsilon_F = h \times 44$kHz. This corresponds to a Fermi wave vector $k_F = 1/2850 a_0$. Furthermore, the width of the resonance is $r^* = 2700 a_0$ so that $k_F r^* \approx 0.95$. In the experiment [64] the mixture in the initial state was strongly spin-imbalanced. In this case, the rf pulse addresses only the low momentum

part of the final state spectral function so that $A_\downarrow(\omega, \boldsymbol{q} = 0)$ is expected to accurately reflect the expected rf response of the system, cf. Eq. (4.60) in Chapter 4. In Fig. B.6(b) we show the experimentally measured rf response from [64]. While the upper panel shows the low power rf response, the lower panel corresponds to the response when the rf is driven at high power saturating the final state spectral function. In Fig. B.6(a) we show our theoretical result for the spectral function $A_\downarrow(\omega, \boldsymbol{q} = 0)$ at zero momentum as function of the inverse, dimensionless interaction strength $1/(k_F a)$ which is expected to reflect rather accurately the rf response. There is no fit parameter involved in the calculation and we use the experimental values of k_F and r^* as input. We find that our result indeed compares remarkably well to the experimental data.

Appendix C

The functional renormalization group

In this Appendix we briefly introduce the functional renormalization group which is a modern realization of Wilson's renormalization group concept [97]. It is used in quantum and statistical field theory, especially when dealing with strongly interacting systems (for reviews see [166, 167, 168, 169, 170, 171, 172, 173, 174, 175], for a review which focuses on the application of the functional renormalization group to the few-body problem, and on which we base this appendix, we refer to [46]). The method combines functional methods of quantum field theory with the physically intuitive renormalization group idea. The main motivation for its development was the observation that it is often more useful and transparent to perform the integration of quantum fluctuations in continuous steps rather than doing this at once. The renormalization technique allows to interpolate smoothly between the known microscopic laws and the complicated macroscopic phenomena. In this sense, it bridges the transition from simplicity of microphysics to complexity of macrophysics.

In quantum field theory (QFT) quantum fields are associated with particles [311, 312]. For example, in the Euclidean, grand canonical action

$$S = \int d\tau \int d^3x \, \left\{ \psi^* \left(\partial_\tau - \tfrac{\Delta}{2m} - \mu \right) \psi + g_\Lambda (\psi^* \psi)^2 \right\}, \tag{C.1}$$

which corresponds to the Hamiltonian in Eq. (1.3), the complex scalar field ψ represents a non-relativistic bosonic particle. In QFT, the effective action Γ is a quantum analogue of the classical action functional S. It depends on the fields of a given theory and includes all quantum fluctuations. Variation of Γ with respect to fields yields exact quantum field equations. Mathematically, Γ is the generating functional of one-particle irreducible vertices. Interesting physics, like propagators (two-point Green functions) and scattering amplitudes (higher-point amputated, connected Green functions), can be extracted from Γ in a straightforward way. In a generic interacting field theory the effective action Γ is, however, difficult to obtain. The functional renormalization group provides a practical tool to calculate Γ based on renormalization group ideas.

The central idea of functional renormalization is the introduction of a scale-dependent effective action functional Γ_k often called average action or flowing action. The average action Γ_k interpolates smoothly between the known microscopic action S and the full quantum effective action Γ where k is the RG sliding scale. The dependence on the sliding scale k is introduced by adding an infrared regulator term to the microscopic action. This regulator term has the purpose to suppress fluctuations below the scale k and it is introduced by defining (for

a bosonic field $\tilde{\psi}$) the k-dependent Schwinger functional $W_k[J]$

$$e^{W_k[J]} = \int \mathcal{D}\tilde{\psi}\, e^{-S[\tilde{\psi}]-\Delta S_k[\tilde{\psi}]+\int_x J\tilde{\psi}}. \tag{C.2}$$

The difference to the standard QFT Schwinger functional $W[J]$ is the additional term $\Delta S_k[\tilde{\psi}]$ in the exponential in Eq. (C.2). $\Delta S_k[\tilde{\psi}]$ is quadratic in the fields. In momentum space it reads

$$\Delta S_k[\tilde{\psi}] = \int_Q \tilde{\psi}^*(Q) R_k(Q) \tilde{\psi}(Q). \tag{C.3}$$

where we use the abbreviations $Q = (q_0, \boldsymbol{q})$ and $\int_Q = \int_{q_0}\int_{\boldsymbol{q}}$ with $\int_{q_0} = \frac{1}{2\pi}\int_{-\infty}^{\infty} dq_0$ (at $T = 0$) and $\int_{\boldsymbol{q}} = \frac{1}{(2\pi)^3}\int d^3q$. The infrared regulator function $R_k(Q)$ is not fixed in the unique way, but must satisfy three important conditions. First $R_k(Q)$ should suppress infrared modes below the scale k, i.e.,

$$R_k(Q) > 0, \tag{C.4}$$

for $Q^2 \ll k^2$. This adds effectively an additional masslike term to the particle suppressing its propagation if its momentum Q is below the RG scale k. Second, the regulator must vanish in the infrared

$$\lim_{k\to 0} R_k(Q) = 0. \tag{C.5}$$

With this condition it is guaranteed that W_k equals the standard, exact Schwinger functional W in the infrared, $W = W_{k=0}$. Finally, we should recover the classical action in the ultraviolet and thus we demand

$$\lim_{k\to\infty} R_k(Q) = \infty. \tag{C.6}$$

Apart from these requirements, the regulator can be chosen arbitrarily. Nevertheless, it is recommended to pick the regulator carefully depending on a concrete physical problem. Moreover, one should better choose a regulator that respects as many symmetries of the studied problem as possible. For our purpose it is convenient to choose $R_k(Q) = R_k(\boldsymbol{q})$ independent of the frequency argument q_0. Often, $R_k(\boldsymbol{q})$ is chosen to decay for large $\boldsymbol{q}^2 \gg k^2$. As can be seen from Eq. (C.2) the regulator R_k suppresses fluctuation modes with momenta $\boldsymbol{q}^2 \lesssim k^2$ by giving them a large "mass" or "gap", while high momentum modes are not (or only mildly) affected. Thus, W_k includes all fluctuations with momenta $\boldsymbol{q}^2 \gtrsim k^2$.

The flowing action Γ_k is now obtained by subtracting from the Legendre transform of the Schwinger functional,

$$\tilde{\Gamma}_k[\psi] = \int J\psi - W_k[J] \tag{C.7}$$

with $\psi = \delta W_k[J]/\delta J$, the cutoff term

$$\Gamma_k[\psi] = \tilde{\Gamma}_k[\psi] - \Delta S_k[\psi]. \tag{C.8}$$

The reason why the flowing action $\Gamma_k[\psi]$ is the central object to study is that it obeys the elegant and exact functional flow equation

$$\partial_k \Gamma_k[\psi] \;=\; \frac{1}{2}\mathrm{STr}\,\partial_k R_k\,(\Gamma_k^{(2)}[\psi]+R_k)^{-1}, \tag{C.9}$$

derived by Wetterich [176]. In Eq. (C.9) ∂_k denotes a derivative with respect to the sliding scale k at fixed values of the fields. The functional differential equation for $\Gamma_k[\psi]$ must be supplemented with the initial condition $\Gamma_{k\to\Lambda} = S$, where the "classical action" $S[\psi]$ describes the physics at the microscopic ultraviolet scale $k = \Lambda$. Importantly, in the infrared limit $k \to 0$ the full quantum effective action $\Gamma[\psi] = \Gamma_{k\to 0}[\psi]$ is obtained. In the Wetterich equation STr denotes a supertrace operation which sums over momenta, frequencies, internal indices, and different fields (taking bosons with a plus and fermions with a minus sign).

It is important to note that the exact flow equation for $\Gamma_k[\psi]$ has a one-loop structure. This is a significant simplification compared for example to perturbation theory where all multi-loop Feynman diagrams must be computed to obtain exact results. Remarkably, the flow equation (C.9) implicitly takes care of this. Note however, that Eq. (C.9) is a nonlinear functional differential equation. Indeed, on the right-hand side in the denominator appears the second functional derivative $\Gamma_k^{(2)}[\psi]$ which is a functional of the fields. For this reason it is usually not possible to find closed solutions to Eq. (C.9) and one has to rely on a truncation of Γ_k.

To make the implications of (C.9) more transparent we write the flowing action as an expansion in some complete set of operators

$$\Gamma_k[\psi] = \sum_{n=0}^{\infty} c_n\, \mathcal{O}[\psi]. \tag{C.10}$$

The renormalization group evolution of Γ_k traces a trajectory in the theory space, which is the infinite-dimensional space of all possible couplings $\{c_n\}$ allowed by the symmetries of the problem. At the microscopic ultraviolet scale $k = \Lambda$ one starts with the initial condition $\Gamma_{k=\Lambda} = S$. As the sliding scale k is lowered, the flowing action Γ_k evolves in theory space according to the functional flow equation (C.9). Accordingly, different couplings c_n become running or flowing under the renormalization group evolution. The choice of the regulator R_k is not unique, which introduces some scheme dependence into the renormalization group flow. For this reason, different choices of the regulator R_k correspond to the different paths in theory space. At the infrared scale $k = 0$, however, the full effective action $\Gamma_{k=0} = \Gamma$ is recovered for every choice of the cutoff R_k, and all trajectories meet at the same point in the theory space. When an approximation of Γ_k is employed, however, a regulator dependence of Γ is introduced.

Appendix D

BCS transition temperature and Gorkov correction from functional renormalization

In this Appendix we show how the critical temperature T_c for superfluid pairing in a spin-balanced Fermi gas can be computed from the functional renormalization group. If one only includes pairing fluctuations in the particle/particle (p/p) channel one arrives at the standard BCS result [247] (for a derivation using the fRG, see e.g. also [213])

$$T_c/T_F = \frac{8e^\gamma}{\pi e^2} e^{-\frac{\pi}{2}\frac{1}{k_F|a|}}. \tag{D.1}$$

This result, however, neglects the effect of particle-hole (p/h) fluctuations which lower the critical temperature by a factor of $(4e)^{1/3} \approx 2.2$ as shown by Gorkov and Melik-Barkhudarov [249]. A physical interpretation of this suppression in terms of the exchange of spin fluctuations is given in [313]. The inclusion of p/h fluctuations in the fRG framework had been studied approximately in previous work [214]. In this Appendix we calculate the correction exactly from fRG flow equations.

D.1 Microscopic action and pairing instability

We consider a Fermi gas described by the purely fermionic, classical action [cf. (4.4)]

$$S = \int_{\boldsymbol{x},\tau} \Big\{ \sum_{\sigma=\uparrow,\downarrow} \psi^*_\sigma [\partial_\tau - \Delta - \mu_\sigma] \psi_\sigma + g_\Lambda \psi^*_\uparrow \psi^*_\downarrow \psi_\downarrow \psi_\uparrow \Big\}. \tag{D.2}$$

which is equivalent to the mixed bosonic-fermionic action [cf. (4.5)]

$$S = \int_{\boldsymbol{x},\tau} \Big\{ \sum_{\sigma=\uparrow,\downarrow} \psi^*_\sigma [\partial_\tau - \Delta - \mu_\sigma] \psi_\sigma + \phi^* m^2_{\phi,\Lambda} \phi + h(\psi^*_\uparrow \psi^*_\downarrow \phi + h.c.) \Big\}, \tag{D.3}$$

obtained by a Hubbard-Stratonovich transformation in the pairing channel with the pairing field $\phi \sim \psi\psi$. Integrating out the pairing field ϕ by, for instance, the insertion of its classical equation of motion

$$\phi^* = -\frac{h}{m^2_\phi} \psi^*_\uparrow \psi^*_\downarrow \tag{D.4}$$

into Eq. (D.3) yields the identification $g_\Lambda = -h^2/m^2_{\phi,\Lambda}$. Thus an attractive contact interaction $g_\Lambda < 0$ directly implies a positive 'mass' gap $m^2_{\phi,\Lambda} > 0$.

We are interested in the regime where $k_F|a| \ll 1$. Then the fermionic propagators are assumed not to be renormalized and according to power-counting the momentum dependence of the fermionic vertex (or the dimer propagator, respectively) can be neglected. Based on this argument we devise a truncation of the effective flowing action Γ_k in a leading order vertex and derivative expansion which amounts in only promoting the couplings g and m^2_ϕ, respectively, to be RG scale dependent, $g \to g_k$, and $m^2_\phi \to m^2_{\phi,k}$. Specifically, the purely fermionic truncation reads

$$\Gamma_k = \int_{\boldsymbol{x},\tau} \Big\{ \sum_{\sigma=\uparrow,\downarrow} \psi^*_\sigma [\partial_\tau - \Delta - \mu_\sigma]\psi_\sigma + g_k \psi^*_\uparrow \psi^*_\downarrow \psi_\downarrow \psi_\uparrow \Big\}. \tag{D.5}$$

The corresponding mixed, bosonic-fermionic truncation is given by

$$\Gamma_k = \int_{\boldsymbol{x},\tau} \Big\{ \sum_{\sigma=\uparrow,\downarrow} \psi^*_\sigma [\partial_\tau - \Delta - \mu_\sigma]\psi_\sigma + \phi^* m^2_{\phi,k} \phi + h(\psi^*_\uparrow \psi^*_\downarrow \phi + h.c.) \Big\}. \tag{D.6}$$

When considering only the flow in the p/p channel, at this level of truncation the identification of g with m^2_ϕ holds on every RG scale,

$$g_k = -\frac{h^2}{m^2_{\phi,k}}. \tag{D.7}$$

Note that when the Gorkov correction due to p/h fluctuations are considered the fermionic truncation (D.5) will be more convenient because staying within the truncation (D.6) then necessitates the use of a rebosonization procedure [214].

The specific values of g_k and $m^2_{\phi,k}$, respectively, depend, besides the scattering length a, on the temperature T and density $n = k_F^3/(3\pi^2)$ set by the chemical potential μ. The onset of (local) superfluidity and the breakdown of Fermi liquid theory is indicated by a divergence in the coupling g_k during the RG flow which is equivalent to the emergence of a negative mass gap $m^2_{\phi,k} < 0$ and a corresponding symmetry breaking in the effective potential $U(\phi^*\phi)$.

The (pseudo-)critical temperature T_c can be determined by tuning the temperature in such a way that the divergence in g_k occurs exactly in the infrared. The condition for the onset of superfluidity then reads

$$g_{IR}\Big|_{T_c} = \infty. \tag{D.8}$$

This condition corresponds to the Thouless criterion and gives strictly speaking only an upper bound on T_c: for $T < T_c$ the flow enters the symmetry broken regime where Goldstone bosons associated with the Mexican hat structure of the effective potential $U(\phi^*\phi)$ in the pairing field ϕ lead to a further suppression of T_c. Indeed, in two spatial dimensions it is for

the Goldstone bosons that symmetry is restored in the flow for *any* finite temperature so that no condensate appears unless $T \equiv 0$ [314, 315, 316]. In fact, if one wants to study the flow also in the symmetry broken phase, it is more convenient to consider the bosonic truncation (D.6) since here the full functional dependence of the effective potential can be studied. In the following we are interested, however, only in the derivation of the critical temperature according to (D.8) and hence we will only consider the purely fermionic truncation (D.5) where the only running coupling is given by g_k.

In order to derive the RG flow equation of g_k we have to find the correct projection of the full RG equation

$$\partial_k \Gamma_k = \frac{1}{2} \tilde{\partial}_k \mathrm{STr} \ln[\Gamma_k^{(2)} + R_k], \tag{D.9}$$

onto g_k. In order to find this projection it is helpful to take a step back and to realize that in general during the RG flow the scale dependent vertex function $\Gamma_k^{(4)}$ corresponding to the interaction term

$$\sim \int_{P_i} \Gamma_k^{(4)}(P_1, P_2, P_1') \psi_\sigma^*(P_1) \psi_{\sigma'}^*(P_2) \psi_{\sigma'}(P_1') \psi_\sigma(P_1 + P_2 - P_1') \tag{D.10}$$

acquires a complicated momentum and energy dependence, where the P_i denote four-momenta $P_i = (\omega_i, \boldsymbol{p}_i)$ as illustrated in Fig. D.1(a). Since we are only interested in the regime where

FIGURE D.1: *(a) The four-fermion vertex $\Gamma^{(4)}$ acquires a complicated dependence on the three independent four-momenta P_1, P_1', and P_2. (b) Reduced momentum dependence. In the weak coupling limit scattering takes place close to the Fermi surface. Considering only the pairing instability, the parametrization of $\Gamma^{(4)}$ in terms of the center-of-mass momentum of the pair $\boldsymbol{q}$ is convenient. For zero-momentum pairs, $\boldsymbol{q} = 0$, and the vertex is only dependent on the angle between $\boldsymbol{p}_1$ and $\boldsymbol{p}_1'$.*

$k_F|a| \ll 1$ and $T \ll T_F$ this dependence can be simplified considerably. First, in this regime the scattering of fermions takes place close to the Fermi surface. For this reason the energy of the incoming atoms is zero according to the perturbative dispersion relation $E = \boldsymbol{p}^2 - \mu$ which vanishes for $|\boldsymbol{p}| = k_F$. This dispersion relation is valid since the fermions are assumed not to be renormalized. Furthermore, we consider the instability towards superfluid pairing. Therefore we may consider the momentum configuration shown in Fig. D.1(b). When studying the full $\boldsymbol{q}$ dependence of the vertex one finds that the leading instability takes place for zero-momentum pairs so that $\boldsymbol{q} = 0$, which implies that no phase of the Fulde-Ferrell-Larkin-Ovchinnikov (FFLO) type appears [309, 310]. This finally implies that the vertex is only a

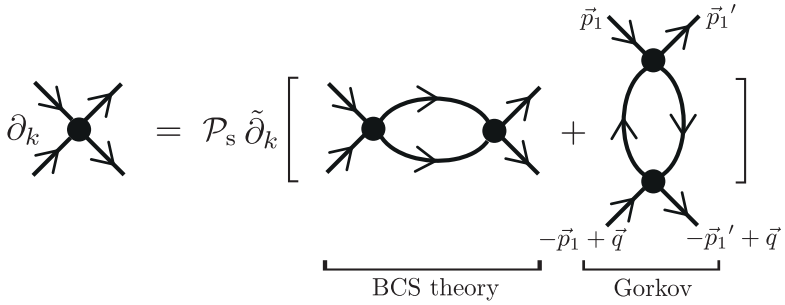

FIGURE D.2: *Diagrammatical representation of the flow equation of the point-like coupling g_k (black solid circle). The operator $\mathcal{P}_s$ denotes the s-wave projection according to Eq.* (D.11) *and the prescription described below Eq.* (D.10).

function of $\boldsymbol{p}_1 - \boldsymbol{p}_1'$, i.e. $\Gamma_k^{(4)} = \Gamma_k^{(4)}(\boldsymbol{p}_1 - \boldsymbol{p}_1')$, and because both momenta are on the Fermi surface, $|\boldsymbol{p}_1| = |\boldsymbol{p}_1'| = k_F$, only the dependence on the angle $\theta = \angle(\boldsymbol{p}_1, \boldsymbol{p}_1')$ remains. As the pairing takes place in the s-wave channel our final projection onto the coupling g_k reads

$$g_k = \frac{1}{2}\int_{-1}^{+1} d\cos\theta\, \Gamma_k^{(4)}(\cos\theta). \tag{D.11}$$

The flow equation of the vertex g_k is shown in terms of diagrams in Fig. D.2 where we also indicate the underlying momentum dependence of the vertex. The flow equation reads

$$\begin{aligned} \partial_k g_k &= -g_k^2 \tilde{\partial}_k \int_Q G^c(Q) G^c(-Q) \\ &\quad -g_k^2 \tilde{\partial}_k \frac{1}{2}\int_{-1}^{1} d\cos\theta \int_Q G^c(\boldsymbol{l} + (\boldsymbol{p}_1' - \boldsymbol{p}_1), \omega_n) G^c(\boldsymbol{l}, \omega_n) \end{aligned} \tag{D.12}$$

where $\int_Q = T\sum_{\omega_n}\int \frac{d^3l}{(2\pi)^3}$, $Q = (\boldsymbol{l}, \omega_n)$, $\theta = \angle(\boldsymbol{p}_1, \boldsymbol{p}_1')$, $|\boldsymbol{p}_1| = |\boldsymbol{p}_1'| = \sqrt{\mu}$, and in the first term we used that the integrand does not depend on θ so that the angular integration over θ is trivial. Now me may invert this flow equation by division by $-g_k^2$. If we kept the momentum dependence of $\Gamma^{(4)}(P_1, P_2, P_1')$, this inversion could not be done as $\Gamma^{(4)}$ then appeared inside the integral. Furthermore, $\tilde{\partial}_k$ commutes with g_k because the derivative $\tilde{\partial}_k$ acts only on the regulators inside the cutoff Green's functions G^c as described in Chapter 4. After the inversion the flow equation for g_k^{-1} reads

$$\begin{aligned} \partial_k g_k^{-1} &= \tilde{\partial}_k \int_Q G^c(Q) G^c(-Q) \\ &\quad +\tilde{\partial}_k \frac{1}{2}\int_{-1}^{1} d\cos\theta \int_Q G^c(\boldsymbol{l} + (\boldsymbol{p}_1' - \boldsymbol{p}_1), \omega_n) G^c(\boldsymbol{l}, \omega_n). \end{aligned} \tag{D.13}$$

Note, we could equally well derive all results in terms of a flow equation for g_k, which would then, however, necessitate a numerical solution.

There are two contributions in Eq. (D.13). The first is a p/p contribution. It is responsible for the pairing instability and will lead to the BCS transition temperature. The second p/h diagram takes into account spin and exchange fluctuations which lead to a suppression of the pairing instability.

D.2 BCS transition temperature from functional renormalization

It is instructive to concentrate on BCS theory first which ignores the second term in Eq. (D.13) altogether. Before calculating T_c in BCS theory we show from the RG flow equation (D.14) below that for arbitrarily weak attraction, $g_\Lambda < 0$, the Fermi liquid is unstable with respect to superfluid pairing at zero temperature.

Superfluid pairing at $T = 0$ for arbitrarily weak attraction

We have to evaluate the flow equation

$$\partial_k g_k^{-1} = \tilde{\partial}_k \int_Q G^c(Q) G^c(-Q). \tag{D.14}$$

In this Appendix we employ sharp regulators in momentum space such that

$$G^c(\boldsymbol{q}, \omega_n) = G(\boldsymbol{q}, \omega_n)\theta(|\boldsymbol{q}^2 - \mu| - k^2). \tag{D.15}$$

At zero temperature Eq. (D.14) can straightforwardly be evaluated. One obtains

$$\begin{aligned} \partial_k g_k^{-1} &= -\int \frac{d\omega}{2\pi} \int \frac{d^3q}{(2\pi)^3} \frac{2k\delta(|\boldsymbol{q}^2 - \mu| - k^2)}{(-i\omega + \xi_{\boldsymbol{q}})(i\omega + \xi_{-\boldsymbol{q}})} \\ &= -\frac{k}{2\pi^2} \left[\int_{\sqrt{\mu}}^{\infty} dq q^2 \frac{\delta(q^2 - \mu - k^2)}{q^2 - \mu} - \int_0^{\sqrt{\mu}} dq q^2 \frac{\delta(\mu - q^2 - k^2)}{q^2 - \mu} \right]. \end{aligned} \tag{D.16}$$

where in the first step we acted with $\tilde{\partial}_k$ on the step function and where we define $\xi_{\boldsymbol{q}} \equiv \boldsymbol{q}^2 - \mu$. In the second step we performed the frequency integration. Here, the two terms arise due to the pole structure of the integrand and the second term appears only for positive chemical potential $\mu > 0$. This becomes in particular important when studying the BEC-BCS crossover in a simple (e.g. Nozieres-Schmitt–Rink like) truncation, where the fermions are not renormalized. Then on the BEC side of the resonance, where $\mu < 0$ this term does not contribute. In Chapter 4 we have seen that in a more elaborate truncation where the fermions are renormalized[1] the second term would even contribute on the far BEC side due to the large self-energy

[1]Note, in a self-consistent Ward-Luttinger approach, which goes far beyond a simple Nozieres-Schmitt–Rink calculation and which was employed by Haussmann *et al.* to study the BEC-BCS crossover [37, 58, 264, 255, 265], this effect is included as well.

of the fermions. Evaluating the δ-distributions in Eq. (D.14) then finally yields

$$\partial_k g_k^{-1} = -\frac{1}{4\pi^2 k}\left[\sqrt{\mu+k^2}+\sqrt{\mu-k^2}\theta(\mu-k^2)\right]. \tag{D.17}$$

At this point let us set the initial condition for g_Λ which is determined by two-body scattering physics and the UV regularization of the contact interaction. In order to obtain g_Λ we have to evaluate Eq. (D.17) at vanishing density, $\mu = 0$, which yields

$$\partial_k g_k^{-1} = -\frac{1}{4\pi^2} \quad \rightarrow \quad \frac{1}{g_\Lambda} = \frac{1}{g_{IR}} - \frac{\Lambda}{4\pi^2} \tag{D.18}$$

so that we obtain

$$\frac{1}{g_\Lambda} = \frac{1}{8\pi a} - \frac{\Lambda}{4\pi^2}. \tag{D.19}$$

The analysis of this simple relation allows for a brief side remark: in Chapter 2 we learned that $1/\Lambda$ can be viewed upon as representing the range of the microscopic interaction potential. In consequence Eq. (D.19) tells us that for microscopic *repulsive* interactions the scattering length a is bounded from above by [209]

$$a < \frac{\pi}{2\Lambda} \quad (\text{for } g_\Lambda > 0). \tag{D.20}$$

For contact interactions, $\Lambda \to \infty$, and thus $a \to 0$, which can be viewed as a reincarnation of the triviality of non-relativistic ϕ^4 theory.

We are, however, interested in *attractive*, microscopic interactions, $g_\Lambda < 0$, for which no such bound applies. Indeed depending on the choice of g_Λ any scattering length a can be achieved as can easily be seen by inversion of Eq. (D.19),

$$a = \frac{1}{\frac{8\pi}{g_\Lambda} + \frac{2}{\pi}\Lambda}. \tag{D.21}$$

Hence a 'shape resonance' condition, cf. Section 2.1 in Chapter 2 is fulfilled for $g_\Lambda = -4\pi^2/\Lambda$.

After having discussed the few-body physics, let us come back to the question of an instability of a Fermi gas towards superfluidity at $T = 0$ for arbitrarily weak attraction, parametrized by a small, negative scattering length a.[2] Eq. (D.17) straightforwardly answers this question: first note that $\partial_k g_k^{-1}$ is negative for all k, which implies that $1/g_k$ increases towards the infrared. In the case of finite density, when $\mu > 0$ we observe that $\partial_k g_k^{-1}$ diverges for $k \to 0$. This in turn means that for any interaction strength $g_\Lambda < 0$, $1/g_k$ will cross zero at some finite RG scale k. Since $g_k = \infty$ implies the onset of symmetry breaking, this shows that the spin-balanced Fermi gas with arbitrarily weak, attractive interactions in unstable towards superfluid pairing at $T = 0$.

[2] From Eq. (D.19) it is then apparent that this implies an arbitrarily weak $g_\Lambda < 0$.

Transition temperature

In order to determine the critical temperature T_c of BCS theory we have to solve Eq. (D.14) at finite temperature and density n. T_c is then given by the criterion for the onset of superfluidity Eq. (D.8). This calculation is a nice and simple example to show the connection between the present fRG approach and resummed perturbation theory. To see this connection we solve the RG flow equation in two different ways which lead to the same result. First we explicitly derive the flow equation for g_k in an analytical form and then integrate the flow from the UV to the IR. Second, we use a more direct, simpler approach which relies on the perturbative assumption of non-renormalization of the fermionic Green's function to instantly integrate the flow without ever calculating the flow equation explicitly.

Let us start with the first approach. The BCS flow equation is given by Eq. (D.14). We act with the derivative $\tilde{\partial}_k$ and perform the Matsubara summation over (fermionic) Matsubara frequencies using

$$\begin{aligned} T\sum_{\omega_n}\frac{1}{-i\omega_n+\xi} &= -n_F(\xi) \\ T\sum_{\omega_n}\frac{1}{i\omega_n+\xi} &= n_F(-\xi)=1-n_F(\xi) \\ n_F(\xi)=\frac{1}{e^{\beta\xi}+1}, &\qquad 1-2n_F(\xi)=\tanh\left[\beta\xi/2\right]. \end{aligned} \tag{D.22}$$

One obtains

$$\begin{aligned} \partial_k g_k^{-1} &= -\frac{k}{2\pi^2}\int_0^\infty dq q^2 \frac{\tanh\left[\beta\xi_{\boldsymbol{q}}/2\right]}{\xi_{\boldsymbol{q}}}\delta(|\xi_{\boldsymbol{q}}|-k^2) \\ &= -\frac{k}{4\pi^2}\left[\int_{-\mu}^\infty d\xi \frac{\sqrt{\xi+\mu}\tanh\left[\beta\xi/2\right]}{\xi}\delta(-\xi-k^2)\right. \\ &\quad \left.+\int_0^\infty d\xi \frac{\sqrt{\xi+\mu}\tanh\left[\beta\xi/2\right]}{\xi}\delta(\xi-k^2)\right], \end{aligned} \tag{D.23}$$

which yields the flow equation in its final form

$$\partial_k g_k^{-1} = -\frac{\tanh\left[\beta k^2/2\right]}{4\pi^2 k}\left[\theta(\mu-k^2)\sqrt{\mu-k^2}+\sqrt{\mu+k^2}\right]. \tag{D.24}$$

The inspection of Eq. (D.24) nicely shows that the divergency encountered in the flow of g_k at $T=0$ is cured by the tanh term. This flow equation can now be integrated analytically from

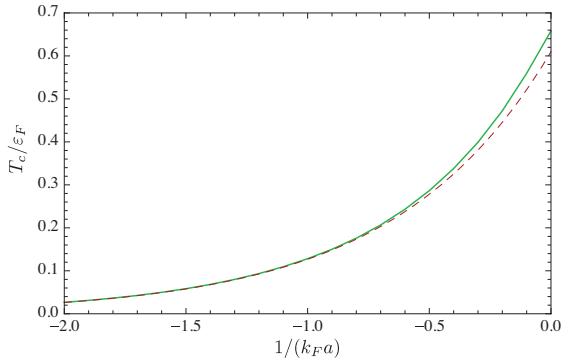

FIGURE D.3: *Dimensionless transition temperature T_c/ε_F towards superfluid pairing taking into account only particle-particle correlations. Analytical, approximate result Eq.* (D.29) *(dashed, red) versus numerical solution of Eq.* (D.26) *(solid, green).*

the UV ($k = \Lambda$) to the IR ($k = 0$)

$$\frac{1}{g_{\mathrm{UV}}} - \frac{1}{g_{\mathrm{IR}}} = -\frac{1}{4\pi^2}\left[\int_0^{\sqrt{\mu}} dk \frac{\tanh\left[\beta k^2/2\right]}{k}\left(\sqrt{\mu+k^2}+\sqrt{\mu-k^2}\right) + \int_{\sqrt{\mu}}^{\Lambda} dk \frac{\tanh\left[\beta k^2/2\right]}{k}\sqrt{\mu+k^2}\right], \tag{D.25}$$

which, after inserting Eq. (D.19), gives

$$\frac{1}{g_{\mathrm{IR}}} = \frac{1}{8\pi a} - \frac{1}{4\pi^2}\left[\Lambda - \int_0^{\sqrt{\mu}} dk \frac{\tanh\left[\beta k^2/2\right]}{k}\left(\sqrt{\mu+k^2}+\sqrt{\mu-k^2}\right) - \int_{\sqrt{\mu}}^{\Lambda} dk \frac{\tanh\left[\beta k^2/2\right]}{k}\sqrt{\mu+k^2}\right]. \tag{D.26}$$

One can arrive at Eq. (D.26) in more direct way by realizing that in the original flow equation (D.14) the only RG scale k-dependence arises due to the regulators appearing explicitly in the cutoff propagators G^c. Therefore we can safely replace the derivative $\tilde{\partial}_k$ by ∂_k. Note, this would neither work if we took into account self-energy corrections of the fermions nor if any k-dependent coupling appeared on the right-hand-side of the flow equation. The replacement $\tilde{\partial}_k \to \partial_k$ becomes possible here only due to the ability to invert the flow equation $g_k \to 1/g_k$ so that g_k does not appear on the RHS of the flow equation. In particular, this would not have worked if we kept any explicit momentum dependence of g_k.

After the replacement $\tilde{\partial}_k \to \partial_k$ in Eq. (D.14) we can directly integrate the RG flow,

$$\frac{1}{g_{\mathrm{IR}}} = \frac{1}{g_\Lambda} - \int_Q G^c(Q)G^c(-Q)\Big|_{R_{k=0}}^{R_{k=\Lambda}}. \tag{D.27}$$

After performing the Matsubara summation using Eqn. (D.22) we find

$$\begin{aligned}\frac{1}{g_{\rm IR}} &= \frac{1}{g_\Lambda}+\int\frac{d^3q}{(2\pi)^3}\frac{1-2n_F(\xi_{\boldsymbol{q}})}{2\xi_{\boldsymbol{q}}}\theta(\Lambda^2-|\xi_{\boldsymbol{q}}|)\\ &= \frac{1}{g_\Lambda}+\int_{-\mu}^{\infty}\frac{d\xi}{8\pi^2}\frac{\sqrt{\xi+\mu}}{\xi}\tanh\left[\beta\xi/2\right]\theta(\Lambda^2-|\xi|).\end{aligned} \tag{D.28}$$

The careful evaluation of the momentum integral shows that the result is again given by Eq. (D.26).

In order to determine T_c, Eq. (D.26) is solved so that the condition (D.8) is fulfilled. In Fig. D.3 we show T_c/ϵ_F as function of the dimensionless interaction strength $1/(k_Fa)$. In the weak coupling limit, $k_Fa\to 0^-$, we recover (for a review of how to solve Eq. (D.26) analytically in the weak coupling limit we refer to [313])

$$T_c=\frac{8e^\gamma}{\pi e^2}e^{-\frac{\pi}{2}\left|\frac{1}{k_Fa}\right|}, \tag{D.29}$$

where $\gamma\approx 0.577$ is the Euler's constant. Deviations from this analytical formula become relevant for larger $|k_Fa|$.

D.3 The Gorkov–Melik-Barkhudarov effect

In this Section we include the effect of p/h fluctuations given by the second term in Eq. (D.13), cf. Fig. D.2, which we omitted so far in our discussion. In order to keep the calculation brief, we will use the second approach taken in the previous Section and integrate the flow (D.13) instantly from the UV to the IR after realizing that also in the p/h contribution any RG scale k-dependence is due to the regulators appearing in the cutoff propagators G^c. Then we may again replace $\tilde{\partial}_k\to\partial_k$ and arrive directly at

$$\begin{aligned}\frac{1}{g_{\rm UV}}-\frac{1}{g_{\rm IR}} &= \overbrace{\int_Q G^c(Q)G^c(-Q)\Big|_{R_{k=0}}^{R_{k=\Lambda}}}^{\delta I_{\rm BCS}}\\ &\quad+\underbrace{\frac{1}{2}\int_{-1}^{1}d\cos\theta\int_Q G^c(\boldsymbol{l}+(\boldsymbol{p}_1'-\boldsymbol{p}_1),\omega_n)G^c(\boldsymbol{l},\omega_n)\Big|_{R_{k=0}}^{R_{k=\Lambda}}}_{\delta I_{\rm GMB}}.\end{aligned} \tag{D.30}$$

$\delta I_{\rm BCS}$ was calculated in the previous Section. Here we concentrate on the correction to the superfluid pairing interaction due to p/h fluctuations given by the term $\delta I_{\rm GMB}$. Employing

the sharp momentum regulator, cf. Eq. (D.15), it is given by

$$\begin{aligned}\delta I_{\mathrm{GMB}} &= \frac{1}{2}\int_{-1}^{1} d\cos\theta T\sum_{\omega_n}\int \frac{d^3l}{(2\pi)^3}\frac{1}{[-i\omega_n+\xi_{\boldsymbol{l}}][-i\omega_n+\xi_{\boldsymbol{l}+(\boldsymbol{p}_1'-\boldsymbol{p}_1)}]} \\ &\quad\times\left[\theta(|\xi_{\boldsymbol{l}}|-\Lambda^2)\theta(|\xi_{\boldsymbol{l}+(\boldsymbol{p}_1'-\boldsymbol{p}_1)}|-\Lambda^2)-1\right], \end{aligned} \tag{D.31}$$

where $|\boldsymbol{p}_1|=|\boldsymbol{p}_1'|=\sqrt{\mu}$, $\xi_{\boldsymbol{q}}=\boldsymbol{q}^2-\mu$, and $\theta=\angle(\boldsymbol{p}_1,\boldsymbol{p}_1')$. In the limit $\Lambda\to\infty$ the term proportional to the step functions vanishes. Performing the Matsubara summation using Eqn. (D.22) and the definition $\boldsymbol{q}=\boldsymbol{p}_1'-\boldsymbol{p}_1$ one obtains

$$\begin{aligned}\delta I_{\mathrm{GMB}} &= -\frac{1}{2}\int_{-1}^{1} d\cos\theta\int\frac{d^3l}{(2\pi)^3}\frac{n_F(\xi_{\boldsymbol{l}+\boldsymbol{q}})-n_F(\xi_{\boldsymbol{l}})}{\xi_{\boldsymbol{l}+\boldsymbol{q}}-\xi_{\boldsymbol{l}}} \\ &= \int_{-1}^{1} d\cos\theta\int\frac{d^3l}{(2\pi)^3}\frac{n_F(\xi_{\boldsymbol{l}})}{\xi_{\boldsymbol{l}+\boldsymbol{q}}-\xi_{\boldsymbol{l}}}, \end{aligned} \tag{D.32}$$

where we shifted the momentum integration variable in the second step and used $\xi_{\boldsymbol{l}}=\xi_{-\boldsymbol{l}}$. To progress further it is convenient to switch to dimensionless momenta $\tilde{l}=|\boldsymbol{l}|/\sqrt{\mu}$ and $\tilde{q}=|\boldsymbol{q}|/(2\sqrt{\mu})$. Eq. (D.32) can then be brought into the form

$$\delta I_{\mathrm{GMB}} = \int_{-1}^{1} d\cos\theta\frac{\mu^{1/2}\theta(\mu)}{16\pi^2\tilde{q}}\int_0^\infty d\tilde{l}\tilde{l}n_F(\tilde{l}\sqrt{\mu})\int_{-1}^{1}dy\frac{1}{\tilde{q}/\tilde{l}+y}, \tag{D.33}$$

where $y=\cos\eta$, and $\eta=\angle(\boldsymbol{q},\boldsymbol{l})$. This yields [317]

$$\delta I_{\mathrm{GMB}}=\int_{-1}^{1} d\cos\theta\frac{\mu^{1/2}\theta(\mu)}{16\pi^2\tilde{q}}\int_0^\infty d\tilde{l}\tilde{l}n_F(\tilde{l}\sqrt{\mu})\ln\left|\frac{\tilde{q}/\tilde{l}+1}{\tilde{q}/\tilde{l}-1}\right|. \tag{D.34}$$

Let us evaluate Eq. (D.34) first at zero temperature, $T=0$. The momentum integral can then be performed analytically,

$$\delta I_{\mathrm{GMB}}^{(T=0)}=\int_{-1}^{1} d\cos\theta\frac{\mu^{1/2}\theta(\mu)}{16\pi^2\tilde{q}}\left[\tilde{q}+\frac{1}{2}(1-\tilde{q}^2)\ln\left|\frac{\tilde{q}+1}{\tilde{q}-1}\right|\right]. \tag{D.35}$$

The last step is the s-wave projection represented by the remaining angular integral. Remarkably, also this can be performed analytically. Here we use $\boldsymbol{q}^2=2\mu(1-\cos\theta)$, $d\cos\theta=-q/\mu dq$ and find

$$\delta I_{\mathrm{GMB}}^{(T=0)}=\frac{\sqrt{\mu}\theta(\mu)}{12\pi^2}(1+\ln 4)=\frac{\sqrt{\mu}\theta(\mu)}{4\pi^2}\ln(4e)^{\frac{1}{3}} \tag{D.36}$$

At this point we note that the few-body problem, which is characterized by $\mu=0$, is not changed by the p/h contribution $\delta I_{\mathrm{GMB}}^{(T=0)}$ which is identically zero in this limit. Thus the initial value for g_Λ given by Eq. (D.19) is not affected by the p/h term and the Gorkov correction

simply appears as an additional term in Eq. (D.26). In the weak coupling regime, where the transition temperature to the superfluid state is very low, cf. Eq. (D.29), we may use Eq. (D.36) to derive the change in T_c due to p/h fluctuations. The term $\delta I_{\rm GMB}^{(T=0)}$ gives then a correction to the p/p contribution solely taken into account in Eq. (D.26). In fact the additional correction to Eq. (D.26) can be absorbed in a redefinition of the scattering length

$$\frac{1}{a'} = \frac{1}{a} + \frac{2}{\pi}\ln(4e)^{1/3}. \tag{D.37}$$

This redefined scattering length then appears in the expression for T_c in Eq. (D.29) and leads

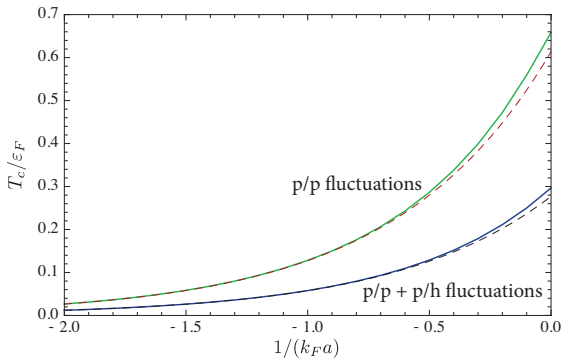

FIGURE D.4: *Dimensionless transition temperature T_c/ε_F towards superfluid pairing taking into account particle-particle as well as particle-hole correlations (lower solid line). Analytical, approximate result Eq.* (D.38) *(dashed, black) versus numerical solution of Eq.* (D.26) *and* (D.34) *(solid, blue). The result from BCS theory is also shown (upper lines), cf. Fig. D.3.*

to a shift of T_c according to

$$T_c^{\rm GMB} = \frac{8e^\gamma}{\pi e^2} e^{\frac{\pi}{2}\frac{1}{k_F a'}} = \frac{1}{(4e)^{1/3}} \frac{8e^\gamma}{\pi e^2} e^{\frac{\pi}{2}\frac{1}{k_F a}}, \tag{D.38}$$

which is the famous shift by a factor of $(4e)^{1/3} \approx 2.2$ we aimed to derive.

When the interaction characterized by $k_F a$ is not arbitrarily weak Eqn. (D.26) and (D.34) have to be evaluated numerically. The resulting critical temperature T_c/ε_F versus the dimensionless interaction strength $1/(k_F a)$ is shown in Fig. D.4.

Finally we comment on the significance of p/h fluctuations in the BEC-BCS crossover, in particular for the unitary Fermi gas where $k_F a$ is infinite. Remarkably, it was found that theories, such as the self-consistent T-matrix approach used in [37, 58, 264, 255, 265], which take into account only the p/p channel, but not the Gorkov correction due to the p/h channel, give very accurate results e.g. for T_c, compared to experiments [34] and state-of-the-art diagrammatic Monte-Carlo calculations [35]. At first this is surprising when considering the large correction by a factor of about 2.2 in T_c due to p/h fluctuations in the weak coupling limit. However, from the inspection of Eq. (D.36) we find that the correction $\delta I_{\rm GMB}$ decreases

for a decreasing value of the chemical potential μ. In the BEC-BCS crossover the chemical potential decreases as the interaction is tuned from the BCS to the BEC regime and μ crosses zero for a specific value of $1/(k_F a)$. Hence within at least a non-self-consistent T-matrix approach, which does not take into account the renormalization of the fermions, the p/h contribution will yield no significant contribution to T_c around unitarity. In a self-consistent T-matrix approach the renormalization of the fermions is taken into account so that this simple argument does not apply. From an RG perspective, and taking into account our findings in the context of the polaron-to-molecule transition in Chapter 4, it seems, however, likely that the flow of the fermionic self-energy is such that the effective 'flowing' chemical potential $\mu + \Sigma(\mathbf{0}, 0)$ remains negative or small until shortly before the IR so that the correction due to p/h fluctuations remains suppressed. This technical argument might give some insight why T-matrix approximations work so well for the unitary Fermi gas in the context of the BEC-BCS crossover as well as for the polaron problem.

Appendix E

Angular average in the derivation of the modified STM equation

The goal is to take the angular average, Eq. (2.53), of Eq. (2.52). The resulting expression is a sum of terms of the form

$$I = c \int_{-1}^{1} d\cos\angle(\boldsymbol{q}_1, \boldsymbol{q}_2) \int_0^\infty dl\, l^2 h(l) \int_{-1}^{1} d\cos\angle(\boldsymbol{l}, \boldsymbol{q}_1) f(q_1, l, \cos\angle(\boldsymbol{l}, \boldsymbol{q}_1)) g(q_2, l, \cos\angle(\boldsymbol{l}, \boldsymbol{q}_2)), \tag{E.1}$$

where c is a numerical constant, $l = |\boldsymbol{l}|$, $q_i = |\boldsymbol{q}_i|$ and the function $h(l)$ does not depend on any angle. Now first the angular average $\int d\cos\angle(\boldsymbol{q}_1, \boldsymbol{q}_2)$ is performed where the vectors $\boldsymbol{q}_1$ and $\boldsymbol{l}$ are chosen to be fixed. The angular integration amounts then in an integration over all $\boldsymbol{q}_2$ on a sphere of constant radius $|\boldsymbol{q}_2|$ and the integrals can be interchanged:

$$I = c \int_0^\infty dl\, l^2 h(l) \int_{-1}^{1} d\cos\angle(\boldsymbol{l}, \boldsymbol{q}_1) f(q_1, l, \cos\angle(\boldsymbol{l}, \boldsymbol{q}_1)) \underbrace{\int_{-1}^{1} d\cos\angle(\boldsymbol{q}_1, \boldsymbol{q}_2) g(q_2, l, \cos\angle(\boldsymbol{l}, \boldsymbol{q}_2))}_{(*)}, \tag{E.2}$$

Since both $\boldsymbol{q}_1$ and $\boldsymbol{l}$ are fixed for the integration marked by $(*)$, one can integrate equally over all angles $\angle(\boldsymbol{q}_1, \boldsymbol{l})$ instead of $\angle(\boldsymbol{q}_1, \boldsymbol{q}_2)$. The resulting expression is then

$$I = c \int_0^\infty dl\, l^2 h(l) \underbrace{\int_{-1}^{1} d\cos\angle(\boldsymbol{l}, \boldsymbol{q}_1) f(q_1, l, \cos\angle(\boldsymbol{l}, \boldsymbol{q}_1))}_{f_s(q_1, l)} \underbrace{\int_{-1}^{1} d\cos\angle(\boldsymbol{q}_2, \boldsymbol{l}) g(q_2, l, \cos\angle(\boldsymbol{l}, \boldsymbol{q}_2))}_{g_s(q_2, l)}. \tag{E.3}$$

One obtains a product of two separate s-wave projections and there is no mixing of partial waves involved which is due to the separation into the two separate functions f and g in Eq. (E.1). Applying Eq. (E.3) to each term in Eq. (2.52) then finally yields, after having performed the l-integration, the expression Eq. (2.54).

Appendix F

List of publications

On the following pages we reprint the open-access versions from arXiv.org of the papers that were published in the context of this thesis:

- S. Moroz, and R. Schmidt,
  Nonrelativistic inverse square potential, scale anomaly, and complex extension,
  Ann. Phys. **325**, 491 (2010).

- R. Schmidt, and S. Moroz,
  Renormalization-group study of the four-body problem,
  Phys. Rev. A **81**, 052709 (2010).

- S. Floerchinger, S. Moroz, and R. Schmidt,
  Efimov Physics from the Functional Renormalization Group,
  Few-body Syst. **51**, 153 (2011).

- R. Schmidt, and T. Enss,
  Excitation spectra and rf response near the polaron-to-molecule transition from the functional renormalization group,
  Phys. Rev. A **83**, 063620 (2011).

- R. Schmidt, T. Enss, V. Pietilä, and E. Demler,
  Fermi polarons in two dimensions,
  Phys. Rev. A **85**, 021602(R) (2012).

- R. Schmidt, S. P. Rath, and W. Zwerger,
  Efimov physics beyond universality,
  Eur. Phys. J. B **85**, 386 (2012).

Nonrelativistic inverse square potential, scale anomaly, and complex extension

Sergej Moroz

Institut für Theoretische Physik Universität Heidelberg

Philosophenweg 16, D-69120 Heidelberg, Germany

Richard Schmidt

Physik Department, Technische Universität München,

James-Franck-Strasse, D-85748 Garching, Germany

(Dated: 9-2009)

Abstract

The old problem of a singular, inverse square potential in nonrelativistic quantum mechanics is treated employing a field-theoretic, functional renormalization method. An emergent contact coupling flows to a fixed point or develops a limit cycle depending on the discriminant of its quadratic beta function. We analyze the fixed points in both conformal and non-conformal phases and perform a natural extension of the renormalization group analysis to complex values of the contact coupling. Physical interpretation and motivation for this extension is the presence of an inelastic scattering channel in two-body collisions. We present a geometric description of the complex generalization by considering renormalization group flows on the Riemann sphere. Finally, using bosonization, we find an analytical solution of the extended renormalization group flow equations, constituting the main result of our work.

I. INTRODUCTION

Exactly solvable problems play an important role in physics. They provide a backbone of our understanding and allow to develop perturbation theory on the basis of an exact solution. In nonrelativistic quantum mechanics the harmonic oscillator and the Coulomb central potential are certainly the two most important examples. Another prominent example of an exactly solvable problem in quantum mechanics is the central, inverse square potential

$$V(r) = -\frac{\kappa}{r^2}. \tag{1}$$

Most remarkably, in any spatial dimension the potential (1) is classically conformal invariant because it is a homogeneous function of degree -2 and has the same scaling as the nonrelativistic kinetic energy. Hence, the classical action is invariant under the nonrelativistic scaling $\vec{r} \to \rho\vec{r}$, $t \to \rho^2 t$. The quantum problem with the potential (1) has a long history and is discussed both in standard textbooks [1, 2] and in the scientific literature [3, 4]. More recently there were a number of renormalization group (RG) studies of this problem [5–15].

The quantum physics of the inverse square potential is well understood. The interaction (1) is an example of a singular potential [16] and must be treated with care. It is known that for the repulsive and weakly attractive coupling ($\kappa < \kappa_{cr}$)[1], the scale symmetry is preserved at the quantum level and the theory provides an example of nonrelativistic conformal field theory [17]. On the other hand, for strong attractions ($\kappa > \kappa_{cr}$) a discrete, geometric bound state spectrum develops in the two-body problem, and the continuous scale symmetry is broken to a discrete subgroup by a quantum anomaly [18]. The anomaly has its origin in the singular short-distance behavior of the inverse square potential. In the RG language the anomaly manifests itself as a limit cycle instead of a scale-invariant fixed point.

The inverse square potential is a paradigmatic system for nonrelativistic conformal invariance and scale anomaly. Remarkably, there is a number of different physical systems, which are described (often only in some restricted domain) by the inverse square potential:

- The celebrated Efimov effect, first derived in [19], consists in the formation of a tower of three-body bound states of identical non-relativistic bosons[2] interacting through a short range potential. Exactly at resonance (unitarity regime) all scales drop out of the

[1] κ_{cr} represents the critical attractive coupling. In d spatial dimensions it is given by $\kappa_{cr} = \frac{(d-2)^2}{4}$.
[2] More generally, for the occurance of the Efimov effect it is sufficient that at least two two-body subsystems

problem and the three-body spectrum becomes infinite and geometric. The three-body problem in quantum mechanics is treated most easily in hyperspherical coordinates [20]. Employing the adiabatic hyperspherical approximation [21], Faddeev decomposition of the wave function [22] and restricting to the zero total angular momentum sector, one arrives at the remarkably simple one-dimensional effective equation [23]:

$$\left[-\frac{d^2}{dr^2} - \frac{s_0^2 + 1/4}{r^2}\right]\psi(r) = E\psi(r) \tag{2}$$

with the Efimov parameter $s_0 \approx 1.0062$. This is a one-dimensional radial Schrödinger equation with the inverse square potential in the overcritical regime ($\kappa > \frac{1}{4}$).

- The interaction of a polar molecule with an electron in three spatial dimensions can be approximated by a point dipole-charged particle anisotropic potential

$$V(\vec{r}) \sim \frac{\cos\theta}{r^2}, \tag{3}$$

where the angle θ is measured with respect to the direction of the dipole moment. As was demonstrated in [24], this anisotropic conformal potential can be reduced to the effective isotropic inverse potential (1) in the zero angular-momentum channel. Remarkably, the dipole-electron system exhibits all interesting features characteristic for the potential (1).

- At the critical coupling κ_{cr} the theory undergoes a transition from the conformal ($\kappa < \kappa_{cr}$) to the non-conformal ($\kappa > \kappa_{cr}$) regime. It has been demonstrated recently in [15] that this transition is closely related to the classical Berezinskii-Kosterlitz-Thouless (BKT) phase transition in two dimensions. In particular, the energy B of the lowest bound state near the critical coupling κ_{cr} in the non-conformal regime vanishes like

$$B \sim \exp\left(-\frac{\pi}{\sqrt{\kappa - \kappa_{cr}}}\right) \tag{4}$$

which is analogous to the behavior of the inverse correlation length as the BKT transition temperature is approached from above [25].

---

have s-wave bound states close to the zero-energy threshold unless two of the three particles are identical fermions.

- Quite unexpectedly, the inverse square potential arises in the near-horizon physics of some black holes. More specifically, this is the case for a massive, scalar field minimally coupled to gravity on the non-extremal spherically-symmetric Reissner-Nordström (RN) black hole background. It was demonstrated in [18] that the Klein-Gordon field equation of the scalar field reduces to the effective Schrödinger equation with the overcritical ($\kappa > \kappa_{cr}$) inverse square potential in the near-horizon limit. The related problem of a scalar particle near an extremal RN black hole was treated in [26] leading to a similar finding.

- Finally, the conformal inverse square potential appears naturally in the context of vacuum AdS/CFT correspondence [27]. The field equation for a scalar field ϕ of mass m in the Euclidean AdS_{d+1} is

$$\partial_r^2\phi - \frac{d-1}{r}\partial_r\phi - \frac{m^2}{r^2}\phi - q^2\phi = 0, \qquad q^2 = (q^0)^2 + \vec{q}^2, \tag{5}$$

  where we transformed to the momentum space on the AdS_{d+1} boundary $(x^0, \vec{x}) \to (q^0, \vec{q})$, and r denotes the radial direction in the AdS_{d+1} space. We can change variable $\phi = r^{(d-1)/2}\psi$ and obtain

$$-\partial_r^2\psi + \frac{m^2 + (d^2-1)/4}{r^2}\psi = -q^2\psi, \tag{6}$$

  which is a one-dimensional Schrödinger equation with an inverse square potential of strength $\kappa = -m^2 - \frac{d^2-1}{4}$ and energy $E = -q^2$. As was emphasized in [15], the overcritical coupling $\kappa > \kappa_{cr}$ corresponds to the violation of the Breitenlohner-Freedman bound in AdS_{d+1}.

In this work we study the quantum problem of the inverse square potential using a functional renormalization method. The plan of this paper is the following: In Sec. II we introduce our method, the physical system of interest, and derive the flow equations using the sharp cut-off regulator. A general mathematical discussion of the flow equation is performed in Sec. III. Our central result is derived in Sec. IV, where we extend the analysis to the complex plane, discuss the fixed point structure and find a numerical solution of the extended set of flow equations. Additionally, we provide a physical interpretation, geometric description and motivation for the complex extension. In Sec. V we bosonize the interaction. This allows us to view the problem from a different angle and, most remarkably, obtain an analytic solution

of the generalized complex flow equations. We draw our conclusions in Sec. VI. Finally, in Appendix A we present the renormalization group flows on the Riemann sphere.

II. THE METHOD, THE MODEL AND THE FLOW EQUATION

In this work we use the functional renormalization group and calculate a scale-dependent effective action functional Γ_k [28] (for reviews see [29–31]) called also average action or flowing action. The method is formulated in Euclidean spacetime and employs the Matsubara formalism if one works at finite temperature. The flowing action Γ_k includes all fluctuations with momenta $q \gtrsim k$. In the infrared (IR) limit $k \to 0$ the full quantum effective action $\Gamma = \Gamma_{k\to 0}$ is recovered and the problem is solved. In practice the dependence on the scale k is introduced by adding a regulator term R_k to the inverse propagator $\Gamma^{(2)}$. The flowing action Γ_k obeys the exact functional flow equation [28], and its bosonic version is given by

$$\partial_k \Gamma_k \;=\; \frac{1}{2}\mathrm{Tr}\,\partial_k R_k\,(\Gamma_k^{(2)} + R_k)^{-1} = \frac{1}{2}\mathrm{Tr}\,\tilde{\partial}_k\,\ln(\Gamma_k^{(2)} + R_k). \tag{7}$$

The functional differential equation for Γ_k must be supplemented by an initial condition $\Gamma_{k\to\Lambda} = S$. The "classical action" S describes the physics at the microscopic ultraviolet (UV) scale $k = \Lambda$ and is assumed to be known. In Eq. (7) Tr denotes a trace which sums over momenta, Matsubara frequencies, internal indices, and fields. The second functional derivative $\Gamma_k^{(2)}$ is the full inverse field propagator, which is modified by the presence of the IR regulator R_k. The momentum dependent regulator function $R_k(q)$ must satisfy three important conditions, but otherwise can be chosen arbitrary [28]. The regulator dependence of the flowing action drops out for $k \to 0$, and one obtains the exact solution of Eq. (7). In the second form of the flow equation (7) $\tilde{\partial}_k$ denotes a scale derivative, which acts only on the IR regulator R_k. This form is convenient because it can be formulated in terms of one-loop Feynman diagrams. It is also convenient to introduce the RG "time" $t \equiv \ln(k/k_0)$, where k_0 is an arbitrary reference scale. The RG evolution towards the UV (IR) corresponds to $t > 0$ ($t < 0$). In the following we will use both t and k.

In most cases of interest Eq. (7) can be solved only approximately. Usually one adopts some type of expansion of Γ_k and then truncates at finite order. This leads to a finite system of ordinary differential equations. The expansions do not necessarily involve any small parameter and are generally of non-perturbative nature.

Although our method allows us to address the quantum many-body problem at finite temperature, in this work we are interested only in the few-body (vacuum) physics, which is characterized by vanishing density ($n = 0$) and vanishing temperature ($T = 0$). In this case the effective action $\Gamma_{k=0}$, being the generating functional of the 1PI vertices, can be easily related to the different scattering amplitudes and bound state energies. Additionally, numerous simplifications arise in the structure of the flow equations (for a detailed discussion see [32, 33]).

Finally, we note that the three-body quantum problem for fermions and bosons was treated with functional renormalization in [32–35]. In this work we apply functional renormalization to solve an arguably simpler problem, and our aim is twofold. First, the inverse square potential is a paradigm and it is important for understanding of other, more challenging problems. Second, working with this simple system, we develop a new renormalization group method of complexified flows in this paper. The method may be useful for more technical few-body problems in the future [36].

In this work we study the nonrelativistic quantum mechanical problem of identical bosons interacting through a long-range potential (1) in d spatial dimensions. The many-body field theory is defined in the UV by the microscopic action S_E

$$\begin{aligned} S_E[\psi,\psi^*] = &\int_0^{1/T} d\tau \int d^dx \psi^*(\tau,\vec{x})[\partial_\tau - \Delta - \mu]\psi(\tau,\vec{x}) \\ &- \frac{\lambda_\psi}{2}\int_0^{1/T} d\tau d^dx \psi^*(\tau,\vec{x})\psi^*(\tau,\vec{x})\psi(\tau,\vec{x})\psi(\tau,\vec{x}) \\ &- \int_0^{1/T} d\tau \int d^dx d^dy \psi^*(\tau,\vec{x})\psi^*(\tau,\vec{y})\frac{\kappa}{|\vec{x}-\vec{y}|^2}\psi(\tau,\vec{y})\psi(\tau,\vec{x}). \end{aligned} \tag{8}$$

Our convention is $\hbar = 2M_\psi = 1$ with the boson mass M_ψ. We work in the Matsubara formalism with Euclidean time $\tau \in (0, 1/T)$. In what follows we will be interested exclusively in the few-body (vacuum) physics. The vacuum state is characterized by zero density, which corresponds to zero chemical potential ($\mu = 0$), and zero temperature ($T = 0$). The bare action (8) is invariant under a global $U(1)$ transformation and possesses Galilean space-time symmetry. The microscopic bare parameter κ characterizes the strength of the long-range potential and is positive in the attractive case. We augmented the theory by a four-boson contact interaction term with a coupling λ_ψ. This is a consequence of the fact that the inverse square potential is singular at the origin [3, 16]. On its own the singular potential is not sufficient to define a quantum mechanical problem and must be augmented by the

boundary condition at the origin [15]. We will see that the introduction of λ_ψ in the UV determines the $r = 0$ boundary condition and makes the problem well-defined.

For our method it is convenient to switch to momentum space. The Fourier transform of the $1/r^2$ potential in d spatial dimensions reads

$$\begin{aligned} F_d(l) &= \int d^d r \frac{1}{r^2} \exp[i\vec{l}\cdot\vec{r}] = (2\pi)^{d/2}|\vec{l}|^{2-d}\int_0^\infty dz z^{d/2-2}J_{d/2-1}(z) = \\ &= \frac{(4\pi)^{d/2}\Gamma(d/2-1)|\vec{l}|^{2-d}}{4} \qquad 2<d<5. \end{aligned} \tag{9}$$

The restriction to dimensions d in the range $2 < d < 5$ can be understood easily by the fact that on the one side, $d = 2$ is a natural lower dimension, in which the integral (9) is IR logarithmically divergent. On the other side, the upper bound $d = 5$ can be relaxed, if we modify the Fourier integral by the introduction of a UV suppression factor $\exp(-\epsilon|\vec{r}|)$ and perform the limit $\epsilon \to 0$ in the very end. Hence, we will use

$$F_d(l) = \frac{(4\pi)^{d/2}\Gamma(d/2-1)|\vec{l}|^{2-d}}{4} \qquad d>2. \tag{10}$$

In what follows we consider only $d > 2$. First, we consider a momentum-independent (pointlike) truncation for the flowing action

$$\begin{aligned} \Gamma_k[\psi,\psi^*] = &\int_Q \psi^*(Q)[i\omega+\vec{q}^2]\psi(Q) - \\ &-\kappa\int_{Q_1,Q_2,\ldots,Q_4} F_d(l)\psi^*(Q_1)\psi(Q_2)\psi^*(Q_3)\psi(Q_4)\delta(-Q_1+Q_2-Q_3+Q_4) \\ &-\frac{\lambda_\psi}{2}\int_{Q_1,Q_2,\ldots,Q_4} \psi^*(Q_1)\psi(Q_2)\psi^*(Q_3)\psi(Q_4)\delta(-Q_1+Q_2-Q_3+Q_4), \end{aligned} \tag{11}$$

where $Q = (\omega, \vec{q})$ and $\int_Q = \int \frac{d\omega}{2\pi}\int \frac{d^dq}{(2\pi)^d}$. The vector $\vec{l} = \vec{q}_2 - \vec{q}_1 = \vec{q}_3 - \vec{q}_4$ gives the spatial momentum transfer during a collision and $l = |\vec{l}|$. In the nonrelativistic vacuum the propagator of the elementary field ψ is not renormalized because the only diagram, which contributes to its flow, contains a hole (antiparticle) in the loop. As there are only particles but not holes in the nonrelativistic vacuum the propagator keeps its microscopic form. Remarkably, the coupling κ, characterizing the strength of the long-range $1/r^2$ potential, is also constant during the renormalization group flow (we discuss this issue in more detail in Sec. V). The only coupling which flows during the RG evolution in our truncation is the contact coupling λ_ψ. Its flow equation is

$$\partial_t\lambda_\psi = \int_L \widetilde{\partial}_t \frac{[\lambda_\psi + 2F_d(l)\kappa]^2}{(i\omega + l^2 + R_k(L))(-i\omega + l^2 + R_k(-L))}. \tag{12}$$

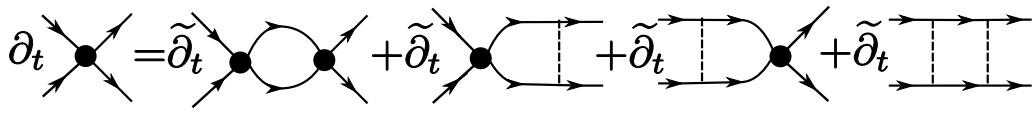

Figure 1: Flow equation of the four-particle contact coupling λ_ψ in form of Feynman diagrams. The solid lines with an arrow denote the boson ψ regularized propagator, the dashed lines correspond to the long-range interaction vertex, and the dark blobs represent the contact coupling λ_ψ.

The flow equation is depicted in terms of Feynman diagrams in Fig. 1. In order to proceed further we must specify the cut-off function $R_k(L)$.

Nevertheless, we note that already at this point it is possible to identify the generic form of the flow equation which reads

$$\partial_t \lambda_\psi = \alpha \lambda_\psi^2 + \beta \lambda_\psi + \gamma \tag{13}$$

with $\alpha, \beta, \gamma \in \mathbb{R}$, which depend on the coupling κ, dimension d and a concrete choice of the cut-off function. We postpone the general analysis of equation (13) until Sec. III.

It is convenient to rewrite Eq. (12) as

$$\partial_t \lambda_\psi = J_{0,d} \lambda_\psi^2 + 4 J_{1,d} \kappa \lambda_\psi + 4 J_{2,d} \kappa^2, \tag{14}$$

where we defined the cut-off dependent integrals

$$J_{n,d} \equiv \int \frac{d\omega}{2\pi} \frac{d^d l}{(2\pi)^d} \partial_t \frac{F_d^n(l)}{(i\omega + l^2 + R_k(L))(-i\omega + l^2 + R_k(-L))}, \tag{15}$$

where $F_d^n(l) \equiv F_d(l)^n$. In the rest of this section we finish the computation by specifying the sharp regulator $R_k(L) = (i\omega + l^2)\left(\frac{1}{\theta(l^2-k^2)} - 1\right)$.

The cut-off function $R_k(L) = (i\omega + l^2)\left(\frac{1}{\theta(l^2-k^2)} - 1\right)$ cuts off quantum fluctuations sharply, i.e. it totally suppresses the modes with $l^2 < k^2$ during the renormalization group evolution. This type of cut-off was used in the closely related three-body problem in [33]. The cut-off satisfies

$$\frac{1}{i\omega + l^2 + R_k(L)} = \theta(l^2 - k^2) \frac{1}{i\omega + l^2}. \tag{16}$$

Employing this property we can calculate $J_{n,d}$ defined in Eq. (15) explicitly as

$$J_{n,d} = \int \frac{d\omega}{2\pi} \frac{d^d l}{(2\pi)^d} \partial_t \theta(l^2 - k^2) \frac{F_d^n(l)}{(i\omega + l^2)(-i\omega + l^2)} = -\frac{\pi S_d}{(2\pi)^{d+1}} k^{d-2} F_d^n(k) \tag{17}$$

with $S_d = \frac{2\pi^{d/2}}{\Gamma(d/2)}$ being the area of a unit sphere in d-dimensional space. The resulting $J_{n,d}$ can be readily substituted in Eq. (14)

$$\partial_t \lambda_\psi = -\frac{k^{d-2}}{(4\pi)^{d/2}\Gamma(d/2)}\lambda_\psi^2 - \frac{2\kappa}{d-2}\lambda_\psi - \frac{(4\pi)^{d/2}\Gamma(d/2)}{(d-2)^2}\kappa^2. \tag{18}$$

The contact coupling λ_ψ has a naive (Gaussian) scaling dimension $[\lambda_\psi] = 2 - d$ and is IR irrelevant in $d > 2$. Our aim is to investigate the fixed point structure of Eq. (18). For this reason we introduce a dimensionless, rescaled coupling $\lambda_{\psi R} \equiv \frac{k^{d-2}\lambda_\psi}{(4\pi)^{d/2}\Gamma(d/2)}$ and its flow equation reads

$$\partial_t \lambda_{\psi R} = -\lambda_{\psi R}^2 + \left(-\frac{2\kappa}{d-2} + d - 2\right)\lambda_{\psi R} - \frac{\kappa^2}{(d-2)^2}. \tag{19}$$

As will be shown in Sec. III, the discriminant D of the quadratic β-function determines the overall behavior of the solution. In our case $D = -4\kappa + (d-2)^2$. The critical κ_{cr} is defined by the condition $D = 0$ yielding

$$\kappa_{cr} = \frac{(d-2)^2}{4}, \tag{20}$$

which is in agreement with the quantum-mechanical non-perturbative calculation [15]. For $\kappa < \kappa_{cr}$ (weak attraction and repulsion) the dimensionless coupling $\lambda_{\psi R}$ has two real fixed points

$$\lambda_{\psi R}^{\pm} = -\frac{\kappa}{d-2} + \frac{d-2}{2} \pm \sqrt{\frac{(d-2)^2}{4} - \kappa} \tag{21}$$

and the theory is scale invariant in the IR respectively UV. For $\kappa > \kappa_{cr}$ (strong attraction) the coupling $\lambda_{\psi R}$ ceases to have real fixed points and scale invariance is lost.

III. GENERAL ANALYSIS OF THE FLOW EQUATION

The flow equation for $\lambda_{\psi R}$ found in Sec. II has the general form

$$\frac{d}{dt}\lambda_{\psi R}(t) = \alpha\lambda_{\psi R}(t)^2 + \beta\lambda_{\psi R}(t) + \gamma, \tag{22}$$

where $\alpha, \beta, \gamma \in \mathbb{R}$ are numerical coefficients. Without loss of generality we consider $\alpha \leq 0$. This choice corresponds to the result obtained in Sec. II. The form of the solution of Eq. (22) is determined by the sign of the discriminant $D = \beta^2 - 4\alpha\gamma$ of the quadratic β-function. We consider the three different cases depicted in Fig. 2

- $D > 0$

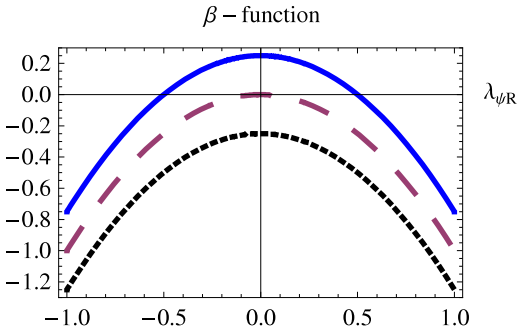

Figure 2: The β-function of the coupling $\lambda_{\psi R}$ for $\alpha = -1$ and $\beta = 0$. The three lines correspond to different values of γ with $D = 1$ (solid blue), $D = 0$ (dashed red) and $D = -1$ (dashed black).

In this case the β-function has two real fixed points $\lambda_{\psi R}^{IR}$ and $\lambda_{\psi R}^{UV}$ with $\lambda_{\psi R}^{IR} < \lambda_{\psi R}^{UV}$. The solution of Eq. (22) depends on the interval, where the UV initial condition $\lambda_{\psi R}$ belongs. For the initial condition $\lambda_{\psi R}^{IR} < \lambda_{\psi R} < \lambda_{\psi R}^{UV}$ the solution is attracted towards the IR by the fixed point $\lambda_{\psi R}^{IR}$ and has the form:

$$\lambda_{\psi R}(t) = \frac{-\beta - \sqrt{D}\tanh\left[\frac{\sqrt{D}}{2}(t+\eta)\right]}{2\alpha}, \tag{23}$$

with η fixed by the UV initial condition $\lambda_{\psi R}(t = 0)$. For the initial condition $\lambda_{\psi R} > \lambda_{UV}$ the flow runs into a positive divergence (Landau pole), but reemerges at negative infinity and subsequently approaches $\lambda_{\psi R}^{IR}$ in the IR. The explicit solution in this case reads

$$\lambda_{\psi R}(t) = \frac{-\beta + \sqrt{D}\coth\left[\frac{\sqrt{D}}{2}(-t+\eta)\right]}{2\alpha}, \tag{24}$$

with η fixed by the UV initial condition. In fact, the case $\kappa = 0$, which leads to $D > 0$, corresponds to the well-studied case of a contact interaction in atomic physics. In this context the appearance of the Landau pole signals the presence of a weakly bound molecular (dimer) state. Finally, for the initial condition $\lambda_{\psi R} < \lambda_{\psi R}^{IR}$ the RG flow is a smooth, monotonic function $\lambda_{\psi R}(t)$, which approaches $\lambda_{\psi R}^{IR}$ with the explicit solution given again by Eq. (24). Notably, for $D > 0$ the IR value $\lambda_{\psi R}(k = 0) = \lambda_{\psi R}^{IR}$ is not sensitive to the concrete choice of the initial condition. We offer an elegant geometric description of the flow in Sec. IV and Appendix A.

- $D = 0$

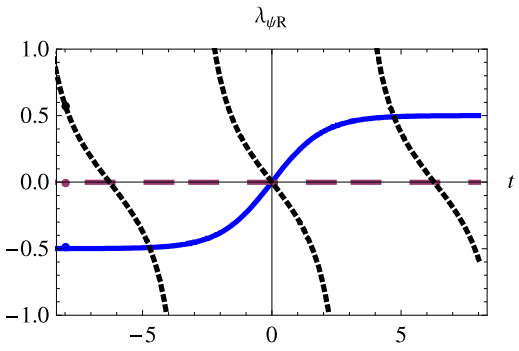

Figure 3: The renormalization group flows of the coupling $\lambda_{\psi R}$ for $\alpha = -1$ and $\beta = 0$ and initial condition $\lambda_{\psi R}(t = 0) = 0$. The different lines correspond to three different choices of γ with $D = 1, \eta = 0$ (solid blue), $D = 0, \eta \to \infty$ (dashed red), and $D = -1, \eta = 0$ (dashed black).

This is a limit of the previous case ($D > 0$) when the two fixed points merge. Excluding the trivial choices $\alpha = \beta = \gamma = 0$ and $\alpha = \beta = 0$; $\gamma \neq 0$, the β-function has a single fixed point $\lambda^*_{\psi R} = -\frac{\beta}{2\alpha}$ (see Fig. 2). The RG equation takes the form

$$\frac{d\lambda_{\psi R}(t)}{dt} = \alpha[\lambda_{\psi R}(t) - \lambda^*_{\psi R}]^2 \tag{25}$$

with the solution

$$\lambda_{\psi R}(t) = \lambda^*_{\psi R} - \frac{1}{\alpha t + \eta}, \tag{26}$$

where η is fixed by the initial condition. The running of the coupling $\lambda_{\psi R}(k)$ is logarithmic (which corresponds to the marginal deformation) and for $\eta < 0$ it hits a IR Landau pole. The coupling runs into the pole at the scale $t = -\frac{\eta}{\alpha}$, nevertheless the RG evolution can be extended beyond this scale and approaches $\lambda^*_{\psi R}$ at $k = 0$.

- $D < 0$

  In this case there are no real fixed points. The formal solution can be written as:

$$\lambda_{\psi R}(t) = \frac{-\beta + \sqrt{-D}\tan\left[\frac{\sqrt{-D}}{2}(t+\eta)\right]}{2\alpha}, \tag{27}$$

  where η is fixed by the initial condition. This solution is periodic with a period $T = \frac{2\pi}{\sqrt{-D}}$. Remarkably, in this case the UV initial condition $\lambda_{\psi R}(k = \Lambda)$ plays an important role as it determines the infrared value $\lambda_{\psi R}(k = 0)$.[3]

[3] This is analogous to the necessity to introduce the well-know three-body parameter in the context of the Efimov effect [23].

We plot the RG flows of $\lambda_{\psi R}$ in the three cases in Fig. 3. While for $D \geq 0$ the flows approach a fixed point in IR, the renormalization group evolution develops a limit cycle[4] for $D < 0$. As the RG scale k can be related to the energy of the particles, the physical interpretation of the limit cycle solution is clear: During the RG flow one hits bound states, manifesting themselves as divergences of the coupling $\lambda_{\psi R}$. And since there are infinitely many divergences one has an infinite tower of bound states with a geometric spectrum for the case $D < 0$.

IV. COMPLEX EXTENSION

In this section we discuss the different subcases, considered in Sec. III, in more detail and extend the analysis to complex values of the interaction coupling. We also present a physical interpretation of this extension.

A. Negative discriminant: complex fixed points

The renormalization group flow equation in our point-like approximation is[5]

$$\partial_t \lambda = \alpha \lambda^2 + \beta \lambda + \gamma \tag{28}$$

with $\alpha, \beta, \gamma \in \mathbb{R}$, and one can vary the parameters β and γ by considering different κ and d in Eq. (19). It is sometimes useful to express Eq. (28) in the alternative form

$$\partial_t \lambda = \alpha(\lambda - \lambda_*)^2 + \Delta\gamma, \qquad \lambda_* = -\frac{\beta}{2\alpha}, \qquad \Delta\gamma = \gamma - \frac{\beta^2}{4\alpha}. \tag{29}$$

If the discriminant $D = \beta^2 - 4\alpha\gamma = -4\alpha\Delta\gamma < 0$, the β-function has a pair of complex roots

$$\lambda^{\pm} = \frac{-\beta \pm i\sqrt{|D|}}{2\alpha} = \lambda_* \pm i\frac{\sqrt{|\alpha\Delta\gamma|}}{\alpha}. \tag{30}$$

[4] Strictly speaking, to find a limit cycle one needs at least two couplings connected by the RG flow equations (see, for example, Eqs. (63, 65)). In the case of a single coupling constant an infinite (unbounded) limit cycle appears only if there are periodic real discontinuities in the RG flow. We provide an elegant description of the infinite limit cycle on the Riemann sphere in Sec. IV.

[5] This equation coincides with Eq. (22). To simplify notation, we denote the coupling $\lambda_{\psi R}$ as λ in this section.

For this reason it is natural to consider the RG evolution of a generally complex variable $\lambda = \lambda_1 + i\lambda_2$ in Eq. (28). The resulting flow equations in the complex plane now read

$$\begin{aligned} \partial_t \lambda_1 &= \alpha\lambda_1^2 - \alpha\lambda_2^2 + \beta\lambda_1 + \gamma \\ \partial_t \lambda_2 &= 2\alpha\lambda_1\lambda_2 + \beta\lambda_2. \end{aligned} \tag{31}$$

Notably, if we start on the real axis (i.e. $\lambda_2(t=0) = 0$), the flow remains real

$$\begin{aligned} \partial_t \lambda_1 &= \alpha\lambda_1^2 + \beta\lambda_1 + \gamma \\ \partial_t \lambda_2 &= 0 \end{aligned} \tag{32}$$

with the periodic solution

$$\lambda_1(t) = \frac{-\beta + \sqrt{-D}\tan[\frac{\sqrt{-D}}{2}(t+\eta)]}{2\alpha}, \tag{33}$$

where η is fixed by the initial condition $\lambda_1(t=0)$. The solution can be nicely identified with a limit cycle if we map the complex plane of the Riemann sphere. On the Riemann sphere the real line corresponds to a great circle and the solution (33) traverses this circle periodically (see Fig. 4 (A) and Appendix A). Remarkably, on the complex plane the real axis is the separatrix of the two complex fixed points.

Let us investigate the properties of the fixed points $\lambda^\pm$ by considering the stability matrices

$$M_{ij}^\pm = \frac{\partial \beta_i}{\partial \lambda_j}|_{\lambda^\pm}. \tag{34}$$

A straightforward computation shows

$$M^\pm = \begin{pmatrix} 0 & -b^\pm \\ b^\pm & 0 \end{pmatrix}, \qquad b^\pm = \pm i\sqrt{|D|}. \tag{35}$$

The stability matrices $M^\pm$ have a pair of complex conjugate pure imaginary eigenvalues

$$\kappa_1^\pm = \pm i\sqrt{|D|} \qquad \kappa_2^\pm = (\kappa_1^\pm)^*. \tag{36}$$

Therefore, the local flow near the fixed points has a form of a circle. The sign of $b^\pm$ in the matrix (35) determines the orientation of the circle. For $b^\pm > 0$ the circulation is anticlockwise, while for $b^\pm < 0$ it is clockwise. Hence the fixed points $\lambda^\pm$ have the opposite circulation.

The phase portrait of the RG flow in the complex plane, computed numerically for specific values of parameters, and the example of the RG flow are depicted in Fig. 5. We observe

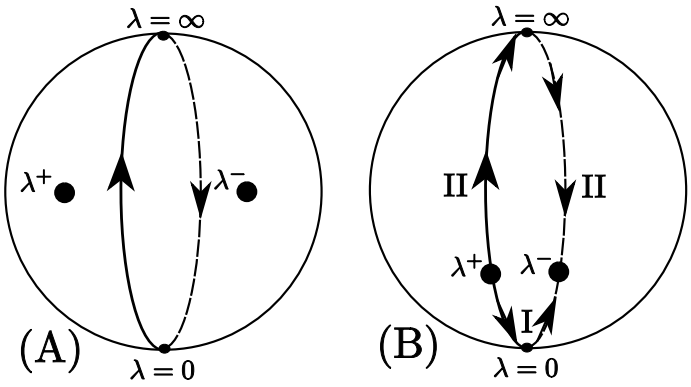

Figure 4: The real flows of λ projected onto the Riemann sphere: Great circle with arrows pointing towards the UV represents the real line. (A) For negative discriminant the fixed points λ^+ and λ^- are complex, and the flow traverses the real great circle periodically generating a limit cycle. (B) For positive discriminant the IR fixed point λ^+ and the UV fixed point λ^- lie on the real great circle. The UV fixed point can be reached from the IR fixed point via two different paths– the "short" path I and the "long" path II.

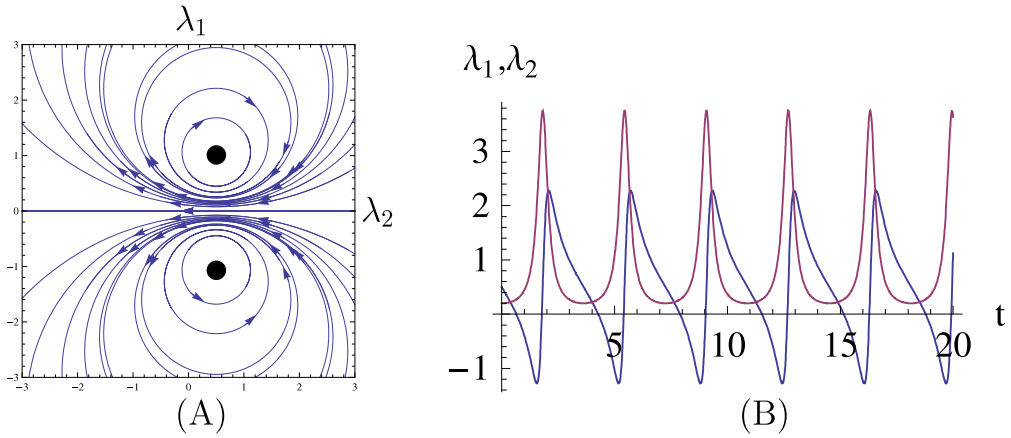

Figure 5: (A) The phase portrait of the flow equations (31) for the specific choice of parameters $\alpha = \gamma = -1$ and $\beta = 1$. Arrows denote the direction towards the UV. (B) Corresponding periodic flows of the real part λ_1 (blue) and the imaginary part λ_2 (red) of the complex coupling λ.

that the periodic divergences of the pure real solution (33) are regularized and the flow of the imaginary part λ_2 develops a tower of resonances. The analytic solution of Eq. (31) for $D < 0$ is given in Sec. V.

B. Positive discriminant: real fixed points

If the discriminant D is positive, the β-function has a pair of real roots

$$\lambda^{\pm} = \frac{-\beta \pm \sqrt{D}}{2\alpha}. \tag{37}$$

As before, we generalize the coupling to complex values $\lambda = \lambda_1 + i\lambda_2$ and obtain the pair of coupled differential equations (31). The phase portrait and a specific solution of the flow equations (31) for $D > 0$ are depicted in Fig. 6. We find the analytic solution of Eq. (31) for $D > 0$ in Sec. V.

The character of the fixed points $\lambda_{\pm}$ can be determined from the stability matrices $M^{\pm}_{ij}$, defined by Eq. (34). For $D > 0$, we obtain

$$M^{\pm} = \begin{pmatrix} \pm\sqrt{D} & 0 \\ 0 & \pm\sqrt{D} \end{pmatrix} = \pm\sqrt{D} I \tag{38}$$

with the degenerate eigenvalues $\kappa^{\pm}$

$$\kappa^{\pm} \equiv \kappa^{\pm}_1 = \kappa^{\pm}_2 = \pm\sqrt{D}. \tag{39}$$

The sign of the real eigenvalue determines whether the fixed point is UV attractive or repulsive. The eigenvalue κ^+ is positive and hence the fixed point λ^+ (left fixed point in Fig. 6(A)) is UV repulsive, meaning that as the sliding scale k is increased the flow is driven away from λ^+. On the other hand κ^- is negative and therefore the fixed point λ^- (right fixed point in Fig. 6(A)) is UV attractive. Notice that any two-component vector is an eigenvector of the fixed points $\lambda^{\pm}$.

We propose a geometric interpretation for the different behavior of the real solution in dependence on the initial conditions, which we observed in Sec. III. For a positive discriminant D both the UV fixed point λ^- and the IR fixed point λ^+ are situated on the large real circle on the Riemann sphere (see Fig. 4 (B) and Appendix A). We note that the UV fixed point can be reached from the IR fixed point following two different paths. Depending on the initial conditions $\lambda_{\text{in}} = \lambda^+ \pm \epsilon$, the flow can follow either a "short" path I or a "long" path II (see Fig. 4 (B)). Path I corresponds to the solution (23), which is a standard way how to regularize the inverse square potential at $\kappa < \kappa_{cr}$. On the other hand, the path II traverses $\lambda = \infty$ on the Riemann sphere and corresponds to the solution (24)

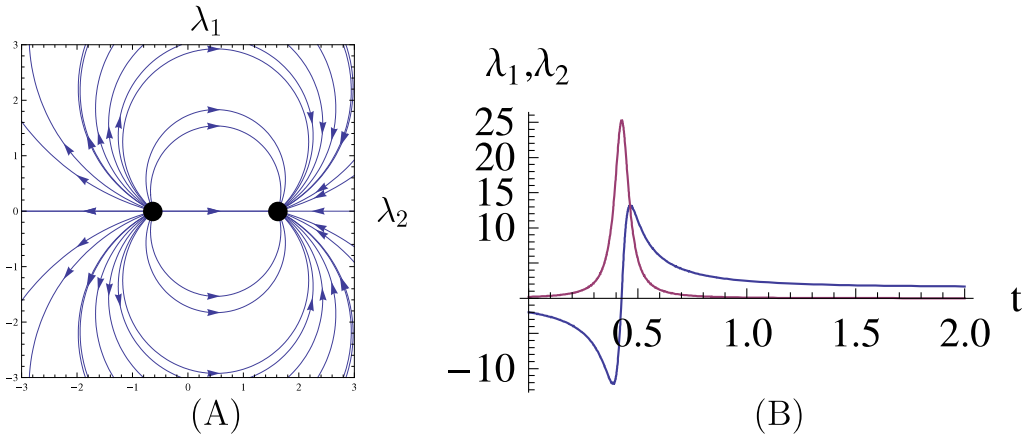

Figure 6: (A) The phase portrait of the flow equations (31) for the specific choice of parameters $\alpha = -1$ and $\beta = \gamma = 1$. Arrows denote the direction towards the UV. (B) Corresponding renormalization group flows of the real part λ_1 (blue) and the imaginary part λ_2 (red) of the complex coupling λ.

with the Landau pole. The divergence during the RG evolution is identified with a single bound state, which, in the case of $\kappa = 0$, becomes the the well-known shallow dimer studied extensively in atomic physics [23]. We notice that on the full Riemann sphere the path II can be continuously deformed into the path I. Thus, the introduction of a small imaginary initial condition $\lambda_2(t = 0)$ for the complex extended flow, which leads to a small deformation of the path II, regularizes the divergence in the real part of the coupling (see Fig. 6 and Appendix A).

C. Zero discriminant: degenerate fixed points

Finally, for $D = 0$, the pair of roots of the β-function becomes degenerate

$$\lambda_* \equiv \lambda^+ = \lambda^- = -\frac{\beta}{2\alpha} \tag{40}$$

which corresponds to a single, real-valued fixed point λ_*.

As it turns out, the stability matrix $M_{ij} = \frac{\partial \beta_i}{\partial \lambda_j}|_{\lambda_*}$ vanishes in the case of $D = 0$. This corresponds to a logarithmic (marginal) renormalization group flow in the vicinity of the fixed point and local properties of the degenerate fixed point λ_* are accounted for by the

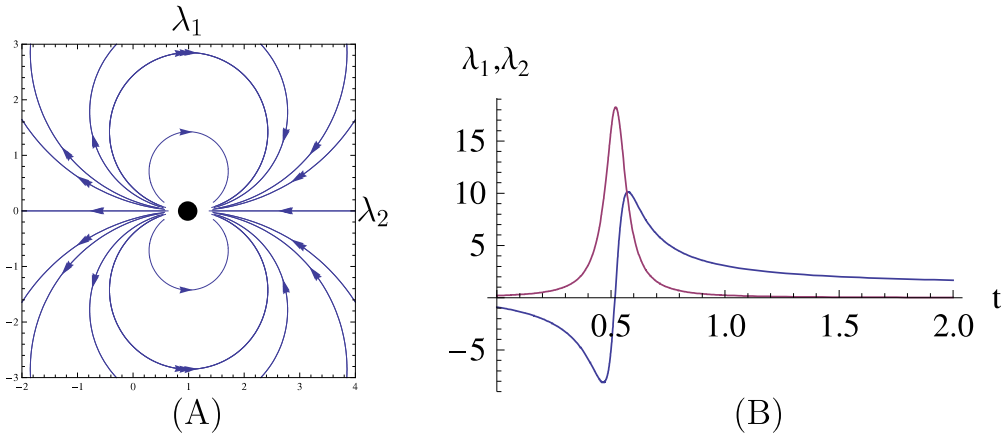

Figure 7: (A) The phase portrait of the flow equations (31) for the specific choice of parameters $\alpha = -1$, $\beta = 2$ and $\gamma = -1$. Arrows denote the direction towards the UV. (B) Corresponding renormalization group flows of the real part λ_1 (blue) and the imaginary part λ_2 (red) of the complex coupling λ.

second derivative of the β-function K_{ijl} at λ_*

$$K_{ijl} = \frac{\partial^2 \beta_i}{\partial\lambda_j \partial\lambda_l}|_{\lambda^*} \qquad i,j,l = 1,2. \tag{41}$$

The only nontrivial components are

$$K_{111} = -K_{122} = K_{212} = K_{221} = 2\alpha. \tag{42}$$

Again, we computed the phase portrait and a specific solution of the flow equations (31) and show the results in Fig. 7. We observe that the Landau pole of the real part of λ is regularized and the imaginary part of λ develops a single resonance.

D. Physical interpretation of the complex extension

One may wonder about the physical meaning of the complex contact coupling λ introduced in this section. To answer this question, we consider inelastic scattering[6] of particles

[6] By definition inelastic collisions change the internal state of the colliding particles and, hence, at least one of the colliding particles must be composite and have some internal structure. For example, in experiments two atoms might collide and fall into energetically deeper lying internal states. The excess in energy will be converted into kinetic energy and the atoms will be lost if the released energy suffices to overcome the trapping potential.

in a central potential in quantum mechanics. Following [2] in three spatial dimensions the scattering amplitude in the center of mass frame can be expanded in partial waves

$$f_k(\theta) = \sum_{l=0}^{l=\infty} (2l+1) f_l(k) P_l(\cos(\theta)), \tag{43}$$

where $P_l(\cos\theta)$ are the Legendre polynomials. From the unitarity constraints the partial waves scattering amplitudes $f_l(k)$ as functions of scattering momentum k are given by

$$f_l(k) = \frac{1}{g_l(k^2) - ik}. \tag{44}$$

Here, $g_l(k^2)$ is an even function of k which is generally complex in the case of presence of inelastic channels.

For low-energy scattering of particles, interacting through a short-range potential, only the s-wave contribution $f = f_0$ is substantial and $g(k^2) = g_0(k^2)$ can be expanded as

$$g(k^2) = -a^{-1} + \frac{1}{2} r_{\text{eff}} k^2 + \ldots, \tag{45}$$

where in the case of elastic scattering a and r_{eff} are real and denote the scattering length and effective range. However, in the inelastic case a may also be regarded as a complex scattering length $a = \alpha + i\beta$ and the effective range r_{eff} might also be complex [37]. In the forthcoming argument it is sufficient to consider low energy scattering and therefore we keep only the scattering length a and neglect the second term in Eq. (45).

The generalized optical theorem for the scattering of indistinguishable particles

$$\text{Im} f(k) = \frac{k}{8\pi} \sigma_{tot} = \frac{k}{8\pi} (\sigma_{el} + \sigma_{in}) \tag{46}$$

holds also in the case of general inelastic scattering [2]. In this case the total scattering cross section σ_{tot} is the sum of the positive elastic σ_{el} and inelastic σ_{in} contributions. The positivity of σ_{in} and the optical theorem (46) imply that the imaginary part of the scattering length β must be negative. At low energies and for sufficiently short-range interactions the complex scattering length fully determines the elastic and inelastic cross sections, and for indistinguishable particles the result reads [2]

$$\begin{aligned} \sigma_{el} &= 8\pi |a|^2 (1 - 2k|\beta|) \\ \sigma_{in} &= 8\pi \frac{|\beta|}{k} (1 - 2k|\beta|). \end{aligned} \tag{47}$$

We observe that a non-vanishing imaginary part of the scattering length β is required to obtain an inelastic contribution to the total cross section[7], which results in loss of particles.

The presented arguments can be connected to a complex generalization of λ by the simple observation that in a system of identical bosons with short-range interactions the physical scattering length a is related to the IR value of the dimensionful, contact coupling λ_ψ in $d = 3$ via the simple formula (in the case of $\kappa = 0$)

$$\lambda_\psi(k = 0) = -8\pi a. \tag{48}$$

Thus, allowing for complex values of λ_ψ during the RG flow corresponds to the presence of inelastic two-body collisions leading to particle loss. This provides a physical interpretation of the complex coupling λ_ψ. We must stress, however, that the local $(\psi^\dagger\psi)^2$ operator with a negative imaginary coefficient can describe inelastic scattering only to deep energetic states, i.e. the gap energy E_{gap} of the state must be large compared to other energy scales in the problem [38]. On the other hand, decay into shallow bound states can be described by introduction of a non-local operator with a complex coefficient. In fact, a large imaginary part of the two-body interaction might also be useful in the context of atomic physics. This case has recently been studied for cold atoms confined to motion in 1D. In particular it has been shown that a Tonks-Girardeau gas, where 1D strongly repulsive bosons exhibit fermionic like behavior, can also be induced by the effect of strong dissipation [39, 40], meaning large imaginary two-body interaction $\lambda_{\psi 2}$.

Finally, we note that our extension of the RG equation to the complex plane can be used as an efficient numerical tool. As was demonstrated in Sec. III, the flow equation (22) has the periodic solution (27) in the non-conformal phase. The running coupling $\lambda_{\psi R}$ diverges periodically during the RG evolution, making the numerical solution impossible beyond the first divergence. We showed in this section that adding a small imaginary part to the initial condition $\lambda_{\psi R}(t = 0)$ makes the solution of Eq. (22) numerically feasible. Physically, this corresponds to converting stable bound states to long-lived resonances. As shown in the next section, the problem considered in this work can be treated analytically and hence the numerical treatment is not necessary. Nevertheless, the extension turns out to be useful in

[7] We note that according to [2] Eq. (47) is valid for sufficiently fast decrease of the interaction potential at large distances (at least $1/r^3$). Thus, it is not strictly applicable in our case of the long-range $1/r^2$ potential, and the presented argument has to be taken as heuristic.

some other few-body problems, which can not be solved analytically [36].

V. BOSONIZATION

In this section we approximate the four-particle vertex by an exchange of a composite particle. In the literature [31] this is known as bosonization procedure and it is a powerful, physically transparent concept. In this work we will bosonize in two distinct ways. The first bosonization corresponds to the exchange of a massless non-dynamical particle in the t-channel. In this realization the composite particle mediates the long-range $1/r^2$ interaction combined with the contact four-particle interaction. Alternatively, one can approximate the contact vertex by the exchange of a massive particle in the s-channel. While at low energies and momenta bosonization simply reproduces the pointlike (momentum-independent) approximation of Sec. II, it resolves some of momentum structure of the interaction at higher energies.

A. t-channel bosonization

In this subsection we approximate the total four-particle interaction vertex by the exchange of a composite massless particle χ in the t-channel.

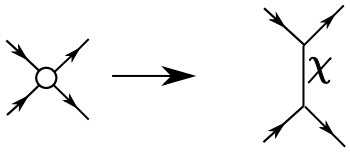

Galilean symmetry of the nonrelativistic vacuum implies that the inverse propagator $P_\chi(\omega, \vec{q})$ of the massless particle depends only on the absolute value of the spatial momentum $\vec{q}$, but not on the frequency ω. Thus, the composite χ is not a dynamical particle and serves only to mediate the two-body long-range interaction.

Mathematically, bosonization is implemented by means of the Hubbard-Stratonovich transformation. At $T = \mu = 0$ one adds an auxiliary part to the microscopic action (8)

$$\begin{aligned} S_{E,aux}[\psi,\psi^*,\chi] = \frac{1}{2}\int_{Q_1,Q_2,\ldots,Q_4} & P_\chi(l)\{\chi(-L) + \frac{g}{2P_\chi(\vec{l})}\psi^*(Q_1)\psi(Q_2)\}\times \\ & \{\chi(L) + \frac{g}{2P_\chi(\vec{l})}\psi^*(Q_3)\psi(Q_4)\}\times \\ & \delta(-Q_1+Q_2-Q_3+Q_4), \end{aligned} \tag{49}$$

where $L = (\omega_l, \vec{l}) = Q_2 - Q_1 = Q_3 - Q_4$ is the momentum transfer $d+1$-vector and χ is a real-valued field. The modified action $S_E^{'} = S_E + S_{E,aux}$ defines an equivalent quantum mechanical problem as the action S_E because the functional integral in the field χ is Gaussian.

Notably, at the UV scale we can achieve the cancellation of the four-particle interaction term by choosing the non-local inverse propagator

$$P_\chi(l) = \frac{g^2}{4}\left[\lambda_\psi^{UV} + 2\kappa F_d(l)\right]^{-1}, \tag{50}$$

where λ_ψ^{UV} is the microscopic (bare) contact coupling in Eq. (8). The modified bare action $S_E^{'}$ now reads

$$\begin{aligned} S_E^{'}[\psi,\psi^*,\chi] = & \int_Q \psi^*(Q)[i\omega + \vec{q}^2]\psi(Q) + \frac{1}{2}\int_Q \chi(-Q)P_\chi(q)\chi(Q) \\ & + g\int_{Q_1,Q_2,Q_3} \psi^*(Q_1)\psi(Q_2)\chi(Q_3)\delta(-Q_1+Q_2+Q_3) \end{aligned} \tag{51}$$

with the four-boson interaction replaced by the Yukawa-like term $\chi\psi\psi^*$. Our truncation for the flowing action is chosen to be

$$\begin{aligned} \Gamma_k[\psi,\psi^*,\chi] = & \int_Q \psi^*(Q)P_\psi(Q)\psi(Q) + \frac{1}{2}\int_Q \chi(-Q)P_\chi(Q)\chi(Q) \\ & + g\int_{Q_1,Q_2,Q_3} \psi^*(Q_1)\psi(Q_2)\chi(Q_3)\delta(-Q_1+Q_2+Q_3) \\ & - \frac{\lambda}{2}\int_{Q_1,Q_2,\ldots,Q_4} \psi^*(Q_1)\psi(Q_2)\psi^*(Q_3)\psi(Q_4)\delta(-Q_1+Q_2-Q_3+Q_4), \end{aligned} \tag{52}$$

where λ is a contact coupling, which is zero in the ultraviolet by construction and is regenerated during the RG flow through a box diagram.

Due to the numerous simplifications of the nonrelativistic vacuum, which are described in detail in [33], we note

- the inverse propagators P_ψ and P_χ are not renormalized during the RG flow

$$P_\psi(Q) = i\omega + \vec{q}, \qquad P_\chi(Q) = \frac{g^2}{4}\left[\lambda_\psi^{UV} + 2\kappa F_d(l)\right]^{-1}. \tag{53}$$

  Technically this arises from the fact that the one-loop Feynman diagrams, which would renormalize P_ψ and P_ϕ, have poles in the same half plane of the complex loop frequency. One can close the integration contour such that it does not enclose any frequency poles. As the result of the residue theorem, the frequency integrals vanish, leading to the non-renormalization of the propagators. We observe the clear manifestation of the non-renormalization of the long-range potential, mentioned already in Sec. II. Another example for this behavior is the boundary sine-Gordon theory, which was studied in [41, 42].

- The coupling g can be chosen arbitrarily, e.g. $g = 1$, at the UV scale. This is a well-know ambiguity of the Hubbard-Stratonovich decoupling. Furthermore, the coupling g is also not renormalized during the renormalization group evolution for the reason mentioned in the previous point.

- Interaction terms of the form χ^n with $n \geq 1$ and $\psi^*\psi\chi^k$ with $k > 1$ are absent in the ultraviolet and are not generated during the flow due to the argument provided above. On the other hand interaction terms of the form $(\psi^*\psi)^2\chi^k$ with $k \geq 0$ are generated through box diagrams during the renormalization group evolution.

- Our truncation is complete up to the two-body sector. This is a result of the special hierarchy of the flow equations in the nonrelativistic vacuum [32, 33], where the couplings from the higher-body sectors do not influence the couplings from the lower-body sectors.

It is straightforward to derive the flow equation of the momentum-independent coupling λ. The result turns out to be given by Eqs. (14, 15) with the substitution $F_d^n(l) \to F_d^n(l) + \frac{\lambda_\psi^{UV}}{2\kappa}$ in Eq. (15). The initial condition $\lambda_\psi(k = \Lambda) = \lambda_\psi^{UV}$ of the one-channel model of Sec. II is implemented directly as the initial condition of the inverse propagator P_χ in the bosonization approach. Otherwise, the flows are completely equivalent at the level of our approximation.

B. s-channel bosonization

We will follow an alternative bosonization procedure in this subsection. In this approach the four-particle contact vertex is approximated by the exchange of a massive ($M_\phi = 2M_\psi$) particle ϕ in the s-channel.

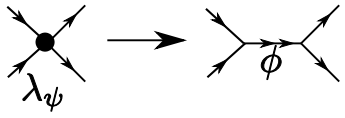

At the level of the microscopic (bare) action this is achieved via the Hubbard-Stratonovich transformation. The auxiliary part, added to the microscopic action (8) at $T = \mu = 0$, reads

$$\begin{aligned} S_{E,aux}[\psi,\psi^*,\phi,\phi^*] = \int_{Q_1,Q_2,\ldots,Q_4} & m^2\{\phi^*(Q_1+Q_3) + \frac{h}{2m^2}\psi^*(Q_1)\psi^*(Q_3)\}\times \\ & \{\phi(Q_2+Q_4) + \frac{h}{2m^2}\psi(Q_2)\psi(Q_4)\}\times \\ & \delta(-Q_1+Q_2-Q_3+Q_4). \end{aligned} \tag{54}$$

For the specific choice $\frac{\lambda_\psi}{2} = \frac{h^2}{4m^2}$, we can cancel the contact term in the modified microscopic action $S_E^{'} = S_E + S_{E,aux}$

$$\begin{aligned} S_E^{'}[\psi,\psi^*,\phi,\phi^*] = & \int_Q \psi^*(Q)[i\omega + \vec{q}^2]\psi(Q) + \int_Q \phi^*(Q)m^2\phi(Q) \\ & + \frac{h}{2}\int_{Q_1,Q_2,Q_3} [\phi^*(Q_1)\psi(Q_2)\psi(Q_3) + \phi(Q_1)\psi^*(Q_2)\psi^*(Q_3)]\,\delta(-Q_1+Q_2+Q_3) \\ & - \kappa\int_{Q_1,Q_2,\ldots,Q_4} F_d(l)\psi^*(Q_1)\psi(Q_2)\psi^*(Q_3)\psi(Q_4)\delta(-Q_1+Q_2-Q_3+Q_4). \end{aligned} \tag{55}$$

During the renormalization group evolution the massive field ϕ becomes dynamical and develops an inverse propagator $P_\phi(Q) = f(i\omega + \frac{\vec{q}^2}{2} + m^2)$, where f is some yet unknown function. The argument of the inverse propagator is fixed by the Galilean symmetry of the nonrelativistic vacuum, while the function f is determined by the dynamics. Our truncation

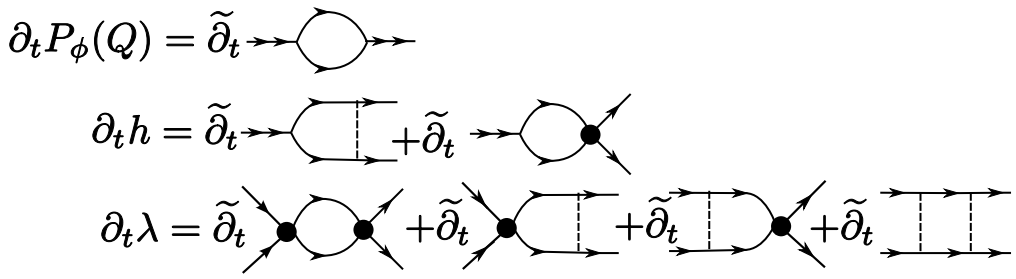

Figure 8: Flow equations of $P_\phi(Q)$, h and λ in the form of Feynman diagrams. The solid lines with one (two) arrow(s) denote regularized propagator for the field ψ (ϕ), the dashed lines correspond to the long-range interaction vertex, the dark blob represents the contact coupling λ.

of the flowing action within the s-channel bosonization approach is

$$\begin{aligned}\Gamma_k[\psi,\psi^*,\phi,\phi^*] = &\int_Q \psi^*(Q)P_\psi(Q)\psi(Q) + \int_Q \phi^*(Q)P_\phi(Q)\phi(Q)\\ &+\frac{h}{2}\int_{Q_1,Q_2,Q_3}\left(\phi^*(Q_1)\psi(Q_2)\psi(Q_3)+\phi(Q_1)\psi^*(Q_2)\psi^*(Q_3)\right)\delta(-Q_1+Q_2+Q_3)\\ &-\kappa\int_{Q_1,Q_2,\ldots,Q_4} F_d(l)\psi^*(Q_1)\psi(Q_2)\psi^*(Q_3)\psi(Q_4)\delta(-Q_1+Q_2-Q_3+Q_4)\\ &-\frac{\lambda}{2}\int_{Q_1,Q_2,\ldots,Q_4}\psi^*(Q_1)\psi(Q_2)\psi^*(Q_3)\psi(Q_4)\delta(-Q_1+Q_2-Q_3+Q_4),\end{aligned} \tag{56}$$

where h denotes the momentum-independent Yukawa-like coupling introduced above and λ stands for the contact four-boson 1PI vertex, which is regenerated during the flow through the box diagram. The non-trivial flow equations for the couplings of the average action (56) are depicted in Fig. 8 in terms of Feynman diagrams.

It is desirable and possible to cancel the RG flow of the coupling λ by absorbing it into the flows of the other couplings. This can be achieved by a rebosonization procedure [43, 44]. The idea is to make the composite field scale-dependent $\phi \to \phi_k$ with the choice

$$\partial_k\phi_k = \alpha_k\psi\psi \qquad \partial_k\phi_k^* = \alpha_k\psi^*\psi^*, \tag{57}$$

where α_k is some real, scale-dependent function. The one-loop flow equation (7) for the average action generalizes to

$$\partial_k\Gamma_k = \frac{1}{2}\mathrm{Tr}\,\partial_k R_k\left(\Gamma_k^{(2)}+R_k\right)^{-1} + \int\frac{\delta\Gamma_k}{\delta\phi_k}\partial_k\phi_k + \int\frac{\delta\Gamma_k}{\delta\phi_k^*}\partial_k\phi_k^*. \tag{58}$$

The unknown scale-dependent coefficient α_k can now be fixed by the condition that the flow of the contact coupling λ is zero

$$\partial_t \lambda = 0 \Rightarrow \lambda = 0. \tag{59}$$

The resulting flow equations (with unspecified cut-off) for the Yukawa coupling h and the inverse propagator $P_\phi(Q)$ now read

$$\begin{aligned} \partial_t P_\phi(Q) &= -\frac{1}{2} h^2 J_{0,d}(Q) \\ \partial_t h &= 2h\kappa J_{1,d} + \frac{4\kappa^2 P_\phi(Q=0) J_{2,d}}{h}, \end{aligned} \tag{60}$$

where $J_{n,d}$ was defined in Eq. (15), and for $J_{0,d}$ we introduce the momentum-dependent generalization

$$J_{0,d}(Q) = \int \frac{d\omega}{2\pi} \frac{d^d l}{(2\pi)^d} \partial_t \frac{1}{[i(\omega+\omega_q) + (\vec{l}+\vec{q})^2 + R_k(L+Q)][-i\omega + \vec{l}^2 + R_k(-L)]}. \tag{61}$$

In order to proceed we must specify the cut-off function and the ansatz for the inverse propagator of the field ϕ. We choose the sharp cut-off, introduced in Sec. II and take the simple ansatz $P_\phi(Q) = A_\phi(i\omega + \frac{q^2}{2}) + m^2$ as used also for the related vacuum 3-body problem in [34]. With this choice the flow equations become

$$\begin{aligned} \partial_t m_R^2 &= (2\xi - d - 2) m_R^2 + \frac{1}{2} h_R^2, \\ \partial_t h_R &= (\xi - 2 - \frac{\kappa}{d-2}) h_R - \frac{\kappa^2}{(d-2)^2} \frac{m_R^2}{h_R}, \\ \partial_t A_{\phi R} &= (2\xi - d) A_{\phi R} - \frac{1}{4} h_R^2, \end{aligned} \tag{62}$$

where we expressed the flows in terms of the rescaled parameters $m_R^2 = k^{-2-d+2\xi} m^2$, $A_{\phi R} = k^{-d+2\xi} A_\phi$, and $h_R = \sqrt{\frac{1}{(4\pi)^{d/2}\Gamma(\frac{d}{2})}} k^{\xi-2} h$. The parameter ξ is not specified yet, but can be identified with the naive scaling dimension of the composite field, i.e. $[\phi] = \xi$. At this point it is convenient to multiply the second equation in (62) by $2h_R$ and obtain flow equations for m_R^2 and h_R^2

$$\begin{aligned} \partial_t m_R^2 &= (2\xi - d - 2) m_R^2 + \frac{1}{2} h_R^2, \\ \partial_t h_R^2 &= -\frac{2\kappa^2}{(d-2)^2} m_R^2 + 2(\xi - 2 - \frac{\kappa}{d-2}) h_R^2. \end{aligned} \tag{63}$$

The equations in (63) form a closed linear system of first order ordinary differential equations. The eigenvalues $\lambda_\pm$ of this system can be readily found

$$\lambda_\pm = 2\xi - 3 - \frac{d}{2} - \frac{\kappa}{d-2} \pm \frac{1}{2}\sqrt{(d-2)^2 - 4\kappa}. \tag{64}$$

We note that $\kappa_{cr} = \frac{(d-2)^2}{4}$, found in Sec. II, provides an important boundary value also in the current analysis. While for $\kappa < \kappa_{cr}$ (repulsion and weak attraction) the eigenvalues are purely real, for $\kappa > \kappa_{cr}$ (strong attraction) $\lambda^{\pm}$ acquires a non-trivial imaginary part.

Let us investigate the latter case in more detail. It is convenient to cancel the real part of $\lambda^{\pm}$ by choosing $\xi = \frac{1}{2}\left(3 + \frac{d}{2} + \frac{\kappa}{d-2}\right)$. With this choice the eigenvalues $\lambda^{\pm}$ are imaginary, leading to a pure oscillatory behavior of the flows of m_R^2 and h_R^2. Choosing the initial conditions $m_R^2(t=0) = M$, $h_R^2(t=0) = H$, we obtain

$$\begin{aligned} m_R^2(t) &= M\cos(\frac{\sqrt{-D}}{2}t) + W_M \sin(\frac{\sqrt{-D}}{2}t) \\ h_R^2(t) &= H\cos(\frac{\sqrt{-D}}{2}t) + W_H \sin(\frac{\sqrt{-D}}{2}t), \end{aligned} \tag{65}$$

where $D = (d-2)^2 - 4\kappa$ is the discriminant of the quadratic β-function introduced in Sec. II and W_M and W_H can be expressed as

$$\begin{aligned} W_M &= \frac{1}{\sqrt{-D}}\left(\left[2 - d + \frac{2\kappa}{d-2}\right]M + H\right) \\ W_H &= -\frac{1}{\sqrt{-D}}\left(\frac{4\kappa^2}{(d-2)^2}M + \left[2 - d + \frac{2\kappa}{d-2}\right]H\right). \end{aligned} \tag{66}$$

As expected, we obtain a finite (bounded) limit cycle solution (65) for the pair (m_R^2, h_R^2) for strong attraction $\kappa > \kappa_{cr}$. It is clear that the infinite number of the two-body bound states, present in this case, manifest themselves as zeros of the mass coupling $m_R^2(t)$ during the RG flow.

It is possible to complexify the flow equations (63) in a similar manner as presented in Sec. IV by extending the couplings h_R^2 and m_R^2 to the complex plane

$$h_R^2 = h_{R1}^2 + i h_{R2}^2 \qquad m_R^2 = m_{R1}^2 + i m_{R2}^2. \tag{67}$$

In this extension the non-zero value of m_{R2}^2 makes the composite particle ϕ unstable. If small compared to m_{R1}^2, it equals to the decay width, which is inverse proportional to the life-time of the particle. Due to the linearity of the evolution equations (63), the flow equations for the pairs (m_{R1}^2, h_{R1}^2), (m_{R2}^2, h_{R2}^2) decouple. They have exactly the same form as Eq. (63) with the solution (65, 66), provided we perform the substitution $m_R^2 \to m_{Ri}^2$, $h_R^2 \to h_{Ri}^2, M \to M_i, H \to H_i$ with $i = 1, 2$. We depict the numerical solution of the complexified system in Fig. 9. As expected, the flow of the coupling $\lambda_R = \frac{h_R^2}{2m_R^2}$ reproduces our finding from Fig. 5.

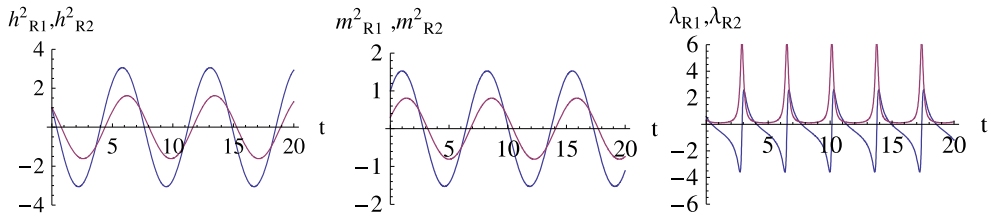

Figure 9: Periodic flows of the real part (blue) and imaginary part (red) of the complex couplings h_R^2, m_R^2 and $\lambda_R = \frac{h_R^2}{2m_R^2}$ for the specific choice of parameters $d = 3$ and $\kappa = 1$. The amplitude of the m_{R2}^2 oscillations is related to the decay rate, which must be fixed by experiment. The width of the peaks of λ_{R2} is of the order of magnitude of the decay rate.

Most importantly, we are now in the position to find an analytical solution of the general non-linear system of flow equations introduced in Sec. IV

$$\begin{aligned} \partial_t \lambda_{R1} &= \alpha \lambda_{R1}^2 - \alpha \lambda_{R2}^2 + \beta \lambda_{R1} + \gamma \\ \partial_t \lambda_{R2} &= 2\alpha \lambda_{R1} \lambda_{R2} + \beta \lambda_{R2}, \end{aligned} \tag{68}$$

with $\alpha, \beta, \gamma \in \mathbb{R}$ and $D = \beta^2 - 4\alpha\gamma < 0$. In order to achieve this goal, it is sufficient to project the complex coupling

$$\lambda_R = \frac{h_R^2}{2m_R^2} = \frac{h_{R1}^2 + i h_{R2}^2}{2[m_{R1}^2 + i m_{R2}^2]} \tag{69}$$

onto its real and imaginary part λ_{R1} and λ_{R2}

$$\lambda_{R1} = \frac{m_{R1}^2 h_{R1}^2 + m_{R2}^2 h_{R2}^2}{2[m_{R1}^4 + m_{R2}^4]} \qquad \lambda_{R2} = \frac{m_{R1}^2 h_{R2}^2 - m_{R2}^2 h_{R1}^2}{2[m_{R1}^4 + m_{R2}^4]}. \tag{70}$$

This expression comprises an explicit solution of the system (68) provided we substitute

$$\begin{aligned} m_{Ri}^2 &= M_i \cos(\frac{\sqrt{-D}}{2} t) + W_{Mi} \sin(\frac{\sqrt{-D}}{2} t) \\ h_{Ri}^2 &= H_i \cos(\frac{\sqrt{-D}}{2} t) + W_{Hi} \sin(\frac{\sqrt{-D}}{2} t) \end{aligned} \tag{71}$$

with $D = \beta^2 - 4\alpha\gamma$ and

$$\begin{aligned} W_{Mi} &= -\frac{1}{\sqrt{-D}} \left(\beta M_i + \alpha H_i\right) \\ W_{Hi} &= \frac{1}{\sqrt{-D}} \left(4\gamma M_i + \beta H_i\right), \end{aligned} \tag{72}$$

where $i = 1, 2$.

We comment on the issue of initial conditions. Obviously, the first-order system (68) must be supplemented with two initial conditions $\lambda_{R1}(t=0)$ and $\lambda_{R2}(t=0)$. In our description, however, there are four unknown constants M_1, M_2, H_1 and H_2 to be fixed. The identification

$$\lambda_{R1}(t=0) = \frac{1}{2}\frac{M_1 H_1 + M_2 H_2}{M_1^2 + M_2^2} \qquad \lambda_{R2}(t=0) = \frac{1}{2}\frac{M_1 H_2 - M_2 H_1}{M_1^2 + M_2^2} \tag{73}$$

fixes only two of them, leaving the remaining two ambiguous. This is the known arbitrariness arising in the Hubbard-Stratonovich transformation. Remarkably, one can fix the remaining two constants almost arbitrarily[8]. An especially convenient choice corresponds to $M_1 = 1$ and $M_2 = 0$. With this choice we have

$$\lambda_{R1}(t=0) = \frac{1}{2}H_1 \qquad \lambda_{R2}(t=0) = \frac{1}{2}H_2. \tag{74}$$

We present also the analytic solution of Eq. (68) in the conformal phase with $D > 0$. The solution is still given by Eq. (70) provided we substitute

$$\begin{aligned} m_{Ri}^2 &= M_i \cosh(\frac{\sqrt{D}}{2}t) + W_{Mi}\sinh(\frac{\sqrt{D}}{2}t) \\ h_{Ri}^2 &= H_i \cosh(\frac{\sqrt{D}}{2}t) + W_{Hi}\sinh(\frac{\sqrt{D}}{2}t) \end{aligned} \tag{75}$$

with

$$\begin{aligned} W_{Mi} &= -\frac{1}{\sqrt{D}}\left(\beta M_i + \alpha H_i\right) \\ W_{Hi} &= \frac{1}{\sqrt{D}}\left(4\gamma M_i + \beta H_i\right). \end{aligned} \tag{76}$$

Finally we note that the analytic solution (69) can be expressed in the unified, compact form

$$\lambda_R = \frac{1}{2\alpha}\left(-\beta - \sqrt{D}\frac{e^{\frac{\sqrt{D}t}{2}} - Ce^{-\frac{\sqrt{D}t}{2}}}{e^{\frac{\sqrt{D}t}{2}} + Ce^{-\frac{\sqrt{D}t}{2}}}\right) \tag{77}$$

for both conformal and non-conformal phase. In the last expression $\sqrt{D} \equiv \sqrt{D+i\epsilon} = i\sqrt{-D}$ for $D < 0$, and the complex constant C determines the initial condition for λ_R. Using Eq. (77) we compute the curvature $\widetilde{\kappa}$ and the related radius R of the complex RG trajectories, which are given by

$$\widetilde{\kappa} = \frac{1}{R} = \frac{|\lambda'_{R1}\lambda''_{R2} - \lambda'_{R2}\lambda''_{R1}|}{[\lambda'^2_{R1} + \lambda'^2_{R2}]^{3/2}}. \tag{78}$$

[8] Some discrete values of two constants lead to a degenerate solution and are therefore forbidden.

Here the primes denote the first and second derivative with respect to t. We observe that the curvature does not depend on the "RG time" t in both the conformal and non-conformal phase. For $D > 0$ the trajectories form arcs of circles of radius $R = |\frac{C}{2\alpha \mathrm{Im} C}|\sqrt{D}$ (see Fig. 6), while for $D < 0$ the trajectories constitute closed circles of radius $R = |\frac{C}{\alpha(1-|C|^2)}|\sqrt{-D}$ (see Fig. 5).

VI. CONCLUSIONS

In this work we investigated the nonrelativistic, quantum-mechanical problem of an inverse square potential problem using functional renormalization. The potential is classically scale-invariant. Additionally, it is singular at the origin and the model must be augmented by a contact term, which is necessary for renormalization. We demonstrated that the RG flow of the contact coupling λ either approaches a real fixed point (conformal phase) in the IR and UV or undergoes a scale anomaly which manifests itself in an infinite, unbounded limit cycle (non-conformal case). The overall behavior is determined by the sign of the discriminant D of the quadratic β-function of the contact coupling, and depends on the strength of the long-range inverse square potential and spatial dimension. Remarkably, in the non-conformal phase ($D < 0$) the β-function possesses a pair of complex conjugate fixed points. This observation led us naturally to the extension of the RG analysis to complex values of the coupling $\lambda \to \lambda_1 + i\lambda_2$. The RG evolution was computed numerically and the phase portraits of the flows were obtained. Additionally, we provided a geometric description of the complex flows on the Riemann sphere. We observed that in the non-conformal phase the real part λ_1 and the imaginary part λ_2 develop a finite (bounded) limit cycle in the complex plane. This suggests that the complex extension can be utilized as an efficient numerical tool for investigation of various problems with infinite (unbounded) limit cycles, as for example, in few-body physics of cold atoms near unitarity. One should simply add a small imaginary part λ_2 to the real part λ_1 and follow the extended RG evolution. This procedure regulates the periodic singularities during the RG flow making the numerical treatment feasible. From a physical point of view, the introduction of the complex coupling constant appears quite natural since it arises from an inelastic channel in the two-body scattering. The bosonization procedure allowed us to view the problem from a different perspective. More importantly, it enabled us to find an analytical solution of the extended set of non-linear flow equations.

Quite surprisingly, a similar RG behavior as in our case of an inverse square potential appears also in the context of chiral dynamics in QCD with a large number of flavors [45, 46]. Here, gluon exchange between the quarks induces quark self-interactions. The flow equations governing the RG evolution of these self-interactions exhibit the same behavior as shown in Fig. 2. Depending on the value of the gauge coupling α the flow equations possess either two fixed points ($\alpha < \alpha_{cr}$) and the system is in the chiral symmetric phase, or as α increases above this critical value α_{cr} one ends up in the chiral symmetry broken phase. The analog to the conformal symmetry breaking in dependence on the value of κ in our simple case of an inverse square potential appears to be quite remarkable.

Finally, we comment on a possible connection between our work and the recent studies of non-Fermi liquids using the AdS/CFT correspondence [47–49]. The authors of [48, 49] studied the relativistic many-body physics of fermions at vanishing temperature in d space-time dimensions by mapping onto a classical gravity problem with an extremal charged black hole in anti-de Sitter spacetime (AdS_{d+1}). In this description the low-energy scaling behavior around the Fermi surface is related to the near-horizon geometry, which turns out to be $AdS_2 \times \mathbb{R}^{d-1}$. Notably, the isometry group of the AdS_2 part is $SO(2,1)$, which is exactly the symmetry group of the quantum mechanics of the inverse square potential in the conformal phase [18]. This suggests that the emergent IR CFT, defined in [49], might be conformal quantum mechanics with the inverse square potential. Another evidence in this direction is given by the observation that the low-energy behavior of the real and imaginary parts of the retarded Green functions, computed numerically in [48, 49], agrees remarkably well with the RG flows of the real and imaginary part of the contact coupling in conformal and non-conformal phases (see Figs. 5, 6). This suggests that the complex extension and its analytical solution, found in this work, might be useful for a better understanding of non-fermi liquids from the AdS/CFT correspondence.

Acknowledgments – It is our pleasure to acknowledge the discussions with S. Floerchinger, H.-W. Hammer, J. M. Pawlowski, D. T. Son, C. Wetterich and W. Zwerger. We are thankful to J. Hošek for critical reading of the manuscript. SM is grateful to KTF for support. RS thanks the DFG for support within the FOR 801 'Strong correlations in multiflavor ultracold quantum gases'.

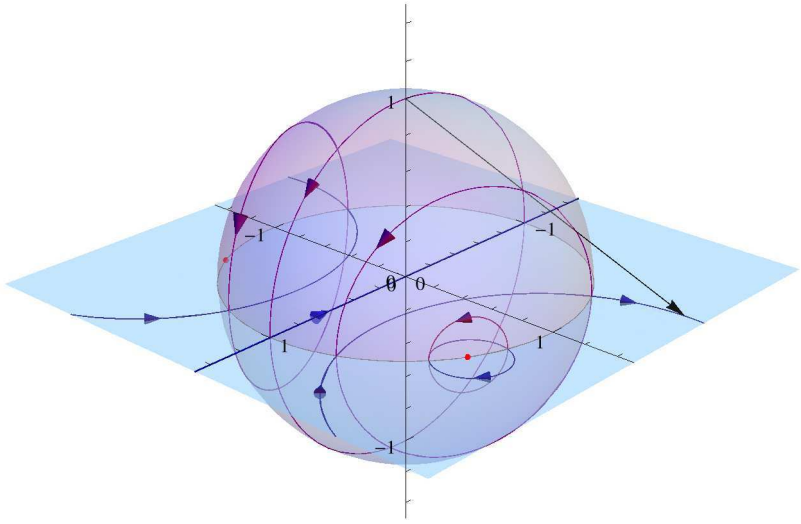

Figure 10: RG flows on the complex plane and the corresponding map onto the Riemann sphere in the non-conformal phase. The pink dots represent the two complex fixed points. The solid lines with arrows, pointing towards the UV, correspond to different RG trajectories. Additionally, the black straight solid line from the north pole illustrates the stereographic projection of the Riemann sphere S^2 onto the complex plane $\mathbb{C}$.

Appendix A: Complex RG flows on the Riemann sphere

As has already been noted in Sec. IV, the generalized RG flow of the complex coupling $\lambda = \lambda_1 + i\lambda_2$ can be most conveniently studied on the Riemann sphere. The Riemann sphere is a unit sphere S^2 in three dimensional real space $\mathbb{R}^3$, which intersects the complex plane $\overline{\mathbb{C}} = \mathbb{C} \cup \{\infty\}$ at the equator. The map σ: $S^2 \to \overline{\mathbb{C}}$ onto the complex plane (λ_1, λ_2) is given by the stereographic projection (see Fig. 10) and reads in the Cartesian coordinates $(x, y, z) \in S^2$

$$\begin{aligned} \lambda_1 = \frac{x}{1-z}, \quad \lambda_2 = \frac{y}{1-z} \qquad & \text{if} \quad (x,y,z) \neq (0,0,1) \\ (\lambda_1, \lambda_2) = \infty \qquad & \text{if} \quad (x,y,z) = (0,0,1). \end{aligned} \tag{A1}$$

The inverse map is given by

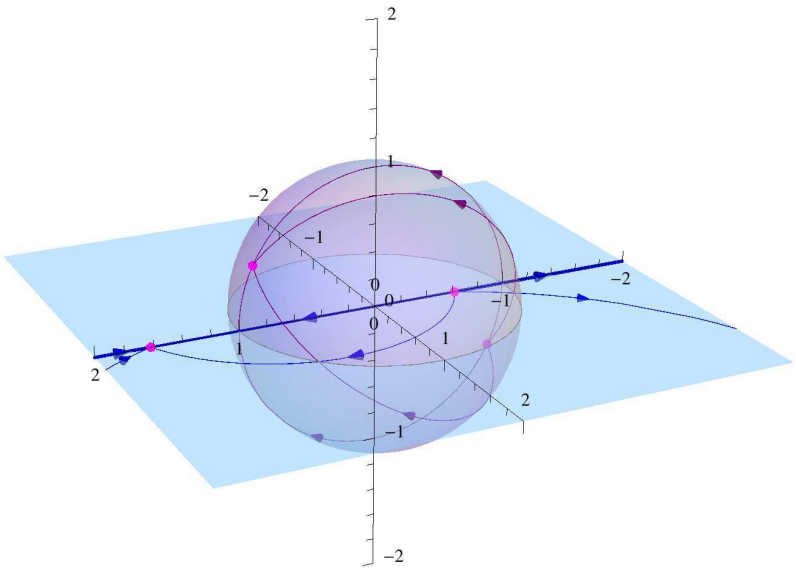

Figure 11: RG flows on the complex plane and the corresponding map onto the Riemann sphere in the conformal phase. The pink dots represent the two real fixed points. The solid lines with arrows, pointing towards the UV, correspond to different RG trajectories.

$$x = \frac{2\lambda_1}{\lambda_1^2+\lambda_2^2+1}, \qquad y = \frac{2\lambda_2}{\lambda_1^2+\lambda_2^2+1}, \qquad z = \frac{\lambda_1^2+\lambda_2^2-1}{\lambda_1^2+\lambda_2^2+1}, \qquad \lambda \neq \infty$$
$$x = 0, \qquad y = 0, \qquad z = 1, \qquad \lambda = \infty. \tag{A2}$$

The analytical solution of the complex flow equations (31) was obtained in Sec. V. We substitute these solutions into Eq. (A2) and obtain the analytical solution on the Riemann sphere, which we plot for both the non-conformal ($D < 0$) and the conformal ($D > 0$) phases in Figs. 10, and 11.

[1] H. Feshbach and P. M. Morse, "Methods of Theoretical Physics II", McGrow-Hill book company, 1953.

[2] L. D. Landau, E. M. Lifshitz, "Quantum Mechanics: Non-relativistic Theory", Pergamon Press, 1977.

[3] K. M. Case, Phys. Rev. **80**, 797 (1950).

[4] V. de Alfaro, S. Fubini and G. Furlan, Nuovo Cim. A **34**, 569 (1976).

[5] E. Kolomeisky and J. P. Straley, Phys. Rev. B **46**, 12664 (1992).

[6] K. S. Gupta and S. G. Rajeev, Phys. Rev. D **48**, 5940 (1993).

[7] S. R. Beane, P. F. Bedaque, L. Childress, A. Kryjevski, J. McGuire and U. v. Kolck, Phys. Rev. A **64**, 042103 (2001).

[8] T. Barford and M. C. Birse, Phys. Rev. C **67**, 064006 (2003).

[9] M. Bawin and S. A. Coon, Phys. Rev. A **67**, 042712 (2003).

[10] E. J. Mueller and T. L. Ho, [arXiv:cond-mat/0403283].

[11] E. Braaten and D. Phillips, Phys. Rev. A **70**, 052111 (2004).

[12] T. Barford and M. C. Birse, J. Phys. A **38**, 697 (2005).

[13] H. W. Hammer and B. G. Swingle, Annals Phys. **321**, 306 (2006).

[14] H. W. Hammer and R. Higa, Eur. Phys. J. A **37**, 193 (2008).

[15] D. B. Kaplan, J. W. Lee, D. T. Son and M. A. Stephanov, arXiv:0905.4752 [hep-th].

[16] W. Frank, D. J. Land and R. M. Spector, Rev. Mod. Phys. **43**, 36 (1971).

[17] Y. Nishida and D. T. Son, Phys. Rev. D **76**, 086004 (2007).

[18] H. E. Camblong and C. R. Ordonez, Phys. Rev. D **68**, 125013 (2003).

[19] V. Efimov, Phys. Lett. **33B**, 563 (1970); V. Efimov, Nucl. Phys. A **210**, 157 (1973).

[20] E. Nielsen, D. V. Fedorov, A. S. Jensen and E. Garrido, Phys. Rep. **347**, 373 (2001).

[21] J. Macek, J. Phys. B **1**, 831 (1968).

[22] L. D. Faddeev, Sov. Phys. JETP **12**, 1014 (1961).

[23] E. Braaten, H.W. Hammer, Phys. Rept. **428**, 259 (2006).

[24] H. E. Camblong, L. N. Epele, H. Fanchiotti and C. A. Garcia Canal, Phys. Rev. Lett. **87**, 220402 (2001).

[25] J. M. Kosterlitz, and D. J. Thouless, J. Phys. C, Solid State Phys., **6**, 1181-1203 (1973).

[26] P. Claus, M. Derix, R. Kallosh, J. Kumar, P. K. Townsend and A. Van Proeyen, Phys. Rev. Lett. **81**, 4553 (1998)

[27] J. M. Maldacena, Adv. Theor. Math. Phys. **2** (1998) 231 [Int. J. Theor. Phys. **38** (1999) 1113]. S. S. Gubser, I. R. Klebanov and A. M. Polyakov, Phys. Lett. B **428** (1998) 105. E. Witten, Adv. Theor. Math. Phys. **2** (1998) 253.

[28] C. Wetterich, Phys. Lett. B **301** (1993) 90.

[29] J. Berges, N. Tetradis and C. Wetterich, Phys. Rept. **363** (2002) 223.

[30] T. R. Morris, Prog. Theor. Phys. Suppl. **131** (1998) 395; K. Aoki, Int. J. Mod. Phys. B **14** (2000) 1249; C. Bagnuls and C. Bervillier, Phys. Rept. **348** (2001) 91; J. Polonyi, Central Eur. J. Phys. **1** (2003) 1; M. Salmhofer and C. Honerkamp, Prog. Theor. Phys. **105** (2001) 1; B. Delamotte, D. Mouhanna and M. Tissier, Phys. Rev. B **69** (2004) 134413; B. J. Schaefer and J. Wambach, hep-ph/0611191.

[31] H. Gies, arXiv:hep-ph/0611146.

[32] S. Diehl, H. C. Krahl, M. Scherer, Phys. Rev. C **78**, 034001 (2008).

[33] S. Moroz, S. Floerchinger, R. Schmidt and C. Wetterich, Phys. Rev. A **79**, 042705 (2009).

[34] S. Floerchinger, R. Schmidt, S. Moroz and C. Wetterich, Phys. Rev. A **79**, 013603 (2009).

[35] R. Schmidt, S. Floerchinger and C. Wetterich, Phys. Rev. A **79**, 053633 (2009).

[36] R. Schmidt, and S. Moroz, in preparation.

[37] M. S. Hussein, arXiv.org:physics/0003081.

[38] E. Braaten, D. Kang and L. Platter, Phys. Rev. A **78**, 053606 (2008).

[39] N. Syassen et. al., Science **320**, 1329 (2008).

[40] M. Kiffner, M. J. Hartmann, arXiv:0908.2055 [quant-ph].

[41] M. P. A. Fisher, and W. Zwerger, Phys. Rev. B **32**, 6190 (1985).

[42] F. Guinea, V. Hakim, and A. Muramatsu, Phys. Rev. Lett. **54**, 263 (1985).

[43] H. Gies and C. Wetterich, Phys. Rev. D **65**, 065001 (2002); Acta Phys. Slov. **52**, 215 (2002).

[44] J. M. Pawlowski, Ann. Phys. (N.Y.) **322**, 2831 (2007).

[45] H. Gies, and J. Jaeckel, Eur. Phys. J. C **46**, 433-438 (2006).

[46] J. Braun, and H. Gies, JHEP 0606 (2006) 024; Phys. Lett. B **645** 53-58 (2007).

[47] S. S. Lee, Phys. Rev. D **79**, 086006 (2009).

[48] H. Liu, J. McGreevy and D. Vegh, arXiv:0903.2477 [hep-th].

[49] T. Faulkner, H. Liu, J. McGreevy and D. Vegh, arXiv:0907.2694 [hep-th].

Renormalization group study of the four-body problem

Richard Schmidt* and Sergej Moroz†
*Physik Department, Technische Universität München, James-Franck-Strasse, D-85748 Garching, Germany
†Institut für Theoretische Physik, Universität Heidelberg, Philosophenweg 16, D-69120 Heidelberg, Germany

We perform a renormalization group analysis of the non-relativistic four-boson problem by means of a simple model with pointlike three- and four-body interactions. We investigate in particular the region where the scattering length is infinite and all energies are close to the atom threshold. We find that the four-body problem behaves truly universally, independent of any four-body parameter. Our findings confirm the recent conjectures of Platter et al. and von Stecher et al. [1–3] that the four-body problem is universal, now also from a renormalization group perspective. We calculate the corresponding relations between the four- and three-body bound states, as well as the full bound state spectrum and comment on the influence of effective range corrections.

PACS numbers: 03.65.Nk, 34.50.-s,11.10.Hi

I. INTRODUCTION

During the last decade few-body physics experienced a renewed interest due to the advent of experiments with ultracold atomic gases. Whereas the study of few-body physics in nuclear systems is hindered by the large complexity of the interparticle potentials, the interactions in ultracold atomic gases are describable to high accuracy with very simple short-range models. In addition, ultracold atomic gases become even more attractive as an ideal theoretical and experimental playground since they do not only offer excellent experimental control but also the amazing possibility of tuning the two-body interaction strength over a wide range using so-called Feshbach resonances [4].

This made it possible, that, about forty years after V. Efimov's seminal prediction [5] of the existence of universal three-body bound states in systems with large two-body interactions, first evidence in favor of the presence of these states had been found in the remarkable experiment by Kraemer et al. in 2006 [6]. In his work, Efimov predicted the existence of infinitely many trimer states for infinitely large scattering length where the two-body interaction is just on the verge of having a bound state. The energy levels form a geometric spectrum and the three-body system is found to be universal in the sense that apart from the s-wave scattering length a only one piece of information about the three-body system enters in the form of a so-called three-body parameter [7]. The findings of Kraemer et al. stimulated extensive activity in the field of three-body physics, both experimentally [8–12] and theoretically; for recent reviews on also the latter see [7, 13] and references therein. As a result, the Efimov effect in three-body systems is a well-understood phenomenon today.

The next natural step is to raise the question what the physics of four interacting particles may be. Early attempts towards an understanding of this system were made in the context of nuclear physics using a variety of approaches [14–17]. Also the four-body physics of ^{4}He atoms has been investigated in much detail, for an overview see, e. g. [18]. The simpler four-body physics of fermions with two spin states, relevant for the dimer-dimer repulsion, has also been studied [19].

In their pioneering work, Platter and Hammer, et al. [1, 2] investigated the four-body problem using effective interaction potentials and made the conjecture that the four-boson system exhibits universal behavior. They also found that no four-body parameter is needed for a self-consistent renormalization of the theory. Calculating the energy spectrum of the lowest bound states in dependence on the scattering length a the existence of two tetramer (four-body bound) states associated with each trimer was conjectured.

Recently, von Stecher, D'Incao, and Greene [3, 20] investigated the four-body problem in a remarkable quantum mechanical calculation. They found that the Efimov trimer and tetramer states always appear as sets of states with two tetramers associated with each of the trimer levels and calculated the bound state energy spectrum of the lowest few sets of states. The calculation suggests that the energy levels within one set of states are related to each other by universal ratios, which were obtained from the behavior of these lowest sets of states. In accordance with the results of Platter et al. [1, 2] the absence of any four-body parameter was also demonstrated. In order to find experimental evidence of the tetramer states extremely precise measurements are required. Remarkably, Ferlaino et al. were able to observe signatures of the lowest two of the tetramer states in a recent experiment [21].

While the calculations by Platter et al. [1, 2] and von Stecher et al. [3, 20] rely on quantum mechanical approaches, in this work we want to shed light onto the four-body problem from a different perspective. A lot of

*Electronic address: richard.schmidt@ph.tum.de
†Electronic address: s.moroz@thphys.uni-heidelberg.de

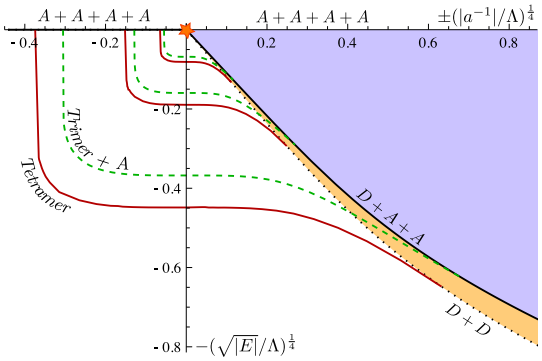

FIG. 1: (Color online) The generalized Efimov plot for four identical bosons. Here, we plot the energy levels of the various bound states as a function of the inverse s-wave scattering length a as numerically calculated in our approximative, effective theory. In order to improve the visibility of the energy levels we rescale both the dimensionless energy E/Λ^2 and the dimensionless inverse scattering length a^{-1}/Λ where Λ denotes the UV cutoff of our model. Also, we only show the first three sets of Efimov levels. The solid black line denotes the atom-atom-dimer threshold, while the dotted black line gives the dimer-dimer threshold. In the three-body sector one finds the well known spectrum of infinitely many Efimov trimer states (green, dashed) which accumulate at the unitarity point $E_\psi = a^{-1} = 0$, indicated by the orange star. In our pointlike approximation the four-body sector features a single tetramer (solid, red) associated with each trimer state.

insight into the three-body problem had been gained from effective field theory and renormalization group (RG) methods [7, 13, 22, 23] and it is desirable to apply these also to the four-body problem. In this paper we will make a first step towards such a description that is complementary to the previous quantum mechanical approaches.

Of special interest is the further investigation of universality in the four-body system. In this context the so-called unitarity point, illustrated by the star in Fig. 1, is of particular importance. In this limit not only the scattering length a is infinite but also all binding energies in the problem accumulate at the atom threshold at zero energy. Only at the unitarity point physics becomes truly universal in the sense that for example the ratio between the binding energies of consecutive trimer levels assumes exactly its universal value, $E_{n+1}/E_n = \exp(-2\pi/s_0)$, with $s_0 \approx 1.00624$ the so-called Efimov parameter. The unitarity point is therefore the most interesting one from a theory point of view. Unfortunately, in the previous calculations only few lowest lying states were determined. The major advantage of the present RG approach is that it allows to investigate analytically the complete spectrum and to address directly the unitarity point in order to extract the universal relations between the three- and four-body bound states in this limit.

We investigate the renormalization group behavior of the relevant four-body interactions with an approximate, but simple and physically intuitive model which allows only for pointlike (i.e. momentum independent[1]) three- and four-body interactions. In the three-body problem universality manifests itself in an RG limit cycle of the three-body coupling. We find that this three-body limit cycle leads in turn to a "self-sustained" limit cycle of the four-body sector leaving no room for any four-body parameter.

The RG method allows furthermore for computations away from the unitarity point. We calculate the bound state energy spectrum in the pointlike approximation (see Fig. 1) and investigate how the relations between tetramer and trimer states approach the universal limit as one comes closer to the unitarity point.

The paper is structured as follows. In Sec. II we introduce the functional renormalization group (FRG) method and set up the microscopic model. Secs. III and IV are devoted to the FRG analysis of the two- and three-body sector. In Sec. V we discuss the four-body sector and present our numerical results. Our findings are summarized in Sec. VI.

II. METHOD AND DEFINITION OF THE MODEL

In this work we are interested in the computation of the few-body properties, such as the bound state spectrum, of four identical bosons. In a quantum field theory approach the information about these properties can be extracted from the effective action Γ which is the generating functional of one-particle irreducible vertex functions $\Gamma^{(n)}$ and which contains all information about a given system. The computation of Γ is a very complicated task as quantum (and, as in the case of nonzero density, statistical) fluctuations have to be integrated out on all length and therefore momentum scales q. In order to cope with this task we rely on the functional renormalization group [24], for detailed reviews we refer to [25, 26].

The central quantity of the FRG is a scale dependent effective action functional, the so-called effective flowing action Γ_k. The effective flowing action Γ_k, which includes all fluctuations with momenta $q \gtrsim k$, interpolates between the classical action S at some ultraviolet (UV) cutoff scale $k = \Lambda$ and the full quantum effective action Γ in the limit $k \to 0$. The underlying idea is similar to Wilson's idea of momentum shell-wise integration of fluctuations. The evolution of Γ_k is governed by the Wetterich equation [24], which is an exact, non-perturbative RG equation. It reads

$$\partial_k \Gamma_k = \frac{1}{2} \mathrm{Tr} \left(\Gamma_k^{(2)} + R_k \right)^{-1} \partial_k R_k, \qquad (1)$$

[1] Throughout the paper we will use the term momentum independence to refer to combined spatial momentum and frequency independence.

where $\Gamma_k^{(2)}$ is the flowing, full inverse propagator and the trace Tr sums over momentum $\vec{q}$ and Matsubara frequency q_0 as well as the internal degrees of freedom such as species of fields. The dependence on the RG scale k is introduced by the regulator R_k. At the UV scale $k = \Lambda$ the effective flowing action Γ_k equals the classical action S and as we want to consider dilute atomic gases the UV scale Λ is set to be of the order of the inverse Bohr radius a_0^{-1}. For most problems, quantum and statistical fluctuations will generate infinitely many terms in Γ_k. Due to this fact it is in practice impossible to solve Eq. (1) exactly. Therefore one has to decide for a truncation of Γ_k, which in turn corresponds to solving the theory only approximately.

In this work we investigate the four-boson problem by approximately solving Eq. (1). Our truncation for the Euclidean flowing action is given by a simple two-channel model

$$\begin{aligned}\Gamma_k &= \int_x \{\psi^*(\partial_\tau - \Delta + E_\psi)\psi \\ &+ \phi^*\left(A_\phi(\partial_\tau - \frac{\Delta}{2}) + m_\phi^2\right)\phi + \frac{h}{2}(\phi^*\psi\psi + \phi\psi^*\psi^*) \\ &+ \lambda_{AD}\phi^*\psi^*\phi\psi + \lambda_\phi(\phi^*\phi)^2 \\ &+ \beta(\phi^*\phi^*\phi\psi\psi + \phi\phi\phi^*\psi^*\psi^*) + \gamma\phi^*\psi^*\psi^*\phi\psi\psi\}, \quad (2)\end{aligned}$$

where Δ denotes the Laplace operator and we use the natural, non-relativistic convention $2M = \hbar = 1$ with the atom mass M. ψ denotes the field of the elementary bosonic atom, while the dimer, the bosonic bound state consisting of two elementary atoms, is represented by the field $\phi \sim \psi\psi$. Both the atom and the dimer field are supplemented with non-relativistic propagators with energy gaps E_ψ and m_ϕ^2, respectively. In our approximation the fundamental four-boson interaction $\sim \lambda_\psi(\psi^*\psi)^2$ is mediated by a dimer exchange, which yields $\lambda_\psi = -h^2/m_\phi^2$ in the limit of pointlike two-body interactions. The dynamical dimer field ϕ allows us to capture essential details of the momentum dependence of the two-body interaction. We introduce a wave function renormalization factor A_ϕ for the dimer field in order to take into account an anomalous dimension of the dimer field ϕ. The only nonzero interaction, present at the microscopic UV scale $k = \Lambda$, is taken to be the Yukawa-type term with the coupling h. Together with the microscopic value of A_ϕ the Yukawa interaction h at the UV scale can be connected to the effective range r_{eff} in an effective range expansion. The atom-dimer interaction λ_{AD} as well as the various four-body interactions λ_ϕ, β, and γ vanish at the UV scale and are built up via quantum fluctuations during the RG flow.

At this stage we want to emphasize the meaning of the term pointlike approximation which must not be confused with the notion of a zero-range (contact) model. Consider for example the two-body contact interaction $\sim \lambda_\psi(\psi^*\psi)^2$, which has no momentum dependence on the UV scale, $k = \Lambda$. In order to describe the scattering of two particles in quantum mechanics one proceeds by solving the two-body Schrödinger equation. From this one obtains the well-known result for the zero-range s-wave scattering amplitude $f_0(p) = (-a^{-1} - ip)^{-1}$ (with $p = |\vec{p}|$ denoting the momentum of the colliding particles). The scattering amplitude becomes momentum dependent. In the RG approach one deals with the effective vertex λ_ψ which varies with the RG scale k. On the UV ($k = \Lambda$) scale λ_ψ is momentum independent. When including more and more quantum fluctuations – meaning lowering the RG scale k from Λ to eventually $k = 0$ – the effective vertex function λ_ψ assumes a momentum dependence which in the IR limit $k = 0$ is equivalent to the result for f_0 in the zero-range model. In a pointlike approximation one ignores this generated momentum dependence. In the simple model Eq. (2) the three- and four-body sector is treated strictly in the pointlike approximation. However, in the two-body sector the momentum dependence of effective vertex λ_ψ is captured by the exchange of the dynamic (i.e. momentum dependent) dimer propagator, such that the two-body sector is treated beyond the pointlike approximation.

In the general case of nonzero density and temperature one works in the Matsubara formalism and the integral in Eq. (2) sums over homogenous three-dimensional space and over imaginary time $\int_x = \int d^3x \int_0^{1/T} d\tau$. Although our method allows us to tackle a full, many-body problem at finite temperature in this way, we are interested solely in the few-body (vacuum) physics in this paper, for which density n and temperature T vanish. For $T = 0$, $\int_x$ reduces to an integral over infinite space and time. Our truncation (2) is based on the simple structure of the non-relativistic vacuum and, as demonstrated in [23, 27], numerous simplifications occur when solving Eq. (1) compared with the general, many-body case. The flowing action (2) has a global $U(1)$ symmetry which corresponds to particle number conservation. In the vacuum limit it is also invariant under spacetime Galilei transformations which restricts the form of the non-relativistic propagators to be functions of $\partial_\tau - \Delta$ for the atoms and $\partial_\tau - \Delta/2$ for the dimers. All couplings present in Eq. (2) are allowed to flow during the RG evolution and are taken to be momentum-independent in Fourier space as explained above.

Besides the ansatz of Γ_k we must choose a suitable regulator function R_k in order to solve Eq. (1). Based on our recent treatment of the closely related three-fermion problem [28, 29], we choose optimized regulators,

$$\begin{aligned}R_\psi &= (k^2 - q^2)\theta(k^2 - q^2), \\ R_\phi &= \frac{A_\phi}{2}(k^2 - q^2)\theta(k^2 - q^2), \quad (3)\end{aligned}$$

with $q = |\vec{q}|$. These regulators are optimized in the sense of [26, 30] and allow to obtain analytical results.

III. TWO-BODY SECTOR

A remarkable and very useful feature of the vacuum flow equations is comprised by a special hierarchy: the flow equations of the N-body sector do not influence the renormalization group flows of the lower $N-1$-body sector [23]. For this reason the different N-body sectors can be solved subsequently. In this spirit we first solve the two-body sector, then investigate the three-body sector in order to finally approach the four-body problem.

The solution for the two-body sector can be found analytically in our approximation[2] (for the analogous problem considering fermions, see [28, 31]). The only running couplings in the two-body sector are the dimer gap m_ϕ^2 and its wave function renormalization A_ϕ. The flow equations of the two-body sector are shown in terms of Feynman diagrams in Fig. 2(a) and read

$$\begin{aligned} \partial_t m_\phi^2 &= \frac{h^2}{12\pi^2}\frac{k^5}{(k^2+E_\psi)^2}, \\ \partial_t A_\phi &= -\frac{h^2}{12\pi^2}\frac{k^5}{(k^2+E_\psi)^3}, \end{aligned} \tag{4}$$

where $t = \ln\frac{k}{\Lambda}$. As there are no possible nonzero flow diagrams for the Yukawa coupling h, it does not flow in the vacuum limit.
The infrared (IR) values of the couplings h and m_ϕ^2 can be related to the low-energy s-wave scattering length a via

$$a = -\frac{h^2(k=0)}{16\pi m_\phi^2(k=0, E_\psi=0)}. \tag{5}$$

Knowing the analytical solution of the two-body sector, this relation can be used to fix the initial values of our model. For the UV value of the dimer gap m_ϕ^2 we find

$$m_\phi^2(\Lambda) = -\frac{h^2}{16\pi}a^{-1} + \frac{h^2}{12\pi^2}\Lambda + 2E_\psi. \tag{6}$$

The first term fixes the s-wave scattering length according to Eq. (5), while the second term represents a counterterm taking care of the UV renormalization of the two-body sector. Finally, the last term accounts for the fact that the dimer consists of two elementary atoms. Additionally, we choose $A_\phi(\Lambda) = 1$ which corresponds to the effective range $r_{\text{eff}} = -\frac{64\pi}{h^2}$.

The action (2) can also be used for a quite accurate description of Feshbach resonances. In this context Eq. (2) is referred to as resonance model. In such a model m_ϕ^2 is proportional to the detuning energy of the molecule in the closed channel with respect to the atom-atom threshold [32] and the coupling h is proportional to the width of the associated Feshbach resonance being a function of the strength of the coupling to the closed channel. The choice $A_\phi(\Lambda) = 1$ then corresponds to the so-called characteristic length $r^* = -\frac{1}{2}r_{\text{eff}}$ often used in literature [7, 33].
In the limit of large, positive scattering length there exists a universal, weakly bound dimer state. In order to find its binding energy we calculate the pole of the dimer propagator, corresponding to the condition $m_\phi^2(E_\psi, k=0) = 0$, which yields in the limit $E_\psi/\Lambda^2 \ll 1$

$$\begin{aligned} E_D = -2E_\psi &= -2\left(\frac{h^2}{64\pi} - \sqrt{\frac{h^4}{(64\pi)^2} + \frac{h^2 a^{-1}}{32\pi}}\right)^2 \\ &= -\frac{2}{r_{\text{eff}}^2}\left(1 - \sqrt{1 - \frac{2r_{\text{eff}}}{a}}\right)^2. \end{aligned} \tag{7}$$

In the limit $h \to \infty$, corresponding to $r_{\text{eff}} \to 0$ one recovers the well-known result $E_D = -2/a^2$. The dimer bound state energy is shown as a function of the inverse scattering length in Fig. 1 (black solid line). The deviation from the universal $1/a^2$ scaling for large inverse scattering lengths is due to the finite size of h which is taken to be $h^2/\Lambda = 10$ in Fig. 1. In the regime of small scattering length a one finds a crossover of the behavior of the dimer binding energy which then has the limiting behavior $E_D = 4/(a r_{\text{eff}})$.

IV. THREE-BODY SECTOR

The bound state spectrum of the three-body sector is much richer than the one of the two-body system. In his seminal papers [5] Efimov showed the existence of an infinite series of three-body bound states for strong two-body interactions. These energy levels exhibit a universal geometric scaling law as one approaches the unitarity point $E_\psi = a^{-1} = 0$. Remarkably, these three-body bound trimer states exist even for negative scattering lengths a where no two-body bound state is present; they become degenerate with the three-atom threshold for negative scattering length and merge into the atom-dimer threshold for positive a. An additional three-body parameter is needed in order to determine the actual positions of the degeneracies [22]. In this section we want to shortly review how Efimov physics can be treated within our approach. For a more detailed account on that matter and an application to the three-component ^{6}Li Fermi gas we refer to [23, 28, 29].

In our truncation, the three-body sector contains a single, pointlike $\phi^*\psi^*\phi\psi$ term with a coupling λ_{AD}, which is assumed to vanish in the UV. It is build up by quantum fluctuations during the RG flow and the corresponding Feynman diagrams of the flow equation for λ_{AD} is shown in Fig. 2(b). First we investigate the unitarity

[2] Remarkably, the atom inverse propagator (one-body sector) is not renormalized in the non-relativistic vacuum.

point, $E_\psi = a^{-1} = 0$. For this limit we are able to obtain an analytical solution for the flow equation of λ_{AD} while away from unitarity we have to rely on a numerical solution.

At the unitarity point all intrinsic length scales drop out of the problem and the system becomes classically scale invariant. At unitarity, the Yukawa coupling h is dimensionless and the only (extrinsic) length scale present is the inverse ultraviolet cutoff Λ^{-1}, which defines the validity limit of our effective theory.
In our approximation the dimer field ϕ develops a large anomalous dimension $\eta = -\frac{\partial_t A_\phi}{A_\phi} = 1$ at unitarity which is consistent with the exact solution of the two-body sector [23, 27]. As the atom and dimer propagators have vanishing gaps in the IR the two-body sector respects a continuous scaling symmetry.

In order to find the solution of the three-body sector we switch to the rescaled, dimensionless coupling $\tilde{\lambda}_{AD} \equiv \frac{k^2}{h^2}\lambda_{AD}$. One finds that the flow equation for $\tilde{\lambda}_{AD}$ becomes independent of k and h,

$$\partial_t \tilde{\lambda}_{AD} = \underbrace{\frac{24}{25}\left(1-\frac{\eta}{15}\right)}_{a}\tilde{\lambda}_{AD}^2 \underbrace{-\frac{14}{25}\left(1-\frac{4\eta}{35}\right)}_{b}\tilde{\lambda}_{AD} + \underbrace{\frac{26}{25}\left(1-\frac{\eta}{65}\right)}_{c}. \quad (8)$$

As was demonstrated in [23, 34], the behavior of the solution of this type of flow equation is determined by the sign of the discriminant D of the right hand side of Eq. (8) which is $D = b^2 - 4ac < 0$. Eq. (8) can be solved analytically and one finds

$$\tilde{\lambda}_{AD}(t) = \frac{-b + \sqrt{-D}\tan\left(\frac{\sqrt{-D}}{2}(t+\delta)\right)}{2a}, \quad (9)$$

where δ is connected to the three-body parameter and determines the initial condition. Most remarkably, the three-body sector exhibits a quantum anomaly: The RG flow of the renormalized coupling $\tilde{\lambda}_{AD}$ exhibits a limit cycle, which, due to its periodicity, breaks the classically continuous scaling symmetry to the discrete subgroup Z. The Efimov parameter can be determined from the period of the limit cycle [23] and is given in our approximation by

$$s_0 = \frac{\sqrt{-D}}{2} \approx 0.925203. \quad (10)$$

The exact result is given by $s_0 \approx 1.00624$ [7]. Considering the simplicity of our pointlike approximation, which, as discussed in Sec. III, does not resolve any momentum or frequency structure of the effective (k dependent) interaction vertex of the three-body sector, the agreement is quite good. In fact, in previous work [23] we have shown how to obtain the exact value of s_0 using the FRG.

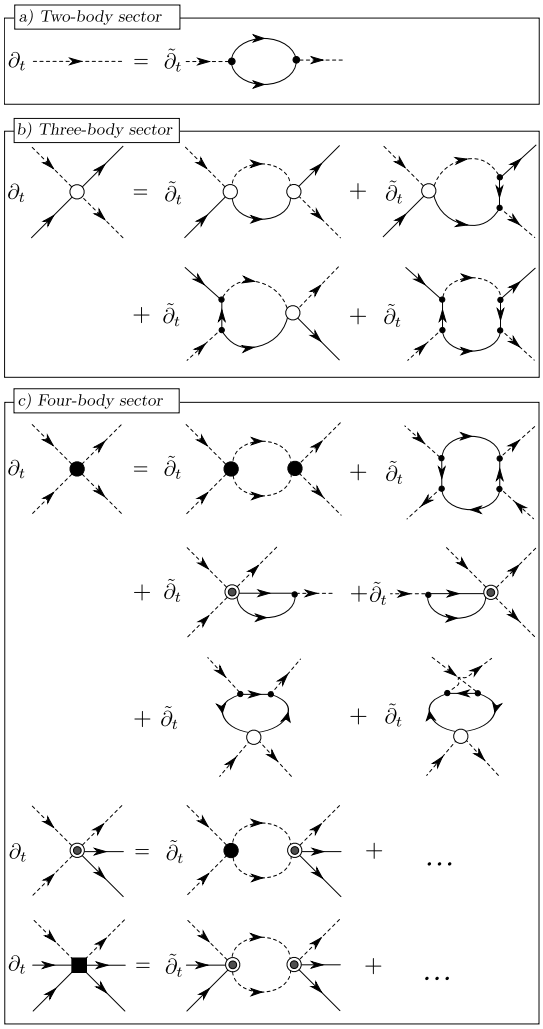

FIG. 2: The flow equations in terms of Feynman diagrams for the (a) two-body, (b) three-body, and (c) four-body sector. All internal lines denote full, regularized propagators. The scale derivative $\tilde{\partial}_t$ on the right hand side of the flow equations acts only on the regulators. Solid lines represent elementary bosons ψ, while dashed lines denote composite dimers ϕ. The vertices are: Yukawa coupling h (small black dot), atom-dimer vertex λ_{AD} (open circle), dimer-dimer coupling λ_ϕ (black circle), coupling β (two circles), and the atom-atom-dimer vertex γ (black square). Due to the large number of diagrams for the latter two vertex functions, we only show two exemplary diagrams.

The presence of N-body bound states leads to divergencies in the corresponding N-body vertices. The periodic divergencies in the analytical solution of $\tilde{\lambda}_{AD}$ in Eq.

(9) correspond therefore to the presence of the infinitely many Efimov trimer states at the unitarity point.

We can use the latter correspondence to calculate the bound state spectrum also away from unitarity. The trimer binding energies are calculated by determining the atom energies E_ψ for which $\tilde{\lambda}_{AD}$ exhibits divergencies in the IR as function of a^{-1}. The trimer binding energy is then given by $E_T = -3E_\psi$. The result is shown in Fig. 1. In this plot the dashed, green lines indicate the binding energies of the Efimov trimer states. For calculational purposes we switch to the static trimer approximation which is completely equivalent to our two-channel model in Eq. (2). We describe this procedure in Appendix A.

At the unitarity point the trimer binding energies form a geometric spectrum and the ratio between adjacent levels is given by

$$\frac{E_T^{(n+1)}}{E_T^{(n)}} = e^{-\frac{2\pi}{s_0}}, \tag{11}$$

which can be understood from the limit cycle flow of λ_{AD}. At each scale $k = \Lambda e^t$, where λ_{AD} diverges, one hits a trimer state. The RG scale k can in turn be connected to the atom energy E_ψ [23, 28, 29] and as the divergencies appear periodically in t one easily obtains Eq. (11).

There is an additional universal relation obeyed by the trimer energy levels which we may take as a measure of the quality of our approximation. It is given as the relation between the trimer binding energy E^* for $a \to \infty$ and value of a for which the trimer becomes degenerate with the atom-dimer (a_+^*) and three-atom threshold (a_-^*), respectively. For comparison we define a wave number κ^* by $E^* = -\hbar^2\kappa^{*2}/M$ (in our convention, $E^* = -2\kappa^{*2}$) and find

$$a_-^*\kappa^* \approx -1.68, \quad a_+^*\kappa^* \approx 0.08 \tag{12}$$

which has to be compared with the exact result $a_-^*\kappa^* = -1.56(5)$, $a_+^*\kappa^* = 0.07076$ from the fully momentum-dependent calculation in [7, 22]. The agreement with our approximate solution suggests that our model should provide a solid basis for the step to the four-body problem.

V. THE FOUR-BODY SECTOR

Recently, the solution of the four-body problem in the low-energy limit has gained a lot of interest. In quantum mechanical calculations the existence of two tetramer (four-body bound) states was conjectured for each of the infinitely many Efimov trimers [1, 2]. By calculating the lowest few sets of bound state levels von Stecher et al. [3, 20] concluded that both ratios of energies between the different tetramers and the trimer state approach universal constants. However, with the quantum mechanical approach the calculation directly at the unitarity point ($a^{-1} = E_\psi = 0$), marked explicitly in Fig. 1, turns out to be difficult, although this point is of great interest when one wants to gather evidence for universality of the four-body system. In fact, in the three-body sector the infinite RG limit cycle appears only exactly at the unitarity point and its universal appearance is directly connected to the breaking of the continuous scale symmetry. Within our approach, the unitarity region is easily accessible.

In order to investigate the four-body sector we include all possible, U(1) symmetric, momentum-independent interaction couplings in the effective flowing action Γ_k. If one assumes all these couplings to be zero at the microscopic UV scale Λ, one can show, by evaluating all possible Feynman diagrams and using the vacuum hierarchy described in [23], that from all possible four-body couplings only the three couplings λ_ϕ, β, and γ are built up by quantum fluctuations and are therefore included in Eq. (2). Couplings other than λ_ϕ, β, and γ, such as, for instance, the term $\sim (\psi^*\psi)^4$ are not generated during the RG evolution. This consideration leads to our ansatz for the effective average action (2).

For the investigation of the unitarity point we first switch to rescaled, dimensionless couplings

$$\tilde{\lambda}_\phi = \frac{k^3}{\pi^2 h^4}\lambda_\phi, \quad \tilde{\beta} = \frac{k^4}{h^3}\beta, \quad \tilde{\gamma} = \frac{\pi^2 k^5}{h^2}\gamma, \tag{13}$$

and obtain the corresponding flow equations by inserting the effective flowing action Γ_k, Eq. (2), into the Wetterich equation (1). By the use of the rescaled couplings we find three coupled ordinary differential equations, which are again coupled to the two- and three-body sectors, but become explicitly independent of h and k. We show the diagrammatic representation of the flow equations in Fig. 2(c). Their analytical form at the unitarity point is given by[3]

$$\partial_t\tilde{\lambda}_{AD} = \frac{128}{125} - \frac{62}{125}\tilde{\lambda}_{AD} + \frac{112}{125}\tilde{\lambda}_{AD}^2, \tag{14}$$

$$\partial_t\tilde{\lambda}_\phi = \frac{1}{16} + \frac{1}{3}\tilde{\beta} - \frac{1}{6}\tilde{\lambda}_{AD} + 3\tilde{\lambda}_\phi + \frac{128}{15}\tilde{\lambda}_\phi^2, \tag{15}$$

$$\begin{aligned}\partial_t\tilde{\beta} &= \frac{188}{125}\tilde{\beta} + \frac{1}{6}\tilde{\gamma} + \frac{128}{125}\tilde{\lambda}_{AD} \\ &+ \frac{224}{125}\tilde{\lambda}_{AD}\tilde{\beta} - \frac{156}{125}\tilde{\lambda}_{AD}^2 + \frac{4384}{375}\tilde{\lambda}_\phi \\ &+ \frac{128}{15}\tilde{\beta}\tilde{\lambda}_\phi - \frac{3968}{375}\tilde{\lambda}_{AD}\tilde{\lambda}_\phi,\end{aligned} \tag{16}$$

$$\begin{aligned}\partial_t\tilde{\gamma} &= \frac{4592}{375} + \frac{8768}{375}\tilde{\beta} + \frac{128}{15}\tilde{\beta}^2 \\ &+ \frac{1}{125}\tilde{\gamma} - \frac{79072}{1875}\tilde{\lambda}_{AD} - \frac{7936}{375}\tilde{\beta}\tilde{\lambda}_{AD} \\ &+ \frac{448}{125}\tilde{\gamma}\tilde{\lambda}_{AD} + \frac{74368}{1875}\tilde{\lambda}_{AD}^2 - \frac{5376}{625}\tilde{\lambda}_{AD}^3.\end{aligned} \tag{17}$$

[3] For illustrative purpose we show the analytical form of the flow equations at the unitarity point only. Away from this limit their explicit expressions become much more complex.

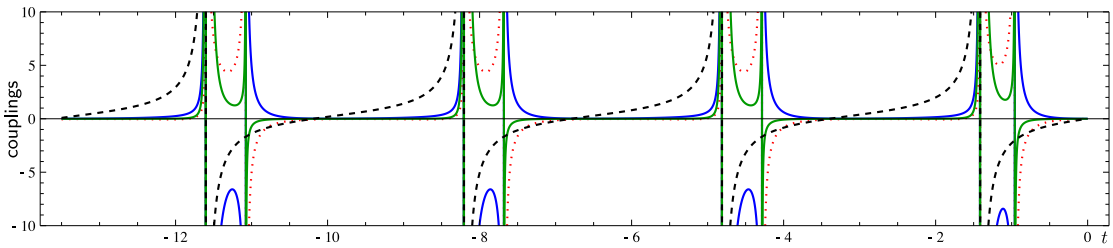

FIG. 3: (Color online) Renormalization group limit cycle behavior of the three- and four-body sector at the unitarity point $E_\psi = a^{-1} = 0$. The real parts of the rescaled, dimensionless couplings $\tilde{\lambda}_{AD,1}$, $4\tilde{\lambda}_{\phi,1}$, $\tilde{\beta}_1/6$, and $\tilde{\gamma}_1/1000$ are plotted as functions of $t = \ln(k/\Lambda)$. Not only the three-body coupling $\tilde{\lambda}_{AD,1}$ (dashed, black) exhibits a limit cycle behavior, but also the four-body sector couplings $\tilde{\lambda}_{\phi,1}$ (red, dotted), $\tilde{\beta}_1$ (blue, solid), and $\tilde{\gamma}_1$ (green, solid) obey a limit cycle attached to the three-body sector with the same period.

We pointed out in the last section that the appearance of bound states is connected with divergent vertex functions $\Gamma_k^{(n)}$ and we exploit this behavior to determine the bound state spectrum of the three- and four-boson system. At this point we must note that these infinities are complicated to handle in a numerical solution of the theory. In particular, the numerical treatment of unbounded limit cycles is problematic due to the periodic infinities during the RG flow. In order to circumvent this difficulty we used the method of complex extension, developed in [34]. The basic idea is to extend the domain of the running couplings to the complex plane

$$\begin{aligned} \lambda_{AD} &\to \lambda_{AD,1} + i\lambda_{AD,2} & \lambda_\phi &\to \lambda_{\phi,1} + i\lambda_{\phi,2} \\ \beta &\to \beta_1 + i\beta_2 & \gamma &\to \gamma_1 + i\gamma_2. \end{aligned} \tag{18}$$

On the one hand this effectively doubles the number of real flow equations and additional initial conditions must to provided. We choose $\lambda_{AD,2} = \epsilon = 10^{-11}$ in our numerical calculation and take all other imaginary parts to be zero in the UV. On the other hand this procedure allows us to perform the numerical integration of the flow equations as it regularizes the periodic infinities in the flow and makes the numerical treatment feasible. Physically, by the complex extension we convert the stable bound states into metastable resonances and by taking different values of ϵ we are able to vary the decay width of the resonances. One may compare this with the procedure of Braaten and Hammer [35] who introduce a parameter η^* in order to model the decay of the trimers to deeply bound states which have not been included in the effective model. In this line we also view our complex extension as a way to include these deeply bound states in the FRG calculation. Specifically, we find that for $\epsilon \ll 1$ the decay width of the $\mathrm{n^{th}}$ Efimov trimer $\Gamma_{\mathrm{T}}^{(n)}$ is given by $\Gamma_{\mathrm{T}}^{(n)} = 4\epsilon E_{\mathrm{T}}^{(n)}$ at unitarity. This is in agreement with the result in [7]

$$\Gamma_{\mathrm{T}}^{(n)} \approx \frac{4\eta^*}{s_0} E_{\mathrm{T}}^{(n)} \tag{19}$$

which holds for small η^*. Thus, for $\epsilon \ll 1$, the relation to the parameter η^* introduced by Braaten and Hammer is given by

$$\epsilon = \frac{\eta^*}{s_0}. \tag{20}$$

The result of the numerical calculation of the four-body sector at unitarity is shown in Fig. 3. Here, we display the RG flows of the real parts of all nonzero three- and four-body sector couplings as a function of the RG scale $t = \ln(k/\Lambda)$. The three-body coupling $\tilde{\lambda}_{AD,1}$ (black dotted line) exhibits the well-known limit cycle behavior, described in Section IV, with the period being connected to the Efimov parameter s_0. Remarkably, there is an additional limit cycle in the flow of the four-body sector couplings with a periodic structure of exactly the same frequency as the three-body sector. This four-body sector limit cycle exhibits resonances which are shifted with respect to the ones of the three-body system. The magnitude of this shift is given by a new universal number, which is inherent to the four-body sector.

Our observation is that the four-body sector is intimately connected with the three-body sector at the unitarity point. It is permanently attached to the running of the three-body sector from the first three-body resonance on. From here on the periodic structure of the flow remains unchanged as one goes to smaller values of k. Due to this tight bond between the three- and four-body sector, there stays no room for an additional four-body parameter.
We also find that the magnitude of the shift beyond the first resonance is neither dependent on the initial values of the four-body sector couplings in the UV nor is it influenced by finite range corrections which we are able to check by choosing different values for the Yukawa coupling h. Arbitrary choices lead to the same behavior. Having done this calculation directly at the unitarity point our conclusion is, that, within our simple approximation, the four-body sector behaves truly universal and independent of any four-body parameter

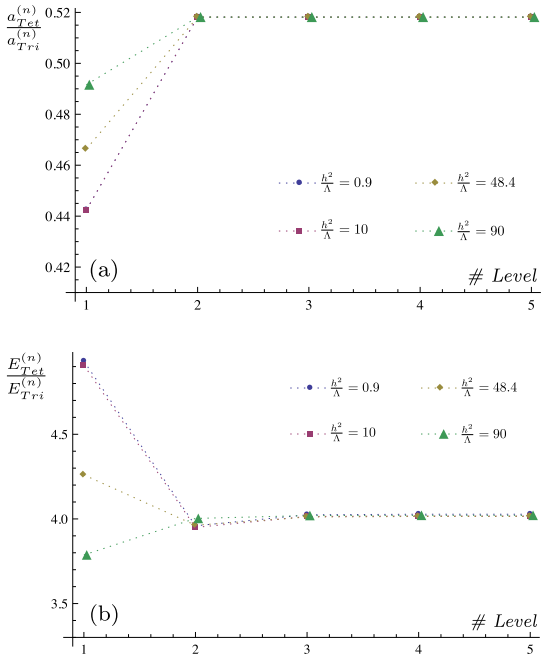

FIG. 4: (Color online) Calculation of the universal ratios for the lowest five set of levels. The calculation is done for different values of the Yukawa coupling h^2/Λ which determines the effective range in our model. The dotted lines are only guide for the eye. (a) Ratios between the values of scattering lengths $a^{(n)}_{Tet}$ and $a^{(n)}_{Tri}$ for which the tetramer and corresponding trimer become degenerate with the four-atom threshold. (b) Ratios between the values of binding energies $E^{(n)}_{Tet}$ and $E^{(n)}_{Tri}$ at resonance $a \to \infty$.

confirming the conjecture made by Platter et al. and von Stecher et al.. We expect that universality will also hold for an improved truncation.

Naively one expects that each resonance in the flow of the vertex functions is connected to the presence of a bound state. As one observes there are also additional resonances in the four-body sector being degenerate with the three-body sector resonances. However, we arrive at the conclusion that these resonances are artifacts of our approximation. The mathematical structure of the flow equations is of a kind that divergencies in the three-body sector directly lead to a divergent four-body sector. We are confident that the resonances at these positions will disappear as one includes further momentum dependencies in the field theoretical model. Therefore we can already infer from the calculation at unitarity that within our approximation we are only able to resolve a single tetramer state attached to each trimer state also away from unitarity. In contrast, the "exact" quantum mechanical calculations in [1–3, 20] predict the existence of two tetramer states which have recently been observed by Ferlaino et al. [21]. As one includes further momentum dependencies, it is well possible that not only the degenerate resonance disappears but also new, genuine resonances associated with the "missing" tetramer state will appear at the same time. This effect indeed occurs in the three-body problem. There, it is essential to include the momentum dependent two-atom vertex. Only under this condition one arrives at the quadratic equation as in (8) which gives rise to the Efimov effect. This can easily be seen by taking a look at the flow equation of λ_{AD} depicted as Feynman diagrams in Fig. 2(b). The assumption of a momentum independent two-atom interaction corresponds to a momentum (and frequency) independent dimer propagator. In this approximation the first term on the RHS of Fig. 2(b) vanishes because all poles of the loop frequency integration lie on the same complex frequency half-plane. This directly leads to the loss of the Efimov effect in this crude level of approximation.

We can also use our model to investigate the full bound state energy spectrum by solving the flow equations for arbitrary values of the scattering length a. The energy levels of the various bound states are then determined by varying the energy of the fundamental atoms E_ψ such that one finds a resonant four-body coupling in the IR. The result of this calculation, using the static trimer approximation presented in Appendix A, is shown in Fig. 1, where we plot the energy levels of the various bound states versus the inverse scattering length. We find one tetramer state attached to each of the Efimov trimer states. These tetramer states become degenerate with the four-atom threshold for negative scattering length and merge into the dimer-dimer threshold for positive a. In the experiment this leads to the measured resonance peaks in the four-body loss coefficient. In order not to overload the plot we show only the first three sets of levels, although the FRG method allows to calculate an arbitrary number of them. One also observes that the shape of the tetramer levels follows the shape of the trimer levels. In analogy to the three-body sector one can calculate a universal formula relating a tetramer binding energy $E^*_{Tet} = -2\kappa^{*2}_T$ at $a \to \infty$ with the corresponding scattering length at which the tetramer becomes degenerate with the four-atom threshold a^*_{T-} and the dimer-dimer threshold a^*_{T+}, respectively. We find

$$a^*_{T-}\kappa^*_T \approx -1.75, \quad a^*_{T+}\kappa^*_T \approx 0.20. \tag{21}$$

In their recent quantum mechanical calculations von Stecher et al. were able to calculate the lowest few sets of bound state energy levels [3]. From their behavior it was inferred that the ratio between the tetramer and trimer binding energies approaches a universal number within these first few sets of levels. Figuratively speaking it is therefore expected that the universal regime in the energy plot in Fig. 1 is reached very fast as one goes to

smaller a^{-1} and E_ψ.

In order to investigate this observation we calculate the behavior of two ratios as a function of the set of level for which they are determined. The first ratio relates the negative scattering lengths $a_{Tet}^{(n)}$ and $a_{Tri}^{(n)}$ for which the n^{th} tetramer and trimer become degenerate with the four-atom threshold. The second is the ratio between the binding energies of the n^{th} tetramer $E_{Tet}^{(n)}$ and the n^{th} trimer $E_{Tri}^{(n)}$ at resonance, $a \to \infty$. The resulting plots are shown in Fig. 4. We calculate the ratios for different values of the microscopic couplings in order to test the degree of universality of the various sets of energy levels. In the plots we show in particular the dependence on the choice of the Yukawa coupling h determining the effective range r_{eff} of the model. As one sees, only the first of the ratios depend on the microscopic details. Already from the second set of levels on the microscopic details are washed out and the ratios become independent of the choice of initial conditions: The regime of universality is reached extremely fast and as a^{-1} and E_ψ are lowered one will ultimately find the four-body limit cycle described above.

For the asymptotic ratios we find

$$a_{Tet}^{(n)} \approx 0.518\, a_{Tri}^{(n)}, \tag{22}$$

$$E_{Tet}^{(n)} \approx 4.017\, E_{Tri}^{(n)}. \tag{23}$$

Von Stecher et al. find $a_{Tet}^{(n)}/a_{Tri}^{(n)} \approx 0.43\,(0.9)$ for the deeper (shallower) bound tetramer and $E_{Tet}^{(n)}/E_{Tri}^{(n)} \approx 4.58\,(1.01)$, respectively. Considering the simplicity of our model the agreement is quite good. With an ultracold bosonic Cs gas Ferlaino et al. found $a_{Tet}^{(n)}/a_{Tri}^{(n)} \approx 0.47\,(0.84)$. In this remarkable experiment only the lowest set of tetramer states in the energy spectrum had been accessible due to the particular scattering length profile. Considering our observation that the deepest set of levels is still strongly dependent on the microscopical details it cannot be expected to find the universal numbers in this particular setting. Therefore more experiments for bosons interacting via a larger scattering lengths would be desirable.

VI. CONCLUSIONS

In this paper, we investigated the four-body problem with the help of the functional renormalization group. Employing a simple two-channel model with pointlike three- and four-body interactions we were able to investigate universal properties at the unitarity point $a \to \infty$, $E_\psi = 0$ as well as to perform computations away from it. In the RG language the Efimov physics of the three-body problem manifests itself as an infinite RG limit cycle behavior of the three-body coupling constant at unitarity. We found that also the four-body sector is governed by such a limit cycle which is solely induced by the RG running of the three-body sector, signaling the absence of a four-body parameter.

We also computed the energy spectrum away from unitarity and were able to obtain the universal relations between four- and three-body observables in our approximation. Our calculation provides an explanation for the findings of von Stecher et al. [3], who found that these ratios approach universal constants very quickly as they are computed for higher and higher excited states. We also found a dependence of the ratios for the lowest level on microscopic details such as the effective range. This in turn is of relevance for the experimental observations by Ferlaino et al. [21]. In this experiment the lowest states have been measured and one can therefore not expect to find the exact universal relations between them.

Considering the simplicity of our model, the agreement with the previous studies in [1–3] is quite good. There had been some disagreement in literature about universality and the absence or existence of a four-body parameter, see e.g. [36–38]. Our RG results support the conclusion that the four-body system is universal and independent of any four-body parameter.

An important shortcoming of the pointlike approximation is the absence of the shallower of the two tetramer states. Obviously the pointlike approximation of the three- and four-body sectors is not sufficient and in future work one should include momentum dependent interactions. From the energy spectrum in Fig. 1 it becomes also evident that the excited tetramer states can decay into an energetically lower lying trimer plus atom. The higher excited states in the four-body system are therefore expected to have an intrinsic finite decay width [2]. Whether this width has a universal character still remains an opened question as well as in which way the corresponding imaginary coupling constants will change the RG analysis.

The inclusion of the full momentum dependencies in the three- and four-body sector seems to be a rather complicated task. In the effective field theory study of the three-boson system the introduction of a dynamical dimer field, often called the di-atom trick [7], has been a decisive step towards the exact solution of the three-body problem. From this perspective we suggest that the inclusion of a dynamical trimer field in the effective action might help to simplify the momentum dependent calculation.

The four boson system remains still a subject with many open questions. With our RG analysis in the pointlike approximation, we made the first step towards a renormalization group description of the four-body problem supplementing the previous quantum mechanical approaches. From this perspective this work provides a starting point for a deeper understanding of universality in the four-body problem.

VII. ACKNOWLEDGMENTS

We thank E. Braaten, S. Floerchinger, C. H. Greene, H. W. Hammer, J. Pawlowski, J. von Stecher, C. Wetterich, and W. Zwerger for stimulating discussions. We are indebted to F. Ferlaino, R. Grimm, and S. Knoop for many insightful discussions and for pointing out the problem to us in the first place. RS thanks the DFG for support within the FOR 801 'Strong correlations in multiflavor ultracold quantum gases'. SM is grateful to KTF for support.

Appendix A: The trimer approximation and rebosonization

In this appendix we will apply the rebosonization method developed in [40] to our model (2). We introduce an additional trimer field χ, representing the bound state of three bosons, which then mediates the atom-dimer interaction. A similar procedure had already been used long time ago by Fonseca and Shanley [17] in the context of nuclear physics and was recently employed by us in [28, 29] for the treatment of the three-component Fermi gas. There are several reasons for employing this procedure. First, it is useful to reduce the number of resonances one has to integrate through in the RG flow. Instead of calculating the divergent coupling λ_{AD} one only has to calculate zero-crossings of the trimer energy gap which is numerically much easier to handle. Secondly, by the introduction of a dynamical trimer field one may be able to mimic some of the complicated momentum structure of the atom-dimer interaction in a simple way which could probably be sufficient to find the missing tetramer state in our calculation. The third point is of a more technical nature and concerns the method of rebosonization, which we will employ here in a quite extensive manner.

In the three-body sector the real atom-dimer coupling λ_{AD} exhibits divergencies when the energy gap of the fundamental atoms E_ψ is tuned such that one hits the trimer bound state in the IR. In the static trimer approximation, the coupling λ_{AD} is mediated by the exchange of a trimer field χ with the non-dynamical, inverse propagator $P_\chi = m_\chi^2$, which can be depicted as

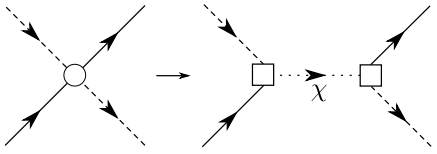

The trimer field $\chi \sim \psi^3$ is introduced on the microscopic scale by a Hubbard-Stratonovich transformation and our ansatz for the effective average action, motivated by the resulting classical action, reads

$$\begin{aligned}\Gamma_k \;=\; \int_x \{&\psi^*(\partial_\tau - \Delta + E_\psi)\psi \\ &+\phi^*\left(A_\phi(\partial_\tau - \frac{\Delta}{2}) + m_\phi^2\right)\phi + \chi^* m_\chi^2 \chi \\ &+\frac{h}{2}(\phi^*\psi\psi + \phi\psi^*\psi^*) + \lambda_{AD}\phi^*\psi^*\phi\psi \\ &+g(\chi^*\phi\psi + \chi\phi^*\psi^*) \\ &+\lambda_\phi(\phi^*\phi)^2 + \beta(\phi^*\phi^*\phi\psi\psi + \phi\phi\phi^*\psi^*\psi^*) \\ &+\gamma\phi^*\psi^*\psi^*\phi\psi\psi + \delta_1\chi^*\psi^*\chi\psi \\ &+\delta_2(\chi^*\psi^*\phi\phi + \chi\psi\phi^*\phi^*) \\ &+\delta_3(\chi^*\psi^*\phi\psi\psi + \chi\psi\phi^*\psi^*\psi^*)\}. \end{aligned} \tag{A1}$$

The Yukawa interaction g couples the trimer field to the dimer and atom field. The δ_i are the additional U(1) symmetric four-body couplings which are generated by quantum fluctuations. All other possible couplings can be shown to stay zero during the RG evolution provided they are zero at the UV scale. Also the coupling λ_{AD} is regenerated through a box diagram in the RG flow. However, it is possible to absorb all these emerging couplings by the use of the rebosonization procedure.
For this matter we promote the trimer field χ to be explicitly scale dependent, $\chi \to \chi_k$, $\chi^* \to \chi_k^*$ and the Wetterich equation generalizes to

$$\begin{aligned}\partial_k\Gamma_k[\Phi_k] \;=\; &\frac{1}{2}\mathrm{Tr}\left(\Gamma_k^{(2)}[\Phi_k] + R_k\right)^{-1}\partial_k R_k \\ &+\left(\frac{\delta}{\delta\Phi_k}\Gamma_k[\Phi_k]\right)\partial_k\Phi_k, \end{aligned} \tag{A2}$$

where Φ_k now includes all fields including the trimer fields (χ, χ^*). The additional term in the generalized flow equation (A2) allows for the absorption of the reemerging couplings since one has the freedom to choose the scale dependence of the trimer fields as a function of fields. In order to continuously eliminate the couplings λ_{AD} and δ_i we choose

$$\begin{aligned}\partial_k\chi_k \;&=\; \phi\psi\zeta_{a,k} + \psi^*\chi_k\psi\zeta_{b,k} \\ &\quad +\psi^*\phi\phi\zeta_{c,k} + \psi^*\phi\psi\psi\zeta_{d,k}, \\ \partial_k\chi_k^* \;&=\; \phi^*\psi^*\zeta_{a,k} + \psi\chi_k^*\psi^*\zeta_{b,k} \\ &\quad +\psi\phi^*\phi^*\zeta_{c,k} + \psi\phi^*\psi^*\psi^*\zeta_{d,k}. \end{aligned} \tag{A3}$$

Upon inserting Eq. (A3) into the generalized Wetterich equation (A2) the condition that the flows of λ_{AD} and δ_i vanish leads to

$$\begin{aligned}\zeta_a \;&=\; -\frac{\partial_k\lambda_{AD}}{2g}, \quad \zeta_b = -\frac{\partial_k\delta_1}{2m_\chi^2} \\ \zeta_c \;&=\; -\frac{\partial_k\delta_2}{m_\chi^2}, \quad \zeta_d = -\frac{\partial_k\delta_3 + g\zeta_b}{m_\chi^2}. \end{aligned} \tag{A4}$$

When one calculates now the flow equations of the remaining flowing couplings by projecting Eq. (A2) onto them, one obtains new contributions due to the presence

of additional terms arising from Eq. (A3).
In our static trimer approximation the trimer field has no dynamical propagator and the model given by Eq. (A1) is completely equivalent to the two-channel model in Eq. (2). Furthermore, no regulator has to be specified for the trimer field since in our approximation the original atom-dimer coupling λ_{AD} is solely replaced by g^2/m_χ^2. At this point it already becomes clear why the modified flow equations will be easier to handle numerically: instead of calculating a divergent λ_{AD} in the three-body sector one has only to deal with zero crossings of m_χ^2 at the values of k where originally λ_{AD} had divergencies. The modified flow equations are given by

$$\begin{aligned} \partial_t g &= \partial_t g|_{\Phi_k} + m_\chi^2 \zeta_a, \\ \partial_t \beta &= \partial_t \beta|_{\Phi_k} + g\zeta_c, \\ \partial_t \gamma &= \partial_t \gamma|_{\Phi_k} + 2g\zeta_d, \end{aligned} \tag{A5}$$

where the first terms in the flows are the original flow equations with the trimer field taken to be scale independent. In fact, by expressing all flow equations in terms of the coupling $G \equiv g^2$ one can also get rid off the problematic g in the denominator of ζ_a in Eq. (A4). We point out that the static trimer approximation allows to calculate easily the three-body sector. In the four-body sector the original divergencies of λ_{AD} still appear since trimers χ appear in the corresponding flow diagrams and therefore one has to deal with terms $\sim 1/m_\chi^2$. For this reason it had been essential to perform the complex extension described in Section V. Finally, the bound state spectrum of the trimers can be computed by calculating the poles of the trimer propagator, $m_\chi^2(k=0, E_\psi) = 0$, in a straightforward manner.

[1] L. Platter, H.-W. Hammer, and Ulf-G. Meißner, Phys. Rev. A **70**, 052101 (2004).
[2] H.-W. Hammer, and L. Platter, Eur. Phys. J. A **32**, 113 (2007).
[3] J. von Stecher, J. P. D'Incao, and C. H. Greene, Nature Phys. **5**, 417-421 (2009).
[4] C. Chin, R. Grimm, P. Julienne, and E. Tiesinga, arXiv:0812.1496 (2008).
[5] V. Efimov, Phys. Lett. B **33**, 563 (1970); V. Efimov, Nucl. Phys. A **210**, 157 (1973).
[6] T. Kraemer et al., Nature **440**, 315 (2006).
[7] E. Braaten, H.W. Hammer, Phys. Rept. **428**, 259 (2006).
[8] S. Knoop *et al.*, Nature Phys. **5**, 277 (2009).
[9] T. B. Ottenstein *et al.*, Phys. Rev. Lett. **101**, 203202 (2008).
[10] J. H. Huckans *et al.*, Phys. Rev. Lett. **102**, 165302 (2009); J. R. Williams *et al.*, arXiv:0908.0789v1 (2009).
[11] M. Zaccanti *et al.*, Nature Phys. **5**, 586 (2009).
[12] G. Barontini *et al.* Phys. Rev. Lett. **103**, 043201(2009).
[13] L. Platter, arXiv:0904.2227 (2009).
[14] O. A. Yakubovsky, Yad. Fiz. **5**, 1312 (1967); [Sov. J. Nucl. Phys. **5**, 937 (1967)].
[15] J. A. Tjon, Phys. Rev. Lett. **56**, 217 (1975).
[16] B. F. Gibson, and D. R. Lehmann, Phys. Rev. C **14**, 685 (1976).
[17] A. C. Fonseca, and P. E. Shanley, Phys. Rev. C **14**, 1343 (1976).
[18] J. A. Tjon, in *Few-body Systems and Nuclear Forces II*, edited by H. Ziegel *et al.* (Springer, Berlin, 1978); D. Blume and C. H. Greene, J. Chem. Phys. **112**, 8053 (2000); K. B. Whaley, Int. Rev. Phys. Chem. **13**, 41 (1994).
[19] D. S. Petrov, C. Salomon, and G. V. Shlyapnikov, Phys. Rev. Lett **93**, 090404 (2004).
[20] J. P. D'Incao, J. von Stecher, and C. H. Greene, Phys. Rev. Lett. **103**, 033004 (2009).
[21] F. Ferlaino, *et al.*, Phys. Rev. Lett. **102**, 140401 (2009).
[22] P. F. Bedaque, H. W. Hammer, and U. van Kolck, Phys. Rev. Lett. **82**, 463 (1999); Nucl. Phys. A **646**, 444 (1999).
[23] S. Moroz, S. Floerchinger, R. Schmidt, and C. Wetterich, Phys. Rev. A **79**, 042705 (2009).
[24] C. Wetterich, Phys. Lett. B **301**, 90 (1993).
[25] K. I. Aoki, Int. J. Mod. Phys. B **14**, 1249 (2000); C. Bagnuls, C. Bervillier, Phys. Rept. **348**, 91 (2001); M. Salmhofer and C. Honerkamp, Prog. Theor. Phys. **105**, 1 (2001); C. Wetterich, Int. J. Mod. Phys. A **16**, 1951 (2001); J. Berges, N. Tetradis, and C. Wetterich, Phys. Rept. **363**, 223 (2002); W. Metzner, Prog. Theor. Phys. Suppl. **160**, 58 (2005); B. Delamotte, e-print arXiv:cond-mat/0702365.
[26] J. M. Pawlowski, Ann. Phys. **322**, 2831 (2007).
[27] S. Diehl, H. C. Krahl, M. Scherer, Phys. Rev. C **78**, 034001 (2008).
[28] S. Floerchinger, R. Schmidt, S. Moroz, and C. Wetterich, Phys. Rev. A **79**, 013603 (2009).
[29] S. Floerchinger, R. Schmidt, and C. Wetterich, Phys. Rev. A **79**, 053633 (2009).
[30] D. F. Litim, Phys. Lett. B **486**, 92 (2000).
[31] S. Diehl, H. Gies, J. M. Pawlowski, and C. Wetterich, Phys. Rev. A **76**, 021602(R) (2007).
[32] S.J.J.M.F. Kokkelmans et al., Phys. Rev. A **65**, 053617 (2002).
[33] I. Bloch, J. Dalibard, and W. Zwerger, Rev. Mod. Phys. **80**, 885 (2008).
[34] S. Moroz, and R. Schmidt, Ann. Phys. **325**, 489 (2010).
[35] E. Braaten, H.-W. Hammer, Phys. Rev. Lett. **87**, 160407 (2001); Phys. Rev. A **70** 042706 (2004).
[36] M. T. Yamashita, L. Tomio, A. Delfino, and T. Frederico, Europhys. Lett. **75**, 555 (2006).
[37] S. K. Adhikari, T. Frederico, and I. D. Goldmann, Phys. Rev. Lett. **74**, 487 (1995).
[38] R. D. Amado, and F. C. Greenwood, Phys. Rev. D **7**, 2517 (1973).
[39] S. Floerchinger, M. Scherer, S. Diehl, and C. Wetterich, Phys. Rev. B **78**, 174528 (2008).
[40] H. Gies, C. Wetterich, Phys. Rev. D **65**, 065001 (2002); Acta Phys. Slov. **52**, 215 (2002).

Efimov physics from the functional renormalization group

Stefan Floerchinger · Sergej Moroz · Richard Schmidt

Abstract Few-body physics related to the Efimov effect is discussed using the functional renormalization group method. After a short review of renormalization in its modern formulation we apply this formalism to the description of scattering and bound states in few-body systems of identical bosons and distinguishable fermions with two and three components. The Efimov effect leads to a limit cycle in the renormalization group flow. Recently measured three-body loss rates in an ultracold Fermi gas of ^{6}Li atoms are explained within this framework. We also discuss briefly the relation to the many-body physics of the BCS-BEC crossover for two-component fermions and the formation of a trion phase for the case of three species.

Keywords Efimov effect · Functional renormalization · Limit cycle

1 Introduction

The physics of two or three non-relativistic particles that can scatter of each other or form bound states can be well described by quantum mechanics. Nevertheless, we present here an approach to these problems that is based on a method borrowed from the modern formulation of quantum field theory. Why should this be useful? There are several reasons. First, to better understand few-body physics it is desirable to have several different approaches at hand. Intuitive pictures and quantitative results can be compared and improved. Second, by applying powerful but also involved methods to rather simple problems one can also learn how to improve these methods. Also, by establishing a unified description of different physical phenomena (possibly on very different energy scales) one can hope for fruitful interference between different fields. Some universal aspects might even be transferred directly. Finally, for the field of ultracold quantum gases one has the very concrete advantage that functional renormalization can not only be applied to few-body problems but allows in a very similar way also the description of many-body phenomena.

Our formalism uses the quantum effective action $\Gamma[\psi]$ which is a functional of the field $\psi(t,\mathbf{x})$ representing in our case non-relativistic particles. Formally speaking, the quantum effective action $\Gamma[\psi]$ is the generating functional of one-particle irreducible Feynman diagrams. This means that tree level expressions for scattering amplitudes are exact when the vertices and the propagators are obtained from functional derivatives of $\Gamma[\psi]$. In some sense the effective action $\Gamma[\psi]$ is similar to the microscopic action $S[\psi]$ but with the difference that all quantum and statistical fluctuations are included. Variation of $\Gamma[\psi]$ with respect to ψ yields exact equations. The functional form of $\Gamma[\psi]$ and the connection to scattering and bound state properties will become more clear below. Here we remark that for a generic interacting field theory the calculation of $\Gamma[\psi]$ is non-trivial. A method for this task is provided by functional renormalization.

S. Floerchinger
Institut für Theoretische Physik, Philosophenweg 16, D-69120 Heidelberg, Germany
now at: Physics Department, Theory Unit, CERN, CH-1211 Genève 23, Switzerland

S. Moroz
Institut für Theoretische Physik, Philosophenweg 16, D-69120 Heidelberg, Germany

R. Schmidt
Physik Department, Technische Universität München, James-Franck-Straße, D-85748 Garching, Germany

A particularly interesting feature of few-body physics relevant for experiments with ultracold quantum gases is universality [1]. Broadly speaking this means that for a large class of microscopic properties (such as the interaction potential between two particles) the macroscopic, low-energy properties are independent of the microscopic details and depend only on a few parameters. In particular if the scattering length is large compared to the effective range of the interaction potential the macroscopic properties can be equivalently calculated from a contact potential (with a vanishing range). In a renormalization group picture universality manifests itself as a (partial) fixed point. A large class of microscopic theories is attracted towards the same RG trajectory during the flow towards the infrared. The low-energy properties of the whole class can be characterized in terms of one representative which is for simplicity chosen to be the contact potential. For this case the microscopic or classical action has a particularly simple form. For a single boson field ψ (as appropriate to describe identical bosons) it reads

$$S = \int d\tau \int d^3x \left\{ \psi^* \left(\partial_\tau - \tfrac{\boldsymbol{\nabla}^2}{2M_\psi} - \mu \right) \psi + \frac{1}{2} \lambda_\psi (\psi^* \psi)^2 \right\}. \tag{1}$$

The microscopic interaction strength λ_ψ will later be related to the s-wave scattering length a. We use in Eq. (1) a formulation with imaginary time τ which is integrated from 0 to $1/T$ in the Matsubara formalism. We also introduced a chemical potential μ. Although we are interested here only in the few-body properties in vacuum, i.e. for vanishing temperature $T = 0$ and particle density $n = 0$, the generalization to many-body physics at nonvanishing temperature is possible and straightforward in principle by adjusting μ and T. Real-time properties can be obtained from analytic continuation $t = i\tau$. Throughout this paper we will use natural units with $\hbar = k_B = 1$. In addition we measure energies in units of momentum squared which leads to $2M_\psi = 1$.

Signatures of universality also arise in few-body physics related to the Efimov effect [2]. A remarkable feature which underlies the Efimov effect is the presence of a discrete scaling symmetry. Specifically, at the unitarity point, where the scattering length diverges, the solution of the Efimov problem remains invariant (self-similar) under rescaling of length by integer powers of some discrete scaling factor. In the renormalization group language the discrete scaling symmetry is reflected in a renormalization group flow that periodically traverses a closed orbit, a so-called limit cycle [3]. Limit cycles encode the essence of the Efimov effect and broaden the concept of few-body universality introduced in the previous paragraph. Recent experiments with ultracold atoms (for a summary see [4]) provided the first clear evidence of how Efimov physics is realized in nature.

Since the three-body sector develops a renormalization group cycle scaling at the unitarity point, one must provide a proper ultraviolet initial condition for the three-body interaction, which is dictated by the details of the microscopic physics such as for instance the underlying interatomic potentials. Phrased in RG language, the limit cycle scaling implies that a three-body term $\sim \lambda_3 (\psi^* \psi)^3$ has a complex anomalous dimension and is exactly marginal at unitarity. For these reasons a three-body interaction term must in principle be included in the microscopic action (1). In the main part of this work we do, however, not concentrate on the direct comparison with particular experiments in which case the microscopical details and correspondingly a three-body term would become of relevance. For the sake of simplicity we tune the three-body parameter λ_3 to zero which is why such a term is not included in the microscopic action (1). In this simple setting all three-body correlations are generated during renormalization group evolution. Only in section 6, where we compare our findings with recent experiments with three-component fermionic ^{6}Li atoms, the three-body term becomes a part the microscopic description.

This paper is organized as follows. In section 2 we give a short introduction to the functional renormalization method with emphasis on the non-relativistic few-body problem. In section 3 we discuss the problem of two identical bosons with contact interaction as well as the problem of three identical bosons at a broad Feshbach resonance where the scattering length diverges. The subsequent section 4 is dedicated to a system of fermions with two species (e.g. hyperfine states). We discuss how the renormalization group flow equations are modified compared to the case of bosons in the few-body sector and sketch how they account for the BCS-BEC crossover physics at non-zero density. Section 5 contains a discussion of our renormalization group treatment for a system with three fermion species. We assume that the fermions have equal properties (apart from their hyperfine spin) and that there is a common Feshbach resonance for all particles leading to a global SU(3) symmetry. We generalize this model to the case where the resonances

occur at different values of the magnetic field in section 6. In this setup we explain three-body loss rates recently measured in experiments with ^{6}Li atoms [5,6]. Finally, we draw our conclusions in section 7.

2 Method

2.1 Functional renormalization group

Functional renormalization is a modern realization of Wilson's renormalization group concept which is used in quantum and statistical field theory, especially when dealing with strongly interacting systems (for reviews see [7]). The method combines functional methods of quantum field theory with the physically intuitive renormalization group idea. The main motivation for its development was the observation that it is often more useful and transparent to perform the integration of quantum fluctuations in continuous steps rather than doing it at once. The renormalization technique allows to interpolate smoothly between the known microscopic laws and the complicated macroscopic phenomena. In this sense, it bridges the transition from simplicity of microphysics to complexity of macrophysics.

In quantum field theory a particular useful quantity is the effective action Γ which is a direct analogue of the classical action functional S. It depends on the fields of a given theory and includes all quantum fluctuations. For a generic interacting field theory the effective action Γ, however, is difficult to obtain. Functional renormalization provides a practical tool to calculate Γ employing the concept of renormalization group.

The central idea of functional renormalization is the introduction of a scale-dependent effective action functional Γ_k often called average action or flowing action. The average action Γ_k interpolates smoothly as a function of the RG sliding scale k between the known microscopic action S and the full quantum effective action Γ. The dependence on the sliding scale k is introduced by adding an infrared regulator term to the microscopic action. This regulator term has the purpose to suppress fluctuations below the scale k and it is introduced by defining (for a bosonic field $\tilde{\psi}$) the k-dependent Schwinger functional $W_k[J]$

$$e^{W_k[J]} = \int \mathcal{D}\tilde{\psi}\, e^{-S[\tilde{\psi}]-\Delta S_k[\tilde{\psi}]+\int_x J\tilde{\psi}}. \tag{2}$$

The difference to the standard QFT Schwinger functional $W[J]$ is the additional term $\Delta S_k[\tilde{\psi}]$ in the exponential in Eq. (2). $\Delta S_k[\tilde{\psi}]$ is quadratic in the fields and in momentum space it reads

$$\Delta S_k[\tilde{\psi}] = \int_Q \tilde{\psi}^*(Q) R_k(Q) \tilde{\psi}(Q). \tag{3}$$

We use the abbreviations $Q = (q_0, \mathbf{q})$ and $\int_Q = \int_{q_0}\int_{\mathbf{q}}$ with $\int_{q_0} = \frac{1}{2\pi}\int_{-\infty}^{\infty} dq_0$ and $\int_{\mathbf{q}} = \frac{1}{(2\pi)^3}\int d^3q$. The infrared regulator function $R_k(Q)$ is not fixed in the unique way, but must satisfy three important conditions. First $R_k(Q)$ should suppress infrared modes below the scale k, i.e.

$$R_k(0) \approx k^2. \tag{4}$$

This adds effectively an additional masslike term to the particle suppressing its propagation if its momentum is below the RG scale k. Second, the regulator must vanish in the infrared

$$\lim_{k\to 0} R_k(Q) = 0. \tag{5}$$

With this condition it is guaranteed that W_k equals the standard, exact Schwinger functional W in the infrared, $W = W_{k=0}$. Finally, we should recover the classical action in the ultraviolet and thus we demand

$$\lim_{k\to\infty} R_k(Q) = \infty. \tag{6}$$

Apart from these requirements, the regulator can be chosen arbitrarily. Nevertheless, it is recommended to pick the regulator carefully depending on a concrete physical problem. Moreover, one should better choose a regulator that respects as many symmetries of the studied problem as possible. For our purpose it is convenient to choose $R_k(Q) = R_k(\mathbf{q})$ independent of the frequency argument q_0. Often, $R_k(\mathbf{q})$ is chosen to decay for large $\mathbf{q}^2 \gg k^2$. As we have seen, in Eq. (2) the regulator R_k suppresses fluctuation modes with

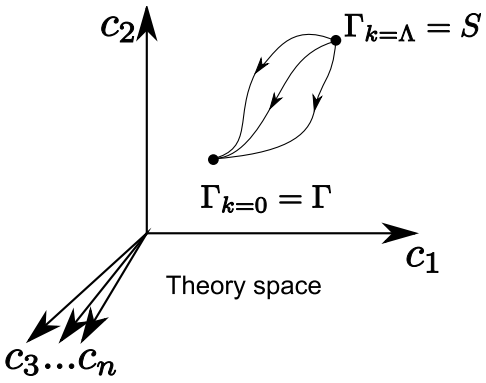

Fig. 1 Renormalization group flow in the theory space of all possible couplings allowed by symmetries. Different trajectories correspond to different choices of the infrared regulator R_k.

momenta $\mathbf{q}^2 \lesssim k^2$ by giving them a large "mass" or "gap", while high momentum modes are not (or only mildly) affected. Thus, W_k includes all fluctuations with momenta $\mathbf{q}^2 \gtrsim k^2$.

The flowing action Γ_k is now obtained by subtracting from the Legendre transform of the Schwinger functional,

$$\tilde{\Gamma}_k[\psi] = \int J\psi - W_k[J] \tag{7}$$

with $\psi = \delta W_k[J]/\delta J$, the cutoff term

$$\Gamma_k[\psi] = \tilde{\Gamma}_k[\psi] - \Delta S_k[\psi]. \tag{8}$$

The reason why the flowing action $\Gamma_k[\psi]$ is the central object to study is that it obeys the elegant and exact functional flow equation

$$\partial_k \Gamma_k[\psi] = \frac{1}{2}\mathrm{STr}\,\partial_k R_k \,(\Gamma_k^{(2)}[\psi] + R_k)^{-1}, \tag{9}$$

derived by C. Wetterich in 1993 [8]. Despite its compact form, the flow equation governs the full quantum dynamics. In Eq. (9) ∂_k denotes a derivative with respect to the sliding scale k at fixed values of the fields. The functional differential equation for $\Gamma_k[\psi]$ must be supplemented with the initial condition $\Gamma_{k\to\Lambda} = S$, where the "classical action" $S[\psi]$ describes the physics at the microscopic ultraviolet scale $k = \Lambda$. Importantly, in the infrared limit $k \to 0$ the full quantum effective action $\Gamma[\psi] = \Gamma_{k\to 0}[\psi]$ is obtained. In the Wetterich equation STr denotes a supertrace operation which sums over momenta, frequencies, internal indices, and different fields (taking bosons with a plus and fermions with a minus sign).

It is important to note that the exact flow equation for $\Gamma_k[\psi]$ has a one-loop structure. This is a significant simplification compared for example to perturbation theory, where all multi-loop Feynman diagrams must be included. Note however, that Eq. (9) is a nonlinear functional differential equation. Indeed, on the right-hand side in the denominator appears the second functional derivative $\Gamma_k^{(2)}[\psi]$. Due to that it is usually not possible to find closed solutions to Eq. (9) in an analytical form.

To make the implications of (9) more transparent we write the flowing action as an expansion in some complete set of operators

$$\Gamma_k[\psi] = \sum_{n=0}^{\infty} c_n \, O[\psi]. \tag{10}$$

The renormalization group evolution of Γ_k traces a trajectory in the theory space, which is the infinite-dimensional space of all possible couplings $\{c_n\}$ allowed by the symmetries of the problem. As schematically shown in Fig. 1, at the microscopic ultraviolet scale $k = \Lambda$ one starts with the initial condition $\Gamma_{k=\Lambda} = S$. As the sliding scale k is lowered, the flowing action Γ_k evolves in theory space according to the functional flow equation (9). Accordingly, different couplings $\{c_n\}$ become running or flowing under the renormalization group evolution. The choice of the regulator R_k is not unique, which introduces some

scheme dependence into the renormalization group flow. For this reason, different choices of the regulator R_k correspond to the different paths in Fig. 1. At the infrared scale $k = 0$, however, the full effective action $\Gamma_{k=0} = \Gamma$ is recovered for every choice of the cutoff R_k, and all trajectories meet at the same point in the theory space.

2.2 Non-relativistic few-body problem

As was mentioned above we use here a field-theoretic formalism with which also many-body problems in thermal and chemical equilibrium can be addressed. In this setup the properties of a few particles such as scattering amplitudes and binding energies are encoded in the n-point correlation functions in vacuum. The projection of the effective action Γ onto the vacuum state was developed in [9,10]. It amounts in cooling the system ($T \to 0$) and making it dilute ($n \to 0$) in such a way, that the temperature T always stays above its critical value in order to avoid many-body effects (e.g., Bose-Einstein condensation). The chemical potentials of different particles in a given problem are related to their binding energies measured with respect to some reference energy level. As usual in non-relativistic physics the absolute energy scale can be shifted, and it is often convenient for us to fix it such that the lowest energy excitation (lowest energy n-particle bound state) has a vanishing energy.

All few-body systems discussed here are translation invariant, i.e. no trapping potential is considered. Moreover, they are invariant under space-time Galilei transformations, which restricts the form of the non-relativistic propagator of a field ψ to be a function of the combination $\partial_\tau - \boldsymbol{\nabla}^2$ of temporal and spatial derivatives (we recall that in our units $2M_\psi = 1$). In addition, all systems possess an internal U(1) symmetry associated with particle number conservation.

As was discussed in detail in [10,11,12,13], numerous mathematical simplifications appear in few-body problems compared with more complicated many-body problems. For instance, all Feynman diagrams with loop lines pointing in the same direction necessarily vanish. This simplification originates from the fact that there are only particles, but no antiparticles or holes as excitations of the non-relativistic vacuum. As a result, a remarkable hierarchy of RG flow equations arises in few-body physics. The flow equations of the n-body sector are not influenced by the higher-body sectors.[1] One can solve the two-particle problem without any information about the three-particle problem and so on. We note that the presence of this hierarchy makes the systematic vertex expansion, discussed in Sec. 2.3.2, very useful for the treatment of few-body problems. The generally applicable strategy thus is to solve n-body problems subsequently by starting with the lower (one-particle, two-particle) sectors and proceeding to the higher ones.

2.3 Truncations

In most cases of interest the flow equation (9) can only be solved approximately. Usually some type of expansion of Γ_k is first performed, which is then truncated at finite order leading to a finite system of ordinary differential equations. The choice of a suitable expansion scheme should be physically motivated and depends on the given problem. The expansions do not necessarily involve a small parameter (like an interaction coupling constant or $1/N$) and thus they are, in general, of nonperturbative nature. Here we describe two different expansion schemes that we used for studying few-body quantum problems with functional renormalization.

2.3.1 Derivative expansion

A particularly simple truncation scheme is the derivative expansion. One expands the flowing action in terms with increasing number of spatial and temporal derivatives.[2] As an example consider bosons with the

[1] The n-body sector is defined here as the set of one-particle irreducible $2n$-point functions expressed in terms of the elementary ψ-fields. For a detailed discussion of the few-body hierarchy as well as a general proof of this feature see [13].

[2] Due to the non-relativistic nature of the problem we can assign to the derivatives the scaling dimensions $[\boldsymbol{\nabla}] = 1$ and $[\partial_\tau] = 2$ which corresponds to the dynamical critical exponent $z = 2$.

microscopic action given in Eq. (1). In the derivative expansion the ansatz for the flowing action is

$$\begin{aligned}\Gamma_k[\psi] = \int_{\tau,\mathbf{x}} \Big\{ & U_k(\psi^*\psi) + Z_1 \psi^* \partial_\tau \psi + Z_2 \psi^* (-\boldsymbol{\nabla}^2)\psi \\ & + V_1 \psi^* (-\partial_\tau^2)\psi + V_2 \psi^* (\partial_\tau \boldsymbol{\nabla}^2)\psi + V_3 \psi^* (-\boldsymbol{\nabla}^4)\psi + \dots \Big\}.\end{aligned} \tag{11}$$

Similar to the effective potential $U_k(\psi^*\psi)$, being a function of $\psi^*\psi$, the coefficients Z_i and V_i are functions of the scale parameter k and depend in principle also on the U(1) invariant combination $\psi^*\psi$. Besides higher order derivatives also terms of the form $\psi^*\psi(-\boldsymbol{\nabla}^2)^n\psi^*\psi$ will appear in Eq. (11).

The derivative expansion is particularly useful for the investigation of many-body problems [7]. In problems where bound state formation plays a role one expects that the derivative expansion in the form (11) is not particularly useful. The reason is that one expects in this case a pole in the effective four-point correlation function. Extracting this object from Eq. (11) by taking the appropriate functional derivatives, one finds that it is given by a combination of terms with different frequency and momentum dependence. However, all these terms are regular and any finite number of them cannot account for a bound state pole.

For this reason, instead of working with the microscopic action in Eq. (1) it is sometimes useful to perform a Hubbard-Stratonovich transformation. One adds a term that is quadratic in the complex auxiliary field ϕ. The action becomes

$$\begin{aligned}S = \int_{\tau,\mathbf{x}} \Big\{ & \psi^*(\partial_\tau - \boldsymbol{\nabla}^2 - \mu)\psi + \tfrac{1}{2}\lambda_\psi(\psi^*\psi)^2 \\ & + \Big(\phi^* - \psi^*\psi^* \tfrac{h}{m_\phi^2}\Big) m_\phi^2 \Big(\phi - \tfrac{h}{m_\phi^2}\psi\psi\Big).\end{aligned} \tag{12}$$

Since the action for ϕ is Gaussian, the field ϕ can be easily integrated out. Hence, the action (12) is equivalent to the original action (1), and under the condition

$$\frac{h^2}{m_\phi^2} + \tfrac{1}{2}\lambda_\psi = 0, \tag{13}$$

the interaction term $\sim \lambda_\psi$ is cancelled. The resulting theory is of the Yukawa type

$$S = \int_{\tau,\mathbf{x}} \Big\{ \psi^*(\partial_\tau - \boldsymbol{\nabla}^2 - \mu)\psi - h(\phi^*\psi\psi + \psi^*\psi^*\phi) + \phi^* m_\phi^2 \phi \Big\}. \tag{14}$$

It is possible to investigate the theory in this form using a derivative expansion for the original field ψ as well as the composite auxiliary (dimer) field ϕ. This will be described in more detail below.

For some purposes it is useful to do the Hubbard-Stratonovich transformation not at a single scale but in a k-dependent way. This is advantageous in particular when the interaction parameter that develops a bound-state pole is due to fluctuation effects and emerges from the functional renormalization flow. An exact flow equation that realizes such a scale-dependent Hubbard-Stratonovich transformation has been derived [14, 15]. For a discussion of this approach to the treatment of bound states in the context of non-relativistic physics see ref. [16].

2.3.2 Vertex expansion

As we advocated in Sec. 2.2, a systematic vertex expansion of Γ_k is especially suitable for studies of few-body problems. The vertex expansion is an expansion in powers of fields, i.e. schematically

$$\Gamma_k = \sum_{n=2}^{\infty} \Gamma_k(n) = \Gamma_k(2) + \Gamma_k(3) + \Gamma_k(4) + ..., \tag{15}$$

where n represents the number of fields in the monomial $\Gamma_k(n)$. We dropped $\Gamma_k(0)$ in (15) which encodes the ground state energy of the non-relativistic (Fock) vacuum. The term linear in fields is absent due to U(1) symmetry. It is important to stress that, even if absent in the microscopic action $S = \Gamma_{k=\Lambda}$, the vertices $\Gamma_k(n)$ become in general nonlocal in position space during the RG flow. Assuming translation invariance it

is convenient to Fourier transform to momentum space, where the monomials $\Gamma_k(n)$ are functions of $n-1$ kinematically independent momenta and energies. At the infrared scale ($k=0$) this kinematic dependence of Γ_k directly translates into energy and momentum dependence of scattering and bound state properties of the system.

To make this construction transparent we consider the example of bosons described by the microscopic action S in Eq. (1). The term $\Gamma_k(3)$ vanishes in this case, and the vertex expansion in Eq. (15) starts with the terms

$$\begin{aligned}\Gamma_k(2) &= \int_Q \psi^*(Q)P_\psi(Q)\psi(Q)\\ \Gamma_k(4) &= \frac{1}{2}\int_{Q_1,\dots Q_4} \lambda_\psi(Q_1,Q_2,Q_3)\psi^*(Q_1)\psi^*(Q_2)\psi(Q_3)\psi(Q_1+Q_2-Q_3),\end{aligned} \tag{16}$$

where $P_\psi(Q)$ is the scale-dependent inverse propagator and $\lambda_\psi(Q_1,Q_2,Q_3)$ is the nonlocal scale-dependent four-particle vertex. Due to the U(1) particle number symmetry only terms with equal number of ψ and ψ^* can appear in the vertex expansion.

3 Identical bosons

In this section we investigate the few-body physics of identical bosons interacting via a contact interaction. The hierarchy of flow equations introduced in section 2.2 turns out to be extremely useful as it allows us to tackle few-body problems step by step. Completely detached from higher n-body sectors we can first analyze the flow equations describing a single particle, then proceed to the two-body sector followed by the three-body system. For solving the n-body problem we only need the solution of the m-body systems with $m<n$.

3.1 Two-body problem

The interacting bosons are governed by the microscopic action in Eq. (1). In the following it will be useful to switch to the formulation after the Hubbard-Stratonovich transformation in Eq. (14).

In order to apply the functional renormalization group equation (9) we first have to choose a truncation for the effective flowing action Γ_k. We choose a vertex expansion as introduced in Eq. (15), which, up to third order in fields, reads in momentum space

$$\begin{aligned}\Gamma_k(2) &= \int_Q \psi^*(Q)(iq_0+\mathbf{q}^2-\mu_\psi)\psi(Q) + \int_Q \phi^*(Q)P_\phi(Q)\phi(Q),\\ \Gamma_k(3) &= \frac{h}{2}\int_{Q_1,Q_2,Q_3}[\phi^*(Q_1)\psi(Q_2)\psi(Q_3)+\phi(Q_1)\psi^*(Q_2)\psi^*(Q_3)]\delta(Q_1-Q_2-Q_3).\end{aligned} \tag{17}$$

We stress that $\Gamma_k(2)$ and $\Gamma_k(3)$ do not have the most general form compatible with Galilean and global U(1) particle number symmetry. This would include a general inverse atom propagator $P_\psi(Q)$ and a momentum dependent Yukawa coupling $h(Q_1,Q_2)$. However, using the special properties of the vacuum one can show that neither $P_\psi(Q)$ nor $h(Q_1,Q_2)$ get renormalized. Indeed, the condition of vanishing density implies that the poles of the propagators with respect to the frequency argument q_0 are restricted to the upper complex half-plane. Therefore diagrams with all internal lines pointing in the same direction (we call these diagrams 'cyclic') have integrands whose poles lie in the upper complex frequency half-plane. By closing the integration contour in the lower half-plane one finds that the corresponding expressions vanish.

Let us investigate now the renormalization of the two-body sector. Here, we have to consider the couplings h, λ_ψ, and the inverse dimer propagator P_ϕ. At the UV scale, $k=\Lambda$, the contact coupling λ_ψ vanishes because it has been replaced by the dimer exchange interaction in the Hubbard-Stratonovich transformation. Yet there is the box diagram corresponding to the β-function $\partial_t\lambda_\psi$, schematically shown in Fig. 2 (left). This diagram potentially regenerates λ_ψ during the RG flow. It is however cyclic and thus one has $\lambda_\psi\equiv 0$ during the whole RG flow. The only possible diagram renormalizing the Yukawa coupling h contains the

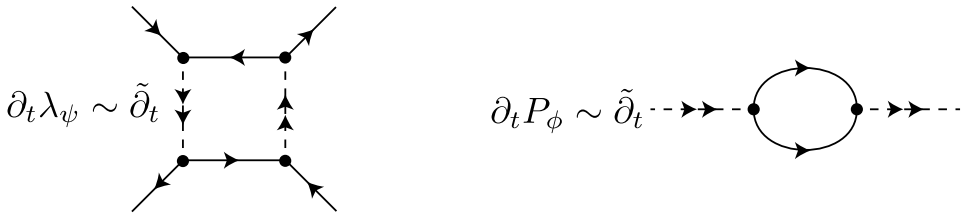

Fig. 2 The beta functions of the coupling λ_ψ (left) and the dimer propagator P_ϕ (right) depicted schematically as one-loop Feynman diagrams. The arrows in Feynman diagrams correspond to flow of particle number associated with U(1) symmetry.

vertex λ_ψ, which is zero. For this reason also h is not renormalized, and one is left with the flow equation for the inverse dimer propagator $P_\phi(Q)$. For this reason, the truncation (17) is complete to third order in fields.

The diagram renormalizing P_ϕ is shown in Fig. 2 (right) and can be written as follows:[3]

$$\partial_t P_\phi(Q) = -\frac{2}{3+p}\int_L \tilde{\partial}_t \frac{h^2}{(P_\psi(L)+R_\psi(L))(P_\psi(Q-L)+R_\psi(Q-L))}, \tag{18}$$

with $p = 1$ for bosons ψ,[4]

$$P_\psi(Q) = iq_0 + \mathbf{q}^2 - \mu_\psi \tag{19}$$

and $R_\psi(Q)$ denotes the atom regulator. In Eq. (18), the symbol $\tilde{\partial}_t$ represents a formal t derivative that hits only the cutoff $R_\psi(Q)$. For the choice of R_ψ we follow [10,11] and choose a frequency and momentum independent cutoff of the simple form $R_\psi = k^2$. It turns out that this masslike regulator allows a relatively simple, analytical integration of the flow equation (18). The two-body problem has also been solved analytically using the so called optimized Litim cutoff by Birse [17]. In contrast to the k^2 regulator, the Litim regulator breaks Galilean invariance such that symmetry restoring counterterms have to be inserted in the UV.

First we perform the frequency loop integration in Eq. (18) with the help of the residue theorem:

$$\begin{aligned}\partial_t P_\phi(Q) &= -\frac{2}{3+p}\int \frac{d^3l}{(2\pi)^3}\tilde{\partial}_t \frac{h^2}{iq_0 + \mathbf{l}^2 + (\mathbf{l}-\mathbf{q})^2 - 2\mu_\psi + 2R_\psi} \\ &= -\frac{2h^2}{3+p}\partial_t \int \frac{d^3l}{(2\pi)^3}\frac{1}{iq_0 + \mathbf{l}^2 + (\mathbf{l}-\mathbf{q})^2 - 2\mu_\psi + 2R_\psi}.\end{aligned} \tag{20}$$

In the second line we replaced $\tilde{\partial}_t$ with ∂_t. The tilde indicates that the derivative acts only upon the k-dependence of the regulator. We are allowed to drop the tilde as neither the Yukawa coupling h nor the atom propagator P_ψ is renormalized such that only the regulator term exhibits a k-dependence. This permits to perform the t integration of the flow equation from the UV scale $t_{\mathrm{UV}} = 0$ to the IR scale $t_{\mathrm{IR}} = -\infty$. Using the specific values of the regulator $R_\psi(t_{\mathrm{IR}}) = 0$ and $R_\psi(t_{\mathrm{UV}}) = \Lambda^2$ we obtain

$$\begin{aligned}&P_\phi^{\mathrm{IR}}(Q) - P_\phi^{\mathrm{UV}}(Q) \\ &= -\frac{2h^2}{3+p}\int \frac{d^3l}{(2\pi)^3}\left(\frac{1}{iq_0 + \mathbf{l}^2 + (\mathbf{l}-\mathbf{q})^2 - 2\mu_\psi} - \frac{1}{iq_0 + \mathbf{l}^2 + (\mathbf{l}-\mathbf{q})^2 - 2\mu_\psi + 2\Lambda^2}\right) \\ &= -\frac{h^2}{3+p}\int \frac{dl}{2\pi^2}\left(\frac{l^2}{l^2 + (\frac{iq_0}{2} + \frac{\mathbf{q}^2}{4} - \mu_\psi)} - \frac{l^2}{l^2 + (\frac{iq_0}{2} + \frac{\mathbf{q}^2}{4} - \mu_\psi + \Lambda^2)}\right) \\ &= -\frac{h^2}{4\pi(3+p)}(\Lambda - \sqrt{\frac{iq_0}{2} + \frac{\mathbf{q}^2}{4} - \mu_\psi}).\end{aligned} \tag{21}$$

[3] Here we use the logarithmic, dimensionless RG scale $t = \ln \frac{k}{\Lambda}$ such that $\partial_t = k\partial_k$.

[4] The scattering physics of two distinguishable particles such as two fermions with opposite spin can be solved analogously with $p = -1$ [11].

In the first line we get rid of the angular integration by substituting $\mathbf{l} \to \mathbf{l} - \mathbf{q}/2$ and the last identity assumes $\Lambda >> |\mu_\psi|, |\mathbf{q}|, |q_0|$.

At this point we have to fix the initial condition for P_ϕ^{UV} at $k = \Lambda$ in order to obtain the physical inverse propagator P_ϕ^{IR} at $k = 0$. The momentum and frequency independent part of the inverse dimer propagator at the microscopic scale can be written as

$$P_\phi^{\mathrm{UV}} = \delta\nu + \nu(a). \tag{22}$$

The physical properties determined by the inverse infrared propagator P_ϕ^{IR}, should be independent of the cutoff scale Λ. From Eq. (21) we see, that this condition determines the term $\delta\nu$,

$$\delta\nu = \frac{h^2}{4\pi(3+p)}\Lambda. \tag{23}$$

Furthermore, as the composite dimer ϕ mediates the interaction between atoms, P_ϕ^{IR} has to correctly describe the scattering physics characterized by the s-wave, zero-range scattering amplitude

$$f(q) = \frac{1}{-a^{-1} - iq}, \tag{24}$$

where $E = 2\mathbf{q}^2$ is the total energy of the two scattered atoms with momenta $\pm\mathbf{q}$ respectively. The scattering amplitude is in turn connected to P_ϕ^{IR}. A simple tree level analysis shows

$$f(0) = -a = \frac{1}{16\pi}\frac{h^2}{P_\phi^{\mathrm{IR}}(0,0,\mu_\psi = 0)}, \tag{25}$$

where the dimer propagator is evaluated for vanishing frequency and momentum. At this point it is important to note, that when describing the s-wave scattering of atoms one deals with atoms at the energy threshold in the in- and outgoing states. For this reason it is necessary to work at vanishing atom energy, $\mu_\psi = 0$. Taking this into account we are in the position to determine $\nu(a)$. Evaluating Eq. (21) for vanishing momentum, energy and atom gap μ_ψ we find

$$\nu(a) = -\frac{h^2}{4\pi(3+p)}a^{-1}. \tag{26}$$

We finally arrive at the solution of the two-body problem encoded in the exact infrared inverse dimer propagator

$$P_\phi(Q) \equiv P_{\phi,k=0}(Q) = \frac{h^2}{4\pi(3+p)}\Big(-a^{-1} + \sqrt{\frac{iq_0}{2} + \frac{\mathbf{q}^2}{4} - \mu_\psi}\Big). \tag{27}$$

This propagator also recovers – after performing the Wick rotation to real energies – the exact (s-wave) zero-range scattering amplitude in Eq. (24).

Quantum mechanics predicts the existence of a universal, weakly bound dimer state for two particles with an interaction characterized by a large, positive scattering length a. Its binding energy can be extracted from a pole of the T-matrix at negative energy. In our approach the T-matrix is given by

$$\tau(E) = -\frac{h^2}{P_\phi^{\mathrm{IR}}(0,0,\mu_\psi = E/2)} \tag{28}$$

and finding its pole therefore corresponds to solving $P_\phi^{\mathrm{IR}}(0,0,\mu_\psi) = 0$ for the atom gap $-\mu_\psi > 0$. This leads to

$$a = \frac{1}{\sqrt{-\mu_\psi}}. \tag{29}$$

As the dimer consists of two atoms we find for its binding energy

$$E_{\mathrm{D}} = 2\mu_\psi = -\frac{2}{a^2}, \qquad E_{\mathrm{D}} = -\frac{\hbar^2}{ma^2}. \tag{30}$$

The second equation is expressed in conventional units and is the well-known universal relation for the binding energy of the shallow dimer. The determination of μ_ψ takes care of the correct vacuum limit. The atom gap $\mu_\psi < 0$ is fixed to the value where the dimer becomes gapless in the infrared. This reflects that for $a > 0$ the dimer is the two-body ground state of the system.

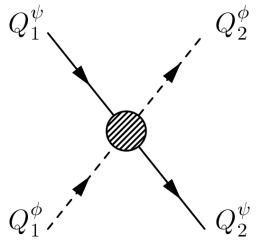

Fig. 3 Kinematics of the vertex $\lambda_3(Q_1^\psi, Q_2^\psi, E)$ in the center-of-mass frame. The atoms and dimers have momenta $Q_1^\psi = (E_{\psi 1}, \mathbf{q}_1)$, $Q_1^\phi = (-E_{\psi 1} + E, -\mathbf{q}_1)$ and $Q_2^\psi = (E_{\psi 2}, \mathbf{q}_2)$, $Q_2^\phi = (-E_{\psi 2} + E, -\mathbf{q}_2)$.

3.2 Three-body problem

In order to treat the three-body system of identical bosons within the vertex expansion scheme, we extend our truncation (17) by the term

$$\Gamma_k(4) = -\int_{Q_1,\dots Q_4} \lambda_3(Q_1, Q_2, Q_3)\phi(Q_1)\psi(Q_2)\phi^*(Q_3)\psi^*(Q_4)\delta(Q_1 + Q_2 - Q_3 - Q_4) \tag{31}$$

with $\lambda_3(Q_1, Q_2, Q_3)$ denoting the atom-dimer vertex. For simplicity we restrict our discussion to unitarity, $a^{-1} = 0$, and demonstrate how Efimov physics emerges from the renormalization group flow equation for the atom-dimer coupling $\lambda_3(Q_1, Q_2, Q_3)$.

First consider the kinematics of the atom-dimer scattering. The 1PI vertex $\lambda_3(Q_1, Q_2, Q_3)$ depends on three independent energies and spatial momenta. In the following we work in the center-of-mass frame and take the incoming atom and dimer to have momenta $\mathbf{q}_1$ and $-\mathbf{q}_1$, and energies $E_{\psi 1}$ and $E - E_{\psi 1}$, while the outgoing particles have momenta $\mathbf{q}_2$ and $-\mathbf{q}_2$ and energies $E_{\psi 2}$ and $E - E_{\psi 2}$. In the following the atom-dimer vertex will be denoted by $\lambda_3(Q_1^\psi, Q_2^\psi, E)$. The kinematics is summarized in Fig. 3.

The closed exact solution of the two-body problem, presented in the previous subsection, provides a simple strategy for the derivation of the renormalization group flow equation for the atom-dimer vertex. In principle, one can introduce completely independent regulators R_ψ and R_ϕ for the atoms ψ and dimers ϕ. Nevertheless, since the presence of the cutoff R_ϕ does not alter the solution of the two-body problem, we choose for the atoms the Galilei-invariant momentum independent cutoff R_ψ, used in subsection 3.1, and lower it first from $R_\psi = \Lambda^2$ to zero while keeping R_ϕ fixed. As the result of this step the dimer inverse propagator is renormalized according to Eq. (27). This also induces interactions between dimers, as for example a term $\sim (\phi^*\phi)^2$. However, these interactions belong to the four-body and higher sectors. By virtue of the vacuum hierarchy, they do not influence the flow of λ_3. Subsequently in the second step, only the dimer cutoff is present and we lower R_ϕ from its UV value to zero. In the second step P_ϕ and P_ψ are fixed according to Eqs. (27) and (19). In this subsection we use a sharp cutoff for the dimer field,

$$R_\phi(Q, k) = P_\phi(Q)\left(\frac{1}{\theta(|\mathbf{q}| - k)} - 1\right). \tag{32}$$

The special feature of this cutoff is that the regularized dimer propagator takes the simple form

$$\frac{1}{P_\phi(Q) + R_\phi(Q, k)} = \theta(|\mathbf{q}| - k)\frac{1}{P_\phi(Q)}. \tag{33}$$

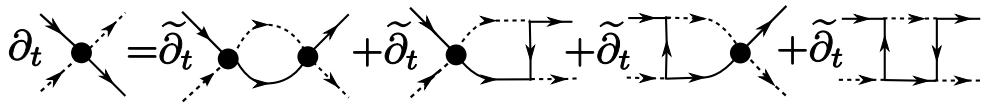

Fig. 4 Graphical representation of the flow equation for the atom-dimer vertex λ_3. Full lines denote atoms ψ and dashed lines dimers ϕ. The shaded circle denotes the atom-dimer vertex λ_3.

Following the procedure described above we derive the flow equation for the atom-dimer vertex $\lambda_3(Q_1^\psi, Q_2^\psi; E)$, which is given by

$$\begin{aligned}\partial_t\lambda_3(Q_1^\psi, Q_2^\psi; E) = -\int_L \frac{k\delta(|\mathbf{l}|-k)}{P_\psi(L)P_\phi(-L+Q)}\Big[&C\lambda_3(Q_1^\psi, L; E)\lambda_3(L, Q_2^\psi; E) \\ &+\frac{B}{2}\Big\{\frac{h^2}{P_\psi(-L+Q_1^\phi)}\lambda_3(L, Q_2^\psi; E) + \lambda_3(Q_1^\psi, L; E)\frac{h^2}{P_\psi(-L+Q_2^\phi)}\Big\} \\ &+A\frac{h^2}{P_\psi(-L+Q_1^\phi)}\,\frac{h^2}{P_\psi(-L+Q_2^\phi)}\Big],\end{aligned} \tag{34}$$

where $Q = Q_1^\phi + Q_1^\psi = (E, \mathbf{0})$, $A = 1$, $B = 2$ and $C = 1$. The graphical representation of this flow equation in terms of one-loop Feynman diagrams can be found in Fig. 4.

Fortunately, at low energies and momenta the flow equation can be considerably simplified (for details see [11]). After introducing the angle-averaged 1PI atom-dimer vertex

$$\lambda_3(q_1, q_2, E) \equiv \frac{1}{2h^2}\int_{-1}^{1} d(\cos\theta)\lambda_3(\mathbf{q}_1, \mathbf{q}_2; E), \qquad \cos(\theta) = \frac{\mathbf{q}_1\cdot\mathbf{q}_2}{|\mathbf{q}_1||\mathbf{q}_2|} \tag{35}$$

and transforming to the real-time formalism, the flow equation reads

$$\begin{aligned}\partial_t\lambda_3(q_1, q_2, E) = -\frac{2(3+p)}{\pi}\frac{k^3}{\sqrt{\frac{3k^2}{4}-\frac{E}{2}-i\epsilon}}\Big[&C\lambda_3(q_1, k, E)\lambda_3(k, q_2, E) + \\ &\frac{B}{2}\left\{\lambda_3(q_1, k, E)G(k, q_2) + G(q_1, k)\lambda_3(k, q_2, E)\right\} + AG(q_1, k)G(k, q_2)\Big],\end{aligned} \tag{36}$$

where we remind that for bosons $p = 1$, and the symmetric function $G(q_1, q_2)$ is defined by

$$G(q_1, q_2) = \frac{1}{4q_1q_2}\log\frac{q_1^2+q_2^2+q_1q_2-\frac{E}{2}-i\epsilon}{q_1^2+q_2^2-q_1q_2-\frac{E}{2}-i\epsilon}. \tag{37}$$

The infinitesimally positive $i\epsilon$ term arises from the inverse Wick rotation and makes both Eqs. (36) and (37) well-defined. Note that Eq. (36) is independent of the Yukawa coupling h and thus is well-defined in the broad resonance limit $h \to \infty$.

The flow equation (36), obtained above, is quite complicated. In order to gain physical understanding, we first employ a crude, but simple and intuitive pointlike approximation. In this approximation the 1PI vertex $\lambda_3(q_1, q_2, E)$ is replaced by a momentum and energy independent coupling λ_3. In the pointlike limit the flow equation (36) takes the simple form

$$\partial_t\lambda_3^R = -\frac{4(3+p)}{\sqrt{3}\pi}\left[\frac{A}{4} + \frac{B}{2}\lambda_3^R + C(\lambda_3^R)^2\right] + 2\lambda_3^R, \tag{38}$$

where the rescaled dimensionless coupling $\lambda_3^R = \lambda_3 k^2$ is introduced. The right-hand side of this differential equation is a quadratic polynomial with constant coefficients. The sign of its discriminant D determines the behavior of the solution of Eq. (38). For the bosonic problem $D \approx -7.762$ and we obtain a periodic solution of the form $\lambda_3^R \sim \tan[\pi t/T]$ with a period $T = \frac{2\pi}{\sqrt{-D}}$. Note that the renormalization group evolution is governed by a limit cycle scaling. RG limit cycles are the manifestation of the Efimov effect. Indeed, we

can give the following intuitive interpretation of the periodic solution: During the RG flow we encounter three-body atom-dimer bound states, which manifest themselves as divergences of the atom-dimer coupling λ_3^R. In the unitary limit there are infinitely many of these bound states, which are equidistant in a logarithmic RG energy scale. In this way the continuous scaling symmetry is broken to the discrete scaling subgroup, and the generalized universality emerges.

It is well-known that at the unitarity point, where the scattering length a diverges, the energy spectrum of Efimov trimers forms a geometric series

$$\frac{E_{n+1}}{E_n} = \exp(-2\pi/s_0) \tag{39}$$

with E_{n+1} and E_n denoting neighboring bound state energies. The Efimov parameter s_0 is given by the solution of a transcendental equation and one finds $s_0 \approx 1.00624$ [1]. By dimensional arguments we can connect the artificial RG sliding scale k^2 with the binding energy E as $E \sim k^2$. The proportionality factor disappears in the ratio of the energies and hence the Efimov parameter can be read off from the RG period

$$\frac{k_{n+1}^2}{k_n^2} = \frac{E_{n+1}}{E_n} = \exp(-2T) \Rightarrow s_0 = \frac{\pi}{T}. \tag{40}$$

In the pointlike approximation we obtain $s_0 \sim 1.393$, which differs from the correct result by 40%. Obviously the simple pointlike approximation is too crude to get the correct quantitative agreement. Nevertheless it provides us with the qualitative picture of how the Efimov effect appears as limit cycles in the functional renormalization group framework.

It is remarkable that for $E = 0$ the flow equation (36) can be solved exactly. Here only the main results will be summarized while for details we refer to [10, 11]. In order to find the exact solution most easily we perform the redefinition

$$f_t(t_1, t_2, E) \equiv 4(3+p)q_1q_2\lambda_3(q_1, q_2, E) \qquad g(t_1, t_2) \equiv 4(3+p)q_1q_2G(q_1, q_2) \tag{41}$$

and introduce the connected, one-particle reducible atom-dimer vertex

$$\bar{f}_t(t_1, t_2) = p f_t(t_1, t_2) + g(t_1, t_2), \tag{42}$$

where from now on we prefer to work with logarithms of momenta $t_1 = \ln(q_1/\Lambda)$ and $t_2 = \ln(q_2/\Lambda)$. The RG scale dependence of the atom-dimer vertex $\bar{f}_t(t_1, t_2, E)$ is denoted by the subscript t. The renormalization group flow equation and the initial condition for $\bar{f}_t$ are given in matrix notation by

$$\partial_t \bar{f}_t = -\frac{p}{\sqrt{3}\pi} \bar{f}_t \cdot A_t \cdot \bar{f}_t, \qquad \bar{f}_{t=0} = g, \tag{43}$$

where A_t has matrix elements $A_t(t_1, t_2) = \delta(t - t_1)\delta(t - t_2)$ and matrix multiplication denotes integration over t. The formal solution of this differential matrix equation reads for $t \in (-\infty, 0)$

$$\bar{f}_t = \left(I + \frac{p}{\sqrt{3}\pi} \int_0^t ds g \cdot A_s \right)^{-1} \cdot g, \tag{44}$$

where I denotes the identity matrix.

In the IR limit $t \to -\infty$, which corresponds to the integration of all quantum fluctuations, $\bar{f} \equiv \bar{f}_{t=-\infty}$ solves the following matrix equation

$$\bar{f} = g + \frac{p}{\sqrt{3}\pi} g \cdot \bar{f}. \tag{45}$$

This is the well-known integral equation for the amputated, connected Green's function obtained by Skorniakov and Ter-Martirosian more than fifty years ago [18].

For illustration purposes we discretized Eq. (44) and solved it numerically. A series of cartoons of the RG evolution of the 1PI vertex $f_t(t_1, t_2)$ is depicted in Fig. 5. In the UV we start with a simple initial condition $f_t(t_1, t_2) = 0$ and observe how a periodic structure (with period $T_{\text{spatial}} \approx 6.2$) gradually develops. This intricate periodic landscape is completely missed in the pointlike approximation which corresponds to a planar landscape with no t_1 and t_2 dependence. The RG evolution of the point $f_t(t_1 = 0, t_2 = 0)$ of the

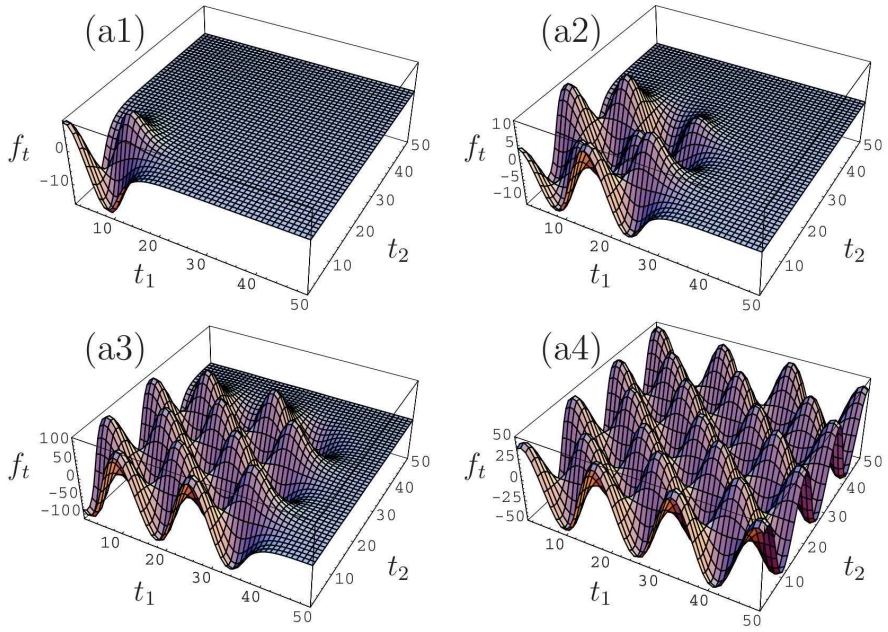

Fig. 5 The RG evolution of the momentum dependent modified vertex $f_l(t_1, t_2) = 4(3 + p)q_1q_2\lambda_3(q_1, q_2, E)$. Spatial momenta t_1, t_2 and the RG time t are discretized to $N = 50$ intervals with a step $\Delta t = 0.4$. The cartoons correspond to the descritized steps $10, 25, 35, 50$.

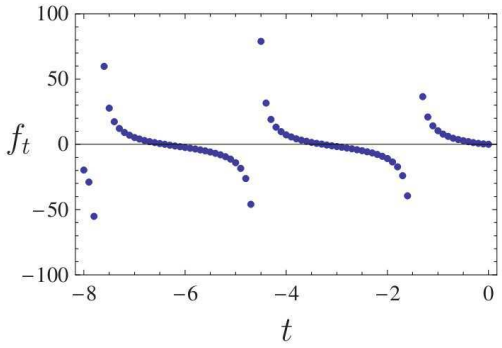

Fig. 6 Numerical evolution of the point $f_l(t_1 = 0, t_2 = 0)$ with the RG time t. Renormalization group develops a limit cycle with a period $T_{temp} \approx 3.1$.

landscape is depicted in Fig. 6. Similar to the solution obtained in the pointlike approximation we observe "temporal" oscillations. The period of these oscillations $T_{\text{temp}} \approx 3.1$ which leads to the Efimov parameter $s_0 = \frac{\pi}{T_{\text{temp}}} \approx 1.0$. This is in a good agreement with the "exact" result $s_0 \approx 1.00624$ obtained from the quantum mechanical treatment and is only limited by our numerical accuracy.

4 Two-component fermions

4.1 Few-body problem

The solution of the two- and three-body problem, presented in the previous section, can be straightforwardly extended to a system consisting of two fermion species with equal masses $M_{\psi_1} = M_{\psi_2}$ near a broad

Feshbach resonance described by the Euclidean action

$$S = \int_{\tau,\mathbf{x}} \Big\{ \psi_i^*(\partial_\tau - \boldsymbol{\nabla}^2 - \mu)\psi_i + \phi^* P_\phi \phi - h(\phi^* \psi_1 \psi_2 + \psi_2^* \psi_1^* \phi) \Big\}. \tag{46}$$

Here, the two species of elementary fermionic atoms ψ_1, ψ_2 are described by Grassmann-valued fields, and ϕ is a composite bosonic dimer with the inverse propagator P_ϕ. Wherever equal indices appear summation is implied. Note that in Eq. (46) the dimer ϕ is just an auxiliary field which has no own dynamics, i.e. its inverse propagator $P_\phi = P_{\phi,k=\Lambda}$ is a constant. This fermionic system has a global SU(2)×U(1) internal symmetry with (ψ_1, ψ_2) transforming as a doublet and ϕ as a singlet of the SU(2) flavor subgroup. Two-species fermion systems (46) near a broad Feshbach resonance have for example been realized experimentally using two hyperfine states of ^{6}Li or ^{40}K ultracold atoms.

The two-body problem can be solved analytically following the very same route that we have taken for bosons in subsection 3.1. The only difference for fermions consists in setting $p = -1$ in Eqs. (18)-(27). Similar to bosons, for $a > 0$ there is a universal dimer bound state with the binding energy given by Eq. (30).

The solution of the fermionic three-body problem is also directly analogous to the computation for bosons, presented in subsection 3.2. For two-component fermions one arrives at the flow equation (34) with coefficients $A = 1$, $B = -2$ and $C = 1$. The solution of this flow equation is, however, qualitatively very different from the bosonic case. This can be understood already in the pointlike limit, where the flow equation is given by (38). Crucially, for fermions the discriminant D is positive. We find $D = 9.881$, and the solution of the flow equation is of the form $\lambda_3^R \sim \tanh\Big(\frac{\sqrt{D}}{2}(t+\kappa)\Big)$, where κ is fixed by the initial condition. The solution in the pointlike approximation approaches fixed points in the IR and UV. The numerical solution of the full RG flow equation (34), detailed account of which can be found in [11], supports this finding. In summary, the renormalization group flow does not develop a limit cycle scaling and there is no Efimov effect in the three-body problem for two-component fermions with equal mass.

4.2 Many-body physics

Although the few-body physics of two-component fermions of equal masses is not as rich as for the case of identical bosons, this system exhibits interesting many-body physics [19,20]. We concentrate on the case of equal densities $\mu = \mu_{\psi_1} = \mu_{\psi_2}$. For small negative scattering length $a \to 0_-$ BCS theory becomes valid. Many-body quantum fluctuations lead to spontaneous U(1) symmetry breaking and a superfluid ground state. Also for small positive scattering length $a \to 0_+$ the ground state will be superfluid, now given by a Bose-Einstein condensate of dimers. In between these two regions one finds a smooth BCS-BEC crossover, including in particular unitarity with $a^{-1} = 0$.

The functional renormalization description of this system has been developed in the recent years [12, 21,22]. It proved to be convenient to work with the Hubbard-Stratonovich transformed microscopic action in Eq. (46) and to use a truncation of the flowing action Γ_k in terms of a derivative expansion. The most elaborate truncation studied so far [22] reads

$$\begin{aligned}\Gamma_k = \int_0^{1/T} d\tau \int d^3x \Big\{ & \psi_i^* Z_\psi (\partial_\tau - \boldsymbol{\nabla}^2 + m_\psi^2)\psi_i + \phi^* (Z_\phi \partial_\tau - \tfrac{1}{2} A_\phi \boldsymbol{\nabla}^2)\phi \\ & + U_k(\phi^*\phi) - h(\phi^*\psi_1\psi_2 + \phi\psi_2^*\psi_1^*) + \lambda_{\phi\psi}\phi^*\phi\psi_i^*\psi_i \Big\}.\end{aligned} \tag{47}$$

Here, the coefficients Z_ψ, m_ψ^2, Z_ϕ, A_ϕ, h, $\lambda_{\phi\psi}$ and the effective potential $U_k(\phi^*\phi)$ are k-dependent quantities.

The truncation in Eq. (47) can be used both for the few-body physics (vacuum) and to describe thermal and chemical equilibrium. In the former case one finds the characteristic binding energy of the dimers as in Eq. (30). Due to simplicity of the truncation it is also rather easy to calculate more complicated observables such as the scattering length of dimers a_M. In the limit $a \to 0_+$ the result $a_M/a = 0.59$ [22] is in good agreement with the exact result $a_M/a = 0.60$ [23] obtained from solving the Schrödinger equation. The dimer-dimer scattering was also recently studied with functional renormalization by the Manchester group [24,25]. In [25] all possible local couplings that can be generated in the fermion four-body problem

were included and it was found that $a_M/a = 0.58 \pm 0.2$, where the error was estimated from the regulator dependence of the final result.

At non-zero density the flow equations are modified, for example the particle-particle diagram renormalizing the boson propagator in Fig. 2 has a stronger effect. As a result for small temperatures the effective potential $U_k(\phi^*\phi)$ becomes of a mexican hat form at the macroscopic scale $k = 0$. This leads to spontaneous U(1) symmetry breaking and superfluidity. For a more detailed discussion of the flow equations as well as for the results of this approach we refer to ref. [12,22,26].

5 Three-component fermions with global SU(3) symmetry

As was discussed in section 4 there is no Efimov effect for two fermion species with equal masses. The main reason for this is Pauli blocking. An obvious question is what happens in the case of three species (flavors) of fermions. The question is of particular interest as systems with three hyperfine states have been realized in recent experimants [5,6]. In this section we will consider the case where all fermion masses are equal as well as the three pairwise scattering lengths such that the system possesses a global SU(3) internal symmetry. The generalization to the experimentally accessible system of ^{6}Li atoms, where the pairwise scattering lengths are not equal, is discussed in section 6.

5.1 Exact solution at unitarity: Vertex expansion

For the case of SU(3) symmetric fermions we extend the action (46) to

$$S = \int_{\tau,\mathbf{x}} \left\{ \psi_i^* \left(\partial_\tau - \boldsymbol{\nabla}^2 - \mu\right) \psi_i + \phi_i^* \left(\partial_\tau - \boldsymbol{\nabla}^2/2 + m_\phi^2\right) \phi_i + \frac{h}{2} \epsilon_{ijk} \left(\phi_i^* \psi_j \psi_k - \phi_i \psi_j^* \psi_k^*\right) \right\}. \tag{48}$$

Eq. (48) is the analog of a two-channel model where the composite bosons ϕ_i have a non-trivial propagator already in the microscopic action. The analog of the single channel model in Eq. (46) corresponds to the limit of broad resonances $h^2 \to \infty$, $m_\phi^2 \to \infty$. The inverse propagator of the bosons is then dominated by the constant part m_ϕ^2. For finite h the action in Eq. (48) can describe also Feshbach resonances of finite width.

The three Grassmann valued fields ψ_i for the fermions can be assembled into a vector $\psi = (\psi_1, \psi_2, \psi_3)$ and the bosonic fields ϕ_i form a vector $\phi = (\phi_1, \phi_2, \phi_3) \sim (\psi_2\psi_3, \psi_3\psi_1, \psi_1\psi_2)$. The action possesses an SU(3)×U(1) internal symmetry with ψ transforming as a triplet $\mathbf{3}$ and ϕ as an anti-triplet $\bar{\mathbf{3}}$ under the SU(3) flavor subgroup. The three dimers mediate the pairwise scattering in the three possible s-wave scattering channels.

What about Efimov physics in such a system? The answer to this question is in fact quite simple and can be understood with the following quantum mechanical argument: To identify the bound state spectrum one has to solve the three-body Schrödinger equation. In the case of fermions the bound state wave function has to be totally antisymmetric. The total wave function can be separated into the orbital and flavor part. If we take the flavor part to be antisymmetric, $(\epsilon_{ijk}|i> |j> |k>)$, the orbital part must be symmetric and therefore has the same symmetry properties as in the bosonic case. As the orbital part solely determines the bound state spectrum in a quantum mechanical calculation, the bound state physics of SU(3) fermions is identical to the bosonic case leading to the same Efimov spectrum.

A proper analysis of the renormalization group flow equations confirms these expectations. It is more complicated than for identical bosons since two different terms $\sim \phi^*\phi\psi^*\psi$ similar to Eq. (31) are allowed by the symmetries. Specifically, the analog to Eqs. (17) and (31) reads

$$\Gamma_k = \int_{\tau,\mathbf{x}} \left\{ \psi^\dagger(\partial_\tau - \boldsymbol{\nabla}^2 - \mu)\psi + \phi^\dagger P_\phi \phi + \frac{h}{2}\epsilon_{ijk}(\phi_i^*\psi_j\psi_k - \phi_i\psi_j^*\psi_k^*) + \lambda_{3a}\phi_i^*\psi_i^*\phi_j\psi_j + \lambda_{3b}\phi_i^*\psi_j^*\phi_i\psi_j \right\}. \tag{49}$$

We have suppressed here the nonlocal structure (momentum dependence) of the inverse propagator P_ϕ and the couplings λ_{3a} and λ_{3b} for simplicity. Nevertheless, in the broad resonance limit $h^2 \to \infty$, the solution of the flow equation at $a^{-1} = 0$ can be constructed in close analogy to the one presented in Sec. 3.2. In particular one finds also a limit cycle with the same Efimov parameter $s_0 \approx 1.00624$. For details we refer to [11].

5.2 Approximate solution away from unitarity: Derivative expansion

Although the foregoing discussion formally resolves the question about the Efimov effect for SU(3) fermions, we want to elaborate a bit more on this case. The solution of the flow equation in terms of the vertex expansion works well (and is numerically exact) at the unitarity point with $a^{-1} = 0$ and $E = 0$. However, one would like to understand also the region away from this point, especially since for experiments the physics directly at the unitarity point is hard to access. In this subsection we develop a simplified truncation of the flowing action in terms of a derivative expansion.

Based on the ansatz (49) our first goal is to find a 'minimal' truncation which still captures the essential features of Efimov physics. Due to fermion statistics the Efimov trimer is expected to be a SU(3) singlet. Only the term proportional to λ_{3a} in Eq. (49) can have a bound state pole due to the combination of all three flavours. From this perspective, the term proportional to λ_{3b}, which plays a similar role as in the two component fermion case, is expected to be less relevant for the description of the three-body bound state. We expect it only to affect quantitative results but not the qualitative features and we will neglect it from here on.

Instead of keeping the full momentum and energy dependence of P_ϕ and λ_{3a} as in the vertex expansion (49) we will employ a derivative expansion

$$\Gamma_k = \int_{\tau,\mathbf{x}} \Big\{ \psi_i^*(\partial_\tau - \boldsymbol{\nabla}^2 - \mu)\psi_i + \phi_i^* \left[A_\phi \left(\partial_\tau - \boldsymbol{\nabla}^2/2 \right) + m_\phi^2 \right] \phi_i + \chi^* \left[A_\chi \left(\partial_\tau - \boldsymbol{\nabla}^2/3 \right) + m_\chi^2 \right] \chi \\ + \frac{h}{2} \epsilon_{ijk} \left(\phi_i^* \psi_j \psi_k - \phi_i \psi_j^* \psi_k^* \right) + g \left(\phi_i^* \psi_i^* \chi - \phi_i \psi_i \chi^* \right) \Big\}. \tag{50}$$

The inverse dimer propagator is now approximated by a gradient expansion in leading order in momentum and energy with a gap term m_ϕ^2 and wave function renormalization A_ϕ. The truncation (50) furthermore contains a single component fermionic field χ which is a singlet under SU(3) and represents the totally antisymmetric combination $\psi_1\psi_2\psi_3$. The Efimov trimer field χ, which we also call sometimes the 'trion', mediates the original atom dimer interaction $\sim \lambda_{3a}$ and is introduced by a Hubbard-Stratonovich transformation analogously to the dimer field introduced in section 2.3. Similar to the dimer we approximate the inverse propagator for the field χ in terms of a derivative expansion.

The Yukawa-type term proportional to g describes how the composite field χ is formed from its constituents. At the microscopic scale $k = \Lambda$ we choose $g = 0$, $A_\chi = 1$ and $m_\chi^2 \to \infty$. The field χ is then an auxiliary field that decouples from the other fields. With this choice we recover the original microscopic action (48) in the broad resonance limit. In the next subsection we will relate the initial values of the dimer gap $m_\phi^2(\Lambda)$ and the Yukawa coupling h to the scattering properties of the elementary fermions ψ_i.

5.2.1 Two-body problem

We proceed as in section 3 by subsequently solving the flow equations in the two- and three-body sector. In the following analysis we will employ the regulator $R_k = r(k^2 - \mathbf{p}^2)\theta(k^2 - \mathbf{p}^2)$ with $r = 1$ for the fermions ψ_i, $r = A_\phi/2$ for the bosons ϕ_i and $r = A_\chi/3$ for the trion field χ. From the arguments presented in Sect. 3.1 it follows that the fermion propagator and the Yukawa coupling h are not renormalized. The flow equation for the boson gap parameter reads

$$\partial_t m_\phi^2 = \frac{h^2}{6\pi^2} \frac{k^5}{(k^2 - \mu)^2}, \tag{51}$$

and for the boson wave function renormalization we obtain

$$\partial_t A_\phi = -\frac{h^2}{6\pi^2} \frac{k^5}{(k^2 - \mu)^3}. \tag{52}$$

Eqs. (51), (52) can be solved by direct integration, for details we refer to ref. [27].

The initial values for A_ϕ, m_ϕ^2, and h can be related to the scattering properties of the elementary fermions close to a Feshbach resonance. We can use the freedom to perform a rescaling of the field ϕ_i and choose $A_\phi(\Lambda) = 1$. To fix the remaining parameters we note that the scattering length between the fermions is given

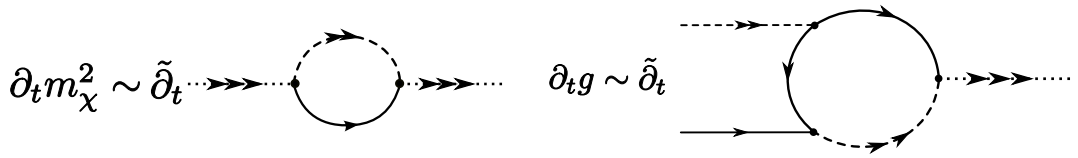

Fig. 7 The beta functions of the three-body couplings m_χ^2 and g depicted as Feynman diagrams. The dotted lines with three arrows denote the composite trimer field χ.

by $a = -\frac{h^2}{8\pi m_\phi^2}$ where the couplings are evaluated at the macroscopic (IR) scale $k = 0$ and for vanishing μ. This fixes the initial value of m_ϕ^2 to be

$$m_\phi^2(\Lambda) = -\frac{h^2}{8\pi} a^{-1} + \frac{h^2}{6\pi^2}\Lambda - 2\mu, \tag{53}$$

where the term -2μ accounts for the fact that the dimer consists of two fermions.

The value of the Yukawa coupling h is related to the width of the Feshbach resonance. The scattering length close to a Feshbach resonance at magnetic field B_0 and width ΔB can be parametrized by [19,28]

$$a = \frac{a_{bg}\Delta B}{B - B_0} \tag{54}$$

with a_{bg} the background scattering length. Furthermore, we may identify the boson gap $m_\phi^2(k = 0, \mu = 0)$ with the energy of the closed channel molecule, $E_c = \mu_M(B - B_0)$, with μ_M being its magnetic moment (for more details see [12]). From this one can see that the Yukawa coupling h^2 is proportional to the width of the Feshbach resonance:

$$h^2 = -8\pi a_{bg}\mu_M \Delta B. \tag{55}$$

Broad Feshbach resonances correspond to $h^2 \to \infty$. However, we can study also the crossover from narrow to broad Feshbach resonances within the two-channel model Eq. (48).

5.2.2 Three-body problem and energy spectrum

The flow equations of the three-body sector read

$$\partial_t m_\chi^2 = \frac{6g^2}{\pi^2} \frac{A_\phi k^5}{(3A_\phi k^2 - 2A_\phi \mu + 2m_\phi^2)^2}, \tag{56}$$

and

$$\partial_t g = m_\chi^2 \partial_t \alpha - \frac{2gh^2}{3\pi^2} \frac{k^5}{(k^2 - \mu)^2} \frac{(6A_\phi k^2 - 5A_\phi \mu + 2m_\phi^2)}{(3A_\phi k^2 - 2A_\phi \mu + 2m_\phi^2)^2}. \tag{57}$$

While the expression in Eq. (56) and the second term in Eq. (57) are straightforwardly found from the diagrams shown in Fig. 7, the first term in Eq. (57) needs further clarification.

Although the original atom-dimer interaction $\sim \lambda_{3a}$ has been replaced on the UV scale by the trion exchange using the Hubbard-Stratonovich transformation, an atom-dimer interaction term of the form

$$\int_{\tau,\mathbf{x}} \lambda_{\phi\psi} \phi_i^* \psi_i^* \phi_j \psi_j \tag{58}$$

builds up again in the RG flow due to the box diagram shown in Fig. 8. As it turns out, it is essential to include this evolution in our RG treatment to recover Efimov physics. In order to do so, we use a scale dependent Hubbard-Stratonovich transformation, a method developed in [14,15]. By this we absorb the regenerated atom-dimer coupling $\lambda_{\phi\psi}$ into the flow of the Yukawa coupling g.

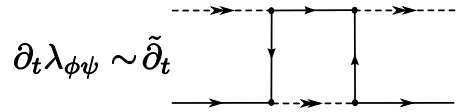

Fig. 8 The box diagram leads to the regeneration of the atom-dimer vertex $\lambda_{\phi\psi}$ in the RG flow. Using a k-dependent Hubbard-Stratonovich transformation it is absorbed in the flow of the Yukawa coupling g.

As was shown in [14, 15], the Wetterich equation gets supplemented by an additional term from the scale dependence of the Hubbard-Stratonovich transformation. We choose this scale dependence such that the box diagram in Fig. 8 gets cancelled. This leads to

$$\partial_t \alpha = -\frac{h^4}{12\pi^2 g}\frac{k^5}{(k^2-\mu)^3}\frac{(9A_\phi k^2 - 7A_\phi \mu + 4m_\phi^2)}{(3A_\phi k^2 - 2A_\phi \mu + 2m_\phi^2)^2}. \tag{59}$$

This determines the first term in Eq. (57) and with this choice $\lambda_{\phi\psi} \equiv 0$ is enforced on all scales k. The scattering between fermions and bosons is now described exclusively by the exchange of the (scale dependent) trion bound state χ.

We now investigate the energies of the different states – elementary fermions ψ_i ("atoms"), composite bosons ϕ_i ("dimers") or composite fermions χ ("trimers") – as a function of the model parameters (e.g. the fermion scattering length a). In general it is not possible to find a simple analytical solution to the flow equations (56), (57) and we have to resort on a numerical solution. To find the energy of the lowest excitation we adjust the chemical potential $\mu \leq 0$ such that the lowest excitation of the vacuum is gapless at $k = 0$.

For a finite UV cutoff scale Λ we find that for $a^{-1} \to -\infty$, the lowest energy state is given by the atoms which implies $\mu = 0$, $m_\phi^2 > 0$, and $m_\chi^2 > 0$. No bound states are present in this regime.

In contrast, for $a^{-1} \to \infty$, the dimer ϕ is the lowest energy state, $\mu < 0$, $m_\phi^2 = 0$, and $m_\chi^2 > 0$. In fact, we can use our analytical solution of the two-body sector to obtain the dimer energy. In the limit $\Lambda/|\mu| \to \infty$ we find

$$\mu = -\left(\frac{h^2}{32\pi} - \sqrt{\frac{h^4}{(32\pi)^2} + \frac{a^{-1}h^2}{16\pi}}\right)^2. \tag{60}$$

which gives the binding energy of the weakly bound dimer state $E_D = 2\mu$. For finite h and the choice $A_\phi(\Lambda) = 1$ the dimer binding energy also depends on the "effective range"

$$r_{\text{eff}} = -\frac{32\pi}{h^2}, \tag{61}$$

according to

$$E_D = 2\mu = -\frac{2}{r_{\text{eff}}}\left(1 - \sqrt{1 - \frac{2r_{\text{eff}}}{a}}\right)^2. \tag{62}$$

In the broad resonance limit (vanishing effective range) one recovers the well-known result $E_D = -2/a^2 = -\hbar^2/(M_\psi a^2)$.

Let us investigate to the regime of strong interaction close to the point with $a^{-1} = 0$. In a region $a_{c1}^{-1} \leq a^{-1} \leq a_{c2}^{-1}$, we find that the lowest energy is given by the trion, such that $\mu < 0$, $m_\phi^2 > 0$, and $m_\chi^2 = 0$ for $k = 0$. In this region the lowest energy state is a bound state of three fundamental fermions $\chi \sim \psi_1\psi_2\psi_3$. The critical scattering length a_{c1}^{-1} (a_{c2}^{-1}), at which the Efimov trimer becomes degenerate with the atom (atom-dimer) threshold, depends on the effective range. For narrow resonances $h^2/\Lambda \ll 1$ we find a linear increase with h^2 as $a_{c1}^{-1} = -0.0013h^2$ and $a_{c2}^{-1} = 0.0085h^2$. For broad Feshbach resonances, $h^2/\Lambda \gg 1$, the depth of the trimer state becomes independent of the effective range and is determined solely by the UV cutoff scale a_{c1}^{-1}, $a_{c2}^{-1} \sim \Lambda$ such that the cutoff scale can be viewed as the additional three-body parameter needed to determine the exact position of the universal Efimov trimer state [1]. This crossover behavior from narrow to broad resonances is shown in Fig. 9 (left).

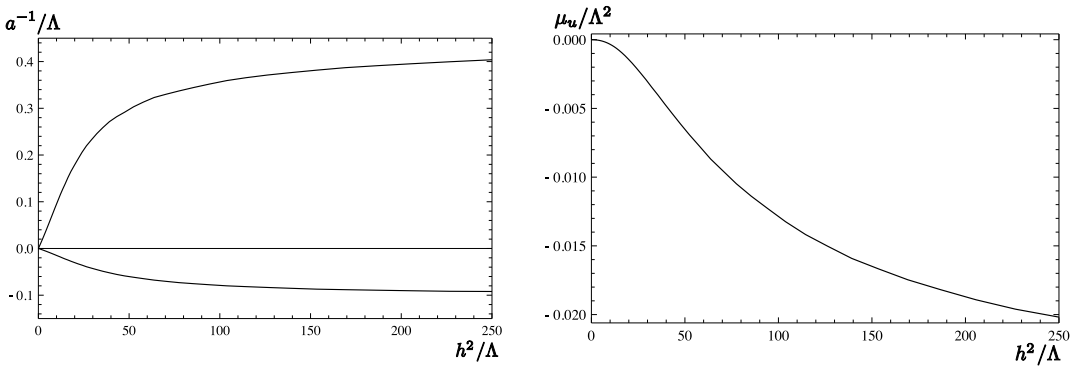

Fig. 9 Crossover from narrow to broad Feshbach resonances. left: Scaling of the critical scattering length $a_{c1}^{-1} < 0$ ($a_{c2}^{-1}/4 > 0$) at which the lowest Efimov trimer becomes degenerate with the atom (atom-dimer) threshold in dependence on the width of the Feshbach resonance given by h. right: Analogous scaling of the lowest trimer binding energy given by the chemical potential μ_u at unitarity.

In Fig. 9 (right) we show our result for the energy per atom μ_u of the trimer as a function of h^2 at unitarity $a^{-1} = 0$. For narrow resonances we find $\mu_u = -2.5 \times 10^{-6} h^4$. In the broad resonance limit $h^2 \to \infty$ also μ_u depends only on the three-body parameter given by the cutoff scale, $\mu_u \sim \Lambda^2$.

From the work of Efimov [2], and as we seen in section 5.1, one expects a whole tower of infinitely many Efimov trimer states close to the resonance. In the following we will calculate this excitation spectrum. In order to do so, we make the following observation. First consider the inverse propagators of the atoms, dimers and trimer after analytical continuation, $\tau = it$, to real frequencies

$$\begin{aligned} P_\psi &= -\omega_\psi + \mathbf{p}^2 - \mu, \\ P_\phi/A_\phi &= -\omega_\phi + \frac{\mathbf{p}^2}{2} - 2\mu + \nu_\phi(\mu + \omega_\phi/2 - \mathbf{p}^2/4), \\ P_\chi/A_\chi &= -\omega_\chi + \frac{\mathbf{p}^2}{3} - 3\mu + \nu_\chi(\mu + \omega_\chi/3 - \mathbf{p}^2/9). \end{aligned} \tag{63}$$

We note that ν_ϕ and ν_χ can dependent only on the particular combinations of μ, ω, and $\mathbf{p}^2$ indicated above. This is a consequence of an additional symmetry of the real-time microscopic action $S = \Gamma_\Lambda$ under the time-dependent U(1) transformation $\psi \to e^{iEt}\psi$, $\phi \to e^{i2Et}\phi$, and $\chi \to e^{i3Et}\chi$ if we also simultaneously change the chemical potential $\mu \to \mu + E$. In vacuum we do not expect any anomalies, such that also the quantum effective action $\Gamma = \Gamma_{k=0}$ possesses this symmetry. As consequence any dependence on μ is accompanied by a corresponding frequency dependence and vice versa. This allows only the particular combinations $\omega_\psi + \mu$, $\omega_\phi + 2\mu$, and $\omega_\chi + 3\mu$ to appear. The additional relation between frequency and momenta is a consequence of Galilean invariance.

The dispersion relations are obtained from the poles of the propagators, that is from solving $P_\phi(\omega_\phi = \mathcal{E}_\phi) = 0$ and analogous for the atoms and the trion. The dimer dispersion for example reads

$$\mathcal{E}_\phi(\mathbf{p}^2) = \frac{\mathbf{p}^2}{2} - 2\mu + \nu_\phi(\mathcal{E}_\phi/2 + \mu - \mathbf{p}^2/4) = \frac{\mathbf{p}^2}{2} + \frac{m_\phi}{A_\phi}. \tag{64}$$

To obtain the dimer and trimer energy levels E_ϕ and E_χ we have to substract two or three times the atom energy $E_\psi = -\mu$ from the dispersion relation at rest such that

$$\begin{aligned} E_\phi &= \mathcal{E}_\phi(\mathbf{p}^2 = 0) + 2\mu = \nu_\phi(\omega_\phi = \mathcal{E}_\phi, \mathbf{p}^2 = 0, \mu), \\ E_\chi &= \mathcal{E}_\chi(\mathbf{p}^2 = 0) + 3\mu = \nu_\chi(\omega_\chi = \mathcal{E}_\chi, \mathbf{p}^2 = 0, \mu). \end{aligned} \tag{65}$$

Here μ is the effective chemical potential which accounts for an shift in the atom energy using the time-dependent U(1) symmetry. The ground and excited states are obtained by the condition that the particular particles are gapless in the IR which corresponds to a gapless dispersion, i. e. for example $\mathcal{E}_\phi(\mathbf{p}^2 = 0) = 0$. This means that the corresponding gap parameter has to vanish in the infrared, i. e. $\mu = 0$, or $m_\phi^2 = 0$, or

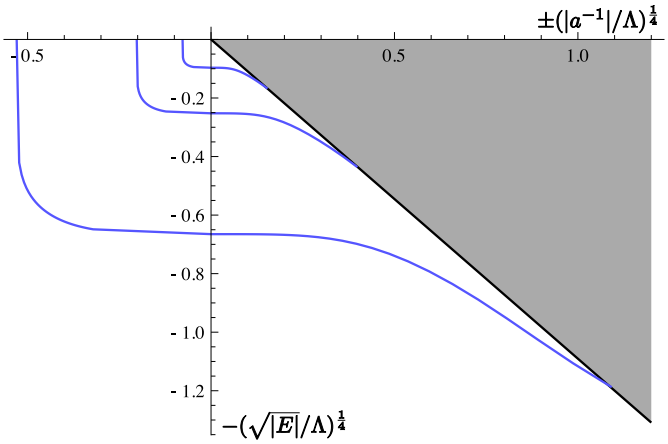

Fig. 10 The Efimov spectrum for SU(3) fermions. We plot the lowest three Efimov trimer levels E_χ (blue). The dimer binding energy is shown as black curve. To improve the visibility of the energy levels, we rescale both the dimensionless inverse scattering length a^{-1}/Λ and the dimensionless energy E/Λ^2. We have chosen the UV cutoff $\Lambda = a_0$ and the Yukawa coupling $h^2\Lambda = 100$ as appropriate for ^{6}Li atoms in the $m_F = 1/2$, $m_F = -1/2$ channel close to the Feshbach resonance at $B_0 \sim 810\,\mathrm{G}$.

$m_\chi^2 = 0$. In practice, we extract the bound state energy levels $E_\phi = 2\mu$, $E_\chi = 3\mu$ by calculating the gaps m_ϕ^2 and m_χ^2 for $k = 0$ such that they vanish for a specific choice of $E_\psi = -\mu$.

As it turns out for the trimer there is not only the ground state solution which we discussed before but a whole infinite set of possible solutions corresponding to the infinite tower of universal Efimov trimer states. The numerical result for the dimer energy level E_ϕ and the lowest three Efimov trimer levels E_χ as function of a^{-1} measured in units of Λ is shown in Fig. 10. In this figure we used a convenient rescaling to make the excited Efimov states visible. We have identified the UV cutoff Λ with the inverse Bohr radius, $\Lambda = a_0^{-1}$, and have additionally chosen $h^2 = 100\Lambda$. This choice corresponds to the width of the Feshbach resonance of ^{6}Li atoms in the $m_F = 1/2$, $m_F = -1/2$ channel relevant for experiments [29].

5.2.3 Limit cycle scaling at the unitarity point

Already in section 3 we have discussed the especially interesting unitarity point in the spectrum where the scattering length diverges and the atom energy is at the threshold, $a^{-1} = E_\psi = -\mu = 0$. It is instructive to consider this limit also within the derivative expansion as it allows us to obtain analytical results. At the unitarity point all length scales drop out of the problem and one obtains a simple scaling solution for the flow equations. In this limit the flow equations for the three-body sector simplify and read

$$\begin{aligned}\partial_t m_\chi^2 &= \frac{36}{25} g^2 \frac{k^2}{h^2} \\ \partial_t g^2 &= -\frac{64}{25} g^2 - \frac{13}{25} m_\chi^2 \frac{h^2}{k^2}.\end{aligned} \tag{66}$$

where we used $A_\phi(k) = h^2/(6\pi^2 k)$ and $m_\phi^2 = A_\phi k^2$ for $k \to 0$. Using $g(\Lambda) = 0$ as initial coupling we find the oscillatory, analytical solution

$$\begin{aligned}m_\chi^2(k) &= \left(\frac{k}{\Lambda}\right)^{-\frac{7}{25}} m_\chi^2(\Lambda)\Big[\cos\left(s_0 \ln\frac{k}{\Lambda}\right) + \frac{7}{\sqrt{419}}\sin\left(s_0 \ln\frac{k}{\Lambda}\right)\Big], \\ g^2(k) &= -\frac{13\,h^2}{\sqrt{419}\,k^2}\left(\frac{k}{\Lambda}\right)^{-\frac{7}{25}} m_\chi^2(\Lambda)\sin\left(s_0 \ln\frac{k}{\Lambda}\right),\end{aligned} \tag{67}$$

with $s_0 = \sqrt{419}/25 \approx 0.82$.[5] From this solution we see that $m_\chi^2(\Lambda)$ drops out of the ratio g^2/m_χ^2 which determines the atom-dimer interaction $\lambda_{3a} \sim g^2/m_\chi^2$. The flow of m_χ^2 and g^2 describes a closed limit cycle

[5] Using the analogous derivative expansion for bosons, where there exists only a single term describing the atom-dimer interaction $\sim \phi^*\psi^*\phi\psi$, one finds $s_0 \approx 0.93$ [30].

with the frequency given by s_0. Considering the simplicity of our approximation this is in reasonable agreement with the 'exact' result, $s_0 \approx 1.00624$. The limit cycle goes on 'forever' only exactly at the unitarity point and at the threshold energy $\mu = 0$. A finite a^{-1} as well as a finite atom energy $E_\psi = -\mu$ act as infrared cutoffs, which stop the limit cycle flow once $k \approx |\mu|$ or $k \approx 3\pi|a^{-1}|/4$, respectively.

5.3 Many-body physics

The simple truncation of the exact functional renormalization group equation in terms of a derivative expansion yields a detailed picture of the spectrum of bound states and scattering in the system with three species of fermions with SU(3) symmetry. Depending on the scattering length a, the lowest energy state may be a fundamental fermion (atom) or a bosonic molecule (dimer) or a composite fermion formed from three atoms (trion). Trions are stable (lowest energy state) in the interval $(a_{c1}^{(1)})^{-1} < a^{-1} < (a_{c2}^{(1)})^{-1}$.

We have so far only considered the flow equations in vacuum, but we can already infer some interesting features of what happens at non-zero density for the many-body ground state at $T = 0$. The qualitative properties for small density follow from our computations and simple arguments of continuity. Importantly, we find that a novel "trion phase" separates the BEC phase and the BCS phase [27].

For nonvanishing density, the chemical potential μ increases above its vacuum value μ_0. At $T = 0$ for $a^{-1} > (a_{c2})^{-1}$ the BEC phase occurs for small density. Due to the symmetries of the microscopic action, the effective potential $U(\rho)$ for the bosonic field depends only on the SU(3) × U(1) invariant combination $\rho = A_\phi \phi^\dagger \phi = A_\phi(\phi_1^* \phi_1 + \phi_2^* \phi_2 + \phi_3^* \phi_3)$. It reads for small $\mu - \mu_0$

$$U(\rho) = \frac{\lambda_\phi}{2}\rho^2 - 2(\mu - \mu_0)\rho, \tag{68}$$

where we use the fact that the term linear in ρ vanishes for $\mu = \mu_0$, i.e. $m_\phi^2(\mu_0) = 0$. The minimum of the potential shows a non-zero condensate

$$\rho_0 = \frac{2(\mu - \mu_0)}{\lambda_\phi}, \qquad U(\rho_0) = -\frac{2}{\lambda_\phi}(\mu - \mu_0)^2, \tag{69}$$

with density

$$n = -\frac{\partial U(\rho_0)}{\partial \mu} = \frac{4}{\lambda_\phi}(\mu - \mu_0). \tag{70}$$

For the BCS phase for $a < a_{c1} < 0$, one has $\mu_0 = 0$. Non-zero density corresponds to positive μ, and in this region the renormalization flow drives m_ϕ^2 always to zero at some finite k_c, with BCS spontaneous symmetry breaking ($\rho_0 > 0$) induced by the flow for $k < k_c$. Both the BEC and BCS phases are therefore characterized by superfluidity with a non-zero $\rho_0 = A_\phi \phi^\dagger \phi$.

As an additional feature compared to the BCS-BEC crossover for a Fermi gas with two components, the expectation value for the bosonic field ϕ in the three component case also breaks the "spin" SU(3) symmetry. Due to the analogy with QCD this is called "Color Superfluidity" [31], see also [32]. For any particular direction of the expection value of ϕ a continuous symmetry SU(2) × U(1) remains. According to the symmetry breaking SU(3) × U(1) → SU(2) × U(1), the effective potential has five flat directions.

For two component fermions the BEC and BCS phases are not separated, since in the vacuum either $\mu_0 = 0$ or $m_\phi^2 = 0$. There is no phase transition, but rather a continuous crossover. For three component fermions, however, we find a new trion phase for $(a_{c1}^{(1)})^{-1} < a^{-1} < (a_{c2}^{(1)})^{-1}$. In this region the vacuum has $\mu_0 < 0$ and $m_\phi^2 > 0$. The atom fluctuations are cut off by the negative chemical potential and do not drive m_ϕ^2 to zero, such that for small density m_ϕ^2 remains positive. Adding a term $m_\phi^2 \rho$ to the effective potential (68) we see that the minimum remains at $\rho_0 = 0$ as long as $m_\phi^2 > 2(\mu - \mu_0)$. No condensate of dimers occurs in the trion phase. The BEC and BCS phases, that show both extended superfluidity through a spontaneous breaking of the SU(3) × U(1) symmetry, are now separated by a phase where $\rho_0 = 0$, such that the SU(3) × U(1) symmetry remains unbroken (or as we argue below will be only partially broken).

Deep in the trion phase, e.g. for very small $|a^{-1}|$, the atoms and dimers can be neglected at low density since they both have a gap. The thermodynamics at low density and temperature is determined by a single species of fermions, the trions. In our approximation it is simply given by a non-interacting Fermi gas,

with fermion mass $3M$ and chemical potential $3(\mu - \mu_0)$. Beyond our approximation, we expect that trion interactions are induced by fluctuations. While local trion interactions $\sim (\chi^*\chi)^2$ are forbidden by Fermi statistics, momentum dependent interactions are allowed. These may, however, be "irrelevant interactions" at low density, since also the relevant momenta are small such that momentum dependent interactions will be suppressed. Even if attractive interactions would induce a trion-trion condensate, this has atom number six and would therefore leave a Z_6 subgroup of the U(1) transformations unbroken, in contrast to the BEC and BCS phase where only Z_2 remains. Furthermore, the trions are SU(3)-singlets such that the SU(3) symmetry remains unbroken in the trion phase. The different symmetry properties between the possible condensates guarantee true quantum phase transitions in the vicinity of a_{c1} and a_{c2} for small density and at $T = 0$. We expect that this phase transition also extends to small non-zero temperature.

While deep in the trion phase the only relevant scales are given by the density and temperature, and possibly the trion interaction, the situation gets more complex close to quantum phase transition points. For $a \approx a_{c1}$ we have to deal with a system of trions and atoms, while for $a \approx a_{c2}$ a system of trions and dimers becomes relevant. The physics of these phase transitions is not clear now, it might be complex and interesting.

6 Three-component fermions without SU(3) symmetry

Quite recently three-component Fermi gases have been realized with ultracold atoms [5,6]. In these experiments ^{6}Li atoms are prepared in three hyperfine states. Using external magnetic fields the scattering length of the different pair of atoms $(1,2)$, $(1,3)$, and $(2,3)$ can be tuned due to the presence of three Feshbach resonances. In the SU(3) invariant system discussed before all pairs of atoms had equal scattering lengths. This is not valid in the case of ^{6}Li atoms as can be seen from the scattering lengths profiles shown in Fig. 11. Although the Feshbach resonances are close to each other, they are still at different magnetic fields and also the profiles of the scattering lengths differ for the different pairs of atoms. In order to compare our calculations with the experimental observations we have therefore to extend the model discussed in section 5.

The experiments by Ottenstein *et al.* [5] and Huckans *et al.* [6] concentrated on the magnetic field region between $B = 100\,\mathrm{G}$ and $B = 550\,\mathrm{G}$ where all scattering lengths are rather large and negative. The main observation was a distinct feature in the atom loss rate which could be attributed to a three-body process and shows up in the three-body coefficient K_3 which is defined by the loss rate:

$$\frac{dn_i}{dt} = K_3 n_i^3, \tag{71}$$

where n_i denotes the density of the various atom species. The measured data points from [5] are shown in Fig. 13 (right) together with our numerical results which will be derived below.

Already from the work of Efimov [2] it is known that trimer bound states should persist in systems were the pairwise scattering lengths of the three involved particles differ from each other as long as at least to of them are large in magnitude. This is the case in the regime investigated by the experiments and in the following we will show how the observed loss features can be explained by Efimov physics using functional renormalization [33]. Similar predictions have been made using different methods by Braaten *et al.* [34] and Naidon und Ueda [35].

6.1 Derivative expansion

First consider the model which we will use to describe the system. We generalize the truncation given by Eq. (50) presented in section 5. The average action then reads

$$\begin{aligned}\Gamma_k = \int_x \Big\{ &\sum_{i=1}^{3} \psi_i^*(\partial_\tau - \nabla^2 - \mu)\psi_i + \sum_{i=1}^{3} \phi_i^* \left[A_{\phi i}\left(\partial_\tau - \boldsymbol{\nabla}^2/2\right) + m_{\phi i}^2\right]\phi_i + \chi^* \left[A_\chi\left(\partial_\tau - \boldsymbol{\nabla}^2/3\right) + m_\chi^2\right]\chi \\ &+ \sum_{i,j,k=1}^{3} \frac{h_i}{2}\epsilon_{ijk}\left(\phi_i^*\psi_j\psi_k - \phi_i\psi_j^*\psi_k^*\right) + \sum_{i=1}^{3} g_i\left(\phi_i^*\psi_i^*\chi - \phi_i\psi_i\chi^*\right)\Big\},\end{aligned} \tag{72}$$

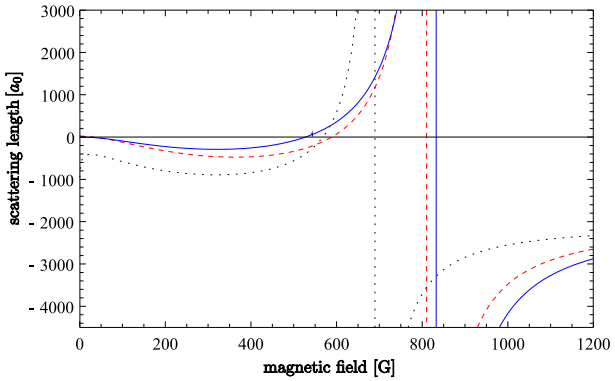

Fig. 11 Two-body scattering lengths a_{12} (solid), a_{23} (dashed), and a_{13} (dotted) in dependence of the magnetic field B of ^{6}Li atoms in the lowest three hyperfine states. These curves were calculated by P. S. Julienne [29] and are taken from Ref. [5].

The generalization consists in allowing for three different inverse boson propagators determined by the six couplings $A_{\phi i}$ and $m^2_{\phi i}$, $i = 1, 2, 3$, and the three independent Yukawa couplings h_i. This enables us to describe the distinct scattering properties of the three channels. Furthermore we allow for three couplings g_i which couple a dimer and a fermion to the trimer bound state χ. As in section 5, the trimer field χ mediates the effective interaction between dimers and atoms $\lambda^{(3)}_{ij}$ such that for vanishing center of mass momentum one has

$$\lambda^{(3)}_{ij} = -\frac{g_i g_j}{m^2_\chi}. \tag{73}$$

By permitting three independent couplings g_i we are able to account for different strength of the atom-dimer interaction. Note, however, that we neglect the atom-dimer scattering channel denoted by λ_{3b} in Eq. (49). We again expect its effect to be subdominant.

6.2 Flow equations and initial conditions

The flow equations of the two-body sector are the straightforward generalization of Eqns. (51) and (52) with the replacements $m^2_\phi \to m^2_{\phi i}$, $A_\phi \to A_{\phi i}$, and $h \to h_i$. Since the Yukawa couplings h_i are not renormalized the flow equations can be immediately integrated. As in section 5, the microscopic values of the gap terms $m^2_{\phi i}$ and the h_i are chosen to reproduce the experimentally measured scattering lengths a_{12}, a_{23}, a_{13} in the infrared. Due to our ignorance of the microscopic details (e. g. effective range) leading to the specific scattering profiles in the regime between $B = 100\,\mathrm{G}$ and $B = 550\,\mathrm{G}$ (see Fig. 11), we choose here large and equal values of $h = h_1 = h_2 = h_3$. This corresponds to contact interactions at the UV scale. However, we use the dependence on the specific choice of h to estimate the error within our truncation. We emphasize that in this problem the bosonic fields ϕ_i are not associated with the Feshbach molecules of the nearby resonance. They should rather be seen as true auxiliary Hubbard-Stratonovich fields representing the T-matrix of the atom-atom scattering.

The flow equations of the three-body sector read for the gap term,

$$\partial_t m^2_\chi = \sum_{i=1}^{3} \frac{2 g_i^2 k^5}{\pi^2 A_{\phi i}(3k^2 - 2\mu + 2m^2_{\phi i}/A_{\phi i})^2} \tag{74}$$

and for the Yukawa-like coupling g_1 one finds

$$\partial_t g_1 = -\frac{g_2 h_2 h_1 k^5 \left(6k^2 - 5\mu + \frac{2m^2_{\phi 2}}{A_{\phi 2}}\right)}{3\pi^2 A_{\phi 2}(k^2-\mu)^2 \left(3k^2 - 2\mu + \frac{2m^2_{\phi 2}}{A_{\phi 2}}\right)^2} - \frac{g_3 h_3 h_1 k^5 \left(6k^2 - 5\mu + \frac{2m^2_{\phi 3}}{A_{\phi 3}}\right)}{3\pi^2 A_{\phi 3}(k^2-\mu)^2 \left(3k^2 - 2\mu + \frac{2m^2_{\phi 3}}{A_{\phi 3}}\right)^2}. \tag{75}$$

The flow equations for g_2 and g_3 can be derived from Eq. (75) by permuting the corresponding indices. There is an additional contribution to the flow of g_i arising from the box diagram which regenerates the

atom-dimer interaction during the RG flow. As explained in the previous section it can be computed using a k-dependent Hubbard-Stratonovich transformation and the flows of the g_i receive the additional contribution

$$m_\chi^2\left(-\frac{\partial_t\lambda_{ij}^{(3)}}{2g_j}-\frac{\partial_t\lambda_{il}^{(3)}}{2g_l}+\frac{g_i\partial_t\lambda_{jl}^{(3)}}{2g_jg_l}\right). \tag{76}$$

Here we define $(i,j,l)=(1,2,3)$ and permutations thereof and find

$$\partial_t\lambda_{ij}^{(3)}=\frac{k^5h_1h_2h_3h_l(9k^2-7\mu+\frac{4m_{\phi l}^2}{A_{\phi l}})}{6\pi^2A_{\phi l}(k^2-\mu)^3(3k^2-2\mu+\frac{2m_{\phi l}^2}{A_{\phi l}})^2}. \tag{77}$$

Although this contribution is essential to obtain the full tower of Efimov states at the resonance it plays only a subdominant role for the properties of the lowest Efimov state. For simplicity we will therefore neglect this term in the computation of the loss coefficient K_3.

In the broad resonance limit, $h_i\to\infty$, Efimov physics is universal in the sense that it is only dependent on the given scattering lengths a_{ij} and an additional three-body parameter [1]. In section 5 we found that this parameter may be given by the cutoff scale Λ. Here, we however use the ratio of the couplings g_i and m_χ^2 at fixed UV scale Λ as the three-body parameter, which is equivalent to using Λ as the parameter itself. Also we choose $g=g_1=g_2=g_3$ at UV scale such that our three-body parameter is given by $\lambda^{(3)}\equiv-g^2(\Lambda)/m_\chi^2(\Lambda)$. Note, however, that the couplings g_i evolve differently during the flow towards the IR.

6.3 Numerical results and comparison with experiment

We solve the flow equations (74) and (75) numerically. We note at this point that the zero-range limit is valid if the magnitude of the scattering length is much larger than the range of interaction given typically by the van der Waals length l_{vdW}, which for ^{6}Li is $l_{vdW}\approx 62.5\,a_0$. Although the loss resonances appear for $|a_{ij}|\gtrsim 2l_{vdW}$ such that the zero-range approximation might be questionable, we will assume its validity. We will, however, estimate the error by using various values for the Yukawa coupling h, which is related to the effective range, as we have seen in section 5.

The trimer energy level can be calculated in the same way as in the case of SU(3) symmetric fermions by determining the chemical potential μ such that $m_\chi^2=0$ for $k=0$. We find $m_\chi^2=0$ for large enough values of a_{ij} which indicates the presence of a trimer bound state. Now, the experimental observations offer a way to determine the three-body parameter inherent to Efimov physics: We simply adjust the initial value of $\lambda^{(3)}$ such that the Efimov trimer becomes degenerate with the atom threshold exactly at the position of the observed loss feature at $B=125\,\mathrm{G}$. This fixes the three-body parameter $\lambda^{(3)}$ to the physical value and we assume that it is constant for all other investigated magnetic field strengths B.

Having determined the three-body parameter we are able to calculate the energy level of the trimer bound state as a first prediction. We find the existence of the trimer in the magnetic field range from $B=125\,\mathrm{G}$ to $B=498\,\mathrm{G}$. The binding energy E_T is shown in Fig. 12 as solid line when choosing $h^2=100\,a_0^{-1}$ as appropriate for ^{6}Li in the $(1,2)$ channel. The shaded region is an error estimate obtained by choosing values $h^2\in(20\,a_0^{-1},300\,a_0^{-1})$. If we include the contribution due to the k-dependence of the Hubbard-Stratonovich transformation given in Eq. (76) we find a reduction of the trimer binding energy. The result is shown as dashed curve.

As a second prediction we determine the loss coefficient K_3 measured in experiments [5,6]. Within our model the observed three-body loss can be explained as follows below, an illustration is shown in Fig. 13 (left). So far we have shown the existence of the Efimov state in the regime of interest. This trimer state may the formed in a collision of three atoms. However, one must keep in mind that ^{6}Li atoms have a complicated substructure with various bound states so that the composite trimer can become unstable. We account for this decay to not further specified degrees of freedom by a phenomenological decay width Γ_χ. For example, the decay might involve the molecular dimer states associated with the nearby Feshbach resonance. The trimer formation from three atoms proceeds via the exchange of the effective bosons ϕ_i.

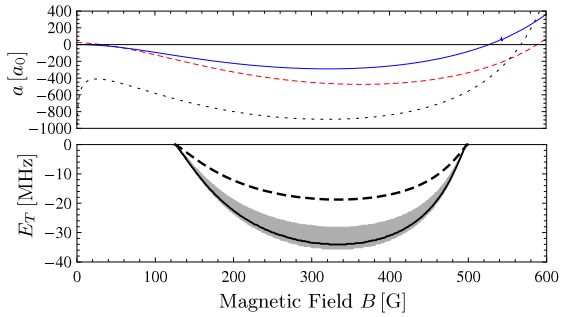

Fig. 12 *Upper panel:* Scattering length a_{12} (solid), a_{23} (dashed) and a_{31} (dotted) as a function of the magnetic field B for ^{6}Li. *Lower panel:* Binding energy E_T of the three-body bound state $\chi \widehat{=} \psi_1\psi_2\psi_3$. The solid line corresponds to the initial value $h^2 = 100\,a_0^{-1}$. The shaded region gives an error estimate by using values of h in the range $h^2 = 20\,a_0^{-1}$ (upper border) to $h^2 = 300\,a_0^{-1}$ (lower border). The dashed line shows the reduction of the trimer energy when the refermionization of the atom-boson interaction is taken into account.

Evaluating the matrix elements corresponding to the diagram shown in Fig. 13 (left) we can estimate the loss coefficient K_3 to be proportional to

$$p = \left| \sum_{i=1}^{3} \frac{h_i g_i}{m_{\phi i}^2} \frac{1}{\left(m_\chi^2 - i\frac{\Gamma_\chi}{2}\right)} \right|^2 . \tag{78}$$

The amplitude for forming a trimer out of three atoms is given by $\sum_{i=1}^{3} h_i g_i / m_{\phi i}^2$. The amplitude for the evolution from the initial state of three atoms to the unknown decay products further involves the inverse trimer propagator which in the real-time formalism reads

$$G_\chi^{-1} = \omega - \frac{\mathbf{p}^2}{3} - m_\chi^2 + i\frac{\Gamma_\chi}{2}. \tag{79}$$

We evaluate it in the limit of small momenta $\mathbf{p}^2 = (\sum_i \mathbf{p}_i)^2 \to 0$, and small on-shell atom energies $\omega_i = \mathbf{p}_i^2$, $\omega = \sum_i \omega_i \to 0$. That the incoming atoms in the recombination process are at the atom threshold also implies that we have an effective chemical potential $\mu = 0$. The trimer gap m_χ^2 is then negative for $B = 125 \ldots 498$ G. A further ingredient of the calculation of the matrix elements in Eq. (78) is the decay width Γ_χ which we first assume to be independent of the magnetic field B. Furthermore the evaluation of K_3 via Fermi's Golden rule involves unknown vertices and phase-space factors for the trimer decay such that our compuation contains an unknown multiplicative factor c_K. In terms of p in Eq. (78) we obtain

$$K_3 = c_K\, p. \tag{80}$$

The resulting curve is shown in Fig. 13 (right) and agrees reasonably well with the experimentally measured data points. To sum up, our estimation of K_3 involved three parameters: The location of the first loss resonance at $B_0 = 125$ G fixes the three-body parameter. The overall amplitude of K_3 at the first resonance is adjusted by c_K and the unkown decay width Γ_χ is tuned to the width of the first resonance yielding a trimer lifetime of ≈ 10 ns. The extension of the curve away from the first resonance then involves no further parameter.

Our calculation predicts a second sharp resonance feature at $B = 498$ G where the trimer becomes again degenerate with the atom threshold. The assumption of a constant Γ_χ fixes the width of this peak. The measured feature is however much broader. This may have a simple explanation: It is plausible to assume that the trimer decays into the molecular dimer states associated with the nearby Feshbach resonances and a free atom. Approaching the Feshbach resonances the molecular state becomes closer to the trimer energy level. Therefore it is reasonable to assume that the matrix element for the decay from the trimer to the dimers becomes larger. This in turn implies a shortening of the lifetime of the trimer as the magnetic field B is increased. We have tested this assumption and indeed found a significant broadening or even disappearance of the second resonance peak. Recently, there had been phenomenological studies of this reasoning in [36].

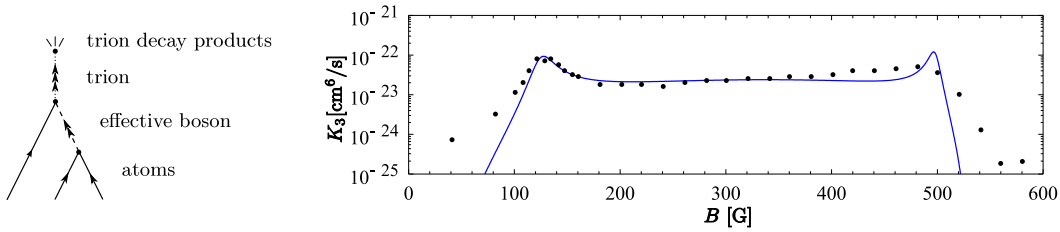

Fig. 13 *left:* Three-body loss involving the Efimov trimer. *right:* Loss coefficient K_3 in dependence on the magnetic field B as measured in [5] (dots). The solid line is the fit of our model to the experimental curve. We use here a decay width Γ_χ that is independent of the magnetic field B.

By now, the system of three-component ^{6}Li atoms is quite well understood also away from the magnetic field range discussed above. This includes theoretical predictions [37,38] as well as experimental measurements [39,40] which also finally led to the first direct association of a Efimov trimer in ultracold atoms by Lompe *et al.* [41].

7 Conclusions

During recent years non-relativistic few-body physics has experienced a revived interest and undergone considerable progress. A wealth of experiments with ultracold atomic gases together with a significant theoretical effort initiated the (re)birth of an exciting field known as Efimov physics. In this paper we reviewed the studies of various aspects related to the Efimov effect using the method of functional renormalization.

By constructing solutions to exact functional renormalization group flow equations, we have obtained a rather detailed picture of non-relativistic few-body problems related to the Efimov effect. We considered identical bosons and fermions with two or three spin components, the latter both for the case of a common Feshbach resonance with a global SU(3) symmetry and for the case of ^{6}Li where this symmetry is broken.

Solving the flow equations in terms of a vertex expansion leads to (numerically) exact solutions. A remarkable hierarchy in the structure of the flow equations allows to construct the parts of the quantum effective action relevant for the one-, two- or three-body problem without further approximations. Beyond the present context it becomes apparent how the quantum mechanical formalism is embedded in non-perturbative quantum field theory.

Besides the vertex expansion we also established the derivative expansion as a way to find approximate solutions. In connection with a k-dependent Hubbard-Stratonovich transformation this allows for a simple and very efficient parameterization of the essential physics. No equivalent approximation scheme is known to us for the quantum mechanical formalism. As we have demonstrated this scheme is particularly valuable in more complex situations where a full solution in the vertex expansion becomes too involved. An example for this was given by the calculation of the three-body loss rate in a system of ultracold ^{6}Li atoms which shows how our theoretical investigations can be directly tested in experiments.

Both in the vertex expansion and in the derivative expansion the Efimov effect shows up as a limit cycle in the solution of the flow equations at the point where the scattering length diverges. This mechanism is very interesting from a theoretical perspective. Realistic models in relativistic quantum field theory that show a similar behavior have not been found so far. Also the universality of the non-relativistic few-body physics is very interesting from a theoretical point of view. While in a renormalization group description universality is usually associated with the presence of fixed points, the Efimov effect with its limit cycle scaling and the connected discrete scaling symmetry goes beyond this standard paradigm. This generalized notion of few-body universality is expected to extend beyond the physics of three particles. First studies of four-body universality using functional renormalization have been undertaken [30].

In conclusion, we believe that the functional renormalization group is a powerful and suitable method for investigation of non-relativistic few-body physics and of the Efimov effect in particular. It allows to address few-body problems from an unconventional perspective and provides an interesting alternative to the standard quantum mechanical and effective field theory treatments. Importantly, the method is not only limited to few-body problems but also is widely used for studying many-body physics. In this way

functional renormalization provides a unified framework for studying an interplay between few-particle and many-particle phenomena.

Acknowledgements We thank M. Birse, E. Braaten, S. Diehl, H. Gies, H.-W. Hammer, H. C. Krahl, J. M. Pawlowski, M. M. Scherer, C. Wetterich, and W. Zwerger for useful discussion and collaboration. We also acknowledge S. Jochim and the members of his group for interesting discussions and providing us with their experimental data. The work of S.F. has been supported by the DFG research group FOR 723 and the Helmholtz Alliance HA216/EMMI. S.M. is thankful to the Klaus Tschira foundation and the DFG research group FOR 723 for support. R. S. thanks the DFG for support within the FOR 801 'Strong correlations in multiflavor ultracold quantum gases'.

References

1. E. Braaten and H. W. Hammer: Universality in few-body systems with large scattering length, Phys. Rep. **428**, 259, (2006).
2. V. Efimov: Energy levels arising from resonant two-body forces in a three-body system, Phys. Lett. **33B**, 563 (1970); V. Efimov: Energy levels of three resonantly-interacting particles, Nucl. Phys. A **210**, 157 (1973).
3. P. F. Bedaque, H. W. Hammer and U. van Kolck, Renormalization of the three-body system with short-range interactions, Phys. Rev. Lett. **82**, 463 (1999).
4. F. Ferlaino, R. Grimm: Forty years of Efimov physics: How a bizarre prediction turned into a hot topic, Physics **3**, 9 (2010).
5. T. B. Ottenstein, T. Lompe, M. Kohnen, A. N. Wenz, and S. Jochim: Collisional Stability of a Three-Component Degenerate Fermi Gas, Phys. Rev. Lett. **101**, 203202 (2008).
6. J. H. Huckans, J. R. Williams, E. L. Hazlett, R. W. Stites, and K. M. O'Hara: Three-Body Recombination in a Three-State Fermi Gas with Widely Tunable Interactions, Phys. Rev. Lett. **102**, 165302 (2009).
7. J. Berges, N. Tetradis and C. Wetterich: Non-perturbative renormalization flow in quantum field theory and statistical physics, Phys. Rept. **363** (2002) 223; T. R. Morris: Elements of the Continuous Renormalization Group, Prog. Theor. Phys. Suppl. **131** (1998) 395; K. Aoki: Introduction to the Non-Perturbative Renormalization Group and its Recent Applications, Int. J. Mod. Phys. B **14** (2000) 1249; C. Bagnuls and C. Bervillier: Exact renormalization group equations: an introductory review, Phys. Rept. **348** (2001) 91; J. Polonyi: Lectures on the functional renormalization group method, Central Eur. J. Phys. **1** (2003) 1; M. Salmhofer and C. Honerkamp: Fermionic renormalization group flows - Technique and Theory, Prog. Theor. Phys. **105** (2001) 1; B. Delamotte: An Introduction to the Nonperturbative Renormalization Group, cond-mat/0702365; B. J. Schaefer and J. Wambach: Renormalization Group Approach towards the QCD Phase Diagram, Phys. Part. Nucl.**39** (2008), 1025; J. M. Pawlowski: Aspects of the Functional Renormalisation Group, Annals Phys. **322** (2007), 2831; O. J. Rosten: Fundamentals of the Exact Renormalization Group, arXiv:1003.1366.
8. C. Wetterich: Exact evolution equation for the effective potential, Phys. Lett. B **301** (1993) 90.
9. S. Diehl and C. Wetterich: Functional integral for ultracold fermionic atoms, Nucl. Phys. B **770**, 206 (2007); Universality in phase transitions for ultracold fermionic atoms, Phys. Rev. A **73** (2006) 033615; S. Diehl: Universality in the BCS - BEC Crossover in Cold Fermion Gases, cond-mat/0701157.
10. S. Diehl, H. C. Krahl, M. Scherer: Three-body scattering from nonperturbative flow equations, Phys. Rev. C **78**, 034001 (2008).
11. S. Moroz, S. Floerchinger, R. Schmidt and C. Wetterich: Efimov effect from functional renormalization, Phys. Rev. A **79**, 042705 (2009).
12. S. Diehl, S. Floerchinger, H. Gies, J. M. Pawlowski and C. Wetterich: Functional renormalization group approach to the BCS-BEC crossover, Ann. Phys. (Berlin) **522**, 615 (2010).
13. S. Floerchinger, *Functional renormalization and ultracold quantum gases*, Doctoral thesis, Universität Heidelberg, 2009.
14. H. Gies, C. Wetterich, Renormalization flow of bound states, Phys. Rev. D **65**, 065001 (2002); Renormalization flow from UV to IR degrees of freedom, Acta Phys. Slov. **52**, 215 (2002).
15. S. Floerchinger and C. Wetterich: Exact flow equation for composite operators, Phys. Lett. B **680**, 371 (2009).
16. S. Floerchinger: Exact flow equation for bound states, Eur. Phys. J. C **69**, 119 (2010).
17. M. C. Birse: Functional renormalization group for two-body scattering, Phys. Rev. C **77**, 047001 (2008).
18. G. V. Skorniakov, K. A. Ter-Martirosian: Three body problem for short range forces 1. Scattering of low energy neutrons by deuterons, Zh. Eksp. Teor. Phys. **31**, 775 (1956), [Sov. Phys. JETP **4**, 648 (1957)].
19. I. Bloch, J. Dalibard, and W. Zwerger: Many-body physics with ultracold gases, Rev. Mod. Phys. **80**, 885 (2008).
20. S. Giorgini, L. P. Pitaevskii, and S. Stringari: Theory of ultracold atomic Fermi gases, Rev. Mod. Phys. **80**, 1215 (2008).
21. M. C. Birse, B. Krippa, J. A. McGovern, and N. R. Walet: Pairing in many-fermion systems: an exact renormalisation group treatment, Phys. Lett. B **605**, 287 (2005); S. Diehl, H. Gies, J. M. Pawlowski, and C. Wetterich: Flow equations for the BCS-BEC crossover, Phys. Rev. A **76**, 021602(R) (2007); Renormalization flow and universality for ultracold fermionic atoms, Phys. Rev. A 76, 053627 (2007); S. Floerchinger, M. Scherer, S. Diehl, and C. Wetterich: Particle-hole fluctuations in BCS-BEC crossover, Phys. Rev. B **78**, 174528 (2008); L. Bartosch, P. Kopietz, and A. Ferraz: Renormalization of the BCS-BEC crossover by order-parameter fluctuations, Phys. Rev. B **80**, 104514 (2009).
22. S. Floerchinger, M. M. Scherer, and C. Wetterich: Modified Fermi sphere, pairing gap, and critical temperature for the BCS-BEC crossover, Phys. Rev. A **81**, 063619 (2010).
23. D. S. Petrov, C. Salomon, and G. V. Shlyapnikov: Weakly Bound Dimers of Fermionic Atoms, Phys. Rev. Lett. **93**, 090404 (2004).
24. B. Krippa, N. R. Walet, M. C. Birse: Renormalization group, dimer-dimer scattering, and three-body forces, Phys. Rev. A **81**, 043628 (2010).
25. M. C. Birse, B. Krippa, N. R. Walet: Convergence of a renormalization group approach to dimer-dimer scattering, arXiv:1011.5852.

26. M. M. Scherer, S. Floerchinger, and H. Gies: Functional renormalization for the BCS-BEC crossover, e-print arXiv:1010.2890.
27. S. Floerchinger, R. Schmidt, S. Moroz, and C. Wetterich: Functional renormalization for trion formation in ultracold fermion gases, Phys. Rev. A **79**, 013603 (2009).
28. S. J. J. M. F. Kokkelmans, J. N. Milstein, M. L. Chiofalo, R. Walser, and M. J. Holland: Resonance superfluidity: Renormalization of resonance scattering theory, Phys. Rev. A **65**, 053617 (2002).
29. M. Bartenstein, A. Altmeyer, S. Riedl, R. Geursen, S. Jochim, C. Chin, J. Hecker Denschlag, R. Grimm, A. Simoni, E. Tiesinga, C. J. Williams, and P. S. Julienne: Precise Determination of 6Li Cold Collision Parameters by Radio-Frequency Spectroscopy on Weakly Bound Molecules, Phys. Rev. Lett. **94**, 103201 (2005).
30. R. Schmidt, and S. Moroz: Renormalization-group study of the four-body problem, Phys. Rev. A **81**, 052709 (2010).
31. A. Rapp, G. Zarand, C. Honerkamp, and W. Hofstetter: Color Superfluidity and "Baryon" Formation in Ultracold Fermions, Phys. Rev. Lett. **98**, 160405 (2007); A. Rapp, W. Hofstetter, and G. Zarand: Trionic phase of ultracold fermions in an optical lattice: A variational study, Phys. Rev. B **77**, 144520 (2008).
32. F. Wilczek, Quantum chromodynamics: Lifestyles of the small and simple, Nature Phys. **3**, 375 (2007).
33. S. Floerchinger, R. Schmidt, and C. Wetterich: Three-body loss in lithium from functional renormalization, Phys. Rev. A **79**, 053633 (2009).
34. E. Braaten, H. W. Hammer, D. Kang and L. Platter: Three-Body Recombination of ^{6}Li Atoms with Large Negative Scattering Lengths, Phys. Rev. Lett. **103**, 073202 (2009).
35. P. Naidon and M. Ueda: Possible Efimov Trimer State in a Three-Hyperfine-Component Lithium-6 Mixture, Phys. Rev. Lett. **103**, 073203 (2009).
36. A. N. Wenz, T. Lompe, T. B. Ottenstein, F. Serwane, G. Zürn, and S. Jochim: Universal trimer in a three-component Fermi gas, Phys. Rev. A **80**, 040702 (R) (2009).
37. H. W. Hammer, D. Kang and L. Platter: Efimov physics in atom-dimer scattering of ^{6}Li atoms, Phys. Rev. A **82**, 022715 (2010).
38. P. Naidon and M. Ueda: The Efimov effect in lithium 6, *eprint:* arXiv:1008.2260v2 (2010).
39. J. R. Williams, E. L. Hazlett, J. H. Huckans, R. W. Stites, Y. Zhang, and K. M. O'Hara: Evidence for an Excited-State Efimov Trimer in a Three-Component Fermi Gas, Phys. Rev. Lett. **103**, 130404 (2009).
40. T. Lompe, T. B. Ottenstein, F. Serwane, K. Viering, A. N. Wenz, G. Zürn, and S. Jochim: Atom-Dimer Scattering in a Three-Component Fermi Gas, Phys. Rev. Lett. **105**, 103201 (2010).
41. T. Lompe, T. B. Ottenstein, F. Serwane, A. N. Wenz, G. Zürn, and S. Jochim: Radio-Frequency Association of Efimov Trimers, Science **330**, 940 (2010).

Excitation spectra and rf-response near the polaron-to-molecule transition from the functional renormalization group

Richard Schmidt and Tilman Enss
Physik Department, Technische Universität München, D-85747 Garching, Germany

A light impurity in a Fermi sea undergoes a transition from a polaron to a molecule for increasing interaction. We develop a new method to compute the spectral functions of the polaron and molecule in a unified framework based on the functional renormalization group with full self-energy feedback. We discuss the energy spectra and decay widths of the attractive and repulsive polaron branches as well as the molecular bound state, and confirm the scaling of the excited state decay rate near the transition. The quasi-particle weight of the polaron shifts from the attractive to the repulsive branch across the transition, while the molecular bound state has a very small residue characteristic for a composite particle. We propose an experimental procedure to measure the repulsive branch in a ^{6}Li Fermi gas using rf-spectroscopy and calculate the corresponding spectra.

PACS numbers: 11.10.Gh, 32.30.Bv, 32.70.Jz, 67.85.Lm

I. INTRODUCTION

A single impurity ↓-atom immersed in a background of ↑-fermions is a screened Fermi polaron [1] below a critical interaction strength. For larger interaction the ground state changes its character and the impurity forms a molecular bound state with the bath atoms. This qualitative change marks the polaron-to-molecule transition and was predicted by Prokof'ev and Svistunov [2]. The transition can be regarded as the modification of the two-body problem due to medium effects: For two non-relativistic particles with an interaction characterized by the s-wave scattering length a, a weakly bound molecule is the ground state for positive a, whereas for negative a the molecular state ceases to exist and the ground state is given by the free atoms.

Related impurity models have been studied for many years, in particular the Kondo effect for a fixed impurity with discrete energy levels immersed in a Fermi sea of conduction electrons [3]. A mobile but very heavy impurity loses its quasi-particle character in low dimensions $d = 1$, related to the orthogonality catastrophe [4]. The transition of the light mobile impurity poses a new and challenging many-body problem.

The polaron-to-molecule transition is observable with ultracold atoms where the scattering length can be tuned via Feshbach resonances [5]. Using radio-frequency (rf) spectroscopy the lineshape, ground-state energy, and polaron quasi-particle weight have been measured across the transition [6]. The ground-state properties near the transition have been calculated using variational wavefunctions [7–13], non-self-consistent T-matrix approximations [8], $1/N$ expansions [14], Wilsonian renormalization group [15], variational Monte Carlo [16] and diagrammatic Monte Carlo (diagMC) [2].

It turns out that even beyond the critical interaction strength the polaron remains as a long-lived excitation above the molecular ground state, and conversely the molecule becomes an excited state on the polaronic side of the transition. The proper description of these excited states and in particular their finite lifetime remains a difficult problem. Using a phenomenological model in a three-loop calculation, Bruun and Massignan have shown that the decay rates of the excited states decrease rapidly as $\Delta\omega^{9/2}$ toward the transition, where $\Delta\omega$ is the energy difference between the ground and excited states [17].

Recently, interest has focused on an additional feature present in the polaron-to-molecule transition: The renormalization of the ↓-spectral function by the strong interactions leads to the appearance of an additional quasi-particle excitation for positive energies. This excitation corresponds to a Fermi polaron interacting repulsively with the ↑-Fermi sea. The repulsive polaron has a finite lifetime which becomes very small at unitarity, $a \to \infty$. In the opposite limit of weak coupling $a \to 0$, the repulsive polaron is long-lived and its spectral weight approaches unity. This justifies perturbative methods which neglect the presence of the molecular channel [18, 19]. The repulsive polaron has been studied theoretically in the context of ultracold gases by Cui and Zhai [20] and more recently by Massignan and Bruun [21]. Experimentally, the repulsive polaron has not yet been observed in the strong-coupling regime. However, it has important implications for the stability of a ferromagnetic phase in Fermi gases [20, 22–26]. Furthermore, a single ↓-fermion in an ↑-Fermi sea corresponds to a strongly imbalanced, two-component Fermi gas near full polarization, and the polaron-to-molecule transition sheds light on a region of the zero-temperature phase diagram of the polarized Fermi gas [10, 15, 27].

So far, there is a lack of theoretical work which describes all of these features within one unified approach. In this paper we present a method capable of doing this: Using a novel numerical implementation of the functional renormalization group (fRG) we are able to determine both the full spectral functions and the quasi-particle features of the polaron-to-molecule transition.

With the renormalization group one usually limits oneself to a few running couplings. In this work we develop a computational tool which allows us to keep track of

the renormalization group flow of fully momentum and frequency dependent Matsubara Green's functions based on an exact renormalization group equation [28]. By introducing an auxiliary bosonic field which mediates the interaction between ↑- and ↓-atoms, we are able to accurately capture the momentum and frequency dependence of both vertex functions and propagators. In particular for non-universal quantities our approach, which complements the proposal by Blaizot, Méndez-Galain, and Wschebor [29], may prove vital, and we demonstrate its efficiency in the polaron problem.

Our main results from the fRG are the following. We give the spectral functions of the ↓-fermion and—for the first time—also of the molecule in a wide range of interaction values. From this we extract the quasi-particle properties including energies, decay rates and residues for both the polaron and the molecule. We connect the quasi-particle weight of the molecule with a measure of its compositeness introduced by Weinberg [30]. We propose a new experimental procedure to measure the repulsive polaron in a ^{6}Li Fermi gas using rf-spectroscopy, and we employ our spectral functions to predict the expected rf-response.

The paper is organized as follows: in section II we introduce the model of the polaron-to-molecule transition and derive appropriate fRG flow equations. These equations are solved in section III for the full frequency and momentum dependent spectral functions, which are presented and interpreted in section IV. Section V is devoted to rf-spectroscopy, and we conclude with a discussion in section VI. In the appendix the fRG flow equations are solved using the simpler derivative expansion, which already gives qualitatively correct results.

II. MODEL AND RG FLOW EQUATIONS

In this work we study a two-component Fermi gas in the limit of extreme population imbalance at $T = 0$. The microscopic action describing the system is

$$S = \int_{\mathbf{x},\tau} \Big\{ \sum_{\sigma=\uparrow,\downarrow} \psi^*_\sigma [\partial_\tau - \Delta - \mu_\sigma]\psi_\sigma + g\psi^*_\uparrow \psi^*_\downarrow \psi_\downarrow \psi_\uparrow \Big\} \quad (1)$$

in natural units $\hbar = 2m = 1$ and with imaginary time τ. The Grassmann-valued, fermionic fields $\psi_\uparrow$ and $\psi_\downarrow$ denote the up and down fermions, which have equal mass m. The associated chemical potentials μ_σ are adjusted such that the ↑-fermions have a finite density $n_\uparrow = k_F^3/(6\pi^2)$ while there is only a single impurity ↓-fermion. The atoms interact via a contact interaction with coupling constant g which is related to the s-wave scattering length a via $g = 8\pi a$. The T-matrix acquires a complicated frequency and momentum dependence in the strong-coupling limit. It is then convenient to perform a Hubbard-Stratonovich transformation of the action (1) introducing a bosonic molecule (pairing) field $\phi \sim \psi_\downarrow \psi_\uparrow$ which mediates the two-particle interaction $g\psi^*_\uparrow \psi^*_\downarrow \psi_\downarrow \psi_\uparrow$. The resulting action is given by

$$S = \int_{\mathbf{x},\tau} \Big\{ \sum_{\sigma=\uparrow,\downarrow} \psi^*_\sigma [\partial_\tau - \Delta - \mu_\sigma]\psi_\sigma + \phi^* G^{-1}_{\phi,\Lambda} \phi + h(\psi^*_\uparrow \psi^*_\downarrow \phi + h.c.) \Big\} \quad (2)$$

with a real Yukawa coupling h for the conversion of two fermions into a molecule. Integrating out the bosonic field ϕ shows that (2) is equivalent to the single-channel model (1) provided that $-h^2 G_{\phi,\Lambda} = g$ and $h \to \infty$ [14, 31]. As $h^2 \sim \Delta B$ this limit corresponds to a broad Feshbach resonance [5].

The physical properties can be accessed via Green's functions which are derivable from generating functionals. The one-particle irreducible vertex functions $\Gamma^{(n)}$ are obtained from the effective quantum action Γ, which can, for instance, be computed perturbatively in a loop expansion. As we are interested in the intrinsically non-perturbative regime of fermions close to a Feshbach resonance where the scattering length a diverges we employ a different approach. Γ includes quantum fluctuations on all momentum and energy scales. The main idea of the functional renormalization group (fRG) is to introduce an interpolating effective flowing action Γ_k which includes only fluctuations on momentum scales $q \gtrsim k$ larger than the renormalization group scale k. At the UV scale $k = \Lambda \to \infty$ the effective flowing action reduces to the microscopic action S which does not include any quantum corrections. In the infrared limit $k \to 0$, Γ_k equals the full quantum action Γ.

The evolution, or flow, of Γ_k with the RG scale k is given by the exact renormalization group equation [28]

$$\partial_k \Gamma_k = \frac{1}{2} \mathrm{STr} \left(\frac{1}{\Gamma^{(2)}_k + R_k} \partial_k R_k \right). \quad (3)$$

The supertrace symbol STr denotes a loop integration over frequency and momentum as well as the summation over all fields and internal degrees of freedom, with a minus sign for fermions. $\Gamma^{(2)}_k$ is the full, field dependent inverse two-point Green's function at scale k, and R_k is a regulator taking care of the successive inclusion of momentum scales. The regulator acts by imposing a large mass term on the modes with momenta $q \lesssim k$ lower than the cutoff scale k. R_k can be chosen freely as long as $R_{k\to 0} \to 0$ and $R_{k\to\infty} \to \infty$. For further details on the fRG we refer to the literature [32–34], and to its application to the BEC-BCS crossover [35].

Γ_k is in general a functional of the fields and contains all possible operators of the fields allowed by the symmetries. For this reason its exact calculation is usually impossible and one has to rely on approximations for Γ_k. In this work we will use the truncation

$$\Gamma_k = \int_{\mathbf{p},\omega} \Big\{ \psi^*_\uparrow [-i\omega + \mathbf{p}^2 - \mu_\uparrow]\psi_\uparrow + \psi^*_\downarrow G^{-1}_{\downarrow,k}(\omega,\mathbf{p})\psi_\downarrow + \phi^* G^{-1}_{\phi,k}(\omega,\mathbf{p})\phi \Big\} + \int_{\mathbf{x},\tau} h(\psi^*_\uparrow \psi^*_\downarrow \phi + h.c.) \quad (4)$$

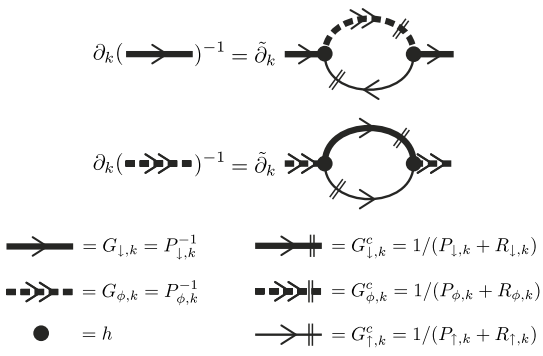

FIG. 1: Diagrammatic representation of the fRG flow equations (8) for the impurity and molecule propagators.

with Matsubara frequency ω. For the momentum and frequency dependence of the k-dependent, or flowing, propagators of the $\downarrow$-fermion $G_{\downarrow,k}$ and the boson $G_{\phi,k}$ we will present a simple approximation in terms of a gradient expansion in the appendix. In the following section III we develop a new numerical method to solve the renormalization group flow of the propagators as completely general functions of ω and $\mathbf{p}$. This will enable us to capture decay rates and dynamic effects which is not possible in a simple gradient expansion.

Within the truncation (4) the Yukawa coupling h is not renormalized which can be seen by a simple argument: In Eq. (4) we neglect a term $\psi^*_\uparrow\psi^*_\downarrow\psi_\downarrow\psi_\uparrow$ which would be regenerated during the flow by particle-hole fluctuations [36]. Similarly, a term $\psi^*_\uparrow\phi^*\psi_\uparrow\phi$ for the atom-dimer interaction is neglected. Both terms would lead to a renormalization of h. Due to their omission, however, there is no diagram generating a flow of h which is why $\partial_k h \equiv 0$ and h remains independent of frequency and momentum. Furthermore, we neglect terms $(\phi^*\phi)^{n\geq 2}$ which would give higher-order corrections to the bosonic self-energy. The majority $\uparrow$-atoms are renormalized only by the single impurity $\downarrow$-atom to order $1/N_\uparrow$, hence one can neglect the renormalization of the $\uparrow$-atoms in the thermodynamic limit, and the chemical potential $\mu_\uparrow = \epsilon_F = k_F^2/(2m)$ is that of a free Fermi gas (we work in units where the Fermi momentum $k_F = 1$) [2].

As Eq. (3) is a (functional) differential equation, it has to be supplemented with appropriate initial conditions at the UV scale Λ, which are obtained from few-body (vacuum) physics. The s-wave vacuum scattering amplitude for the interaction of an $\uparrow$- and $\downarrow$-fermion with momenta $\mathbf{q}$, $-\mathbf{q}$ in the center-of-mass frame is given by ($q = |\mathbf{q}|$)

$$f(q) = \frac{1}{-1/a - iq}. \tag{5}$$

$f(q)$ is related to the full molecule propagator $G^{\text{vac}}_{\phi,\text{R}}$ evaluated at the infrared RG scale $k = 0$,

$$f(q) = \frac{h^2}{8\pi}\, G^{\text{vac}}_{\phi,\text{R}}(\omega = 2q^2, \mathbf{p} = 0), \tag{6}$$

where $\omega = 2q^2$ is the total kinetic energy of the interacting atoms. The subscript R indicates that the analytical continuation to the retarded function of real frequencies ($i\omega \to \omega + i0$) has been performed. In [37] the exact vacuum molecule propagator $G^{\text{vac}}_{\phi,\text{R}}$ has been calculated using the fRG and agrees with the well-known result

$$[G^{\text{vac}}_{\phi,\text{R}}(\omega,\mathbf{p})]^{-1} = \frac{h^2}{8\pi}\left(-a^{-1} + \sqrt{-\frac{\omega}{2} + \frac{\mathbf{p}^2}{4} - i0}\right). \tag{7}$$

This expression for $G^{\text{vac}}_{\phi,\text{R}}$ reproduces the correct scattering amplitude (5) when inserted into Eq. (6), and dictates the form of the UV propagator $G^{-1}_{\phi,\Lambda}$ for a given choice of regulator.

Furthermore, the initial condition for the fermions is given by their form in the microscopic action (2), $G^{-1}_{\sigma,k=\Lambda}(\omega,\mathbf{p}) = -i\omega + \mathbf{p}^2 - \mu_\sigma$. As we will see in the following, the momentum and frequency dependence of both propagators, $G_{\phi,k}$ and $G_{\downarrow,k}$, is strongly renormalized during the fRG flow toward the infrared, which leads to a rich structure of the spectral functions.

After inserting the truncation (4) into the flow equation (3), the flow of $G_{\downarrow,k}$ and $G_{\phi,k}$ is derived by taking the appropriate functional derivatives of Eq. (3) with respect to the fields. One obtains the fRG flow equations

$$\begin{aligned}\partial_k P_{\downarrow,k}(P) &= h^2\tilde{\partial}_k \int_Q G^c_{\phi,k}(Q)G^c_{\uparrow,k}(Q-P)\\ \partial_k P_{\phi,k}(P) &= -h^2\tilde{\partial}_k \int_Q G^c_{\downarrow,k}(Q)G^c_{\uparrow,k}(P-Q)\end{aligned} \tag{8}$$

with the multi-indices $P = (\omega,\mathbf{p})$ and $Q = (\nu,\mathbf{q})$. The $P_k \equiv G_k^{-1}$ on the left-hand side are the flowing inverse propagators *without* the regulator from Eq. (4), while the propagators G^c_k on the right-hand side are regulated:

$$G_k \equiv 1/P_k \qquad\qquad G^c_k \equiv 1/(P_k + R_k). \tag{9}$$

The tilde on $\tilde{\partial}_k$ indicates that the derivative with respect to the RG scale k acts only on the regulator term R_k in the cutoff propagators G^c_k: specifically, the single-scale propagators read $\tilde{\partial}_k G^c_k = -(G^c_k)^2\partial_k R_k$ in Eq. (8). Note that the flow equations (8), which are depicted in Fig. 1, have a one-loop structure but contain the *full* propagators at scale k: by integrating the flow, diagrams of arbitrarily high loop order are generated and constantly fed back into each other. It is especially for the latter reason that our approach goes beyond other approximations used for the description of the polaron problem such as for example the non-self-consistent T-matrix approximation [8, 21]. The goal of this paper is to solve the system of differential flow equations (8).

In the following we choose sharp cutoff functions R_k which strictly cut off all momentum modes with $|\mathbf{p}| < k$ while the frequencies are not restricted [54]. Then the regulated Green's functions G^c_k take the particularly sim-

ple form (for unoccupied ↓-atoms)

$$G^c_{\downarrow,k}(\omega,\mathbf{p}) = \frac{\theta(|\mathbf{p}|-k)}{P_{\downarrow,k}(\omega,\mathbf{p})}, \tag{10}$$
$$G^c_{\phi,k}(\omega,\mathbf{p}) = \frac{\theta(|\mathbf{p}|-k)}{P_{\phi,k}(\omega,\mathbf{p})},$$
$$G^c_{\uparrow,k}(\omega,\mathbf{p}) = \frac{\theta(|\mathbf{p}^2-\mu_\uparrow|-k^2)}{P_{\uparrow,k}(\omega,\mathbf{p})}.$$

For the ↑-atoms it is crucial to regularize the low-energy modes around the Fermi energy $\mu_\uparrow$. Using the Dyson equation

$$P_k(\omega,\mathbf{p}) = G_k^{-1}(\omega,\mathbf{p}) = G_0^{-1}(\omega,\mathbf{p}) - \Sigma_k(\omega,\mathbf{p}),$$

where $G_0 = G_{k=\Lambda}$ denotes the free (UV) and G_k the full Green's function at scale k, we can in particular identify the gap term

$$m^2_{\downarrow,k} := P_{\downarrow,k}(0,\mathbf{0}) = -\mu_\downarrow - \Sigma_{\downarrow,k}(0,\mathbf{0}). \tag{11}$$

The chemical potential $\mu_\downarrow$ is the energy required to add one ↓-atom to the system,

$$\mu_\downarrow = E(N_\downarrow) - E(N_\downarrow - 1), \tag{12}$$

and is independent of the cutoff scale k. The interaction effects on the ↓-fermion, which are successively included during the flow, are captured by the k-dependent self-energy $\Sigma_k(\omega,\mathbf{p})$. In the polaron problem we are interested in a two-component Fermi gas in the limit of extreme population imbalance where one considers only a single ↓-atom, $N_\downarrow = 1$, and relation (12) is used to determine the ground-state energy of the system. This value of the chemical potential $\mu_\downarrow$ then marks the phase transition from a degenerate, fully polarized ↑-Fermi gas to a phase of finite ↓-fermion density [10]. Accordingly, for all choices of $\mu'_\downarrow \le \mu_\downarrow$ there has to be a vanishing occupation of both ↓-fermions and molecules at every RG scale k, which leads to the condition

$$P_{\downarrow,k}(0,\mathbf{0},\mu'_\downarrow) \ge 0, \quad P_{\phi,k}(0,\mathbf{0},\mu'_\downarrow) \ge 0 \quad \forall \mu'_\downarrow \le \mu_\downarrow. \tag{13}$$

In order to have only a single ↓-atom or molecule, $\mu_\downarrow$ has to be determined self-consistently such either the ↓-atom or the molecule ϕ is gapless in the infrared, $P_{\downarrow/\phi,k=0}(0,\mathbf{0}) = 0$ (ground state). We find that depending on the value of the dimensionless coupling $(k_F a)^{-1}$, either the polaron or the molecule becomes the ground state, see Table I. The polaron-to-molecule transition occurs at the critical interaction strength $(k_F a_c)^{-1}$ at which $m^2_\phi = m^2_\downarrow = 0$.

coupling	$(k_F a)^{-1} < (k_F a_c)^{-1}$	$(k_F a)^{-1} > (k_F a_c)^{-1}$
ground state	polaron	molecule
↓ gap	$P_\downarrow(0,\mathbf{0}) = m^2_\downarrow = 0$	$P_\downarrow(0,\mathbf{0}) = m^2_\downarrow > 0$
ϕ gap	$P_\phi(0,\mathbf{0}) = m^2_\phi > 0$	$P_\phi(0,\mathbf{0}) = m^2_\phi = 0$

TABLE I: Conditions for the polaron and molecule ground states.

III. RG FOR FULL SPECTRAL FUNCTIONS

The main goal of this work is to solve the system of flow equations (8) without imposing any constraints on the frequency and momentum dependence of the polaron and molecule propagators. This problem can only be solved numerically, and the inverse, flowing Green's functions $P_{\downarrow/\phi,k}(\omega,\mathbf{p})$ are evaluated on a discrete grid in frequency and momentum space,

$$P_{\downarrow,k}(\omega,\mathbf{p}) \to P_{\downarrow,k}(\omega_i,p_j) = P^{ij}_{\downarrow,k}$$
$$P_{\phi,k}(\omega,\mathbf{p}) \to P_{\phi,k}(\omega_i,p_j) = P^{ij}_{\phi,k}. \tag{14}$$

We choose a logarithmically spaced, finite grid with $\omega_i \in (0,\dots,\omega_{\max})$ and $p_j \in (0,\dots,p_{\max})$. As a result of rotational invariance the propagators depend only on the magnitude of spatial momentum $p = |\mathbf{p}|$, and due to the condition $P^*(\omega) = P(-\omega)$ for Euclidean (Matsubara) propagators it is sufficient to consider positive frequencies only [39]. The full (ω,p) dependence is reconstructed from the finite number of couplings $P^{ij}_{\downarrow/\phi,k}$ by cubic spline interpolation,

$$P_{\downarrow/\phi,k}(\omega,p) = \mathrm{Spline}(\{P^{ij}_{\downarrow/\phi,k}\})$$
$$= \sum_{\xi,\vartheta=0}^{3} c^{ij,\xi\vartheta}_{\downarrow/\phi,k}(\omega-\omega_i)^\xi (p-p_j)^\vartheta, \tag{15}$$

with $\omega \in (\omega_i,\omega_{i+1})$, $p \in (p_j,p_{j+1})$ and $c^{ij,\xi\vartheta}_{\downarrow/\phi,k}$ the corresponding spline coefficients. For the asymptotics of the propagators for high frequency and momentum modes, $\omega > \omega_{\max}$ and/or $p > p_{\max}$, we choose the simple fit models

$$P^{>}_{\downarrow,k}(\omega,\mathbf{p}) = -i\omega + \mathbf{p}^2 - \mu_\downarrow \tag{16}$$
$$P^{>}_{\phi,k}(\omega,\mathbf{p}) = \frac{h^2}{8\pi}\left(-a^{-1} + \sqrt{-\frac{i\omega}{2} + \frac{\mathbf{p}^2}{4} + f_{\phi,k}}\right)$$

with $f_{\phi,k}$ determined by a continuity condition from the numerical value of $P_{\phi,k}$ for the largest momenta $|\mathbf{p}| = p_{\max}$.

In order to keep the numerical cost of computing the flow equations (8) low it is advantageous to employ the sharp momentum regulator functions $R_{\downarrow,k}$, $R_{\uparrow,k}$, and $R_{\phi,k}$ defined by Eq. (10). This reduces the number of loop integrations by one. The flow equations evaluated by our algorithm are then given by

$$\partial_k P_{\downarrow,k}(\omega,\mathbf{p}) = -\frac{h^2}{(2\pi)^3}\int_{-1}^{1} dx \int_{-\infty}^{\infty} d\nu \int_0^\infty q^2\, dq$$
$$\times \frac{\chi_k(p,q,x)}{P_{\phi,k}(\nu,\mathbf{q})P_{\uparrow,k}(\nu-\omega,\mathbf{q}-\mathbf{p})}$$
$$\partial_k P_{\phi,k}(\omega,\mathbf{p}) = \frac{h^2}{(2\pi)^3}\int_{-1}^{1} dx \int_{-\infty}^{\infty} d\nu \int_0^\infty q^2\, dq$$
$$\times \frac{\chi_k(p,q,x)}{P_{\downarrow,k}(\nu,\mathbf{q})P_{\uparrow,k}(\omega-\nu,\mathbf{p}-\mathbf{q})} \tag{17}$$

where we have defined the characteristic function

$$\chi_k(p,q,x) = \delta(q-k)\theta(|(\mathbf{p}-\mathbf{q})^2-\mu_\uparrow|-k^2) + 2k\theta(q-k)\delta(|(\mathbf{p}-\mathbf{q})^2-\mu_\uparrow|-k^2) \quad (18)$$

and $x = \cos\theta$ expresses the angle θ between the momentum vectors $\mathbf{p}$ and $\mathbf{q}$ such that $|\mathbf{p}\pm\mathbf{q}|^2 = p^2+q^2\pm 2pqx$.

The initial condition at the UV scale $k=\Lambda$ is determined by the few-body calculation (7). As we employ no approximation for the momentum and frequency dependence of the molecule propagator we are able to incorporate the *exact* two-body scattering amplitude (5), in contrast to the calculation in the appendix using the derivative expansion where this is not possible. The vacuum problem can be solved exactly using the sharp regulators (10), which leads to the UV molecule propagator

$$P_{\phi,\Lambda}(\omega,\mathbf{p}) = -\frac{h^2}{8\pi a}+\frac{h^2\Lambda}{4\pi^2} - \frac{h^2}{2}\int_{\mathbf{q}}\left[\frac{\theta(|\mathbf{q}-\frac{\mathbf{p}}{2}|-\Lambda)\,\theta(|\mathbf{q}+\frac{\mathbf{p}}{2}|-\Lambda)}{q^2+\left(-\frac{i\omega}{2}+\frac{\mathbf{p}^2}{4}-\mu_{\mathrm{vac}}\right)}-\frac{\theta(q-\Lambda)}{q^2}\right].$$

At each RG step we first perform the q integration in Eq. (17) which is trivial due to the δ-functions in the characteristic function χ_k. Next the frequency integration in Eq. (17) is carried out. The computational speed is greatly enhanced by mapping the numerical integration onto an *analytical* integration using the spline polynomials in the interval $(-\omega_{\max},\omega_{\max})$. $\omega_{\max}$ is chosen such that the error in the ω integration of the outer regime $\omega > \omega_{\max}$ introduced due to the approximation (16) is smaller than the accuracy of the numerical solution of the system of differential equations (8). For the final angular integration in $x=\cos\theta$ on the right-hand side of the flow equation (17) we use a numerical integration with adaptive nodes in order to cope with discontinuities of the integrand.

In order to obtain a stable numerical result it is sufficient to calculate the flow of the propagators for roughly 1500 grid points (ω_i, p_j) in frequency and momentum space. The corresponding system of ordinary differential equations is straightforwardly solved using a Runge-Kutta algorithm, which we have implemented in a version with adaptive stepsize in RG time $t=\ln(k/\Lambda)$. An adaptive stepsize is essential in order to detect the kinks in the RG flow due to the sharp Fermi surface of the $\uparrow$-fermions at zero temperature. We observe that about 10^4 RG steps are necessary to obtain an error smaller than $\epsilon\sim 10^{-5}$.

Finally, when the flow reaches the infrared, $k=0$, we end up with the full Matsubara Green's functions $G_{\downarrow,k=0}(\omega,p)$ and $G_{\phi,k=0}(\omega,p)$. The initial value of $\mu_\downarrow$ for a given $k_F a$ is adjusted such that a vanishing macroscopic occupation of $\downarrow$-atoms and molecules is obtained at the end of the flow, as discussed in section II. In order to access the spectral functions we perform the analytical continuation to real frequencies using a Padé approximation.

IV. FULL SPECTRAL FUNCTIONS

We now present our numerical results for the spectral functions of the polaron and molecule across the whole transition region. First, the Matsubara Green's functions at the end of the RG flow, $G_{\downarrow/\phi,k=0}(\omega,\mathbf{p})$, are continued analytically to retarded Green's functions of real frequency, $G_{\downarrow/\phi,\mathrm{R}}(\omega,\mathbf{p})$, using the Padé approximation. The spectral functions are defined as

$$A_{\downarrow/\phi}(\omega,\mathbf{p}) = 2\,\mathrm{Im}\,G_{\downarrow/\phi,\mathrm{R}}(\omega,\mathbf{p}). \quad (19)$$

In Fig. 2 the zero-momentum spectral functions $A_{\downarrow/\phi}(\omega,\mathbf{p}=0)$ are shown as functions of frequency and coupling $(k_F a)^{-1}$.

The coherent single-particle excitations at zero momentum are determined by the solutions ω_{qp} of the equation

$$G^{-1}_{\downarrow/\phi,\mathrm{R}}(\omega,\mathbf{p}=0)\Big|_{\omega=\omega_{\mathrm{qp}}} = 0 \quad (20)$$

for ω in the complex lower half-plane. Near each quasi-particle pole the retarded propagator can be approximated by the form

$$G_{\downarrow/\phi,\mathrm{R}}(\omega,\mathbf{p}=0) \approx \frac{Z_{\downarrow/\phi}}{\omega_{\mathrm{qp}}-\omega-i0} \quad (21)$$

where the real part of ω_{qp} determines the quasi-particle energy

$$E_{\mathrm{qp}} = \mu_\downarrow + \mathrm{Re}[\omega_{\mathrm{qp}}]. \quad (22)$$

We have shifted the ground-state energy, which is zero in our calculation (vanishing gap), to the conventional value $\mu_\downarrow$ from Eq. (12). The imaginary part of the pole position determines the decay width

$$\Gamma_{\mathrm{qp}} = -\,\mathrm{Im}[\omega_{\mathrm{qp}}]. \quad (23)$$

A Fourier transform in time relates the decay width to the quasi-particle lifetime

$$\tau_{\mathrm{qp}} = \hbar/\Gamma_{\mathrm{qp}}. \quad (24)$$

The quasi-particle weight $Z_{\downarrow/\phi}$ is obtained from the frequency slope at the complex pole position,

$$Z^{-1}_{\downarrow/\phi} = -\frac{\partial}{\partial\omega}G^{-1}_{\downarrow/\phi,\mathrm{R}}(\omega,\mathbf{p}=0)\Big|_{\omega=\omega_{\mathrm{qp}}}. \quad (25)$$

Note that an alternative definition of the decay width in terms of the self-energy evaluated not at the complex pole position but on the real frequency axis,

$$\Gamma_{\mathrm{alt}} = \mathrm{Im}\,\Sigma_{\downarrow/\phi,\mathrm{R}}(\omega,\mathbf{p}=0)\Big|_{\omega=\mathrm{Re}\,\omega_{\mathrm{qp}}}, \quad (26)$$

agrees with our definition for Γ_{qp} only for a single quasi-particle pole (21) with $Z=1$. However, for the polaron problem there are further excited states and $Z<1$.

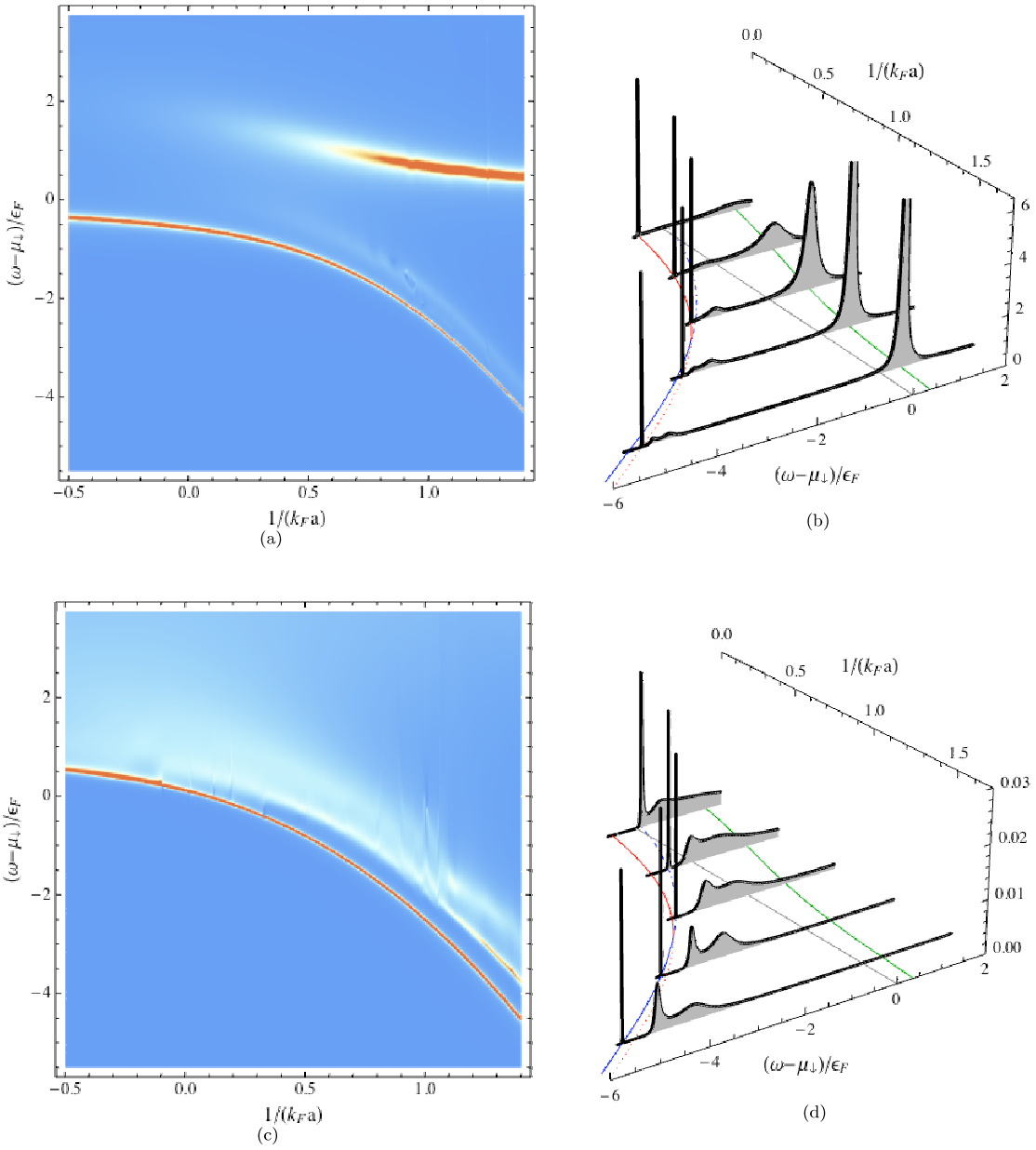

FIG. 2: (color online). Spectral functions at zero momentum in dependence on $1/(k_F a)$. (a), (b): Polaron spectral function $A_\downarrow(\omega, \mathbf{p} = 0)$. (c), (d): Molecule spectral functions $A_\phi(\omega, \mathbf{p} = 0)$. In order to make the δ-function peak for the ground state visible we introduced an artificial width of the quasi-particles of $0.007\,\epsilon_F$.

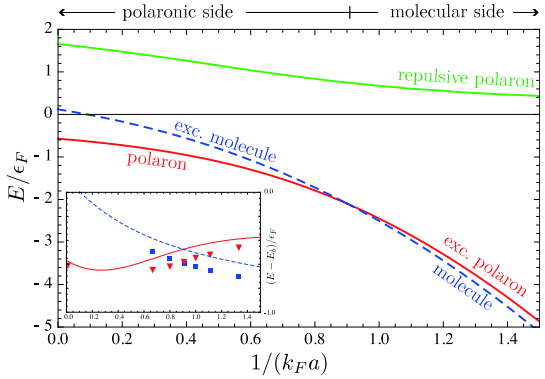

FIG. 3: (color online). Energy spectrum of the single-particle excitations of the polaron-to-molecule transition. In the inset we show our fRG result for the ground-state energy (with the universal dimer binding energy $E_b = -\hbar^2/(ma^2)$ subtracted) in comparison to the results obtained with diagMC by Prokof'ev and Svistunov [2] (symbols).

Hence, only $\Gamma_{\rm qp}$ from Eq. (23) can be interpreted as the half-width of the peaks in the spectral function and as the inverse lifetime.

We will now in turn discuss the features seen in the spectral functions: the peak position ($E_{\rm qp}$), width ($\Gamma_{\rm qp}$) and weight (Z), first for the polaron (upper row of Fig. 2) and then for the molecule (lower row).

A. Attractive and repulsive polaron

Energy spectrum. Let us first look at the energy spectrum of the quasi-particle excitations depicted in Fig. 3 in dependence on the coupling strength $(k_Fa)^{-1}$. From our data we find two coherent quasi-particle states for the $\downarrow$-atom, the attractive and the repulsive polaron, and one bound state for the molecule. The attractive polaron (red solid line) is the ground state for $(k_Fa)^{-1} < (k_Fa_c)^{-1}$ (polaronic side) but becomes an excited state for $(k_Fa)^{-1} > (k_Fa_c)^{-1}$ (molecular side). Conversely, the molecule is the ground state on the molecular side (blue dashed line) and an excited state on the polaronic side, in accordance with the discussion at the end of section II. For the critical coupling strength we obtain $(k_Fa_c)^{-1} = 0.904(5)$, which agrees with the value $(k_Fa_c)^{-1} = 0.90(2)$ obtained using diagrammatic Monte Carlo (diagMC) by Prokof'ev and Svistunov [2]. As shown in the inset of Fig. 3, also the values for the energies agree well with diagMC (symbols). At unitarity, $(k_Fa)^{-1} = 0$, we obtain the ground-state energy $\mu_\downarrow = -0.57\,\epsilon_F$ while diagMC gives the value $\mu_\downarrow = -0.615\,\epsilon_F$. Having treated the full frequency and momentum dependence of the propagators in the truncation (4), we can attribute the residual deviation in the ground state energy to the omission of the terms $\psi^*_\uparrow\psi^*_\downarrow\psi_\downarrow\psi_\uparrow$ and $\phi^*\psi^*_\sigma\phi\psi_\sigma$. The latter term describes the atom-dimer interaction and is expected to further reduce the ground-state energy in the transition regime in accordance with the results from the variational wave function approach [10, 11]. The term $\psi^*_\uparrow\psi^*_\downarrow\psi_\downarrow\psi_\uparrow$, generated by particle-hole fluctuations, is expected to give the main correction in the unitarity regime [9]. Both terms can be included in the fRG flow as additional flowing couplings, or implicitly by using the Katanin scheme [40] or rebosonization [41].

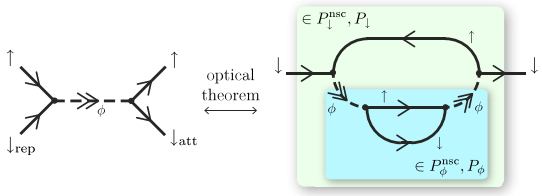

FIG. 4: (color online). Decay channel for the repulsive polaron. **(left)** Two-body process which leads to the decay of the repulsive polaron. **(right)** Corresponding contribution to the $\downarrow$-atom self-energy via the optical theorem.

Until recently [22] most experiments with ultracold Fermi gases have focused on the lower, attractive branch on the BEC side $(k_Fa)^{-1} > 0$. There exists, however, also the repulsive polaron branch (solid green line) which corresponds to a higher excited state of the $\downarrow$-atom interacting *repulsively* with the $\uparrow$-Fermi sea. Our results for the energy of the repulsive branch agree with the weak-coupling results [18] for $(k_Fa)^{-1} \gtrsim 1$. In the strong-coupling regime our energies lie between the result from the non-self-consistent T-matrix approach [21] and the MC results for square well potentials [24]. In the polaron spectral function, cf. Fig. 2(b), one can clearly discern the attractive polaron branch as a very sharp peak at low frequencies, and the much broader repulsive polaron branch at higher frequencies.

Decay widths. The repulsive polaron has a large decay width $\Gamma_{\rm rep}$, as calculated from Eq. (23) and depicted in Fig. 5, and correspondingly a short lifetime. The leading-order decay channel for the repulsive polaron is the process shown in Fig. 4(left) where the repulsive polaron, which is an excited state, decays to the attractive, and energetically lower lying, polaron due to the interaction with an $\uparrow$-atom. This diagram can be translated via the optical theorem into a contribution to the imaginary part of the $\downarrow$-atom self-energy, as depicted in Fig. 4(right). This self-energy diagram is already included in the non-self-consistent T-matrix propagator $P^{\rm nsc}_\downarrow$, and has been studied recently using this approximation [21]. Of course, this diagram is also included in our fRG approach.

In the weak-coupling limit $(k_Fa)^{-1} \to \infty$ the excitation becomes sharp, $\Gamma_{\rm rep} \to 0$, and the repulsive polaron

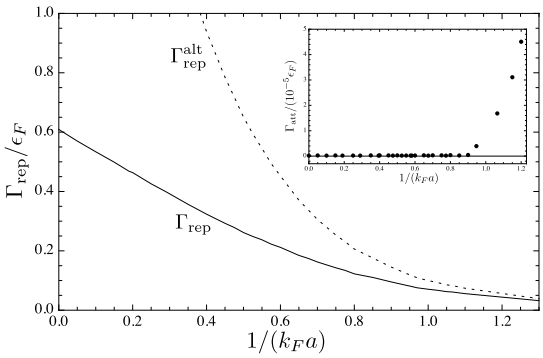

FIG. 5: Decay width $\Gamma_{\rm rep}$ of the repulsive polaron as a function of the coupling $(k_Fa)^{-1}$. We also show the width according to the approximate formula Eq. (26) (dotted line). Inset: Decay width $\Gamma_{\rm att}$ of the attractive polaron.

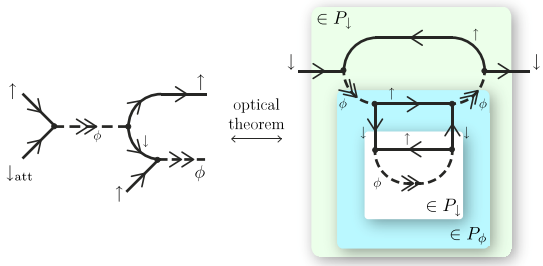

FIG. 6: (color online). Decay channel for the attractive polaron. **(left)** Three-body recombination process which leads to the decay of the attractive polaron. **(right)** Corresponding contribution to the ↓-atom self-energy via the optical theorem (there is also a contribution with crossed lines).

is a well-defined quasi-particle. Toward unitarity, $\Gamma_{\rm rep}$ grows but remains a well-defined, finite quantity even at unitarity. We find that indeed $\Gamma_{\rm rep}$, and not the approximation $\Gamma_{\rm rep}^{\rm alt}$ from Eq. (26), is the correct half-width at half-height of the respective peak in the polaron spectral function in Fig. 2(b). For $(k_Fa)^{-1} < 0.6$ the energy $E_{\rm rep}$ of the repulsive branch exceeds the bath Fermi energy, $E_{\rm rep} > \epsilon_F$. At this point it is energetically favorable to spin-flip the impurity atom, which can be interpreted as the condition for the onset of saturated ferromagnetism [20, 26]. At the same time the decay width $\Gamma_{\rm rep} > 0.2\,\epsilon_F$ is large, which potentially destabilizes a ferromagnetic phase [25].

On the polaronic side $(k_Fa)^{-1} < (k_Fa_c)^{-1}$ the attractive polaron is the stable ground state with decay width $\Gamma_{\rm att} = 0$, while on the molecular side it is an excited state with finite lifetime and decay width $\Gamma_{\rm att} > 0$, see Fig. 5(inset). This decay is much weaker and also qualitatively different from the repulsive channel. The attractive polaron can decay by a three-body recombination process as shown in Fig. 6(left). Via the optical theorem this process can be translated into a contribution to the ↓-atom self-energy as depicted in Fig. 6(right), plus an additional contribution with crossed lines. This decay channel has recently been studied using an explicit three-loop calculation [17]. The resulting finite lifetime cannot be seen in the non-self-consistent T-matrix approximation, where the self-energy corrections of the ↓-atom—indicated by the inner white box $P_\downarrow$—are *not* fed back into the T-matrix $\sim P_\phi^{-1}$ [8, 21]. In contrast to the non-self-consistent T-matrix calculation, our fRG includes the full feedback of both the ↓ and ϕ self-energies, denoted by bold internal lines in the flow equations in Fig. 1. Therefore, the contributions from the decay diagram in Fig. 6(right), and many more, are automatically included in our approach.

Quasi-particle weights. Fig. 7 depicts the quasi-particle weights of the attractive and repulsive polaron computed using Eq. (25). On the polaronic side the attractive polaron state contains most of the weight, but as one moves toward the molecular side the spectral weight gradually shifts to the repulsive branch, and the corresponding peak in the polaron spectral function in Fig. 2(b) becomes larger. We find that the attractive and repulsive branches almost completely make up the total spectral weight, hence the contribution from the incoherent background is very small. This is also apparent in the polaron spectral function in Fig. 2(b).

Our results for the quasi-particle weights agree well with those from the non-self-consistent T-matrix and variational wave-function approaches. At unitarity we obtain for the attractive polaron $Z_{\downarrow,\rm att} = 0.796$ compared to the variational value $Z_{\downarrow,\rm att} = 0.78$ [7, 10]. For the repulsive polaron at $(k_Fa)^{-1} = 1$ we find $Z_{\downarrow,\rm rep} = 0.71$, in agreement with the recent non-self-consistent T-matrix calculation [21].

Note that there is an alternative definition of the quasi-particle weight [10]

$$Z_\downarrow^{\rm alt} = \lim_{t\to\infty} \big|G_\downarrow(t, \mathbf{p}=0)\big|. \tag{27}$$

This definition has to be treated with care: on the molecular side of the transition the polaron acquires a finite decay width $\Gamma_\downarrow > 0$ but nonetheless continues to be a well-defined quasi-particle with finite spectral weight, as can be seen from Fig. 2. However, definition (27) yields zero as soon as $\Gamma_\downarrow > 0$ and in this case cannot be interpreted as a measure of spectral weight anymore. In contrast, the definition (25) remains correct for a finite decay width and accordingly our data for $Z_\downarrow$ shows no discontinuity at the transition. In the experiment the finite lifetime of the attractive polaron on the molecular side complicates the direct measurement of $Z_\downarrow$ by radio-frequency spectroscopy because the molecular state and not the attractive polaron becomes occupied as the initial state (cf. section V).

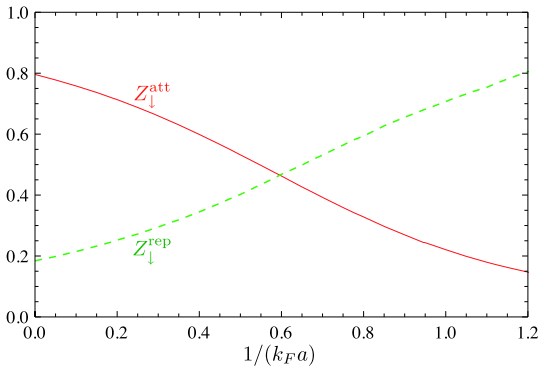

FIG. 7: (color online). Quasi-particle weight $Z_\downarrow$ of the attractive (solid line) and repulsive (dashed line) polaron. The weights of the two quasi-particle peaks in the $\downarrow$ spectral function almost completely make up the total spectral weight, and the contribution from the incoherent background is very small.

B. Molecule

Energy spectrum. The molecule spectral function in Fig. 2(d) displays a sharp quasi-particle peak of the bound state at low frequencies, followed by an incoherent background at higher frequencies which actually carries most of the spectral weight. Note that this background is not taken into account in the simple derivative expansion in the appendix nor in the Wilsonian RG approach [15]. On the molecular side $(k_F a)^{-1} > (k_F a_c)^{-1}$ the molecule is the ground state and is clearly separated from the incoherent continuum. On the polaronic side of the transition the molecule becomes an unstable, excited state and develops a clearly visible finite decay width in the spectral function.

Decay widths. The leading decay channel of the excited molecule state is via the three-body recombination process shown in Fig. 8(left). Via the optical theorem this process can be translated into a contribution to the molecule self-energy as depicted in Fig. 8(right). Similarly to the attractive polaron, in the non-self-consistent T-matrix approximation the $\downarrow$-atom self-energy corrections in $P_\downarrow$ are *not* fed back into the T-matrix $\sim P_\phi^{-1}$, and the molecule does not decay. In contrast, the diagram Fig. 6(right) is included in the fRG, which leads to the visible broadening in the spectral function.

Ref. [17] shows by an analytical calculation of the phase space for three-loop diagrams of the type in Fig. 8 that the decay width of the molecule scales as

$$\Gamma_\phi \propto \Delta\omega^{9/2} \qquad \Delta\omega = E_\phi - E_{\downarrow,\rm att} \tag{28}$$

where $\Delta\omega$ is the difference between the energy levels of the excited molecule and the attractive polaron ground state. In Fig. 9 we show Γ_ϕ as a function of $\Delta\omega$ in a double logarithmic plot. The large fluctuations of our numerical data are due to the accuracy of the Runge-Kutta integration as well as due to the restriction to a finite number of Matsubara frequencies. We have estimated the corresponding error by comparing the results for different grids with varying number and position of (Matsubara) frequencies. The solid line in Fig. 9 indicates the power law $\Delta\omega^{9/2}$. The triangles in Fig. 9 correspond to a calculation with a higher number of frequencies and we find a convergence to the solid curve for decay widths larger than our numerical integration accuracy $\epsilon = 10^{-5}$. This indicates that the error for larger Γ_ϕ can be attributed to the Padé approximation, while for $\Gamma_\phi < \epsilon$ the accuracy of our results becomes limited by the absolute error of our numerical integration. With our fRG calculation we are thus able to verify the prediction by Bruun and Massignan [17], and the correctness of the power law attests to the strength of our method to describe many features of the polaron-to-molecule transition in one unified approach.

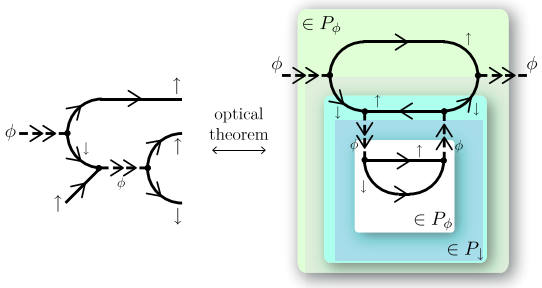

FIG. 8: (color online). Leading decay channel for the excited molecular state. **(left)** Three-body recombination process which leads to the decay of the molecular state. **(right)** Corresponding contribution to the molecule self-energy via the optical theorem (there is also a contribution with crossed lines).

Quasi-particle weight and compositeness. The quasi-particle weight Z_ϕ of the molecular bound state in the spectral function in Fig. 2(d) is very small, $Z_\phi \approx 0.002$ at unitarity, and increases slowly toward the molecular limit, see Fig. 10(inset). For broad resonances, $h^2 \sim \Delta B \to \infty$, the two-channel model (2) is equivalent to the single-channel model (1) where $Z_\phi = 0$ [31]. Specifically, we obtain for the weight of the bound state in vacuum

$$Z_\phi = \frac{32\pi}{h^2 a} \qquad (\text{vacuum}, \Lambda \to \infty). \tag{29}$$

This is consistent with the interpretation of Z_ϕ as the closed-channel admixture (cf. Eq. (29) in [5]). In our calculation we set the physical UV cutoff scale to $\Lambda = 10^3 k_F$, which is of the order of the inverse Bohr radius, and choose $h^2 < \infty$. We observe $Z_\phi \propto 1/(k_F a)$ on the BEC side and a deviation from the vacuum scaling close to unitarity, which may be due to a combination of finite

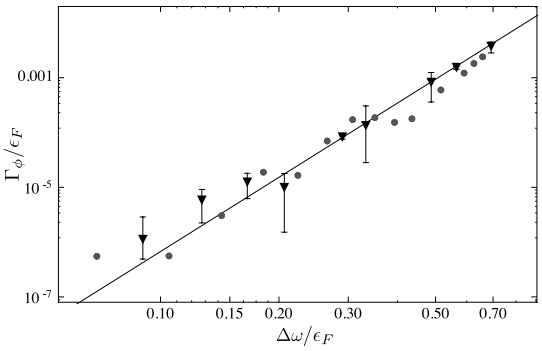

FIG. 9: The decay width Γ_ϕ of the excited molecular state as a function of the energy difference $\Delta\omega = E_\phi - E_{\downarrow,\mathrm{att}}$ between the excited molecule and attractive polaron ground state. The solid line indicates the power-law scaling $\Gamma_\phi \propto \Delta\omega^{9/2}$.

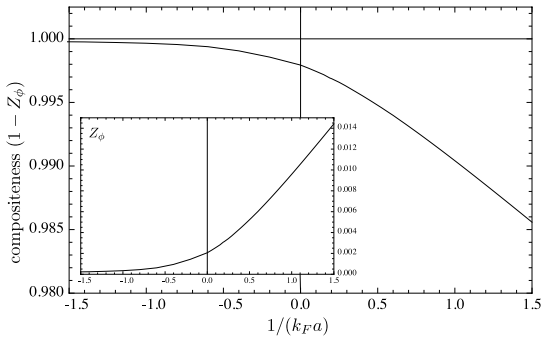

FIG. 10: Compositeness $(1-Z_\phi)$ of the molecular bound state. A value of 100% would indicate that the molecule has no overlap with elementary closed-channel bosons. Inset: Molecular residue Z_ϕ.

density corrections and the admixture of closed-channel molecules in the microscopic action by choosing finite values of h and Λ.

Furthermore, the quasi-particle weight Z can be interpreted as the overlap between the "true" particles and the "elementary", or bare, particles in the microscopic action (2). The attractive Fermi polaron becomes elementary, $Z_{\downarrow,\mathrm{att}} \to 1$, in the BCS limit ($k_F a \to 0^-$), while in the opposite limit of $k_F a \to 0^+$ the repulsive Fermi polaron becomes elementary, $Z_{\downarrow,\mathrm{rep}} \to 1$. Near unitarity, both excitations have a sizable weight. In contrast, the molecular bound state is almost exclusively a composite particle in the whole transition region. Indeed, the deviation of the quasi-particle weight from unity, $1 - Z_\phi$, is a well-established measure of compositeness in nuclear physics [30], and in Fig. 10 we show that for our choice of the Yukawa coupling h the compositeness of the molecule is very large ($> 98\%$). This is consistent with the measurement of a small molecular weight Z_ϕ for a balanced ^{6}Li Fermi gas close to a broad Feshbach resonance by Partridge *et al.* [42]. In experiments with a narrow Feshbach resonance the compositeness will decrease and a single-channel description becomes invalid. A strength of the fRG approach is that both situations are naturally described by tuning the values of h and $G_{\phi,\Lambda}$.

In the vacuum there exists no molecular state for negative scattering length a as can easily seen from Eq. (7), which has no bound-state pole. In the presence of a medium of $\uparrow$-fermions, however, the molecule propagator develops an excited bound-state pole also for negative scattering length a. This bound state will become the superfluid ground state if the impurity density exceeds a critical threshold [10].

V. RF-RESPONSE OF THE ^{6}LI FERMI GAS

As a final application we want to connect our results for the polaronic spectral function to experimentally observable radio-frequency (rf) spectra. The attractive branch of the polaron-to-molecule transition has been studied experimentally by Schirotzek *et al.* [6] using a population imbalanced, two-component mixture of ^{6}Li atoms. In the experiment the rf-response of the system has been used to infer information about the low-frequency behavior of the fermionic spectral functions. For instance, the ground-state energy and the residue $Z_\downarrow$ of the $\downarrow$-fermions were measured and confirmed the theoretical predictions.

In order to measure the rf-response, an rf-pulse is applied to the system which drives the transition of the atoms to a third, initially empty state. In Fig. 11 we show the scattering length profile of ^{6}Li versus the magnetic field. In the experiment [6] a mixture of fermions initially in the hyperfine states $|1\rangle$ and $|3\rangle$ had been prepared in a range of the external magnetic field $B = 630 \ldots 690\,\mathrm{G}$ (shaded area). In this regime the scattering length a_{13} in the initial state is large and positive, while the final state scattering lengths a_{12}, a_{23} are rather small.

Information about the spectral function can be accessed from rf-spectroscopy, for example by populating the particle under investigation up to the energies one is interested in and then driving the transition to a weakly interacting final state for which the spectral function is well-known. This route had been taken for the study of the attractive polaron. The repulsive polaron branch, on the other hand, has not yet been observed directly in experiments. The main complication is that the repulsive polaron has a very short lifetime in the strong-coupling regime of interest (cf. Fig. 5). Hence, its macroscopic population is inhibited on longer time scales, and even after a fast ramp to the desired magnetic field most minority atoms will have decayed into the respective ground state. A similar situation arises in the detection

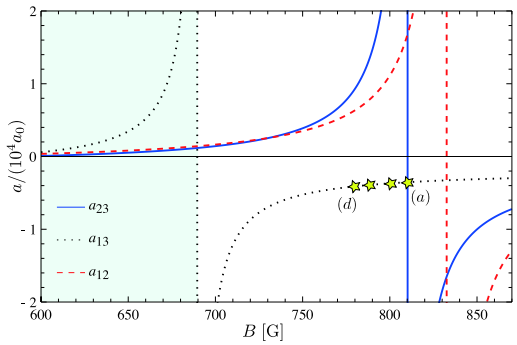

FIG. 11: (color online). Scattering length profile of ^{6}Li atoms in the three lowest hyperfine states as calculated by P. S. Julienne based on the model described in [43]. The stars indicate the magnetic field values for which we determine the rf-response of the imbalanced Fermi gas in Fig. 13.

of Efimov trimers in a three-component mixture of ^{6}Li atoms [44, 45]. The decay of the repulsive branch is also of relevance for the balanced system and the competition between ferromagnetic order and molecule formation [22, 25].

In this section we propose an experimental procedure to circumvent these difficulties and directly analyze the spectral function of the repulsive polaron. A strongly imbalanced two-component ^{6}Li Fermi gas is prepared in hyperfine states $|1\rangle$ and $|3\rangle$ for magnetic fields $B > 690\,\mathrm{G}$ across the $(1,3)$ Feshbach resonance. In this regime the initial scattering length is negative, $a_{13} < 0$. One then drives an rf-transition to the final state $|2\rangle$ which is characterized by large, positive scattering lengths a_{12} and a_{23} and thus strong interactions. Because the attractive polaron spectral function of the initial state, with its negative scattering length a_{13}, is well understood both experimentally and theoretically, the final-state spectral function can then be analyzed in a controlled fashion.

Within linear response theory the induced transition rate from the initial state $|i\rangle$ to the final state $|f\rangle$ is given by [46–48]

$$I(\omega_L) = 2\Omega^2\,\mathrm{Im}\,\chi_\mathrm{R}(\mu_f - \mu_i - \omega_L) \qquad (30)$$

where the Rabi frequency Ω is given by the coupling strength of the rf-photon to the atomic transition, μ_i (μ_f) the initial (final) state chemical potential, and ω_L denotes the rf-frequency offset with respect to the free rf-transition frequency. Neglecting the momentum of the rf-photon, the retarded rf-susceptibility χ_R is given by the analytical continuation to real frequencies of the correlation function in imaginary time τ (Matsubara frequency ω)

$$\chi(\omega) = -\int_\mathbf{r}\int_{\mathbf{r}'}\int_\tau e^{i\omega\tau}\langle T_\tau \psi_f^\dagger(\mathbf{r},\tau)\psi_i(\mathbf{r},\tau) \times \psi_i^\dagger(\mathbf{r}',0)\psi_f(\mathbf{r}',0)\rangle, \qquad (31)$$

	B field [G]	$(k_F a_{13})^{-1}$	$(k_F a_{23})^{-1}$	$(k_F a_{12})^{-1}$
(a)	810.3	-1.88	0.0	0.39
(b)	800.8	-1.80	0.2	0.58
(c)	788.2	-1.70	0.5	0.86
(d)	780.6	-1.62	0.7	1.04

TABLE II: Interaction parameters at the four transitions indicated in Fig. 11, using $k_{F\uparrow} = 0.00015\,a_0^{-1}$.

where T_τ is the imaginary time-ordering operator. Eq. (31) leads to various diagrammatic contributions which are in general difficult to handle if the final-state interactions are not negligible [49]. Here we will calculate Eq. (31) in a simple approximation with full Green's functions but without vertex corrections. In this approximation Eq. (31) yields the susceptibility in Matsubara frequency

$$\chi(\omega) = \int_{\mathbf{k},\nu} G_i(\mathbf{k},\nu)\,G_f(\mathbf{k},\nu+\omega). \qquad (32)$$

The rf-response in real frequency is then given by

$$I(\omega_L) = \Omega^2 \int_\mathbf{k}\int_0^{\mu_i-\mu_f+\omega_L}\frac{d\nu}{2\pi} \times A_f(\mathbf{k},\nu)\,A_i(\mathbf{k},\nu+\mu_f-\mu_i-\omega_L) \qquad (33)$$

where $\mu_i - \mu_f + \omega_L > 0$.

In Eq. (33) the initial-state spectral function A_i is probed for negative frequencies only. Hence, there is no rf-response for the pure polaron problem at vanishing density and chemical potential $\mu_\downarrow^{(0)}$. In the experiment one has, however, a small but finite concentration $x = n_\downarrow/n_\uparrow$ of $\downarrow$-fermions which leads to an observable rf-response. In order to describe the experimental situation we therefore need a calculation for a finite minority ($\downarrow$) density characterized by a chemical potential $\mu_i = \mu_\downarrow > \mu_\downarrow^{(0)}$. Within the fRG framework such a calculation requires the regulator $R_\downarrow$ in Eq. (10) to be adjusted in order to cope with the finite Fermi surface of $\downarrow$-fermions which complicates the computation. Fortunately, our calculation for the polaron problem shows that for negative scattering length, where the polaron is the ground state and decay processes do not matter, the fRG results are in excellent agreement with the results from a non-self-consistent T-matrix approach. We may therefore use this approach instead of a full-feedback fRG for the calculation of the imbalanced Fermi gas of finite densities $n_\uparrow$ and $n_\downarrow$ in order to determine the initial-state spectral function. The non-self-consistent calculation was also done by Punk and Zwerger [46] and is obtained in our fRG formulation by simply switching off the feedback of the $\downarrow$-atom self-energy into the molecule flow.

Because the occupation of $\downarrow$-atoms is small only the low-momentum modes are relevant. The $\downarrow$-atoms form a

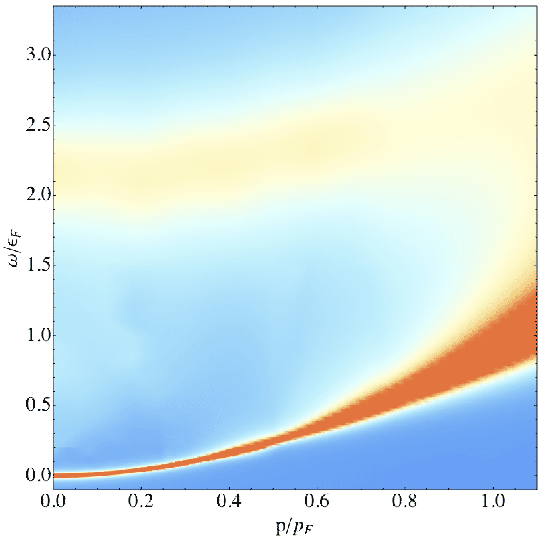

FIG. 12: (color online). Full momentum and frequency dependence of the polaron spectral function $A_\downarrow(\omega, \mathbf{p})$ at unitarity $(k_F a)^{-1} = 0$.

degenerate Fermi gas of polaronic quasi-particles and the spectral function can be approximated by [16]

$$A_i(\omega, \mathbf{p}) = 2\pi Z_i \, \delta\Big(\omega - \frac{\mathbf{p}^2}{2m^*_\downarrow} + \Delta\Big), \tag{34}$$

where Z_i is the residue and $m^*_\downarrow$ is the effective mass of the impurity atoms. Δ determines the impurity concentration x.

We have calculated the parameters $m^*_\downarrow$, Z_i, and Δ as functions of $(k_F a)^{-1}$ via the non-feedback (non-self-consistent T-matrix) calculation. μ_i is determined self-consistently to ensure the correct impurity density. Inserting the spectral function Eq. (34) into the susceptibility (33) we obtain for the rf-response

$$I(\omega_L) = \frac{\Omega^2 Z_i}{2\pi^2} \int_0^{\sqrt{2m^*_\downarrow \Delta}} dk \mathbf{k}^2 \times A_f\Big(\mathbf{k}, \mu_i - \mu_f + \omega_L - \Delta + \frac{\mathbf{k}^2}{2m^*_\downarrow}\Big). \tag{35}$$

For the final state $|f\rangle$ we use the spectral function obtained in section IV from the full fRG calculation. In Fig. 12 we show an example of the full final-state spectral function in dependence of frequency and momentum which enters the momentum sum in Eq. (35). One can clearly discern the broadening of the attractive polaron branch at larger momenta, as well as the broad repulsive branch at higher frequencies. A similar feature appears in the spectral function for the balanced Fermi gas above T_c

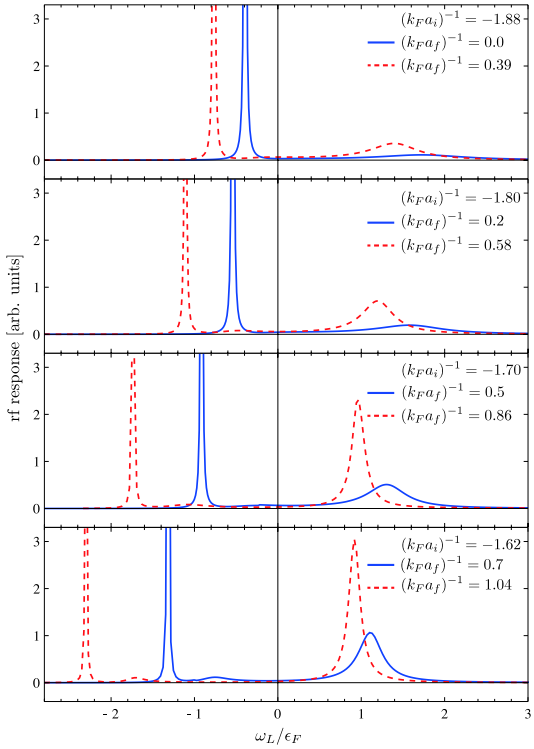

FIG. 13: (color online). rf-spectra $I(\omega_L)$ for minority species $|1\rangle$ (solid blue lines) and minority species $|3\rangle$ (dashed red lines). The interaction parameters correspond to the four magnetic field values marked in Fig. 11, and listed in Table II: (a) top—(d) bottom.

as calculated by Haussmann *et al.* [48]. The fermionic spectral functions and rf-spectra in this work were determined using state-of-the-art *self-consistent* T-matrix (2PI) approximations and form the basis for a full linear response calculation including vertex corrections [50].

Initially, the gas is prepared in a $|1\rangle$ and $|3\rangle$ mixture, and both states can serve as minority or majority species, for example, $|\uparrow\rangle = |3\rangle$ and $|\downarrow\rangle = |1\rangle$ such that $|i\rangle = |1\rangle$ and $|f\rangle = |2\rangle$. The initial occupation of the minority $|\downarrow\rangle$ states is small and for our numerical calculation we use $x = n_\downarrow/n_\uparrow = 0.01$. The energy scale is set by the Fermi momentum of the majority species $k_{F\uparrow} = 0.00015\, a_0^{-1}$ as appropriate for the MIT experiment [6]. We calculate the rf-spectra at four values of the magnetic field indicated as stars in Fig. 11, and listed in Table II. The resulting spectra are shown in Fig. 13: the solid blue lines indicate the response for minority species $|1\rangle$, while the dashed red lines correspond to minority species $|3\rangle$. In the latter case the sign of the frequency offset ω_L is changed because the state $|3\rangle$ is energetically above the final state.

The position of the sharp attractive polaron peak at

negative frequency offset ω_L shifts with the interaction parameter $(k_F a_f)^{-1}$ in accordance with the energy spectrum Fig. 3. One observes that the attractive polaron loses quasi-particle weight on the molecular side, cf. Fig. 7. In contrast, the repulsive polaron branch gains quasi-particle weight toward the molecular side, and the respective peak in the rf-spectra becomes both larger and narrower, and one can read of the increasing lifetime.

The spectra in Fig. 13 are convolved with a sinc function $\mathrm{sinc}^2(\omega T/2)$ which gives the response to an rf-pulse with a rectangular profile of length $T = 20\,\mathrm{ms}$ [48]. While our curves are computed for zero temperature, a finite temperature $\sim 0.01\,T_F$ would lead only to a slight broadening of the experimental rf-peaks. The broadening of the attractive polaron due to the finite lifetime on the molecular side $(k_F a_f)^{-1} > (k_F a_c)^{-1}$, however, is too small to be resolved. Note that we have included both final-state and initial-state interaction in our calculation: the knowledge of the spectral function for the initial state allows for a detailed study of the final-state spectral function.

VI. DISCUSSION

We have presented a new computational method to solve the non-perturbative, exact renormalization group equation (3) and have demonstrated its efficiency for the Fermi polaron problem as a specific example. The inclusion of the full frequency and momentum dependence of the propagators opens up new perspectives to apply the functional renormalization group to problems where the detailed dynamics of the relevant degrees of freedom becomes important [51]. In particular, the method draws its strength from the possibility to successively bosonize further channels of the interaction via additional auxiliary fields (Hubbard-Stratonovich transformation) [52]. In this way one can partially capture the complicated analytical structure of higher-order vertex functions $\Gamma^{(n)}$, including possible quasi-particle poles and branch cuts, as we have explicitely shown for the s-wave scattering channel in the polaron problem. In combination with the recently developed flowing rebosonization technique [41] our numerical method can be extended to also incorporate re-emerging vertices. Our approach complements the proposal for bosons [29] and additionally includes fermions.

For the Fermi polaron problem we achieve a unified description of many dynamical effects beyond thermodynamics. We verify the non-trivial power-law scaling of decay rates [17] and determine the properties of the repulsive polaron with a method beyond the non-self-consistent T-matrix approximation [20, 21]. This is of value in the ongoing debate about the possible occurrence of ferromagnetism in ultracold Fermi gases with short-range interactions [20–26]. The polaron problem sheds light on this question in the limit of strong population imbalance. For the repulsive polaron we find the critical interactions strength $k_F a = 1.57$ from our numerical data (Fig. 3). Going to a finite density of $\downarrow$-fermions is straightforward within the fRG and involves only a slight modification of the regulator of the $\downarrow$-fermions (10) as long as no spontaneous symmetry breaking occurs. By continuity we can infer that the repulsive branch will remain to exist for small but finite $\downarrow$-population and will exceed the critical energy ϵ_F for the presumed onset of saturated ferromagnetism. It is an open question whether for larger impurity concentrations the repulsive branch is so strongly renormalized that saturated ferromagnetism can be ruled out [26], or whether competition with molecule formation may preclude the observation of ferromagnetic domains [25]. Answering these questions will require a full non-equilibrium calculation.

There has been much theoretical progress on the repulsive Fermi gas with short-range interactions, but relatively few experiments have been completed. While the repulsive ^{3}He Fermi gas has been studied extensively in experiment, it is not dilute and has a large repulsive hard-core potential [53]. In contrast, ultracold Fermi gases offer the realization of a proper contact interaction of tunable strength. We predict rf-transition rates for the repulsive branch and propose a possible route to measure these excited states in a ^{6}Li Fermi gas. This is a challenging problem because the final repulsive polaron state is highly unstable. One possible approach could involve fast tomographic imaging similar to the MIT experiment [6], another might be to measure the loss in the final state which is expected to scale with the rf-transition rate for a constant rf-pulse time but may be suppressed by the quantum Zeno effect [44]. Hence, the possible observation of the repulsive polaron represents not only a test of theoretical predictions but poses an interesting challenge touching several aspects of many-body physics.

Acknowledgments

We wish to thank M. Barth, N. Dupuis, T. Hyodo, S. Jochim, N. Kaiser, S. Moroz, M. Punk, S. Rath, and W. Zwerger for many useful discussions and P. Julienne, N. Prokof'ev, B. Svistunov, and M. Zwierlein for kindly providing their data for comparison. Part of this work was supported by the DFG within the Forschergruppe 801.

Appendix A: Derivative expansion

In this appendix we qualitatively study the polaron-to-molecule transition using a simple approximation for the renormalized Green's functions $G_{\downarrow,k}$ and $G_{\phi,k}$. As we have seen, $G_{\downarrow,k}$ and $G_{\phi,k}$ generally develop a complicated frequency and momentum $(\omega, \mathbf{p})$ dependence. Here, we will use an expansion in small frequencies and momenta (derivative or gradient expansion) which allows for an analytical evaluation of the loop integrals on the right-hand

side of the flow equation (8). The derivative expansion proves to be a good approximation if one is interested in physics determined by the structure of the Green's functions close to their poles as, for example, in the description of phase transitions and critical phenomena [32]. In the derivative expansion the dependence of the inverse propagators $P_{\downarrow/\phi,k}(\omega,\mathbf{p})$ on the RG scale k is approximated by

$$\begin{aligned} P_{\downarrow,k}(\omega,\mathbf{p}) &= A_{\downarrow,k}\cdot(-i\omega+\mathbf{p}^2)+m^2_{\downarrow,k} \\ P_{\phi,k}(\omega,\mathbf{p}) &= A_{\phi,k}\cdot(-i\omega+\mathbf{p}^2/2)+m^2_{\phi,k}. \end{aligned} \tag{A1}$$

In this approximation, which is similar to the one used in the Wilsonian RG approach to the polaron problem [15], we assume that the renormalization of the frequency and momentum coefficients is given by common wave-function renormalizations $A_{\downarrow,k}$ and $A_{\phi,k}$, respectively, which in turn are related to the quasi-particle weights via $Z_{\downarrow/\phi}=A^{-1}_{\downarrow/\phi}$. The flowing gap terms $m^2_{\downarrow,k}$ and $m^2_{\phi,k}$ are related to the flowing static self-energy via Eq. (11).

From equation (8) one can derive the flow equations for the four running couplings $A_{\downarrow,k}$, $A_{\phi,k}$, $m^2_{\downarrow,k}$, and $m^2_{\phi,k}$. The $\uparrow$-fermions are not renormalized, $A_{\uparrow,k}=1$ and $m^2_{\uparrow,k}=-\mu_\uparrow$. With the sharp cutoff (10), the frequency as well as the momentum integrations can be performed analytically. The resulting flow equations read

$$\begin{aligned} \partial_k A_\downarrow &= -\frac{2h^2k}{\pi^2 A_\phi}\theta(\mu_\uparrow-2k^2)\Big[\frac{\sqrt{\mu_\uparrow-k^2}}{(k^2+\mu_\uparrow+2m^2_\phi/A_\phi)^2} \\ &\quad +\frac{k}{(-k^2+2\mu_\uparrow+2m^2_\phi/A_\phi)^2}\Big] \\ \partial_k m^2_\downarrow &= \frac{h^2k}{\pi^2 A_\phi}\theta(\mu_\uparrow-2k^2)\Big[\frac{\sqrt{\mu_\uparrow-k^2}}{k^2+\mu_\uparrow+2m^2_\phi/A_\phi} \\ &\quad +\frac{k}{-k^2+2\mu_\uparrow+2m^2_\phi/A_\phi}\Big] \\ \partial_k A_\phi &= -\frac{h^2k}{2\pi^2 A_\downarrow}\,\frac{\sqrt{\mu_\uparrow+k^2}}{(2k^2+\mu_\uparrow+m^2_\downarrow/A_\downarrow)^2} \\ \partial_k m^2_\phi &= \frac{h^2k}{2\pi^2 A_\downarrow}\,\frac{\sqrt{\mu_\uparrow+k^2}}{(2k^2+\mu_\uparrow+m^2_\downarrow/A_\downarrow)}. \end{aligned} \tag{A2}$$

The initial conditions for this system of differential equations (A2) are specified at the UV scale $k=\Lambda$. We note that the derivative expansion (A1) of the molecule propagator $P_{\phi,k}(\omega,\mathbf{p})$ cannot account for the correct vacuum scattering amplitude (5), because the term iq is rooted in the non-analytical structure of the molecule propagator (7). We therefore focus only on the correct calculation of the scattering length a for $q=0$, which leads to the infrared condition $(m^{\rm vac}_{\phi,k=0})^2=-h^2/(8\pi a)$ for $\mu_\downarrow=\mu_\uparrow=0$. In this case of two-body physics $P_{\downarrow,k}$ is not renormalized, $A_{\downarrow,k}=1$ and $m^2_{\downarrow,k}=0$, and the differential equations for $A_{\phi,k}$ and $m^2_{\phi,k}$ decouple and can be solved analytically. The integration of (A2) in the vacuum limit yields

$$(m^{\rm vac}_{\phi,k=0})^2 = m^2_{\phi,\Lambda}-\frac{h^2\Lambda}{4\pi^2}. \tag{A3}$$

This leads to the UV condition for the molecule gap,

$$m^2_{\phi,\Lambda}=\frac{h^2}{8\pi}(2\Lambda/\pi-a^{-1}), \tag{A4}$$

which incorporates the correct regularization of the UV divergence Λ in Eq. (A3). At the UV scale the momentum and frequency dependence of $P_{\phi,\Lambda}$ can be neglected due to the large bosonic gap $m^2_{\phi,\Lambda}$, and we set $A_{\phi,\Lambda}=1$.

For a finite density of $\uparrow$-atoms the system of differential equations (A2) is solved numerically. The initial values for the $\downarrow$ propagator are then given by $m^2_{\downarrow,\Lambda}=-\mu_\downarrow$ and $A_{\downarrow,\Lambda}=1$. The down chemical potential $\mu_\downarrow$ is determined in the way discussed in section II. We find that the polaron is indeed the ground state for interaction strengths $(k_Fa)^{-1}<(k_Fa_c)^{-1}$ whereas the molecule becomes the ground state for $(k_Fa)^{-1}>(k_Fa_c)^{-1}$, with $(k_Fa_c)^{-1}=0.96$.

The energy spectrum from the simple derivative expansion is in qualitative agreement and even in rough quantitative agreement with the results obtained from our new numerical method and other theoretical calculations. A drawback of the derivative expansion is that it is impossible to extract a reasonable spectral function from an ansatz of the form (A1) as it only accounts for a single coherent quasi-particle excitation. Neither higher excited states, such as the repulsive polaron, nor the incoherent background, which comprises the major weight for the molecule (cf. section IV), can be captured with this ansatz. Furthermore, although decay processes lead to a finite lifetime of the excited polaron and molecule branches, in the simple approximation (A1) these states have a vanishing decay width. Note that the finite lifetime of excited states can be obtained neither from simple variational wave functions [7] nor from the non-self-consistent T-matrix approach [8]. Their description requires the full self-energy feedback developed in section III.

[1] L. D. Landau, Phys. Z. Sowjetunion **3**, 644 (1933).
[2] N. V. Prokof'ev and B. V. Svistunov, Phys. Rev. B **77**, 020408 (2008); N. V. Prokof'ev and B. V. Svistunov, Phys. Rev. B **77**, 125101 (2008).
[3] A. C. Hewson, *The Kondo problem to heavy fermions* (Cambridge University Press, 1997).
[4] A. Rosch and T. Kopp, Phys. Rev. Lett. **75**, 1988 (1995).
[5] I. Bloch, J. Dalibard, and W. Zwerger, Rev. Mod. Phys. **80**, 885 (2008).
[6] A. Schirotzek, C.-H. Wu, A. Sommer, and M. W. Zwier-

lein, Phys. Rev. Lett. **102**, 230402 (2009).
[7] F. Chevy, Phys. Rev. A **74**, 063628 (2006).
[8] R. Combescot, A. Recati, C. Lobo, and F. Chevy, Phys. Rev. Lett. **98**, 180402 (2007).
[9] R. Combescot and S. Giraud, Phys. Rev. Lett. **101**, 050404 (2008).
[10] M. Punk, P. T. Dumitrescu, and W. Zwerger, Phys. Rev. A **80**, 053605 (2009).
[11] C. Mora and F. Chevy, Phys. Rev. A **80**, 033607 (2009).
[12] R. Combescot, S. Giraud, and X. Leyronas, Europhys. Lett. **88**, 60007 (2009).
[13] M. Ku, J. Braun, and A. Schwenk, Phys. Rev. Lett. **102**, 255301 (2009).
[14] P. Nikolić and S. Sachdev, Phys. Rev. A **75**, 033608 (2007).
[15] K. B. Gubbels and H. T. C. Stoof, Phys. Rev. Lett. **100**, 140407 (2008).
[16] C. Lobo, A. Recati, S. Giorgini, and S. Stringari, Phys. Rev. Lett. **97**, 200403 (2006).
[17] G. M. Bruun and P. Massignan, Phys. Rev. Lett. **105**, 020403 (2010).
[18] R. F. Bishop, Ann. Phys. (N.Y.) **78**, 391 (1973).
[19] T. D. Lee and C. N. Yang, Phys. Rev. **105**, 1119 (1957); K. Huang and C. Yang, Phys. Rev. **105**, 767 (1957).
[20] X. Cui and H. Zhai, Phys. Rev. A **81**, 041602 (2010).
[21] P. Massignan and G. M. Bruun (2011), preprint arXiv:1102.0121.
[22] G. B. Jo, Y. R. Lee, J. H. Choi, C. A. Christensen, T. H. Kim, J. H. Thywissen, D. E. Pritchard, and W. Ketterle, Science **325**, 1521 (2009).
[23] G. J. Conduit, A. G. Green, and B. D. Simons, Phys. Rev. Lett. **103**, 207201 (2009); G. J. Conduit and E. Altman (2009), Phys. Rev. A **83**, 043618 (2011); G. J. Conduit and B. D. Simons, Phys. Rev. A **79**, 053606 (2009); A. Recati and S. Stringari, Phys. Rev. Lett. **106**, 080402 (2011); S. Zhang and T.-L. Ho (2011), preprint arXiv:1102.5687.
[24] S. Pilati, G. Bertaina, S. Giorgini, and M. Troyer, Phys. Rev. Lett. **105**, 030405 (2010).
[25] D. Pekker, M. Babadi, R. Sensarma, N. Zinner, L. Pollet, M. W. Zwierlein, and E. Demler, Phys. Rev. Lett. **106**, 050402 (2011).
[26] M. Barth and W. Zwerger (2011), Ann. Phys. (NY) in press, preprint arXiv:1101.5594.
[27] A. Bulgac and M. McNeil Forbes, Phys. Rev. A **75**, 031605 (2007).
[28] C. Wetterich, Phys. Lett. B **301**, 90 (1993).
[29] J. P. Blaizot, R. Méndez-Galain, and N. Wschebor, Phys. Lett. B **632**, 571 (2006).
[30] S. Weinberg, Phys. Rev. **137**, B672 (1965).
[31] D. Lurié and A. J. Macfarlane, Phys. Rev. **136**, B816 (1964).
[32] J. Berges, N. Tetradis, and C. Wetterich, Phys. Rep. **363**, 223 (2002).
[33] M. Salmhofer and C. Honerkamp, Prog. Theor. Phys. **105**, 1 (2001); W. Metzner, Prog. Theor. Phys. Suppl. **160**, 58 (2005); B. Delamotte (2007), preprint arXiv:cond-mat/0702365; O. J. Rosten (2010), preprint arXiv:1003.1366.
[34] J. Pawlowski, Ann. Phys. (N.Y.) **322**, 2831 (2007).
[35] M. C. Birse, B. Krippa, J. A. McGovern, and N. R. Walet, Phys. Lett. B **605**, 287 (2005); S. Diehl, H. Gies, J. M. Pawlowski, and C. Wetterich, Phys. Rev. A **76**, 021602 (2007); S. Diehl, H. Gies, J. M. Pawlowski, and C. Wetterich, Phys. Rev. A **76**, 053627 (2007); L. Bartosch, P. Kopietz, and A. Ferraz, Phys. Rev. B **80**, 104514 (2009).
[36] S. Floerchinger, M. Scherer, S. Diehl, and C. Wetterich, Phys. Rev. B **78**, 174528 (2008).
[37] S. Diehl, H. C. Krahl, and M. Scherer, Phys. Rev. C **78**, 034001 (2008).
[38] S. Liao, J. Polonyi, and M. Strickland, Nucl. Phys. B **567**, 493 (2000); D. F. Litim, Phys. Lett. B **486**, 92 (2000).
[39] A. A. Abrikosov, L. P. Gorkov, and I. E. Dzyaloshinski, *Methods of quantum field theory in statistical physics* (Dover, 1975).
[40] A. A. Katanin, Phys. Rev. B **70**, 115109 (2004).
[41] H. Gies and C. Wetterich, Phys. Rev. D **65**, 065001 (2002); S. Floerchinger and C. Wetterich, Phys. Lett. B **680**, 371 (2009); S. Floerchinger, Eur. Phys. J. C **69**, 119 (2010).
[42] G. B. Partridge, K. E. Strecker, R. I. Kamar, M. W. Jack, and R. G. Hulet, Phys. Rev. Lett. **95**, 020404 (2005).
[43] M. Bartenstein *et al.*, Phys. Rev. Lett. **94**, 103201 (2005).
[44] T. Lompe, T. B. Ottenstein, F. Serwane, A. N. Wenz, G. Zürn, and S. Jochim, Science **330**, 940 (2010).
[45] S. Nakajima, M. Horikoshi, T. Mukaiyama, P. Naidon, and M. Ueda, Phys. Rev. Lett. **106**, 143201 (2011).
[46] M. Punk and W. Zwerger, Phys. Rev. Lett. **99**, 170404 (2007).
[47] M. Punk, Ph.D. thesis, Technical University Munich (2009).
[48] R. Haussmann, M. Punk, and W. Zwerger, Phys. Rev. A **80**, 063612 (2009).
[49] P. Pieri, A. Perali, and G. C. Strinati, Nature Phys. **5**, 736 (2009).
[50] T. Enss, R. Haussmann, and W. Zwerger, Ann. Phys. (N.Y.) **326**, 770 (2011).
[51] C. Honerkamp, H. C. Fu, and D. H. Lee, Phys. Rev. B **75**, 014503 (2007).
[52] C. Husemann and M. Salmhofer, Phys. Rev. B **79**, 195125 (2009).
[53] P. Wölfle and D. Vollhardt, *The Superfluid Phases of Helium 3* (Taylor and Francis, 1990).
[54] While the solution of the un-truncated flow equation (3) does not depend on the particular choice of the cutoff function, the results from the truncated flow become cutoff dependent. We have implemented a class of smooth cutoff functions interpolating between a k^2 and the sharp cutoff and found minimal sensitivity [34, 38] and also best agreement with Monte Carlo data for the limit of the sharp cutoff.

Fermi polarons in two dimensions

Richard Schmidt and Tilman Enss
Physik Department, Technische Universität München, D-85747 Garching, Germany

Ville Pietilä and Eugene Demler
Physics Department, Harvard University, Cambridge, Massachusetts 02138, USA
(Dated: February 8, 2012)

We theoretically analyze inverse radiofrequency (rf) spectroscopy experiments in two-component Fermi gases. We consider a small number of impurity atoms interacting strongly with a bath of majority atoms. In two-dimensional geometries we find that the main features of the rf spectrum correspond to an attractive polaron and a metastable repulsive polaron. Our results suggest that the attractive polaron has been observed in a recent experiment [Phys. Rev. Lett. **106**, 105301 (2011)].

PACS numbers: 67.85.Lm, 68.65.-k, 03.65.Ge, 32.30.Bv

The behavior of a mobile impurity (polaron) interacting strongly with a bath of particles is one of the basic many-body problems studied in condensed matter physics [1–4]. With the advent of ultracold atomic gases [5], the Fermi polaron problem in which a single spin-↓ atom interacts strongly with a Fermi sea of spin-↑ atoms, has become a subject of intensive research [6]. In three dimensions it was found that the polaron state splits into two branches, a low-energy state interacting attractively with the bath of fermions, and the repulsive polaron, which is an excited, metastable state [7–9]. In this way the polaron exemplifies a more general paradigm of a many-body system driven into a nonequilibrium state where a small number of high energy excitations interact strongly with the surrounding degrees of freedom [10, 11]. The polaron is the limiting case of a Fermi gas with strong spin imbalance, and the repulsive polaron provides insight into the question whether a quenched, repulsive Fermi gas may undergo a transition to a ferromagnetic state even though it is highly excited [7–9, 12, 13]. Similarly, the ground state of the polaron problem has important implications for the phase diagram of a strongly interacting Fermi gas [14–16].

It is a key question how many-body properties are affected by reduced dimensionality, and the polaron is a case in point. The combination of optical lattices and Feshbach resonances [5] provides a unique setting to experimentally study strongly interacting low dimensional systems using ultracold atoms [17, 18]. Recent advances in radiofrequency (rf) spectroscopy afford to measure energy spectra [14] and give access to excited states as well as full spectral functions using momentum resolved rf [19, 20]. So far, only the ground state of the two-dimensional polaron problem has been investigated theoretically [21–23] with the focus on a possible polaron to molecule transition. This is similar to the 3D situation where for strong interactions it becomes energetically favorable for the impurity to form a molecular bound state [24]. The structure of high energy excitations and the experimental polaron signatures in rf spectroscopy have remained open questions which we address in this work. We derive the spectral functions of both the molecule and the impurity atom (Fig. 1 left) and find that the impurity state splits into the attractive and the repulsive branch. We compute rf spectra for homogeneous 2D systems (Fig. 1 right) as well as for the experimentally

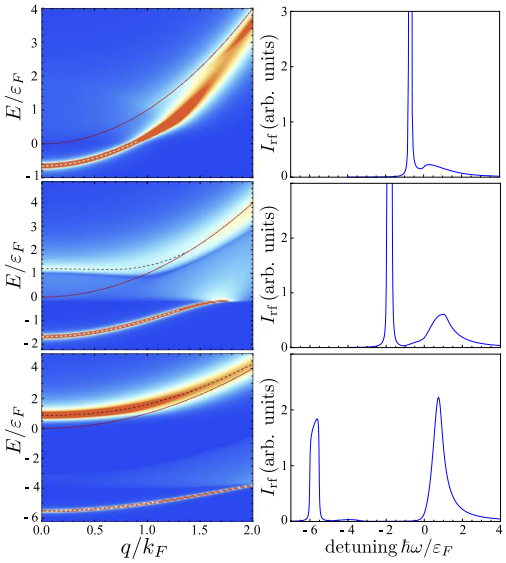

FIG. 1: (color online). **Left panels:** spectral function $\mathcal{A}_\downarrow(q, E-\mu_\downarrow)$ for impurity atoms interacting with a 2D Fermi sea. Red lines indicate the free particle dispersion and white (black) dashed lines mark the dispersion of the attractive (repulsive) polaron. **Right panels:** corresponding rf spectra illustrating how weight is shifted from the attractive polaron state (peak at negative frequencies) to the new repulsive polaron state at positive frequencies. The two-body bound state energy is (a) $\varepsilon_B/\varepsilon_F = 0.1$, (b) $\varepsilon_B/\varepsilon_F = 1$, (c) $\varepsilon_B/\varepsilon_F = 5$.

relevant quasi-2D geometries (Fig. 4). Finally, we argue that our calculation provides an alternative explanation of the recent experiment by Fröhlich et al. [17] in terms of the polaron picture.

A quasi-2D geometry can be realized experimentally using an optical lattice in one direction with associated trapping frequency ω_z. In this case, a confinement induced two-body bound state exists for an arbitrarily weak attractive interaction [25–27] with binding energy $\varepsilon_B > 0$. The spatial extent of the bound state is related to the 2D scattering length given by $a_{2D} = \hbar/\sqrt{m\varepsilon_B} > 0$. In the weak coupling BCS regime of small 3D scattering length $a_{3D} < 0$ [5] these dimers are large and weakly bound ($\varepsilon_B \ll \hbar\omega_z$); in the BEC limit of small $a_{3D} > 0$, the weakly interacting molecules are too tightly bound to feel the confinement ($\varepsilon_B \sim \hbar^2/(ma_{3D}^2) \gg \hbar\omega_z$). Around the Feshbach resonance ($a_{3D}^{-1} = 0$) there is a strong coupling regime where the binding energy attains the universal value $\varepsilon_B = 0.244\,\hbar\omega_z$ [5, 27].

At finite densities the majority atoms form a Fermi gas with Fermi energy ε_F and the two-body scattering is replaced by many-body scattering which gives rise to important qualitative differences, most notably the emergence of two polaron branches. Spectral weight is shifted from the attractive to the repulsive polaron in the non-perturbative regime where the interaction parameter $1/\ln(\varepsilon_B/2\varepsilon_F)$ diverges [28] and the confinement induced resonance appears [5, 29].

We consider a two-component 2D Fermi gas in the limit of extreme spin imbalance, described by the grand canonical Hamiltonian

$$H = \sum_{\boldsymbol{k}\sigma} (\varepsilon_{\boldsymbol{k}\sigma} - \mu_\sigma) c^\dagger_{\boldsymbol{k}\sigma} c_{\boldsymbol{k}\sigma} + \frac{g}{A} \sum_{\boldsymbol{k}\boldsymbol{k}'\boldsymbol{q}} c^\dagger_{\boldsymbol{k}\uparrow} c^\dagger_{\boldsymbol{k}'\downarrow} c_{\boldsymbol{k}'-\boldsymbol{q}\downarrow} c_{\boldsymbol{k}+\boldsymbol{q}\uparrow},$$

with single-particle energies $\varepsilon_{\boldsymbol{k}\sigma} = \boldsymbol{k}^2/2m_\sigma$ for species σ ($\hbar = 1$), chemical potentials μ_σ and system area A. Having in mind the experiment of Ref. [17], we focus on the case of equal masses $m_\uparrow = m_\downarrow = m$. Generalizations to mass imbalanced situations are straightforward [21, 22]. In the low-energy limit the attractive s-wave contact interaction g can act only between different species due to the Pauli principle. The majority atoms are not renormalized by the presence of a single impurity with finite mass such that $\mu_\uparrow = \varepsilon_F = k_F^2/2m$ at zero temperature. The chemical potential $\mu_\downarrow$ of the impurity atom is determined such that the impurity state $|\downarrow\rangle$ has vanishing macroscopic occupation. Furthermore, $\mu_\downarrow$ is negative due to the attractive interaction between $\uparrow$ and $\downarrow$ atoms.

Dressed molecule. The two-body scattering of a spin-$\uparrow$ atom and a spin-$\downarrow$ atom is described by the exact two-body T-matrix [26]

$$T_0(E) = \frac{4\pi/m}{\ln(\varepsilon_B/E) + i\pi}\,. \tag{1}$$

The pole of the T-matrix at $E = -\varepsilon_B$ corresponds to the molecular bound state, and the associated vacuum scattering amplitude for two particles with relative momenta $\boldsymbol{k}$ and $-\boldsymbol{k}$ in the center-of-mass frame is $f(k = |\mathbf{k}|) = mT_0(2\varepsilon_{\boldsymbol{k}}) = 4\pi/[\ln(1/k^2a_{2D}^2) + i\pi]$ [5].

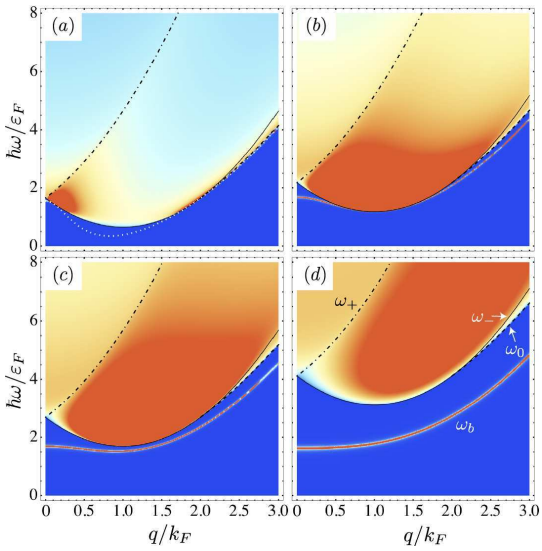

FIG. 2: (color online). Molecular spectral function $\mathcal{A}_{\rm mol}(\boldsymbol{q},\omega)$ for different values of the two-body binding energy $\varepsilon_B/\varepsilon_F$: (a) 0.1, (b) 0.5, (c) 1.0, (d) 2.5. The dashed lines mark the log continuum ω_0, dash-dotted and solid the root continuum $\omega_\pm$.

In the presence of a Fermi sea of spin-$\uparrow$ atoms, the molecular state is dressed by fluctuations and described by the many-body T-matrix. This can be calculated in the Nozieres–Schmitt-Rink approach [30], as done in the 2D case by Engelbrecht and Randeria [31, 32]. We generalize these results to the case of spin imbalance and obtain

$$T^{-1}(\boldsymbol{q},\omega) = T_0^{-1}(\omega + i0 + \mu_\uparrow + \mu_\downarrow - \varepsilon_{\boldsymbol{q}}/2) + \int \frac{d^2k}{(2\pi)^2} \frac{n_F(\varepsilon_{\boldsymbol{k}} - \mu_\uparrow) + n_F(\varepsilon_{\boldsymbol{k}+\boldsymbol{q}} - \mu_\downarrow)}{\omega + i0 + \mu_\uparrow + \mu_\downarrow - \varepsilon_{\boldsymbol{k}} - \varepsilon_{\boldsymbol{k}+\boldsymbol{q}}}, \tag{2}$$

with the Fermi function $n_F(\varepsilon)$. At zero temperature where $\mu_\uparrow = \varepsilon_F$ and $\mu_\downarrow < 0$, we obtain an analytical expression for the many-body T-matrix

$$T(\boldsymbol{q},\omega) = T_0\Big(\tfrac{1}{2}z \pm \tfrac{1}{2}\sqrt{(z-\varepsilon_{\boldsymbol{q}})^2 - 4\varepsilon_F\varepsilon_{\boldsymbol{q}}}\Big) \tag{3}$$

with $z = \omega + i0 - \varepsilon_F + \mu_\downarrow$ and $\pm = \mathrm{sgn}\,\mathrm{Re}(z - \varepsilon_{\boldsymbol{q}})$. Due to the constant density of states in 2D the many-body T-matrix can be expressed as the two-body T-matrix with the argument shifted by Pauli blocking. The molecular spectral function $\mathcal{A}_{\rm mol}(\boldsymbol{q},\omega) = -2\,\mathrm{Im}\,T(\boldsymbol{q},\omega)$ is shown in Fig. 2 for several values of the interaction strength parametrized by the two-body binding energy ε_B. One

observes a bound state peak at low energies and the particle-particle continuum at higher energies.

The continuum of dissociated molecules arises mathematically from the branch cut of the square root (3) in the region $\omega_-(q) < \omega < \omega_+(q)$, $\omega_\pm = \varepsilon_F(1 \pm q/k_F)^2 - \mu_\downarrow$ (dash-dotted/solid lines), as well as from the branch cut of the logarithm (1) for $\omega > \omega_+(q)$ and for $\omega_0 = \varepsilon_{\boldsymbol{q}}/2 - \varepsilon_F - \mu_\downarrow < \omega < \omega_-(q)$ if $q > 2k_F$ (dashed lines).

The bound state pole of the many-body T-matrix has the dispersion relation [21]

$$\omega_b(\boldsymbol{q}) = \frac{\varepsilon_{\boldsymbol{q}}/2(\varepsilon_{\boldsymbol{q}}/2 - \varepsilon_F) + \varepsilon_B(\varepsilon_F - \varepsilon_B)}{\varepsilon_{\boldsymbol{q}}/2 + \varepsilon_B} - \mu_\downarrow \qquad (4)$$

which changes qualitatively with the two-body binding energy ε_B (see Fig. 2): for $\varepsilon_B < 2\varepsilon_F$ the bound state has minimum energy at a finite wave vector with positive effective mass $m^*/m = (2 - 2/k_F a_{2D})^{-1}$ [33].

Polaron and quasi-particle properties. The impurity atom is dressed with virtual molecule-hole excitations and becomes a quasi-particle with self-energy [32–34]

$$\Sigma_\downarrow(\boldsymbol{q}, \omega) = \int_{k<k_F} \frac{d^2k}{(2\pi)^2}\, T(\boldsymbol{k} + \boldsymbol{q}, \varepsilon_{\boldsymbol{k}} - \mu_\uparrow + \omega)\,, \qquad (5)$$

which leads to the same ground state energy as a variational ansatz [35]. Here we have used the fact that in the zero-temperature polaron problem the molecule has vanishing macroscopic occupation. Hence it has spectral weight only at positive frequencies (cf. Fig. 2) where the Bose distribution vanishes. We perform the integral in (5) numerically and obtain the spectral function of impurity atoms

$$\mathcal{A}_\downarrow(\boldsymbol{q}, \omega) = -2\,\mathrm{Im}[\omega + i0 + \mu_\downarrow - \varepsilon_{\boldsymbol{q}} - \Sigma_\downarrow(\boldsymbol{q}, \omega)]^{-1}. \qquad (6)$$

The frequency and momentum dependence of the spectral function is shown in Fig. 1 (left panel) for three values of the interaction strength. In Fig. 3 we display the zero-momentum spectral function $\mathcal{A}_\downarrow(q = 0, E - \mu_\downarrow)$ versus interaction parameter $\eta = \ln(k_F a_{2D}) = -\ln(\varepsilon_B/2\varepsilon_F)/2$. In both figures we set the reference energy to the free atom threshold by subtracting the chemical potential $\mu_\downarrow$.

At weak binding $\varepsilon_B \ll \varepsilon_F$ (Fig. 1a) the attractive polaron is a well-defined quasi-particle at small momenta but for $q \gtrsim k_F$ it scatters off virtual molecules and acquires a large decay width. For intermediate binding (Fig. 1b) a new repulsive polaron state appears at positive energies. It is a metastable state with broad decay width, and it is shifted to higher energy due to the repulsive interaction with the Fermi sea of spin-↑ atoms. The dispersion of the repulsive polaron has a minimum at finite momentum $q \sim k_F$ reflecting a similar feature in the molecular spectral function (Fig. 2c); for larger momenta it approaches the free particle dispersion. Finally, for strong binding (Fig. 1c) both polaron branches are well separated and the repulsive polaron becomes an increasingly long-lived and stable quasi-particle. Between the attractive and the repulsive polaron branches appears the molecule-hole continuum (see also Fig. 3). Its spectral weight is small in the case of a broad Feshbach resonance studied here, but it is enhanced for narrow resonances by an admixture of closed channel molecules [8].

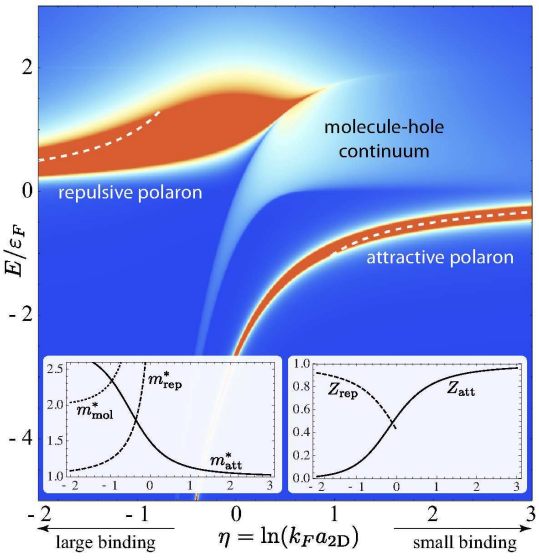

FIG. 3: (color online). Polaron spectral function $\mathcal{A}_\downarrow(q = 0, E - \mu_\downarrow)$ versus the interaction parameter η. The dashed lines indicate the perturbation theory of Ref. [28]. **Left inset:** effective mass m^*/m of the attractive and repulsive polaron as well as the molecule. **Right inset:** crossover of the quasi-particle weight Z from the repulsive to the attractive polaron.

It is instructive to see how the quasi-particle properties of the polaron change as the interaction parameter η is varied. The right inset of Fig. 3 shows a continuous crossover where the quasi-particle weight $Z = 1/[1 - \partial_\omega \Sigma(\boldsymbol{q} = 0, \omega)]$ evaluated at the quasi-particle pole, shifts from the attractive to the repulsive polaron branch: for small binding ($\eta > 0$), the attractive polaron is the dominant excitation and the weight is gradually transferred toward the repulsive branch for increasing binding ($\eta < 0$). This crossover is also reflected in the effective mass m^*/m (Fig. 3 left inset). Our strong coupling calculation reproduces the perturbative results [28] for the attractive and repulsive polaron energies in the weak and strong binding limits (dashed lines in Fig. 3).

Radiofrequency spectroscopy. The spectral properties of the imbalanced Fermi gas can be accessed experimentally using rf spectroscopy. We assume that an rf pulse is used to drive atoms from an initial state $|i\rangle$ to an initially empty final state $|f\rangle$. We choose the final state to be strongly interacting with a bath of a third species $|\uparrow\rangle$ such that $|f\rangle$ is in fact the impurity state, $|f\rangle = |\downarrow\rangle$.

This inverse rf procedure interchanges the roles of $|i\rangle$ and $|f\rangle$ with respect to Ref. [14]; it has been proposed in Refs. [8, 9] and realized in the experiment by Fröhlich et al. [17].

Within linear response theory, the rf transition rate is given by [36]

$$I_{\rm rf}(\omega_{\rm rf}) = -2\Omega_{\rm rf}^2 \,{\rm Im}\,\chi^R(-\omega_{\rm rf} - \mu_i + \mu_f) \qquad (7)$$

where $\Omega_{\rm rf}$ is the Rabi frequency, $\omega_{\rm rf}$ the detuning of the rf photon from the bare transition frequency and $\mu_{i(f)}$ the initial (final) state chemical potential. The retarded correlation function χ^R can be computed from the corresponding time-ordered correlation function $-i\theta(t-t')\langle[\psi_f^\dagger(\boldsymbol{r},t)\psi_i(\boldsymbol{r},t), \psi_i^\dagger(\boldsymbol{r}',t')\psi_f(\boldsymbol{r}',t')]\rangle$ [34, 37]. In general vertex corrections are crucial [38, 39], but we find that they vanish in the case of negligible initial state interactions as appropriate for the experiment [17]. At $T = 0$, we obtain

$$I_{\rm rf}(\omega_{\rm rf}) = \Omega_{\rm rf}^2 \int_{\varepsilon_{\boldsymbol{q}}<\mu_i} \frac{d^2q}{(2\pi)^2}\, A_\downarrow(\boldsymbol{q}, \omega_{\rm rf} + \varepsilon_{\boldsymbol{q}} - \mu_\downarrow)\,. \qquad (8)$$

The integral in equation (8) is calculated numerically and the resulting rf spectra are shown in Fig. 1 (right panel). The rf probes the final $|\downarrow\rangle$ state spectral function along the free-particle dispersion up to the initial state chemical potential μ_i. As in the experiment [17], we assume a balanced initial state mixture with $\mu_i = \mu_\uparrow$. We find a peak in the rf spectrum once the detuning $\omega_{\rm rf}$ reaches the final state chemical potential $\mu_\downarrow$ ($\mu_\downarrow$ is negative in the polaron problem). The transfer of spectral weight from the attractive to the repulsive polaron can be directly observed in Fig. 1.

Comparison to experiments. In order to relate our results to harmonically confined Fermi gases, we have to connect the strict 2D calculation to the quasi-2D geometry relevant to experiments [5, 27]. Well below the confinement energy $\hbar\omega_z$ where only the lowest transverse mode is occupied, this can be done by replacing ε_B with the exact quasi-2D two-body binding energy. Thus ε_B becomes a function of both the 3D scattering length $a_{\rm 3D}$ and the confinement length $\ell_z = \sqrt{\hbar/m\omega_z}$ ([27], cf. Eq. 82 in [5]).

Recently the quasi-2D geometry has been realized experimentally with a Fermi gas of ^{40}K atoms [17]. Following the inverse rf procedure described above, an initially non-interacting balanced mixture is driven into a strongly interacting final state. As long as its occupation remains small the final state is a Fermi polaron, and our calculation predicts the experimental rf response.

In Fig. 4 we show our trap averaged rf spectra versus magnetic field. We use the experimental parameters of Ref. [17] with $\omega_z = 2\pi \times 80$ kHz, $\omega_\perp = 2\pi \times 125$ Hz, and express $a_{\rm 3D}$ in terms of the magnetic field [5, 40]. We incorporate the radial trapping in the 2D plane using the local density approximation; the local Fermi energy is $\varepsilon_F(r) = \varepsilon_F - m\omega_\perp^2 r^2/2$ with peak Fermi energy $\varepsilon_F = 9$ kHz. Finally, we average over 30 pancakes in the z direction [17].

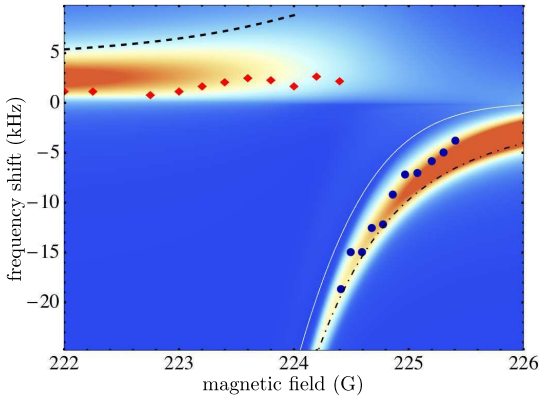

FIG. 4: (color online). Trap averaged rf spectra of a quasi-2D Fermi gas: rf detuning versus magnetic field B. The experimental data points (blue and red diamonds) are taken from Ref. [17]. Also shown are the energy of the repulsive (dashed) and attractive (dash-dotted) polaron as well as the two-body binding energy (solid, white) in a homogeneous system.

We observe that the lower branch of the experimental spectra (circles) agrees well with the attractive polaron picture (Fig. 4) and our calculation provides an alternative interpretation to the two-body bound state (solid line) put forward in Ref. [17]. We note that also the measured frequency shift in 3D as shown in [17] fits the polaron picture [8]. Our results show a second rf peak at positive detunings corresponding to the repulsive polaron. The dashed line in Fig. 4 indicates its quasiparticle energy in the bulk (cf. Fig. 3). As similar for the attractive polaron energy (dash-dotted line) the trap average leads to a significant shift of the rf peaks to lower energies. The experimental data (diamonds) in this magnetic field range agrees qualitatively with our calculation. One possible reason for the remaining discrepancy is the large final state occupation in the experiment.

In conclusion, we studied Fermi polarons in two dimensions which exhibit an attractive and repulsive branch and computed their rf spectra. Additional work is needed to understand discrepancies between theory and experiment for repulsive polarons. As an example, pump and probe experiments in the form of a sequence of two short pulses may shed further light on this issue.

We thank M. Köhl and his group for kindly providing us with their data, and M. Köhl, M. Punk and W. Zwerger for useful discussions. We acknowledge financial support from Harvard-MIT CUA, DARPA OLE program, NSF Grant No. DMR-07-05472, AFOSR Quantum Simulation MURI, AFOSR MURI on Ultracold-Molecules, and the ARO-MURI on Atomtronics (VP and

ED), Academy of Finland (VP) and DFG through FOR 801 (RS and TE).

[1] P. W. Anderson, Phys. Rev. Lett. **18**, 1049 (1967).
[2] T. K. Mitra, A. Chatterjee, and S. Mukhopadhyay, Phys. Rep. **153**, 91 (1987).
[3] J. T. Devreese and A. S. Alexandrov, Rep. Prog. Phys. **72**, 066501 (2009).
[4] L. Radzihovsky and D. E. Sheehy, Rep. Prog. Phys. **73**, 076501 (2010).
[5] I. Bloch, J. Dalibard, and W. Zwerger, Rev. Mod. Phys. **80**, 885 (2008).
[6] F. Chevy and C. Mora, Rep. Prog. Phys. **73**, 112401 (2010).
[7] X. Cui and H. Zhai, Phys. Rev. A **81**, 041602 (2010).
[8] R. Schmidt and T. Enss, Phys. Rev. A **83**, 063620 (2011).
[9] P. Massignan and G. M. Bruun, Eur. Phys. J. D **65**, 83 (2011).
[10] F. Schmitt *et al.*, Science **321**, 1649 (2008).
[11] J. K. Freericks, H. R. Krishnamurthy, and T. Pruschke, Phys. Rev. Lett. **102**, 136401 (2009).
[12] G. B. Jo *et al.*, Science **325**, 1521 (2009).
[13] D. Pekker *et al.*, Phys. Rev. Lett. **106**, 050402 (2011).
[14] A. Schirotzek, C.-H. Wu, A. Sommer, and M. W. Zwierlein, Phys. Rev. Lett. **102**, 230402 (2009).
[15] S. Nascimbène *et al.*, Phys. Rev. Lett. **103**, 170402 (2009).
[16] M. Punk, P. T. Dumitrescu, and W. Zwerger, Phys. Rev. A **80**, 053605 (2009).
[17] B. Fröhlich *et al.*, Phys. Rev. Lett. **106**, 105301 (2011).
[18] P. Dyke *et al.*, Phys. Rev. Lett. **106**, 105304 (2011).
[19] J. T. Stewart, J. P. Gaebler, and D. S. Jin, Nature **454**, 744 (2008).
[20] M. Feld, B. Fröhlich, E. Vogt, M. Koschorrek, and M. Köhl, Nature **480**, 75 (2011).
[21] S. Zöllner, G. M. Bruun, and C. J. Pethick, Phys. Rev. A **83**, 021603(R) (2011).
[22] M. M. Parish, Phys. Rev. A **83**, 051603(R) (2011).
[23] M. Klawunn and A. Recati, Phys. Rev. A **84**, 033607 (2011).
[24] N. V. Prokof'ev and B. V. Svistunov, Phys. Rev. B **77**, 020408 (2008).
[25] L. D. Landau and E. M. Lifshitz, *Quantum Mechanics* (Butterworth-Heinemann, Oxford, 1981).
[26] M. Randeria, J.-M. Duan, and L.-Y. Shieh, Phys. Rev. Lett. **62**, 981 (1989).
[27] D. S. Petrov and G. V. Shlyapnikov, Phys. Rev. A **64**, 012706 (2001).
[28] P. Bloom, Phys. Rev. B **12**, 125 (1975).
[29] D. S. Petrov, M. Holzmann, and G. V. Shlyapnikov, Phys. Rev. Lett. **84**, 2551 (2000).
[30] P. Nozieres and S. Schmitt-Rink, J. Low Temp. Phys. **59**, 195 (1985).
[31] J. R. Engelbrecht and M. Randeria, Phys. Rev. Lett. **65**, 1032 (1990).
[32] J. R. Engelbrecht and M. Randeria, Phys. Rev. B **45**, 12419 (1992).
[33] See Supplementary Material for details of the derivation.
[34] M. Punk and W. Zwerger, Phys. Rev. Lett. **99**, 170404 (2007).
[35] R. Combescot, A. Recati, C. Lobo, and F. Chevy, Phys. Rev. Lett. **98**, 180402 (2007).
[36] R. Haussmann, M. Punk, and W. Zwerger, Phys. Rev. A **80**, 063612 (2009).
[37] P. Massignan, G. M. Bruun, and H. T. C. Stoof, Phys. Rev. A **77**, 031601(R) (2008).
[38] P. Pieri, A. Perali, and G. C. Strinati, Nature Phys. **5**, 736 (2009).
[39] T. Enss, R. Haussmann, and W. Zwerger, Ann. Phys. (N.Y.) **326**, 770 (2011).
[40] N. Strohmaier *et al.*, Phys. Rev. Lett. **104**, 080401 (2010).

Supplementary material

Many-body T-matrix. The molecular spectral function displayed in Fig. 2 changes qualitatively with the binding energy. For large binding $\varepsilon_B > 2\,\varepsilon_F$ (Fig. 2d), the bound state (4) has minimum energy $\omega_b = \varepsilon_F - \varepsilon_B - \mu_\downarrow$ at $q = 0$ and we find an effective mass $m^*/m|_{q=0} = 2/(1 - 2\varepsilon_F/\varepsilon_B) > 2$. While it is well known that the T-matrix does not yield the correct binding energy of the molecule in the BEC limit [22] the repulsive polaron, which is the focus of our work, is reproduced correctly [28]. For smaller binding $\varepsilon_B < 2\,\varepsilon_F$ (Fig. 2b-c), the effective mass at $q = 0$ becomes negative and a new minimum appears at finite wave vector $q_c = 2\sqrt{k_F a_{2D} - 1}/a_{2D}$ [21] and with positive effective mass $m^*/m|_{q=q_c} = (2 - 2/k_F a_{2D})^{-1}$. For decreasing binding energy ε_B the bound state eventually touches the continuum at momenta $q_\pm/k_F = 1 \pm \sqrt{1 - 2\varepsilon_B/\varepsilon_F}$ (dotted line in Fig. 2a). For $q_- < q < q_+$ the bound state has negative residue and it ceases to exist.

Polaron self-energy. We compute the many-body T-matrix in the ladder approximation which is represented diagrammatically in Fig. 5d. The self-energy of the $\downarrow$ atom is given by scattering an $\uparrow$ hole off a molecule as depicted in Fig. 5b. Explicitly, the self-energy reads

$$\Sigma^R_\downarrow(\boldsymbol{q},\omega) = \int \frac{d^2k}{(2\pi)^2}\frac{dz}{\pi}\big[n_B(z)G^A_\uparrow(\boldsymbol{k}-\boldsymbol{q}, z-\omega)\,\mathrm{Im}\,T(\boldsymbol{k},z) - n_F(z)\,\mathrm{Im}\,G^R_\uparrow(\boldsymbol{k},z)\,T(\boldsymbol{k}+\boldsymbol{q}, z+\omega)\big] \quad (9)$$

where $G^{A,R}_\uparrow$ refers to advanced/retarded $\uparrow$ Green's functions. The first contribution comes from the pole and branch cuts of the T-matrix. In the polaron problem neither the $\downarrow$ state nor the molecular state are macroscopically occupied at zero temperature, hence the molecular spectral function $\propto \mathrm{Im}\,T$ has weight only at positive frequencies $z > 0$ where $n_B(z)$ vanishes, cf. Fig. 2. The second contribution of (9) with the bare $\uparrow$ spectral function $\mathrm{Im}\,G^R_\uparrow(\boldsymbol{k},z) = -i\pi\delta(z - \varepsilon_{\boldsymbol{k}} + \mu_\uparrow)$ directly yields Eq. (5). The $\downarrow$ self-energy yields the $\downarrow$ Green's function via the Dyson equation (6) depicted diagrammatically in Fig. 5c.

Local density approximation. To incorporate the radial trapping potential we use the local density approx-

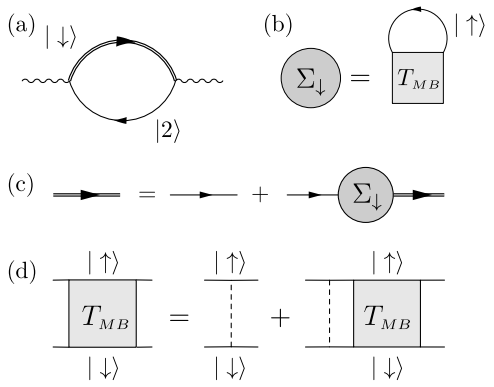

FIG. 5: Diagrammatic representation of (a) the rf photon self-energy, (b) the self-energy of spin-↓ atoms, (c) the Dyson equation for the dressed Green's function $G_\downarrow$, and (d) the many-body T-matrix between states $|\uparrow\rangle$ and $|\downarrow\rangle$.

imation (LDA). In the experiment [17] not only a single (central) 2D layer is populated but also additional pancakes along the axial direction. For each of these layers we calculate the rf response

$$I^{(\nu)}_{\rm trap}(\omega) = \int d^2r\, \rho^{(\nu)}_{\rm LDA}(\boldsymbol{r})\, I^{(\nu)}_{\rm rf}(\omega, \boldsymbol{r}). \qquad (10)$$

The various pancakes are indicated by the index ν and $\rho^{(\nu)}_{\rm LDA}(\boldsymbol{r}) = m\varepsilon^{(\nu)}_F(r)/2\pi\hbar^2$ is the Thomas-Fermi distribution of the density of non-interacting fermions within a single layer. $I^{(\nu)}_{\rm rf}(\omega, \boldsymbol{r})$ is the rf response in Eq. (8) computed for a homogeneous system with local Fermi energy $\varepsilon^{(\nu)}_F(r)$ and interaction parameter $\eta^{(\nu)}(r) = -\ln(\varepsilon_B/2\varepsilon^{(\nu)}_F(r))/2$. In the experiment [17] 30 layers have been populated. To obtain the complete rf response of the trapped system we finally sum over 30 contributions $I^{(\nu)}_{\rm trap}$ where we assume that the peak density of each layer, $\epsilon^{(\nu)}_F(0)$, varies according to a Thomas-Fermi profile along the lattice direction.

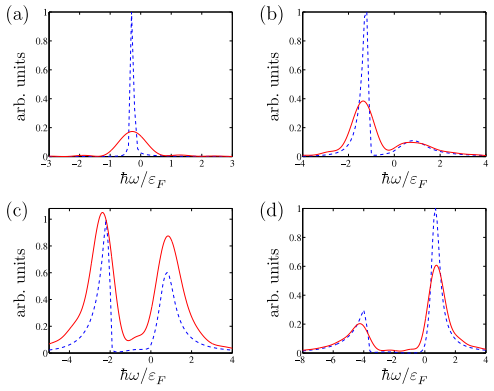

FIG. 6: (color online). RF spectrum of a trapped quasi-2D Fermi gas for (a) $B = 227$ G, (b) $B = 225$ G, (c) $B = 224.5$ G, and (d) $B = 224$ G. The attractive polaron gives rise to the peak at negative frequencies and the repulsive polaron corresponds to the peak at positive frequencies. The dashed line depicts the trap averaged signal $I_{\rm trap}$ while the solid line shows the expected experimental signal $I_{\rm exp}$ which takes into account a rectangular rf pulse of duration $T = 100\,\mu$s (not to scale) [17].

Shape and length of the rf pulse. The line shape of the rf spectra has a strong dependence on the rf pulse shape. The rf pulse used in Ref. [17] is approximately rectangular with duration $T = 100\,\mu$s. We compute the experimental rf signal as the convolution of $I_{\rm trap}(\omega)$ with the Fourier spectrum of the rf field [36]

$$I_{\rm exp}(\omega) = \frac{T}{2\pi}\int d\omega'\, I_{\rm trap}(\omega - \omega')\, {\rm sinc}^2(\omega' T/2). \qquad (11)$$

In Fig. 6 we show the resulting rf spectra for different values of the external magnetic field. Note that the broadening may shift the apparent peak position, see e.g. Fig. 7b.

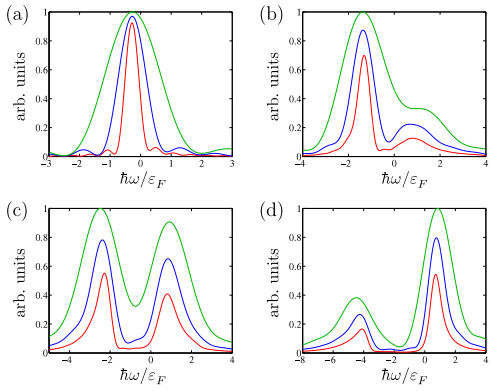

FIG. 7: (color online). Same as Fig. 6 but for different rf pulse duration (from top to bottom) $T = 50\,\mu$s, $T = 100\,\mu$s, and $T = 200\,\mu$s (not to scale).

EPJ manuscript No.
(will be inserted by the editor)

Efimov physics beyond universality

Richard Schmidt, Steffen Patrick Rath, and Wilhelm Zwerger

Physik Department, Technische Universität München, 85747 Garching, Germany

Received: date / Revised version: date

Abstract. We provide an exact solution of the Efimov spectrum in ultracold gases within the standard two-channel model for Feshbach resonances. It is shown that the finite range in the Feshbach coupling makes the introduction of an adjustable three-body parameter obsolete. The solution explains the empirical relation between the scattering length a_- where the first Efimov state appears at the atom threshold and the van der Waals length $l_{\rm vdw}$ for open-channel dominated resonances. There is a continuous crossover to the closed-channel dominated limit, where the scale in the energy level diagram as a function of the inverse scattering length $1/a$ is set by the intrinsic length $r^\star$ associated with the Feshbach coupling. Our results provide a number of predictions for the deviations from universal scaling relations between energies and scattering lengths that can be tested in future experiments.

1 Introduction

Most of the basic features that distinguish quantum from classical physics show up already at the single particle level. Genuine two-particle effects like the Hong-Ou-Mandel two-photon interference are typically a consequence of particle statistics, not of interactions [1]. Surprisingly, novel quantum effects in which statistics and interactions are combined appear at the level of three particles. As shown by Efimov in 1970 [2], three particles which interact via a resonant short-range attractive interaction exhibit an infinite sequence of three-body bound states or trimers. Remarkably, the trimers exist even in a regime where the two-body interaction does not have a bound state. Efimov trimers thus behave like Borromean rings: three of them are bound together but cutting one of the bonds makes the whole system fly apart. While theoretically predicted in a nuclear matter context, Efimov states have finally been observed with ultracold atoms [3]. The assumption of short range interactions is perfectly valid in this case and, moreover, the associated scattering lengths can be tuned by an external magnetic field, exploiting a Feshbach resonance [4]. An important feature of the Efimov trimers is that the binding energies exhibit universal scaling behavior. In the limit where the two-body interaction is just at the threshold to form a bound state, the ratio $E^{(n)}/E^{(n+1)}$ of consecutive binding energies approaches the universal value $e^{2\pi/s_0} \simeq 515.028$ for $n \gg 1$ with the Efimov number $s_0 \approx 1.00624$. One key experimental signature of Efimov physics is the resonant enhancement of the three-body recombination rate when the nth Efimov state meets the atom threshold at a scattering length $a_-^{(n)}$. Also here the universal scaling law prevails: the ratio of consecutive values of $a_-^{(n)}$ approaches $a_-^{(n+1)}/a_-^{(n)} \to e^{\pi/s_0} \simeq 22.6942$. The origin of this universality can be understood from an effective field theory approach to the three-body problem [5,6]. There remains, however, a non-universal aspect in the theory: Although the relative position of the trimer states is universal, this does not fix their absolute position in the (a, E) plane which is determined by the so-called three-body parameter (3BP). It is presumed that the 3BP is highly sensitive to microscopic details of the underlying two-body potential as well as genuine three-body forces [7].

In practice, it is often only the lowest Efimov state at $a_- = a_-^{(0)}$ that can be observed because of large atom losses as the scattering length increases. As more experimental data have been accumulated in recent years [8–15], a puzzling observation came to light: In most experiments, the measured values for a_- clustered around $a_- \approx -9.45\, l_{\rm vdw}$, no matter which alkali atoms were used. Since a_- determines the overall scale of the whole Efimov spectrum, this observation suggests a three-body parameter which is independent of the microscopic details. But where does this apparent 'universality of the three-body parameter' come from? A possible answer to this question is based on the observation that, typically, Efimov trimers which are accessible with ultracold atoms appear in a situation where the scattering length is tuned via an open-channel dominated Feshbach resonance. Such resonances are well described by a single-channel picture. Irrespective of the short distance behavior, the associated *two*-body problem is then known to have $l_{\rm vdw}$ as the only relevant length scale at energies much smaller than the depth of the potential well [16]. In the absence of genuine three-body forces, it is plausible that this result extends to the three-particle Efimov problem and thus, that $l_{\rm vdw}$ provides the characteristic scale for the 3BP. This has in fact been shown in recent, independent work on this problem

by Chin [17] and by Wang *et al.* [18], using single-channel potentials with a van der Waals tail.

While being consistent with the observed correlation between a_- and the van der Waals length $l_{\rm vdw}$ for a number of different alkalis, such a single-channel description does not apply in general and thus suggests a universality of the ratio $a_-/l_{\rm vdw}$ which is far too general even within the constraint that only two-body interactions play a role. In particular, it fails for closed-channel dominated Feshbach resonances. In fact, in this case, it is known that the 3BP is set by the intrinsic length $r^\star$ which determines the strength of the Feshbach coupling [19,20]. In the following, we present an exact solution for the Efimov spectrum within a standard two-channel model [4] which incorporates the finite range of the Feshbach coupling and properly recovers both limits of open-channel *and* closed-channel dominated resonances. It provides a complete description of the trimer spectrum in terms of only two, experimentally accessible, parameters: the van der Waals length $l_{\rm vdw}$ and the intrinsic length $r^\star$. Depending on the dimensionless resonance strength $s_{\rm res} = 0.956\, l_{\rm vdw}/r^\star$ [4], there is a continuous change in the relation between the trimer energy spectrum and the scattering length, with the lowest Efimov state appearing at $a_- \approx -8.3\, l_{\rm vdw}$ as $s_{\rm res} \gg 1$ while $a_- \approx -10.3\, r^\star$ in the opposite limit $s_{\rm res} \ll 1$. This model provides a minimum description of the Efimov spectrum which is based on two-body physics only and has no adjustable parameter. It explains why the ratio $a_-/l_{\rm vdw}$ is in the observed range for open-channel dominated resonances and predicts strong deviations from this in the intermediate regime $s_{\rm res} = \mathcal{O}(1)$. Our results are consistent with most of the experimental data, even though no details of the interatomic potentials at short distances or three-body forces are included. As an important additional feature, we find that the experimentally accessible lowest Efimov states exhibit strong deviations from the universal ratios that characterize the scaling limit, which have apparently been observed in recent experiments [21,22].

2 Two-channel model

We consider non-relativistic bosons described by the microscopic action (in units where $2m = \hbar = 1$)

$$S = \int_{\mathbf{r},t} \Big\{ \psi^*(\mathbf{r},t)[i\partial_t - \nabla^2]\psi(\mathbf{r},t) + \phi^*(\mathbf{r},t) P_\phi^{\rm cl} \phi(\mathbf{r},t) \Big\} + \frac{g}{2} \int_{\mathbf{r}_1,\mathbf{r}_2,t} \chi(\mathbf{r}_2 - \mathbf{r}_1) \times \Big[\phi(\frac{\mathbf{r}_1+\mathbf{r}_2}{2},t) \psi^*(\mathbf{r}_1,t) \psi^*(\mathbf{r}_2,t) + c.c. \Big], \qquad (1)$$

where ψ denotes the atoms and ϕ the molecule in the closed channel. Here $P_\phi^{\rm cl} = i\partial_t - \nabla^2/2 + \nu$ with $\nu(B) = \mu(B - B_{\rm res})$ the bare detuning from the resonance and μ is the difference in the magnetic moment between the molecule and the open-channel atoms. For a description of universal features of Efimov trimers like the asymptotic ratio $a_-^{(n+1)}/a_-^{(n)} \to e^{\pi/s_0}$, the atom-molecule conversion amplitude $\sim g$ may be taken as pointlike in coordinate space [5,6]. In reality, however, the coupling has a finite range σ which is determined by the scale of the wave function overlap between the open- and closed-channel states. As has been pointed out by a number of authors [23–28], this can be accounted for by a form factor $\chi(r)$ in Eq. (1). The solution of the modified Skornyakov-Ter-Martirosian (STM) equation (7) below, can then be used to fit the location of three-body resonances for different alkali atoms by adjusting the associated range parameter σ [26–28]. The precise form of the form factor $\chi(r)$ depends on details of the interatomic potentials. As will show below, however, its characteristic length σ is given by the van der Waals or the mean scattering length $\bar{a}$. In physical terms, this reflects the fact that the classical turning point in the closed-channel states is of the order of $l_{\rm vdw}$ because for typical magnetic field-tuned Feshbach resonances, it is only the bound states close to the continuum threshold that are experimentally accessible. Specifically, we choose an exponential form factor $\chi(r) \sim e^{-r/\sigma}/r$, which leads to $\chi(p) = 1/(1+\sigma^2 p^2)$ in momentum space. In contrast to the more standard Gaussian cutoff [23–25], this choice is in fact optimal in the sense that the resulting effective range $r_e = 3\,\bar{a}$ of two-body scattering near an open-channel dominated Feshbach resonance (see Eq. (3) below) agrees very well with the standard result $r_e \approx 2.92\,\bar{a}$ [16] for a single-channel potential with a $1/r^6$ tail. It is important to note that the action (1) can also be used to describe the situation where the interaction is dominated by a large background scattering length $a_{\rm bg}$. Indeed, integrating out the closed-channel field ϕ, one obtains a contribution $\sim (\psi^*\psi)^2$ that properly describes background scattering of range σ and scattering length $\sim g^2/\tilde{\nu}$, provided the Feshbach coupling $g^2 = 32\pi/r^\star \gg 1/l_{\rm vdw}$ is strong enough such that the momentum dependence of $P_\phi^{\rm cl}$ can be neglected. In the opposite limit of closed-channel dominated resonances, however, using a proper two-channel model cannot be avoided [24,26–28].

3 Determination of the model parameters

In our model the scattering of two atoms is mediated by the exchange of the closed-channel or dimer field ϕ. The two-body problem is thus solved by computing the renormalization of the inverse propagator of the dimer $\mathcal{G}_\phi^{-1}$. Evaluation of the standard ladder diagram yields

$$\mathcal{G}_\phi^{-1}(E,\mathbf{q}) = P_\phi^{\rm cl}(E,\mathbf{q}) - \frac{g^2/(32\pi)}{\sigma \left[1 + \sigma \sqrt{-\frac{E}{2} + \frac{\mathbf{q}^2}{4} - i\epsilon} \right]^2} \qquad (2)$$

with $P_\phi^{\rm cl}(E,\mathbf{q}) = -E + \mathbf{q}^2/2 - \nu(B) - i\epsilon$. The two-atom scattering amplitude now follows from $f(k) = g^2\chi(k)^2 \times \mathcal{G}_\phi(2k^2,\mathbf{0})/(16\pi)$. Its standard low-energy expansion then determines the scattering length a and the effective range r_e via

$$\frac{1}{a} = \frac{1}{2\sigma} - \frac{16\pi}{g^2}\nu(B), \quad r_e = -2r^* + 3\sigma\left(1 - \frac{4\sigma}{3a}\right). \qquad (3)$$

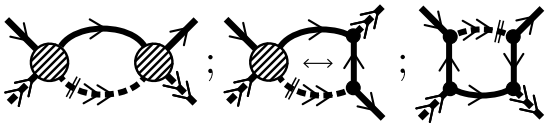

Fig. 1. Feynman diagrams contributing to the renormalization of the atom-dimer vertex $\lambda_3^{(k)}$ (large circle). The small black circle represents the atom-dimer coupling $\sim g$ and the solid (dashed) line denotes the atom (dimer) propagator.

This allows to express the bare parameters g, σ, and $\mu B_{\rm res}$ which appear in (1) in terms of fixed, experimental parameters. Close to a Feshbach resonance at magnetic field B_0, the scattering length can be written as $a(B) = -1/r^*\tilde{\nu}(B)$ where $\tilde{\nu}(B) = \mu(B - B_0)$ is the renormalized detuning in units of a wavenumber squared, while $r^\star > 0$ is the intrinsic length scale which characterizes the strength of the Feshbach coupling [4,29]. This fixes $g^2 = 32\pi/r^*$. Moreover, the resonance shift is given by $\mu(B_0 - B_{\rm res}) = 1/(r^\star\sigma)$, which is always positive in our model. This resonance shift has previously been calculated using microscopic interaction potentials that have a van der Waals tail [30]. Comparison with this result yields the identification $\sigma = \bar{a}$, with the so-called mean scattering length $\bar{a} = 4\pi/\Gamma(1/4)^2 l_{\rm vdw} \approx 0.956\, l_{\rm vdw}$ [31]. All parameters of our model (1) are thus fixed by two-body physics.

4 Functional renormalization group solution of the three-body problem

Based on the knowledge of the full two-body scattering amplitude, the three-body problem can be solved exactly, keeping only s-wave interactions. In particular, the three-boson scattering can be expressed in terms of an atom-dimer interaction $\sim \phi^*\psi^*\phi\psi$. The corresponding one particle irreducible atom-dimer vertex $\lambda_3(Q_1, Q_2, Q_3)$ [$Q_i = (E_i, \mathbf{q}_i)$] develops a complicated energy and momentum dependence which determines the full Efimov spectrum for arbitrary values of the scattering length. The derivation becomes particularly simple using the functional renormalization group (fRG) [32]. The central quantity of the fRG is an RG scale k dependent effective action Γ_k which interpolates between the microscopic action $S = \Gamma_{k=\Lambda}$ and the full quantum effective action $\Gamma = \Gamma_{k=0}$ by successively including quantum fluctuations on momentum scales $q \gtrsim k$. Here, we adopt an RG strategy adjusted to the few-body problem as discussed in [33,34], where the flowing action Γ_k is of the form of S in (1) but with $P_\phi^{\rm cl}$ replaced by $1/\mathcal{G}_\phi$ from (2) and an additional three-body term

$$\Gamma_k^{\rm 3B} = -\int_{Q_1,Q_2,Q_3} \lambda_3^{(k)}(Q_1,Q_2,Q_3)\times \phi^*(Q_1)\psi^*(Q_2)\phi(Q_3)\psi(Q_1+Q_2-Q_3). \quad (4)$$

Since we do not consider a microscopic three-body force here, we have $\lambda_3^{(\Lambda)} = 0$ at the UV scale Λ. The atom-dimer vertex $\lambda_3^{(k)}$ is then the only running coupling in Γ_k. It is important to note that the truncation of Γ_k is complete for the solution of the three-body problem as no additional couplings can be generated in the RG flow [33,34]. In our scheme the propagator of the bosons ψ is not regularized and the dimer ϕ is supplemented with a sharp momentum regulator. In Fig. 1 we show the Feynman diagrams contributing to the flow of $\lambda_3^{(k)}$. The number of independent energies and momenta is reduced by working in the center-of-mass frame and by noting that the loop frequency integration puts one internal atom on mass-shell [6]. After performing the s-wave projection $\lambda_3^{(k)}(q_1,q_2;E) = 1/(2g)\int d\cos\theta \lambda_3^{(k)}(\mathbf{q}_1,\mathbf{q}_2;E)$, $\theta = \angle(\mathbf{q}_1,\mathbf{q}_2)$, one finds the RG equation

$$\partial_k \lambda_3^{(k)}(q_1,q_2;E) = -\frac{g^2k^2\mathcal{G}_\phi(E-k^2,k)}{2\pi^2}\times \Big[\lambda_3^{(k)}(q_1,k;E)\lambda_3^{(k)}(k,q_2;E) + \lambda_3^{(k)}(q_1,k;E)G_E(k,q_2) + G_E(q_1,k)\lambda_3^{(k)}(k,q_2;E) + G_E(q_1,k)G_E(k,q_2)\Big], \quad (5)$$

where

$$G_E(p,q) \equiv \frac{1}{2}\int_{-1}^{1} d\cos\theta \frac{\chi(|\mathbf{p}+\frac{\mathbf{q}}{2}|)\chi(|\mathbf{q}+\frac{\mathbf{p}}{2}|)}{-E+\mathbf{p}^2+\mathbf{q}^2+(\mathbf{p}+\mathbf{q})^2-i\epsilon}. \quad (6)$$

Making use of the binomial form of Eq. (5) the flow can be integrated analytically and yields

$$f_E(q_1,q_2) = g_E(q_1,q_2) - \int_0^\Lambda dl\, g_E(q_1,l)\,\zeta_E(l)\,f_E(l,q_2), \quad (7)$$

which is a modified form of the well-known STM equation [35] with $f_E(q_1,q_2) = g_E(q_1,q_2) + \tilde{\lambda}_E(q_1,q_2)$, $g_E(q_1,q_2) = 16q_1q_2G_E(q_1,q_2)$, $\tilde{\lambda}_E(q_1,q_2) = 16q_1q_2\,\lambda_3(q_1,q_2;E)$, and $\zeta_E(l) = -g^2\mathcal{G}_\phi(E-l^2,l)/(32\pi^2)$.

In a standard treatment of Efimov physics with contact interactions [6], the STM equation (7) has to be regularized and the resulting dependence on the UV cutoff scale Λ reflects the presence of the three-body parameter. The exact position of the Efimov states is then adjusted by choosing an appropriate value of Λ. In our case, the situation is fundamentally different. Due to the presence of the form factor χ in g_E and the finite range corrections in Eq. (2), the UV limit $\Lambda \to \infty$ can safely be taken and the usual three-body parameter completely disappears from the theory. As a result, the exact position of the states in the Efimov spectrum is predicted without any adjustable parameter.

The knowledge of the full vertex λ_3 gives all information about the scattering of three bosons, such as bound states, recombination rates, and lifetimes, by evaluating the corresponding tree-level diagrams [6]. In the following we compute the trimer bound state spectrum by identifying the poles of λ_3 as a function of the energy E. As shown recently [36,37], such poles also exist in higher order vertices λ_N for $N \geq 4$ which are not considered in our work. Indeed, it is likely that there are N-body bound states for arbitrary large N,[1] a conjecture consistent with a re-

[1] This has been shown numerically up to $N = 13$, see [38].

cent theorem by Seiringer [39] which states that any pairwise interaction potential with negative scattering length a has an N-body bound state for some value of N, no matter how small $|a|$ may be. In the vicinity of a bound state pole the atom-dimer vertex can be parametrized as $\lambda_3(q_1,q_2;E) \approx \mathcal{B}(q_1,q_2)/[E+E^{(n)}+i\Gamma^{(n)}]$. When inserted into Eq. (7) an integral equation for $\mathcal{B}$ is obtained which is solved by discretization and amounts to evaluating the determinant $\det[\mathcal{C}-\mathbb{I}]=0$ with $\mathcal{C}(q_1,q_2) = g^2 g_E(q_1,q_2)\mathcal{G}_\phi(E-q_2^2,q_2)/(32\pi^2)$. $\mathcal{C}$ has a log-periodic structure where low-momentum modes are suppressed by any finite $1/a \neq 0$ and energy $E<0$ below the atom-dimer threshold. High-momentum modes are suppressed due to the finite range potential of our model.

5 Universal Efimov spectrum

In Fig. 2 we show the resulting Efimov spectrum including the atom-dimer threshold for an open-channel dominated Feshbach resonance and one of intermediate strength in dimensionless units. The position of the trimer states in the $(1/a,E)$ plane is completely fixed by our calculation. The overall appearance of the spectrum remains similar as the strength of the resonance is varied. In the limit $s_{\rm res} \ll 1$, it gets pushed towards the unitarity point $E=1/a=0$, while for open-channel dominated resonances it reaches a maximal extent in the $(1/a,E)$ plane. The detailed position of the lowest energy levels depends on both the value of the van der Waals length and the resonance strength $s_{\rm res}$. Only in the experimentally hardly accessible limit, $n \gg 1$, the ratios of $a_-^{(n)}$, $a_*^{(n)}$ (the scattering length for which the trimer meets the atom-dimer threshold), and $E^{(n)}$ of consecutive levels approach their universal values. It is instructive to quantify to which extent the lowest states deviate from this within our model. In Table 1 and Fig. 3 we show our results for various dimensionless ratios for Feshbach resonances of widely different strengths. Apparently, already for the third state the results are close to the asymptotic behavior determined by the universal

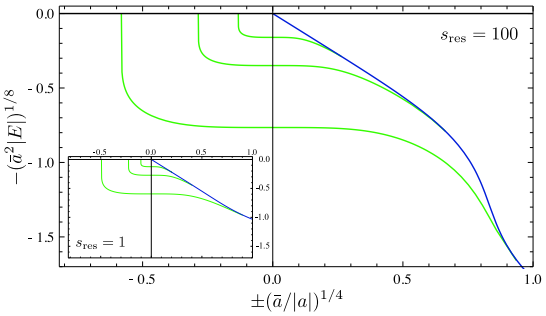

Fig. 2. (color online). The Efimov spectrum in dimensionless units for a open-channel dominated Feshbach resonance of strength $s_{\rm res}=100$. The inset shows the spectrum for a resonance of intermediate strength $s_{\rm res}=1$. The dimer binding energy is shown in blue.

$s_{\rm res}$	n	0	1	2	$n \gg 1$
100	$E^{(n)}/E^{(n+1)}$	530.871	515.206	515.035	515.028
	$a_-^{(n+1)}/a_-^{(n)}$	17.083	21.827	22.654	22.694
	$a_*^{(n+1)}/a_*^{(n)}$	3.980	40.033	23.345	22.694
	$\kappa_*^{(n)}a_-^{(n)}$	2.121	1.573	1.512	1.5076
1	$E^{(n)}/E^{(n+1)}$	515.830	515.039	515.035	515.028
	$a_-^{(n+1)}/a_-^{(n)}$	22.869	22.650	22.690	22.694
	$a_*^{(n+1)}/a_*^{(n)}$	17.183	22.303	22.716	22.694
	$\kappa_*^{(n)}a_-^{(n)}$	1.500	1.511	1.508	1.5076
0.1	$E^{(n)}/E^{(n+1)}$	521.273	515.059	515.010	515.028
	$a_-^{(n+1)}/a_-^{(n)}$	26.230	22.964	22.71	22.694
	$a_*^{(n+1)}/a_*^{(n)}$	26.965	21.286	22.48	22.694
	$\kappa_*^{(n)}a_-^{(n)}$	1.296	1.489	1.506	1.5076

Table 1. The ratio between consecutive trimer energies $E^{(n)} = \hbar^2(\kappa_*^{(n)})^2/m$ and threshold scattering lengths ($a_{-,*}^{(n)}$) as well as the product $a_-^{(n)}\kappa_*^{(n)}$ for a open-channel ($s_{\rm res}=100$), intermediate ($s_{\rm res}=1$) and closed-channel dominated ($s_{\rm res}=0.1$) Feshbach resonance for the three lowest-lying Efimov states $n=0,1,2$. The rightmost column shows the ratios in the universal scaling limit ($E=1/a=0$).

Efimov number $s_0 \approx 1.00624$, regardless of the value of $s_{\rm res}$. By contrast, the experimentally most relevant lowest states exhibit large deviations. Remarkably, our prediction $a_-^{(1)}/a_- = 17.08$ for open-channel dominated resonances is in reasonable agreement with recent measurements of the position of the second Efimov trimer in ^{6}Li, which find a ratio near 19.7 [21,22], definitely smaller than the asymptotic value 22.69. Surprisingly, for intermediate Feshbach resonances ($s_{\rm res}\approx 1$), the interplay between the scales r^* and σ leads to ratios close to their asymptotic ones even for the lowest states (see Fig. 3). Note that the values of $a_*^{(n)}$ for small n are highly sensitive to the precise form of the two-body bound state spectrum which, on its own, is strongly non-universal. The ratios between the lowest $a_*^{(n)}$ are therefore in general not suitable for a measurement of universal ratios. Instead one has to access the states with $n \gg 1$ near threshold, where the dimer binding energy has the universal form $\epsilon_b = \hbar^2/ma^2$.

To investigate generic features of the trimer spectrum which are independent of the precise form of the dimer energy, we study the dependence of $a_-^{(n)}$ and $\kappa_*^{(n)}$ on the strength of the Feshbach resonance. In Fig. 4 the behavior for the lowest, experimentally accessible, state is shown. For open-channel dominated resonances $a_-/\bar{a}$ and $\bar{a}\kappa_*$ become independent of $s_{\rm res}$ and thus of r^* and we find $a_- \approx -8.27\,l_{\rm vdw}$ and $\kappa_* l_{\rm vdw} = 0.26$. In the limit of closed-channel dominated resonances, the van der Waals length becomes irrelevant and the scale for the full Efimov spectrum is set by r^* only. Specifically, we find $a_-^{(n)} = \xi^{(n)} r^*$ and $\kappa_*^{(n)} r^* = \eta^{(n)}$ with numbers $\xi^{(n)}$ and $\eta^{(n)}$ which approach universal values as $n \to \infty$. In fact, we accurately reproduce the results for the universal scaling limit ($n \gg 1$) of closed-channel dominated Feshbach resonances, $a_-(n\gg 1) = -12.90\,r^*$ and $\kappa_*(n\gg 1)r^* = 0.117$, which were previously derived within a zero range model

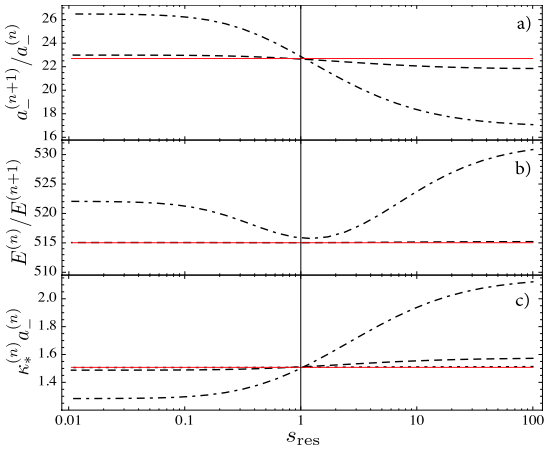

Fig. 3. (color online). Various dimensionless ratios as function of the Feshbach resonance strength $s_{\rm res}$. Shown are the results for the lowest levels (black). The universal scaling result is shown in red. a) Ratio of scattering lengths $a_-^{(n+1)}/a_-^{(n)}$ where the consecutive trimer states meet the atom threshold at $E = 0$. b) Ratio $E^{(n)}/E^{(n+1)}$ of the consecutive trimer energies at unitarity $1/a = 0$. c) Ratio $\kappa_*^{(n)} a_-^{(n)}$ as a measure of the distortion of the trimer levels from their universal shape in the (a, E) plane.

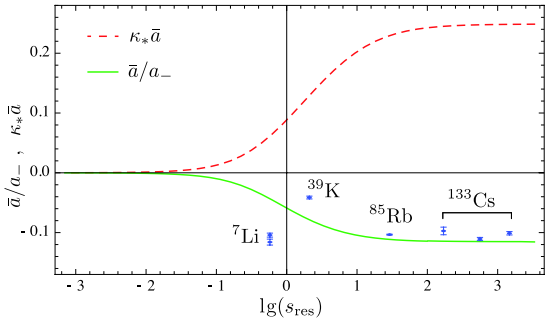

Fig. 4. (color online). Inverse threshold scattering length a_- (solid line) and wavenumber $\kappa_* = \kappa_*^{(0)}$ (dashed line) in units of $\bar{a}$ as functions of the resonance strength $s_{\rm res}$. The dots with error bars show the experimental results for ^{7}Li [13,10], ^{39}K [11], ^{85}Rb [15] and ^{133}Cs [14].

where $\sigma = 0$ [19,20]. The low-lying Efimov states however deviate from this limiting scaling behavior and our model predicts for example for the lowest Efimov state the ratios $a_- = -10.3\, r^*$ and $\kappa_* r^* = 0.125$. The precise numbers which quantify the deviations from the universal scaling predictions are specific for our model (1) with an exponential form factor $\chi(r)$. Note that it is also possible to study these deviations using a systematic expansion in the small parameter $l_{vdw}/|a|$ within effective field theory as done by Ji and coworkers [40]. Such an approach, however, requires not only an adjustable three-body parameter, but in addition further counterterms which are necessary to renormalize the theory with an interaction of finite range at finite scattering lengths a.

6 Comparison to experiments

Comparing to the experimental data, the open-channel dominated resonances in ^{85}Rb [15] and in ^{133}Cs [14] fit well into our prediction, see Fig. 4. The 12 % deviation between the value $a_- \approx -9.45\, l_{\rm vdw}$ inferred from averaging the results from different experiments and our ratio -8.27 shows that there is no true universality of the 3BP in a strict sense: short range physics which enters into the details of the form factor $\chi(r)$ leads to slightly different numbers. From both the empirical data and a study of how much our numbers change for various choices of the form factor $\chi(r)$, they are generically at the ten percent level. As mentioned above, the van der Waas length does not set the scale for the Efimov spectrum in general. In particular, in the regime of Feshbach resonances of intermediate strength $s_{\rm res} \approx 1$ both scales r^* and σ become relevant. Our approach equally applies to this regime, which is realized, e.g., in the case of ^{39}K, where $s_{\rm res} \simeq 2.1$ [11]. As shown in Fig. 4, the observation [11] of a considerable deviation from the result $a_- \approx -9.45\, l_{\rm vdw}$ in this case is in qualitative agreement with our model[2]. By contrast, the case of ^{7}Li, which seems to follow nicely the result $a_- \approx -9.45\, l_{\rm vdw}$ [10,13] for open-channel dominated resonances despite the even smaller value $s_{\rm res} \simeq 0.58$ [13] of the resonance strength is *not* consistent with our prediction. A possible origin of this discrepancy may be three-body forces of the Axilrod-Teller type [42], which lead to substantial changes in the position of the first Efimov trimer [7]. Their magnitude, in fact, depends quite sensitively on the choice of how these forces are modeled at short distances. Whether it is indeed three-body forces or other effects not captured by our model that will account for the discrepancy between the observed a_- in ^{7}Li and our prediction is unknown at present. Note, however, that irrespective of this problem, an explanation of the observed result for a_- in ^{7}Li within a single-channel description [18] is likely to be inadequate due to the rather small value of $s_{\rm res} \simeq 0.58$.

7 Conclusion

We have presented a simple, exactly solvable model, containing only r^* and $l_{\rm vdw}$ as experimentally accessible parameters, in which the full Efimov spectrum is fixed in quantitative terms without an adjustable 3BP. Our results provide an explanation for the observed proportionality between the scattering length a_- where the first Efimov trimer appears and the van der Waals length $l_{\rm vdw}$, which

[2] note added: new experimental data suggests that the value of $l_{\rm vdw}/a_-$ reported in [11] has to be corrected and is shifted to a larger value [41].

is often interpreted as a 'universality' of the 3BP. This relation applies for open-channel dominated resonances and in situations in which three-body forces are negligible. A continuous crossover is found into the regime of closed-channel dominated resonances, where the scale for the 3BP is set by $r^\star$, recovering previous exact solutions [19, 20]. Our results provide a clue for why the ratio $a_-/l_{\rm vdw}$ in ^{39}K is quite different from those in the open-channel dominated resonances. It remains an open question, however, why the ^{7}Li resonance, which is far from being open-channel dominated, has an a_- that fits perfectly the open-channel dominated limit. Finally, we have shown that for the lowest Efimov states within a given trimer spectrum, there are appreciable deviations from the asymptotic scaling relations, consistent with experiments. Clearly, a more systematic investigation of these non-universal ratios and of resonances with intermediate strength $s_{\rm res} = \mathcal{O}(1)$ is necessary to clarify to which extent the generic features of the Efimov effect in ultracold atoms are captured by our simple model, in which the complete trimer spectrum is obtained without any adjustable parameter from two-body physics only.

We thank Francesca Ferlaino, Rudi Grimm, Selim Jochim, Robert Seiringer, Felix Werner and Matteo Zaccanti for useful discussions and acknowledge support by the DFG through FOR 801.

References

1. C. K. Hong, Z. Y. Ou, and L. Mandel, Phys. Rev. Lett. **59**, 2044 (1987).
2. V. Efimov, Phys. Lett. **33B**, 563 (1970); V. Efimov, Nucl. Phys. A **210**, 157 (1973).
3. T. Kraemer, M. Mark, P. Waldburger, J. G. Danzl, C. Chin, B. Engeser, A. D. Lange, K. Pilch, A. Jaakkola, H.-C. Nägerl, and R. Grimm, Nature **440**, 315 (2006).
4. C. Chin, R. Grimm, P. S. Julienne, and E. Tiesinga, Rev. Mod. Phys. **82**, 1225 (2010).
5. P. F. Bedaque, H.-W. Hammer and U. van Kolck, Phys. Rev. Lett. **82**, 463 (1999); P. F. Bedaque, H.-W. Hammer and U. van Kolck, Nucl. Phys. A **646**, 444 (1999).
6. E. Braaten, H.-W. Hammer, Phys. Rept. **428**, 259 (2006).
7. J. P. D'Incao, C. H. Greene, and B. D. Esry, J. Phys. B **42**, 044016 (2009).
8. T. B. Ottenstein, T. Lompe, M. Kohnen, A. N. Wenz, and S. Jochim, Phys. Rev. Lett. **101**, 203202 (2008).
9. J. H. Huckans, J. R. Williams, E. L. Hazlett, R. W. Stites, and K. M. O'Hara, Phys. Rev. Lett. **102**, 165302 (2009).
10. S. E. Pollack, D. Dries, and R. G. Hulet, Science **326**, 1683 (2009).
11. M. Zaccanti, B. Deissler, C. D'Errico, M. Fattori, M. Jona-Lasinio, S. Müller, G. Roati, M. Inguscio, and G. Modugno, Nature Phys. **5**, 586 (2009).
12. N. Gross, Z. Shotan, S. Kokkelmans, and L. Khaykovich, Phys. Rev. Lett. **103**, 163202 (2009).
13. N. Gross, Z. Shotan, S. Kokkelmans, and L. Khaykovich, Phys. Rev. Lett. **105**, 103203 (2010).
14. M. Berninger, A. Zenesini, B. Huang, W. Harm, H.-C. Nägerl, F. Ferlaino, R. Grimm, P. S. Julienne, and J. M. Hutson, Phys. Rev. Lett. **107**, 120401 (2011).
15. R. J. Wild, P. Makotyn, J. M. Pino, E. A. Cornell, and D. S. Jin, Phys. Rev. Lett. **108**, 145305 (2012).
16. V. V. Flambaum, G. F. Gribakin, and C. Harabati, Phys. Rev. A **59**, 1998 (1999).
17. C. Chin, arXiv:1111.1484v2 (2011).
18. J. Wang, J. P. D'Incao, B. D. Esry, C. H. Greene, Phys. Rev. Lett. **108**, 263001 (2012).
19. D. S. Petrov, Phys. Rev. Lett. **93**, 143201 (2004).
20. A. O. Gogolin, C. Mora, and R. Egger, Phys. Rev. Lett. **100**, 140404 (2008).
21. A. N. Wenz, T. Lompe, T. B. Ottenstein, F. Serwane, G. Zürn, and S. Jochim, Phys. Rev. A **80**, 040702(R) (2009).
22. J. R. Williams, E. L. Hazlett, J. H. Huckans, R. W. Stites, Y. Zhang, and K. M. O'Hara, Phys. Rev. Lett. **103**, 130404 (2009).
23. M. H. Szymańska, K. Góral, T. Köhler, and K. Burnett, Phys. Rev. A **72**, 013610 (2005).
24. P. Massignan and H. T. C. Stoof, Phys. Rev. A **78**, 030701(R) (2008).
25. F. Werner, L. Tarruell, and Y. Castin, Eur. Phys. J. B **68**, 401 (2009).
26. L. Pricoupenko, Phys. Rev. A **82**, 043633 (2010).
27. M. Jona-Lasinio, and L. Pricoupenko, Phys. Rev. Lett. **104**, 023201 (2010).
28. L. Pricoupenko, and M. Jona-Lasinio, Phys. Rev. A **84**, 062712 (2011).
29. I. Bloch, J. Dalibard, and W. Zwerger , Rev. Mod. Phys. **80**, 885 (2008).
30. K. Góral, T. Köhler, S. A. Gardiner, E. Tiesinga, and P. S. Julienne, J. Phys. B **37**, 3457 (2004).
31. G. F. Gribakin and V. V. Flambaum, Phys. Rev. A **48**, 546 (1993).
32. C. Wetterich, Phys. Lett. B **301**, 90 (1993).
33. S. Diehl, H. C. Krahl, M. Scherer, Phys. Rev. C **78**, 034001 (2008).
34. S. Moroz, S. Floerchinger, R. Schmidt, and C. Wetterich, Phys. Rev. A **79**, 042705 (2009).
35. G. V. Skornyakov, K. A. Ter-Martirosian, Zh. Eksp. Teor. Phys. **31**, 775 (1956), [Sov. Phys. JETP **4**, 648 (1957)].
36. J. v. Stecher, J. P. D'Incao, and C.H. Greene, Nat. Phys. **5**, 417, (2009).
37. R. Schmidt, and S. Moroz, Phys. Rev. A **81**, 052709 (2010).
38. J. v. Stecher, J. Phys. B **43**, 101002 (2010).
39. R. Seiringer, J. Spec. Theo. **2**, 321 (2012).
40. C. Ji, D. R. Phillips, and L. Platter, Eur. Phys. Lett. **92**, 12003 (2010).
41. G. Modugno, private communication.
42. B. M. Axilrod, and E. Teller, J. Chem. Phys. **11**, 299 (1943).

Bibliography

[1] A. L. Fetter and J. D. Walecka, *Quantum theory of many-particle systems*, International series in pure and applied physics (John Dirk, San Francisco, McGraw-Hill, 1971).

[2] A. A. Abrikosov, L. P. Gorkov and I. E. Dzyaloshinski, *Methods of quantum field theory in statistical physics* (Dover Publications, 1975).

[3] L. Landau, E. Lifshitz and L. Pitaevskii, *Statistical Physics, Part 2*, no. 9 in Course of Theoretical Physics (Elsevier Science, 1980).

[4] G. D. Mahan, *Many particle physics* (Springer, 2000).

[5] A. Altland and B. Simons, *Condensed matter field theory* (Cambridge University Press, 2006).

[6] I. Bloch, J. Dalibard and W. Zwerger, *Many-body physics with ultracold gases*, Rev. Mod. Phys. **80**, 885 (2008).

[7] W. Ketterle and M. W. Zwierlein, *Making, probing and understanding ultracold Fermi gases*, in M. Inguscio, W. Ketterle and S. C. (eds.), *Ultracold Fermi Gases Proceedings of the International School of Physics 'Enrico Fermi', Course CLXIV, Varenna 2006* (IOS Press, Amsterdam, 2008).

[8] N. W. Ashcroft and N. D. Mermin, *Solid State Physics* (Brooks/Cole, Belmont, 1976).

[9] G. Baym and C. Pethick, *Physics of Neutron Stars*, Annual Review of Astronomy and Astrophysics **17**, 415 (1979).

[10] J. M. Lattimer and M. Prakash, *The Physics of Neutron Stars*, Science **304**, 536 (2004).

[11] L. P. Pitaevskii and S. Stringari, *Bose-Einstein Condensation* (Oxford University Press, 2003).

[12] K. B. Davis, M. O. Mewes, M. R. Andrews, N. J. van Druten, D. S. Durfee, D. M. Kurn and W. Ketterle, *Bose-Einstein Condensation in a Gas of Sodium Atoms*, Phys. Rev. Lett. **75**, 3969 (1995).

[13] M. H. Anderson, J. R. Ensher, M. R. Matthews, C. E. Wieman and E. A. Cornell, *Observation of Bose-Einstein Condensation in a Dilute Atomic Vapor*, Science **269**, 198 (1995).

[14] B. DeMarco and D. S. Jin, *Onset of Fermi Degeneracy in a Trapped Atomic Gas*, Science **285**, 1703 (1999).

[15] M. W. Zwierlein, C. H. Schunck, A. Schirotzek and W. Ketterle, *Direct observation of the superfluid phase transition in ultracold Fermi gases*, Nature **442**, 54 (2006).

[16] W. Zwerger (ed.), *BCS–BEC Crossover and the Unitary Fermi Gas* (Lecture Notes in Physics, Springer, 2012).

[17] J. F. Babb, *Casimir Effects in Atomic, Molecular, and Optical Physics*, in P. B. E. Arimondo and C. Lin (eds.), *Advances in Atomic, Molecular, and Optical Physics*, *Advances In Atomic, Molecular, and Optical Physics*, vol. 59, 1 – 20 (Academic Press, 2010).

[18] L. Landau and E. Lifshitz, *Quantum Mechanics* (Butterworth-Heinemann, Oxford, UK, 1980).

[19] M. Greiner, O. Mandel, T. Esslinger, T. W. Hansch and I. Bloch, *Quantum phase transition from a superfluid to a Mott insulator in a gas of ultracold atoms*, Nature **415**, 39 (2002).

[20] I. Bloch, J. Dalibard and S. Nascimbene, *Quantum simulations with ultracold quantum gases*, Nature Physics **8**, 267 (2012).

[21] W. S. Bakr, J. I. Gillen, A. Peng, S. Folling and M. Greiner, *A quantum gas microscope for detecting single atoms in a Hubbard-regime optical lattice*, Nature **462**, 74 (2009).

[22] J. F. Sherson, C. Weitenberg, M. Endres, M. Cheneau, I. Bloch and S. Kuhr, *Single-atom-resolved fluorescence imaging of an atomic Mott insulator*, Nature **467**, 68 (2010).

[23] M. Cheneau, P. Barmettler, D. Poletti, M. Endres, P. Schausz, T. Fukuhara, C. Gross, I. Bloch, C. Kollath and S. Kuhr, *Light-cone-like spreading of correlations in a quantum many-body system*, Nature **481**, 484 (2012).

[24] M. Baranov, L. Dobrek, K. Góral, L. Santos and M. Lewenstein, *Ultracold Dipolar Gases – a Challenge for Experiments and Theory*, Physica Scripta **2002**, 74 (2002).

[25] Y. Nishida and S. Tan, *Universal Fermi Gases in Mixed Dimensions*, Phys. Rev. Lett. **101**, 170401 (2008).

[26] G. Lamporesi, J. Catani, G. Barontini, Y. Nishida, M. Inguscio and F. Minardi, *Scattering in Mixed Dimensions with Ultracold Gases*, Phys. Rev. Lett. **104**, 153202 (2010).

[27] S. Stellmer, R. Grimm and F. Schreck, *Production of quantum-degenerate strontium gases*, Phys. Rev. A **87**, 013611 (2013).

[28] F. M. Spiegelhalder, A. Trenkwalder, D. Naik, G. Kerner, E. Wille, G. Hendl, F. Schreck and R. Grimm, *All-optical production of a degenerate mixture of* ^{6}Li *and* ^{40}K *and creation of heteronuclear molecules*, Phys. Rev. A **81**, 043637 (2010).

[29] M. W. Zwierlein, A. Schirotzek, C. H. Schunck and W. Ketterle, *Fermionic Superfluidity with Imbalanced Spin Populations*, Science **311**, 492 (2006).

[30] J. Dalibard, F. Gerbier, G. Juzeliūnas and P. Öhberg, *Colloquium : Artificial gauge potentials for neutral atoms*, Rev. Mod. Phys. **83**, 1523 (2011).

[31] C. Weitenberg, M. Endres, J. F. Sherson, M. Cheneau, P. Schausz, T. Fukuhara, I. Bloch and S. Kuhr, *Single-spin addressing in an atomic Mott insulator*, Nature **471**, 319 (2011).

[32] C. Salomon, G. V. Shlyapnikov and L. F. Cugliandolo, *Many-Body Physics with Ultracold Gases: Lecture Notes of the Les Houches Summer School: Volume 94, July 2010*, vol. 94 (OUP Oxford, 2012).

[33] R. Feynman, *Simulating physics with computers*, International Journal of Theoretical Physics **21**, 467 (1982).

[34] M. J. H. Ku, A. T. Sommer, L. W. Cheuk and M. W. Zwierlein, *Revealing the Superfluid Lambda Transition in the Universal Thermodynamics of a Unitary Fermi Gas*, Science **335**, 563 (2012).

[35] K. Van Houcke, F. Werner, E. Kozik, N. Prokof'ev, B. Svistunov, M. J. H. Ku, A. T. Sommer, L. W. Cheuk, A. Schirotzek and M. W. Zwierlein, *Feynman diagrams versus Fermi-gas Feynman emulator*, Nature Physics **8**, 366 (2012).

[36] W. Zwerger, *Mott–Hubbard transition of cold atoms in optical lattices*, Journal of Optics B: Quantum and Semiclassical Optics **5**, S9 (2003).

[37] R. Haussmann, W. Rantner, S. Cerrito and W. Zwerger, *Thermodynamics of the BCS-BEC crossover*, Phys. Rev. A **75**, 023610 (2007).

[38] D. Jaksch and P. Zoller, *The cold atom Hubbard toolbox*, Annals of Physics **315**, 52 (2005).

[39] D. Jaksch, H.-J. Briegel, J. I. Cirac, C. W. Gardiner and P. Zoller, *Entanglement of Atoms via Cold Controlled Collisions*, Phys. Rev. Lett. **82**, 1975 (1999).

[40] M. D. Lukin, M. Fleischhauer, R. Cote, L. M. Duan, D. Jaksch, J. I. Cirac and P. Zoller, *Dipole Blockade and Quantum Information Processing in Mesoscopic Atomic Ensembles*, Phys. Rev. Lett. **87**, 037901 (2001).

[41] A. Gezerlis and J. Carlson, *Strongly paired fermions: Cold atoms and neutron matter*, Phys. Rev. C **77**, 032801 (2008).

[42] T. Schäfer, *Nearly perfect fluidity*, Physics **2**, 88 (2009).

[43] G. Dvali and C. Gomez, *Black Holes as Critical Point of Quantum Phase Transition*, arXiv:1207.4059 (2012).

[44] V. Efimov, *Energy levels arising from resonant two-body forces in a three-body system*, Physics Letters B **33**, 563 (1970).

[45] T. Kraemer, M. Mark, P. Waldburger, J. G. Danzl, C. Chin, B. Engeser, A. D. Lange, K. Pilch, A. Jaakkola, H. C. Naegerl and R. Grimm, *Evidence for Efimov quantum states in an ultracold gas of caesium atoms*, Nature **440**, 315 (2006).

[46] S. Floerchinger, S. Moroz and R. Schmidt, *Efimov Physics from the Functional Renormalization Group*, Few-Body Systems **51**, 153 (2011).

[47] M. Berninger, A. Zenesini, B. Huang, W. Harm, H.-C. Nägerl, F. Ferlaino, R. Grimm, P. S. Julienne and J. M. Hutson, *Universality of the Three-Body Parameter for Efimov States in Ultracold Cesium*, Phys. Rev. Lett. **107**, 120401 (2011).

[48] J. von Stecher, J. P. D'Incao and C. H. Greene, *Signatures of universal four-body phenomena and their relation to the Efimov effect*, Nature Physics **5**, 417 (2009).

[49] G.-B. Jo, Y.-R. Lee, J.-H. Choi, C. A. Christensen, T. H. Kim, J. H. Thywissen, D. E. Pritchard and W. Ketterle, *Itinerant Ferromagnetism in a Fermi Gas of Ultracold Atoms*, Science **325**, 1521 (2009).

[50] D. Pekker, M. Babadi, R. Sensarma, N. Zinner, L. Pollet, M. W. Zwierlein and E. Demler, *Competition between Pairing and Ferromagnetic Instabilities in Ultracold Fermi Gases near Feshbach Resonances*, Phys. Rev. Lett. **106**, 050402 (2011).

[51] C. Sanner, E. J. Su, W. Huang, A. Keshet, J. Gillen and W. Ketterle, *Correlations and Pair Formation in a Repulsively Interacting Fermi Gas*, Phys. Rev. Lett. **108**, 240404 (2012).

[52] G. J. Conduit, A. G. Green and B. D. Simons, *Inhomogeneous Phase Formation on the Border of Itinerant Ferromagnetism*, Phys. Rev. Lett. **103**, 207201 (2009).

[53] G. J. Conduit and B. D. Simons, *Itinerant ferromagnetism in an atomic Fermi gas: Influence of population imbalance*, Phys. Rev. A **79**, 053606 (2009).

[54] G. J. Conduit and E. Altman, *Effect of three-body loss on itinerant ferromagnetism in an atomic Fermi gas*, Phys. Rev. A **83**, 043618 (2011).

[55] M. Barth and W. Zwerger, *Tan relations in one dimension*, Annals of Physics **326**, 2544 (2011).

[56] S. Zhang and T.-L. Ho, *Atom loss maximum in ultra-cold Fermi gases*, New Journal of Physics **13**, 055003 (2011).

[57] J. M. Luttinger and J. C. Ward, *Ground-State Energy of a Many-Fermion System. II*, Phys. Rev. **118**, 1417 (1960).

[58] R. Haussmann, *Crossover from BCS superconductivity to Bose-Einstein condensation: A self-consistent theory*, Zeitschrift für Physik B **91**, 291 (1993).

[59] N. Prokof'ev and B. Svistunov, *Fermi-polaron problem: Diagrammatic Monte Carlo method for divergent sign-alternating series*, Phys. Rev. B **77**, 020408 (2008).

[60] N. V. Prokof'ev and B. V. Svistunov, *Bold diagrammatic Monte Carlo: A generic sign-problem tolerant technique for polaron models and possibly interacting many-body problems*, Phys. Rev. B **77**, 125101 (2008).

[61] B. Fröhlich, M. Feld, E. Vogt, M. Koschorreck, W. Zwerger and M. Köhl, *Radio-Frequency Spectroscopy of a Strongly Interacting Two-Dimensional Fermi Gas*, Phys. Rev. Lett. **106**, 105301 (2011).

[62] R. Schmidt and T. Enss, *Excitation spectra and rf response near the polaron-to-molecule transition from the functional renormalization group*, Phys. Rev. A **83**, 063620 (2011).

[63] R. Schmidt, T. Enss, V. Pietilä and E. Demler, *Fermi polarons in two dimensions*, Phys. Rev. A **85**, 021602 (2012).

[64] C. Kohstall, M. Zaccanti, M. Jag, A. Trenkwalder, P. Massignan, G. M. Bruun, F. Schreck and R. Grimm, *Metastability and coherence of repulsive polarons in a strongly interacting Fermi mixture*, Nature **485**, 615 (2012).

[65] M. Koschorreck, D. Pertot, E. Vogt, B. Frohlich, M. Feld and M. Kohl, *Attractive and repulsive Fermi polarons in two dimensions*, Nature **485**, 619 (2012).

[66] E. Braaten and H.-W. Hammer, *Universality in few-body systems with large scattering length*, Physics Reports **428**, 259 (2006).

[67] F. Dalfovo, S. Giorgini, L. P. Pitaevskii and S. Stringari, *Theory of Bose-Einstein condensation in trapped gases*, Rev. Mod. Phys. **71**, 463 (1999).

[68] J. O. Andersen, *Theory of the weakly interacting Bose gas*, Rev. Mod. Phys. **76**, 599 (2004).

[69] J. Cardy, *Scaling and Renormalization in Statistical Physics* (Cambridge University Press, 1996).

[70] S. Sachdev, *Quantum Phase Transitions* (Cambridge University Press, 2000).

[71] S. Diehl and C. Wetterich, *Universality in phase transitions for ultracold fermionic atoms*, Phys. Rev. A **73**, 033615 (2006).

[72] P. Nikolic and S. Sachdev, *Renormalization-group fixed points, universal phase diagram, and 1/N expansion for quantum liquids with interactions near the unitarity limit*, Phys. Rev. A **75**, 033608 (2007).

[73] S. Sachdev, *Dilute Fermi and Bose Gases*, in W. Zwerger (ed.), *BCS–BEC Crossover and the Unitary Fermi Gas* (Lecture Notes in Physics, Springer, 2012).

[74] G. Zürn, T. Lompe, A. N. Wenz, S. Jochim, P. S. Julienne and J. M. Hutson, *Precise Characterization of* ^{6}Li *Feshbach Resonances Using Trap-Sideband-Resolved RF Spectroscopy of Weakly Bound Molecules*, Phys. Rev. Lett. **110**, 135301 (2013).

[75] P. Arnold, J. E. Drut and D. T. Son, *Next-to-next-to-leading-order epsilon expansion for a Fermi gas at infinite scattering length*, Phys. Rev. A **75**, 043605 (2007).

[76] Y. Nishida, *Ground-state energy of the unitary Fermi gas from the ϵ expansion*, Phys. Rev. A **79**, 013627 (2009).

[77] M. M. Forbes, S. Gandolfi and A. Gezerlis, *Resonantly Interacting Fermions in a Box*, Phys. Rev. Lett. **106**, 235303 (2011).

[78] G. F. Bertsch, *Many-Body Challenge Problem*, see R. F. Bishop, Int. J. Mod. Phys. B **15** (2001).

[79] E. Burovski, N. Prokof'ev, B. Svistunov and M. Troyer, *Critical Temperature and Thermodynamics of Attractive Fermions at Unitarity*, Phys. Rev. Lett. **96**, 160402 (2006).

[80] O. Goulko and M. Wingate, *Thermodynamics of balanced and slightly spin-imbalanced Fermi gases at unitarity*, Phys. Rev. A **82**, 053621 (2010).

[81] V. Efimov, *Weakly-bound states of three resonantly-interacting particles*, Sov. J. Nucl. Phys. **12**, 101 (1971).

[82] T. K. Lim, K. Duffy and W. C. Damer, *Efimov state in the 4He trimer*, Phys. Rev. Lett. **38**, 341 (1977).

[83] R. Brühl, A. Kalinin, O. Kornilov, J. P. Toennies, G. C. Hegerfeldt and M. Stoll, *Matter Wave Diffraction from an Inclined Transmission Grating: Searching for the Elusive* ^{4}He *Trimer Efimov State*, Phys. Rev. Lett. **95**, 063002 (2005).

[84] R. Amado and J. Noble, *On Efimov's effect: A new pathology of three-particle systems*, Physics Letters B **35**, 25 (1971).

[85] R. D. Amado and J. V. Noble, *Efimov's Effect: A New Pathology of Three-Particle Systems. II*, Phys. Rev. D **5**, 1992 (1972).

[86] V. Efimov, *Low-energy properties of three resonantly interacting particles*, Sov. J. Nucl. Phys. **29**, 546 (1979).

[87] U. Fano, *Sullo spettro di assorbimento dei gas nobili presso il limite dello spettro d'arco*, Il Nuovo Cimento **12**, 154 (1935).

[88] H. Feshbach, *Unified theory of nuclear reactions*, Annals of Physics **5**, 357 (1958).

[89] U. Fano, *Effects of Configuration Interaction on Intensities and Phase Shifts*, Phys. Rev. **124**, 1866 (1961).

[90] H. Feshbach, *A unified theory of nuclear reactions. II*, Annals of Physics **19**, 287 (1962).

[91] E. Timmermans, P. Tommasini, M. Hussein and A. Kerman, *Feshbach resonances in atomic Bose-Einstein condensates*, Physics Reports **315**, 199 (1999).

[92] C. Chin, R. Grimm, P. Julienne and E. Tiesinga, *Feshbach resonances in ultracold gases*, Rev. Mod. Phys. **82**, 1225 (2010).

[93] T. Frederico, L. Tomio, A. Delfino and A. E. A. Amorim, *Scaling limit of weakly bound triatomic states*, Phys. Rev. A **60**, R9 (1999).

[94] A. S. I.V. Simenog, *Effect of long-range interaction in a three-body system with short-range forces*, Doklady Academy of Sciences of the Ukrainian SSR, Ser. A **11**, 74 (1981).

[95] L. H. Thomas, *The Interaction Between a Neutron and a Proton and the Structure of* H^3, Phys. Rev. **47**, 903 (1935).

[96] S. Moroz, S. Floerchinger, R. Schmidt and C. Wetterich, *Efimov effect from functional renormalization*, Phys. Rev. A **79**, 042705 (2009).

[97] K. G. Wilson, *Renormalization Group and Strong Interactions*, Phys. Rev. D **3**, 1818 (1971).

[98] S. D. Glazek and K. G. Wilson, *Limit Cycles in Quantum Theories*, Phys. Rev. Lett. **89**, 230401 (2002).

[99] S. Albeverio, R. Haegh-Krohn and T. T. Wu, *A class of exactly solvable three-body quantum mechanical problems and the universal low energy behavior*, Physics Letters A **83**, 105 (1981).

[100] P. Bedaque, H.-W. Hammer and U. van Kolck, *The three-boson system with short-range interactions*, Nuclear Physics A **646**, 444 (1999).

[101] P. F. Bedaque, H.-W. Hammer and U. van Kolck, *Renormalization of the Three-Body System with Short-Range Interactions*, Phys. Rev. Lett. **82**, 463 (1999).

[102] T. Barford, *The renormalisation group and applications in few-body physics*, Ph.D. thesis, University of Manchester, arXiv:nucl-th/0404072 (2004).

[103] T. Barford and M. C. Birse, *Effective theories of scattering with an attractive inverse-square potential and the three-body problem*, Journal of Physics A: Mathematical and General **38**, 697 (2005).

[104] R. Mohr, R. Furnstahl, H.-W. Hammer, R. Perry and K. Wilson, *Precise numerical results for limit cycles in the quantum three-body problem*, Annals of Physics **321**, 225 (2006).

[105] S. Floerchinger, R. Schmidt, S. Moroz and C. Wetterich, *Functional renormalization for trion formation in ultracold fermion gases*, Phys. Rev. A **79**, 013603 (2009).

[106] R. Schmidt and S. Moroz, *Renormalization-group study of the four-body problem*, Phys. Rev. A **81**, 052709 (2010).

[107] T. Enss, *Quantum critical transport in the unitary Fermi gas*, Phys. Rev. A **86**, 013616 (2012).

[108] D. Son and M. Wingate, *General coordinate invariance and conformal invariance in nonrelativistic physics: Unitary Fermi gas*, Annals of Physics **321**, 197 (2006).

[109] D. T. Son, *Vanishing Bulk Viscosities and Conformal Invariance of the Unitary Fermi Gas*, Phys. Rev. Lett. **98**, 020604 (2007).

[110] T. Enss, R. Haussmann and W. Zwerger, *Viscosity and scale invariance in the unitary Fermi gas*, Annals of Physics **326**, 770 (2011).

[111] S. Moroz and R. Schmidt, *Nonrelativistic inverse square potential, scale anomaly, and complex extension*, Annals of Physics **325**, 491 (2010).

[112] H. E. Camblong and C. R. Ordóñez, *Anomaly in conformal quantum mechanics: From molecular physics to black holes*, Phys. Rev. D **68**, 125013 (2003).

[113] Y. Nishida and D. T. Son, *Nonrelativistic conformal field theories*, Phys. Rev. D **76**, 086004 (2007).

[114] H. R. Lewis, *Class of Exact Invariants for Classical and Quantum Time-Dependent Harmonic Oscillators*, J. Math. Phys. 1976 (1968).

[115] V. S. Popov and A. M. Perelomov, J. Exp. Theor. Phys. 738 (1969).

[116] G. M. Bruun and C. W. Clark, *Ideal gases in time-dependent traps*, Phys. Rev. A **61**, 061601 (2000).

[117] Y. Castin, *Exact scaling transform for a unitary quantum gas in a time dependent harmonic potential*, Comptes Rendus Physique **5**, 407 (2004).

[118] S. Moroz, *Scale-invariant Fermi gas in a time-dependent harmonic potential*, Phys. Rev. A **86**, 011601 (2012).

[119] V. Efimov, *Level spectrum of three resonantly interacting particles*, Sov. Phys. JETP Lett. 34 (1972).

[120] V. Efimov, *Energy levels of three resonantly interacting particles*, Nuclear Physics A **210**, 157 (1973).

[121] P. O. Fedichev, M. W. Reynolds and G. V. Shlyapnikov, *Three-Body Recombination of Ultracold Atoms to a Weakly Bound s Level*, Phys. Rev. Lett. **77**, 2921 (1996).

[122] T. Weber, J. Herbig, M. Mark, H.-C. Nägerl and R. Grimm, *Three-Body Recombination at Large Scattering Lengths in an Ultracold Atomic Gas*, Phys. Rev. Lett. **91**, 123201 (2003).

[123] B. D. Esry, C. H. Greene and J. P. Burke, *Recombination of Three Atoms in the Ultracold Limit*, Phys. Rev. Lett. **83**, 1751 (1999).

[124] E. Nielsen and J. H. Macek, *Low-Energy Recombination of Identical Bosons by Three-Body Collisions*, Phys. Rev. Lett. **83**, 1566 (1999).

[125] P. F. Bedaque, E. Braaten and H.-W. Hammer, *Three-body Recombination in Bose Gases with Large Scattering Length*, Phys. Rev. Lett. **85**, 908 (2000).

[126] E. Braaten and H.-W. Hammer, *Three-Body Recombination into Deep Bound States in a Bose Gas with Large Scattering Length*, Phys. Rev. Lett. **87**, 160407 (2001).

[127] J. P. D'Incao, H. Suno and B. D. Esry, *Limits on Universality in Ultracold Three-Boson Recombination*, Phys. Rev. Lett. **93**, 123201 (2004).

[128] T. B. Ottenstein, T. Lompe, M. Kohnen, A. N. Wenz and S. Jochim, *Collisional Stability of a Three-Component Degenerate Fermi Gas*, Phys. Rev. Lett. **101**, 203202 (2008).

[129] O. Machtey, Z. Shotan, N. Gross and L. Khaykovich, *Association of Efimov Trimers from a Three-Atom Continuum*, Phys. Rev. Lett. **108**, 210406 (2012).

[130] J. H. Huckans, J. R. Williams, E. L. Hazlett, R. W. Stites and K. M. O'Hara, *Three-Body Recombination in a Three-State Fermi Gas with Widely Tunable Interactions*, Phys. Rev. Lett. **102**, 165302 (2009).

[131] S. E. Pollack, D. Dries and R. G. Hulet, *Universality in Three- and Four-Body Bound States of Ultracold Atoms*, Science **326**, 1683 (2009).

[132] M. Zaccanti, B. Deissler, C. D'Errico, M. Fattori, M. Jona-Lasinio, S. Muller, G. Roati, M. Inguscio and G. Modugno, *Observation of an Efimov spectrum in an atomic system*, Nature Physics **5**, 586 (2009).

[133] N. Gross, Z. Shotan, S. Kokkelmans and L. Khaykovich, *Observation of Universality in Ultracold* ^{7}Li *Three-Body Recombination*, Phys. Rev. Lett. **103**, 163202 (2009).

[134] N. Gross, Z. Shotan, S. Kokkelmans and L. Khaykovich, *Nuclear-Spin-Independent Short-Range Three-Body Physics in Ultracold Atoms*, Phys. Rev. Lett. **105**, 103203 (2010).

[135] R. J. Wild, P. Makotyn, J. M. Pino, E. A. Cornell and D. S. Jin, *Measurements of Tan's Contact in an Atomic Bose-Einstein Condensate*, Phys. Rev. Lett. **108**, 145305 (2012).

[136] S. Roy, M. Landini, A. Trenkwalder, G. Semeghini, G. Spagnolli, A. Simoni, M. Fattori, M. Inguscio and G. Modugno, *Universality of the three-body Efimov parameter at narrow Feshbach resonances*, arXiv:1303.3843 (2013).

[137] S. Floerchinger, R. Schmidt and C. Wetterich, *Three-body loss in lithium from functional renormalization*, Phys. Rev. A **79**, 053633 (2009).

[138] S. Knoop, F. Ferlaino, M. Mark, M. Berninger, H. Schobel, H. C. Nagerl and R. Grimm, *Observation of an Efimov-like trimer resonance in ultracold atom-dimer scattering*, Nature Physics **5**, 227 (2009).

[139] E. Braaten and H.-W. Hammer, *Enhanced dimer relaxation in an atomic and molecular Bose-Einstein condensate*, Phys. Rev. A **70**, 042706 (2004).

[140] A. N. Wenz, T. Lompe, T. B. Ottenstein, F. Serwane, G. Zürn and S. Jochim, *Universal trimer in a three-component Fermi gas*, Phys. Rev. A **80**, 040702 (2009).

[141] T. Lompe, T. B. Ottenstein, F. Serwane, A. N. Wenz, G. Zürn and S. Jochim, *Radio-Frequency Association of Efimov Trimers*, Science **330**, 940 (2010).

[142] S. Nakajima, M. Horikoshi, T. Mukaiyama, P. Naidon and M. Ueda, *Measurement of an Efimov Trimer Binding Energy in a Three-Component Mixture of* ^{6}Li, Phys. Rev. Lett. **106**, 143201 (2011).

[143] J. Wang, J. P. D'Incao, B. D. Esry and C. H. Greene, *Origin of the Three-Body Parameter Universality in Efimov Physics*, Phys. Rev. Lett. **108**, 263001 (2012).

[144] C. Chin, *Universal scaling of Efimov resonance positions in cold atom systems*, arXiv:1111.1484v2 (2011).

[145] V. V. Flambaum, G. F. Gribakin and C. Harabati, *Analytical calculation of cold-atom scattering*, Phys. Rev. A **59**, 1998 (1999).

[146] D. S. Petrov, *Three-Boson Problem near a Narrow Feshbach Resonance*, Phys. Rev. Lett. **93**, 143201 (2004).

[147] A. O. Gogolin, C. Mora and R. Egger, *Analytical Solution of the Bosonic Three-Body Problem*, Phys. Rev. Lett. **100**, 140404 (2008).

[148] G. F. Gribakin and V. V. Flambaum, *Calculation of the scattering length in atomic collisions using the semiclassical approximation*, Phys. Rev. A **48**, 546 (1993).

[149] F. Werner, L. Tarruell and Y. Castin, *Number of closed-channel molecules in the BEC-BCS crossover*, Eur. Phys. J. B **68**, 401 (2009).

[150] M. H. Szymańska, K. Góral, T. Köhler and K. Burnett, *Conventional character of the BCS-BEC crossover in ultracold gases of* ^{40}K, Phys. Rev. A **72**, 013610 (2005).

[151] M. Holland, S. J. J. M. F. Kokkelmans, M. L. Chiofalo and R. Walser, *Resonance Superfluidity in a Quantum Degenerate Fermi Gas*, Phys. Rev. Lett. **87**, 120406 (2001).

[152] J. N. Milstein, S. J. J. M. F. Kokkelmans and M. J. Holland, *Resonance theory of the crossover from Bardeen-Cooper-Schrieffer superfluidity to Bose-Einstein condensation in a dilute Fermi gas*, Phys. Rev. A **66**, 043604 (2002).

[153] P. Massignan and H. T. C. Stoof, *Efimov states near a Feshbach resonance*, Phys. Rev. A **78**, 030701 (2008).

[154] L. Pricoupenko, *Crossover in the Efimov spectrum*, Phys. Rev. A **82**, 043633 (2010).

[155] M. Jona-Lasinio and L. Pricoupenko, *Three Resonant Ultracold Bosons: Off-Resonance Effects*, Phys. Rev. Lett. **104**, 023201 (2010).

[156] L. Pricoupenko and M. Jona-Lasinio, *Ultracold bosons in the vicinity of a narrow resonance: Shallow dimer and recombination*, Phys. Rev. A **84**, 062712 (2011).

[157] K. Góral, T. Köhler, S. A. Gardiner, E. Tiesinga and P. S. Julienne, *Adiabatic association of ultracold molecules via magnetic-field tunable interactions*, Journal of Physics B: Atomic, Molecular and Optical Physics **37**, 3457 (2004).

[158] P. K. Soerensen, D. V. Fedorov, A. S. Jensen and N. T. Zinner, *Efimov physics and the three-body parameter within a two-channel framework*, Phys. Rev. A **86**, 052516 (2012).

[159] P. K. Soerensen, D. V. Fedorov, A. S. Jensen and N. T. Zinner, *Finite Range Effects in Energies and Recombination Rates of Three Identical Bosons*, arXiv:1212.1398 (2012).

[160] E. P. Wigner, *Lower Limit for the Energy Derivative of the Scattering Phase Shift*, Phys. Rev. **98**, 145 (1955).

[161] H.-W. Hammer and D. Lee, *Causality and the effective range expansion*, Annals of Physics **325**, 2212 (2010).

[162] G. V. Skornyakov and K. A. Ter-Martirosyan, *Three body problem for short-range forces. Low energy neutron scattering by deuterons*, Zh. Eksp. Teor. Fiz 775 (1956).

[163] G. S. Danilov and V. I. Lebedev, *Calculation of the doublet neutron-deuteron scattering length in the theory of zero range forces*, Sov. Phys. JETP 1015 (1963).

[164] Y. Tanizaki, *Flow equation of functional renormalization group for three-body scattering problems*, arXiv preprint arXiv:1304.3286 (2013).

[165] S. Floerchinger, *Few-body hierarchy in non-relativistic quantum field theory and a decoupling theorem*, arXiv:1301.6542v2 (2013).

[166] K.-I. Aoki, *Introduction to the non-perturbative renormalization group and its recent applications*, International Journal of Modern Physics B **14**, 1249 (2000).

[167] C. Bagnuls and C. Bervillier, *Exact renormalization group equations: an introductory review*, Physics Reports **348**, 91 (2001).

[168] M. Salmhofer and C. Honerkamp, *Fermionic Renormalization Group Flows*, Progress of Theoretical Physics **105**, 1 (2001).

[169] C. Wetterich, *Effective average action in statistical physics and quantum field theory*, International Journal of Modern Physics A **16**, 1951 (2001).

[170] J. Berges, N. Tetradis and C. Wetterich, *Non-perturbative renormalization flow in quantum field theory and statistical physics*, Physics Reports **363**, 223 (2002).

[171] W. Metzner, *Functional Renormalization Group Computation of Interacting Fermi Systems*, Progress of Theoretical Physics Supplement **160**, 58 (2005).

[172] J. M. Pawlowski, *Aspects of the functional renormalisation group*, Annals of Physics **322**, 2831 (2007).

[173] B. Delamotte, *An Introduction to the Nonperturbative Renormalization Group*, in A. Schwenk and J. Polonyi (eds.), *Renormalization Group and Effective Field Theory Approaches to Many-Body Systems*, *Lecture Notes in Physics*, vol. 852, 49–132 (Springer Berlin Heidelberg, 2012).

[174] O. J. Rosten, *Fundamentals of the exact renormalization group*, Physics Reports **511**, 177 (2012).

[175] W. Metzner, M. Salmhofer, C. Honerkamp, V. Meden and K. Schönhammer, *Functional renormalization group approach to correlated fermion systems*, Rev. Mod. Phys. **84**, 299 (2012).

[176] C. Wetterich, *Exact evolution equation for the effective potential*, Physics Letters B **301**, 90 (1993).

[177] S. Diehl, H. C. Krahl and M. Scherer, *Three-body scattering from nonperturbative flow equations*, Phys. Rev. C **78**, 034001 (2008).

[178] R. Schmidt, S. Rath and W. Zwerger, *Efimov physics beyond universality*, The European Physical Journal B **85**, 1 (2012).

[179] C. Husemann and M. Salmhofer, *Efficient parametrization of the vertex function, Ω scheme, and the t,t' Hubbard model at van Hove filling*, Phys. Rev. B **79**, 195125 (2009).

[180] K.-U. Giering and M. Salmhofer, *Self-energy flows in the two-dimensional repulsive Hubbard model*, Phys. Rev. B **86**, 245122 (2012).

[181] C. Husemann and W. Metzner, *Incommensurate nematic fluctuations in the two-dimensional Hubbard model*, Phys. Rev. B **86**, 085113 (2012).

[182] C. Husemann, K.-U. Giering and M. Salmhofer, *Frequency-dependent vertex functions of the (t, t') Hubbard model at weak coupling*, Phys. Rev. B **85**, 075121 (2012).

[183] R. Seiringer, *Absence of bound states implies non-negativity of the scattering length*, Journal of Spectral Theory 321 (2012).

[184] J. von Stecher, *Weakly bound cluster states of Efimov character*, Journal of Physics B: Atomic, Molecular and Optical Physics **43**, 101002 (2010).

[185] J. R. Williams, E. L. Hazlett, J. H. Huckans, R. W. Stites, Y. Zhang and K. M. O'Hara, *Evidence for an Excited-State Efimov Trimer in a Three-Component Fermi Gas*, Phys. Rev. Lett. **103**, 130404 (2009).

[186] C. Ji, D. R. Phillips and L. Platter, *Beyond universality in three-body recombination: An effective field theory treatment*, Europhysics Letters **92**, 13003 (2010).

[187] B. M. Axilrod and E. Teller, *Interaction of the van der Waals Type Between Three Atoms*, J. Chem. Phys. 299 (1943).

[188] L.-Y. Tang, Z.-C. Yan, T.-Y. Shi, J. F. Babb and J. Mitroy, *The long-range non-additive three-body dispersion interactions for the rare gases, alkali, and alkaline-earth atoms*, The Journal of Chemical Physics **136**, 104104 (2012).

[189] O. A. Yakubovsky, Sov. J. Nucl. Phys. 1312 (1967).

[190] J. Tjon, *Bound states of 4He with local interactions*, Physics Letters B **56**, 217 (1975).

[191] B. F. Gibson and D. R. Lehman, *Four-body bound states from the Schrödinger equation with separable potentials*, Phys. Rev. C **14**, 685 (1976).

[192] A. C. Fonseca and P. E. Shanley, *Soluble model involving four identical particles*, Phys. Rev. C **14**, 1343 (1976).

[193] J. A. Tjon, *Few-body Systems and Nuclear Forces II* (Springer, Berlin, 1978).

[194] D. Blume and C. H. Greene, *Monte Carlo hyperspherical description of helium cluster excited states*, The Journal of Chemical Physics **112**, 8053 (2000).

[195] K. B. Whaley, *Structure and dynamics of quantum clusters*, International Reviews in Physical Chemistry **13**, 41 (1994).

[196] D. S. Petrov, C. Salomon and G. V. Shlyapnikov, *Weakly Bound Dimers of Fermionic Atoms*, Phys. Rev. Lett. **93**, 090404 (2004).

[197] G. Röpke, A. Schnell, P. Schuck and P. Nozières, *Four-Particle Condensate in Strongly Coupled Fermion Systems*, Phys. Rev. Lett. **80**, 3177 (1998).

[198] P. Schuck, T. Sogo and G. Röpke, *Many Body Theory for Quartets, Trions, and Pairs in Low Density Multi-Component Fermi-Systems*, International Journal of Modern Physics A **24**, 2027 (2009).

[199] T. Sogo, G. Röpke and P. Schuck, *Many-body approach for quartet condensation in strong coupling*, Phys. Rev. C **81**, 064310 (2010).

[200] L. Platter, H.-W. Hammer and U.-G. Meißner, *Four-boson system with short-range interactions*, Phys. Rev. A **70**, 052101 (2004).

[201] H.-W. Hammer and L. Platter, *Universal properties of the four-body system with large scattering length*, The European Physical Journal A **32**, 113 (2007).

[202] J. P. D'Incao, C. H. Greene and B. D. Esry, *The short-range three-body phase and other issues impacting the observation of Efimov physics in ultracold quantum gases*, Journal of Physics B: Atomic, Molecular and Optical Physics **42**, 044016 (2009).

[203] F. Ferlaino, S. Knoop, M. Berninger, W. Harm, J. P. D'Incao, H.-C. Nägerl and R. Grimm, *Evidence for Universal Four-Body States Tied to an Efimov Trimer*, Phys. Rev. Lett. **102**, 140401 (2009).

[204] F. Ferlaino, A. Zenesini, M. Berninger, B. Huang, H.-C. Nägerl and R. Grimm, *Efimov Resonances in Ultracold Quantum Gases*, Few-Body Systems **51**, 113 (2011).

[205] A. Zenesini, B. Huang, M. Berninger, S. Besler, H.-C. Nägerl, F. Ferlaino, R. Grimm, C. H. Greene and J. von Stecher, *Resonant Five-Body Recombination in an Ultracold Gas*, arXiv:1205.1921 (2012).

[206] M. T. Yamashita, L. Tomio, A. Delfino and T. Frederico, *Four-boson scale near a Feshbach resonance*, Europhysics Letters **75**, 555 (2006).

[207] G. J. Hanna and D. Blume, *Energetics and structural properties of three-dimensional bosonic clusters near threshold*, Phys. Rev. A **74**, 063604 (2006).

[208] L. Platter, *Low-Energy Universality in Atomic and Nuclear Physics*, Few-Body Systems **46**, 139 (2009).

[209] S. Floerchinger and C. Wetterich, *Functional renormalization for Bose-Einstein condensation*, Phys. Rev. A **77**, 053603 (2008).

[210] S. Floerchinger, *Functional renormalization and ultracold quantum gases*, Ph.D. thesis, Universität Heidelberg (2009).

[211] D. F. Litim, *Optimisation of the exact renormalisation group*, Physics Letters B **486**, 92 (2000).

[212] S. Diehl, H. Gies, J. M. Pawlowski and C. Wetterich, *Flow equations for the BCS-BEC crossover*, Phys. Rev. A **76**, 021602 (2007).

[213] S. Diehl, *The BCS – BEC Crossover in Ultracold Fermion Gases*, Ph.D. thesis, Universität Heidelberg (2006).

[214] S. Floerchinger, M. Scherer, S. Diehl and C. Wetterich, *Particle-hole fluctuations in BCS-BEC crossover*, Phys. Rev. B **78**, 174528 (2008).

[215] S. Diehl, S. Floerchinger, H. Gies, J. Pawlowkski and C. Wetterich, *Functional renormalization group approach to the BCS-BEC crossover*, Annalen der Physik **522**, 615 (2010).

[216] S. Floerchinger, M. M. Scherer and C. Wetterich, *Modified Fermi sphere, pairing gap, and critical temperature for the BCS-BEC crossover*, Phys. Rev. A **81**, 063619 (2010).

[217] S. Moroz, *Few-body Physics with Few-body physics with functional renormalization*, Ph.D. thesis, Universität Heidelberg (2011).

[218] E. Braaten and H.-W. Hammer, *Enhanced dimer relaxation in an atomic and molecular Bose-Einstein condensate*, Phys. Rev. A **70**, 042706 (2004).

[219] H. Gies and C. Wetterich, *Renormalization flow of bound states*, Phys. Rev. D **65**, 065001 (2002).

[220] S. Floerchinger and C. Wetterich, *Exact flow equation for composite operators*, Physics Letters B **680**, 371 (2009).

[221] A. Rapp, G. Zaránd, C. Honerkamp and W. Hofstetter, *Color Superfluidity and "Baryon" Formation in Ultracold Fermions*, Phys. Rev. Lett. **98**, 160405 (2007).

[222] A. Rapp, W. Hofstetter and G. Zaránd, *Trionic phase of ultracold fermions in an optical lattice: A variational study*, Phys. Rev. B **77**, 144520 (2008).

[223] F. Wilczek, *Quantum chromodynamics: Lifestyles of the small and simple*, Nature Physics **3**, 375 (2007).

[224] R. D. Amado and F. C. Greenwood, *There Is No Efimov Effect for Four or More Particles*, Phys. Rev. D **7**, 2517 (1973).

[225] S. K. Adhikari, T. Frederico and I. D. Goldman, *Perturbative Renormalization in Quantum Few-Body Problems*, Phys. Rev. Lett. **74**, 487 (1995).

[226] L. D. Landau, *Electron motion in crystal lattices*, Phys. Z. Sowjetunion **3**, 644 (1933).

[227] H. Fröhlich, *Electrons in lattice fields*, Advances in Physics **3**, 325 (1954).

[228] J. Kondo, *Resistance Minimum in Dilute Magnetic Alloys*, Progress of Theoretical Physics **32**, 37 (1964).

[229] K. G. Wilson, *The renormalization group: Critical phenomena and the Kondo problem*, Rev. Mod. Phys. **47**, 773 (1975).

[230] A. C. Hewson, *The Kondo Problem to Heavy Fermions* (Cambridge University Press, 1997).

[231] F. Chevy, *Universal phase diagram of a strongly interacting Fermi gas with unbalanced spin populations*, Phys. Rev. A **74**, 063628 (2006).

[232] C. Lobo, A. Recati, S. Giorgini and S. Stringari, *Normal State of a Polarized Fermi Gas at Unitarity*, Phys. Rev. Lett. **97**, 200403 (2006).

[233] R. Combescot, A. Recati, C. Lobo and F. Chevy, *Normal State of Highly Polarized Fermi Gases: Simple Many-Body Approaches*, Phys. Rev. Lett. **98**, 180402 (2007).

[234] R. Combescot and S. Giraud, *Normal State of Highly Polarized Fermi Gases: Full Many-Body Treatment*, Phys. Rev. Lett. **101**, 050404 (2008).

[235] K. B. Gubbels and H. T. C. Stoof, *Renormalization Group Theory for the Imbalanced Fermi Gas*, Phys. Rev. Lett. **100**, 140407 (2008).

[236] M. Punk, P. T. Dumitrescu and W. Zwerger, *Polaron-to-molecule transition in a strongly imbalanced Fermi gas*, Phys. Rev. A **80**, 053605 (2009).

[237] C. Mora and F. Chevy, *Ground state of a tightly bound composite dimer immersed in a Fermi sea*, Phys. Rev. A **80**, 033607 (2009).

[238] R. Combescot, S. Giraud and X. Leyronas, *Analytical theory of the dressed bound state in highly polarized Fermi gases*, Europhysics Letters **88**, 60007 (2009).

[239] M. Ku, J. Braun and A. Schwenk, *Finite-Size and Confinement Effects in Spin-Polarized Trapped Fermi Gases*, Phys. Rev. Lett. **102**, 255301 (2009).

[240] A. Schirotzek, C.-H. Wu, A. Sommer and M. W. Zwierlein, *Observation of Fermi Polarons in a Tunable Fermi Liquid of Ultracold Atoms*, Phys. Rev. Lett. **102**, 230402 (2009).

[241] G. M. Bruun and P. Massignan, *Decay of Polarons and Molecules in a Strongly Polarized Fermi Gas*, Phys. Rev. Lett. **105**, 020403 (2010).

[242] S. Pilati, G. Bertaina, S. Giorgini and M. Troyer, *Itinerant Ferromagnetism of a Repulsive Atomic Fermi Gas: A Quantum Monte Carlo Study*, Phys. Rev. Lett. **105**, 030405 (2010).

[243] X. Cui and H. Zhai, *Stability of a fully magnetized ferromagnetic state in repulsively interacting ultracold Fermi gases*, Phys. Rev. A **81**, 041602 (2010).

[244] A. Recati and S. Stringari, *Spin Fluctuations, Susceptibility, and the Dipole Oscillation of a Nearly Ferromagnetic Fermi Gas*, Phys. Rev. Lett. **106**, 080402 (2011).

[245] F. Chevy and C. Mora, *Ultra-cold polarized Fermi gases*, Reports on Progress in Physics **73**, 112401 (2010).

[246] H. K. Onnes, *The superconductivity of mercury*, Comm. Phys. Lab. Univ. Leiden **119**, 122 (1911).

[247] J. Bardeen, L. N. Cooper and J. R. Schrieffer, *Theory of Superconductivity*, Phys. Rev. **108**, 1175 (1957).

[248] L. N. Cooper, *Bound Electron Pairs in a Degenerate Fermi Gas*, Phys. Rev. **104**, 1189 (1956).

[249] L. P. Gorkov and T. K. Melik-Barkhudarov, *Contribution to the theory of superfluidity in an imperfect Fermi gas*, Sov. Phys. JETP **13**, 1018 (1961).

[250] A. M. Clogston, *Upper Limit for the Critical Field in Hard Superconductors*, Phys. Rev. Lett. **9**, 266 (1962).

[251] B. S. Chandrasekhar, *A note on the maximum critical field of high-field superconductors*, Appl. Phys. Lett. **1**, 7 (1962).

[252] P. F. Bedaque, H. Caldas and G. Rupak, *Phase Separation in Asymmetrical Fermion Superfluids*, Phys. Rev. Lett. **91**, 247002 (2003).

[253] Y.-i. Shin, C. H. Schunck, A. Schirotzek and W. Ketterle, *Phase diagram of a two-component Fermi gas with resonant interactions*, Nature **451**, 689 (2008).

[254] D. T. Son and M. A. Stephanov, *Phase diagram of a cold polarized Fermi gas*, Phys. Rev. A **74**, 013614 (2006).

[255] R. Haussmann, M. Punk and W. Zwerger, *Spectral functions and rf response of ultracold fermionic atoms*, Phys. Rev. A **80**, 063612 (2009).

[256] M. Punk, *Many particle physics with ultracold gases*, Ph.D. thesis, Technical University Munich (2009).

[257] S. Pilati and S. Giorgini, *Phase Separation in a Polarized Fermi Gas at Zero Temperature*, Phys. Rev. Lett. **100**, 030401 (2008).

[258] P. Massignan and G. Bruun, *Repulsive polarons and itinerant ferromagnetism in strongly polarized Fermi gases*, The European Physical Journal D **65**, 83 (2011).

[259] P. Nozieres and S. Schmitt-Rink, *Bose condensation in an attractive fermion gas: From weak to strong coupling superconductivity*, Journal of Low Temperature Physics **59**, 195 (1985).

[260] D. Lurié and A. J. Macfarlane, *Equivalence Between Four-Fermion and Yukawa Coupling, and the $Z_3 = 0$ Condition for Composite Bosons*, Phys. Rev. **136**, B816 (1964).

[261] Y. Nishida, *Casimir interaction among heavy fermions in the BCS-BEC crossover*, Phys. Rev. A **79**, 013629 (2009).

[262] A. Bulgac and S. Yoon, *Induced P-wave superfluidity within the full energy- and momentum-dependent Eliashberg approximation in asymmetric dilute Fermi gases*, Phys. Rev. A **79**, 053625 (2009).

[263] P. Pieri, A. Perali and G. C. Strinati, *Enhanced paraconductivity-like fluctuations in the radiofrequency spectra of ultracold Fermi atoms*, Nature Physics **5**, 736 (2009).

[264] R. Haussmann, *Self-consistent quantum-field theory and bosonization for strongly correlated electron systems*, Lecture Notes in Physics M **56** (1999).

[265] R. Haussmann and W. Zwerger, *Thermodynamics of a trapped unitary Fermi gas*, Phys. Rev. A **78**, 063602 (2008).

[266] F. Werner and Y. Castin, *General relations for quantum gases in two and three dimensions: Two-component fermions*, Phys. Rev. A **86**, 013626 (2012).

[267] F. Werner and Y. Castin, *General relations for quantum gases in two and three dimensions. II. Bosons and mixtures*, Phys. Rev. A **86**, 053633 (2012).

[268] M. Punk and W. Zwerger, *Theory of rf-Spectroscopy of Strongly Interacting Fermions*, Phys. Rev. Lett. **99**, 170404 (2007).

[269] A. A. Katanin, *Fulfillment of Ward identities in the functional renormalization group approach*, Phys. Rev. B **70**, 115109 (2004).

[270] R. Bishop, *On the ground state of an impurity in a dilute fermi gas*, Annals of Physics **78**, 391 (1973).

[271] Y. Nagaoka, *Ferromagnetism in a Narrow, Almost Half-Filled s Band*, Phys. Rev. **147**, 392 (1966).

[272] R. Shankar, *Renormalization-group approach to interacting fermions*, Rev. Mod. Phys. **66**, 129 (1994).

[273] S. Weinberg, *Evidence That the Deuteron Is Not an Elementary Particle*, Phys. Rev. **137**, B672 (1965).

[274] G. B. Partridge, K. E. Strecker, R. I. Kamar, M. W. Jack and R. G. Hulet, *Molecular Probe of Pairing in the BEC-BCS Crossover*, Phys. Rev. Lett. **95**, 020404 (2005).

[275] M. Bartenstein, A. Altmeyer, S. Riedl, R. Geursen, S. Jochim, C. Chin, J. H. Denschlag, R. Grimm, A. Simoni, E. Tiesinga, C. J. Williams and P. S. Julienne, *Precise Determination of* ^{6}Li *Cold Collision Parameters by Radio-Frequency Spectroscopy on Weakly Bound Molecules*, Phys. Rev. Lett. **94**, 103201 (2005).

[276] T. Enss and R. Haussmann, *Quantum Mechanical Limitations to Spin Diffusion in the Unitary Fermi Gas*, Phys. Rev. Lett. **109**, 195303 (2012).

[277] C. Honerkamp, H. C. Fu and D.-H. Lee, *Phonons and d-wave pairing in the two-dimensional Hubbard model*, Phys. Rev. B **75**, 014503 (2007).

[278] J.-P. Blaizot, R. Mandez-Galain and N. Wschebor, *A new method to solve the non-perturbative renormalization group equations*, Physics Letters B **632**, 571 (2006).

[279] D. Vollhardt and P. Wölfle, *The superfluid phases of helium 3* (CRC, 1990).

[280] S.-S. Lee, *Non-Fermi liquid from a charged black hole: A critical Fermi ball*, Phys. Rev. D **79**, 086006 (2009).

[281] J. Maldacena, *The Large-N Limit of Superconformal Field Theories and Supergravity*, International Journal of Theoretical Physics **38**, 1113 (1999).

[282] H. Liu, J. McGreevy and D. Vegh, *Non-Fermi liquids from holography*, Phys. Rev. D **83**, 065029 (2011).

[283] S. Sachdev and B. Keimer, *Quantum criticality*, Physics Today **64**, 29 (2011).

[284] N. V. Prokof'ev and B. V. Svistunov, *Polaron Problem by Diagrammatic Quantum Monte Carlo*, Phys. Rev. Lett. **81**, 2514 (1998).

[285] D. Fay and J. Appel, *Coexistence of p-state superconductivity and itinerant ferromagnetism*, Phys. Rev. B **22**, 3173 (1980).

[286] Y. Zhang, W. Ong, I. Arakelyan and J. E. Thomas, *Polaron-to-Polaron Transitions in the Radio-Frequency Spectrum of a Quasi-Two-Dimensional Fermi Gas*, Phys. Rev. Lett. **108**, 235302 (2012).

[287] P. W. Anderson, *Infrared Catastrophe in Fermi Gases with Local Scattering Potentials*, Phys. Rev. Lett. **18**, 1049 (1967).

[288] T. Mitra, A. Chatterjee and S. Mukhopadhyay, *Polarons*, Physics Reports **153**, 91 (1987).

[289] J. T. Devreese and A. S. Alexandrov, *Fröhlich polaron and bipolaron: recent developments*, Reports on Progress in Physics **72**, 066501 (2009).

[290] L. Radzihovsky and D. E. Sheehy, *Imbalanced Feshbach-resonant Fermi gases*, Reports on Progress in Physics **73**, 076501 (2010).

[291] F. Schmitt, P. S. Kirchmann, U. Bovensiepen, R. G. Moore, L. Rettig, M. Krenz, J.-H. Chu, N. Ru, L. Perfetti, D. H. Lu, M. Wolf, I. R. Fisher and Z.-X. Shen, *Transient Electronic Structure and Melting of a Charge Density Wave in TbTe3*, Science **321**, 1649 (2008).

[292] J. K. Freericks, H. R. Krishnamurthy and T. Pruschke, *Theoretical Description of Time-Resolved Photoemission Spectroscopy: Application to Pump-Probe Experiments*, Phys. Rev. Lett. **102**, 136401 (2009).

[293] S. Nascimbène, N. Navon, K. J. Jiang, L. Tarruell, M. Teichmann, J. McKeever, F. Chevy and C. Salomon, *Collective Oscillations of an Imbalanced Fermi Gas: Axial Compression Modes and Polaron Effective Mass*, Phys. Rev. Lett. **103**, 170402 (2009).

[294] P. Dyke, E. D. Kuhnle, S. Whitlock, H. Hu, M. Mark, S. Hoinka, M. Lingham, P. Hannaford and C. J. Vale, *Crossover from 2D to 3D in a Weakly Interacting Fermi Gas*, Phys. Rev. Lett. **106**, 105304 (2011).

[295] J. T. Stewart, J. P. Gaebler and D. S. Jin, *Using photoemission spectroscopy to probe a strongly interacting Fermi gas*, Nature **454**, 744 (2008).

[296] M. Feld, B. Frohlich, E. Vogt, M. Koschorreck and M. Kohl, *Observation of a pairing pseudogap in a two-dimensional Fermi gas*, Nature **480**, 75 (2011).

[297] S. Zöllner, G. M. Bruun and C. J. Pethick, *Polarons and molecules in a two-dimensional Fermi gas*, Phys. Rev. A **83**, 021603 (2011).

[298] M. M. Parish, *Polaron-molecule transitions in a two-dimensional Fermi gas*, Phys. Rev. A **83**, 051603 (2011).

[299] M. Klawunn and A. Recati, *Fermi polaron in two dimensions: Importance of the two-body bound state*, Phys. Rev. A **84**, 033607 (2011).

[300] M. Randeria, J.-M. Duan and L.-Y. Shieh, *Bound states, Cooper pairing, and Bose condensation in two dimensions*, Phys. Rev. Lett. **62**, 981 (1989).

[301] D. S. Petrov and G. V. Shlyapnikov, *Interatomic collisions in a tightly confined Bose gas*, Phys. Rev. A **64**, 012706 (2001).

[302] J. R. Engelbrecht and M. Randeria, *New collective mode and corrections to Fermi-liquid theory in two dimensions*, Phys. Rev. Lett. **65**, 1032 (1990).

[303] J. R. Engelbrecht and M. Randeria, *Low-density repulsive Fermi gas in two dimensions: Bound-pair excitations and Fermi-liquid behavior*, Phys. Rev. B **45**, 12419 (1992).

[304] P. Bloom, *Two-dimensional Fermi gas*, Phys. Rev. B **12**, 125 (1975).

[305] D. S. Petrov, M. Holzmann and G. V. Shlyapnikov, *Bose-Einstein Condensation in Quasi-2D Trapped Gases*, Phys. Rev. Lett. **84**, 2551 (2000).

[306] N. Strohmaier, D. Greif, R. Jördens, L. Tarruell, H. Moritz, T. Esslinger, R. Sensarma, D. Pekker, E. Altman and E. Demler, *Observation of Elastic Doublon Decay in the Fermi-Hubbard Model*, Phys. Rev. Lett. **104**, 080401 (2010).

[307] C. Trefzger and Y. Castin, *Impurity in a Fermi sea on a narrow Feshbach resonance: A variational study of the polaronic and dimeronic branches*, Phys. Rev. A **85**, 053612 (2012).

[308] P. Massignan, *Polarons and dressed molecules near narrow Feshbach resonances*, Europhysics Letters **98**, 10012 (2012).

[309] P. Fulde and R. A. Ferrell, *Superconductivity in a Strong Spin-Exchange Field*, Phys. Rev. **135**, A550 (1964).

[310] A. Larkin and Y. N. Ovchinnikov, *Nonuniform state of superconductors*, Zh. Eksperim. i Teor. Fiz. **47** (1964).

[311] W. Greiner and J. Reinhardt, *Field quantization* (Springer Verlag, 1996).

[312] A. Zee, *Quantum field theory in a nutshell* (Princeton University Press, 2010).

[313] C. J. Pethick and H. Smith, *Bose-Einstein condensation in dilute gases* (Cambridge University Press, 2001).

[314] N. D. Mermin and H. Wagner, *Absence of Ferromagnetism or Antiferromagnetism in One- or Two-Dimensional Isotropic Heisenberg Models*, Phys. Rev. Lett. **17**, 1133 (1966).

[315] P. C. Hohenberg, *Existence of Long-Range Order in One and Two Dimensions*, Phys. Rev. **158**, 383 (1967).

[316] J. M. Kosterlitz and D. J. Thouless, *Ordering, metastability and phase transitions in two-dimensional systems*, Journal of Physics C: Solid State Physics **6**, 1181 (1973).

[317] I. N. Bronstein, K. A. Semendjajew, G. Musiol and H. Mühlig, *Taschenbuch der Mathematik* (Harri Deutsch, 2001).

Acknowledgements

First of all I want to thank Wilhelm Zwerger for giving me the opportunity to work in his group, for his great and continuous support, and for sharing his ideas and deep understanding of physics with me. He not only had always an open door for long, most enlightening and inspiring discussions, but also supported me in pursuing questions of my own choice for which I am very grateful. Also I would like to thank him for his generous financial support for going to many conferences, workshops and schools, many of which he pointed out to me. I thank Walter Metzner for co-examining the thesis.

In particular I thank Tilman Enss, Sergej Moroz, and Steffen Patrick Rath for the many hours of discussions, and the continuous, good and productive collaboration.

I thank Marcus Barth and Francesco Piazza for insightful discussions and all members of T34 for the great atmosphere in our group.

I acknowledge valuable discussions with Eugene Demler, Rudi Grimm, Selim Jochim, Jan Pawlowski, Ville Pietilä, Lode Pollet, Matthias Punk, Christof Wetterich, and Matteo Zaccanti.

I thank Daniela Neufang for the administrative as well as Stefan Recksiegel for the IT support.

Most importantly I want to thank my parents Margarete and Hartwig for always being there.

Finally I want to thank Sarah for all the support she has been and is giving me. Without you this would not have been possible.